Frontiers of Nanoscience
Series Editor: Richard E. Palmer

Nanostructured Materials

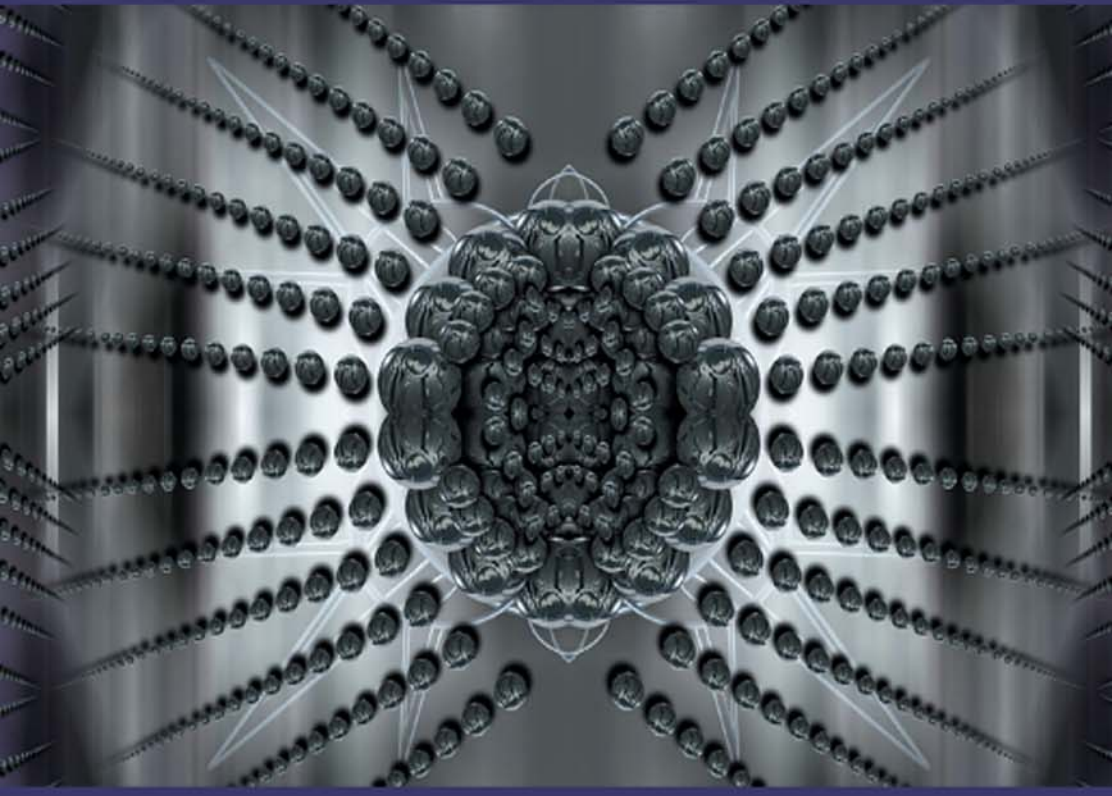

Edited by
Gerhard Wilde

Nanostructured Materials

FRONTIERS OF NANOSCIENCE

Series Editor: Richard E. Plamer
The Nanoscale Physics Research Laboratory,
The School of Physics and Astronomy,
The University of Birmingham, UK

Vol. 1 **Nanostructured Materials** edited by
Gerhard Wilde

Nanostructured Materials

Edited by

Gerhard Wilde
Forschungzentrum Karlsruhe,
Institute of Nanotechnology,
Karlsruhe, Germany

ELSEVIER

Amsterdam • Boston • Heidelberg • London • New York • Oxford
Paris • San Diego • San Franciso • Singapore • Sydney • Tokyo

Elsevier
The Boulevard, Langford Lane, Kidlington, Oxford OX5 1GB, UK
Radarweg 29, PO Box 211, 1000 AE Amsterdam, the Netherlands

First edition 2009

Copyright © 2009, Elsevier Ltd. All rights reserved

No part of this publication may be reproduced, stored in a retrieval system or transmitted in any form or by any means electronic, mechanical, photocopying, recording or otherwise without the prior written permission of the publisher

Permissions may be sought directly from Elsevier's Science & Technology Rights Department in Oxford, UK: phone (+44) (0) 1865 843830; fax (+44) (0) 1865 853333; email: permissions@elsevier.com. Alternatively you can submit your request online by visiting the Elsevier web site at http://elsevier.com/locate/permissions, and selecting *Obtaining permission to use Elsevier material*

Notice
No responsibility is assumed by the publisher for any injury and/or damage to persons or property as a matter of products liability, negligence or otherwise, or from any use or operation of any methods, products, instructions or ideas contained in the material herein. Because of rapid advances in the medical sciences, in particular, independent verification of diagnoses and drug dosages should be made

British Library Cataloguing in Publication Data
A catalogue record for this book is available from the British Library

Library of Congress Cataloging-in-Publication Data
A catalog record for this book is available from the Library of Congress

ISSN: 1876-2778

ISBN: 978-0-08-044965-4

For information on all Elsevier publications
visit our web site at books.elsevier.com

Printed and bound in Great Britain

09 10 10 9 8 7 6 5 4 3 2 1

Working together to grow
libraries in developing countries

www.elsevier.com | www.bookaid.org | www.sabre.org

ELSEVIER BOOK AID International Sabre Foundation

CONTENTS

List of Contributors **vii**

1. Functional Nanostructured Materials – Microstructure, Thermodynamic Stability and Atomic Mobility **1**
S. Divinski, H. Rösner and G. Wilde

2. Reliability of Nanostructured Materials **51**
K.A. Padmanabhan and S. Balasivanandha Prabu

3. Mechanical Properties of Nanocomposite Materials **127**
A.V. Sergueeva, D.M. Hulbert, N.A. Mara and A.K. Mukherjee

4. Nanostructured Supported Catalysts for Low-Temperature Fuel Cells **173**
Suk Bon Yoon, Baizeng Fang, Minsik Kim, Jung Ho Kim and Jong-Sung Yu

5. Nanocrystalline Solar Cells **232**
Gary Hodes and Arieh Zaban

6. Nanoscale Materials for Hydrogen and Energy Storage **270**
Maximilian Fichtner

7. Materials with Structural Hierarchy and their Optical Applications **298**
Chantal Paquet, Andrew Paton and Eugenia Kumacheva

8. Interfacial Assembly of Nanoparticles into Higher-order Patterned Structures **326**
Xiaodong Chen and Lifeng Chi

Index **367**

This page intentionally left blank

CONTRIBUTORS

Xiaodong Chen
Physikalisches Institut and Center for Nanotechnology (CeNTech), Westfälische Wilhelms-Universität, 48149 Münster, Germany

Lifeng Chi
Physikalisches Institut and Center for Nanotechnology (CeNTech), Westfälische Wilhelms-Universität, 48149 Münster, Germany

S. Divinski
Institute of Materials Physics, University of Münster, Wilhelm-Klemm-Str. 10, 48149 Münster, Germany

Baizeng Fang
Department of Chemistry, Hannam Univerisity, Daejeon, 306-791, Korea

Maximilian Fichtner
Forschungszentrum Karlsruhe, Institute for Nanotechnology, PO Box 3640, D-76021 Karlsruhe, Germany

Gary Hodes
Department of Materials and Interfaces, Weizmann Institute of Science, Rehovot 76100, Israel

D.M. Hulbert
Chemical Engineering & Materials Science Department, University of California, One Shields Avenue, Davis, CA 95616, USA

Jung Ho Kim
Department of Chemistry, Hannam Univerisity, Daejeon, 306-791, Korea

Minsik Kim
Department of Chemistry, Hannam Univerisity, Daejeon, 306-791, Korea

Eugenia Kumacheva
Department of Chemistry, University of Toronto, Toronto, Ontario M5S 3H6, Canada

N.A. Mara
Chemical Engineering & Materials Science Department, University of California, One Shields Avenue, Davis, CA 95616, USA

A.K. Mukherjee
Chemical Engineering & Materials Science Department, University of California, One Shields Avenue, Davis, CA 95616, USA

K.A. Padmanabhan
Materials Science and Engineering Division, Department of Mechanical Engineering, Anna University, Chennai-600 025, India

Chantal Paquet
Department of Chemistry, University of Toronto, Toronto, Ontario M5S 3H6, Canada

Andrew Paton
Department of Chemistry, University of Toronto, Toronto, Ontario M5S 3H6, Canada

S. Balasivanandha Prabu
Materials Science and Engineering Division, Department of Mechanical Engineering, Anna University, Chennai-600 025, India

H. Rösner
Institute of Materials Physics, University of Münster, Wilhelm-Klemm-Str. 10, 48149 Münster, Germany

A.V. Sergueeva
Chemical Engineering & Materials Science Department, University of California, One Shields Avenue, Davis, CA 95616, USA

G. Wilde
Institute of Materials Physics, University of Münster, Wilhelm-Klemm-Str. 10, 48149 Münster, Germany

Suk Bon Yoon
Department of Chemistry, Hannam Univerisity, Daejeon, 306-791, Korea

Jong-Sung Yu
Department of Chemistry, Hannam Univerisity, Daejeon, 306-791, Korea

Arieh Zaban
Department of Chemistry, Bar Ilan University, Ramat Gan, 52900, Israel

CHAPTER 1

Functional Nanostructured Materials – Microstructure, Thermodynamic Stability and Atomic Mobility

S. Divinski, H. Rösner and G. Wilde

SCOPE OF THE BOOK

One way to distinguish nanostructured materials is based on their dimensionality, i.e. according to the number of spatial dimensions in which the materials are ***not*** nanoscaled. In recent years, much attention has been devoted to zero-, one- and two-dimensional nanostructures, e.g. nanoparticles (0-D), nanotubes and nanowires (1-D) or thin films and multilayer systems (2-D) with a fair number of overview and review volumes published in these areas. However, hierarchical structures as analysed in Chapter 7 or porous nanocrystalline films (Chapter 5) do not fit well into such a classification scheme, since the respective functional property depends sensitively on both the size confinement and interface contributions due to the nanoscale building blocks and also on the structure and structuring on the micrometre level. It is believed that both dependencies are crucial and necessarily need to be regarded for any functional nanosystem that should be transferred into a device application. Thus, this book focuses on functional aspects of nanostructured materials that have a high relevance to immediate applications, such as catalysis (Chapter 4), energy harvesting (Chapter 5), energy storage (Chapter 6), optical properties (Chapter 7) and surface functionalization via self-assembly (Chapter 8). Additionally, Chapters 1–3 are devoted to massive nanostructured materials and composites and deal with basic properties and requirements of this new class of engineering materials. In particular the issues concerning stability and reliability and those concerning mechanical performance are mandatory aspects that need to be regarded carefully for any nanostructured engineering material.

Institute of Materials Physics, University of Münster, Wilhelm-Klemm-Str. 10, 48149 Münster, Germany

Nanostructured Materials © 2009 Elsevier Ltd.
978-0-08-044965-4 All rights reserved.

1. INTRODUCTION

The technological progress of recent decades has mostly been driven by the scientific and technological developments in the area of information technology. The ever-faster progress is to a large extent a result of achieving and controlling smaller and smaller feature sizes of the functional and structural components, thus allowing for higher integration densities, higher speed or lower energy consumption and lower costs. At the same time, the term 'nanotechnology' has found its way to the funding organizations and, in recent years, also to the media, thus reaching the general public. In many cases, the research trends in the nanosciences and in nanotechnology have been mapped directly onto expectations and projections from the information technology sphere, for example the famous Moore's 'law', since the developments proceeded roughly at the same time and since many aspects concerning the progress in information technology are directly related to, or are rather dependent on, the advances made in nanotechnological research.

However, if nanotechnology as a whole is addressed, then a broader range of scientific aspects needs to be considered, with additional research areas such as nanoparticle research that have already entered everyday life, e.g. nanosized particulates for scratch protection on eye glasses, for UV light absorption in sun protection lotions or for viscosity adjustment and wear minimization in the rubber of car tyres. With these applications, it is the reduced size alone that serves the purpose. Yet, there are vast areas of research on nanoscale systems that have just begun to surface, with prominent examples such as an atomic-scale electrical switch [1], inorganic/organic composite structures for bio-mimicked structural applications [2], nano-biological transporter systems for targeted drug delivery [3] or the bio-functionalization of surfaces for advancing new nano-lithography techniques [4], to mention just a few. With most of the future applications that are in the background of today's basic research, not only the functional units need to be nanosized; but also the material used for interfacing the micro- or even the macro-world to the nanosized systems such as substrates, supports or leads will have to be structured on the nanoscale. Thus, the respective material property or the combination of properties that makes the material suitable and desirable for the specific application needs to be analysed in terms of the specific size dependence [5].

Properties of materials are often modified for spatially confined or finite-size systems [5,6]. Depending on the type of property, this behaviour is explained by the crossing of length scales when characteristic interaction lengths or wavelengths become comparable with the system size. This type of argument is usually invoked for explaining the well-known size dependence of electronic properties, e.g. optical or magnetic properties, of nanostructured materials. In these cases, the size of the nanoscale structural unit (the nanoparticle or the nanocrystalline grain) becomes equal to or smaller than a characteristic correlation length. Concerning, e.g., ferromagnetism, the ferromagnetic correlation length $L_0 = \sqrt{A/K_1}$, with the exchange interaction constant, A, and the local magnetocrystalline anisotropy, K_1 [7] becomes comparable with or even smaller than the

average diameter of the particles or grains if size effects become significant. Within this volume, Chapter 7 on optical applications of nanomaterials with hierarchical structures by E. Kumacheva et al., Chapter 5 on porous nanocrystalline films for advanced solar cells by G. Hodes and A. Zaban and Chapter 8 on interfacial self-assembly by L. Chi and X. Chen are strongly concerned with this first type of finite-size effect. A second type of argument concerning the size dependence of properties is related to the presence of interfaces or, more specifically, the presence of a large fraction of the atoms of the system at or near a surface or an internal interface. In addition, and as will be shown here, the atomistic details of these interfaces matter[6].

Traditionally, the impact of the internal or external interfaces has been implemented into the description of interface-controlled property modifications by describing the interface and the core of the particles or grains as two separate phases with intrinsically different properties. One aspect of such 'two-phase' models considers that the atoms situated at or near such an interface are energetically in a different state compared with the atoms in the core of the crystallite or the nanoparticle. Transport properties or parameters that describe the gas–solid interactions, e.g. in the context of hydrogen storage in interstitial sites [8], are current examples for property modifications that are discussed by two-phase descriptions. Similar approaches also apply for describing reversible phase transformations between thermodynamically stable phases, which are often modified for spatially confined or finite-size systems [9]. Within this volume, specifically, Chapter 4 on catalysis and fuel cells by J.-S. Yu et al., Chapter 6 on energy storage by M. Fichtner, Chapter 3 on the mechanical properties of nanocomposites by A. Mukherjee et al. and Chapter 2 on stability and reliability issues of nanomaterials by K.A. Padmanabhan and S. Balasivanandha Prabu are addressing topics within this area of interface controlled properties.

2. NANOSTRUCTURED AND NANOCRYSTALLINE MATERIALS

In addition to materials that are to be structured by means that control the shape and feature size on the nanometre scale, an entire range of promising property modifications, such as mechanical or magnetic properties of *nanocrystalline materials* [5], generate the desire to synthesize and stabilize *massive nanocrystalline materials*, i.e. polycrystalline materials with bulk shape consisting of a dense array of crystallites in the size range well below 100 nm. It was Herbert Gleiter who proposed at the Risø conference in 1981 the basic idea of such a new class of materials in which 50% or more of the atoms are situated at grain boundaries. In distinction to nanostructured materials, the details of the nanocrystal assembly concerning the position and orientation of individual nanocrystals are not controlled, but irreversible processes and non-equilibrium processing steps generate an ensemble of nanosized crystals with properties that are defined for the average of the thermodynamic ensemble. Yet, however different nanostructured and nanocrystalline materials are, with respect to the respective synthesis routes, two issues need to be addressed for both situations that are crucial for any

application: first, the size dependence of the properties must be understood for any meaningful materials design or property prediction. Secondly, the material needs to be stabilized against detrimental coarsening such that the nanoscaled microstructure is at least kinetically stabilized. This is a basic precondition for obtaining properties that are independent of time within the lifetime of the respective product or device application. In view of the similar requirements concerning the materials aspects for both nanostructured and nanocrystalline materials, both types of material are considered interchangeably in the following.

3. BULK NANOCRYSTALLINE MATERIALS

Nanostructured materials and composites can be produced by a variety of different methods. Besides the fabrication of clusters, thin films and coatings from the gas or liquid phase, chemical methods such as sol–gel processes and electrodeposition are common methods of processing. As a versatile alternative, however, mechanical methods have been developed which allow fabricating nanostructured or nanocrystalline materials in large quantities with a broad range of chemical compositions and atomic structures and even in bulk shape. These methods, which are schematically shown in Figure 1.1, can be applied to powder samples, to thin foils and to the surface of bulk samples and are characterized by the application of extremely large plastic strain levels.

While some of the methods such as equal channel angular pressing [10] mostly yield material with submicron grain sizes in the range of a few hundred nanometers – so-called *ultrafine grained material* – and other methods such as high pressure torsion straining [11] are inherently limited to small amounts of material, some techniques, such as repeated cold-rolling [12,13], have been shown to allow the production of bulk quantities of truly nanocrystalline material. In fact,

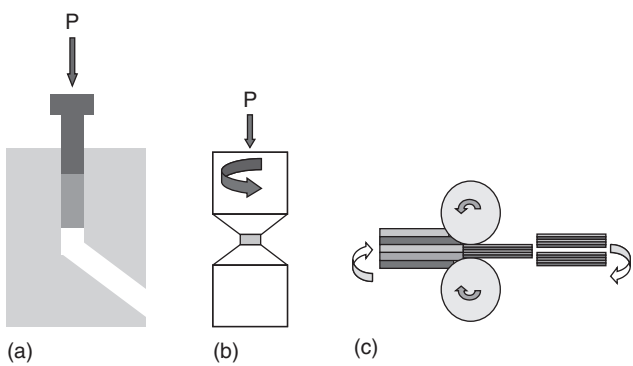

FIGURE 1.1 Schematic representation of three important methods for performing severe plastic deformation. (a) Equal channel angular pressing (ECAP), where a massive cylindrical sample is pressed repeatedly through a knee; (b) high pressure torsion (HPT) straining, where a disc-shaped specimen is torsion strained under very high pressure; and (c) repeated cold-rolling (RCR) with intermediate folding, where sheet metal is repeatedly rolled and folded.

one recent example showed that massive samples of pure Ni with an average grain size as small as 10 nm diameter could be obtained by repeated cold-rolling (Figure 1.2a) [13]. Yet, although important with respect to the exceptional mechanical properties of these materials [14], synthesizing kinetically stabilized two-phase composite nanostructures by plastic deformation processing does not seem

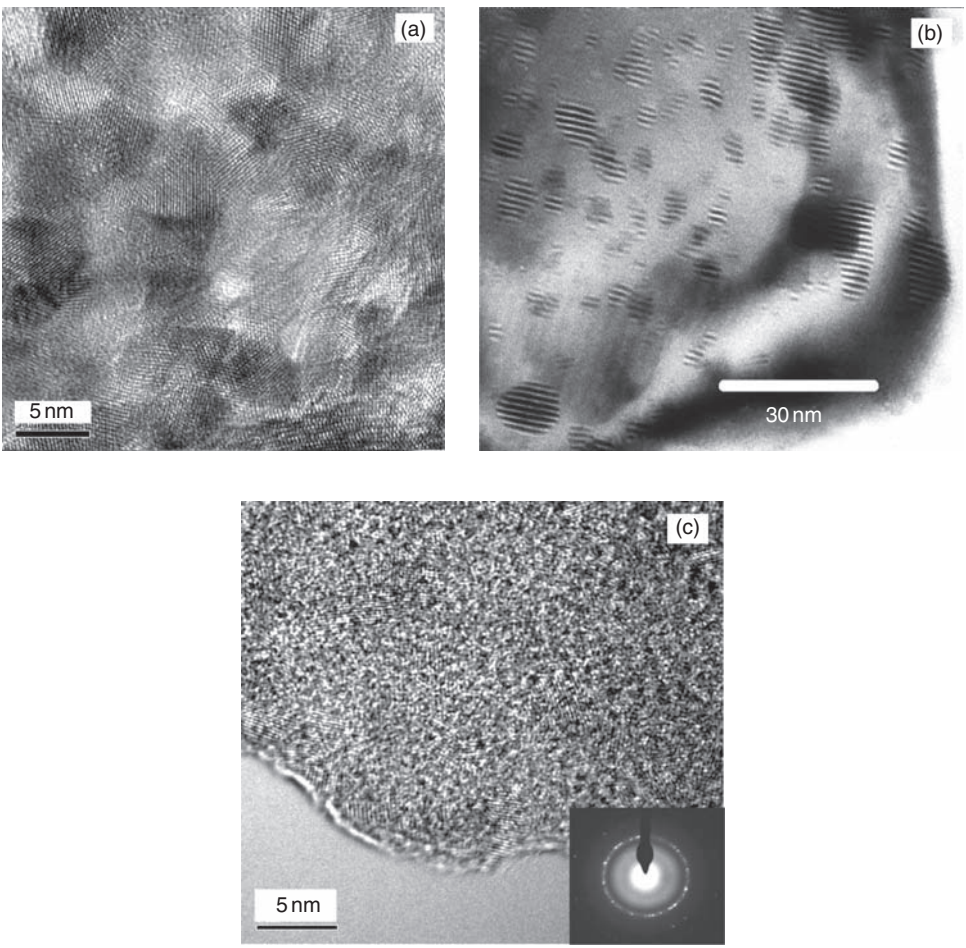

FIGURE 1.2 Bulk nanocrystalline materials synthesized by severe plastic deformation treatments. (a) Nanocrystalline Ni with an average grain size of 10 nm diameter synthesized by repeated cold-rolling. (b) Immiscible Al–Pb nanocomposite obtained by ball milling. (c) Ni–Ti nanocomposite obtained by repeated cold-rolling. The average grain size amounts to only 3–4 nm. Yet, alloying or phase formation during plastic deformation is not observed. The inset of (c) shows a selected area electron diffraction pattern of the Ni–Ti specimen. The broad intensity distribution near the centre indicates the presence either of an amorphous phase or of crystallites with grain sizes in the range of a few nanometres.

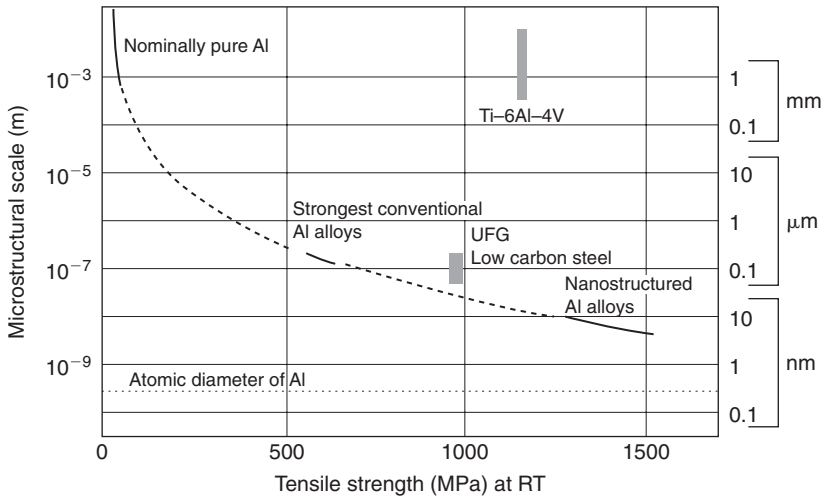

FIGURE 1.3 Relationship between the characteristic scale of the microstructure and the tensile strength at room temperature for Al-based alloys. Strength values for a Ti alloy and for an ultrafine grained (UFG) steel are shown for comparison. The results indicate the enormous benefits that can be entailed with nanostructuring. They also indicate the importance of retaining the size of the microstructure on the nanoscale.

to be straightforward, although nanocomposites of two immiscible components [15] or of two components that require large activation energies for mixing [16] have been obtained, as indicated in Figure 1.2b,c.

An alternative non-equilibrium synthesis route utilizes an initial rapid quenching step for synthesizing a vitreous precursor structure that forms parent phase and matrix for creating *in-situ* nanocomposites within a bulk material, which avoids issues related to contamination and powder compaction. For so-called marginal glass formers – a class of alloys based on Al, Mg or Fe that show the formation of extremely large number densities of primary-phase nanocrystals [17,18] – the unusually high nanocrystal number densities offer improved performance in magnetic and structural applications and exceptional property combinations. Fe-based alloys that transform via a similar mechanism are already applied as nanostructured soft or hard material depending on the specific alloy chemistry, with extremely low or high coercivity values at high saturation magnetization [19,20]. Al-based systems show a combination of high tensile strength of up to 1500 MPa, a high hardness and a low mass density of about 3 g/cm^3 as long as the microstructure scale is of the order of 10 nm or below (Figure 1.3, after [21]).

In addition, the composite nanostructure is self-stabilizing due to overlapping diffusion fields surrounding the nanocrystals [22,23]. Thus, the key strategy in enhancing the nanocrystal number density, and thus to improve both property performance *and* microstructure stability, is to promote the nucleation density of nanocrystals while minimizing the change of the amorphous matrix phase. One new opportunity for enhancing the number density of nanocrystals is presented

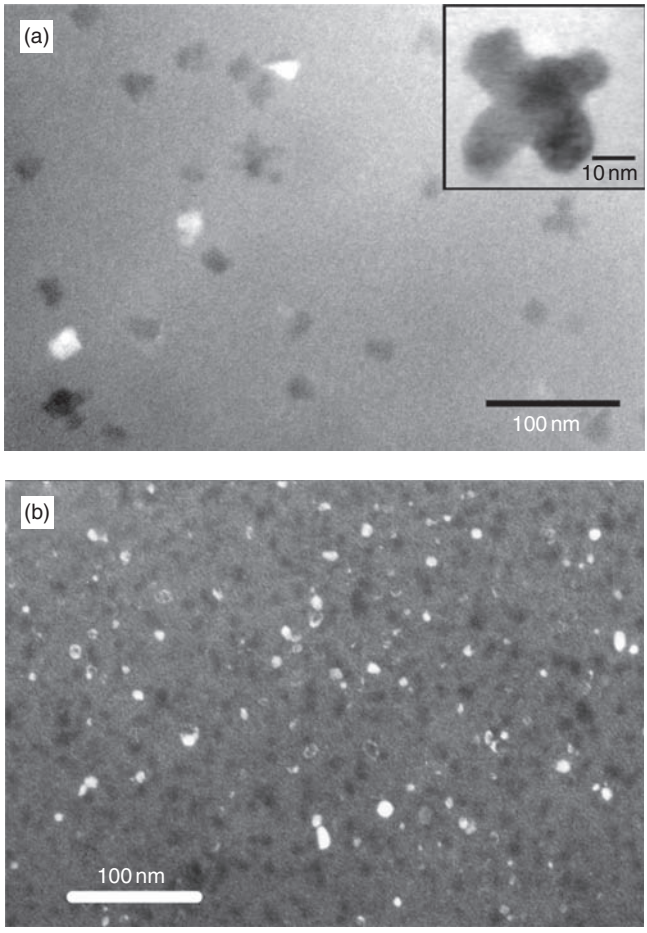

FIGURE 1.4 $Al_{88}Y_7Fe_5$ *in-situ* composites consisting of almost pure fcc-Al nanocrystals embedded in a residual amorphous matrix. Nanocrystallization can be induced by thermal annealing (a) or with a much higher number density by plastic deformation (b). The inset of (a) shows a dendritic nanocrystal at higher magnification.

by severe plastic deformation of rapidly quenched marginally glass-forming alloys [24,25]. In addition to nanostructure formation, the deformation treatment serves as a consolidation step, which is important for producing bulk shapes. Figure 1.4 shows representative examples of partially nanocrystallized $Al_{88}Y_7Fe_5$ samples after (a) thermally induced and (b) deformation-induced nanocrystallization. The comparison indicates clearly the enhanced nanocrystal number density that can be obtained by combining different non-equilibrium processing pathways sequentially. These initial results together with results from combining different plastic deformation treatments indicate an entire range of advanced processing routes for obtaining bulk nanostructured materials or bulk nanocomposites that yet waits to be explored.

4. MICROSTRUCTURE OF NANOCRYSTALLINE MATERIALS

Nanocrystalline materials are single- or multiphase polycrystals with typical grain diameter significantly less than 100 nm. Owing to decreasing dimensions, the fraction of surface atoms located at grain boundaries or interfaces increases for nanocrystalline materials. A simple geometrical estimation, where the grains are assumed as spheres or cubes, yields for the volume fraction of the interfaces the following values: 50% for 5 nm grains, 30% for 10 nm grains and about 3% for 100 nm grains [26]. In fact, many properties of nanocrystalline samples (as for instance strength/hardness ductility, elastic moduli, diffusivity, specific heat, thermal expansion coefficient or soft magnetic properties) are found to be fundamentally different compared with their conventional coarse-grained counterparts. In order to predict these unique properties, it is essential to understand how the structures vary with decreasing crystallite sizes, since for all these new superior properties the grain size is the dominant structural parameter governing a material's properties. Therefore, microstructural investigations are essential to elucidate the underlying mechanisms.

An appropriate way to investigate the microstructures of nanocrystalline materials is to image them in a transmission electron microscope (TEM). In the following, the advantages and disadvantages of TEM as an appropriate tool for the characterization of nanocrystalline materials are described.

4.1 Transmission Electron Microscopy (TEM) – Conventional TEM

Conventional TEM is based on amplitude or scattering contrast owing to the fact that the electron beam is scattered in crystalline material. Two modes are usually used for imaging: bright-field (BF) where deflected electrons are blocked away from the optical axis of the microscope by placing the objective aperture to allow the unscattered electrons only to pass through, and dark-field (DF) using diffracted electrons to form the image. Both imaging modes are illustrated by Figures 1.5 and 1.6.

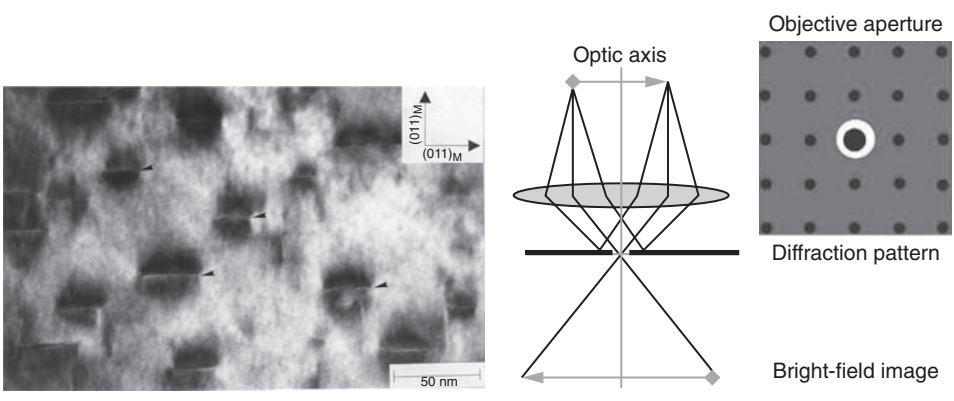

FIGURE 1.5 Left: bright-field image displaying coffee bean contrast due to misfit strains around plate-like precipitates in $Ti_{50}Ni_{25}Cu_{25}$ (taken from reference [27]). Right: schematic sketch showing the principle of bright-field imaging.

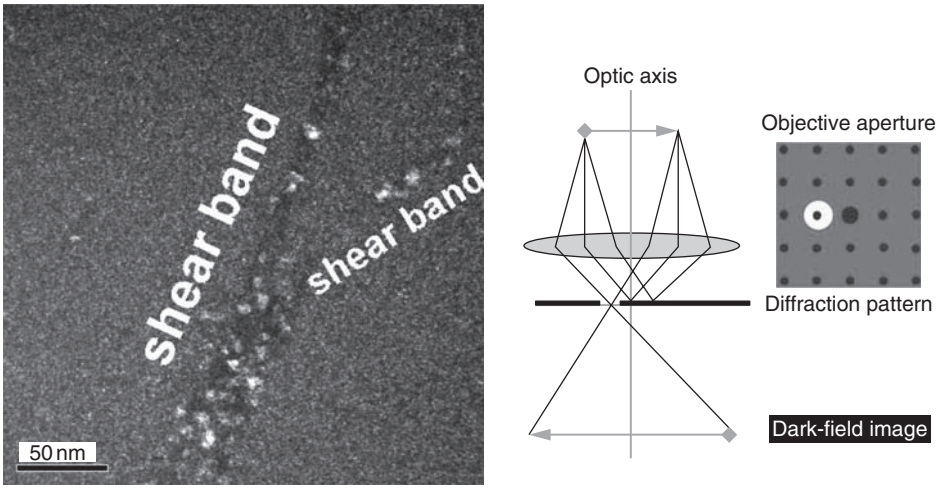

FIGURE 1.6 Left: dark-field image displaying shear bands with nanocrystals (taken from reference [28]). Right: schematic sketch showing the principle of dark-field imaging.

In particular, hollow-cone DF imaging is a rather useful technique for nanocrystalline materials where the tilted beam is rotating over the whole diffraction ring in order to image all grains meeting the Bragg condition. Furthermore, diffraction patterns, which yield information from the k-space, can be obtained simultaneously by selected area electron diffraction (SAED). These techniques are sufficient with respect to panoramic views and statistical analysis of grain size distribution. Due to the small grain sizes of nanocrystalline materials, it is difficult to image dislocations or other defects by conventional TEM since the dislocation contrast is based on its strain field which overlaps with the usual strain contrast of the nanometre-sized grains. Accordingly, and due to the fact that interfaces are dominating the material's behaviour, there is a need for investigations with better resolution to elucidate the operating processes in more detail.

4.2 Transmission Electron Microscopy (TEM) – High-Resolution TEM

High-resolution TEM is a technique developed since the 1970s to image the atomic structure of materials. A decade ago, the technique was restricted to a few research laboratories with highly specialized equipment and staff. Due to the continued development of TEMs, especially the introduction of digital controllers and the improvement of microscope stability, state-of-the-art microscopes with a resolution of 0.2 nm and below are commercially available. High-resolution TEM uses the phase contrast, which is based on the coherent interference of many electron beams, to show lattice fringes and atomic structures. Figure 1.7 shows the principle of high-resolution imaging.

The contrast arises from the difference in the phase of the electron waves scattered through a thin specimen. Phase contrast images are in most cases difficult to interpret because they are very sensitive to many factors such as thickness, orientation,

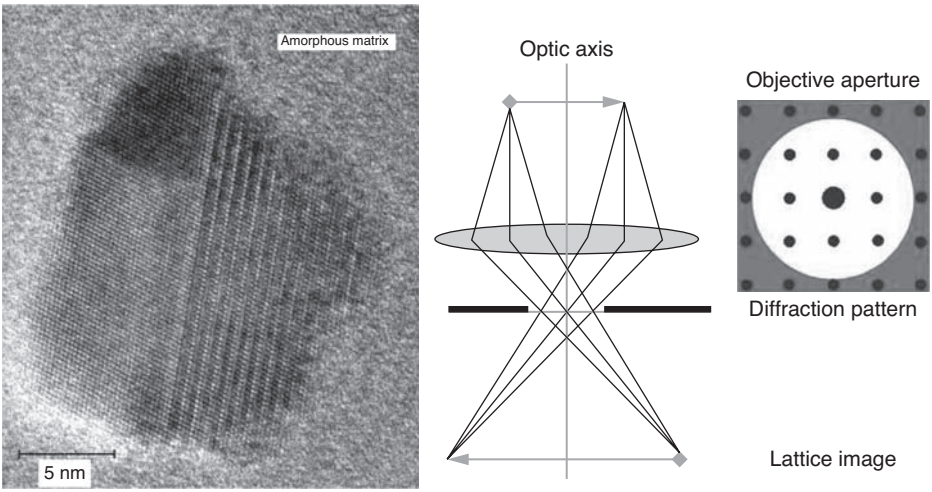

FIGURE 1.7 Left: experimental lattice image using many beams of a [110] zone axis. A nanocrystal (Al dendrite) embedded in an amorphous matrix is imaged with atomic resolution. Note the defects (twins) appearing as stairs on the right side of the Al dendrite. Right: schematic sketch showing the principle of high-resolution imaging.

scattering factor of the specimen and focus and astigmatism of the objective lens. Hence, for the correct interpretation of high-resolution images, numerical simulations, matching the experimental images with computer simulated ones, are required taking the aberrations of the microscope as well as the actual specimen conditions into account. To overcome these difficulties, the following approaches are suggested:

1. imaging of simple well-known structures (for instance metals) having lattice spacings near the point resolution of the TEM using Scherzer focus conditions;
2. reconstruction of the exit wave from a through-focus series (e.g. 20 images) with different defocus values when a microscope equipped with a field-emission gun is used;
3. using an aberration-corrected TEM since the spherical aberration of the objective lens leads to a delocalization of the information. The compensation of the spherical aberration improves the image quality and enhances the reliability for determining the atomic positions in high-resolution TEM [29,30].

In the following, conventional and high-resolution TEM are applied to practical problems in nanocrystalline materials in order to demonstrate the relevance for materials characterization.

5. PLASTICITY IN NANOCRYSTALLINE MATERIALS

The mechanisms of deformation in nanocrystalline materials differ from those of conventional, coarse-grained materials. Molecular dynamic (MD) simulations have

delivered new insight into structure and deformation processes in nanocrystalline materials [31–34]. A transition in the mechanical behaviour from dislocation-based deformation mechanisms to grain boundary (GB)-mediated ones [35], which manifests in change of slope or even a change of the sign of the slope of the Hall–Petch relationship [36], has been found for decreasing grain sizes. A recent review on the results of MD simulations of nanocrystalline materials is given by Wolf et al. [37]. Observations of an 'inverse Hall–Petch' behaviour were explained in terms of diffusion creep by fast transport along the numerous disordered grain boundaries [38–40]. For lower strain rates, a mechanism based on grain-boundary sliding and on coplanar alignment of grain boundaries to form so-called 'mesoscopic glide planes' has been suggested by Hahn and Padmanabhan [41]; this provides explanations for the occurrence of the 'inverse Hall–Petch' behaviour and for a moderate work hardening, respectively. Markmann et al. [42] have shown that, similar to what is known for conventional materials, the dominant deformation mechanism in nanocrystalline materials is a function of the strain rate. Diffusion creep is dominant in the limit of very low strain rate and, in nanocrystalline materials, it becomes noticeable at much lower temperatures than in coarse-grained materials. The following chapter by Padmanabhan elucidates this important point in greater detail. At higher strain rates, partial dislocations must be active as evidenced by the creation of stacking faults. In addition, the absence of a deformation texture indicates that grain-boundary sliding and grain rotation take place along with the dislocation-based plasticity. The experimental findings at large strain rate in nanocrystalline materials agree with predictions from MD simulations, where even higher strain rates are imposed: dislocation activity, i.e. the emission of partial dislocations from grain boundaries, as well as grain-boundary sliding were predicted based on these studies [34,43–49].

Defect structures of plastically deformed nanocrystalline Pd investigated by high-resolution transmission electron microscopy (HRTEM) are presented in this section. Material with an average grain size of about 15 nm was prepared by inert gas condensation and this was plastically deformed by cold-rolling up to a true strain of 0.32 at a strain rate of about 0.3 s^{-1}. Abundant deformation twinning on [111] planes was found and Shockley partial dislocations were identified [50]. Remarkably, in each grain, twinning occurs only on a single set of parallel planes, as shown in Figure 1.8.

This implies that only one out of the five independent slip systems required for the general deformation of a grain is active, a finding which suggests that rigid-body grain rotation and grain boundary sliding must be active along with twinning.

5.1 Transmission Electron Microscopy (TEM) – *in-situ* TEM

In-situ tensile tests performed in a transmission electron microscope (TEM) in combination with high-resolution TEM are feasible. Furthermore, this method is appropriate to elucidate the deformation processes in nanocrystalline materials directly. Until now, only hints of the mechanisms at play have been obtained through changes in contrast, which indicate that dislocations [51–53] as well as

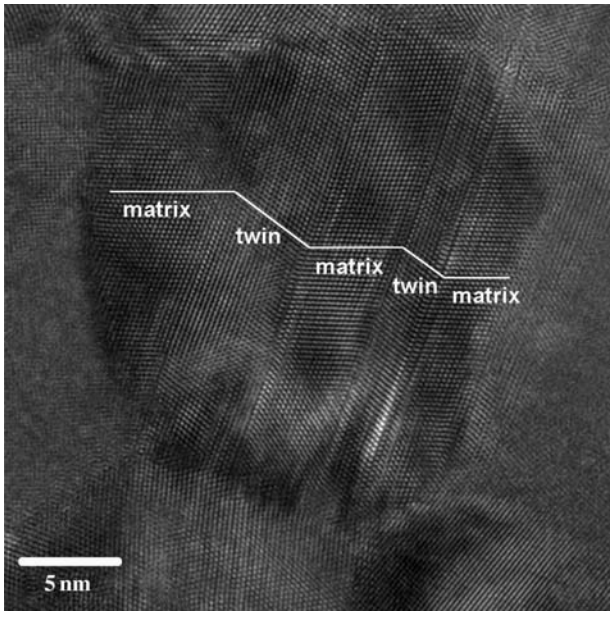

FIGURE 1.8 High-resolution TEM micrograph of a Pd grain (nanocrystalline) oriented along the [011]-direction exhibiting several cases of deformation twinning as indicated by the white lines. Note that the grain boundaries on top and bottom showing the transition to the neighbouring grains are imaged. The [111]-planes bend in an angle of about 14° in both cases (top and bottom).

GB rotation [54] are activated in the nanometre-sized grains. Thus, there is a need for further TEM investigations, especially with better resolution, to elucidate the existing deformation processes in more detail. In the following, a new experimental strategy combining high-resolution TEM with *in-situ* tensile tests is introduced. A new experimental set-up is described and the results obtained reveal clear evidence that deformation twinning and GB processes are activated in nanocrystalline Pd when the foils have been stretched in the TEM.

The material has been cut into rectangular slices having the following dimensions: 4.5 mm in length, 1.2 mm in width and a final thickness of about 100 μm after grinding. After this, the samples have been dimpled down to about 40 μm thickness followed by ion thinning (PIPS, Gatan Model 691) at 3.5 keV and an incident angle of 4°. Such specimens were glued onto a Cu template with superglue as shown in Figure 1.9 and subsequently attached to the tensile stage by two screws.

The *in-situ* TEM tensile tests revealed that cracks were formed while the sample was elongated. A representative example is shown in Figure 1.10 (left). Such cracks occurred suddenly. The regions along the crack as well as the crack tip itself mark the starting points for a comprehensive TEM study of deformation processes in nanocrystalline materials while the TEM sample is still under full load. The TEM experiment was pushed ahead using very low strain rates and stopped for further investigations when changes occurred. The investigation

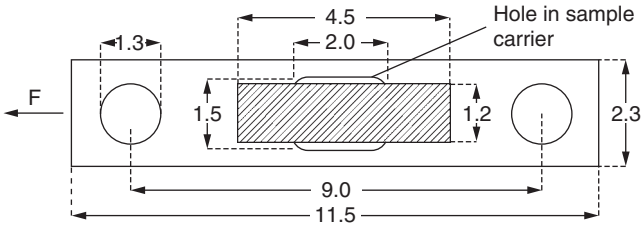

FIGURE 1.9 Schematic sketch showing the dimensions (mm) of a miniaturized *in-situ* TEM tensile test sample which was glued onto a Cu frame.

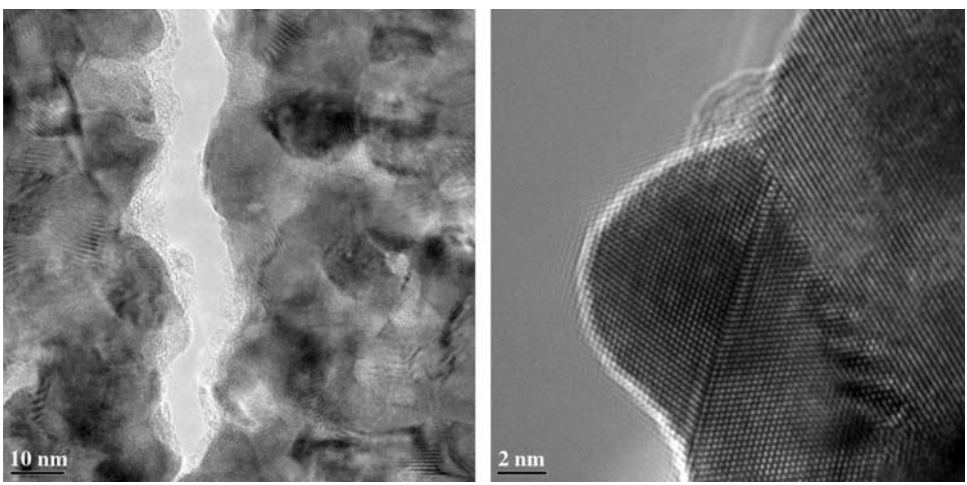

FIGURE 1.10 Left: TEM bright-field micrograph showing an overview of a crack formed during an *in-situ* tensile test in nanocrystalline Pd along the grain boundaries. The average grain size was about 10 nm ± 2 nm, according to X-ray diffraction (XRD) measurements. In order to separate out the grain size from inhomogeneous strain contributions in the broadened Bragg peaks, the method of Williamson–Hall has been used [55]. Right: high-resolution micrograph taken under full load during an *in-situ* TEM tensile test. The crack has propagated along the grain boundaries. A twin has been formed in a grain next to the crack.

revealed that the nanocrystalline Pd ruptured along grain boundaries. Twins were formed in the grains next to the crack as exhibited in Figure 1.10 (right) indicating that the deformation processes must have emerged from the grain boundaries. The observation of deformation twinning confirms furthermore the results of former TEM studies of plastically deformed nanocrystalline Pd [42,50].

5.2 Transmission Electron Microscopy (TEM) – Geometric Phase Analysis (GPA)

Geometric phase analysis (GPA) has been developed independently by M. Takeda, J. Suzuki, [56] and M. Hÿtch [57,58]. GPA is a method for analysing variations in structure from high-resolution TEM images. In Fourier theory, the image of a

perfect crystal can be considered as the sum of sinusoidal lattice fringes having constant amplitude and phase given by the corresponding Fourier component. Imperfections, such as dislocations, are introduced by these Fourier components as a function of position, thus combining real space and reciprocal space information. GPA allows separating amplitude and phase from an image which then is interpreted in terms of image detail and structural variations. Relationships are derived between the phase images and displacement fields due to distortions of the lattice fringes and variations in the local reciprocal lattice vector.

The TEM image is a complex image composed of amplitude $A_g(r)$ and phase $P_g(r)$. For the image of a perfect crystal, the intensity at a position **r**, I(**r**), can be written as a Fourier sum:

$$I(r) = \sum_g H_g(r) \exp(2\pi\, ig \cdot r) \tag{1.1}$$

where **g** corresponds to a Bragg reflection and H_g the corresponding Fourier components. Variations can be described by allowing these Fourier components to be a function of position, giving them a local value in the image, $H_g(\mathbf{r})$.

The complex image $H_g(\mathbf{r})$ is interpreted in terms of its amplitude, Ag(**r**), and phase, Pg(**r**), defined by:

$$H_g(r) = A_g(r) \exp\{iP_g(r)\} \tag{1.2}$$

The amplitude, Ag(r), describes the local contrast of the lattice fringes and the phase, Pg(**r**), describes their positions. Therefore, any displacement of the lattice fringes with respect to the reference will result in a phase shift, i.e. a change in the value of the phase at the position corresponding to the displacement. The phase image is described as:

$$P_g(r) = -2\pi\, g \cdot u \tag{1.3}$$

where u(**r**) is the displacement with respect to position. The phase image, $P_g(\mathbf{r})$, gives the component of the displacement field in the direction of **g**. The strain tensor, ε_{ij}, and the rigid-body rotation, ω_{ij}, can be obtained by differentiation of the displacement field:

$$\varepsilon_{ij} = \frac{1}{2}\left(\frac{\partial u_i}{\partial x_j} + \frac{\partial u_j}{\partial x_i}\right) \qquad \omega_{ij} = \frac{1}{2}\left(\frac{\partial u_j}{\partial x_i} - \frac{\partial u_i}{\partial x_j}\right) \tag{1.4}$$

This method has been applied to learn more about the strain distribution along the Al–Pb interfaces. Following the application for grain boundaries/interfaces as described in reference [59], the strain components e_{xx}, $e_{xy,}$ and e_{yy} have been generated using the two [111]-directions as indicated schematically in Figure 1.11(left). Pb was used as the reference lattice. Figure 1.11(right) and Figure 1.12 show the resulting strain maps. Stress peaks can be seen which arise

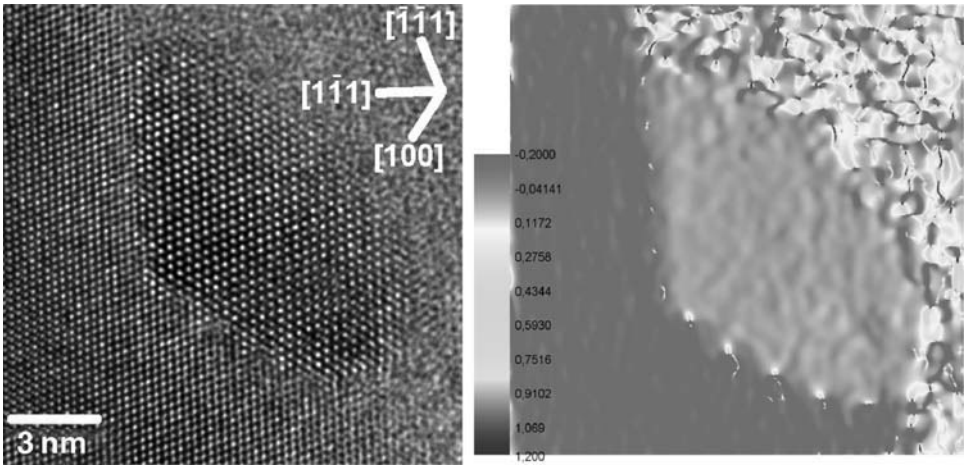

FIGURE 1.11 Left: high-resolution TEM micrograph of an uncovered Pb inclusion at Scherzer focus ($\Delta f = -68$ nm) showing a hetero-interface with the Al matrix remaining on two sides. Right: geometric phase analysis (GPA) showing strain component e_{xx}. Note the stress peaks occurring at the interface where the misfit dislocations are located.

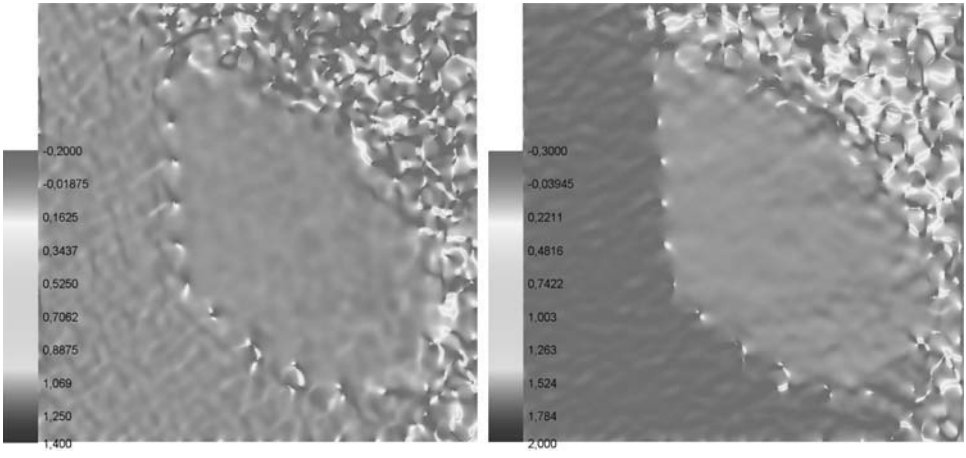

FIGURE 1.12 Left: GPA showing the strain component e_{xy}. Right: GPA showing strain component e_{yy}. Note the stress peaks occurring at the interface where the misfit dislocations are located.

from the misfit dislocation cores. The intermediate regions appear to be smooth and relaxed. Thus, this analysis gives new insight in the understanding of Al–Pb interfaces at which no elastic distortions have been observed so far. The regions indicated by the hot spots, which have high strains, are likely to be nucleation sites for melting.

6. THERMODYNAMIC STABILITY OF NANOSTRUCTURED MATERIALS

As nanostructured materials are structures far away from thermodynamic equilibrium and since they have short transport pathways, fast diffusion and rapid transformation kinetics often lead to coarsening and to the deterioration of the microstructure and the associated properties. Thus, ensuring the stability of the nanoscale structures is a key issue. Aside from restricting the range of candidate materials to the class of refractories such as ceramics or high-melting point metals that are kinetically stabilized at or near ambient conditions, a composite approach involving either two nanosized phases or an extended polycrystalline or amorphous matrix and a nanocrystalline pore phase are obvious solutions for the latter issue since the material transport required for coarsening is severely hampered by a composite structure with limited mutual solubility. This route also includes surface-functionalized nanoparticles as, for example, presented by metallic nanoparticles with a shell consisting of organic ligands or of a natural oxide of the metal [60]. However, it is inherent to nanocrystalline materials that the analysis of microstructure-property relations needs to consider internal interfaces rather than the surface of the nanoscaled structural units. Especially with two-phase nanocomposites, heterophase interfaces with the additional degree of freedom given by the position-dependent composition and possible concentration gradients need to be regarded. An important and basic aspect concerning the functionality of a given material is presented by the respective phase equilibrium that determines the stable structure and the phase distribution and thus the related materials properties. In fact, modifying the phase equilibrium by alloying to improve the performance of a material has been the first and most successful step to modern materials science. However, the phase diagrams are mostly unknown for nanostructured materials. In fact, some observations on ligand-capped magnetic nanoparticles indicate that the energetic contribution due to the bonds at the interface effectively shift the underlying phase stability ranges such that the equilibrium phase is different for the coarse-grained or the nanocrystalline material [60]. Yet, as will be shown below, already the presence of internal heterophase interfaces contributing an excess free energy is sufficient to modify severely the phase equilibrium and the associated phase transformations in nanosize alloy systems. Even the accepted rules to construct phase diagrams need to be modified if nanoscaled alloy systems are considered [61].

6.1 Size-Dependent Melting of Elemental Nanoparticles

It is one of the earliest findings concerning finite-size effects on materials properties that a decrease of the diameter, D, of a particle leads to a shift of the melting temperature, $T_{m,D}$, compared to the bulk melting temperature, $T_{m,0}$ [62]. When the size of a particle is reduced, then the excess free energy – the product of the surface area A and of an interfacial free energy density γ – diminishes more slowly than the free energies of the bulk phases and capillary effects will therefore increasingly affect the thermodynamic equilibrium. In the last few decades, the melting of nanoscale Pb particles embedded in Al has been of interest since

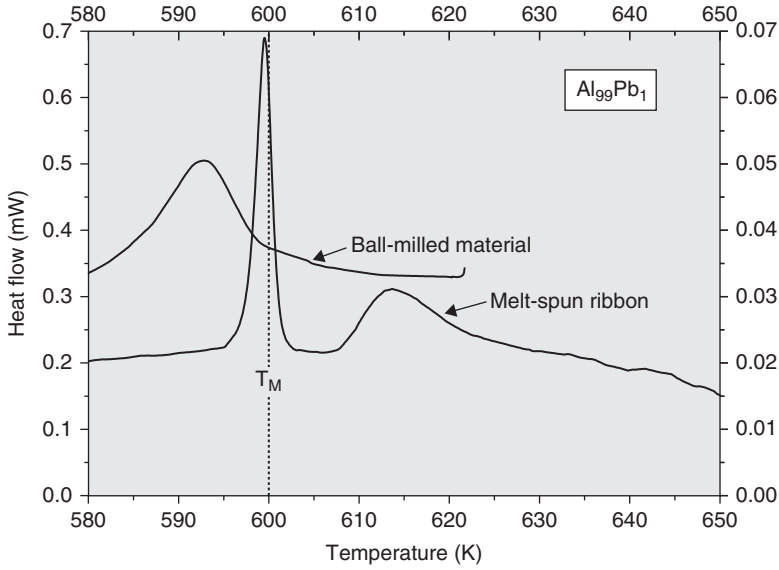

FIGURE 1.13 Comparison of melting signals of nanometre-sized Pb inclusions embedded in Al matrix fabricated by melt spinning and ball milling, respectively. The first peak of the melt-spun material, close to the nominal melting point of bulk Pb, is related to the melting signal of larger Pb inclusions located at the grain boundaries of the Al matrix. The smaller peak represents the melting of the smaller faceted Pb particles in the grain interior of the polycrystalline matrix grains.

Pb–Al nanocomposites serve as model systems to investigate the size-dependent melting phenomenon [63–65].

Nanometre-sized Pb particles embedded in an Al host were produced by different techniques, as for instance melt spinning, ball milling or ion implantation. The melting point of nanometre-sized Pb particles was found to deviate strongly from the bulk melting point of Pb. For instance, an elevated melting point of the Pb inclusions was found in DSC, TEM and XRD *in-situ* heating experiments for melt-spun material [66–71].

On the other hand, material of identical composition and similar average particle size that was fabricated by ball milling revealed a significant depression of the melting point. Figure 1.13 displays the different melting behaviour of ball-milled and melt-spun material, respectively.

The observation of a melting point shift was always linked to the size and morphology of the Pb inclusions, as shown in Figure 1.14. It should be noted that, for both cases, the nanometre-sized Pb inclusions do exhibit a cube-on-cube orientation relationship. Pb inclusions in ball-milled material show a spherical morphology whereas they appear faceted in melt-spun material.

Remarkably, it has been shown that an increase in the melting point of ball-milled Al–Pb composites can be achieved by a heat treatment at high temperatures leading to an increased amount of faceted Pb particles [72]. From the findings attained so far, the melting process at small system sizes seems to be

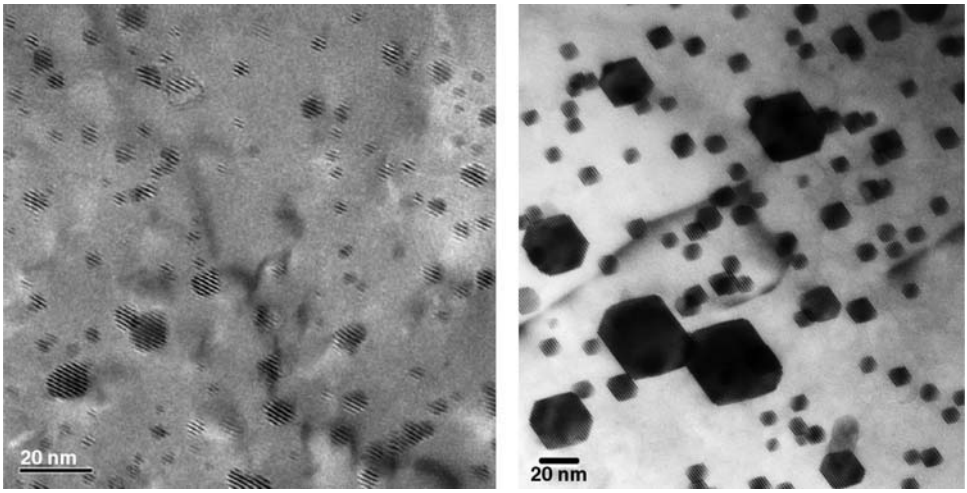

FIGURE 1.14 Comparison of the morphology of Pb inclusions located in the grain interior of the Al matrix. Left: ball-milled material. Right: melt-spun material.

determined by the interface energy and the related interface topology rather than merely by the size of the particle. Thus, a more detailed understanding of the interface morphology is required. One point is to elucidate the reason for a strict maintenance of a cube-on-cube orientation relationship of Pb inclusions, which has been observed after rapid melt quenching as well as for ball-milled material (Figure 1.14). Several interface studies based on high-resolution TEM were undertaken [73–75] revealing that the total excess free energy can be minimized (for a given particle size) by an efficient accommodation of misfit in the form of interfacial dislocations that is energetically particularly favourable if the 'classical' cube-on-cube orientation relationship is maintained, since then the lowest number of misfit dislocations is needed to accommodate the misfit. As a result, for both morphologies, e.g. faceted or spherical, the misfit was found to be accommodated via misfit dislocations (Figure 1.15) on about every fifth Al plane.

6.2 Thermodynamics of Multicomponent Nanoparticles

In addition to the energetic contribution of the external surface, a qualitatively similar contribution arises due to the excess energy associated with internal heterophase interfaces in multiphase, multicomponent nanosystems that are necessarily formed due to temperature- or composition-dependent variations of the relative amount of matter per phase. Therefore, the free energy balance must contain terms of the form $\gamma\ \Delta A$ (specific interface free energy density of the heterophase interface multiplied by the change in area of that interface), on top of the term $A\ \Delta\gamma$ which is dominant in elemental systems, as indicated in the previous section.

Much less work has been devoted to phase equilibria of nanoscale *alloys*, despite their importance for future nanotechnology devices, which will require

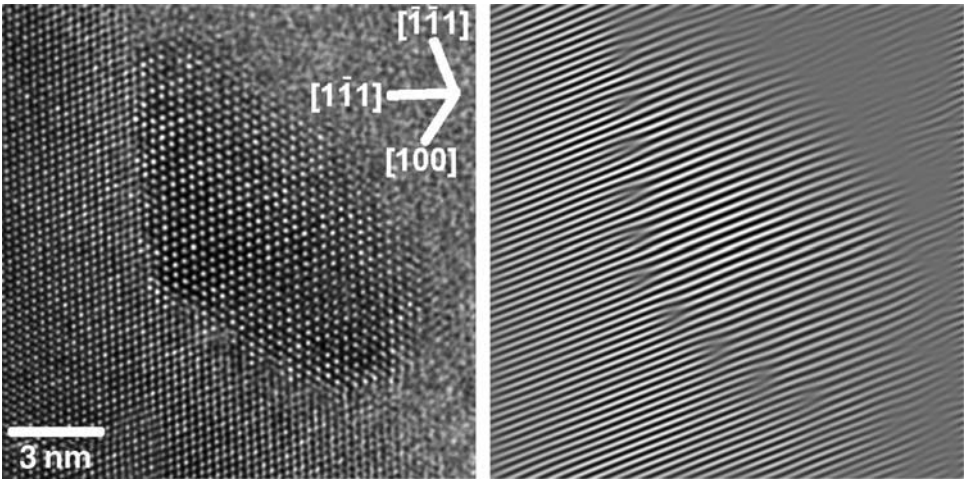

FIGURE 1.15 Left: high-resolution TEM micrograph of an unvovered Pb inclusion (ball-milled material) at Scherzer focus ($\Delta f = -68$ nm) showing a hetero-interface with the Al matrix remaining on two sides. Such Pb particles were located in the amorphous edge area of the TEM specimen. Right: Bragg-filtered image using the [−1,−1,1] reflection only for a better visibility of the misfit dislocations at the Al–Pb interfaces.

the extra degrees of freedom in materials design provided by the use of alloys as opposed to elemental solids. Alloys differ from elemental materials in the fact that constitutional alloy phase diagrams exhibit intervals of temperature and composition in which two (or more) phases coexist at equilibrium. In the following, and without loss of generality, attention will be restricted to binary alloys where, at constant pressure, at maximum three phases can coexist in defined points of the phase diagram (zero degrees of freedom for three-phase coexistence, according to Gibbs' phase rule). The central questions in modelling size-dependent alloy phase diagrams are therefore: can two phases coexist in a small particle and how are the conditions of equilibrium defined? As compared to elemental particles these questions raise a new issue related to the energetics of the internal interface separating the phases within the particle, since varying the relative amount of matter in the phases requires the creation or removal of internal interface area. While it is established that interfacial enrichment or depletion in solute (interfacial segregation) [76] and elastic interactions between the interfaces and the bulk (interface stress) [8] can significantly affect the relative stability of *single-phase* states in nanoscale alloys at constant interfacial area, the consequences of capillarity for the two-phase coexistence within a particle remain widely unexplored. Yet, the capillary energy of the interface between coexisting phases can lead to significant changes in the constitutional phase diagram, i.e. of the composition–temperature fields in which the different phases represent the thermodynamically stable state, and which may be observable even for sizes as large as 100 nm, i.e. well above the structure size of next-generation microelectronics devices. These changes are not mere shifts of temperatures or of compositions at equilibrium; instead, several

qualitative rules, which are universally obeyed in conventional alloy phase diagrams of macroscopic systems, are no longer applicable at the nanometre scale.

In order to analyse the impact of this internal interface to the thermodynamic equilibrium at different particle sizes, an idealized particle embedded in a solid matrix is regarded where the matrix, as in an experiment, serves to prevent coarsening; this implies that the particle shape and consequently (when volume changes during the phase transition can be neglected) the particle-matrix interface area are fixed. The excess free energy due to the outer surface of the particle is then a constant, which can be ignored altogether since it does not affect the phase equilibrium. Thus, in the following discussion, the notion of an interfacial area *A* refers exclusively to the internal interfaces between coexisting phases.

The free energy per particle, G, can be related to the molar free energy, g_0, by:

$$G(T,N,x) = Ng_0(T,x) + \sum_i \gamma_i(T)A_i(T,N,x) \tag{1.5}$$

where the subscript labels the possible interfaces. N is the total amount of matter, i.e. the sum of the amounts of solvent, N_1 and solute, N_2 and x denotes the solute fraction, $x = N_2/N$. At equilibrium, the A_i are not independent state variables, but internal thermodynamic parameters which are functions of T, N, x, determined by the Wulff construction [77]. Generally, the functional dependence of the A_i on N is not linear; this leads to the size-dependence of the chemical potentials of single-phase particles embodied in Gibbs–Thompson–Freundlich-type equations.

In cases where the particle contains two phases, φ and β, e.g. solid, S and liquid, L, that coexist, the Gibbs free energy, $\widetilde{G}$, of the two-phase state with arbitrary compositions (that are not necessarily the compositions at equilibrium that minimize the free enthalpy) is given as:

$$\widetilde{G} = (N^{\varphi}/N)\cdot G^{\varphi} + (1-(N^{\varphi}/N))\cdot G^{\beta} \tag{1.6}$$

The phase fractions for the macroscopic case are then given by the lever rule.

However, the formation of a new phase necessarily entails changes of the area of interfaces and the creation of new interfaces. Thus, the dependence of $\widetilde{G}$ on the phase fraction will cease to be linear, contrary to Eq. (1.6), and consequently the Gibbs free energy of *two-phase* states (in a nanoparticle) is expressed as [61]:

$$\widetilde{G} = (N^{\varphi}/N)\cdot G^{\varphi} + (1-(N^{\varphi}/N))\cdot G^{\beta} + \Delta G_c \tag{1.7}$$

The term ΔG_c represents the deviation from linearity and becomes equal to zero for single-phase particles. Between two single-phase states, a curved graph, as indicated in Figure 1.16a, must result. Thus, the capillary term, $\delta A/\delta V^{\beta}$, in general, removes the coincidence of the tangent lines at equilibrium, as indicated in Figure 1.16a. It should be noted that Eq. (1.7) holds, in general, also for the macroscopic case. However, when the capillary term is negligible, as for macroscopic bulk systems, the condition that the tangents coincide at two-phase coexistence holds and deviations are negligible. The compositions of the coexisting phases in the bulk case are then given by the points of tangency of the common tangent to

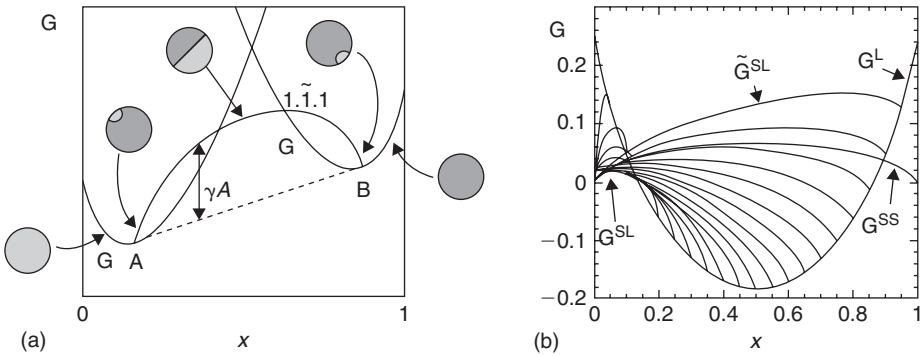

FIGURE 1.16 (a) Schematic diagram of molar Gibbs free energies G^{φ} (red) and G^{β} (blue) versus solute fraction *x* for two phases φ and β. Construction of the Gibbs free energy curve for the two-phase coexistence of alloys represented by points A and B. Black dashed: macroscopic system; solid green: finite size system. Inserts represent cross-sections through the particle, illustrating the geometric arrangement of the phases (red – phase φ, blue – phase β) and the maximum of the interfacial area *A* for equal amounts of phase φ and β. (b) Example of the molar Gibbs free energies (in units of the enthalpy of melting) with various values for x_L used in the computation. Parameters are $T/T_M = 0.75$ and $D = 5$ nm. G^L represents the Gibbs free energy of the single-phase liquid state, G^{SS} represents the two-phase solid state and $G^{SL}(T,x)$ is the lower envelope of the set of functions $\tilde{G}^{SL}(T,x,x_L)$.

the free energy functions G^{φ} and G^{β}; at each temperature these compositions are constants in the two-phase state, independent of the overall composition and the tangent line represents the total free energy.

For small particles, however, the energetic contribution of the internal interface becomes significant and leads to a convex free enthalpy curve as indicated in Figure 1.16a. Different geometric assemblies of the two phases are possible, depending on the relative values of the γ_i but, in general, ΔG_c is a non-linear function of the phase fraction. The most important consequence of the loss of linearity is that the tangent rule ceases to apply. Instead, the compositions of the two coexisting phases at *equilibrium* is not *a priori* known and is determined by energy minimization: the entire set of functions $\tilde{G}^{SL}$ with the solute fraction of the liquid as a parameter needs to be calculated (see Figure 1.16b). The set of curves for $\tilde{G}^{SL}$ also indicates that the composition of the coexisting phases cannot be read from the phase boundaries as in the case of the bulk material. The respective stable states are given by the lower enveloping curve of the Gibbs free energy of all possible phase states and the transition between different phase states that define the minimum of the total Gibbs free energy marks the boundaries of the stability ranges of the different phases.

For the bulk case, the well-known phase diagrams result from an equivalent treatment that minimizes the total Gibbs free energy (Figure 1.17a). However, it is important to note that, for nanoscale systems, not only the topology of the phase boundaries is changed, but the way in which the resulting 'phase diagrams' are to be used is completely different: the compositions of the coexisting phases are no longer invariant upon isothermal variations of the solute fraction and the

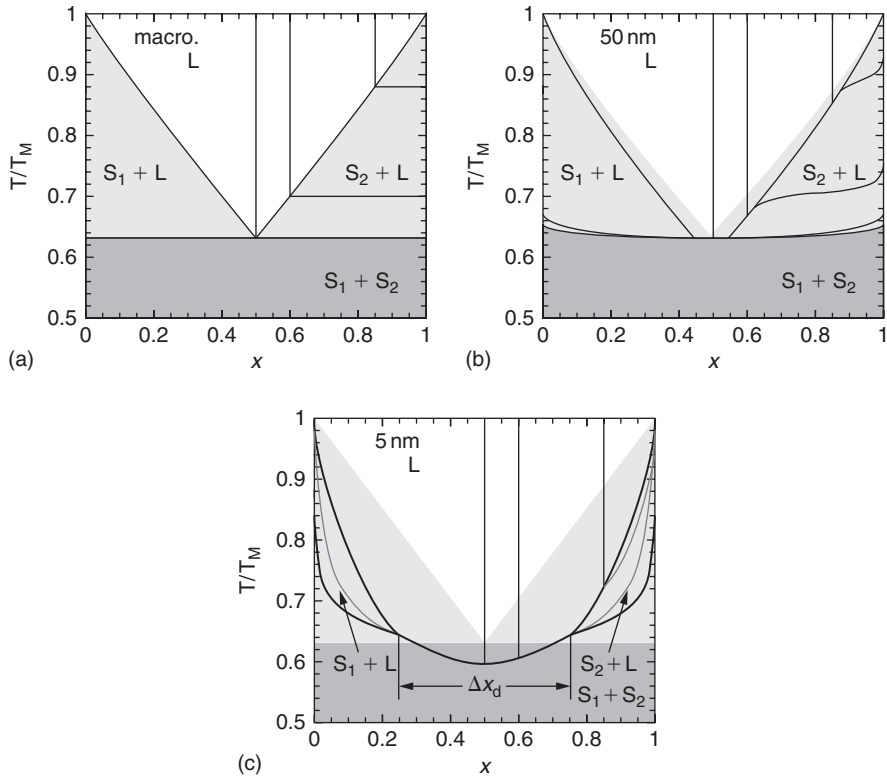

FIGURE 1.17 (a) Phase diagram of a bulk eutectic alloy with no solid solubility. Black: phase coexistence lines; coloured: lines of equal solute fraction x_L in the liquid phase for three arbitrarily chosen values of x_L. (b) and (c) as in (a), but finite size systems with particle diameters D = 50 nm and D = 5 nm respectively. Δx_d: discontinuous melting interval where a direct transition from a two-phase solid to a single-phase liquid without three-phase coexistence occurs. Capital letters indicate the phases that are stable in the respective regions of temperature/composition space. $S_{1,2}$: solid phases; L: liquid. The grey shades represent the topologic features of the bulk phase diagram for easier comparison.

composition of the majority phase is no longer continuous across phase boundary lines [78]. Thus, at first sight, a more appropriate term for the resulting phase diagrams would be '*stability*' diagrams since the properties conventionally associated with phase diagrams are no longer applicable for nanoscaled alloys. It should be emphasized, however, that these properties merely result from the applicability of linear approximations in the macroscopic world – in principle the results derived here for nanoscale systems are generally applicable; they just become significant at small system size and – this is important to note – the calculated diagrams as well as the construction rules extrapolate to the accepted behaviour for large system sizes.

In order to compute phase diagrams (or stability diagrams) for different particle sizes, assumptions for the equations of state need to be done. A simple case is

given by an alloy with no solid solubility and an ideal liquid solution which, for the bulk case, results in a simple eutectic phase diagram that is symmetric concerning the equi-atomic composition. In a reduced representation, the three materials constants that need to be specified (basically the atomic volume, melting entropy and interfacial free energy in scaled representations) are similar for most metals. Details of the computation as well as concerning the analytical model are given elsewhere [61]. The resulting phase diagrams for the bulk system and for two alloy particles with different sizes are summarized in Figure 1.17. It is seen that, as the particle size is reduced, the phase diagram undergoes several qualitative changes, each of which breaks one of the rules that apply universally to the construction of the phase diagram for macroscopic systems. First, it is observed that the invariance of the solidus temperature is lost in favour of a significant composition-dependence. Second, as illustrated by the lines representing states of identical composition x_L of the liquid phase at equilibrium, the compositions of the constituent phases in two-phase equilibria are no longer invariant at constant temperature. Thirdly, the equi-composition lines lose their continuity at the intersection with the liquidus line [79]. This implies that there is a discrete jump in liquid fraction across the liquidus of the small alloy particles, consistent with the result of numerical modelling matched to Sn–Bi nanoparticles [80], where the ends of the tie lines were found to detach from the phase boundary lines. It should be stressed that relaxing the stringent boundary conditions that were used for constructing a simple model system does not qualitatively change the resulting phase equilibria. In fact, recent calculations based on a model eutectic with finite solubility of the terminal phases have shown that the stability fields of the different one- and two-phase states are shifted and that the two-phase solid–liquid stability fields are detached from the terminal phases [M. Gährken and G. Wilde, personal communication] as also found by numerical calculations [80]. However, the most fundamental consequence of the finite system size is a topological change in the phase diagram, the degeneration of the eutectic point of the macroscopic system into a line representing an interval of compositions Δx_d (defined in Figure 1.17c) for which the particle undergoes a discontinuous transition between the two-phase solid–solid state and the single-phase liquid state. In the macroscopic system, three phases can coexist at equilibrium at the eutectic point; by contrast, discontinuous melting in this model is a transition between a two-phase equilibrium (solid–solid) and a single-phase state, without three-phase equilibrium (clearly, three phases will coexist during melting, but this situation resembles a transient, non-equilibrium configuration). It is because of this loss of three-phase equilibrium in the finite-size system that the transition from a eutectic point to a discontinuous melting line can be reconciled with the phase rule. In fact, recent experimental studies of isothermal composition variation within the electron microscope [81] as well as calorimetric investigations on a Bi–Cd eutectic that closely resembles the assumptions of the simple model eutectic [82,83] are in complete agreement with the model results.

In order to verify the results of the theoretical study, experimental analyses were performed on a series of $Al_{98}(Bi_x–Cd_{1-x})_2$ alloys that had been synthesized via melt-spinning. The Bi–Cd system presents similar conditions concerning the constitutive behaviour as assumed in our simplified theoretical model system, especially

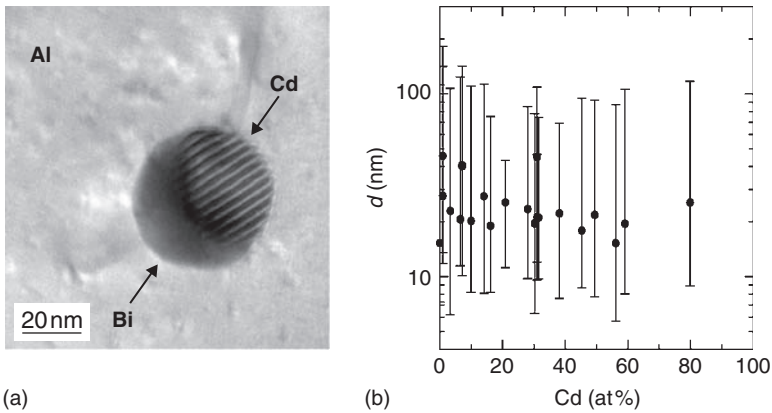

FIGURE 1.18 (a) TEM bright-field image of a Bi–Cd particle embedded in an Al grain. The particle belongs to the 'smaller' fraction that shows pronounced size dependence of the melting behaviour. The two differently appearing parts of the particle (i.e. with or without Moiré effect) are due to the eutectic nature of the particle with one side consisting of Bi and the other of Cd. (b) Average particle diameter as measured from TEM bright-field images. The particle sizes refer to the 'smaller' particles that are located within the Al grains. The error bars indicate the 95% confidence range. The results indicate clearly that the average size of the particles is independent of the alloy composition.

concerning the negligible mutual solubility of Bi and Cd in the solid state and the negligible solubility of both components in solid Al. Thus, eutectic Bi–Cd nanoparticles embedded in an Al matrix were obtained after rapid quenching, as indicated in the TEM bright-field image in Figure 1.18a. However, the melt-spinning process resulted in a bimodal size distribution of the Bi–Cd particles with larger particles located at grain boundaries of the Al matrix and small particles within the Al grains, as already observed for the Al–Pb alloys. *In-situ* melting experiments within the TEM have served to associate the calorimetric melting signals with the respective particle fractions. Thus, the melting signal of the different size fractions could be deconvoluted. Quantitative analyses of the size distribution from TEM bright-field images have shown that the average sizes of the smaller and the larger particles does not depend on the alloy composition (Figure 1.18b). Figure 1.19a shows the experimental results of calorimetric melting experiments on a series of $Al_{98}(Bi_x–Cd_{1-x})_2$ alloys with $x \in [0, 1]$. The two different peaks that are labelled as peak 1 and peak 2, respectively, refer to the melting signals of the two size fractions. It is clear from the calorimetric results in conjunction with the *in-situ* TEM melting experiments that peak 2 is associated with the melting process of the smaller particles that are located within the Al grains. This peak shows an onset temperature about 3°C above the signal maximum due to the larger particles (peak 1) at small Cd concentration but decreases significantly with increasing Cd concentration. At about 60 at% Cd, the onset of melting of the smaller particles is about 6°C below the onset for the larger particles. Thus, the total variation of the onset temperature

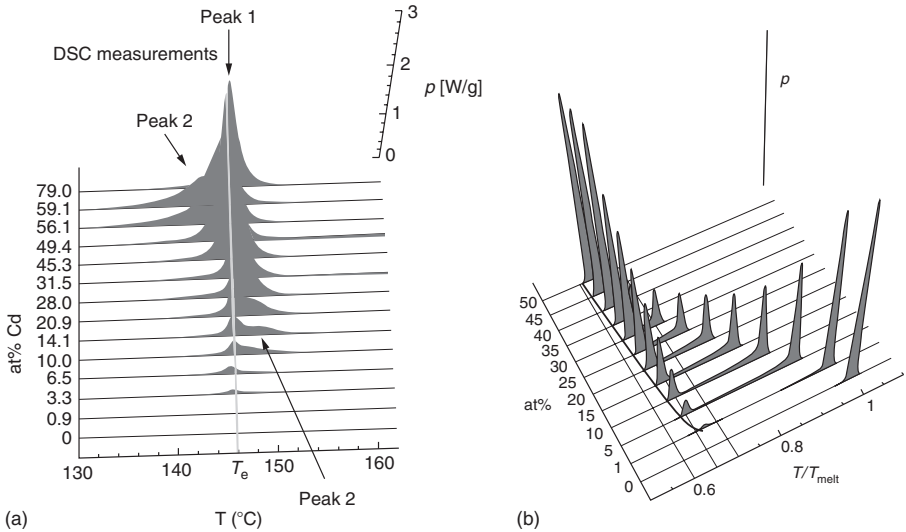

FIGURE 1.19 (a) Calorimetric results showing the onset of melting of a series of $Al_{98}(Bi_x–Cd_{1-x})_2$ alloys. P denoted the calorimetric signal in [W/g]. The two peaks that are indicated in the figure refer to the fraction of larger (peak 1) and smaller (peak 2) particles. The results indicate that the onset of melting (the 'eutectic' temperature) for the smaller particles depends on the alloy composition and is no longer constant as for the larger particles or the bulk alloy. (b) Calculated calorimetry curves based on the theoretical model eutectic for a particle diameter of 20 nm (i.e. similar to the average particle size observed experimentally). The curve outlines the onset of melting for the different alloy compositions. The variation of the melting onset is comparable to the experimental results shown in Figure 1.19a.

is about 9°C. Since the standard deviation for the onset of melting (determined on the same macroscopic alloy system) is only about ±0.8°C, these results indicate the validity of the theoretical approach. In fact, calculating calorimetric curves for the theoretical model system for the same particle size as observed experimentally results in a similar variation of the onset temperature for melting with a dependence on the alloy composition (Figure 1.19b). It should be emphasized that observing a dependence of the solidus temperature on the alloy composition is clear evidence for the importance of the interface contributions since, for macroscopic systems and according to standard phase diagram construction, the solidus temperature in a bulk eutectic system such as Bi–Cd would strictly remain constant.

7. INTERFACE DIFFUSION IN BULK NANOCRYSTALLINE ALLOYS

As was stated above, the attractive application potential of materials with nanometre-sized grains is related to the high fraction of grain boundaries (GBs) and triple junctions (TJs) between grains in these materials. The high values of the diffusion coefficient along the GBs and TJs [84], combined with the high volume

fraction of the atoms positioned inside these defects (up to 30–50%) lead to an unusually high effective diffusion permeability of the nanomaterials at low temperatures and may even change the plasticity mechanism from a dislocation- to a diffusion-controlled one (e.g. see [85]). The detailed consideration of the effect of nanosize on creep-related properties can be found in Chapter 2. However, there are two basic questions: are the GBs in nanomaterials and their coarse-grained counterparts fundamentally different or not? Does only the grain size affect the diffusion permeation of nanoscaled materials?

The atomic structure of GBs can be studied by high-resolution transmission electron microscopy, as discussed earlier in this chapter. However, even small changes of the interatomic configurations result in corresponding changes of the energy barriers for atom jumps. Since the diffusion rates depend *exponentially* on these energy barriers (i.e. on the migration energies), a rather strong impact of changes of the atomic-level structure of grain boundaries on the resulting GB diffusion is expected. Investigations of the diffraction contrast at GBs for ultrafine grained (UFG) materials produced by severe plastic deformation indicated elastic strains in near-GB areas due to a high density of extrinsic GB dislocations and partial disclinations [86]. The term 'non-equilibrium' has been introduced to describe these non-relaxed states of interfaces between grains and to differentiate them from relaxed GBs in well-annealed coarse-grained materials [87]. Again, diffusion measurements can help to verify such a non-equilibrium state of GBs.

Diffusion does not only represent a way to examine the structure and kinetic state of internal interfaces in a nanomaterial. Diffusion phenomena can also be applied for the fabrication of unique nanoscaled materials. For example, the Kirkendall effect (which involves an unbalanced counterdiffusion through a reaction interface) has been widely applied for the fabrication of nanoscale hollow structures [88]. These and other applications, such as the analysis of plasticity of nanomaterials as discussed earlier in this chapter but also in Chapters 2 and 3 require detailed knowledge of diffusion on a nanoscale. The diffusion-induced reactions at interfaces demand also a special consideration when nanoscale distances or short diffusion times are involved [89,90].

Since the pioneering work [91], diffusion in nanocrystalline materials has been the subject of numerous researches. The first decade of research was reviewed in famous articles by H. Gleiter [92,93]. A status report has recently been published by Würschum et al. [94]. Theoretical models of diffusion enhancement associated with transformations of GB defects in nanocrystalline materials were reviewed by Ovid'ko [95]. In the last decade, the focus of diffusion studies has been shifted to full density nanoscaled and ultrafine grained materials produced by different methods of severe plastic deformation. These new findings will be summarized here.

In spite of a considerable progress in our understanding of diffusion in nanocrystalline materials, a number of fundamental problems remains still unresolved: to what extent do GBs in nanocrystalline materials differ from the relaxed boundaries in coarse-grained materials and to what extent do the various types of grain boundaries in the same material differ; what is the relation between the GB structure and the corresponding energetic and kinetic properties; could one

apply the concept of an 'averaged grain boundary' in a nanomaterial; what is the effect of the production route? Here, we will address these and related problems systematically.

7.1 Experiments on Diffusion along Interfaces: General Remarks

The measurement of GB diffusion is not a trivial task. Grain boundaries in a polycrystalline material represent short-circuit diffusion paths. The relation $D_{gb} \gg D_v$ is usually anticipated, although there are important exceptions, e.g. ionic conductors or some semiconductors, where GB diffusion occurs at a lower rate and with a higher activation enthalpy with respect to bulk diffusion [96]. Here D_{gb} and D_v are the GB and bulk diffusivities, respectively. The mathematical treatment of the GB diffusion problem and the parameters which can be determined from an experiment depend critically on the ratio between GB and bulk diffusion fluxes. Following Harrison [97], the GB diffusion measurements in a polycrystalline material can generally be classified into three types: C, B and A (Figure 1.20):

C regime. At low temperatures (short times of diffusion anneal), the bulk diffusion length is small with respect to the GB width δ and the tracer atoms concentrate exclusively in the GBs (Figure 1.20a). In this kinetic regime, the GB diffusivity D_{gb} can directly be determined from an experimental concentration profile applying, for example, the Gaussian solution of the diffusion problem.

B regime. With increasing temperature, the bulk diffusion length becomes much larger than the GB width and diffusion leakage from the GBs into the bulk cannot be neglected. If the bulk diffusion fluxes from neighbouring GBs do not overlap (Figure 1.20b), the conditions of the B kinetics are fulfilled and the only parameter that can experimentally be determined is the so-called double product P of the GB width δ and the GB diffusivity D_{gb}: $P = \delta \cdot D_{gb}$ [128]. In the case of solute diffusion, the double product has to be replaced by the triple product $P{:}P = s \cdot \delta \cdot D_{gb}$, where s is the solute segregation factor [98].

A regime. At even higher temperatures (very long diffusion times), the bulk diffusion fluxes from different GBs overlap (Figure 1.20c) and diffusion proceeds in an effectively homogeneous medium characterized by an effective diffusion

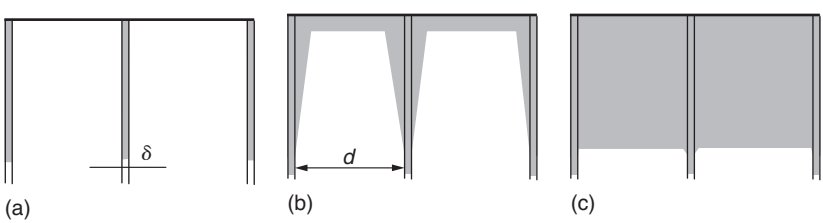

FIGURE 1.20 Schematic classification of GB diffusion regimes after Harrison [97]: the *C* (a), *B* (b) and *A* (c) kinetics. The tracer distribution after a given diffusion anneal is shown (grey regions). The grain boundaries are considered as homogeneous slabs of width δ and diffusivity D_{gb}. The grain size *d* is indicated.

coefficient $D_{eff} = gD_{gb} + (1 - g)D_v$, where $g = sf/(1 - f + sf)$ with f being the fraction of GBs in the polycrystal [84].

Whereas the dominant majority of GB diffusion investigations on coarse-grained materials were carried out in the B kinetics regime [99], diffusion studies on nanocrystalline materials were predominantly performed in the C-type kinetics regime. Experiments in the C kinetics regime on typical coarse-grained materials require a very high sensitivity of the radionuclide counting system, since tiny amounts of tracer have to be detected in each section of the GB diffusion profile. On the other hand, higher temperatures, which are required for the B-type measurements, invoke almost inevitably GB motion and recrystallization in a nanomaterial. This demands certain precautions by comparing the GB diffusion data measured in a nanomaterial and its coarse-grained counterpart.

The Harrison classification has been further refined for diffusion in homogeneous ultrafine grained materials [100] depending on the grain size, diffusion temperature and time, the GB segregation level in the case of impurity diffusion and other parameters. New kinetic regimes are introduced for short-circuit diffusion in a very important case of hierarchical nanocrystalline microstructures [101]; see the case of diffusion in sintered nanomaterials below. The formation of hierarchic structures and their effect on optical properties of metals and polymers are described in Chapter 7. One has to recognize that not only are the bulk properties affected by the hierarchy, but the interface properties, too. The effect may be even more pronounced, since different free volume is typically associated with different types of internal interface. The given types of interface are important at different structure levels and GB diffusion is a property that reflects directly and sensitively the respective boundary structures.

7.2 Effect of the Production Route on Diffusion Behaviour

The diffusion properties of nanocrystalline and ultrafine grained materials will be considered below in relation to the production route.

7.2.1 Inert gas condensation

Inert gas condensation [91] is capable of producing a microstructure that is usually texture-free and consists of equiaxed grains. However, it has several limitations including specimen volume and yield, incomplete densification and difficulties associated with retaining the fine grain size during consolidation.

The state of the art of the research on the diffusion behaviour of interfaces in pure nanocrystalline copper produced by inert gas condensation is illustrated in Figure 1.21, where the data for self- (Cu [102]) and solute (Ag [103], Bi [104]) grain boundary diffusion in nano-Cu are compared with the corresponding diffusivities determined for the coarse-grained (cg) material. Note that different methods of diffusion study were applied: the radiotracer technique (Cu diffusion [102]), electron-beam microanalysis (Ag diffusion) [103] and Rutherford backscattering (Bi diffusion) [104].

One recognizes that GB diffusion of Cu in both nano- and cg-materials (both measured with a radiotracer technique) proceeds with similar rates. In the original

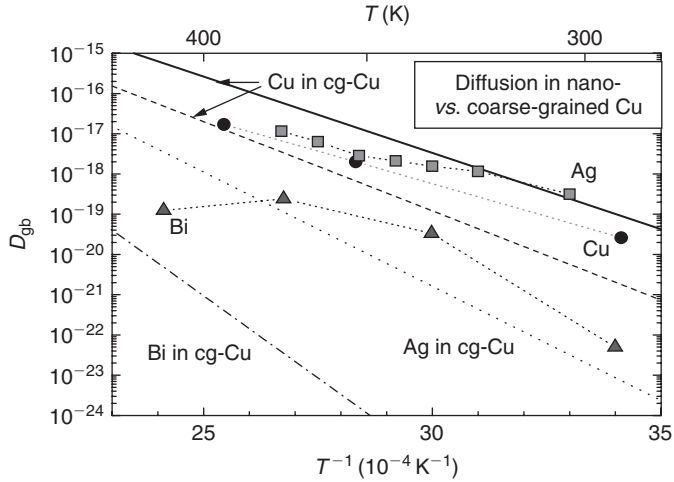

FIGURE 1.21 Self-diffusion of Cu [102] and solute diffusion of Ag [103] and Bi [104] in nanocrystalline Cu (symbols) in comparison with their diffusivities in coarse-grained material (cg-Cu) [105–107] (straight lines). GB self-diffusion of Cu in coarse-grained samples was measured in the materials of purities 5N (dashed line) and 5N8 (solid line) [105].

paper [102], it was claimed that Cu GB diffusion at room temperature in nanocrystalline copper is faster than that in coarse-grained material by several orders of magnitude at room temperature. However, literature data on moderately pure copper were used for the comparison. More recent measurements have discovered a tremendous effect of the purity on GB self-diffusion: the purer the material is, the faster is the GB self-diffusion and the smaller is the corresponding activation enthalpy [105]. Similar effects have been established for solute diffusion of Ni in coarse-grained Cu, too [108]. Due to the high volume fraction of GBs in a nanomaterial, their impurity content is relatively low and must be compared to that in a coarse-grained, high-purity material.

GB diffusivities of solutes in nano-Cu (especially of Bi) appear to be significantly enhanced with respect to the corresponding values in cg-Cu. This enhancement becomes more pronounced with decreasing temperature and approaches about seven orders of magnitude for Bi at T = 350 K (see Figure 1.21). How reliable is this comparison? It is known that the radiotracer technique is superior with respect to electron-beam microanalysis and to Rutherford backscattering regarding sensitivity and dynamical range of the analysed concentration penetration profiles. It would be beneficial to apply the radiotracer method as the most sensitive one for a systematic investigation of diffusion of a solute in copper as a function of the grain size.

The coefficients of GB self-diffusion in nanocrystalline Fe (with relative density higher than 91%) have been determined by Würschum and co-workers [109]. The self-diffusivities were found to be similar to those extrapolated from high temperature data of conventional GBs. These results suggest that the GBs in the high-density nano-Fe prepared by compaction of the inert gas condensate are similar to those in conventional polycrystalline Fe.

7.2.2 Controlled crystallization of amorphous precursors

The controlled crystallization of amorphous precursors is also used for production of nanoscaled materials, as described earlier in this chapter. In such a case, the experimental measurements of GB diffusion are highly complicated by the presence of a residual fraction of an amorphous phase [110]. Selected diffusion data, which were mainly obtained by Würschum and co-workers in Fe-based alloys, are summarized in Figure 1.22. In this case, interfacial diffusion is observed to be similar to or even slower than that in respective coarse-grained materials. This behaviour is explained by residual intergranular amorphous phase [110]. In $Fe_{90}Zr_7B_3$ and $Fe_{90}Zr_{10}$ alloys, a second, faster diffusion process is observed in addition to the slower one [111]. Adopting general treatment of diffusion in hierarchic structures (see below), the diffusivities of the faster diffusion paths were determined and it was found that the diffusivity is similar to diffusion along conventional GBs. These faster diffusion paths are related to intercrystalline regions in the alloys. Intergranular melting of the UFG $Nd_2Fe_{14}B$ alloy was also observed [112].

Similar results were established for Mo tracer diffusion in an $Fe_{76}Mo_8Cu_1B_{15}$ alloy which was studied using a serial sectioning method in the temperature range 548 to 648 K [113].

7.2.3 Electrodeposition

By electrodeposition, sheets with a thickness of 100 μm or more with minimum average grain sizes of about 10 to 40 nm can be produced [114]. However, the use of additives, such as saccharin, in the plating bath often results in carbon and sulphur as impurities in the materials that often are found to be segregated at the grain boundaries and strongly affect GB diffusion. This route allows the production of

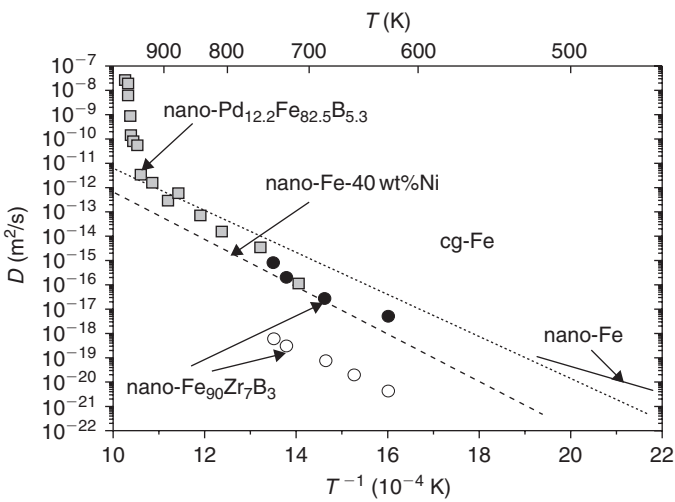

FIGURE 1.22 Interfacial diffusion of Fe in nanocrystalline Fe-based alloys produced by crystallization of amorphous phase: $Pd_{12.2}Fe_{82.5}B_{5.3}$ [112], $Fe_{90}Zr_7B_3$ [111]. The data on GB diffusion in coarse-grained Fe [125], nano-Fe (produced by inert gas condensation) [110], and nano-Fe-40wt%Ni [122] are also presented.

nanotwinned or nanostructured copper with a very small grain size, down to several tens of nanometres [115]. There are presently no direct measurements of tracer diffusion in such materials, although such a study can address a very interesting effect of (nano-) twins on the diffusion permeability of crystals.

7.2.4 Ball milling

Diffusion studies on nanocrystalline ceramics prepared by high-energy ball milling of coarse-grained source materials were recently reviewed by Heitjans and Indris [116,117]. The applied experimental techniques are both tracer diffusion or conductivity methods and nuclear magnetic resonance techniques. It was possible to discriminate between highly mobile ions in the interfacial regions and immobile ions in the grains. Investigations on composite materials exhibited phenomena which can be explained by the percolation of fast diffusion pathways being formed by the interfaces between the two components. In general, diffusion in the nanocrystalline systems was found to be fast compared to that in the corresponding microcrystalline source materials. However, although mechanical milling (i.e. ball milling) and compaction can produce reasonably sized billets, the process also suffers from contamination, in this case from the milling media and/or atmosphere and often involves coarsening of the nanocrystalline aggregates during consolidation.

7.2.5 Sintering

Pressureless sintering of ball-milled powders represents an attractive route for producing a bulk nanocrystalline material with almost theoretical density [118]. The nanocrystalline Fe–Ni alloy was produced during hydrogen reduction of ball-milled oxide powders. The detailed preparation scheme is completely described in Knorr et al. and Divinski et al. [119,120]. Micrometre-large Fe_2O_3 and NiO powders were mixed together to the Fe-40wt% Ni composition. The mixture was ball-milled in a stainless-steel attritor. After drying in an oven, the material was sieved down to a grid size of 100 μm. The powder mixture was then reduced in hydrogen atmosphere at 873 K for 1 h resulting in nucleation and growth of a nanocrystalline γ-Fe-40wt% Ni alloy with the average grain size of about 30 nm.

The material was compacted at room temperature under a pressure of 1.25 GPa and then sintered for 1 h at 1123 K in hydrogen atmosphere. The heating and cooling proceeded at the rate of 10 K/min. As a result, cylindrical discs of 10 mm in diameter and 2 to 3 mm in height were produced. A density of about 98% of the theoretical density was obtained. The chemical composition of the samples was controlled by electron microprobe analysis.

7.3 Interface Diffusion in Hierarchic Microstructures

During sintering, the grain size increased from 30 to about 100 nm, which was checked by X-ray diffraction and scanning electron microscopy studies. The nanocrystalline structure turned out to be quite stable and, even after thermal anneals at 1100 K for 100 h, no pronounced changes in the grain size were observed [120,121].

The investigation of the microstructure revealed the existence of a hierarchic microstructure in the material: the nanocrystalline grains ($d \approx 100$ nm)

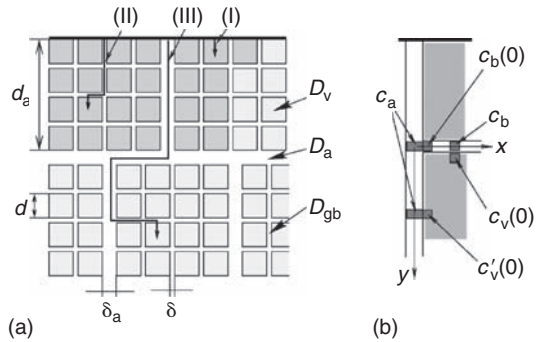

FIGURE 1.23 Schematic representation of the hierarchic microstructure of the nanocrystalline Fe–Ni alloy (a). Small nanograins (of the size d) are clustered in agglomerates of the size d_a. δ and δ_a are the widths of nano-GBs and interagglomerate boundaries, respectively; D_v, D_{gb}, and D_a are the bulk, nano-GB and interagglomerate boundary diffusivities, respectively. Possible diffusion paths of individual tracer atoms, which contribute to the fluxes (I), (II) and (III) (see text), are illustrated. (b) The concentrations (see text p. 34), which are relevant to the definitions of the segregation factors s and s_a, are indicated.

turned out to be clustered in agglomerates with the average size d_a from 30 to 50 μm [121,122]. This microstructure is schematically presented in Figure 1.23a. Thus, several different types of internal interface existed in the material under investigation.

The small residual porosity of the material (below 2% of the volume) is mainly related to the interagglomerate boundaries and microvoids which decorate these interfaces [121]. However, the individual microvoids are well separated and do not serve as an additional short-circuit diffusion path in the material.

The effect of a hierarchical microstructure on diffusion in a nanomaterial has partially been considered by Bokstein with co-workers [123]. The complete analysis of interface diffusion in different possible kinetic regimes has been carried out by Divinski et al. [121,122,124].

7.3.1 Kinetic regimes of GB diffusion in a material with a hierarchical structure

In the case of the nanocrystalline materials with a complex hierarchic microstructure (see Figure 1.23a), the kinetics of diffusion transport deviates from Harrison's scheme (see Figure 1.20) and demands detailed consideration. Three potential diffusion paths should simultaneously be taken into account:

1. short-circuit diffusion along the interagglomerate boundaries. Each of such interfaces is assumed to be represented by a homogeneous slab of width δ_a and the diffusivity D_a;
2. short-circuit diffusion along nanocrystalline GBs which are considered as homogeneous slabs of width δ and the diffusivity D_{gb};
3. bulk diffusion with the diffusion coefficient D_v.

It is important that (and this was experimentally verified [121,124]) in the temperature interval under consideration the following condition holds:

$$D_a \gg D_{gb} \gg D_v \tag{1.8}$$

Taking this relation into account, three different diffusion fluxes can generally be introduced (counted according to the values of the relevant penetration depths; see Figure 1.23a):

I. diffusion along interagglomerate boundaries with subsequent outdiffusion to nanoboundaries and then into the grain bulk;
II. GB diffusion along nanocrystalline boundaries with subsequent outdiffusion into the grain interior; and
III. direct volume diffusion from the sample surface into the nanograins.

Thus, the regimes of interface diffusion for processes (II) and (III) have to be specified separately in order to describe the overall diffusion kinetic. Bearing this in mind, a two-letter designation was suggested [124], such as *C–B*. Each letter corresponds to the given Harrison kinetic regime [97] which is satisfied for the particular interface type: at first for the nano-GB and then for the interagglomerate boundary diffusion. Therefore, for example, the *C–B* regime describes the case when the *C* regime of diffusion along the nanocrystalline GBs (no outdiffusion into bulk) is satisfied and when simultaneously the (quasi) *B* regime of diffusion along the interagglomerate boundaries (fast diffusion along the interagglomerate boundaries with subsequent outdiffusion into the adjacent nano-GBs) is fulfilled.

In the case of solute diffusion, the segregation of the solute to both types of internal interfaces has to be taken into account. More than one segregation coefficient has to be introduced. The solute atoms can generally be in excess in (see Figure 1.23b):

1. the interagglomerate interfaces with respect to the adjacent positions in the nano-GBs which intersect this interagglomerate interface;
2. interagglomerate interfaces with respect to the adjacent bulk; and
3. nanocrystalline GBs with respect to the adjacent bulk.

In view of relation (1.8), two segregation factors are required to describe the diffusion problem under consideration: s, which characterizes the solute excess in a nano-GB with respect to an adjacent bulk plane, and s_a, which corresponds to an excess of the solute in the interagglomerate boundary with respect to the adjacent position in the nanocrystalline GB:

$$s = \frac{c_b}{c_v(0)} \tag{1.9}$$

and

$$s_a = \frac{c_a}{c_b(0)} \tag{1.10}$$

Here, $c_v(0)$, c_b, $c_b(0)$ and c_a are the corresponding solute concentrations in the bulk just near a nanocrystalline GB, in a nano-GB, in a nano-GB just near an interagglomerate boundary and in an interagglomerate boundary, respectively. The definition of these concentrations is illustrated in Figure 1.23b.

The segregation factor $s_{av} = c_a/c'_v(0)$ (the case (2) above) is not important in the present consideration, since we have neglected *direct* outdiffusion from the interagglomerate boundaries into the bulk (here $c'_v(0)$ is the bulk solute concentration just near the interagglomerate boundary, Figure 1.23b). Note that the excess of solute atoms in the interagglomerate boundaries with respect to the bulk, s_{av}, may be presented as $s_{av} = s_a s$, if the segregation behaviour corresponds to the dilute limit conditions (linear segregation). The segregation factor s is important for the flux (II) and both factors, s and s_a, affect the flux (III).

Depending on the given kinetic conditions, five regimes (*C–C*, *C–B*, *B–B*, *A–B*, and *A*) and one subregime (*AB–B*) were introduced to describe diffusion in a material with a bimodal distribution of internal interfaces [121].

The C–C regime. This regime corresponds to very low temperatures and short diffusion times which suppress any outdiffusion from the internal interfaces into the material. Bulk and GB diffusion are negligible. If the tracer enters the nanocrystalline GBs, it stops there (Figure 1.24a).

Since nano-GB diffusion is almost 'frozen out', the tracer is dominantly located in the interagglomerate boundaries. The diffusion profile corresponds to the error function or Gaussian solution of the diffusion equation in dependence on the given initial conditions. An example of such a profile, experimentally measured for Ag solute diffusion in the nanocrystalline γ-FeNi alloy [124], is shown in

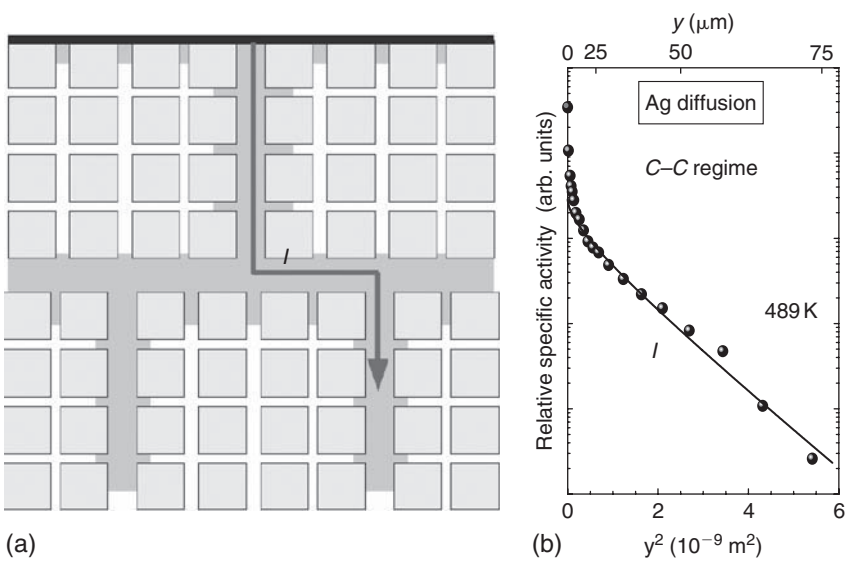

FIGURE 1.24 Scheme of diffusion flux I (a) and the corresponding penetration profile (b) measured for Ag diffusion in nano-FeNi alloy with the hierarchic microstructure in the *C–C* regime. The tracer (grey region) is mainly located in interagglomerate boundaries.

Figure 1.24b. Due to the small solid solubility of Ag in the FeNi alloy, the initial conditions corresponded to the thick layer solution and the error function fitting was applied to extract the diffusivity D_a of interagglomerate boundaries in that case. Due to the applied mechanical sectioning method, the nanocrystalline GB diffusivity D_{gb} could not be analysed in that experiment.

The C–B regime. With increasing temperature of diffusion anneals, the diffusion length along the nano-GBs increases and outdiffusion from the interagglomerate boundaries is becoming important, $\sqrt{D_{gb}t} \gg s_a \cdot d$. This introduces the formal *B* regime conditions for diffusion along the interagglomerate boundaries. However, since bulk diffusion is still suppressed, the *C* kinetic conditions assert for nano-GB diffusion. These conditions define the *C–B* diffusion regime in the material with a hierarchic interface structure.

In this diffusion regime, not the values s_a, δ_a or D_a, but only their product $P_a = s_a\delta_a D_a/\lambda$ can be determined from the penetration profiles. The specific feature of the interagglomerate boundaries is that outdiffusion does not proceed uniformly but only at positions where the nano-GBs intersect the interagglomerate boundaries. The density of such intersection points, λ, enters explicitly into the expression for the product P_a (for cubic grains $\lambda = 2\delta/d$). The diffusion length for diffusion along the nanocrystalline GBs, $\sqrt{D_{gb}t}$, should be smaller than the size d_a of the agglomerates in this regime (Figure 1.25a).

An example of such penetration profile measured for Fe diffusion in nano-γ-FeNi [122] is presented in Figure 1.25b. A two-stage shape of the penetration profile is clearly seen. The first part, which is characterized by the $\ln c \approx y^2$ depth

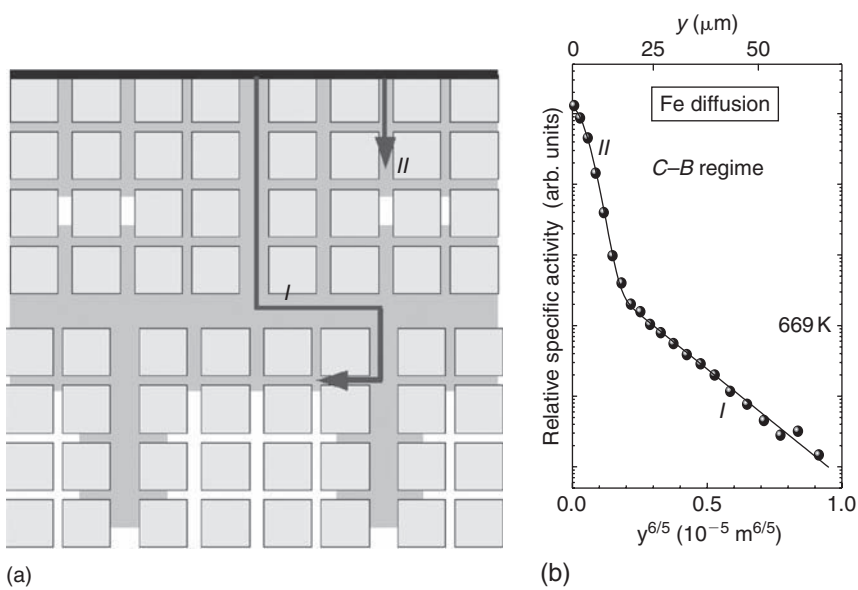

FIGURE 1.25 Scheme of diffusion fluxes I and II (a) and corresponding penetration profile (b) measured for Fe diffusion in nano-FeNi alloy with the hierarchic microstructure in the *C–B* regime. The tracer is located in interagglomerate interfaces and GBs between nanocrystallites.

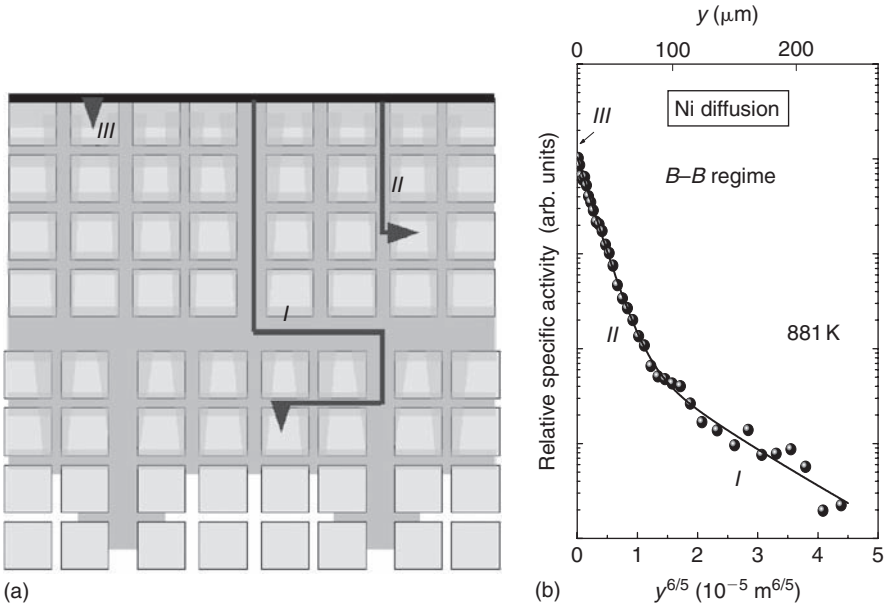

FIGURE 1.26 Scheme of diffusion fluxes I, II and III (a) and corresponding penetration profile (b) measured for Ni diffusion in nano-FeNi alloy with the hierarchic microstructure in the *B–B* regime. The part of the penetration profile corresponding to the flux III cannot be resolved by the applied serial sectioning technique due to small penetration depth of volume diffusion <100 nm.

dependence of the concentration profile (c is the layer tracer concentration and y the penetration depth), corresponds to nano-GB diffusion in the *C* regime. As a result, the nano-GB diffusivity D_{gb} can directly be determined from this part.

The second part of the penetration profile in Figure 1.25b corresponds to the faster diffusion mode from the surface into the interagglomerate boundaries with subsequent outdiffusion into adjacent nanocrystalline GBs. Since formal *B*-type conditions are fulfilled in this diffusion mode, the Suzuoka solution [126] of the interface diffusion problem has to be applied [123]. The solid line in Figure 1.25b represents the relevant fit. The diffusivity P_a of interagglomerate boundaries was determined for Fe, Ni and Ag diffusion in this regime [121,122,124].

The B–B regime. If temperature and/or time of the diffusion anneal increases further, the bulk diffusion flux becomes more significant and cannot be neglected. Then the diffusion process will be dominated by two fluxes (Figure 1.26a):

I. GB diffusion along the nanocrystalline GBs with subsequent outdiffusion into the grain interior; and
II. faster diffusion along interagglomerate boundaries with subsequent outdiffusion to nano-boundaries and then into the grains.

Since the bulk diffusion length, $\sqrt{D_v t}$, has to be smaller than the grain size to satisfy the conditions of this *B–B* regime, the total contribution of direct

volume diffusion from the sample surface into the nanograins can be neglected. Correspondingly, two-stage penetration profiles should be observed. An example of such a profile, which was measured for Ni diffusion in nano-γ-FeNi [121], is shown in Figure 1.26b.

The B regime conditions are satisfied for the flux (II). Therefore, the Suzuoka solution of the GB diffusion problem is applied to analyse this term [123]. As a result, the first part of the penetration profile should be linear in the coordinates of $\ln c$ *vs.* $y^{6/5}$ and only the triple product $P = s\delta D_{gb}$ can be determined, but not the nano-GB diffusivity D_{gb} itself. The parameter $\beta = P/2D_v\sqrt{D_v t}$ has to be large enough in order to observe a distinct GB diffusion-related tail. The effect of β on the accuracy in the determination of P was analysed by Monte-Carlo simulation of GB diffusion and $\beta \geq 2$ can be used as a lower limit of the B regime [120].

The diffusion flux (I) represents a fundamentally new situation, which was analysed for self- and solute diffusion, respectively [121,124]. The Fisher model [127] of interface diffusion was elaborated to the case of a hierarchic structure [121]. The analysis has shown that the logarithm of concentration c should linearly decrease with the penetration depth y. A more careful numerical solution of this diffusion problem resulted in a power-law dependence of the logarithm of concentration, $\ln c \approx y^n$, on $n \approx 1.05$ [121]. The relevant fitting of the experimental penetration profile allows the determination of the triple product P_a for inter-agglomerate boundary diffusion in the B–B regime: $P_a = s_a\delta_a D_a/\lambda$. The fit in Figure 1.26b describes the experimental points well, over almost four decades of decrease in concentration, supplying reliable data on both nano-GB and inter-agglomerate boundary diffusion.

The AB–B, A–B and A regimes. At higher temperatures, diffusion could proceed under conditions of the regimes AB–B, A–B or A. They were introduced and analysed in detail [121,124]. The temperature and time of diffusion annealing as well as the grain and agglomerate sizes determine the given kinetics. In these conditions, a substantial overlap of diffusion fluxes from individual nanocrystalline GBs is expected.

Since these conditions correspond to increased temperatures and long diffusion time, a substantial grain growth may be expected. The grain growth in nanocrystalline materials represents a serious problem, which may complicate analysis of diffusion or even result in incorrect data if it is not taken into account.

7.3.2 Effect of GB migration on diffusion

Grain boundary motion during diffusion annealing treatment changes the pertinent kinetic conditions. As a result, the penetration profiles become linear against depth instead of depth squared in the formal C kinetics [128]. Fortunately, in our investigation of diffusion in nanocrystalline γ-FeNi alloys, we were able to measure penetration profiles over four to six orders of magnitude in the concentration. Correspondingly, one can differentiate kinetic conditions even by the shape of penetration profiles (Figure 1.27).

In the particular case of Fe diffusion in the nanocrystalline-FeNi alloy, the GB motion was effectively suppressed and undisturbed interface diffusion has been measured at elevated temperatures. The penetration profiles presented in

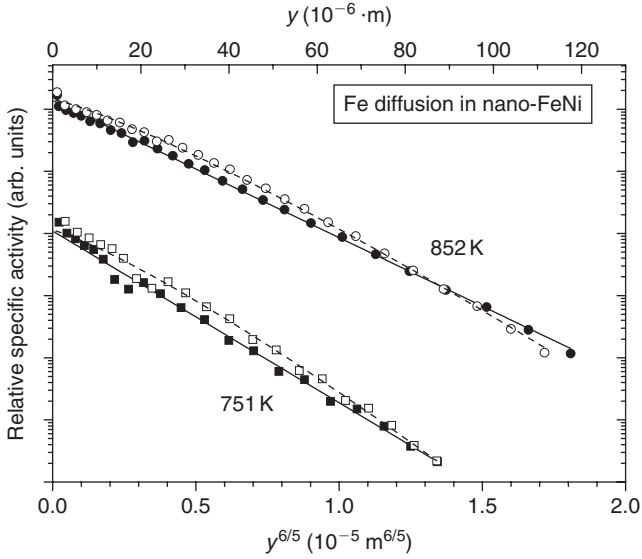

FIGURE 1.27 Penetration profiles plotted against depth *y* (open symbols, upper *x*-axis) and depth to the power 6/5 (full symbols, bottom *x*-axis). It is obvious that the profiles are systematically curved when plotted against depth and become almost linear against $y^{6/5}$ (as it is expected for the formal B-type conditions). The particular measurements of Fe diffusion were performed in the nanocrystalline FeNi alloy with hierarchic microstructure in the *C–B* regime.

Figure 1.27 provide strong support for the correctness of the diffusion measurements and data processing in such complex nanomaterials with a hierarchic microstructure.

7.3.3 Systematics of interface diffusion in nano-FeNi with a hierarchic microstructure

Diffusion of Fe, Ni and Ag in nanocrystalline γ-FeNi alloy was intensively measured in the extended temperature interval from about 500 to 1200 K. The penetration profiles were analysed according to the strict mathematical conditions of the given kinetic regimes. For the analysis of Fe and Ni diffusion, the relevant segregation factors s_{Fe} and s_{Ni} are close to unity. Fe and Ni show complete mutual miscibility in the γ-phase and one may expect only slight (if any) segregation of both Fe and Ni to internal interfaces in the γ-Fe–40wt% Ni alloy. On the other hand, Ag reveals very low solubility in FeNi and a strong Ag segregation to internal interfaces was established [124].

Since $s = s_a = 1$ for diffusion of Fe and Ni, it is relatively easy to identify the kinetic regime for self-diffusion. Ni diffusion in the nanocrystalline γ-FeNi alloy was measured in the kinetics *C–B*, *B–B*, *AB–B*, whereas Fe diffusion was analysed in the regimes *C–B*, *B–B*, *AB–B* and *A–B* (Figure 1.28a,b).

The nano-GB diffusivity D_{gb} was directly determined in the *C–B* and *AB–B* regimes. In the absence of segregation, the triple product *P* is reduced to the

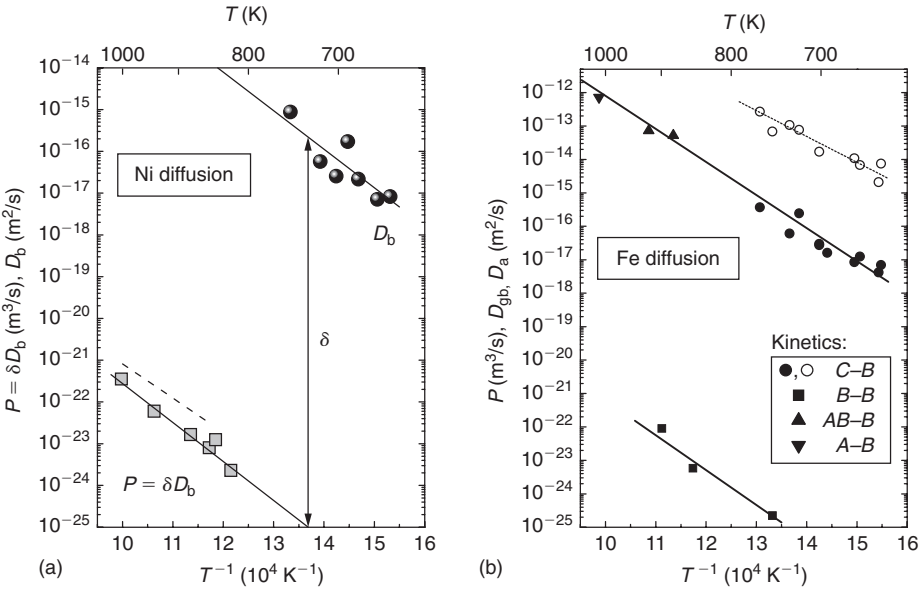

FIGURE 1.28 Arrhenius diagram for Ni [121] (a) and Fe [120,122] (b) diffusion in nanocrystalline γ-Fe-40wt% Ni alloy with the hierarchic microstructure. The filled symbols represent the diffusivity of nanocrystalline GBs and open symbols correspond to interagglomerate boundary diffusion. The comparison of the directly measured double product $P = \delta D_{gb}$ and the nano-GB diffusivity D_{gb} for Ni (a) and Fe (b) diffusion gives an estimate for the GB width, $\delta \approx 0.5$ nm. The dashed line in (a) represents the GB diffusivity of Ni in coarse-grained FeNi alloy [KLD04]. The estimate $\delta_a = 1$ nm was used to recalculate the measured P_a values to the relevant diffusivities D_a for Ni (a) and Fe (b) diffusion.

double product $P = \delta D_{gb}$. Having determined the double product P in the *B–B* regime and having measured D_{gb} directly, the GB width δ can be determined as $\delta = P/D_{gb}$.

In Figure 1.28a and b, the resulting values for Ni and Fe diffusion along nanocrystalline GBs are plotted as functions of the inverse temperature. It is obvious that the P values are systematically below the values of D_{gb}. It is the ratio P/D_b which is equal to the diffusion width of the GBs. The direct estimates give $\delta = (5.5 \pm 4.3) \times 10^{-10}$ m and $(7.3 \pm 5.2) \times 10^{-10}$ m for Ni and Fe diffusion, respectively. This value fits reasonably the commonly accepted value of the GB width, $\delta = 0.5$ nm [129]. This value of δ is used for the comparison of diffusion data derived in different kinetic regimes. The effective diffusivity $D^a{}_{eff}$ determined in the *A–B* kinetics gives the value of the nano-GB diffusivity $D_{gb} = 2D^a{}_{eff}/f_b$. Presenting the volume fraction of nano-GBs f_b as $f_b = \delta/d$ and using the same estimate of the GB width $\delta = 0.5$ nm, the diffusivity D_{gb} can be determined as: $D_{gb} = 2dD^a{}_{eff}/\delta$. The temperature dependencies of Ni and Fe diffusivities D_{gb} along nanocrystalline GBs are presented in Figure 1.28a and b, respectively (filled symbols; the kind of symbol depends on the given kinetic regime). Although Fe and Ni diffusion were

Table 1.1 Arrhenius parameters of self- and solute diffusion along nano-GBs and interagglomerate boundaries in nanocrystalline γ-FeNi alloy

Tracer	GBs between nanocrystallites				Interagglomerate interfaces		Reference
	$P_0 = s\delta D_0$ (m³/s)	Q_{gb} (kJ/mol)	D_0 (m²/s)	H_{gb} (kJ/mol)	$P_0 = \delta_a D^a{}_0/\lambda$ (m³/s)	Q_a (kJ/mol)	
Fe	3.2×10^{-12}	189	6.4×10^{-3}	189	3.4×10^{-13}	148	[122]
Ni	4.6×10^{-13}	177	9.2×10^{-4}	177	1.9×10^{-13}	134	[121]
Ag	8.1×10^{-14}	126	4.7×10^{-4}	173	4.8×10^{-13}	91	[124]

measured in very different kinetic regimes and different mathematical treatments were applied in different regimes, the results show a systematic behaviour and the nano-GB diffusivity follows an Arrhenius type of temperature dependence in an extended interval. The relevant Arrhenius parameters are listed in Table 1.1.

In Figure 1.28a, the Ni GB diffusivity in coarse-grained γ-FeNi alloy [130], which is of similar composition to the nano-γ-FeNi alloy, is plotted in comparison with diffusion in nano-γ-FeNi. Ni diffusion in both materials was found to be similar. In the nanocrystalline material (the grain size $d \approx 100$ nm), the GB structure is well relaxed and is similar to that in the coarse-grained material.

Diffusion in interagglomerate boundaries was measured in the *C–B* kinetics for Fe tracer and in the *C–B*, *B–B* and *AB–B* kinetics for Ni tracer. The diffusivity of the interagglomerate boundaries is much faster than that of nanocrystalline boundaries and the activation enthalpy Q_a is remarkably smaller. The value of Q_a (especially for Ni diffusion) approaches values of activation enthalpies which are typical for surface diffusion. This behaviour is related to an increased free volume at such boundaries [121].

Ag diffusion in the nanocrystalline γ-FeNi was measured in various diffusion regimes. The succession of the kinetics *C–C*, *C–B*, *AB–B* and *A* was observed and the diffusivities of both nano-GBs and interagglomerate boundaries were determined.

The diffusivity D_{gb} of the nanocrystalline GBs was directly determined in the *C–B* kinetics. In order to establish the limits of relevant kinetic regimes and to analyse the experimental data, the knowledge of the segregation factor s is imperative. Due to the strong segregation, it was impossible to measure GB diffusion of Ag under formal B kinetic conditions with the aim to estimate the pertinent segregation factor s (see the case of special ultrafine grained material [100]).

This fundamental difficulty was overcome by the *B*-type GB diffusion measurements in the coarse-grained material of the same chemical composition (with a remarkably larger value of the grain size d). The key point is that the close similarity between Ni self-diffusion in the coarse-grained and nanocrystalline γ-FeNi alloy suggests similar GB structures in these materials. The measurements of Ag diffusion in the coarse-grained γ-FeNi alloy yielded the triple product $P = s\delta D_{gb}$ as a function of temperature (diamonds in Figure 1.29). The data on P for Ag diffusion (determined for the coarse-grained material) can thus be combined

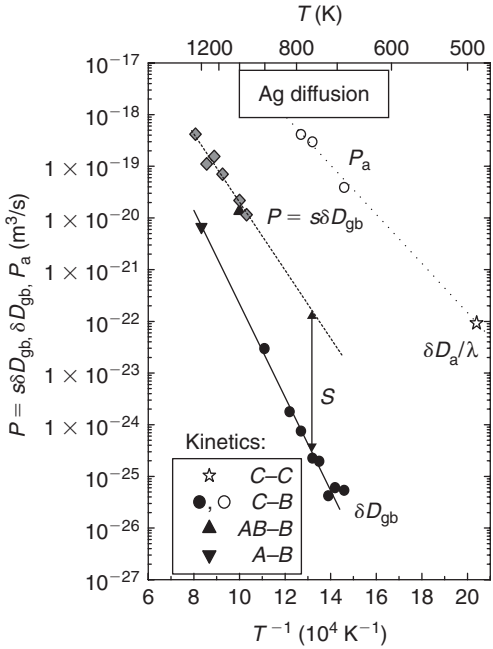

FIGURE 1.29 Arrhenius diagram for Ag [124] interface diffusion in nanocrystalline γ-Fe-40wt% Ni alloy. Filled symbols represent the diffusivity of nanocrystalline GBs and open symbols correspond to interagglomerate boundary diffusion. The estimate $\delta_a = 1$nm was used to recalculate measured P_a values to the relevant diffusivities D_a. The triple product P for Ag diffusion in coarse-grained FeNi alloy is also shown (diamonds). The method of calculation of the segregation factor s for Ag in FeNi is illustrated.

with the direct data on D_{gb} (determined for the nanocrystalline material). As a result, the temperature dependence of the segregation factor s can be derived (Figure 1.29). Taking $\delta = 0.5$nm, as it follows from direct measurements for Ni and Fe diffusion in *the same* material (see above), the following expression was derived:

$$s = 0.35 \times \exp\left\{-\frac{-47\,\mathrm{kJ/mol}}{RT}\right\} \tag{1.11}$$

Ag segregates strongly at GBs in the γ-Fe-40wt% Ni alloy, e.g. $s = 1000$ at $T \approx 700$K. The Arrhenius parameters of Ag nano-GB diffusion in the nano-γ-FeNi alloy are given in Table 1.1.

Having determined the segregation factor s, a special GB diffusion experiment in the nanocrystalline material was designed, in which the conditions of the *AB–B* kinetics were satisfied (the *B–B* kinetics cannot be fulfilled for formal reasons). For this purpose, the time and temperature of the diffusion anneal have to be chosen very carefully. The value determined for sD_{gb} is multiplied by the GB width δ and is plotted in Figure 1.29 (triangle up). Almost perfect agreement with the data of $P = s\delta D_{gb}$ measured in coarse-grained material (diamonds) is obtained (Figure 1.29).

This fact supports the conclusion that the diffusivities of the nanocrystalline ($d \approx 100$ nm) and coarse-grained ($d \approx 0.5$ mm) materials are very similar.

Ag diffusion along the interagglomerate boundaries proceeds much faster than along the nano-GBs (Figure 1.29, open symbols). Having determined $P_a = s_a\delta_a D_a/\lambda$ and D_a separately in the *C–B* and *C–C* regimes, respectively, the factor $s_a\delta_a/\lambda$ can be estimated. Taking λ as $\lambda = 2\delta/d$ with $\delta = 0.5$ nm and $d = 100$ nm, an upper estimate of the product $s_a\delta_a$ is obtained, $s_a\delta_a \approx 1$ nm. Since the interagglomerate boundaries present a more open structure with respect to the nano-GBs, the value of $\delta_a \approx 1$ nm seems to be a good estimate [124]. Thus, the segregation factor s_a for Ag seems to be about unity. This means that there is practically no excess of Ag atoms in the interagglomerate boundaries with respect to the nanocrystalline GBs, Eq. (1.4) and the segregation behaviour of these two internal interfaces with respect to the bulk is similar. In Figure 1.29, the value of D_a measured in the *C–C* regime is multiplied by the factor δ_a/λ (using the estimates $\delta_a = 1$ nm and $\lambda = 0.01$) for comparison with the P_a values measured in the *C–B* regime (open star and circles, respectively). Assuming $s_a = 1$, the temperature dependence of P_a can be presented by the linear Arrhenius relationship (Table 1.1 and dotted line in Figure 1.29).

The whole amount of diffusion data supports the conclusion that the diffusivity of nano-GBs in the present nanocrystalline material (grain size $d \approx 100$ nm) is similar to that of conventional grain boundaries in coarse-grained material. The reason is the grain growth which occurred in the present nano-material during the sintering process (from 30 to $\approx$100 nm) which contributed crucially to relaxation of the nano-GB structure.

The presence of interagglomerate boundaries in the present material affected considerably the diffusion processes and altered the kinetic regimes of interface diffusion in the material. These interagglomerate boundaries present the fastest short-circuit diffusion paths in the material and therefore have to be taken into account in the analysis of diffusion and sintering processes in nano-alloys produced by the powder metallurgy method. Moreover, establishing an optimum size of agglomerates provides a unique route to optimize the functional properties of the materials and to decrease the sintering temperature significantly [118].

7.4 Diffusion after Severe Plastic Deformation

Recently, severe plastic deformation (SPD) processes have been studied extensively due to their potential to produce full density fine-grained structures with attractive and rather unusual mechanical properties [86,131]. The grain sizes achieved so far for pure and rather ductile metals such as Cu, Ni or Ti are actually outside the nanocrystalline regime, in the range of about 150–350 nm for most SPD methods. With repeated cold rolling and folding, however, quite large samples are synthesized in nanocrystalline form with extremely small grain size (down to tens of nanometres) without application of a high hydrostatic pressure [132].

It has been claimed in the literature that, because of high dislocation activity during severe plastic deformation, the grain boundaries in the final ultrafine microstructure exhibit higher energy, higher density of extrinsic grain boundary dislocations, higher excess volume and higher microstrain than their counterpart in

coarse-grained material [95]. Thus, these non-relaxed GBs have been termed *non-equilibrium GBs*. Most phenomenological and structural models of non-equilibrium GBs are based on dislocation-GB interaction. According to Nazarov et al. [133], the non-equilibrium GBs evolved from cell boundaries by absorbing lattice dislocations during plastic deformation. These dislocations are stored in non-periodic, disordered arrays that result in long-range stress fields associated with such newly formed GBs. In spite of the fact that the hypothesis of non-equilibrium grain boundaries is quite plausible, its unequivocal experimental proof is still lacking.

Lian et al. [134] have estimated the parameters of GB self-diffusion in severely deformed Cu from the grain growth kinetics. The corresponding activation enthalpy was about 71 and 107 kJ/mole at low and higher temperatures, respectively. The increase of the activation enthalpy was considered to result from relaxation of the non-equilibrium structure of GBs. However, these data can also be interpreted in terms of an impurity effect on GB self-diffusion in copper: the newly created GBs after severe plastic deformation are relatively free from residual impurities and their segregation can be induced by subsequent heat treatment at higher temperatures. An activation enthalpy of 72 kJ/mol was measured for GB self-diffusion in high-purity copper, whereas this value increased to 80–90 kJ/mol for copper of lesser purity [105].

The creep measurements in UFG Cu of technical purity yielded also higher values of the creep rate than expected from the measurements on coarse-grained materials in conditions of GB sliding-controlled creep [135]. This indicates an enhanced diffusivity of the non-equilibrium GBs. Model-based estimates of the GB diffusivity from the creep data resulted in numerical values of the activation enthalpies for GB diffusion of about 70–78 kJ/mole. These are the values of GB self-diffusion in high-purity coarse-grained copper. Thus, a direct verification of enhanced diffusivities in highly-deformed materials due to the structure of the GBs is still missing.

There exist several investigations of GB diffusion in materials produced by severe plastic deformation [136–139]. Using secondary ion mass spectroscopy (SIMS), diffusion of Cu was exemplarily studied in nanostructured Ni produced by ECAP [137]. It was concluded that copper diffuses along GBs of the nanostructured material by several orders of magnitude faster than in coarse-grained material. On the other hand, annealing treatments before the diffusion experiment allowed GB relaxation and, as a result, similar diffusion rates were observed in both materials [136,137]. However, these conclusions should be treated with caution, since only shallow penetration profiles were recorded in the corresponding measurements. In contrast with the above reports, Würschum et al. [138] have found that the GB diffusivity of ^{59}Fe in UFG Pd was comparable with that for coarse-grained Pd. Similarly, Fujita et al. [140] observed no enhanced diffusivity in ECAP-processed UFG Al and Al-3wt% Mg alloy containing small precipitates that stabilized the UFG microstructure against grain growth. Therefore, if non-equilibrium GBs exist in the as-deformed state, they may rapidly relax during the initial stages of the diffusion anneals in the considered cases of UFG Pd and Al.

Recently, GB diffusion in ECAP-produced UFG Cu–0.17wt% Zr alloy was investigated [139]. The addition of Zr was used to stabilize the microstructure of the UFG

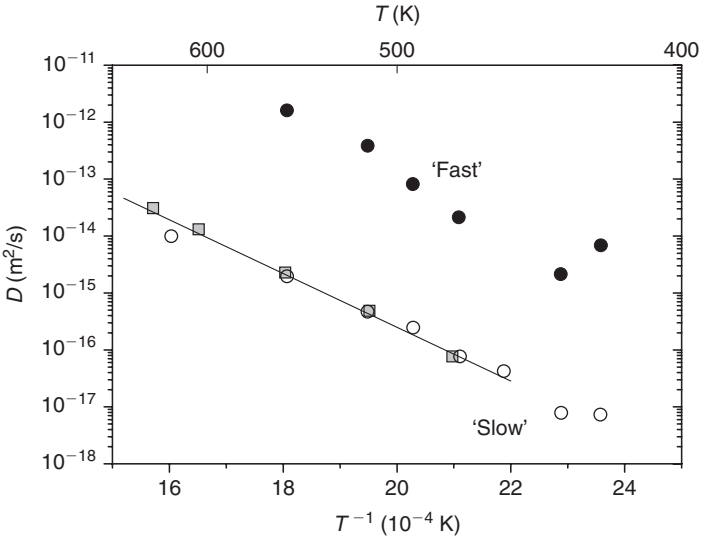

FIGURE 1.30 GB diffusion of Ni in UFG Cu–0.17wt% Zr alloy deformed by ECAP [139] (circles) in comparison to the Ni diffusivity in high-purity coarse-grained Cu [108] (squares). The diffusivities of 'slow' (open circles) and 'fast' (full circles) short-circuit diffusion paths in UFG Cu alloy are shown.

alloy in the range of temperatures and annealing times suitable for GB diffusion measurements. The main finding is a clear bimodality of the GB diffusivities in the severely deformed UFG Cu–0.17wt% Zr alloy: while the majority of GBs exhibit the diffusivities which are very close to those of HAGBs in high purity coarse-grained copper, there is a fraction of GBs which exhibit unusually high diffusivities. The detailed analysis of diffusion data allowed proposing a model of GB character distribution in a severe plastically deformed material. It was concluded that the 'fast' GBs are well separated from each other and form a micrometre-large skeleton embedded in the network of 'slow' GBs. The space separating the latter corresponds to the grain size of the UFG material, namely several hundred nanometres. This hierarchic model resembles the situation observed in the nanocrystalline FeNi alloy produced by pressureless sintering as considered above, although the nature of the 'fast' diffusion paths is completely different in these two cases.

The diffusion along the 'fast' GBs was found to be faster by more than two orders of magnitude than along the 'slow' GBs (Figure 1.30). One should not be misled by the term 'slow' – these interfaces are not, for example, twin or low-angle GBs in a form as they occur in a well-annealed coarse-grained material. Although the short-circuit diffusion paths with a lower diffusivity are referred to as 'slow' paths, they are not 'slow' at all in absolute terms – their diffusivity is similar to that for general high-angle GBs in coarse-grained high-purity copper, where these are the *fastest* short-circuit diffusion paths (Figure 1.30).

Whereas agglomerate formation can naturally occur in ball-milled and sintered powder materials, what can be a reason for the strong bimodality of the GB

diffusivities in a material after severe plastic deformation? Amouyal et al. [139] have associated the major part of the 'fast' GBs with the original high-angle GBs in the coarse grain ingots which existed in the samples prior to severe deformation. Such GBs accumulate additional dislocations and evolve to non-equilibrium GBs during the deformation process. The non-equilibrium state of some of the GBs after ECAP was recently supported by scanning force microscopy measurements of the relative GB energy in severe plastically deformed Cu [141]. Thus, the newly formed high-angle GBs are then likely to represent the network of 'slow' GBs in the UFG copper.

The diffusion measurements [139] suggest that 'slow' short-circuit diffusion paths in the UFG CuZr alloy have diffusivities very similar to those of conventional high-angle GBs in coarse-grained copper (see Figure 1.30). The investigation of Amouyal et al. [139] indicates the strong heterogeneity of GB diffusivities in a heavily deformed material. A similar conclusion was made for hydro-extruded Al [142]. Although this fact complicates the direct comparison of the diffusion data in UFG and coarse-grained materials, reliable conclusions can be drawn only after detailed investigation of the microstructure and extended diffusion measurements.

Is it theoretically possible to measure the diffusion contribution of non-equilibrium GBs? According to Nazarov [143] the relaxation time τ of the non-equilibrium state of GBs can be represented by:

$$\tau = \frac{kTd^3}{A\delta G\Omega D_{\mathrm{gb}}} \tag{1.12}$$

where d and δ are the grain size and the GB width, G the shear modulus, Ω the atomic volume and A the numerical factor, which depends on the specific model of the relaxation and is about 150. The direct estimations for copper give rise to a small value of $\tau = 1$ s at $T = 200$°C and even $\tau = 2.3 \times 10^4$ s at room temperature. The diffusion times are typically considerably larger than τ [139]. First, the absorption of lattice dislocations by non-equilibrium GBs in highly deformed UFG material is not included in the derivation of Eq. (1.12). Secondly, as was estimated in Amouyal et al. [139], the relaxation times of diffusion-controlled climb processes were larger than the actual annealing times mainly due to the fact that the driving force for climb of GB dislocations is associated with the elastic interaction between them which rapidly decreases with increasing dislocation spacing. At the same time, the entropic driving force for radiotracer diffusion is decoupled from the short-range elastic fields and can drive the diffusing atoms over distances which are one to two orders of magnitude larger than the average grain size. Therefore, the pre-existing GBs could at least partially preserve an increased density of GB dislocations (beyond that of the geometrically necessary number density) and associated with it a large excess free volume and high diffusivity during the whole duration of diffusion annealing.

The investigation of GB diffusion in a pure metal with a UFG microstructure can be significantly complicated by simultaneous recrystallization. This problem has recently been considered for Ni diffusion in UFG Cu produced by ECAP [144]. The detailed analysis of the microstructures obtained after annealing treatments

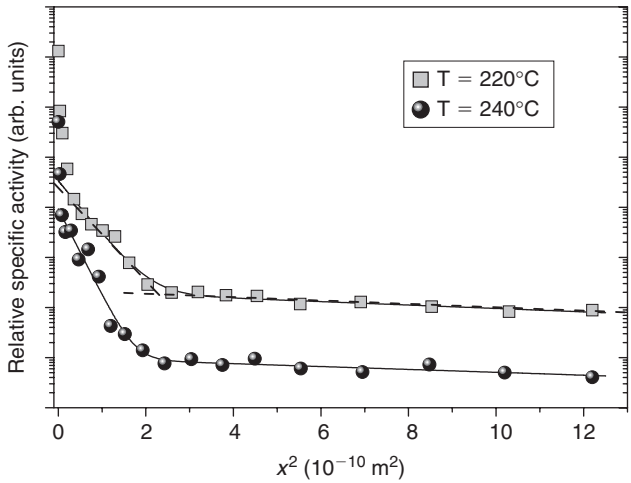

FIGURE 1.31 Penetration profiles measured exemplarily for Ni diffusion in nanostructured Cu produced by ECAP [S. Divinski et al., personal communication]. The contributions of two short-circuit diffusion paths are seen (the two dashed lines for the profile measured at $T = 220°C$). x is the penetration depth. The bulk diffusion length is less than 1 nm and the solid lines represent the only short-circuit diffusion contributions.

at different times and temperatures allowed a quantitative description of the recrystallization kinetics in terms of the Johnson–Mehl–Avrami–Kolmogorov (JMAK) formalism. Using the JMAK-type expression for the volume fraction of the recrystallized area, a model that considers simultaneous diffusion and recrystallization was developed. This model enables quantitative derivation of the diffusion parameters from experimentally measured penetration profiles [144].

The experimentally measured penetration profiles exhibited two distinct branches with different slopes [S. Divinski et al., personal communication] (Figure 1.31) and were quite similar to those observed earlier in the thermally stable Cu–0.17wt% Zr alloy [139]. The similarity of diffusion penetration profiles measured in the structurally stable CuZr alloy [139] and in pure Cu [144] [S. Divinski et al., personal communication] implies that a hierarchical microstructure is typical for UFG materials produced by ECAP.

The enhanced diffusivity of nanocrystalline materials was also proposed to be explained by the contribution of triple junctions [113,145]. Quantitative estimates [113] indicate that triple junction diffusion can formally explain anomalies of several orders of magnitude in materials with a very small grain size, of the order of 10 nm. However, there is presently no direct experimental evidence of the importance of the triple junction contribution to the diffusion phenomena in nanomaterials. A comprehensive study of the grain size dependence of diffusivity of nanomaterials could provide further insight into this problem.

In summary, the investigations concerning the atomic mobility within nanocrystalline materials indicated that the grain boundaries of nanocrystalline materials *per se* are not different from common high angle grain boundaries in conventional coarse-grained materials. Yet, no matter what synthesis method was

used, the existence of a distribution of the properties of internal interfaces was observed. As far as diffusion is concerned, the presence of fast pathways for matter transport open up new opportunities for shape forming at low temperatures and comparably low stresses. However, concerning an in-depth description of the relation between the microstructure of nanocrystalline materials and their associated properties, immediate questions concerning the dependence of these 'unusual' internal interfaces on the synthesis and processing routes or concerning the impact of the presence of 'fast' grain boundaries on the stability of the microstructure and on the homogeneity of the grain size distribution need to be addressed.

8. SUMMARY

New routes for nanostructure formation are presented by sequentially combining different non-equilibrium processing pathways that are based, for example, on rapid cooling or continuous strain energy input. The available permutations offer a wide range of options for tailoring the microstructure and the shape and quantity of the product nanostructure and, at the same time, present a wide field yet to be explored. Moreover, these strategies allow the preparation of stable, metastable or even unstable product phases with bulk shape and with properties that are improved or even completely unique. One basic requirement for any application of these advanced materials is their stability under loading conditions as well as their reliability characteristics. While a broad range of basic issues still need to be addressed concerning the coupling between stabilization strategies and materials properties, it seems clear that a composite approach that enables an effective diffusion control is suitable and most probably also necessary. In this respect – concerning the synthesis of nanostructured composites – solid-state processing methods seem especially suitable.

However, as shown in the previous sections, there are several aspects concerning the thermodynamic stability and the interface diffusion that are drastically affected by the presence and atomic structure of heterophase interfaces as well as by the selection of the synthesis and processing pathways. The modification of phase stabilities and phase diagrams for nanostructured materials as well as the seemingly inherent presence of high-mobility interfaces have to be described in detail, since these important characteristics have to be regarded for utilizing these new materials in any engineering application. At the same time, the observed behaviour, such as a shift of the melting temperature either to higher or to lower temperature depending solely on the atomic structure of the interface or the presence of interfaces with diffusivities that are several orders of magnitude higher than usual, again apparently depending simply on the atomic-scale structure of the interface, highlights the future potential and the newly available range of opportunities for property modification that is uniquely offered by the class of nanocrystalline materials.

ACKNOWLEDGEMENTS

The continuous financial support by the Deutsche Forschungsgemeinschaft is gratefully acknowledged. The authors would like to thank all the colleagues

and co-workers who have contributed to this topic over the past years for their collaboration and stimulating discussions, in particular Drs N. Boucharat (Münster, Germany), G.P. Dinda (Ann Arbor, USA), H. Gleiter, H. Hahn, J. Weissmüller (Karlsruhe, Germany), J.H. Perepezko (Madison, USA) and R. Valiev (Ufa, Russia).

References

1. Xie FQ, Nittler L, Obermair C, Schimmel T. Phys. Rev. Lett. 2004; 93:128303.
2. Hahn H. Adv. Eng. Mater. 2003; 5:277.
3. Brunner C, Ernst KH, Hess H, Vogel V. Nanotechnology 2004; 15:S540.
4. Keren K, Krueger M, Gilad R, Ben-Yoseph G, Sivan U, Braun E. Science 2002; 297:72.
5. Gleiter H. Acta Mater. 2000; 48:1.
6. Gleiter H. Nanostruct. Mater. 1995; 6:3.
7. Herzer G. IEEE Trans. Magn. 1990; 26:1397.
8. Weissmüller J, Lemier C. Phys. Rev. Lett. 1999; 82:213.
9. Cahn RW. Nature 1986; 323:668.
10. Valiev RZ, Krasilnikov NA, Tsenev NK. Mater. Sci. Eng. A 1991; 137:35.
11. Valiev RZ, Korznikov AV, Mulyukov RR. Mater. Sci. Eng. A 1993; 168:141.
12. Wilde G, Dinda GP, Rösner H. Adv. Eng. Mater. 2005; 7:11.
13. Dinda GP, Rösner H, Wilde G. Scripta Mater. 2005; 52:577.
14. Wilde G, Boucharat N, Dinda GP, Rösner H, Valiev RZ. Mater. Sci. Forum 2006; 503–504:425.
15. Ehrhardt H, Weissmüller J, Wilde G. Mater. Res. Soc. Symp. Proc. 2001; 634:B8.6.1.
16. Dinda GP, Rösner H, Wilde G. Solid State Phenom. 2005; 101–102:55.
17. Kim YH, Inoue A, Masumoto T. Mater. Trans. JIM 1990; 32:599.
18. Chen H, He Y, Shiflet GJ, Poon SC. Scripta Metall. Mater. 1991; 25:1421.
19. Croat JJ, Herbst JF, Lee RW, Pinkerton FE. J. Appl. Phys. 1984; 55:2078.
20. Suzuki K, Kataoka N, Inoue A, Masumoto T. Mater. Trans. JIM 1991; 32:93.
21. Greer AL. Science 1995; 267:1947.
22. Allen DR, Foley JC, Perepezko JH. Acta Mater. 1998; 46:431.
23. Wilde G, Boucharat N, Hebert RJ, Rösner H, Tong S, Perepezko JH. Adv. Eng. Mater. 2003; 5(3):125–130.
24. Boucharat N, Hebert RJ, Rösner H, Valiev RZ, Wilde G. Scripta Mater. 2005; 53:823–828.
25. Boucharat N, Rösner H, Wilde G. J. Non-Crystalline Solids 2008; 354:592–596.
26. Lu K. Mater. Sci. Eng. 1996; R16:161–221.
27. Rösner H, Schloßmacher P, Shelyakov AV, Glezer AM. Acta Mater. 2001; 49:1541.
28. Hebert RJ, Perepezko JH, Rösner H, Wilde G. Scripta Mater. 2006; 54:25–29.
29. Haider M, Uhlemann S, Schwan E, Rose H, Kabius B, Urban K. Nature 1998; 392:768.
30. Rose H. Optik 1971; 33:1.
31. Van Swygenhoven H, Derlet PM, Hasnaoui A. Phys. Rev. B 2004; 66: 024101.
32. Derlet PM, Van Swygenhoven H, Hasnaoui A. Phil. Mag. A 2003; 83:3569.
33. Schiøtz J, Jacobsen KW. Science 2003; 301:1357.
34. Yamakov V, Wolf D, Phillpot SR, Gleiter H. Acta Mater. 2003; 51:4135.
35. Argon AS, Yip S. Phil. Mag. Lett. 2006; 86:713.
36. Schiøtz J, Di Tolla FD, Jacobsen KW. Nature 1998; 391:561.
37. Wolf D, Yamakov V, Phillpot SR, Mukherjee AK, Gleiter H. Acta Mater. 2005; 53:1.
38. Chokshi AH, Rosen A, Karch J, Gleiter H. Scripta Metall. 1989; 23:1679.
39. Karch J, Birringer R, Gleiter H. Nature 1987; 330:556.
40. Yamakov V, Wolf D, Phillpot SR, Mukherjee AK, Gleiter H. Nat. Mater. 2002; 1:45.
41. Hahn H, Padmanabhan KA. Phil. Mag. B 1997; 76:559.
42. Markmann J, Bunzel P, Rösner H et al. Scripta Mater. 2003; 49:637.
43. Yamakov V, Wolf D, Salazar M, Phillpot SR, Gleiter H. Acta Mater. 2001; 49:2713.
44. Yamakov V, Wolf D, Salazar M, Phillpot SR, Gleiter H. Acta Mater. 2002; 50:61.
45. Yamakov V, Wolf D, Phillpot SR, Gleiter H. Acta Mater. 2002; 50:5005.

46. Derlet PM, Hasnaoui A, Van Swygenhoven H. Scripta Mater. 2003; 49:629.
47. Van Swygenhoven H, Derlet PM. Phys. Rev. B 2001; 64, 224105.
48. Van Swygenhoven H, Derlet PM, Hasnaoui A. Phys. Rev. B 2002; 66: 024101.
49. Van Swygenhoven H, Derlet PM, Hasnaoui A. Adv. Eng. Mater. 2003; 5:345.
50. Rösner H, Markmann J, Weissmüller J. Phil. Mag. Lett. 2004; 84:321.
51. Hugo RC, Kung H, Weertman JR, Mitra R, Knapp JA, Follstaedt DM. Acta Mater. 2003; 51:1937.
52. Mitra R, Chiou W-A, Weertman JR. J. Mater. Res. 2004; 19:1029.
53. Kumar KS, Suresh S, Chisholm MF, Horton JA, Wang P. Acta Mater. 2003; 51:387.
54. Shan ZW, Stach EA, Wiezorek JMK, Knapp JA, Follstaedt PM, Mao SX. Science 2004; 305:654.
55. Williamson GK, Hall WH. Acta Metall. 1953; 1:22.
56. Suzuki J. Opt. Soc. Am. A 1996; 13:1495.
57. Hÿtch MJ. Microsc. Microanal. Microstruct. 1997; 8:41.
58. Hÿtch MJ, Snoeck E, Kilaas R. Ultramicroscopy 1998; 74:131.
59. Hÿtch MJ, Putaux J-L, Thibault J. Phil. Mag. 2006; 86:4641.
60. Stahl B, Gajbhiye NS, Wilde G et al. Adv. Mater. 2002; 14:24.
61. Weissmüller J, Bunzel P, Wilde G. Scripta Mater. 2004; 51:813.
62. Buffat Ph, Borel J-P. Phys. Rev. A 1976; 13:2287.
63. Johnson E, Andersen HH, Dahmen U. Microsc. Res. Techniq. 2004; 64:356.
64. Chattopadhyay K, Goswami R. Prog. Mater. Sci. 1997; 42:287.
65. Mei QS, Lu K. Prog. Mater. Sci. 2007; 52:1175.
66. Moore KI, Chattopadhyay K, Cantor B. Proc. Roy. Soc. Lond. A 1987; 414:499.
67. Zhang DL, Cantor B. Acta Metall Mater. 1991; 39:1595.
68. Sheng HW, Ren G, Peng LM, Hu ZQ, Lu K. Phil. Mag. Lett. 1996; 73:179.
69. Moore KI, Zhang DL, Cantor B. Acta Metall. Mater. 1990; 38:1327.
70. Sheng HW, Lu K, Ma E. NanoStruc. Mater. 1998; 10:865.
71. Gabrisch H, Kjeldgaard L, Johnson E, Dahmen U. Acta Mater 2001; 49:4259.
72. Rösner H, Scheer P, Weissmüller J, Wilde G. Phil. Mag. Lett. 2003; 83:511.
73. Rösner H, Weissmüller J, Wilde G. Phil. Mag. Lett. 2004; 84:673.
74. Rösner H, Weissmüller J, Wilde G. Phil. Mag. Lett. 2006; 86:623.
75. Rösner H, Freitag B, Wilde G. Phil. Mag. Lett. 2007; 87:341.
76. Weissmüller J. Nanostruct. Mater. 1993; 3:61.
77. Wulff GZ. Krystallogr 1901; XXXIV:449.
78. Wilde G, Bunzel P, Rösner H, Weissmüller J. J. Alloys Comp. 2007; 434–435:286–289.
79. Wilde G. Surface Interface Anal. (SIA) 2006; 38:1047–1062.
80. Jesser WA, Shiflet GJ, Allen GL, Crawford JL. Mater. Res. Innovat. 1999; 2:211.
81. Lee JG, Mori H. Phil. Mag. 2004; 84:2675.
82. Bunzel P, PhD-Thesis, Saarland University, 2004.
83. Bunzel P, Wilde G, Rösner H, Weissmüller J. In Solidification and Crystallization, DM Herlach (ed.). Wiley: Weinheim, 2004; 157–165.
84. Kaur I, Mishin Y, Gust W. Fundamentals of grain and interphase boundary diffusion. Wiley: Chichester, 1995.
85. Estrin Y, Gottstein G, Shvindlerman LS. Scripta Mater. 2004; 50:993.
86. Valiev R. Nature Mater. 2004; 3:511–516.
87. Valiev RZ, Razumovskii IM, Sergeev VI. Phis. Status Solidi 1993; 139:321–335.
88. Fan HJ, Knez M, Scholz R et al. Nano Lett. 2007; 7:993–997.
89. Gas P, Girardeaux C, Mangelinck D, Portavoce A. Mater. Sci. Engin. B 2003; 101:43–48.
90. Beke DL, Erdelyi Z, Langer GA, Csik A, Katona GL. Vacuum 2005; 80:87–91.
91. Birringer R, Gleiter H, Klein HP, Marquardt P. Phys. Lett. A 1984; 102:365.
92. Gleiter H. Phys. Stat. Sol., B 1992; 17:241.
93. Gleiter H. Z. Metallknd. 1995; 86:78.
94. Würschum R, Herth S, Brossmann U. Adv. Eng. Mater. 2003; 5:365.
95. Ovid'ko IA. Int. Mater. Rev. 2005; 50:65.
96. Stolwijk NA, Poisson C, Bernardini J. J. Phys. 1996; 8:5843.
97. Harrison LG. Trans. Faraday Soc. A 1961; 8:1191–1197.
98. Gibbs GB. Phys. Stat. Sol. 1966; 16:K27.

99. Kaur I, Gust W, Kozma L. Handbook of grain and interphase boundary diffusion data. Ziegler Press: Stuttgart, 1989.
100. Mishin Y, Herzig C. Nanostruct. Mater. 1995; 6:859–862.
101. Divinski S, Lee JS, Herzig C. J. Metastable Nanostr. Mater. 2004; 19:55.
102. Horváth J, Birringer R, Gleiter H. Solid State Communs. 1987; 62:319.
103. Schumacher S, Birringer R, Strauss R, Gleiter H. Acta Metall. 1989; 37:2485.
104. Höfler HJ, Averback RS, Hahn H, Gleiter H. J. Appl. Phys. 1993; 74:3832.
105. Surholt T, Herzig C. Acta Mater. 1997; 45:3817.
106. Divinski S, Lohmann M, Herzig C. Acta Mater. 2001; 49:249.
107. Divinski S, Lohmann M, Herzig C. Acta Mater. 2001; 52:3973.
108. Divinski S, Ribbe J, Schmitz G, Herzig C. Acta Mater. 2007; 55:3337–3346.
109. Herth S, Michel T, Tanimoto et al. Defect Diffusion Forum 2001; 94:199–204.
110. Würschum R, Michel T, Scharwaechter P, Frank W, Schaefer HE. Nanostruct. Mater. 1999; 12:555–558.
111. Herth S, Eggersmann M, Eversheim PD, Würschum R. J. Appl. Phys. 2004; 95:5075–5080.
112. Eggersmann M, Ye A, Herth S, Gutfleisch O, Würschum R. Interface Sci. 2001; 9:337.
113. Chen Y, Schuh CA. Scripta Mater. 2007; 57:253–256.
114. Zhang HD, Jiang ZH, Lian JS, Jiang Q. Adv. Engineer. Mater. 2008; 10:41–45.
115. Shen YF, Lu L, Dao M, Suresh S. Scripta Mater. 2006; 55:319–322.
116. Heitjans P, Indris S. J. Phys. Condensed Matter 2003; 15:R1257–R1289.
117. Heitjans P, Indris S. J. Mater. Sci. 2004; 39:5091–5096.
118. Lee J-S, Cha B-H, Kang Y-S. Adv. Engin. Mater. 2005; 7:467–473.
119. Knorr P, Nam JG, Lee JS. Metall. Mater. Trans. 2000; A31:503–510.
120. Divinski S, Hisker F, Kang YS, Lee JS, Herzig C. Z. Metallk. 2002; 93:256.
121. Divinski S, Hisker F, Kang YS, Lee JS, Herzig C. Interface Sci. 2003; 11:67.
122. Divinski S, Hisker F, Kang YS, Lee JS, Herzig C. Z. Metallk. 2002; 93:265.
123. Balandin IL, Bokstein BS, Egorov VK, Kurkin PV. Nanostruct. Mater. 1997; 8:37.
124. Divinski S, Hisker F, Kang YS, Lee JS, Herzig C. Acta Mater. 2004; 52:631.
125. Divinski SV, Geise J, Rabkin E, Herzig C. Z. Metallk. 2004; 95:945–952.
126. Suzuoka T. J. Phys. Soc. Jap. 1964; 19:839.
127. Fisher JC. J. Appl. Phys. 1951; 22:74.
128. Glaeser AM, Evans JW. Acta Metal. 1986; 34:1545–1552.
129. Sommer J, Herzig C. J. Appl. Phys. 1992; 72:2758.
130. Kang YS, Lee JS, Divinski SV, Hisker F, Herzig C. Z. Metallk. 2004; 95:76.
131. Salishchev G, Zaripova R, Galeev R, Valiakhmetov O. Nanostruct. Mater. 1995; 6:913.
132. Dinda GP, Rösner H, Wilde G. Scripta Mater. 2005; 52:577–582.
133. Nazarov AA, Romanov AE, Valiev RZ. Nanostruct. Mater. 1994; 4:93.
134. Lian J, Valiev RZ, Baudelet B. Acta Metall. Mater. 1995; 43(11):4165–4170.
135. Valiev RZ, Kozlov EV, Ivanov YF, Lian J, Nazarov AA, Baudelet B. Acta Metall. Mater. 1994; 42:2467–2475.
136. Kolobov YuR, Grabovetskaya GP, Ivanov MB, Zhilyaev AP, Valiev RZ. Scripta Mater. 2001; 44:873.
137. Grabovetskaya GP, Ratotska IV, Kolobov YuR, Puchkareva LN. Fiz. Metall. Metall. 1997; 83:112.
138. Würschum R, Reimann K, Gruss S et al. Phil. Mag. B 1997; 76:407.
139. Amouyal Y, Divinski SV, Estrin Y, Rabkin E. Acta Mater. 2007; 55:5968–5979.
140. Fujita T, Horita Z, Langdon TG. Phil. Mag. A 2002; 82(11):2249.
141. Amouyal Y, Rabkin E. Acta Mater. 2007; 55:6681.
142. Beke DL, Godeny I, Erdelyi G, Kedves F. J. Phil. Mag. A 1987; 56:659–671.
143. Nazarov AA. Interface Sci. 2000; 8:315–322.
144. Amouyal Y, Divinski SV, Klinger L, Rabkin E. Acta Mater. 2008, doi: 10.1016/S.actamat. 2008.07.029.
145. Ribbe J, Schmitz G, Amouyal Y, Estrin Y, Sivinski SV. Mater. Sci. Forum 2008; 380:584–586.
146. Ovid'ko IA, Sheinerman AG. Rev. Adv. Mater. Sci. 2004; 6:41–47.

CHAPTER 2

Reliability of Nanostructured Materials

K.A. Padmanabhan and S. Balasivanandha Prabu

1. INTRODUCTION

Reliability may be defined as the probability of survival in service of a component at a predetermined property level for a given length of time. Therefore, it is primarily concerned with the statistics of failure time, which may be regarded as the most important variable in Reliability Theory. It establishes an absolute limit to the (useful) lifetime of a component. For example, in the case of structural nanomaterials, parameters like strength and ductility have to be related to the failure time. Concepts associated with reliability are applied in all fields of engineering design and have been used extensively in the case of electronic and structural components and in materials assemblies that may comprise several dissimilar materials. It is self-evident that other considerations like materials selection, economics, productivity, strength-to-weight ratio and stiffness/flexibility become relevant only if the reliability of components in service can be ensured. Reliability of advanced materials is even more difficult to accomplish because they are used in the most demanding conditions, where conventional materials will prove to be inadequate.

The ability of nanostructured materials to display properties that are different from those of their conventional analogues or are entirely new has made the currently available databases irrelevant/unusable. Therefore, reliability of nanostructured materials is primarily concerned with structure–property correlations with a view to ensuring the retention of the assumed design values of properties during the service life of a component and the capacity to predict its residual

Materials Science and Engineering Division, Department of Mechanical Engineering, Anna University, Chennai-600 025, India

Nanostructured Materials © 2009 Elsevier Ltd.
978-0-08-044965-4 All rights reserved.

life at any given point in time. This suggests the need for a multidisciplinary, systems-oriented approach to producing nanostructures/nanomaterials that function reliably in service. Common features/mechanisms that need to be addressed in order to increase the reliability of nanostructures are: surface quality, fracture, fatigue, creep, interface stability, phase stability and thermal stability. In this chapter, the reasons for the instability and unreliability of nanostructures that could arise will be examined and possible ways of improving the situation discussed.

2. INSTABILITY DUE TO SIZE EFFECTS

2.1 Behaviour at Ambient and Low Temperatures

The strength, hardness and plastic deformation features of metals and alloys depend strongly on their micro- and nanoscale structural characteristics [1]. When the grain size is in the nanometre regime, lattice dislocation movement becomes difficult and the metallic materials could acquire very high strength and hardness. Such nanocrystalline (nc) materials often display low tensile ductility at room temperature [2]. But there are also publications in which good ductility at ambient temperatures is reported. This has led to many academic discussions, often from different points of view. In our opinion, the latter observation could be as genuine as the former and a clear delineation of the boundary between the two types of behaviour could lead to some useful industrial applications.

Nanocrystalline materials are synthesized in many ways and the microstructural features depend on the processing conditions [3,4]. A number of methods are available for synthesizing nanopowders. Irrespective of the powder processing routes, metals are easily consolidated and sintered, but ceramic powders are more difficult to densify. Following room temperature consolidation, the porosity level in a ceramic can be at times as high as 60%, while it could be about 20% in metals. Sintering response depends on the material, powder morphology, temperature, consolidated state of the specimen, and applied pressure and method of its application. The strength/hardness increases linearly with the density of the compact. Hot isostatic pressing (HIP) may be used to remove closed pores present following pressureless sintering. To keep the final grain size below 100 nm, hot pressing/sinter forging should be done below about 0.5 Tm (Tm = melting temperature on the absolute scale) [5–10].

During pressure-assisted sintering, pore curvature dominates the driving force for densification, when the grain size is about 2–3 nm but, when the grain size is about 100 nm, the magnitude of the applied pressure is more important. In the range in between, both the effects are significant. The results are interpreted to imply that a threshold stress, which is inversely related to the grain size (and is needed to create additional surface area by grain boundary sliding), has to be overcome before the densification rate can be increased. Microstructural features including grain size, shape, pores and their distribution, other flaws, surface condition, impurity level and crystal defects all affect mechanical properties [11].

There are still two major obstacles to the development of bulk nc materials. First, it is difficult to manufacture porosity- and contamination-free samples.

Second, most of the current techniques of synthesizing bulk nc materials are not adapted to produce industrial scale quantities due to limitations on sample size and cost [12]. The effect of contaminants on strength is often believed to be minimal because of their relatively low volume fraction [13]. For contamination-free grain boundaries in pure metals, low-angle grain boundaries are more fracture-resistant than high-angle boundaries. (This conclusion is based on a simple energy-based argument.) The problem becomes more complicated when impurity segregation along the grain boundaries is involved. There has been a long-standing effort to use grain boundary engineering to improve the fracture resistance of metals [12].

A significant number of early investigations on the mechanical properties of nanocrystalline materials used the inert gas condensation technique. Shortcomings of this technique are the possibility of contamination of the powders and porosity due to insufficient consolidation [14]. The main problems with mechanical alloying (MA) are contamination and grain growth in the powders during processing [5,15,16]. The disadvantage of ball milling for producing nanocrystalline powders is the contamination of products from the milling media (balls and vial) and the atmosphere [17]. For example, the powders may be contaminated with Fe, if steel balls and containers are used. The equipment used also seems to be important. For instance, the Fe impurity level from the high-energy shaker mill is much larger than that from the conventional mill. It is believed that dynamic recovery and cold welding are reduced significantly during cryo-milling, and thus the grain size is refined much faster to a minimum value. In this case, liquid nitrogen provides control over the processing temperature and reduces the contamination of the powders during milling. Liquid nitrogen also serves as a reactive agent to form nitrides and these, along with the oxide particles formed because of the atmosphere, facilitate the retarding of grain growth in the synthesized powders of Al and its alloys obtained by MA processing [16].

The highest hardness values (of about 100 GPa) were reported by Veprek and Reiprich [18] for some Ti–Si–N films. However, these results appeared to be reproducible only with great difficulty and degradation of properties was likely, if there was oxygen contamination [19]. During the fabrication of nanocrystalline amorphous coating nc-Me_n N/a-Si_3N_4 (where Me is a transition metal such as Ti, Zr, V, Nb, W), a low contamination of the deposit with chlorine of less than 0.3–0.5 at% from the transition metal chlorides, used as reactants under conditions of plasma chemical vapour deposition (CVD) in an intense low pressure glow discharge, was encountered. Obviously, plasma CVD is the first choice for the deposition technique because it provides both a high chemical activity of nitrogen and the activation energy necessary for segregation to occur [20].

There are several studies in the literature which report a decrease in creep resistance with time and this has been attributed to Coble creep. But in Coble creep, the creep rate is proportional to d^{-3}. Experimental results report a creep resistance much greater than the Coble prediction. This could be due to the contamination of the grain boundaries by impurities, which act as 'brakes' to grain-boundary sliding [14]. Other physical factors could also be responsible for this observation (see section 2.3).

Important technological issues include the synthesis of high purity materials with a large yield in an economically and environmentally friendly fashion, characterization of the new structures and properties of nanophase materials, fabrication of products of full density and low contamination from other nanoparticles and retention of the ultrafine grain size in service in order to preserve the properties associated with the nanometre scale [1,21].

There is a suggestion that when nano (n-) metals of different grain sizes are prepared by varying the cluster size, the hardness increases with decreasing grain size but, in samples in which the grain size is increased by annealing, a decrease in grain size is accompanied by a decrease in hardness. The grain size ranges and the presence of artifacts when such observations are encountered have not been identified carefully with sufficient attention.

Conventional polycrystalline metals and alloys show an increase in yield strength (σ_y) with decreasing grain size (d) in accordance with the well-known Hall–Petch (H–P) equation [12,14,16,22–28]:

$$\sigma_y = \sigma_o + kd^{-1/2} \tag{2.1}$$

where σ_o is the friction stress that arises in the lattice from the resistance to the glide of dislocations and k is the Hall–Petch slope, which is a measure of the resistance of the grain boundary to slip transfer across grains. In analogy, hardness (H_v) can be related to the grain size by the equation:

$$H_v = H_o + k_H d^{-1/2} \tag{2.2}$$

where H_o and k_H are constants. (Hardness, which is directly related to the yield stress, is a measure of the local resistance of a material to plastic deformation under the application of an indenting load.) As the H–P effect in conventional coarse-grained materials is attributed to the grain boundaries acting as obstacles to dislocation motion, a dislocation pile-up is considered to form inside a grain against the grain boundary concerned. The slip transfer across the interface, which controls the value of k in the Hall–Petch equation, depends on the nature of the interface and the elastic modulus mismatch across the contiguous grains [25].

Tjong (Tjony and chen [16]) has compiled the hardness-grain size results of several workers for nanocrystalline Cu and Pd samples (Figure 2.1a,b). Apparently, the H–P slope for Cu varies gradually from positive, zero to negative. These figures reveal that a deviation from the H–P relation and a negative slope is observed for both the inert gas condensation (IGC) Cu and Pd samples prepared by Chokshi et al. [25]. In contrast, results of other workers only reach a plateau, as the grain size decreases. The Cu and Pd samples used in the plots were all prepared from inert gas condensed and compacted powders. Therefore, it is clear that the conditions of production and consolidation of IGC powders, which determined the density of the compacts, greatly affect the mechanical properties of nanocrystalline metals. A plateau was found in the hardness versus grain size curve when the grain sizes were less than 20 nm. The level of porosity could have been more in the samples of Chokshi et al. [25] for which a negative slope was obtained.

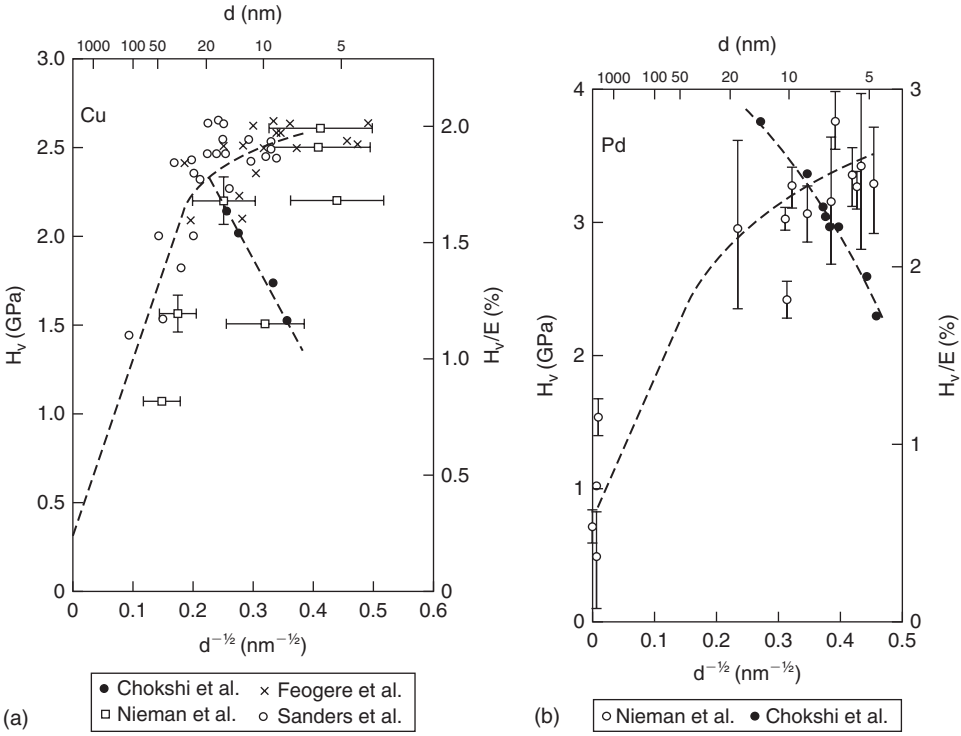

FIGURE 2.1 Hall–Petch plots of the hardness of (a) nanocrystalline Cu and (b) nanocrystalline Pd [16].

This raises the issue of whether the inverse/inverted H–P behaviour is inherited from the intrinsic effect of nanograin size or results from extrinsic defects introduced in the samples during fabrication [29].

In contrast, Zhou et al. [28] have suggested that the dependence of hardness on grain size is according to Figure 2.2.

Koch and Narayan [30] (see ref. [31] also) have identified the problems associated with obtaining artifact-free samples and the accurate determination of grain size and its distribution. To date, there are four sets of results reporting inverse Hall–Petch effect, which are considered to be non-controversial:

1. in laser ablated Zn;
2. in electrodeposited Ni;
3. in electrodeposited Ni tested by a nanoscratch technique; and
4. in pulsed laser deposited Cu [30,31].

Figure 2.3 shows the inverse Hall–Petch plot for nc-Zn made by laser ablation or mechanical attrition.

Several quantitative explanations for the complex deformation behaviour are available. These include grain boundary sliding, diffusion, motion of triple junctions, presence of pores and impurities [1]. At grain sizes below 100–200 nm,

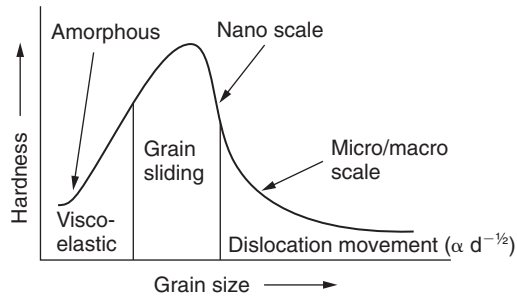

FIGURE 2.2 Schematic depiction of hardness as a function of grain size [28].

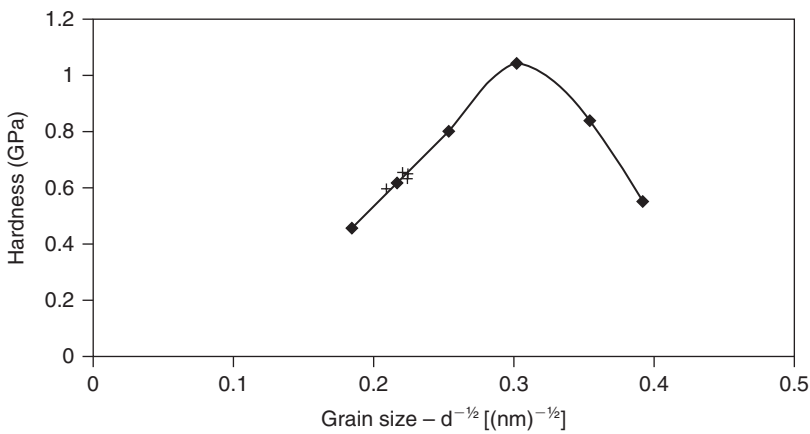

FIGURE 2.3 Hardness vs. inverse grain size, $d^{-0.5}$, in the case of nanocrystalline Zn made by laser ablation or mechanical attrition [30].

deformation occurs via grain boundary dislocation emission; at grain sizes below, say, 20–30 nm, deformation may occur instead by the emission of partial dislocations or formation of deformation twins and, at even finer grain sizes, deformation could occur by grain boundary sliding. These mechanisms, and the grain size ranges of their operation, are influenced by temperature, lattice spacing and stacking fault energy [32,33]. In computer-generated specimens and simulated deformation, the deformation mechanism at grain sizes below 10 nm is characterized by:

1. the absence of intergranular dislocation slip;
2. atomic shuffling; and
3. stress-assisted free volume migration in the grain boundaries [34].

At larger grain sizes, molecular dynamic (MD) simulations [35–37] have shown additional evidence for slip characterized by the emission of partial dislocations from the grain boundary (GB) into the grain and their absorption by the opposite GB [36,38–41]. MD simulation has been extensively used for studying grain-boundary

diffusion creep in nanocrystalline palladium [42]. Yamakov et al. [42] studied the mechanisms of dislocation–dislocation and dislocation–twin boundary reactions that take place under a sufficiently high stress in nanocrystalline Al. Further, they have reported MD simulations of grain growth in an impurity-free model nanocrystalline palladium microstructure containing only high-energy GBs [42]. Haslam et al. [43] studied the effects of grain growth on grain boundary diffusion creep and grain boundary sliding during the high temperature deformation of a nanocrystalline Pd model microstructure using molecular dynamics simulations. Experimental evidence for the absence of dislocations in grains of nc-Pd of grain size of about 33 nm, even after room temperature rolling by more than 40% at a strain rate of $\approx 0.06\ s^{-1}$, has been reported by Markmann et al. [44].

If grain boundary sliding is restricted while the grain size is in the lower nanometre range, a superhard material becomes possible. Therefore, nanocomposite coatings display no inverse Hall–Petch relationship; in fact they display a notable increase in hardness [45]. A strong increase in hardness is found in the region of 10–20 nm crystallite size in some novel superhard nanocrystalline composites [46]. Embedding hard grains of 3–4 nm diameter into a hard amorphous matrix (with about 1 nm grain separation) produces nanocomposite coatings of superior hardness (e.g. 80–100 GPa) [47].

Upon deformation, many nc metals are found to reach their fracture stress in, or slightly beyond, the elastic regime. As full-density bulk nc metals are difficult to produce, poor sample quality is an obvious reason for the low fracture strength, causing premature failure under tensile stresses – sometimes even before yielding has a chance to start. This is especially true when the bulk sample is consolidated from loose nanoparticles [48].

In general, the fracture stress, σ_f, increases with decreasing grain size, d. It is important to realize that in the nc regime σ_f can be depressed for two reasons. First, the intrinsic toughness of the material may be lower for the extremely small d. This could happen when the dislocation-mediated plasticity is eliminated or severely reduced, concurrent with an extraordinarily large population of grain boundaries with high interfacial energies that would allow the cracks to propagate across the sample in an intergranular manner. Secondly, samples of full density with tiny grains are difficult to make and hence often thin and small specimens are made, in which even a minor surface flaw or roughness becomes a source for the initiation of sufficiently large cracks that could induce catastrophic failures, with or without flaws and porosity inside the bulk. As a result of these two factors acting alone or in concert, the ductility of nc-Cu could be controlled by early fracture due to the instability of crack nucleation and growth [48]. Such early failure may be preceded or promoted by extremely localized plastic deformation. Such plastic instability, if present in the form of catastrophic shear banding in the initial stage of straining, is another important factor that can lead to very low apparent ductility. This tendency for plastic deformation in nc metals to become unstable and severely localized very early is related to their diminishing strain hardening capacity. The latter is expected because the extremely small grains cannot store dislocations to increase their density by orders of magnitude, as is possible in coarse-grained metals and alloys.

Tensile deformation may be stabilized by different stabilizing mechanisms, viz. control of grain structure (through a bimodal or multimodal grain size distribution, grain boundary character distribution or deformation mechanisms), or by selecting appropriate tensile deformation conditions (e.g. deformation temperature and strain rate). At low temperatures (77 K), strain rate hardening does not help much as the strain rate sensitivity index (m) is very low for both dislocation-mediated and diffusion mechanisms but, at room temperature, where dynamic recovery is difficult to suppress in the normal strain rate range, m could play a role. In the low temperature range mentioned above, one needs extra scope for strain hardening (such as a bimodal grain structure), or needs to induce strain rate sensitivity, in the absence of strain hardening. Achieving simultaneously high rates of strain hardening and strain rate hardening remains a challenging task. Then, it may be possible to achieve increased ductility.

The enhanced grain boundary diffusivity and early evidence of ductility in nanoceramics led researchers to believe that in the nanometre range:

1. metals would retain the ductility; and
2. intrinsically brittle coarse-grained ceramics and intermetaleics would be ductilized.

Nanomaterials were believed to have the potential for providing the improvements needed for future gas turbine engines with improved reliability and performance [49], but experimental observations made so far seem to suggest that inherent limitations exist so far as strength and ductility of nanomaterials are concerned. Overcoming these is likely to result in large economic gains for the industry.

2.2 Grain Boundary Sliding and High-Strain-Rate Superplasticity in Nanocrystalline Materials

Significant differences have been observed in the deformation characteristics of nanocrystalline (nc) materials at elevated temperatures compared with their microcrystalline (mc) counterparts. Grain boundaries (GBs) and triple junctions crucially affect the outstanding mechanical properties of nanocrystalline materials. The contribution of lattice dislocation slip to plastic flow gradually decreases with decreasing grain size [50,51].

According to contemporary views on plastic flow processes in nanocrystalline materials, the following deformation mechanisms could operate:

- lattice dislocation slip;
- GB sliding;
- GB diffusional creep (Coble creep);
- triple junction diffusional creep;
- rotational deformation occurring via movement of GB disclinations;
- twin deformation arising through partial dislocations emitted from GBs [51].

It is known that by reducing the grain size or increasing the temperature of deformation, it is possible to increase the superplastic strain rate [52–54].

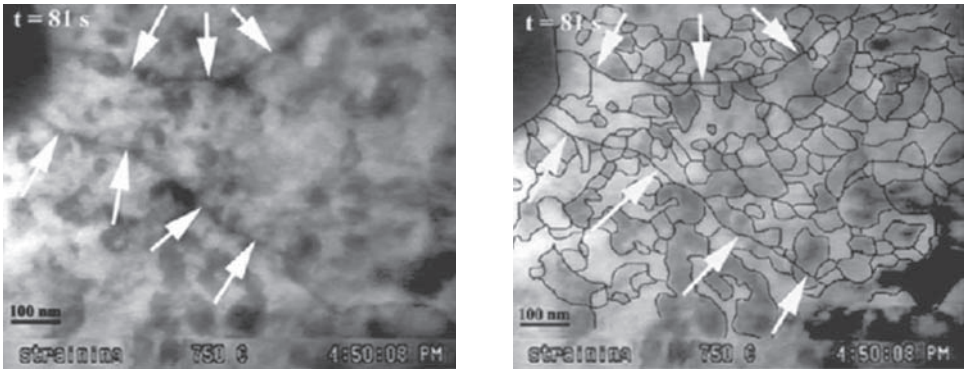

(a) (b)

FIGURE 2.4 (a) SEM images of nanocrystalline Ni_3Al extracted from a real-time video of an *in-situ* tensile test at 750°C. Highlighting of recognizable GB in (b) helps to reveal sliding surfaces, which are pointed out by arrows [50].

Both aspects happen to have attractive technological significance. As grain size is decreased, slip accommodation should become more difficult. An increasing role of grain boundaries in nc materials, especially as sources and sinks of mobile dislocations, was clearly demonstrated by molecular dynamics (MD) simulation. Deformed nanomaterials have shown very little dislocation activity. GB sliding is the dominant mode of superplastic deformation in such materials. In this context, it is highly interesting to understand the specific features of GB sliding and its role in high-strain-rate superplasticity in nanocrystalline material produced by severe plastic deformation.

The bright field micrographs in Figure 2.4a and b show a formation of sliding surfaces (marked by arrows), which supports the idea that cooperative (mesoscopic) grain boundary sliding took place during the deformation of nanocrystalline grains in Ni_3Al alloy. Pre-polished surfaces of superplastically deformed samples of Ni_3Al were also analysed by scanning electron microscopy (SEM) and they too revealed specific features that are usually attributed to cooperative grain boundary sliding. These features included offsets of reference marks, which are indicative of shear events in two directions at 45° to the tensile straining direction. The geometrical size of the offsets and the shear bands was a few orders of magnitude larger than the mean grain size of the material, suggesting that large groups of grains were involved in the sliding process.

Grains can move collectively relative to one another due to the formation of mesoscopic shear planes – the 'mesoscopic boundary sliding planes' in the model of Padmanabhan and coworkers [3,31,55–58] (see later). Special low-angle grain boundaries or those with misorientation close to the twin boundary can offer resistance to this kind of sliding and the local shear planes can concentrate around these grain boundaries creating a cluster of grains embedded in a sliding environment.

2.3 Models for the Deformation of Nanocrystalline Materials

2.3.1 Hall–Petch effect

Models proposed to explain the strengthening due to refining of grain size are based on the motion of dislocations. They account well for the grain size (L) dependence of stress, σ (the Hall–Petch equation), when L is in the μm range. These may be referred to generally as dislocation pile-up-based models. In physical terms, to derive the Hall–Petch relation, the role of grain boundaries as a barrier to dislocation motion is considered [39] and this leads to stress concentration and the activation of dislocation sources and slip in the contiguous grains, a reduction in the mean free paths of dislocations and strain hardening. In such an analysis, a linear dependence of σ on $d^{-1/2}$ results only when there are many dislocations in the pile-up, which is equivalent to assuming that the grain size in the polycrystal under consideration is large. Further, at smaller grain sizes, this mechanism should cease when there are only two dislocations in the pile-up. When the number of dislocations falls to one, no further increase in the yield stress is possible and it should saturate.

In modelling the Hall–Petch relation for nanocrystals using the pile-up calculations, the main technical issues [59] are the:

1. effect of a small number of dislocations;
2. effect of locked dislocations of a different Burgers vector;
3. effect of anisotropy;
4. effect of curved dislocations;
5. effect of discrete or continuum approximation;
6. effect of yield criterion chosen;
7. effect of using single or double ended pile-ups.

For small grain sizes, curved dislocations are more appropriate, but circular and straight dislocations differ in the continuum approximation only by predictable constant factors. There are two yield criteria that are equivalent in the continuum approximation:

1. the overcoming of a barrier stress by the stress field of the dislocations in the pile-up; or
2. the achievement of a critical separation of the first two dislocations in the pile-up.

The pile-up model [59] is shown in Figure 2.5, where mb is the Burgers vector of the locked dislocation, L the length of the pile-up, which is taken as nearly equal to the grain size and σ is the applied stress. Using a virtual work argument, the stress at the tip for any number of dislocations in the pile-up is given as:

$$\sigma_{rtip} = [(n + m - 1)/m]\sigma$$

where n is the number of dislocations in the pile-up.

One needs to assume that permanent deformation takes place when a dislocation source in a given grain is activated and it generates dislocation loops.

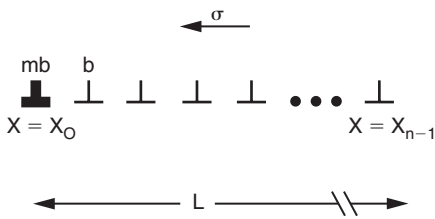

FIGURE 2.5 Pile-up model with a locked dislocation of strength mb [59].

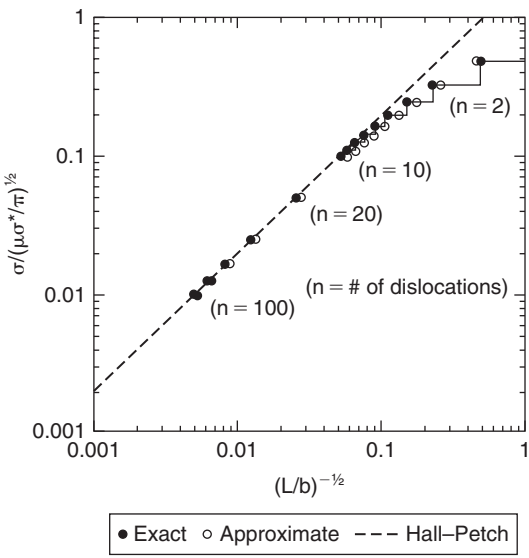

FIGURE 2.6 Exact and approximate comparison [59].

In the pile-up model, this necessary stress is transmitted by the leading dislocation of a pile-up of dislocations located in an adjacent grain. It is readily shown that the stress concentration on the leading dislocation is proportional to the external shear stress and the number, n, of dislocations in the pile-up.

The results are presented graphically in Figure 2.6, where c is scaled to $(\mu\sigma^*/\pi)^{1/2}$ and L is scaled to b. It is seen that the Hall–Petch relation is valid for $n > 20$ but, at values of $n < 20$, the exact (calculated from the data) and the approximate curves exhibit discrete steps and begin to level off (σ^* is the barrier stress).

For a grain size of about 10–15 nm grain boundary sliding and dislocation glide were predicted, whereas at a grain size of about 5 nm or less no dislocation activity was observed. The reasons for this behaviour are still a subject of debate, although it is known that dislocation sources within grains are not expected to operate at these grain sizes. In fact, there is no documented evidence of dislocation pile-ups in deformed specimens and any dislocation activity is primarily believed to originate and terminate at grain boundaries. Furthermore, it has been reported in many cases that the nanocrystalline metals are less ductile than their

microcrystalline counterparts because of very limited/negligible work hardening. These experimental observations severely limit the usefulness of dislocation pile-up based models for explaining the mechanical response of nc materials, particularly when the grain size is in the lower end of the nm range.

Clearly, at sufficiently small grain sizes, the Hall–Petch model based upon dislocations may not be operative. However, in this region, Coble creep could be operating, i.e. grain boundary diffusional creep [60]. However, it is a deformation process that leads to homogeneous elongation of grains along the tensile direction, and grain elongation along the tensile direction has not been observed in deformed specimens of nanocrystalline materials. Moreover, the observed creep resistance was more than what is predicted by the Coble creep model and the grain size dependence of the creep rate also was not in accordance with this model [61]. It appears at this stage that going from the dislocation pile-up model to Coble creep with a decrease in grain size does not account well for the presence of an inverse Hall–Petch effect in nanocrystalline materials.

2.3.2 Inverse Hall–Petch effect

Based on an approach rooted in micromechanics, inverse Hall–Petch effect in nanocrystalline materials was predicted in 1995 by extending and refining an earlier model for mesoscopic (cooperative) grain/interphase boundary sliding controlled flow in microcrystalline materials [3,4,31,55,56,58].

As was noted earlier, the creep resistance of nanocrystalline materials is more than what is warranted by Coble creep. The creep rate also does not vary as L^{-3}, where L is the (average) grain size. Diffusion models like Coble creep assume that grain boundary sliding is always faster than the diffusion process. In that view, grain boundary sliding can lead only to small creep strains because steric hindrance due to the presence of blocking grains prevents any extended deformation or superplastic deformation. The assumption in all previous models is that the stoppage of flow at triple junctions is overcome by diffusion processes or dislocation motion. As a result, the internal stresses which build up during sliding are reduced and plastic deformation can proceed [31,58]. The dominance of grain boundary sliding during superplastic flow was noted even in the early work of Pearson [62]. Many later workers reinforced this finding. Ball and Hutchison [63], after stating the predominant role of grain boundary sliding during extensive superplastic flow, suggested that boundary sliding is 'possibly controlled by dislocation motion within the grains'. Climb of the dislocation at the head of the pile-up present near the grain boundary will then control the rate of flow. In contrast, the boundary sliding controlled flow model assumes that rate controlling flow is confined to a three-dimensional continuous network of grain and interphase boundaries that surround grains which do not deform except for what is required to ensure strain and geometric compatibility. That this grain boundary network in 3D could form an infinite continuum for deformation was appreciated early enough [64], but the microstructural details could be spelt out only after a clear view emerged that the *expansion* present at high-angle boundaries cannot be understood by resolving those boundaries into dislocations, but by only treating them as free volume [65,66]. Dislocation emission from the boundaries sliding

into the grains and diffusion that will be needed for the grain strain to ensure geometric compatibility and coherent strain across grains are regarded as faster accommodation processes and so they do not enter the strain rate equation.

A high angle/high energy grain/interphase boundary is divided into a number of atomic scale ensembles that surround free volume sites present at discrete locations characteristic of a boundary. Each of these ensembles constitutes a basic unit of sliding (where due to the presence of free volume the shear resistance is less than in the rest of the boundary). Sliding occurs by the movement of similar boundary volume elements, of oblate spheroid shape with ground area $\pi\delta^2$ and height δ, located symmetrically on the boundary plane so that the height on either side of the boundary is $(\delta/2)$. Here δ is the grain boundary width. To produce substantial sliding on a mesoscopic scale, two or more grains must cooperate to form a plane interface by boundary migration which, by further interconnection with other plane interfaces, will lead to long-range sliding [56]. The driving force for plane interface formation is the minimization of the total free energy of the system caused by the much larger anisotropic work done by the applied stress, compared with the surface free energies associated with the concerned grain boundaries. Once a plane interface is formed, the localized sliding shears can lead to mesoscopic sliding over dimensions of many grains and eventually lead to large strains and superplastic deformation. For mathematical development, the grain shape is assumed to be either tetrakai decahedral (ideal) or rhombic dodecahedral (real crystals) and the grain size, L, constant (Figures 2.7 and 2.8). (If grain growth is present, L would be obtained from a secondary kinetic equation in which L is a function of strain, strain rate and temperature.) Within the *actually deforming* network of boundaries, flow in the region where sliding is least easy will determine the overall rate of deformation.

The threshold stress in the shear mode (τ_0) needed for the onset of mesoscopic boundary sliding was first determined by Padmanabhan and Schlipf [56] and simplified further in later works [31,68]. That is:

$$\tau_0 = [(2G\Gamma_B \Delta A/A)/\propto_f \sqrt{NA}]^{0.5} \tag{2.3}$$

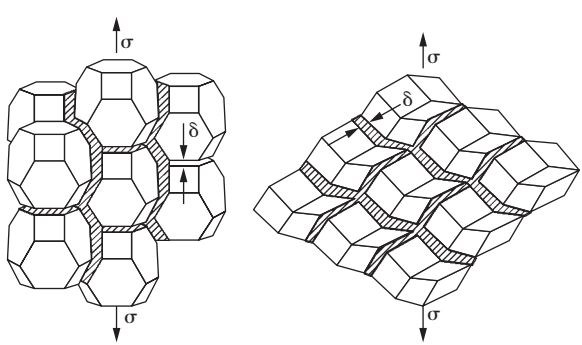

FIGURE 2.7 Tetrakai decahedral (left) and rhombic dodecahedral (right) shapes in an idealized grain arrangement with grain boundaries (shaded areas) separating the grains [56,67,68].

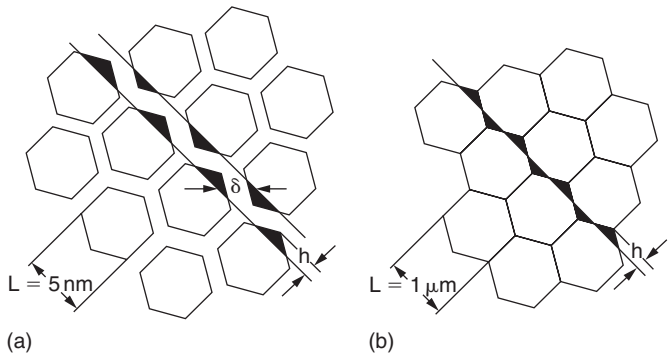

FIGURE 2.8 2D schematic of a grain arrangement in a (a) nano- ($\delta/L = 0.1$, $L = 5$ nm) and (b) polycrystalline ($\delta/L = 0.0005$, $L = 1\mu$m) material. A mesoscopic plane interface can be formed by grain boundary migration. Atoms located in the darker regions have to be rearranged [67]. δ is grain boundary width.

where G is the shear modulus, Γ_B the specific grain boundary energy (assumed to be isotropic), ΔA the boundary area per grain, A the ground area in the boundary region of the given grain, $\propto_f$ a form factor of the order of unity and N the number of grain boundaries participating in the mesoscopic sliding event.

Further, the temperature dependence of τ_0 can be deduced from Eq. (2.3). If the grain size is stable, i.e. if grain growth can be neglected, the temperature dependence of τ_0 is given by the temperature dependence of the expression:

$$\tau_0 = (G\Gamma_B/\sqrt{N})^{0.5} \tag{2.4}$$

Here N depends strongly on temperature, impurity content and grain size distribution. G and Γ_B also are temperature dependent.

If $\tau_{0disloc}$ is the threshold stress in the shear mode, when boundary migration takes place by a combination of dislocation emission and diffusion over a length scale less than unit interatomic distance on average and τ_{0diff}, its value when boundary migration is caused entirely by diffusion over a length scale of 1–2 interatomic distance [58]:

$$\tau_{0disloc} = \frac{C_1}{L}; \quad C_1 = \left(\frac{8G\Gamma_B r}{3^{0.25}}\right)^{0.5}, \quad L > L_{max} \tag{2.5}$$

$$\tau_{0diff} = C_2 \frac{(L - L_0)^{0.5}}{LN^{0.25}}; \quad L_0 = 2\delta\sqrt{6}$$

$$C_2 = \left[\frac{2^{1.5} G\Gamma_B}{3^{0.75}}\right]^{0.5}, \quad L \leq L_{max}$$

where L_{max} is the value of the grain size above which boundary migration can take place only by a combination of dislocation emission and diffusion. If the

grain size dependence of N is ignored in the narrow interval where the inverse Hall–Petch effect is observed:

$$\tau_{0\text{diff}} \approx C_3\left[\frac{(L-L_0)^{0.5}}{L}\right]; \quad C_3 = C_2 N^{-0.25} \tag{2.6}$$

when L_0 is neglected in comparison with L, this reduces to the inverse H–P effect. In addition, the analysis leads to the following relationships:

$$N^{0.5} = 5.7325\left[\frac{D_{\text{gb}}\text{a}C\Gamma_{\text{B}}}{kT\dot{\gamma}_{\text{sp}}}\right]\left[\frac{L-L_0}{L^3}\right]; \quad L \le L_{\max}$$

$$L_{\max} = \left[\frac{28.0835 D_{\text{gb}}\text{a}C\Gamma_{\text{B}} r}{kT\dot{\gamma}_{\text{sp}}}\right]^{1/3}$$

$$\dot{\gamma}_{\text{sp}} = \left(\frac{2.0944 W^4 \gamma_0{}^2 \nu}{kTL}\right)(\tau - \tau_0)\exp\left(\frac{-\Delta F_0}{kT}\right) \tag{2.7}$$

where r is the average boundary misfit removed by diffusion, D_{gb} the grain boundary diffusivity, a the atomic diameter, C the vacancy concentration at any high angle/high energy grain boundary at the temperature of deformation ($\approx 10^{-4}$), ν the thermal vibration frequency and k the Boltzmann constant. τ_0 is either $\tau_{0\text{disloc}}$ or $\tau_{0\text{diff}}$, depending on grain size and $\dot{\gamma}_{sp}$ is the external shear strain rate. If von Mises yield behaviour is assumed, $\dot{\gamma}_{sp} = \sqrt{3}\dot{\varepsilon}_{sp}$. The threshold stress in uniaxial tension mode, $\sigma_0 = \sqrt{3}\tau_0$. If the Taylor factor is used, $\dot{\gamma}_{sp} = 3\,\dot{\varepsilon}_{sp}$ and $\sigma_0 = 3\tau_0$ [31].

When boundary migration/plane interface formation takes place by a combination of dislocation emission and diffusion, as H, the hardness of material and its flow stress are directly related, it follows that:

$$H = A_1 - \frac{B_1}{L} \tag{2.8}$$

where A_1 and B_1 are constants. When boundary migration is entirely by diffusion over a distance of the order of unit interatomic distance in the boundary region:

$$H = A_2 - \left(\frac{B_2}{L}\right)(L - B_3)^{0.5} \tag{2.9}$$

with A_2, B_2 and B_3 ($=2\sqrt{6}\delta = L_0$) as constants. Figure 2.9 shows the validation of the microhardness vs. grain size relationship predicted by the grain/interface sliding controlled model [31] using data considered to be non-controversial by Koch and Narayan [30].

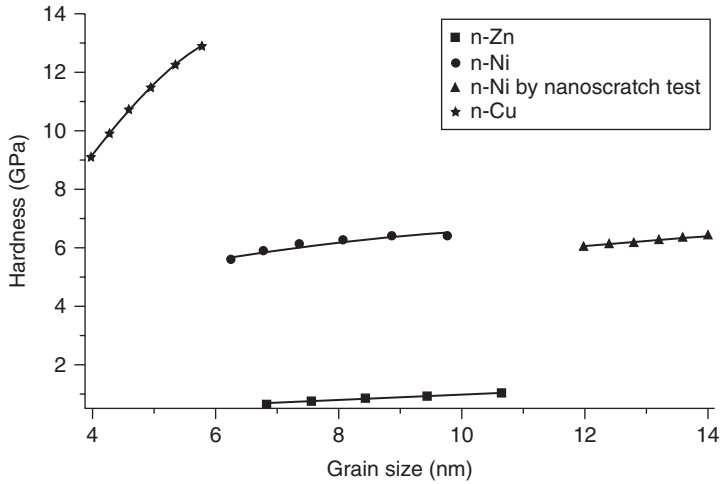

FIGURE 2.9 Inverse Hall–Petch effect in four systems. Symbols represent experimental points. Full curve is according to Eq. (2.8). Dashed curve is as per Eq. (2.9). (■) n-Zn. Best fit values: $A_1 = 1.76$, $B_1 = 7.50$; $A_2 = 3.95$, $B_2 = 10.70$, $B_3 = 2.45$ (i.e. $\delta = 0.5$ nm). Maximum error in the fit as per Eq. (2.8) is 2.18%; as per Eq. (2.9) is 4.37%. (●) n-Ni. Best fit values: $A_1 = 7.94$, $B_1 = 13.72$; $A_2 = 13.38$, $B_2 = 24.50$, $B_3 = 2.45$ (i.e. $\delta = 0.5$ nm); maximum error in the fit as per Eq. (2.8) is 0.13%; as per Eq. (2.9) is 0.07%.(★) n-Cu: best fit values: $A_1 = 21.60$, $B_1 = 50.00$; maximum error in the fit as per Eq. (2.8) is 0.11%. Eq. (2.9) gave a poor fit for this set of data [31].

In physical terms, in metallic systems, the deviation from the Hall–Petch relation, which eventually leads to the inverse Hall–Petch behaviour, could be attributed to competition between the grain boundary sliding controlled process and dislocation dominated deformation. These are two independent mechanisms and the one that requires less stress (energy) will be the favoured mode of deformation under a given set of experimental conditions. Evidently, when grain boundary sliding is dominant, grain refinement will weaken the material (inverse Hall–Petch), but when crystallographic deformation is dominant (conventional Hall–Petch), grain refinement will strengthen the material. This transition region from inverse Hall–Petch to Hall–Petch relationship is yet to be placed in a strict, quantitative framework.

In the above analysis, the threshold stress needed to be overcome before the onset of mesoscopic/cooperative boundary sliding is obtained from an energy balance equation based in thermodynamics. Ovid'ko et al. [51] have provided a physical picture for localized grain boundary migration, which leads to the onset of mesoscopic boundary sliding, as follows.

When a load is applied, mobile GB dislocations (with Burgers vector parallel to GB planes) move causing GB sliding (Figure 2.10a) (GB dislocation motion at high-angle boundaries as the mechanism of boundary sliding is a questionable concept.). They are stopped at triple junctions of GBs, where GB planes are curved and thereby dislocation movement is hampered. In general,

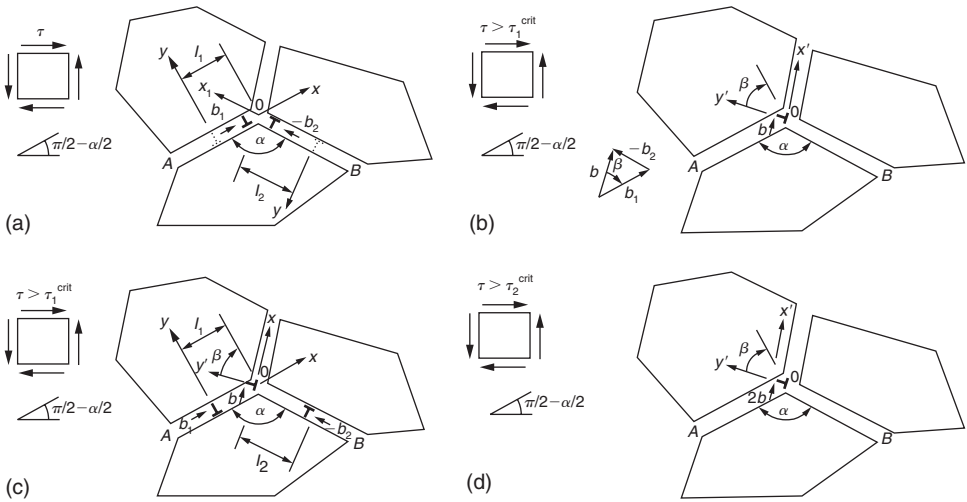

FIGURE 2.10 Transformations of GB dislocations near a triple junction. (a) Initial (0th) state of defect configuration. Two gliding GB dislocations move towards the triple junction O; (b) sessile dislocation with the Burgers vector b is formed. Triple junction is displaced by the vector b_2 from its initial position shown in (a); (c) generation of two new gliding GB dislocations that move towards the triple junction; (d) a new sessile dislocation is formed. The triple junction is transformed by the vector $2b_2$ from its initial position shown in (a) [69].

GB dislocations stopped near a triple junction are capable of overcoming the junction obstacle and enter a dislocation reaction when the shear stress reaches some critical value. In nanocrystalline materials with their high-density ensembles of triple junctions, the critical shear stress needed for GB dislocations to overcome triple junctions specifies the contribution of GB sliding to the yield stress. In so doing, it should be noted that an elementary act of GB sliding is a transfer of the GB dislocation with Burgers vector $-b_2$ across a triple junction (Figure 2.10). This transfer over a short distance l_2 becomes energetically favourable at a critical shear stress σ_1^{crit}. The transfer is accompanied by a dislocation reaction which involves the GB dislocations with Burgers vectors b_1 and $-b_2$ and results in both the formation of a sessile GB dislocation with Burgers vector $b = b_1 - b_2$ and a displacement of the triple junction by vector b_2 (Figure 2.10b).

The configuration consists of two GB dislocations with Burgers vectors b_1 and $-b_2$ parallel to the corresponding GB planes adjacent to the triple junction. GB dislocations are stopped by the triple junction (Figure 2.10a) when $\tau < \tau_1^{crit}$. Thus, the storage of sessile GB dislocations at triple junctions causes a strengthening effect that dominates at the first long stage of mesoscopic sliding/superplastic deformation. (At the same time, it must be said that the movement of GB dislocations across a triple junction can be accompanied by either GB migration or the formation of a triple junction nanocrack [51]). The schematic representation

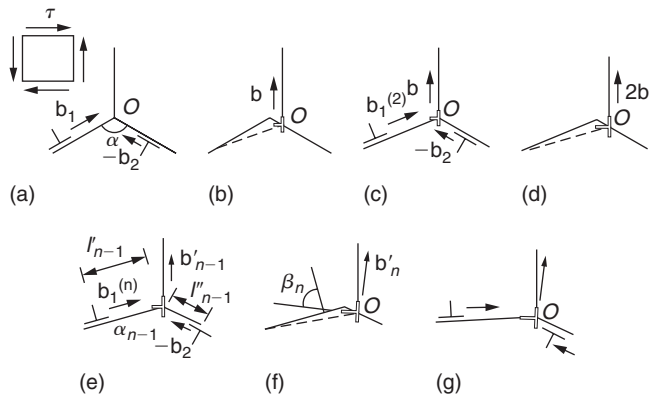

FIGURE 2.11 Numerous acts of transfer of GB dislocations across a triple junction and accompanying local migration of GBs make GB planes (adjacent to the triple junction) temporarily parallel to each other [50,69].

of transfer of GB dislocations across a triple junction and accompanying local migration of GBs is shown in Figure 2.11.

3. PHASE INSTABILITIES

3.1 Phase Instability of Nanostructured Metallic Materials

In this section, the mechanism(s) underlying the unusual behaviour of nanostructures with respect to phase stability, and its implications for designing and fabricating nanostructured materials that display desired functional properties, will be discussed. Meaningful inferences based on these mechanism(s) will be attempted because such a step is essential for ensuring safe industrial applications.

The study of phase transformations in nanocrystalline materials over the past 20 years has established clearly that the temperature (range) below which a high-temperature phase becomes unstable is dependent on the grain size of the material. (A nanophase is said to be stable when the transformation of a high-temperature phase to a low-temperature phase continues to be suppressed below the temperature (range) at which the same material of a coarse grain size would have transformed to the low-temperature phase.) Only very limited research on the effect of grain (particle) size in the nanometre scale on the reversal phase transformation during heating has been reported [70]. The available experimental results lead to conflicting conclusions. The reversal transformation temperature is affected only to a limited extent by particle (grain) size in Fe–Ni alloys [71,72], gets lowered with decreasing particle size of anatase TiO_2 [73], or becomes lower with a decrease in Co grain size when the size is in the range 15–100 nm, but increases when it is smaller than 15 nm [72]. These differences have not yet been accounted for. From the above described experiments, it appears that there is a critical size for ensuring the stability of a low-temperature phase at high temperatures.

Again, the related theory is yet to be established. Broadly, phase stability requires two conditions to be met:

1. *Necessary condition*: the high-temperature phase must form during the preparation of the nanocrystalline material.
2. *Sufficient condition*: the resultant grains must be smaller than a critical grain (particle) size during subsequent cooling [70].

Research on diffusionless phase transformations, including allotropic, polymorphic and martensitic transformations, and phase stability has been carried out on different categories of nc materials using various preparation methods with a view to rationalizing the knowledge gained under widely varying conditions of synthesis and service. Many experiments have demonstrated that the transformation from a high-temperature phase to a low-temperature phase is indeed suppressed when the grain (particle) size is smaller than a certain critical size. In other words, the stability of the high-temperature phase at low temperatures has been established [70].

Al–Ag alloys are of interest because they represent one of the simplest cases of a phase transformation involving a change in crystal structure, namely that of face-centred cubic (fcc) → hcp [74]. Another alloy system that undergoes transformation is the Al–Mg–Si alloys, which are commonly used in the automotive industry. In the bake-hardening process of AA6xxx alloys, a high-density nanometre-size $Mg_xSi_yAl_z$ precipitate is responsible for the large increase in strength. A large number of structures and compositions are present between the initial supersaturated solid solution (SSSS) and the stable Mg_2Si phase. The generic precipitation sequence that is 'generally accepted' for the Mg–Si–Al alloys is the following and the detailed representation is given in Figure 2.12 [75]:

$$\text{SSSS} \rightarrow \text{GP zones } (Mg_1Si_1) \rightarrow \text{pre-}\beta'' \rightarrow \beta''(Mg_5Si_6) \rightarrow (\text{U1}(Mg_1Si_2Al_2), \text{U2}\ (Mg_4Si_4Al_4), \text{B}'(Al_3Mg_9Si_7), \beta'\ (Mg_9Si_5) \rightarrow \beta(Mg_2Si))$$

The transition from pre-β″ to β″ phase marks the transition from fcc-type structures to non-fcc-type structures. A new pre-β″ phase has been identified with a composition Mg_4Si_7 that is energetically very favourable. The fcc-type pre-β″ Mg_4Si_7 structure is the most favoured structure because of the size effect. Although the late precipitate phases (β″, β′, U1, U2 and U3) are very different in composition and crystallography, if the activation energy for the phase transformation from pre-β″ $Mg_4Si_6Al_1$ to β″ $Mg_4Si_6Al_1$ is low, it may be energetically more favourable to transform into β″ $Mg_4Si_6Al_1$ instead of pre-β″ Mg_4Si_7.

It is shown in Figure 2.13 that they share the same substructures consisting of Mg hexagons, which enclose a parallelogram of four atoms. Phase transitions are characterized by columnar and planar shifts of these substructures and not by a total rearrangement of all the atoms [75].

The abnormal thermal stability of nanocrystalline materials, as the basis of phase stability in the forward and the backward (reversal) transformations, revealed in many experiments, has been explained by different mechanisms of grain-growth kinetics.

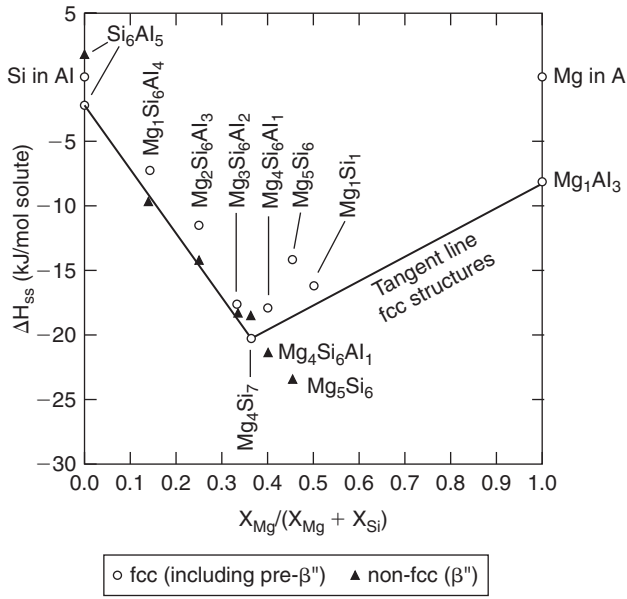

FIGURE 2.12 Formation enthalpy ΔH_{ss} (kJ/mol solute) plotted as a function of ratio of solutes for fully relaxed geometries (both atomic positions and lattice parameters) calculated using VASP-GGA. Here, the pre-β" structures are compared with the β" structures [75].

It was shown that vacancies produced as a result of the reduction in the grain boundary area resulting from grain growth, i.e. by the elimination of the excess volume, increase the free energy of the system. Therefore, the 'injection' of vacancies into the bulk of the material acts as an inhibiting factor leading to a decrease in the grain growth rate. In this approach, uninhibited grain growth is considered to be present only during a limited time, t*. It is assumed that after that time, on reaching the condition when the time derivative of the Gibbs free energy becomes positive, 'locking' of grain growth occurs. A sequence of such locking–unlocking events is considered to represent the grain growth kinetics. The effective grain growth rate, V_{eff}, is given by the equation [76]:

$$V_{\text{eff}} = V \cdot \left(\frac{t^*}{\tau}\right) = \frac{1}{24} \cdot \frac{\gamma D_{SD}}{NkTZ(\delta\beta)^2} \cdot \left(\frac{R}{d}\right)^2 \tag{2.10}$$

which is valid below a certain critical grain size

$$R_c = 24NkTZ(\delta\beta)^2 \frac{m}{D_{SD}} \tag{2.11}$$

Here, V is the 'unperturbed' rate of grain growth driven by the boundary energy; γ, δ, β and m are GB characteristics: free energy per unit area, grain boundary

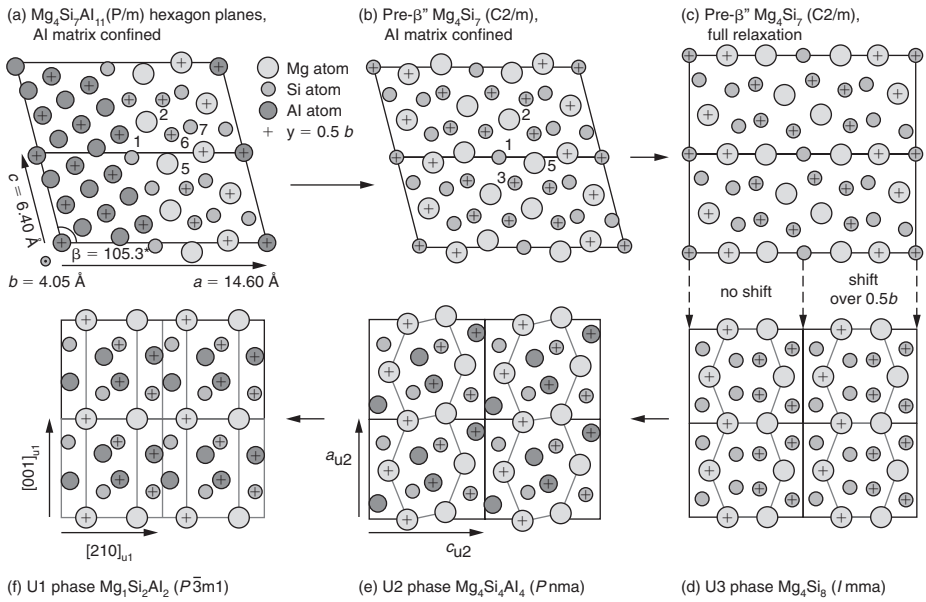

FIGURE 2.13 Phase transformation sequence from pre-β" to U2 to U1. The lattice parameter perpendicular to the plane is coherent or semi-coherent with the Al lattice (y = $[010]_{Al}$ = 4.05Å). (a) Early stage showing the correspondence of the Mg_4Si_7 phase with the Al matrix. It actually consists of one hexagon slice separated by an Al slab of the same thickness. (b) Pre-β" Mg_4Si_7 phase when confined to Al lattice dimensions. (c) Pre-β" Mg_4Si_7 phase after full relaxation of the unit cell. The monoclinic cell is almost rectangular. (d) U3 phase, which follows from the Mg_4Si_7 phase by the addition of one Si atom (Mg_4Si_7 + Si = Mg_4Si_8) and a shift along 0.5b of half the unit cell (i.e. shift one hexagon slice). (e) U2 phase, which can be formed from the U3 phase by partial substitution of Si atoms by Al atoms. (f) Triclinic U1 phase displayed along the [110] axis. This phase can be formed from the U2 phase by removing two Mg atoms per Mg hexagon [75].

thickness, the relative excess free volume, and mobility, respectively; R is the average grain radius, D_{SD} the bulk self-diffusion coefficient, N the number of atoms per unit volume, and Z is the coordination number; kT has the usual meaning. Dv is the vacancy diffusivity and d is the characteristic vacancy sink spacing. τ is the total time of exposure at temperature T.

Rong [77] has reported that the reversal transformation temperatures of the low-temperature phases in nanocrystalline Co bulk metal and Fe–30Niwt% alloy are significantly raised by over 800°C when their grain sizes are smaller than about 15 nm, while in the reported experiments of Asaka et al. [78] on nanocrystalline particles and films, the reversal transformation temperature decreased with decreasing grain size or was practically independent of grain size. The critical size for the high-temperature fcc phase being stable at room temperature was calculated as 18 nm for b-multiple twinned icosahedron shape or 110 nm for b-Wulff polyhedrons (Figure 2.14).

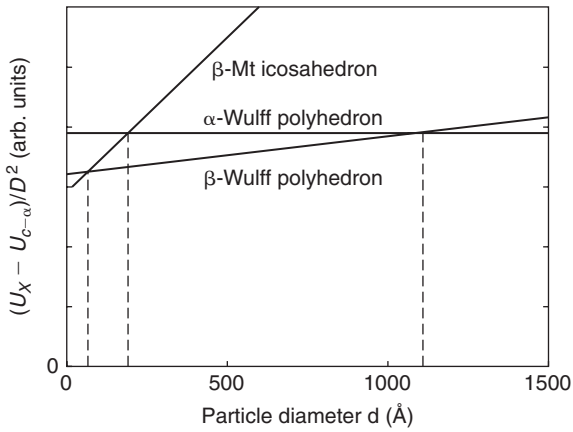

FIGURE 2.14 Calculated energy diagram of a Co fine particle as a function of particle diameter d for three different crystalline states, viz., a β-MT icosahedron, a β-Wulff polyhedron and an α-Wulff polyhedron. $U_{c-\alpha}$ corresponds to the cohesive energy of an α-Co particle [79].

The total free energy for a particle with the Wulff polyhedron shape shown in Figure 2.15 can be expressed as:

$$U_{\text{wulff}-\alpha} = -U_{c-\alpha} + U_{s-\alpha} + U_{sf} \tag{2.12}$$

where $U_{c-\alpha}$, $U_{s-\alpha}$, and U_{sf} denote the cohesive energy, the surface energy and the stacking fault energy, respectively. Since stacking faults parallel to the [0001] plane were frequently observed in the α-Co particles, the third term is added, although this term is negligible compared with the other two.

The energy terms in Eq. (2.12) are given by:

$$U_{c-\alpha} = E_{c-\alpha}\ V_{\alpha}(D) \tag{2.13}$$

$$U_{s-\alpha} = \gamma_{00.1} + \Sigma S_{00.1} + \gamma_{01.1}\Sigma S_{01.1} \tag{2.14}$$

$$U_{sf} = \gamma_{sf}\Sigma S_{sf} \tag{2.15}$$

where $E_{c-\alpha}$ is the cohesive energy of α-Co per unit volume, $V_{\alpha}(D)$ is the volume of the Wulff polyhedron and is equal to $0.409D^3$, $\gamma_{hk.l}$ is the surface energy of (hk.l) plane, $S_{hk.l}$ is the surface area of each (hk.l) plane, γ_{sf} is the stacking fault energy per unit area and S_{sf} is the surface area of each stacking fault plane, with D the particle diameter. Assuming that each α-Co particle contains seven stacking fault planes, the total area can be derived as $\Sigma S_{sf} = 6.93D^2$. On substituting these values into Eqs (13–15), Eq. (2.12) can be rewritten as:

$$\begin{aligned} U_{\text{Wulff}-\beta} &= -E_{c-\alpha}V_{\alpha}(D) + 9.56 \times 10^{-20} D^2 + 0.16 \times 10^{-20} D^2 \\ &= -E_{c-\alpha}V_{\alpha}(D) + 9.72 \times 10^{-20} D^2 \ \text{(joule)} \end{aligned} \tag{2.16}$$

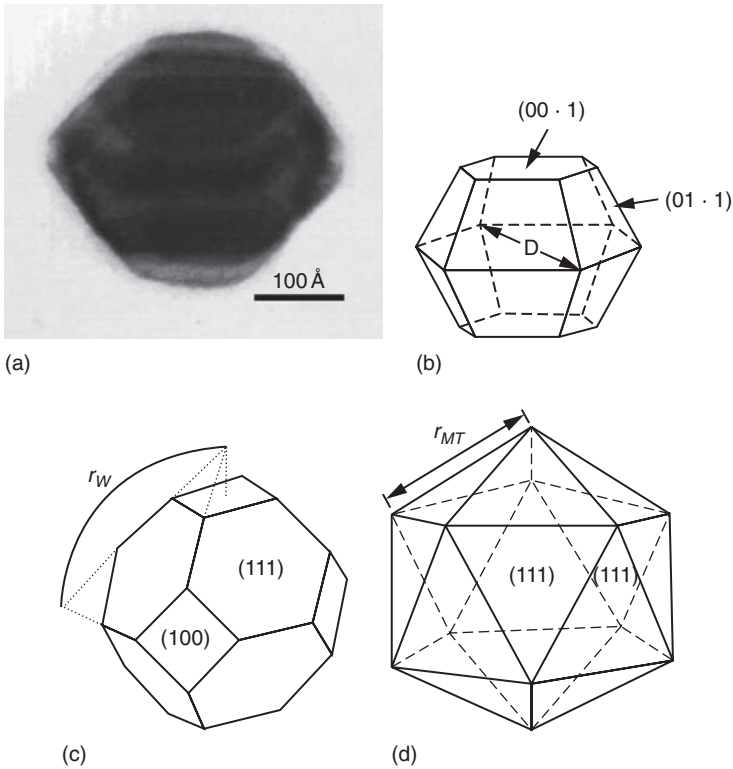

FIGURE 2.15 (a) An external shape of an α-Co particle grown at an Ar gas pressure of 0.35 Torr and (b) the Wulff polyhedron of α-Co constructed by the Gibbs–Wulff relation. Both external shapes look very similar. (c) A β-Wulff polyhedron surrounded by eight [111] and six [100] faces. (d) A multiple twinned (MT) icosahedron composed of twenty tetrahedrons, each of which is surrounded by four β [111] faces. The icosahedron consists of one nucleus, and three primary, six secondary, six tertiary, three quartic and one quintic twins [79].

Here, D is in angstroms. Similarly, the total energy for a β-Wulff polyhedron, β-MT icosahedron (see Figure 2.15c) can be expressed as:

$$U_{\text{wulff}-\beta} = -E_{c-\alpha} V_{\beta}(r_w) + 1.54 \times 10^{-23} + 7.97 \times 10^{-20} D^2 \tag{2.17}$$

$$U_{b-MT} = -U_{c-\alpha} + 13.0 \times 10^{-23} D^3 + 7.29 \times 10^{-20} D^2 \text{ (joule)} \tag{2.18}$$

We note from Figure 2.15 that the relationships of the three energy levels $U_{\text{Wulff}-\beta}$, $U_{\beta-\text{MT}}$, and $U_{\text{Wulff}-\alpha}$ are given as:

$$U_{\text{Wulff}-\beta} \leq U_{\beta-\text{MT}} \leq U_{\text{Wulff}-\alpha} \quad \text{for } 60 \leq D \leq 180 \text{ Å} \tag{2.19}$$

$$U_{\text{Wulff}-\beta} \leq U_{\text{Wulff}-\alpha} \leq U_{\beta-\text{MT}} \quad \text{for } 180 \leq D \leq 1100 \text{ Å} \tag{2.20}$$

$$U_{\text{Wulff}-\alpha} \leq U_{\text{Wulff}-\beta} \leq U_{\beta-\text{MT}} \quad \text{for D} \geq 1100\ \text{Å} \tag{2.21}$$

Co particles with particle sizes smaller than about 20 nm retain the fcc structure at room temperature (RT), while the hcp (α) $\rightarrow$ fcc (β) martensitic transformation takes place at 693 K in coarse-grained bulk samples. The phase stability also depends on the processing methods. For example, by using magnetron sputtering, Rong [77] got a granular film of Co, with an average grain size of 10 nm, consisting of ε-hcp (α-Co) martensite and fcc (β-Co), rather than a single fcc (β-Co) high-temperature phase, even though the grains were smaller than the predicted critical value of 18 nm.

Since the preparation of nanocrystalline materials is often under non-equilibrium conditions, the processing parameters affect structure markedly and, in turn, the phase transformation behaviour. Different combinations of phases in the same grain size range have been observed in many experiments. The difference between the grain (particle) shapes could have led to some extent to a distribution in the values of the critical size needed to form a stable phase. The stability of a nanocrystalline low-temperature phase at high temperatures seen in bulk Co or Fe–30Ni alloy, when the grain size was smaller than a certain size (about 15 nm), however, could not be observed in nanocrystalline particles or films [77]. The behaviour of Fe–Ni samples could be explained to a reasonable extent by some of the theories of grain-growth kinetics, e.g. solute drag, vacancy generation and the role of triple junctions. For example, Figure 2.16 shows a minimum on the total molar Gibbs free energy in the vicinity of a grain size of about 15 nm for the given alloy. The presence of this minimum suggests the possibility of inhibiting the grain-growth process and stabilizing the nanocrystalline structure, if the initial grain size values are lower than that corresponding to the Gibbs free energy minimum. The solute drag mechanism mentioned above has been

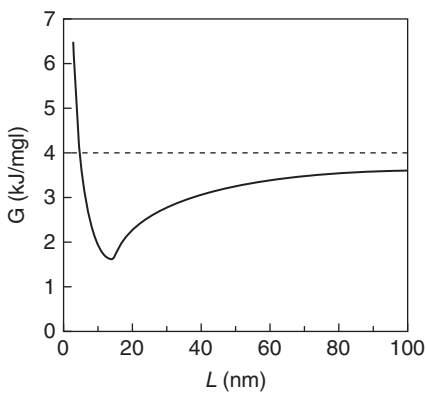

FIGURE 2.16 Variation of the molar Gibbs free energy, G, of a binary alloy polycrystal, with grain size *L* at fixed *P*, *T* and fixed overall solute concentration $x_\beta = 0.05$. The dotted line denotes the Gibbs free energy of the solid solution single crystal with the same x_β [77].

verified by grain growth in nanocrystalline powders of $Pd_{1-x}Zr_x$. At a supersaturated concentration of x = 0.2, little or no grain growth was observed up to about 500°C. The solute drag mechanism may well be used to explain the stability of the nanocrystalline structure in Surface Mechanical Attrition Treated (SMAT) Fe–30Ni alloy [77].

Various recent studies have pointed out that the temperature–pressure phase diagrams of coarse-grained specimens are not valid for nanostructured materials. For example, the relative phase stability was found to be reversed due to the enhanced surface energy contribution at very fine particle sizes [80].

Nanostructured thin film multilayers, comprising alternating A/B layers, can display metastable structures in one or both the layers. From a classical thermodynamics viewpoint, the reduction in the interfacial energy is primarily responsible for this stabilizing effect. Based on this idea, a model has been constructed in which phase stability regions are represented as functions of both the bilayer thickness and the volume fraction of one of the layers. In this model, a normalized free energy with respect to the surface area of the film, Δg, is used to describe the total free energy of the multilayer. This can be seen below in the equation [81]:

$$\Delta g = 2\Delta\gamma + [\Delta G_A f_A + \Delta G_B f_B]\lambda \tag{2.22}$$

where $\Delta\gamma$ is the change in interfacial free energy between the metastable and the bulk equilibrium phases, ΔG_i is the allotropic volume free energy change of component i (where i is A or B), f_i the volume fraction of component i, and λ is the bilayer thickness of layer *A* plus layer *B*. For simplicity, all terms that scale with volume are contained in the ΔG free energy and all terms that scale with area are contained in the $\Delta\gamma$ free energy.

By plotting the inverse of λ against f_i, phase stability diagrams, referred to as a biphase diagram, are constructed. These diagrams map out regions of phase stability and provide a quick and convenient tool for predicting the combinations of volume fraction and length scale, λ, that will lead to changes in phase. Such diagrams are seen in Figures 2.17 and 2.18.

It has been reported [81] that Zr undergoes a phase transformation from hcp to bcc Zr in Zr/Nb multilayers when the bilayer thickness, λ, is reduced below 3.2 nm for a 50% Zr/50% Nb multilayer. Using this result and the thermodynamic model described above, additional phase stabilities, as a function of length scale, λ, and volume fraction, f_{Nb}, were explored for Zr/Nb. Based on the chemical similarities between Ti and Zr, changes in phase stability for Ti in Ti/Nb multilayers could also be investigated. It is evident that understanding in this fascinating area is emerging only very slowly at present.

3.2 Phase Instability of Nanocrystalline Ceramics

Nanocrystalline ceramics are considered to be very promising materials, with enhanced mechanical properties for applications at intermediate and high temperatures and for applications arising from their unique functional properties.

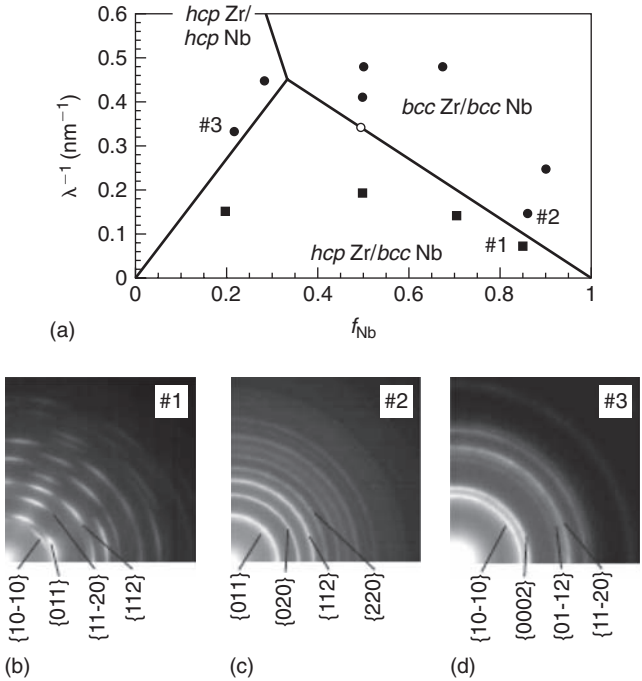

FIGURE 2.17 (a) The biphase diagram for Nb/Zr multilayers. TEM plan view diffraction patterns: (b) hcp Zr/bcc Nb, (c) bcc Zr/bcc Nb, (d) hcp Zr/hcp Nb [81].

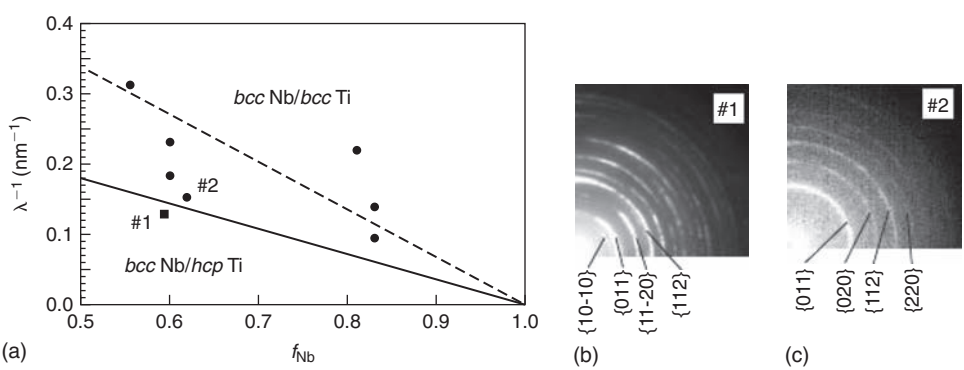

FIGURE 2.18 (a) Biphase diagram for the Ti/Nb system. The dashed line represents the bcc/bcc boundary in Zr/Nb for comparison. TEM plan view diffraction patterns: (b) hcp Ti/bcc Nb, (c) bcc Ti/bcc Nb [81].

One of the challenges in processing these materials is to maintain the nanocrystalline grain structure in the fully dense ceramics after sintering and deformation. A low sintering temperature is a necessary, but not sufficient, condition for achieving the required nanoscale microstructure [82].

Production of dense, bulk nanocrystalline oxides is very challenging since grain growth is inevitable at the relatively high sintering temperatures needed for

densification. MgO has a high melting temperature (≈2850°C) and temperatures as high as 1700°C were reported for pressureless sintering of micrometre-size MgO powder to full density. Decrease in the particle size of the MgO powder into the nanometre range (11–260 nm) resulted in nearly 100% dense specimens with sub-micrometre grain sizes [83]. One of the significant factors in the sintering and densification of nanocrystalline powder compacts is the high specific surface area that acts as a driving force for sintering and densification. Surface diffusion is an active and, under some conditions, even the dominating diffusion mechanism during sintering, compared with grain boundary and lattice diffusion [84].

The experimental data obtained at temperatures above 750°C tend towards lower densities, whereas those below 750°C tend towards higher densities. Several reasons may explain this experimental observation. Hot-pressing experiments of the same nc-MgO powder between 720°C and 790°C showed that the immediate volume shrinkage rate, after the application of a pressure of 150 MPa, increased with an increase in temperature. Therefore, at the higher spark plasma sintering (SPS) temperatures of 775°C and 800°C, one expects that a major portion of the shrinkage in achieving <90% density would take place in a shorter duration than at 750°C (20 s). At the lower temperatures of 725°C and 700°C, the main shrinkage will take place over longer durations than at 750°C. Consequently, grain growth above 90% density, which discourages densification processes, will be greater at the higher temperatures [84]. In order to reduce or suppress grain growth, the mobility of grain and phase boundaries can be reduced, for example, by the presence of impurities, pores or particles of a second phase. It has been shown that second-phase particles are especially effective in suppressing static and dynamic grain growth [85].

Very large grain growth can be present if the particle distribution is inhomogeneous, the size of the second phase particles are too large or the volume fraction of the second phase is too low to pin all the grain boundaries [85].

The grain size/density regime that can be obtained during the sintering of different materials is an important aspect in discussing the different types of grain growth behaviour. A plot of grain size versus relative density in n-ZrO_2 and n-ZrO_2–Al_2O_3 composites is shown in Figure 2.19. The grain size in pure n-ZrO_2 shows a drastic increase at densities in excess of 90%, when pinning by pores (pore drag) becomes less pronounced. In order to provide efficient grain boundary pinning, the particles of the second phase have to fulfil several of the following conditions [85,86]:

1. small diffusion coefficients into the matrix for the atomic species of the particles;
2. small or no solubility of the particles in the matrix;
3. small interfacial energy between the two phases;
4. a homogeneous distribution of the second phase;
5. stability against dissolution and coarsening.

The prevention of grain growth in nanocrystalline ceramics remains a critical task that needs to be accomplished in order to:

1. expand their technological applicability;
2. improve the effectiveness of processing methods; and
3. study their properties at high temperatures [87].

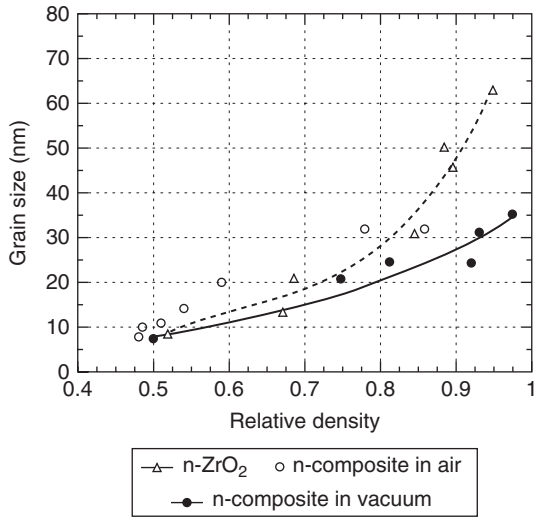

FIGURE 2.19 Grain size as a function of relative density of pure n-ZrO_2 and n-ZrO_2–Al_2O_3 composite after sintering in air and vacuum [85].

Table 2.1 The effect of grain size on the phase structure of ZrO_2 at 1273 K [77]

Hold time (min)	Grain size (nm)	Structure	
		t-phase (%)	m-phase (%)
0.5	14	100	0
2	18	51	49
3	21	36	64
30	31	0	100

The composite ceramic shows a different sintering behaviour, leading to a different grain size/density regime than for pure n-ZrO_2. It is obvious from the grain size/density curves that the atmosphere influences the sintering behaviour of the n-composite. The highest density obtained by sintering in air at the highest temperature of 1200°C was 86% at an average grain size of 32 nm. In contrast, the grain size and density of the n-composite sintered in vacuum at 1200°C were 35 nm and 98%, respectively.

The variations in particle size and phase structure of ZrO_2 with annealing time are given in Table 2.1.

These results clearly demonstrate the effect of grain (particle) size on phase stability since conventional coarse-grain (particle) ZrO_2 undergoes the t → m martensitic transformation at a temperature of 1273 K during cooling [77]. Needless to say, phase stability and thermal stability are interrelated.

Table 2.2 Structure and properties of $FeSi_2$ nanowire phases [88]

Phase	Lattice parameter (Å)	Lattice	Property
α	a = 2.684 c = 5.128	Tetragonal P4/mm	Metallic
β	a = 9.863 b = 7.791 c = 7.833	Orthorhombic Cmca	Semiconducting
γ	a = 5.39	Cubic (fcc) Fm3m (CaF_2)	Metallic and magnetic
s	a = 2.7	Cubic (bcc) Pm3m (CsCl)	Metallic

Transition-metal silicides play an important role in current microelectronic and optoelectronic devices [88]. Among the transition metal silicides, $FeSi_2$ is the only reported light emitter. The transformation of phases in $FeSi_2$ nanowire is presented in Table 2.2.

It is reported by Liang et al. [88] that self-assembled epitaxial iron silicide nanowires (NWs) grown on Si (1 1 0) can be converted from a cubic s-phase $FeSi_2$ to an orthorhombic β-phase $FeSi_2$ by annealing at 800°C for 1 h. The transformation temperature of 800°C is considerably higher than that observed in thin films (200–500°C), due to the small thickness and large interface area of the NWs, which stabilize the s-phase. NW shapes survive annealing at 800°C for 1 h, while the films are normally disrupted. These two phases (γ and s) are metallic and magnetic vs. semiconducting, in thin films. The possibility of single crystal magnetic or semiconducting NWs grown on Si represents a good opportunity for nanoelectronic applications.

3.3 Thermal Stability of Nanostructured Materials

One of the fundamental requirements is that the nanosized microstructure and the resultant attractive properties should be retained for the desired period of time in a specified temperature range. Changes in the structure of nanomaterials with respect to temperature could affect vastly the reliability of the materials/devices at the service temperature. Thermal stability is a general term used to describe the change (or the absence) of material properties as a function of temperature. These properties include oxidation tendency, structure, composition, and mechanical properties. Thermal stressing and relaxation caused by temperature variations could lead to instability.

Structure and thermal stability are natural concerns/fundamental issues in nanocrystalline materials, especially in nanometals [89,90]. High thermal stability is one of the many important properties required for the industrial application of hard and superhard coatings on cutting tools. Unfortunately, not all superhard nanostructured coatings that have been reported in the last decade meet this condition [91].

In recent years, considerable attention has been focused on ternary nitrides containing a low amount of Si, particularly on Ti–Si–N [92–96], W–Si–N [97],

Zr–Si–N [97], Ta–Si–N, Mo–Si–N and Cr–Si–N. The addition of Si as the third element in the ternary nitride is based on the fact that Si easily forms Si_3N_4 and causes the structure of Si_3N_4 to remain amorphous up to high temperature due to the crystallization temperature considerably exceeding 1000°C. The amorphous structure is an excellent barrier to the penetration of oxygen to the substrate surface through the coating and thus improved oxidation resistance is expected to be achieved if the Me–Si–N films contain a reasonable amount of amorphous Si_3N_4 (beyond the percolation threshold). Moreover, incorporation of Si into the film results in (a) a substantial reduction in the macro-stress and (b) an increase in the thermal stability of the mechanical properties, particularly the hardness, H [97].

The reason for the high hardness of these coatings is not well understood. Recent experiments with Zr–Si–N and Ta–Si–N indicate that films composed of amorphous Si_3N_4 and overstoichiometric $MeN_{x>1}$ phases could exhibit high thermal stability up to temperatures in excess of 1000°C.

Nanocrystalline films with high hardness have great potential for wear-resistant applications. Specifically, Ti–B–N layers have been shown to exhibit enhanced hardness, good corrosion, wear resistance and thermal stability, which could give rise to different industrial applications. TiB_2 offers outstanding properties like high hardness, good abrasive and sliding wear resistance and high inertness against liquid alumina [98]. A thorough understanding of the thermal stability of the nanostructured alloys is necessary before one could consider engineering applications that will prove successful in the long run [99].

3.3.1 Nanostructured aluminium alloys

The following is a discussion of the changes in the properties and structure in high temperature environments of nc-Al alloys. In Figure 2.20, values of the mean size, size diversity and grain shape, quantified by $E(d_2)$, $CV(d_2)$ and $E(d_{max}/d_2)$, respectively, are plotted against the annealing temperature.

One can infer from Figure 2.20 that, in the nanostructured aluminium alloy, the grain size is stable up to an annealing temperature of about 300°C (573 K). This is approximately 0.65 of the melting point of 873 K. At higher temperatures, the mean grain size begins to increase and, on annealing at 400°C, the mean equivalent diameter reaches 12 μm. An analysis of the changes in the coefficient of variation CV (d_2) versus annealing temperature (Figure 2.20) indicates that the grain size distribution becomes more homogeneous with an increase in the annealing temperature. These changes in the size and size distribution are accompanied by an equilibration of the shape of the grains, which become more equiaxed. Hence, there is a reliability issue at the higher temperatures [100].

Proper structural modifications will result in a thermally stable structure and the reliability of the materials could be improved greatly. Improvement in thermal stability is achieved by suppressing the migration of grain boundaries through the segregation of solute atoms or the pinning of the boundaries by dispersed particles. However, the reduction in grain boundary mobility due to solute drag is temperature-limited on account of faster diffusion at higher temperatures. Grain boundary pinning by dispersed particles is very effective up to very high temperatures, but recent investigations have shown that the presence

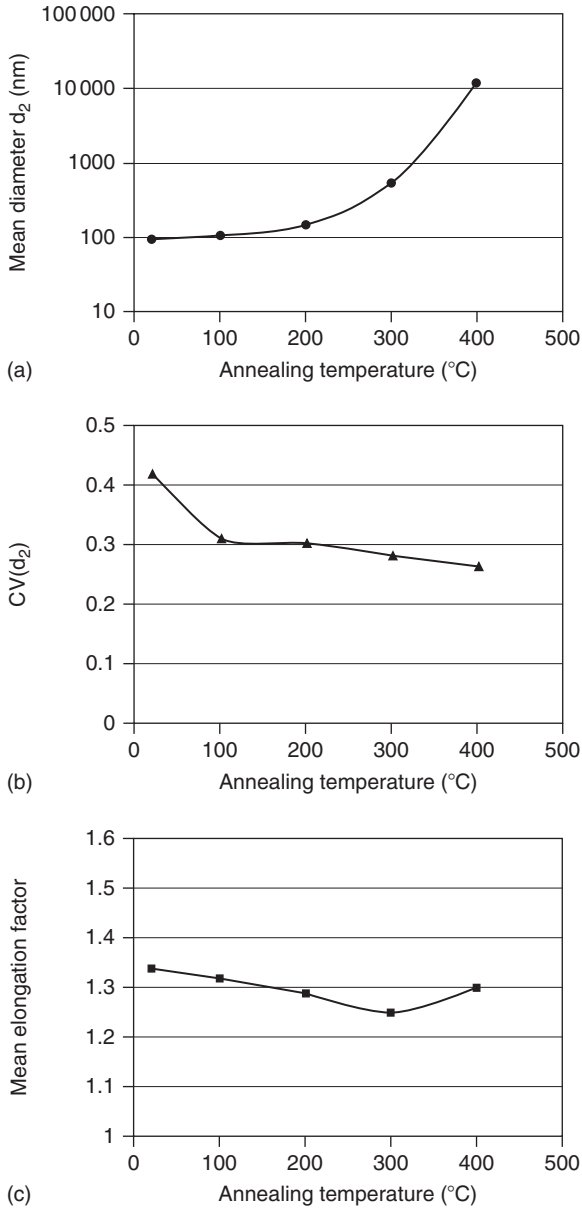

FIGURE 2.20 Plot of (a) the mean equivalent diameter, (b) the coefficient of variation of grain size and (c) the grain elongation factor, against the annealing temperature [100].

of fine, non-shearable dispersoids inhibits the formation of cells, dense dislocation walls and high-angle grain boundaries. This, in turn, delays the development of uniform nanostructures even at very high strains. A reduction in density may reduce this unfavourable role of the dispersed particles, but this will result in less

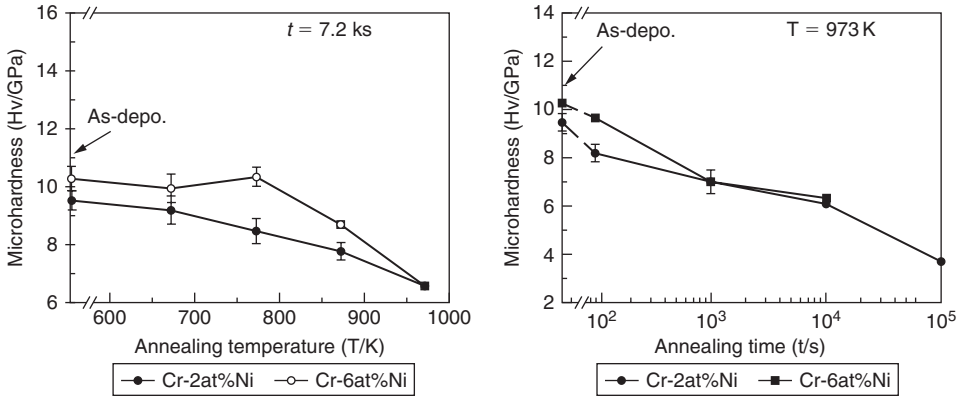

FIGURE 2.21 Change in microhardness of Cr–Ni alloys with annealing temperature and time. The grain sizes of un-annealed sputtered material are 83 and 69 nm for the Cr-2at% Ni and Cr-6at%Ni alloy, respectively [99].

effective pinning of the grain boundaries. The above considerations lead to a conclusion that new methods of improving the thermal stability of nanocrystalline Al-alloys are still of great interest, particularly with regard to severe plastically deformed (SPD) materials [100].

3.3.2 Nanostructured Cr–Ni alloys

Cr–Ni alloys prepared by sputtering have nanometre-sized grains and high hardness. The hardness variation with annealing temperature and time is displayed in Figure 2.21.

The hardness of both the alloys decreases monotonically on increasing the annealing time, up to an annealing temperature of 973 K. The structures of both the alloys change from bcc single phase to a mixture of bcc + fcc phases. Although the secondary phase of nickel appears at a certain annealing time, the effect of precipitation of the nickel phase is not revealed by the microhardness change. It suggests that an increase in the grain size of the alloys (Figure 2.22) decreases the microhardness of the alloys significantly, after high temperature annealing at 973 K [99]. The acceleration in grain growth will reduce the reliable performance of these materials.

3.3.3 Austenitic stainless steel AISI 304

As of now, the production of nanocrystalline bulk materials is expensive and very time-, equipment- and cost-intensive. On the other hand, most failure mechanisms of engineering materials such as fatigue crack nucleation, corrosion or wear, take place at the surface. Therefore, an alternative to bulk nanocrystalline material could be material with a nanocrystalline surface layer, which is easier to produce and is more cost-efficient [101].

The microstructure of AISI 304 surface layer is stable during short isothermal annealing up to 600°C for up to 0.3 h annealing time. Long-time annealing

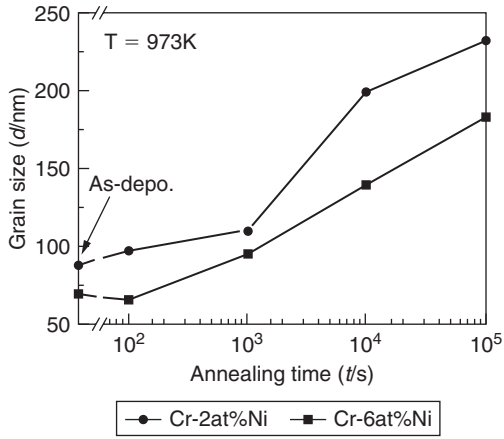

FIGURE 2.22 Change in grain size of Cr-2at%Ni and Cr-6at%Ni alloys with annealing time at an annealing temperature of 973 K [99].

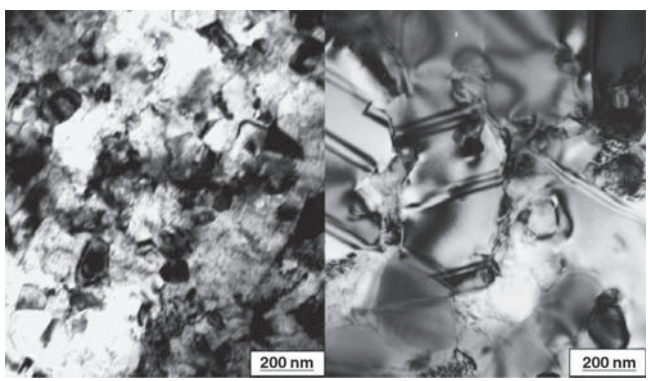

FIGURE 2.23 TEM micrographs of the deep rolled and annealed surface region of AISI 304 for different annealing times at 600°C (1 h (left) and 100 h (right)) [101].

at 600°C (10–100 h) led to recrystallization. After 10 h at 600°C, the nanocrystalline layer transformed into a fine, equiaxed grain structure with an average grain size of about 150–200 nm from an initial grain size of 30 nm. After 100 h at 600°C almost complete recrystallization of the nanocrystalline layer had taken place and the grain size was greater than 200 nm [101]. Figure 2.23 displays a TEM micrograph of the annealed region of AISI 304 after different annealing times (1 h (left) and 100 h (right)) at 600°C.

4. THERMAL STABILITY OF COATINGS

The superhard coatings possess an unusual combination of mechanical and chemical properties such as high fracture toughness, high oxidation resistance and

high thermal and chemical stability [102–104]. Efforts towards the development of superhard coatings, defined by hardness values greater than 40 GPa, have increased significantly in the last 15 years because of the scientific challenges and industrial applications. It is important to evaluate the thermal stability of hard coatings because, at high working temperatures, the mechanical and the tribological properties deteriorate.

There are two main reasons for the high hardness found in coatings: it could be due either to high compressive stresses or a nanoscale structure [105]. Veprek et al. [106–108] have pointed out that superhardness is the result of a well-defined interface of high cohesive strength (along with the small grain size), which prevents crack propagation along the grain boundaries. Only compounds exhibiting a certain affinity for each other, combined with a wide miscibility gap, answer these criteria and exhibit high hardness and thermal stability. The application of a high biaxial compressive stress acts as a driving force for recovery, i.e. the higher the compressive stress, the lower is the thermal activation energy needed to initiate recovery. Thus, a high biaxial compressive stress increases superhardness, but reduces the thermal stability of the coating. The microscale compressive stress inside the coating is increased by the presence of dislocations and this also promotes recovery. In contrast, in nanoscale coatings, the small grain size and heterostructure restrict grain growth and large-scale boundary sliding and thereby the thermal stability is enhanced. The net result of these counteracting effects is complex [107,109–111].

Superhard coatings may be classified into four separate groups [112]:

1. intrinsically superhard materials like diamond, diamond-like carbon (DLC) and cubic boron nitride (c-BN);
2. thin coatings in which the hardness is due to a complex, synergistic effect of ion bombardment during their deposition by plasma chemical or physical vapour deposition (PECVD or PVD);
3. nanocomposite coatings which require thermodynamically driven phase segregation; and
4. multilayer structures.

Superhard coatings are considered to exhibit high thermal stability if hardness and grain size (which depend on the nanostructure and composition), measured at room temperature, remain unchanged upon annealing at a temperature of (at least) 1100°C. Researchers have employed different methods to investigate the thermal stability of superhard coatings:

1. measuring the hardness at room temperature after annealing at high temperatures;
2. measuring the dependence of hardness on composition (the segregation stability and diffusion between the substrate and coating);
3. measuring the stability of the superlattice period (L) as a function of annealing temperature;
4. measuring the biaxial stresses in the coatings in the as-deposited state and after the stress relaxation resulting from heat treatment [112].

The nanolayers (or nanocomposites) must have a well-defined interface of high cohesive strength, because the small grains hinder dislocation formation and movement and a well-defined interface, due to non-availability of very large thermal activation, hinders grain boundary sliding. Another hardness-enhancing mechanism is residual compressive stress. A high residual compressive stress increases the coating hardness towards the superhard level but, as mentioned earlier, reduces the coating stability on account of stress relaxation on annealing at high temperatures.

4.1 Nanocrystalline Films

Nanocrystalline films that have high hardness are of significance in view of their potential wear-resistant applications. Ti–Si–N and Ti–B–N possess high thermal stability. Ti–B–N layers have also been shown to display excellent combination of properties like extreme hardness, high toughness, chemical inertness and good thermodynamic stability at high temperatures [113,114]. Although TiB_2 offers outstanding properties (like high hardness, good abrasive and sliding wear resistance and high inertness against liquid alumina), its brittleness, due to the strong covalent bonds in the hexagonal B network, reduces its usefulness. Deposition of multicomponent and multiphase coatings offers the possibility of overcoming such use-limiting properties [114,115].

A number of publications [20,27,46,104,107,110,116–118] are available on superhard 'Ti-Si-N' coatings as also the generic concept for the design of superhard nc-TiN/a-Si_3N_4 and other nc-Me_nN/a-Si_3N_4 (Me = W, V) nanocomposites, with hardness greater than 50 GPa. Unlike the heterostructures and nanocrystalline metals which show softening when the crystallite size or lattice period decreases below about 5–6 nm, the hardness of the composites increases strongly with decreasing crystallite size in that range also (Figure 2.24). From Figure 2.24

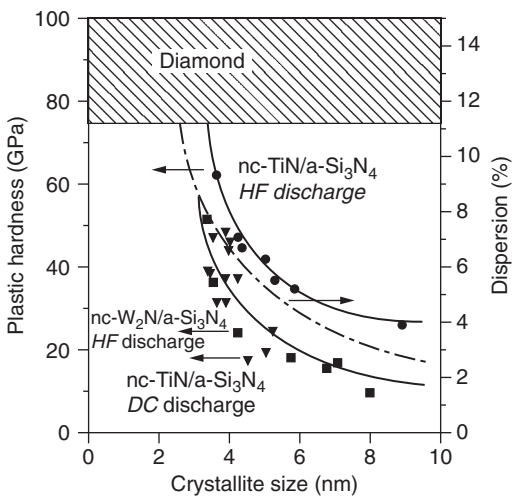

FIGURE 2.24 Dependence of the measured Vickers hardness (left scale) and the estimated degree of dispersion (right scale) on the crystallite size [106].

displaying the dependence of the measured Vickers hardness on the average crystallite size for the nc-TiN/a-Si_3N_4 and nc-W_2N/a-Si_3N_4, one can see that the hardness increase correlates well with an increase in the degree of dispersion $N_s/(N_s + N_v)$, i.e. with the relative fraction of the atoms in the interface between the nanocrystalline transition metal nitride and amorphous silicon nitride, where N_s is the number of atoms in the interfaces between the nc metal nitride and the amorphous silicon nitride and N_v is the number of atoms within the crystallites and the amorphous matrix.

The structural disorder within the grain boundaries and the incommensurability of the grain boundaries result in an excess lattice energy due to the lattice strain and a lower cohesive energy of the grain boundary interface, which result in an increase in the free energy of formation and therefore in the thermodynamic instability of the nanocrystalline phase with respect to a coarse-grained material. As result, all these systems show coarsening, i.e. an increase in the crystallite size upon annealing at a temperature where diffusion is sufficiently fast, which is typically at $T/Tm > 0.5$, with Tm the melting or decomposition point (this phenomenon is called 'Ostwald ripening') on the absolute scale [106].

Figure 2.25 shows the experimentally established dependence of the crystallite size and hardness of nc-TiN/a-Si_3N_4 films on the measured content of Si_3N_4. One notices that with increasing content of Si_3N_4, the crystallite size of TiN decreases, passes a minimum at an Si_3N_4 content of about 16–20 mol% and increases again. The minimum crystallite size correlates well with the maximum

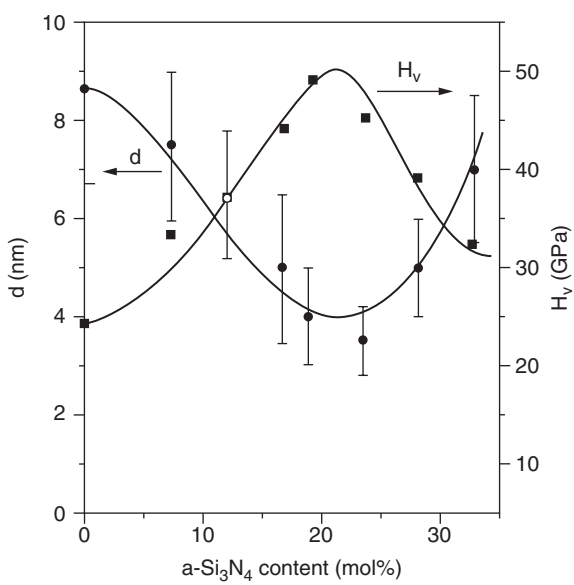

FIGURE 2.25 Dependence of the measured average crystallite size and hardness of nc-TiB/a-Si_3N_4 on the fraction of Si_3N_4 which shows minimum and maximum, respectively, at the percolation threshold. Deposition temperature: 550°C; plasma CVD from $TiCl_4$ and SiH_4 with a large excess of N_2 and H_2 [119].

hardness of the films and both occur at an a-Si_3N_4 content which corresponds to the percolation threshold for Si_3N_4 in the fcc lattice of TiN [119].

The concept for the design of novel superhard nanocomposites is based on the formation of two or more phase systems which display a thermodynamically driven segregation into a nanophase with a grain size less than about 10 nm [119]. A superhardness of 50–70 GPa was achieved by Veprek et al. [118]. Their nanocomposite was based primarily on grain boundary hardening, which is described well by the Hall–Petch relationship, albeit with a different slope.

The phase segregation in the ternary Ti–Si–N systems is chemically of spinodal nature at the nitrogen pressure and deposition temperature typically used for the deposition of the superhard nc-TiN/a-Si_3N_4 nanocomposites, viz., $p_{N2} \geq 10^{-3}$ mbar and T_{dep} 550–600°C, respectively. This segregation occurs provided the nitrogen pressure and deposition temperature are high enough, as explained in Zhang and Veprek [117].

- When deposited under the conditions of a sufficiently high nitrogen pressure (0.3–1 mbar) that provides the thermodynamic driving force and sufficiently high temperature (≥550°C) that ensures that the diffusion rate-controlled phase segregation is completed during deposition, the crystallite size is fairly uniform.
- In systems that display a larger misfit between the phases, such as nc-TiN/a-BN, the 'optimal' crystallite size, where the TiN nanocrystals are covered by about one monolayer of BN and the hardness reaches a maximum, is larger than nc-TiN/a-Si_3N_4, where this misfit is smaller.
- Coatings that were not deposited under the optimal conditions, so that the phase segregation was not completed during the deposition, show an increase in hardness upon annealing at 700°C or more. This is accompanied by the 'adjustment' of the crystallite size to the 'optimal' value of about 3–4 nm, which can be larger or smaller than the original crystallite size in the as-deposited coatings.

In Figure 2.26 the variation in the hardness and the modulus of the coatings with the annealing temperature is presented.

The hardness of the $TiB_{0.80}N_{0.83}$ films (#2) increased initially up to $T_a \leq 800$°C, due to the formation of compact interface boundaries. Then it decreased at $T_a \geq 900$°C (Figure 2.26), because the probability for dislocation formation and plastic deformation increases with an increase in grain size. However, the nanoindentation modulus, E, of Ti–B–N increases from ≈332 GPa in the as-deposited state to ≈375 GPa after annealing at $T_a \geq 900$°C. This has been attributed to a reduction in the volume fraction of the disordered phase. Thus, the elastic modulus of nanocrystalline materials is expected to increase as the grain boundary disordered phase thickness decreases [98,103]. At this stage, this can only be regarded as a conjecture, because there is no clear experimental evidence for a change in the grain boundary thickness on annealing. Also, this result (i.e. increasing E in a range where H is decreasing) is not in line with the commonly held view that the hardness of a material is directly related to its elastic modulus. More detailed examination of these results is essential.

High-resolution transmission electron microscopy (HRTEM) pictures on $TiB_{2.4}$ (#3) of Figure 2.26, presented in Figure 2.27, revealed that these coatings have a

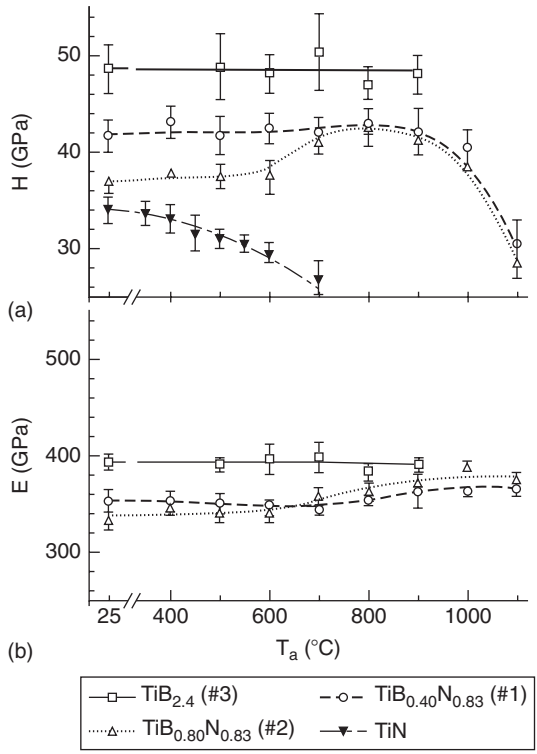

FIGURE 2.26 Hardness, H (a) and nanoindentation modulus, E (b), of PACVD $TiB_{0.40}N_{0.83}$ (#1), PVD $TiB_{0.80}N_{0.83}$ (#2) and PVD $TiB_{2.4}$ (#3) coatings as a function of the annealing temperature, T_a. For comparison, H vs. T_a is also shown for TiN coatings [103].

columnar structure, with an average feature size of ≈20 nm and (0001) preferred orientation. As-deposited $TiB_{0.80}N_{0.83}$ coatings (#2 in Figure 2.26) have a relatively equiaxed (i.e. non-columnar) nanocrystalline structure. The columns are encapsulated in excess B and are themselves composed of smaller stoichiometric TiB_2 subcolumns with an average diameter of ≈5 nm, separated by a thin B-rich tissue phase of thickness 1–2 monolayers (ML). The high cohesive strength of the thin B-rich tissue phase prevents grain-boundary sliding.

The reliability of Ti–B–N thin films at elevated temperatures depends strongly on the microstructure and the phase configuration. High thermal stability was present usually at an optimal composition, which also has a high microhardness value. Thermodynamic stability of Ti–B–N thin films is believed to be affected strongly by phase configuration and composition, which has been studied only rarely. Therefore, a more detailed investigation on the effect of nitrogen on phase segregation and microstructure evolution and the corresponding change in mechanical behaviour and thermal stability is necessary [113].

The dependence of microhardness and elastic modulus values on nitrogen content is shown in Figure 2.28. It is found that the microhardness and elastic modulus values of $TiB_{0.65}$ are about 23 GPa and 235 GPa, respectively. Both values

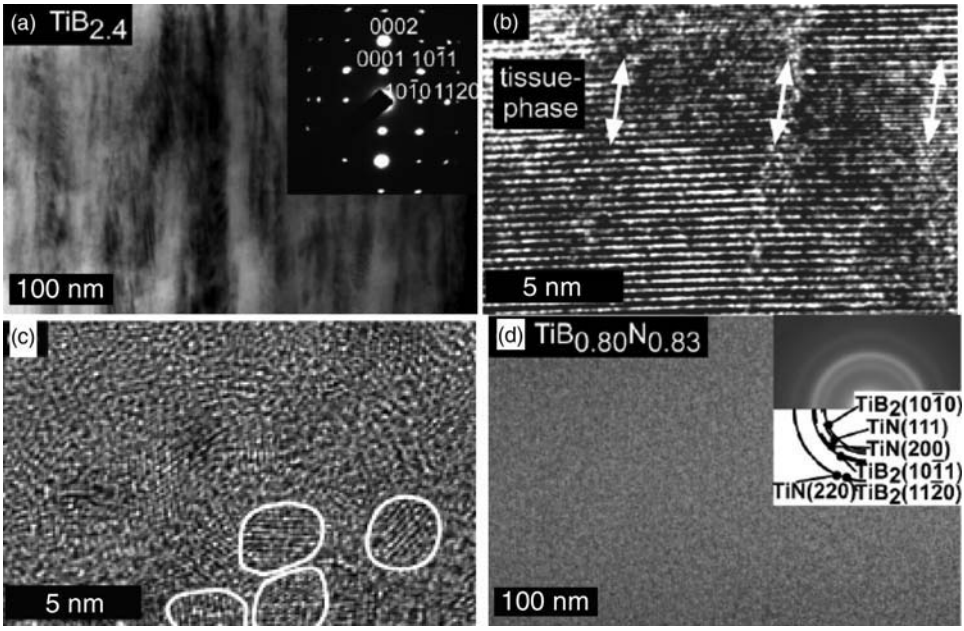

FIGURE 2.27 Cross-sectional bright-field TEM with SAED pattern (a, d) and HRTEM (b, c). (a, b) Images of as-deposited $TiB_{2.4}$. The white arrows indicate the B-rich tissue phase; (c, d) as-deposited $TiB_{0.80}N_{0.83}$ film [103].

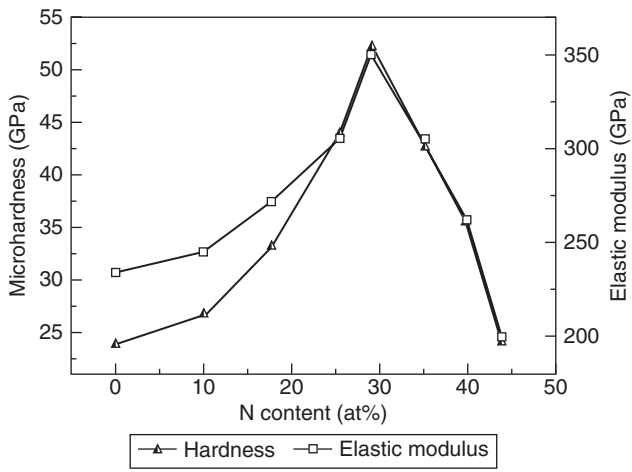

FIGURE 2.28 Microhardness and elastic modulus values as a function of nitrogen content [113].

increase with an increase in the N content. When the N content was increased to about 27 at%, both hardness and elastic modulus reached their maximum values of about 52 GPa and 350 GPa, respectively. Further addition of N decreased the hardness and the elastic modulus.

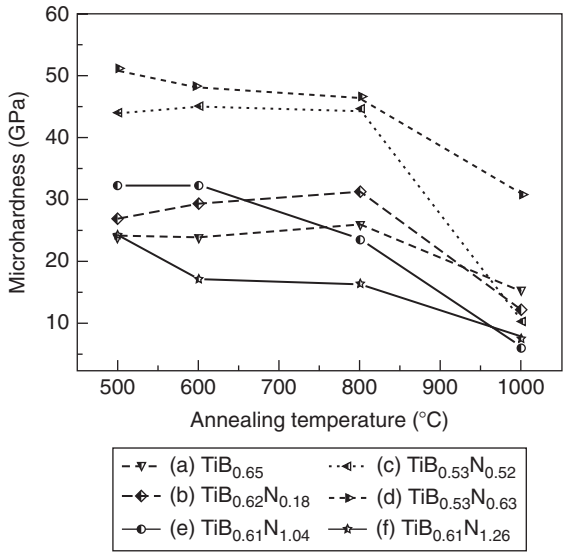

FIGURE 2.29 Microhardness values of (a) $TiB_{0.65}$, (b) $TiB_{0.62}N_{0.18}$, (c) $TiB_{0.53}N_{0.52}$, (d) $TiB_{0.53}$ $N_{0.63}$, (e) $TiB_{0.61}N_{1.04}$ and (f) $TiB_{0.61}N_{1.26}$ thin films as a function of annealing temperature [113].

The thermal stability of thin films depends strongly on phase composition and microstructure. The microstructures are believed to indicate incomplete phase segregation due to a lack of nitrogen addition. The self-hardening in this group is related to some changes in this type of microstructure at low temperatures (≈600°C) and a consequent phase segregation at a higher temperature (above 800°C). In the case of the second group of films, $TiB_{0.53}N_{0.52}$ and $TiB_{0.53}N_{0.63}$, the microstructures are very stable and do not show any obvious change after annealing at 600°C and 800°C. In other words, high thermal stability was present, as can be seen from Figure 2.29. For the third group of films, $TiB_{0.61}N_{1.04}$ and $TiB_{0.61}N_{1.26}$, the compositions are located in the three-phase zone of TiN, TiB_2 and BN in the Ti–B–N phase diagram and they have low hardness values. Under these conditions, the mole fraction of the amorphous phase had increased and appears to be in excess of that needed for the optimal composition. As a result, the grain boundary becomes unstable. With increasing temperature, nanostructural relaxation of the amorphous matrix at low temperatures and crystallization of the amorphous matrix or the recrystallization of the nanocrystallites at high temperatures were present. Then, the microhardness values continuously fell with an increase in the annealing temperature, as displayed in Figure 2.29 (e) [113].

Nitrogen content had a significant effect on phase segregation and the formation of a nanocomposite structure. An amorphous Ti–TiB_2 compound thin film was formed without nitrogen doping. Addition of a small amount of nitrogen (10 at% N in this study) caused phase segregation, which resulted in the formation of nanocomposite nc-TiN/a-TiB_2 thin films. Increasing the nitrogen content accelerated further segregation of the phases, which was followed by the formation

of nanocomposite nc-TiN/a-TiB_2 thin films. Further increase in the N content accelerated the formation of BN bonding and the corresponding nanocomposite nc-TiN/a-TiB_2/a-BN thin films were formed [113].

4.2 W–Si–N Films

Recrystallization in the W–Si–N system as a result of annealing at 900°C increases the hardness. Annealing at still higher temperatures results in recovery, grain growth and a decrease in hardness. Further, when oxygen was added to W–N coatings, the hardness of the coating and its thermal stability decreased [97,102].

The addition of N into the W–Si film strongly changes its structure. The W–Si–N films, with a low (<1.33) ratio of N/Si, exhibit a crystalline structure and those with a high (>1.33) ratio of N/Si are amorphous. The amorphous films contain a high (>50 vol%) amount of the Si_3N_4 phase [97].

4.3 Superhard Coatings

Friction between the cutting tool and the work-piece causes intense heating, which affects the coating and substrate properties. This heat accelerates stress relaxation, recrystallization and grain growth, diffusion between the coating and substrate and oxidation. Thus, the most important properties required of a high-temperature superhard coating are:

1. high oxidation resistance;
2. low miscibility between the coating compounds, in order to prevent diffusion among them;
3. low residual compressive stress;
4. low solubility at high temperatures between the substrate and the work-piece.

Figure 2.30 compares the thermal stability of a superhard nanocomposite (nc-TiN/a-Si_3N_4) with that of ordinary coatings that have their hardness enhanced by energetic ion bombardment during their deposition. It can be seen that nc-TiN/a-Si_3N_4, prepared according to the generic design principle, shows high hardness and thermal stability. In contrast, superhard coatings such as HfB_2, ZrN/Cu and ZrN/Ni, fabricated by energetic ion bombardment during their deposition, show low thermal stability and their hardness rapidly decreases with increasing annealing temperature [112].

Some superlattice coatings such as Cu/Ni, TiN/NbN exhibit low thermal stability. This is due to these materials having coherent low-energy interfaces. Usually they are miscible, i.e. they suffer from rapid interdiffusion at elevated temperatures, and this leads to low thermal stability [112].

The other types of multilayer coating used in the industry are nitride/nitride multilayers, including TiN/AlN, CrN/WN and TiN/NbN multilayer coatings. These coatings display high hardness, chemical inertness and toughness. They have a high hardness value at ambient temperatures. But, in these types of coating, two critical issues have to be faced if heat treatment in air at elevated temperatures is to be employed. One is the interdiffusion of the two nitride layers,

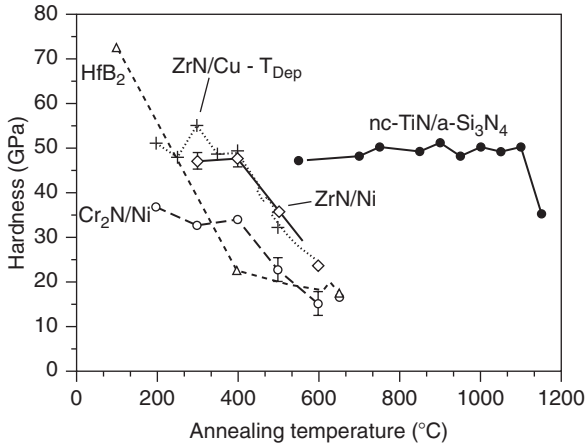

FIGURE 2.30 Hardness variation with annealing temperature [112,117].

Table 2.3 Characteristics of CrN/AlN and TiN/AlN multilayer coatings as-deposited and after different heat treatments [106]

Coating	As-deposited		800°C for 1 h		Film thickness (nm)	Onset temperature for oxidation (°C)
	H(GPa)	R_a(nm)	H(GPa)	R_a(nm)		
CrN/AlN	30.1 ± 1.6	2.8	23.7 ± 0.4	3.1	1000	850
TiN/AlN	28.9 ±1.2	2.5	8.2 ± 2.1	10.6	400	762

which causes the disappearance of the nanolayered structure. The other more serious issue is the formation of a loose and soft oxide on the surface. Both the changes will reduce the hardness of the multilayer coatings [105].

At 800°C, which was above the onset temperature for oxidation of 762°C, crystalline TiO_2 had formed underneath a dense Al_2O_3 layer, indicating that oxygen had diffused inward through the Al-rich layer to react with TiN. The path for the inward diffusion of oxygen could have been the grain boundaries between the oxides and oxygen vacancies [106]. Table 2.3 presents the onset temperature for oxidation for different coatings.

Figure 2.31 displays TEM images of a TiN/AlN multilayer coating after heat treatment at 800°C for 1 h. The bilayer structure of the film after heat treatment at 800°C still persisted and the interface between the nitride layers remained distinct. A thick oxide film (≈260 nm) was found on the TiN/AlN multilayer coating. The oxide film was divided into three regions, as displayed in the TEM image. Location 1 in Figure 2.31a was an Al-rich oxide layer with excess oxygen and it exhibited nanocrystalline structure. The Al-depleted layer with a grain size ranging from 30 to 80 nm was a stoichiometric TiO_2 phase (location 3 in Figure 2.31a).

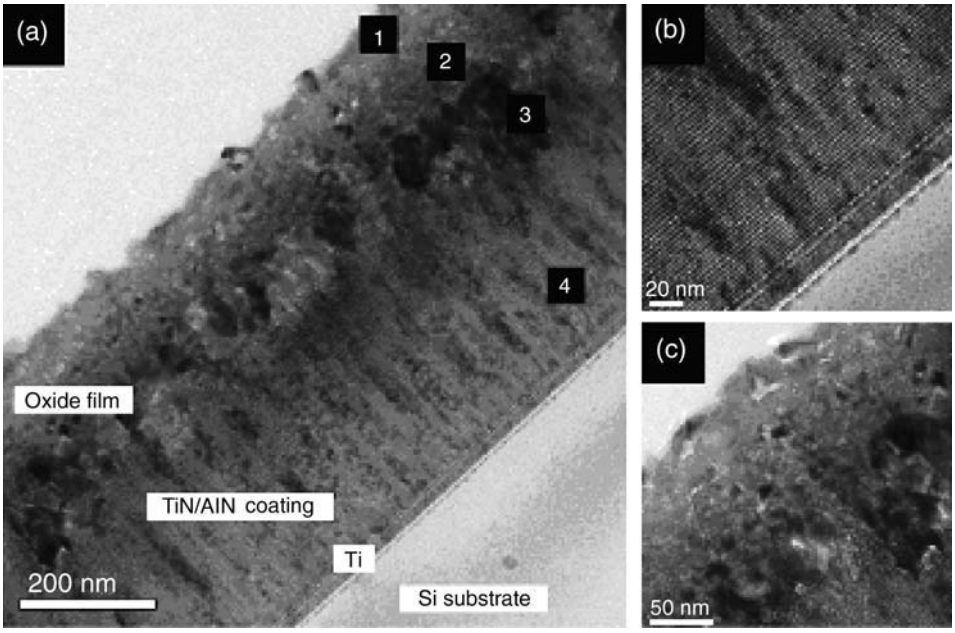

FIGURE 2.31 (a) TEM image of TiN/AlN multilayer coating annealed at 800°C for 1 h; (b) enlarged image of unreacted film; and (c) enlarged image of oxide layer [106].

In between, mixed nanocrystalline TiO_2 and Al_2O_3 layers also could be identified clearly (location 2 in Figure 2.31a).

Superhard coatings deposited by energetic ion beam bombardment, such as HfB_2, ZrN/Cu and ZrN/Ni, show low thermal stability and their hardness decreases drastically with increasing annealing temperature. For high thermal stability, the material structure should exhibit stable thermodynamic behaviour (among the coating components) and form coherent low-energy interfaces. Most of the materials that have coherent low-energy interfaces are isostructural (e.g. Cu/Ni, TiN/NbN). Non-isostructural nanolayers made up of combined metallic and compound layers, e.g. (nc-MeN/Metal), Mo/NbN, W/NbN and W/ZrN, exhibit excellent thermal stability and lattice match. Among the miscible superlattice structures, the TiN/NbN couple shows relatively high stability up to 700°C [112].

Raveh et al. [111] have stated that instability of coating arises from the presence of air. Further, they have reported that Muntz and his group [119] have developed superlattice coatings consisting of $TiAlCr_{0.03}N$ and TiAlYN with L = 1.7 nm, TiAlN/VN and CrN/NbN with L = 3.5 nm. The former sustained its stability up to 950°C, when used for the high-speed machining of die steels. But the latter was stable only up to 680°C.

A deeper understanding of the interactions among the fabrication parameters, film-growing techniques, film structures and composition is the key to ensuring the thermal stability of superhard coatings.

5. STABILITY OF METALLIC GLASSES AGAINST THERMO-MECHANICAL FACTORS

'Metallic glasses' constitute a distinct class of materials. Their relevance to a discussion on the stability of nanocrystalline materials is only because their low-temperature processing can lead to hybrid structures in which nanocrystalline particles are embedded in an amorphous matrix. Such structures exhibit some very useful and improved functional and mechanical properties, e.g. soft magnetic properties with improved strength properties.

In the past two decades, many bulk metallic glasses (BMGs) have been synthesized in multicomponent alloy systems, such as La-, Zr-, Fe- and Cu-based alloys [120–123]. Many Ti-based metallic glasses have been developed based on Ti–Cu–Ni–Sn [124], Ti–Cu–Ni–Si–B, Ti–Cu–Ni–Sn–Be, Ti–Cu–Ni–Sn-Mo, Ti–Zr–Hf–Cu–Ni–Si, Ti–Cu–Ni, Ti–Cu–Ni–Co, Ti–Cu–Ni–Zr, Ti–Cu–Ni–Zr–Sn, Ti–Cu–Ni–Sn–B–Si, Ti–Cu–Ni–Sn–B, Ti–Cu–Ni–Zr–B, Ti–Cu–Ni–Zr–Hf–Si and Ti–Cu–Ni–Zr–Nb(Ta) systems [125,126]. Most of the bulk amorphous formers, like those based on Zr, Pd and the rare-earth (RE) elements, have multicomponents with clearly different atomic sizes. These alloys usually have high packing density and are located in a deep eutectic, making it easier for the melt to cool down from the liquidus temperature, T_1, to below the glass transition temperature, T_g, even at a low cooling rate without undergoing a transformation [127]. Since 1988, various glassy alloy systems with high glass-forming ability (GFA) and a large supercooled liquid region have been synthesized and the main alloy systems have been extended to late transition metal (LTM)-based systems like Fe-, Co- and Ni-based alloys. Among the LTM bulk glassy alloys, much attention has been paid to Fe-based alloys exhibiting good soft magnetic properties. It has been reported that Fe-based bulk glassy alloys with a high GFA and good magnetic properties are formed in Fe–B–Si–Nb and Fe–(Al, Ga)–(P, C, B, Si) systems. Fe-based bulk metallic glasses (BMG) developed to date are classified into the following five groups of Fe–(Al, Ga)–P–C–B, Fe–(Zr, Hf, Nb, Ta)–B, Fe–(Cr, Mo)–(C, B) [128], Fe–Co–Ln–B and Fe–B–Si–Nb [129–131]. Pd–Cu–Ni–P and Zr–Ti–Cu–Ni–Be bulk glasses belong to the group of the most stable metallic bulk glasses. The stability of these glasses is linked to the nature and nucleation kinetics of the crystalline phases which form during the heat treatment of the glass. Glasses of both (Pd–Cu–Ni–P and Zr–Ti–Cu–Ni–Be) alloy families crystallize by formation of several phases which differ in structure and composition, i.e. the crystallization must always be correlated with the decomposition of the glass [132].

Low viscosity and high thermal stability are properties that are required of BMGs for processing, as against crystallization, in the supercooled liquid (SCL) state [133]. Bulk metallic glasses have unique mechanical properties including high strength and low Young's modulus. Moreover, they have good formability in the vicinity of the glass transition temperature. In this temperature regime, the stability of the amorphous structure and creep behaviour are important attributes essential for engineering applications [134].

Crystallization behaviour of bulk BMGs has been studied for at least two reasons. First, it is critical for the achievement of partially or fully nanocrystallized

BMG composites, which show superior mechanical properties or enhanced physical properties, like soft magnetism. Secondly, it is critical for the thermal stability assessment of BMGs, considering that they are potentially good industrial materials and yet in metastable states, compared with their crystalline counterparts [135]. Inoue [135] has concluded that the formation of a nanocrystalline structure in a BMG should satisfy the following criteria:

1. a multistage crystallization process;
2. high nucleation frequency;
3. low growth rate; and
4. enhancement of the thermal stability of the remaining glassy phase, caused by the redistribution of solute elements at the nanocrystalline/glassy interface.

However, different effects could be present in different alloy systems after the annealing of glassy precursors. For example, some glassy alloys become very brittle after partial crystallization, e.g. Fe–Si–B–Nb alloy [137].

Three empirical rules [125,129,130,138–141] have been evolved for the production of bulk amorphous alloy systems. These are:

1. requirement of three or more elements in the alloy;
2. a significant difference in the atomic size ratios, above about 12%, among the three main constituent elements; and
3. negative heats of mixing among the three main constituent elements.

The third rule reflects an experimental observation that the glass formation composition range generally coincides with a eutectic region and a low melting temperature, so that the reduced glass transition temperature, $T_{rg} = T_g/T_1$ (T_1 is the liquidus temperature and T_g is the glass transition temperature), is about 0.6 or higher for easy glass formers. Although these empirical rules give useful directions, they are rather general and the development of new bulk metallic glasses is still a very challenging process of selection and screening of different element combinations [142]. In this section, discussions are based on a few examples of bulk metallic glasses, and how their thermal stability is related to the temperature, deformation and constituent elements.

Figure 2.32 shows the influence of viscous deformation at various temperatures on the T_g and ΔT_x (temperature interval between the glass transition temperature, T_g and the crystallization temperature, T_X). ΔT_x decreases with increasing deformation temperature, indicating that the thermal stability of, for example, the $Zr_{55}Cu_{30}Al_{10}Ni_5$ bulk glassy alloy, decreases following viscous flow. Since Tg increases slightly with increasing deformation temperature, the decrease in ΔT_x is attributed mainly to the decrease of the onset temperature of crystallization [143].

The hardness of the glassy alloy, $Zr_{55}Cu_{30}Al_{10}Ni_5$, subjected to viscous deformation, is shown in Figure 2.33.

Hardness increases slowly with increasing temperature, when it is below 723 K. At lower temperatures, structural relaxation would reduce the free volume. Production of additional free volume due to deformation can counteract the influence of structural relaxation, but the additional free volume is not stable. When measuring the hardness, reordering, even through nanocrystallization,

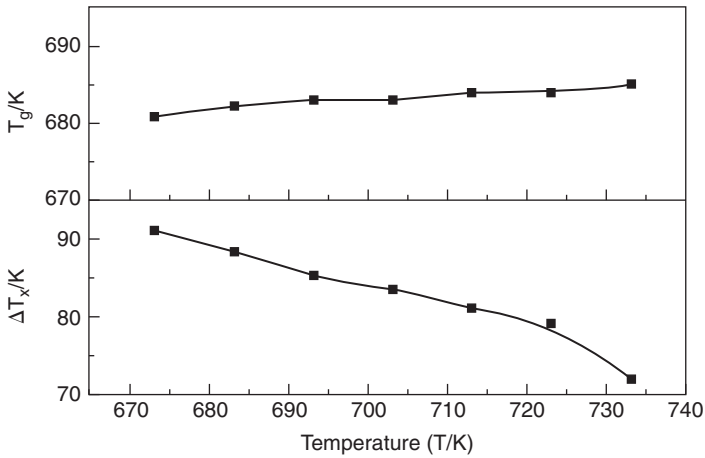

FIGURE 2.32 Temperature dependence of T_g and ΔT_x of the $Zr_{55}Cu_{30}Al_{10}Ni_5$ bulk glassy alloy subjected to high-temperature compression [143].

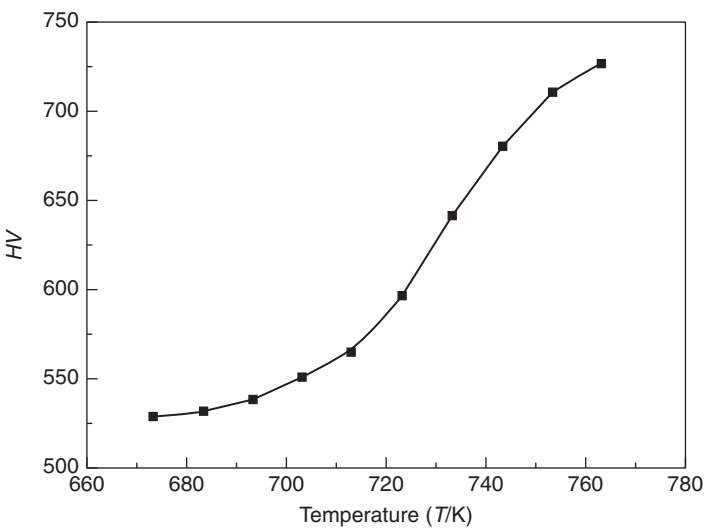

FIGURE 2.33 Temperature dependence of microhardness of the $Zr_{55}Cu_{30}Al_{10}Ni_5$ bulk glassy alloy subjected to high-temperature compression [143].

would occur in the deformation zone underneath the Vickers indenter. At a higher viscous flow temperature, larger deformation is obtained. Then, the density of unstable additional free volume produced by viscous deformation is greater. Nanocrystallization occurs at temperatures between 703 K and 723 K, which can be deduced from Figure 2.34. Then, the nanocrystalline volume fraction increases with increasing temperature at higher temperatures. The reasons given above explain why the hardness increases slowly with increasing temperature below 723 K.

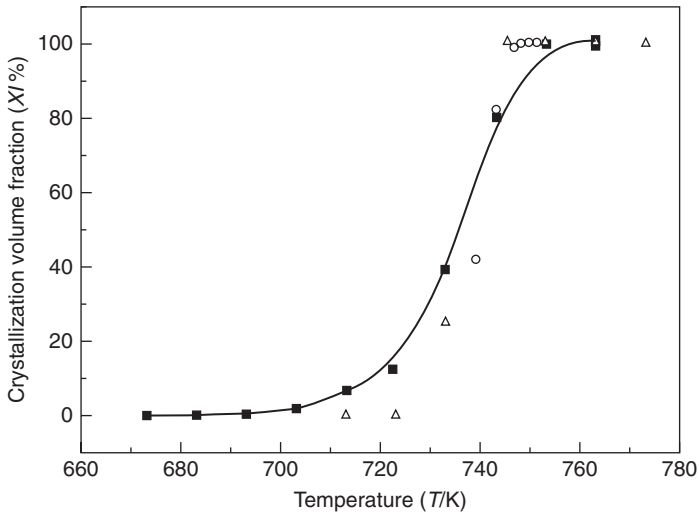

FIGURE 2.34 Temperature dependence of crystallized volume fraction in $Zr_{55}Cu_{30}Al_{10}Ni_5$ bulk glassy alloy subjected to high-temperature compression (O: Liu et al. [143]; △: Gao et al. [144,145]).

At temperatures in excess of 723 K, the large increase in the hardness of the deformed, originally glassy alloy is due to crystallization, which leads to significant decreases in plasticity and ductility. This change in properties will have adverse effects on viscous-flow-formed products of glassy alloys.

The effect of plastic deformation on thermal stability was found to be different for $Zr_{65}Al_{7.5}Cu_{27.5}$ and $FeZr_2$ amorphous alloys. Figures 2.34 and 2.35 reveal that the consequences of plastic deformation are complex. Since a temperature rise and contamination during rolling were ruled out, the shift in the crystallization temperature of the as-rolled samples should be attributed to the structural changes induced by plastic deformation [122].

Figure 2.35a shows the peak temperature change ($Tp - Tp_0$) of the first crystallization with increasing net elongation, ε (Tp and Tp_0 represent the peak crystallization temperature of the as-rolled and the as-quenched samples, respectively). It is evident that the effect of plastic deformation is different for the two amorphous alloys. After rolling, the crystallization temperature decreased in the $Zr_{65}Al_{7.5}Cu_{27.5}$ glass, while it did not change at all in the $FeZr_2$ amorphous alloy. The enthalpy change of each peak remained almost unchanged after plastic deformation in the two amorphous alloys (Figure 2.35b). This reveals that no detectable crystallization was induced by plastic deformation up to a net elongation of 200–250%. The crystallization products and the transformation fraction at each peak did not change after the treatment [122].

The melting and solidification behaviour of $Co_{50}Cr_{15}Mo_{14}C_{15}B_6$ and $Co_{48}Cr_{15}Mo_{14}C_{15}B_6Er_2$ alloys is shown in Figure 2.36.

The two alloys exhibit a nearly identical eutectic temperature (T_m) of 1355 K for the Er-free alloy and 1350 K for the Er-containing alloy. However, the apparent

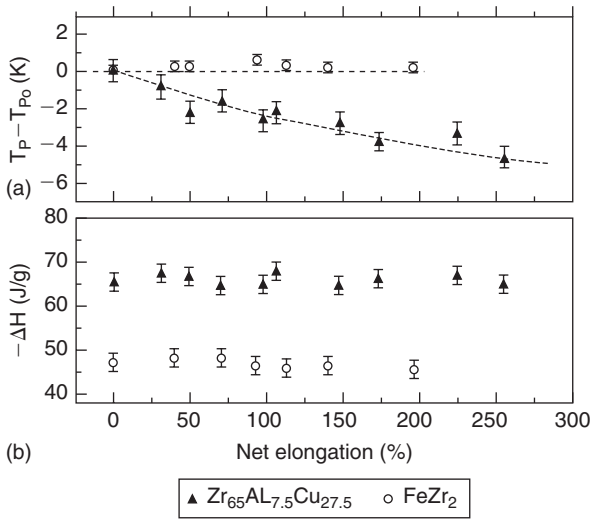

FIGURE 2.35 Variation of the peak crystallization temperature (a) and enthalpy of each peak (b) with degree of deformation for two amorphous alloys [122].

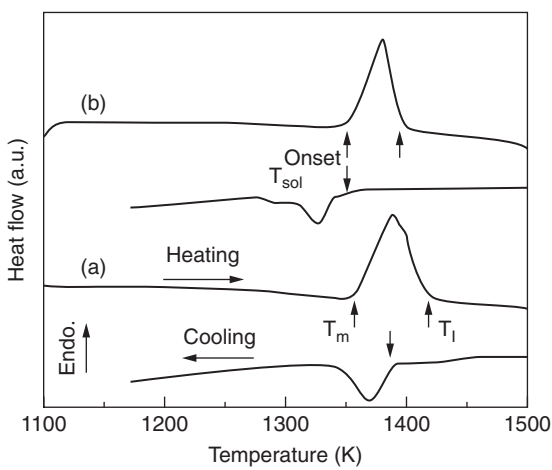

FIGURE 2.36 Melting and solidification behaviour of (a) $Co_{50}Cr_{15}Mo_{14}C_{15}B_6$ and (b) $Co_{48}Cr_{15}Mo_{14}C_{15}B_6Er_2$ alloys [123].

liquidus temperature (T_1) of the Er-free alloy decreases from 1417 K to 1394 K with the addition of Er. As a result, the temperature span between the onset and the end temperature of melting reduces from 62 K for the Er-free alloy to 44 K for the Er-containing alloy. The reduced glass transition temperature (T_{rg}) is defined as T_g/T_1 and the Er-containing glassy alloy has a slightly larger T_{rg} than the Er-free alloy, 0.61 versus 0.58. In addition, only one major exothermic peak could be observed on the cooling traces of both the alloys. Therefore, it could be confirmed that the two alloy compositions are at or very close to the eutectic. With the

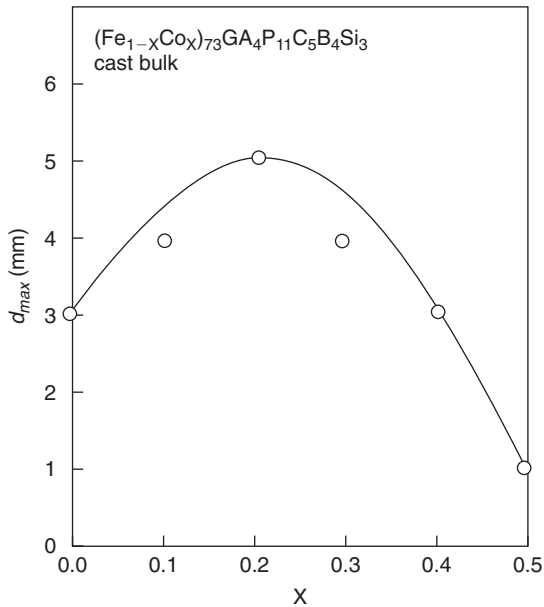

FIGURE 2.37 Plots of the glassy rod critical diameter for the formation of a single glassy phase (d_{max}), as a function of Co content for the $(Fe_{1-x}Co_x)_{73}Ga_4P_{11}C_5B_4Si_3$ alloy [130].

addition of Er, the onset temperature of codification (T_{sol}^{onset}) for the Er-free alloy reduces by about 38 K, from 1388 K to 1350 K. It is implied that the undercooling ability of the Er-free liquid is enhanced due to the addition of Er. That is, the undercooled liquid of the Er-containing alloy is more stable than the Er-free alloy. In general, an increase in the magnitude of T_{rg} and an enhanced stability of the undercooled liquid indicate better glass-forming ability [123].

The replacement effects of Co for Fe on the glass-forming ability (GFA) and magnetic properties in the (Fe, Co)–Ga–(P, C, B, Si) systems were investigated by Amiya et al. [130].

The compositional dependence of the critical diameter for the formation of the single glassy phase (d_{max}) was examined in the $(Fe_{1-x}Co_x)_{73}Ga_4P_{11}C_5B_4Si_3$ alloy. Figure 2.37 displays a plot of d_{max} as a function of Co content for this alloy. The d_{max} of the glassy alloy rod was 3 mm for $Fe_{73}Ga_4P_{11}C_5B_4Si_3$. However, the d_{max} value increased significantly to 5 mm at $x = 0.2$ and decreased to 2 mm at $x = 0.5$, indicating clearly the composition dependence of GFA [130].

Figure 2.38 shows the change in the liquidus temperature (T_1), solidification temperature (T_s), and the degree of undercooling (ΔT), T_g, T_x and ΔT_x as a function of Co content. T_1 decreases gradually from 1310 to 1270 K in the Co content range between 0 and 0.5. T_s obtained at a cooling rate of 0.17 Ks^{-1} was 1235 K for Co = 0, followed by a minimum of 1230 K for Co = 0.2, and then a monotonic increase to 1250 K for Co = 0.5. The degree of undercooling ($\Delta T = T_1 - T_s$) was evaluated as 40 K for x = 0.2. All samples showed that the glass transition was followed by a supercooled liquid region and then crystallization took place.

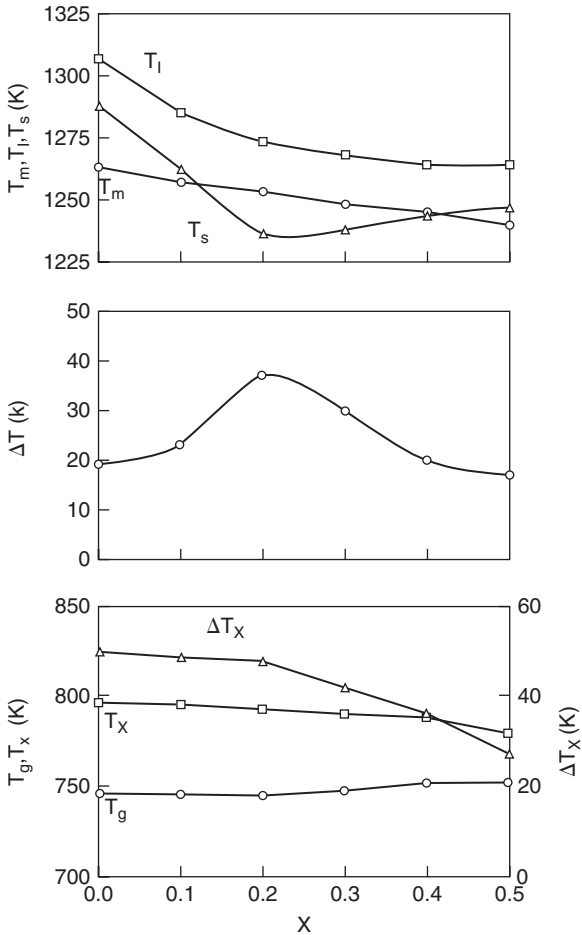

FIGURE 2.38 Thermal property changes of the liquidus temperature (T_l), the solidification temperature (T_s), and the supercooling rate (ΔT), T_g,T_x and ΔT_x, measured by DSC and DTA, as a function of Co content [130].

The ΔT_x keeps a constant value of about 50 K in the composition range from x = 0 to 0.2 and decreases significantly to 27 K in the higher Co content range [130].

The reason for the effectiveness of the replacement of Fe by Co in the Fe–Ga–P–C–B–Si alloys on the GFA has been attributed to these alloys satisfying the three empirical component rules. The atomic size of Co is almost the same as that of Fe, but Co has significant atomic size mismatches against the other constituent elements. Co also has large negative heats of mixing against the other constituent elements and the heats of mixing for the atomic pairs between Co and Ga, P, C, B, or Si are −51, −141, −7, −57, −91 kJ/mol, respectively [130].

Moreover, the Co addition makes the rearrangement of the constituent atoms to allow the proceeding of the crystallization reaction rather difficult. This leads to the suppression of crystallization and the enhancement of GFA. Compounds

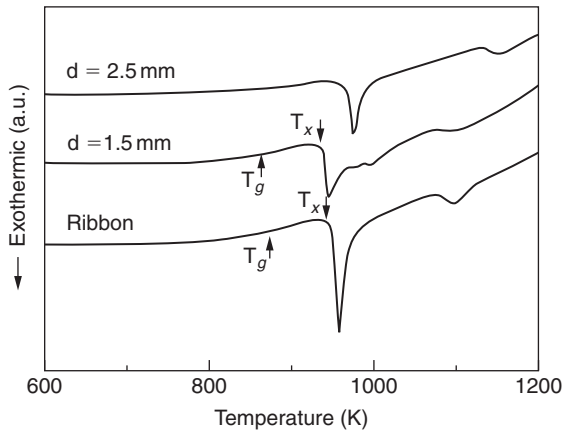

FIGURE 2.39 DSC curves of glassy $Fe_{56}Co_7Ni_2Zr_{10}Mo_5B_{20}$ rods with diameters of 1.5 and 2.5 mm (heating rate is 20 K/mm). The data for the melt-spun glassy ribbon are also shown for comparison [145].

could be detected in which Co was the main constituent element in both in the as-cast and the air-cooled alloys of the (Fe, Co)–Ga–P–C–B–Si system. This indicated that Co had gone into solution in the precipitated phases [130].

Two exothermic peaks are clearly seen, which are indicative of the multistage crystallization process in amorphous $Fe_{56}Co_7Ni_2Zr_{10}Mo_5B_{20}$ alloy. The metallic glass exhibits the sequential transition of glass transition, supercooled liquid region and crystallization. The thermal stability parameters, including the glass transition temperature(T_g), the onset temperature of crystallization (T_x), supercooled liquid region, ΔT_x (defined as the temperature interval between T_g and T_x) and reduced glass transition temperature $T_{rg}(T_g/T_m)$ for the as-cast rod of 1.5 mm diameter were measured to be 868, 937, 69 K and 0.596, respectively. In comparison with the data for the melt-spun amorphous ribbon shown in Figure 2.39, the T_g and T_x for the as-cast glassy rod of 1.5 mm diameter are lower, but the supercooled liquid region ΔT_x is almost the same.

Bletry and coworkers [146] investigated the homogeneous deformation of a zirconium-based bulk metallic glass $Zr_{52.5}Al_{10}Cu_{22}Ti_{2.5}\ Ni_{13}$ in the glass transition region. Compression tests at different temperatures and strain rates were conducted. The mechanical behaviour was analysed in the framework of a free volume model, taking into account the dependence of the defect concentration on the deformation process. High values of the activation volume for plastic deformation could be indicative of a cooperative motion of a group of a few tens of atoms per elementary plastic event. It has been claimed that the validity of the activation volume analysis and the measurement ensures the validity of the scaling law of glass viscosity versus strain rate and temperature (Figure 2.40).

From the mechanical tests, it is possible to estimate the relative variation of the steady-state defect concentration with strain rate and, knowing the equilibrium defect concentration and the activation volume, a method has been proposed to

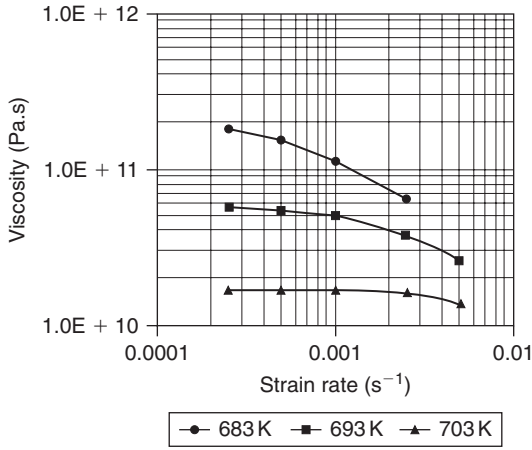

FIGURE 2.40 Viscosity vs. $\dot{\varepsilon}$ for three temperatures [146].

determine a_x/k_r (the ratio of the strain-induced defect creation rate to the recovery constant) and $\dot{\varepsilon}_{0,c}$ (migration rate).

$$\frac{a_x}{k_r} = \frac{\dfrac{\dot{\varepsilon}}{\dot{\varepsilon}_{0,c}\,\sinh(\sigma V/2\sqrt{3}kT)} - C_{f,eq}}{\dot{\varepsilon}\ln^2\left(\dfrac{\dot{\varepsilon}}{\dot{\varepsilon}_{0,c}\,\sinh(\sigma V/2\sqrt{3}kT)}\right)}$$

Here

$$C_{f,eq} = C_0\,\exp\left(-\frac{\Delta G^f}{kT}\right)$$

where V is the activation volume for the stress bias, $\dot{\varepsilon}$ plastic strain rate, ΔG^f formation free energy of the flow defects and $c_{f,eq}$ defect concentration at equilibrium.

On account of the exponential law that links free volume and defect concentration developing during flow, it is impossible to determine the absolute value of the thermal equilibrium defect concentration $c_{f,eq}$ [147]. This statement needs to be reconciled with the claim of establishing the validity of the scaling law of glass viscosity with strain rate and temperature.

The glass-formation ability (GFA) of Al-based glasses does not follow the atomic size criteria employed for producing other bulk metallic glass-forming alloys, but, till now, no bulk metallic glass based on Al with a thickness exceeding 1 mm has been produced [127].

Both Al–Ni and Al–Y binary Al-rich phase diagrams were characterized by a distinct asymmetry, due to which the liquidus rises rapidly from the eutectic point towards the intermetallics. In the ternary Al–Ni–Y phase diagram, as indicated in Figure 2.41a, there exist two ternary phases Al_4NiY and $Al_{16}Ni_3Y$ and so

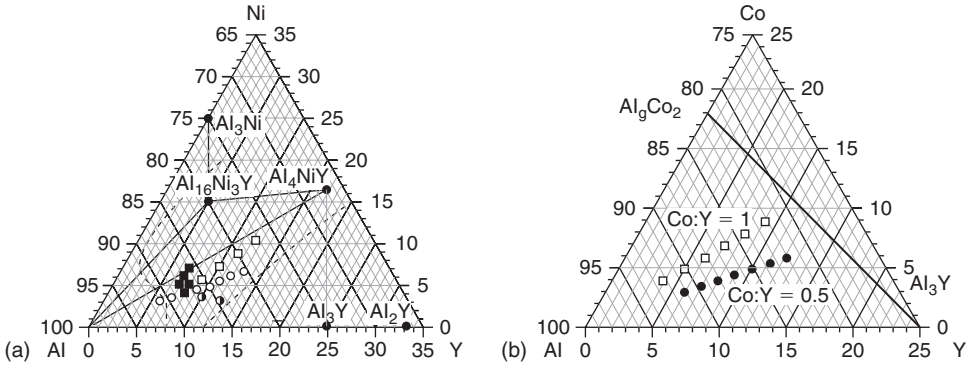

FIGURE 2.41 Schematic diagrams of the Al-rich corner of the ternary (a) Al–Ni–Y and (b) Al–Co–Y systems. The glass-forming range is marked by dashed line [127].

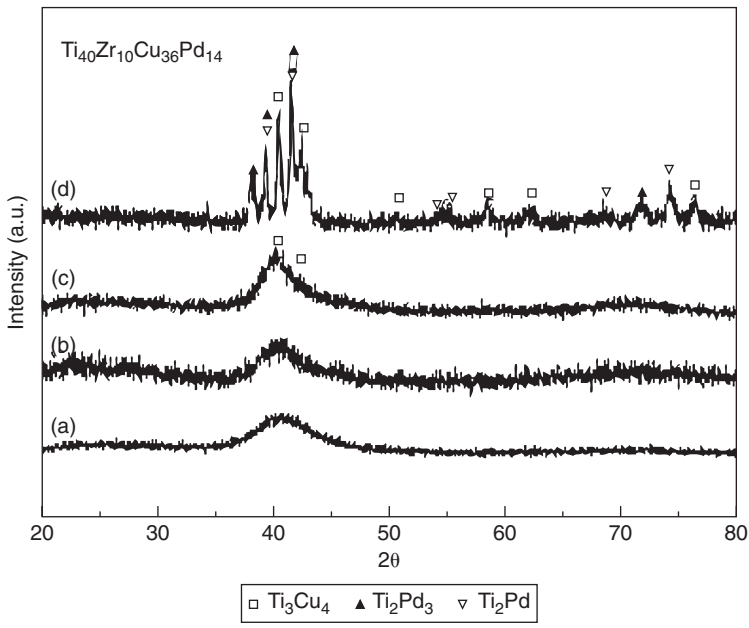

FIGURE 2.42 XRD patterns of the $Ti_{40}Zr_{10}Cu_{36}Pd_{14}$ bulk metallic glass and its annealed (for 10 min) alloys: as-cast (a), annealed at 693 K (b), 723 K (c) and 823 K (d) [137].

the Al-rich corner of this diagram is divided into three regions. As glass formation has been reported only in the binary Al–Y system and not in the Al–Ni system, only the triangle of Al–Al_3Y (Al_2Y)–Al_4NiY is of interest here [127].

The XRD patterns of the as-cast $Ti_{40}Zr_{10}Cu_{36}Pd_{14}$ bulk metallic glass and its annealed alloys at different temperatures are shown in Figure 2.42. It is clear that only a halo peak appears in the XRD pattern of the as-cast alloy, indicating that a glassy phase has been formed. Although no obvious crystalline peaks appear

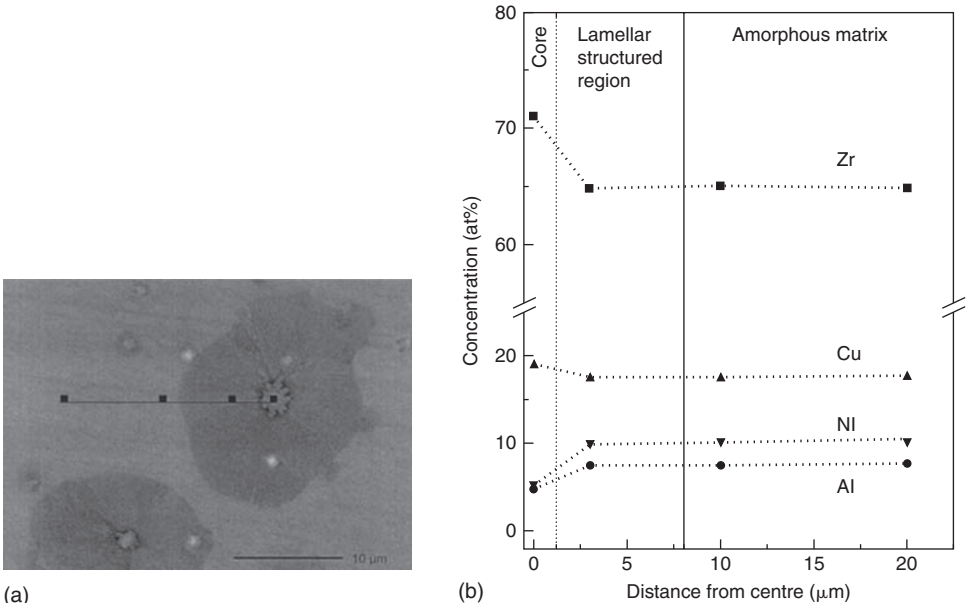

FIGURE 2.43 (a) SEM image (BSE mode) of crystalline inclusions in an amorphous $Zr_{65}Al_{7.5}Cu_{17.5}Ni_{10}$ sample with 0.28 at% oxygen. (b) Elements distribution (electron probe microanalysis) starting from the centre of a crystalline inclusion towards the amorphous matrix in a sample with 0.28 at% oxygen (compare with (a): ■- experimental points) [150].

in the XRD pattern after annealing at 693 K, the main peak becomes sharper as compared with the as-cast alloy and some weak diffraction peaks identified as Ti_3Cu_4 appear in the pattern of the alloy annealed at 723 K. The low-intensity peaks of the precipitates indicate the possibility of the formation of a nanocrystalline structure in the glassy matrix of the samples annealed at 693 and 723 K. This could not be established unequivocally by XRD [137].

Inoue et al. [147] reported from empirical relations between the critical cooling rate (maximum sample thickness) and the reduced glass transition temperature, T_g/T_m (Tm: melting temperature) or ΔT_x that a large glass-forming ability requires, besides a high Tg/Tm, a large ΔT_x value. Lin et al. [148] investigated the effect of oxygen on crystal nucleation in undercooled melts of zirconium-based alloys and concluded that the critical cooling rate for glass formation depends dramatically on the oxygen impurity level. Furthermore, they found that the degree of overheating above T_m is decisive for determining the kind of nucleation, i.e. homogeneous or heterogeneous, in the undercooled melt. However, they did not give any information on the phases formed or the microstructures of samples with different oxygen content [150].

The dependence of T_g, T_x and ΔT_x on oxygen content is illustrated in Figures 2.43 and 2.44. For comparison, values obtained for amorphous ribbons are also given. It is obvious that the size of the supercooled liquid region decreases with increasing oxygen content in both the cases, i.e. the slowly cooled bulk samples and the

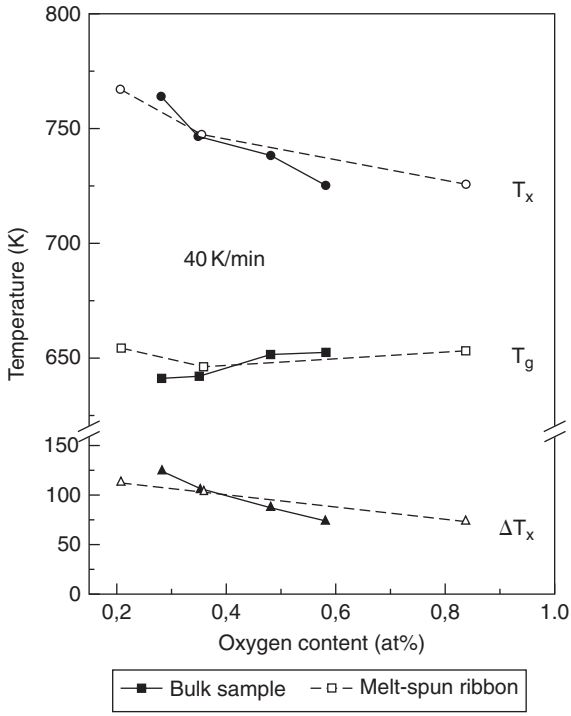

FIGURE 2.44 Dependence of T_g, T_x and ΔT_x on the oxygen content in $Zr_{65}Al_{7.5}Cu_{17.5}Ni_{10}$ bulk samples and ribbons [150].

rapidly quenched ribbons. Investigations on the ribbons, which were isothermally annealed above the glass transition temperature, revealed that oxygen triggered the formation of metastable phases which subsequently transformed into stable equilibrium compounds at higher temperatures. In detail, the fcc $NiZr_2$ phase was mainly found in samples with up to about 0.6 at% oxygen as an intermediate metastable phase, which transforms into hexagonal $NiAl_2Zr_6$ at higher temperatures. Tetragonal $CuZr_2$ also forms. In addition, a quasicrystalline phase was detected in samples with a higher oxygen content (about 0.8 at%), which transforms into tetragonal $CuZr_2$ [150].

An increase in oxygen content changes the crystallization behaviour from a single to a double-step process, indicating a change in the mode of crystallization from simultaneous precipitation of two phases to a successive step-wise transformation into the equilibrium compounds. This indicates that the same oxygen-induced crystallization processes proceed in both types of sample. The first exothermic peak in the DSC scans for $Zr_{65}Al_{7.5}Cu_{17.5}Ni_{10}$ samples with higher oxygen content is related to oxygen-triggered formation of the metastable fcc $NiZr_2$-type phase. In addition, tetragonal $CuZr_2$ was found. The region of existence of the metastable fcc phase extends to lower temperatures with increasing oxygen content. Therefore, the nucleation of fcc $NiZr_2$ becomes the determining

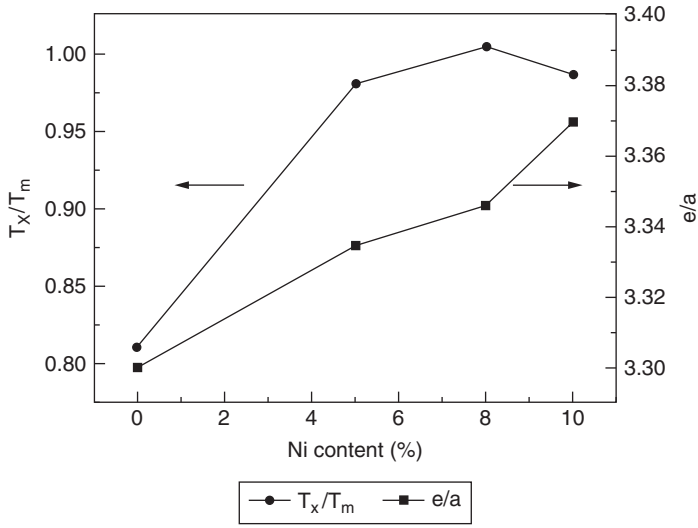

FIGURE 2.45 Reduced crystallization temperature and valence concentration of as-cast $(Nd_{60}Fe_{30}Al_{10})_{92}Ni_8$ as a function of Ni content [152].

step for the initiation of crystallization with increasing oxygen content and, in turn, T_x shifts to lower temperatures at a given heating rate. Furthermore, the temperature span between the formation of fcc $NiZr_2$ and its transformation into the tetragonal $NiAl_2Zr_6$ equilibrium compound becomes larger with increasing oxygen content, which accounts for the occurrence of two well-separated exothermic DSC peaks for samples with relatively large oxygen content. These findings prove, similar to what is found for cooling from the overheated melt, that the oxygen-triggered nucleation of the metastable fcc phase is the initial step in crystallization, which leads to the reduced stability of the supercooled liquid [151].

Often, the more the elements involved, the lower is the possibility for the formation of viable crystal structures.

In order to understand the thermal stability and GFA of the BMG-forming systems further, the change in the reduced crystallization temperature T_r ($=T_x/T_m$) and the valence concentration, e/a (e and a are the valence number of electrons and the atomic number in a unit cell, respectively), of $(Nd_{60}Fe_{30}Al_{10})_{100-x}Ni_x$ alloys were determined for different percentages of Ni and these are shown in Figure 2.45. Without Ni, the value of T_r is about 0.81, which is slightly below the value of 0.85 reported by Inoue et al. [147] for an alloy of the same composition. Figure 2.45 shows that T_r increases significantly to 0.98, when the Ni content is 5%, and up to 1.01 when it is 8%. It is believed that the anomalously high value (>1) of T_r is related to the existence of two amorphous phases, with different thermal stabilities. The melting temperature of the unstable amorphous phase could be lower than the crystallization temperature of the stable one.

It is clear that significantly more work needs to be done before a clear physical understanding can emerge.

6. RELIABILITY UNDER CREEP CONDITIONS

Creep deformation is a ubiquitous reliability problem in nanomaterials. With the development of the depth-sensing indentation technique, it is now possible routinely to determine mechanical properties, including creep, using very small volumes of materials. Creep in nanocrystalline materials has been studied only in recent years owing to the many experimental complications involved. First is the limitation with regard to synthesizing bulk nanomaterials free of defects (porosity and impurities), with a uniform grain size distribution that could provide reliable data to understand the deformation processes. Second is the significant increase in the volume fraction of grain boundaries and intercrystalline defects such as triple lines and quadruple junctions that render the creep mechanism complicated [14,36].

There is no universal agreement on the creep mechanisms. In recent years, improving the elevated-temperature properties has become a critical issue for possible applications of cast Mg alloys in components that operate at high homologous temperatures. Several approaches have been adopted to improve the creep properties of Mg alloys, which are mostly focused on the effects of thermally stable grain boundary particles. However, it has been shown recently that, in Mg–Sn-based alloys, the presence of thermally stable nanoparticles within the matrix also can significantly improve the creep resistance [105].

In the case of ceramics, past studies on mechanical properties were mainly focused on the amorphous state of the precursor-derived ceramics. For example, compression creep studies on amorphous Si–C–N and Si–B–C–N ceramics in the temperature range from 1400 to 1550°C at stresses between 30 and 250 MPa demonstrated that these materials exhibit an unusually high creep resistance. A similar observation is made with respect to amorphous metallic glasses, if they are annealed at temperatures above the glass transition. Nevertheless, the structural stability of these ceramic materials and, consequently, their respective mechanical properties might have been improved substantially by crystallization. It has been shown that after crystallization, β-SiC and eventually Si_3N_4 nanocrystallites are embedded in a turbostratic 'B–C–N' matrix consisting of amorphous carbon and boron nitride domains [153].

Silicon carbide is the first phase to nucleate in the temperature range between 1400 and 1500°C, whereas silicon nitride nucleates at and above 1700°C. Below 1350°C the ceramic material was found to remain purely amorphous. The size of the SiC nanocrystallites was determined by high-resolution TEM studies, from which values between 2 and 5 nm were obtained [153]. Figure 2.46 shows TEM images of nanocrystalline Si–B–C–N Ceramics crystallized at 1800°C, 1 h/10 bar N_2 pressure, 1800°C, 3 h/10 bar N_2 pressure and 1800°C, 3 h/100 bar N_2 pressure.

It is shown that, depending on the actual annealing conditions, SiC and Si_3N_4 nanocrystallites are formed, which are distributed in an amorphous B–C–N matrix consisting of amorphous carbon and boron nitride domains. The high temperature mechanical properties of the various annealed Si–B–C–N samples and of a representative amorphous specimen were examined by compression creep experiments. Constant load experiments were carried out at 1400°C which showed that

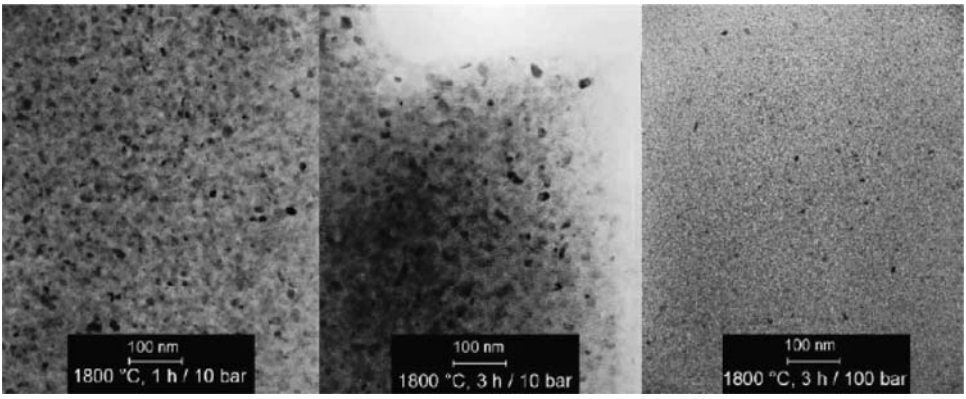

FIGURE 2.46 TEM images of nanocrystalline Si–B–C–N ceramics crystallized at 1800°C, 1 h/10 bar N_2 pressure, 1800°C, 3 h/10 bar N_2 pressure and 1800°C, 3 h/100 bar N_2 pressure [153].

improved creep resistance exists for the annealed Si–B–C–N samples, containing SiC and Si_3N_4 nanocrystallites (Figure 2.47a).

In Figure 2.47b the deformation rate, $\dot{\varepsilon}$, of the annealed samples I–IV are shown, along with that of the amorphous counterpart (sample V). It can be seen that the time dependence of $\dot{\varepsilon}$ for the amorphous and the annealed nanocrystalline ceramics is almost identical, including the absence of any asymptotic behaviour even after 300 h of testing time. However, there is a significant difference in the creep strength of the annealed and the amorphous Si–B–C–N samples, as the former display a significantly increased creep resistance. The annealed material, therefore, exhibits in the entire time interval of the test, deformation rates, $\dot{\varepsilon}$ and strains, which are about one order of magnitude less than those of their amorphous counterpart (sample V).

6.1 Nanocomposites

Discontinuously reinforced metal–matrix composites (MMCs) are attractive for their high specific modulus and strength, good wear resistance and good dimensional stability. Compared with monolithic fine-grained Al_2O_3, Al_2O_3 nanocomposites reinforced with SiC nanoparticles display an especially high modulus of rupture as well as reduced creep strain. Extensive research has been carried out on the creep behaviour of Si_3N_4/SiC [154,155], Ni/$Si_3N_{4(W)}$ [156] and Al_2O_3/SiC [157] nanocomposites.

The main factor determining the creep strain appears to be SiC nanoparticles pinning the grain boundaries with a consequent:

- decrease in grain boundary sliding;
- viscoelastic contribution to creep; and
- enhancement in the grain boundary strength, which allows plastic deformation of grains through dislocations motion [157].

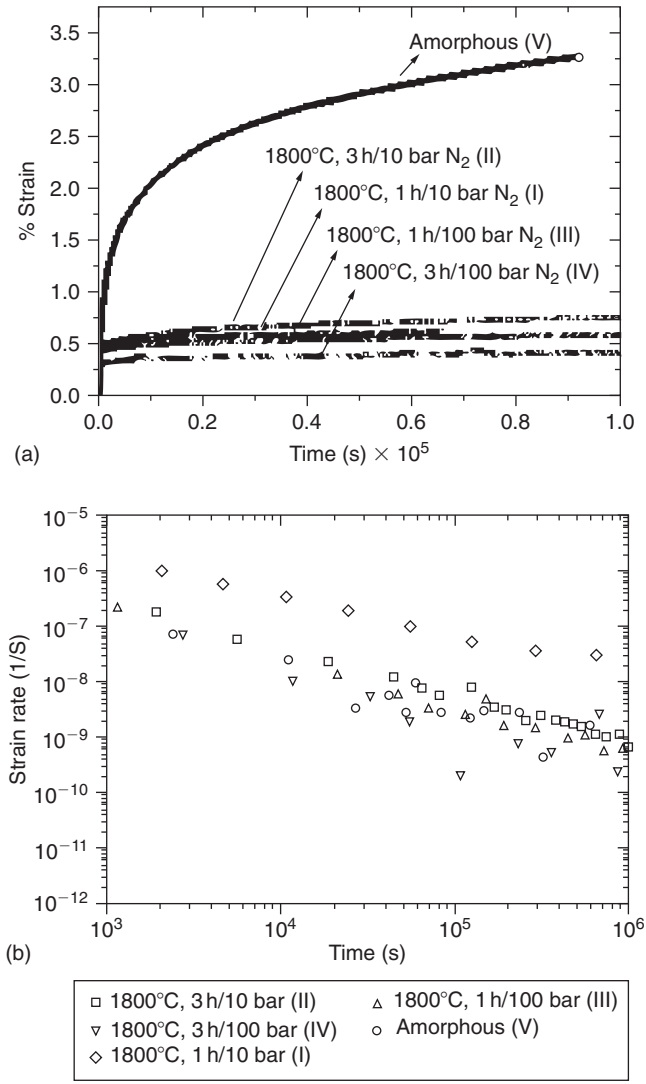

FIGURE 2.47 (a) Deformation curves of four different Si–B–C–N samples, annealed at 1800°C with the conditions (holding time, N_2 pressure) indicated in the figure and of the corresponding amorphous specimen. The experiments were performed at 1400°C with a compressive stress of 100 MPa and (b) deformation rates of an annealed Si–B–C–N sample [153].

It has been suggested that the creep behaviour was governed by grain boundary sliding, accommodated by dissolution of secondary phases in the amorphous intergranular phase and diffusion through the glass and reprecipitation, with diffusion the rate controlling step [155]. When this occurs, rearrangement is stopped and only lattice mechanisms based on dislocation motion and, to a lesser extent,

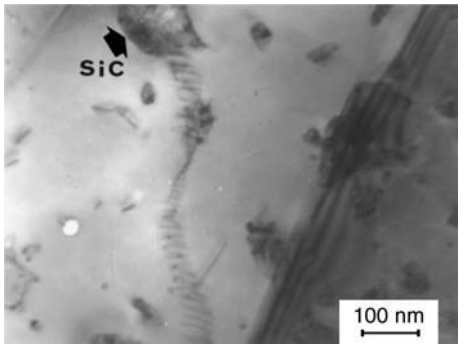

FIGURE 2.48 TEM micrograph of a nanocomposite showing dislocations associated with intergranular SiC particles [157].

a viscoelastic mechanism, still contribute to the creep process. Figure 2.48 shows up the dislocations associated with the SiC particles [157].

The sliding rearrangement phenomenon is transient in nature and, in addition to the viscoelastic behaviour, explains why at a given temperature the onset of the steady state is delayed in nanocomposite materials. According to the authors, the deformation mechanism, which is mainly based on increased bonding between grains, is also in agreement with the room temperature mechanical properties as well as with the wear and machining behaviour. Indeed, such a mechanism necessarily promotes strengthening at the expense of toughening mechanisms, such as crack deflection or microcracking, both of which involve the propagation of the main crack along the grain boundaries [157].

The main feature observed was the large number of pores, particularly at triple junctions in the material after creep (Figure 2.49a). As creep proceeded these pores grew into finger-like cavities and, if creep were further continued, their interlinking would give rise to premature failure of the sample. Enhancement of grain boundary cohesion depresses grain boundary sliding. Figure 2.49b shows that, where substantial sliding had occurred, some grains were forced into their neighbours causing deformation in the latter and also giving rise to dislocation motion in the deformed grains. Interpretation of such topological details is difficult because figures like Figure 2.49b are 2D projections of a 3D situation, taken from a given perspective. At this stage, it is noted that these features are analogous to those seen during creep in materials of conventional grain sizes, where grain boundary sliding is impeded by grain boundary particles and other obstacles so that the local rate of accommodation falls below the boundary sliding rate.

6.2 Low-Temperature Creep

Nanocrystalline materials exhibit creep and superplasticity at lower temperatures compared with their conventional micrograined counterparts. Nanocrystalline Cu, Pd and Al–Zr are often made by the inert gas condensation and *in-situ* compaction

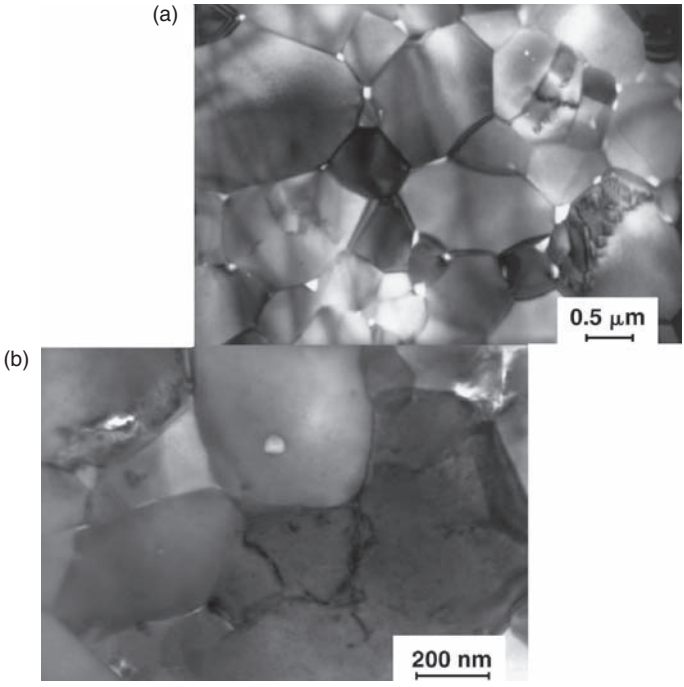

FIGURE 2.49 (a) TEM micrograph of monolithic alumina after creep showing extensive cavitation mainly at triple junctions; (b) TEM micrograph of the nanocomposite after creep showing the presence of deformed grains due to plastic accommodation of grain boundary sliding [157].

methods. Sanders et al. [157] studied over a wide temperature range the creep behaviour of nanocrystalline Cu, Pd and Al–Zr alloy, made by these two methods. They suggested that the observed low creep rates were due to the high fraction of low-energy grain boundaries, together with the limitation on dislocation activity in the small nanograin size range. Wang et al. [158] investigated the room temperature creep behaviour of nanocrystalline Ni produced by the electrodeposition technique. They concluded that grain boundary sliding and diffusion through intercrystalline regions are the major deformation mechanisms. No rate controlling mechanism has been suggested. In contrast, Padmanabhan and coworkers [8,31,58,67,68] have suggested that grain boundary sliding is the dominant rate controlling mechanism of creep and have also derived a rate equation for a microstructure of uniform constant grain size.

Figure 2.50 is an example of creep curves obtained in the case of nanograined pure Cu. It can be seen that the creep curve contains the primary and the steady state stages, as usually seen during high-temperature creep in coarse-grained metals, but the tertiary stage is very short. These results indicate that the steady state creep rate (SSCR) is proportional to the effective stress. The activation energy for creep of 0.72 eV [1] is clearly smaller than that for lattice diffusion (2.0 eV) [160] and grain boundary diffusion (1.08 eV) [160] in coarse-grained Cu, but it is close

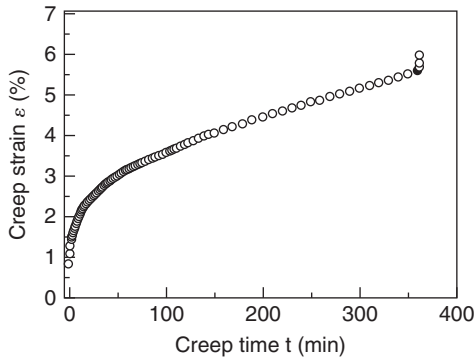

FIGURE 2.50 Creep curve of nanograined pure Cu at 40°C and 142 MPa [160].

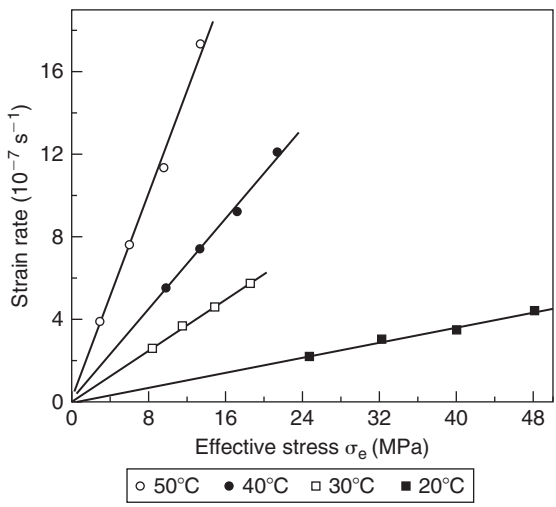

FIGURE 2.51 Steady state creep rate as a function of effective stress, σ_e, for nanograined pure Cu at different temperatures [160].

to that for grain boundary diffusion in nanograined Cu (0.69 eV, 0.64 eV) [161]. Hence, creep in this material could be associated with grain boundary diffusion but, as grain boundary sliding is also dominant, in the absence of microstructural/topological evidence an unequivocal inference on the rate controlling mechanism is not possible.

Figure 2.51 shows the steady state creep rate (SSCR) as a function of effective stress, σ_e. It can be seen from the figure that the SSCR is proportional to the effective stress and increases with increasing temperature. Hence, the SSCR can be expressed as:

$$\dot{\varepsilon} = \frac{A\sigma_e}{kT} \exp\left(-\frac{Q}{kT}\right) \tag{2.23}$$

where A is a constant, Q the activation energy for creep and k and T have their usual meaning. For dimensional consistency, the effective stress should be used in the equation in a dimensionless form. But, it is cautioned that the procedure adopted in this work for obtaining the effective stress from the applied stress appears to be *ad hoc*.

The predicted creep rates based on Coble (diffusion) creep reveal that there is an increase in strain rate by six orders of magnitude when the grain size is decreased from 1 μm to 10 nm. Such a sharp increase in strain rate has not been observed experimentally. Therefore, Coble creep as a rate controlling process does not appear to be attractive. Also, this mechanism predicts grain elongation, for which there is no experimental support.

Nanostructured metals exhibit notable anelastic relaxation even at ambient temperatures, compared with their coarse-grained counterparts, due to the fact that an extremely fine grain size results in a high volume fraction of disordered interfaces, as well as a decrease in dislocation activity in the matrix [162,163].

A general theory of interfacial segregation was developed on the basis of thermodynamic equilibrium for the distribution of different types of species between the bulk and the interface. For a multicomponent system, the mole fraction of a particular interstitial at the interface may be written as:

$$\frac{X_I^{\phi}}{X^{0\phi} - \sum_J^{M-1} X_J^{\phi}} = \frac{X_I}{1 - \sum_J^{M-1} X_J} \exp\left(-\frac{\Delta G_I}{RT}\right) \tag{2.24}$$

where $X^{\theta\phi}$, X^{ϕ}_I and X_I are the total ratio of all sites available at the interface for segregation, the mole fractions of element I at the interface ϕ and in the bulk, respectively, and ΔG_I is the free energy of segregation to the grain boundary. The free energy of segregation is approximately equal to the segregation enthalpy, as the segregation entropy may be relatively small, for example, for sulphur in nickel [162].

In Mg–Sn alloys, grain boundaries are decorated by semicontinuous particles, which consist mostly of Mg_2Sn particles with small amounts of Mg_2Si and $Mg_{17}Al_{12}$ particles. Mg_2Si particles are present as the globular type, instead of a Chinese-script type, which is usually formed under slow cooling conditions. Besides the grain boundary particles, fine (<50 nm) Mg_2Sn particles are present within the matrix of the alloy also. One important characteristic of these Mg_2Sn particles is that they have been reported to have no orientation relationship with the Mg matrix. Non-existence of any orientation relationship between the Mg_2Sn particles and the Mg matrix is surprising. It is known that Mg–Sn alloys show pronounced age hardening behaviour, with the precipitation of Mg_2Sn. Although the orientation relationship between Mg_2Sn precipitates and Mg matrix has not been identified so far, it is expected that there exists a certain orientation relationship since precipitates usually have an orientation relationship with the matrix. The present result further suggests that Mg_2Sn particles found in die-cast TAS 831 alloy were formed during solidification [164]. Creep deformation of this alloy occurs by dislocation climb controlled flow, which is controlled by dislocation movements through obstacles, such as these precipitates, dispersoids and other

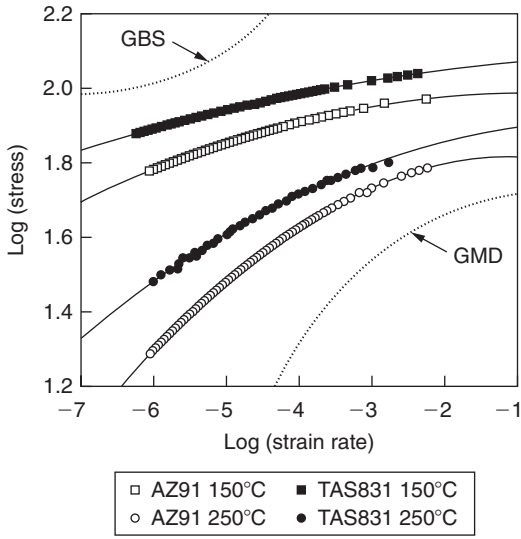

FIGURE 2.52 Load-relaxation flow curves of die-cast AZ91 and TAS831 alloys [164].

dislocations. The presence of thermally stable Mg_2Sn and Mg_2Si particles along grain boundaries retards grain boundary migration during high-temperature exposure, resulting in an improvement in the creep resistance.

In an internal-variable theory, grain boundary sliding and grain matrix deformation have a mutually accommodating relationship, competing against each other at high temperatures. In the load-relaxation curve, grain boundary sliding is shown as a concave curve and grain matrix deformation is shown as a convex curve (see schematic in Figure 2.52).

In summary, the creep stability or its absence in nanostructured materials is mainly dominated by the size effects, grain boundaries, interphase boundaries, particles residing at the boundaries and the type of processing. Extensive research will be needed to establish the roles of all these aspects before unequivocal conclusions on the operating/rate controlling mechanisms can be drawn.

7. STABILITY IN CORROSIVE ENVIRONMENTS

The use of nanoscale, compositionally modulated structures can offer a combination of properties such as high hardness and wear resistance, coupled with reasonable corrosion resistance [165]. In recent years, there has been a substantial improvement in nanocoating technology which prevents the material from being exposed to the corrosive environment. Chromate conversion coatings can be successfully used for the corrosion protection of aluminium alloys. However, the environmental laws in many countries have imposed severe restrictions on the use of chromate due to its high toxicity and consequent environmental hazards [166]. In this context, CrN/NbN nanoscale multilayered coatings have

performed particularly well in corrosion-resistant applications because of the use of the chemically stable metals Nb and Cr, with a nanoscale multilayer architecture [167].

Electrochemical measurements have revealed that a nanocrystalline surface layer on 316L stainless steel fabricated by cavitation followed by low-temperature annealing displays lower susceptibility to pitting corrosion in 0.9 wt% NaCl solution at 25°C [167]. The conducting polyaniline (PANI) hybrid coating, containing nanoparticulate ZnO in poly (vinyl acetate) PVAc matrix, showed remarkable improvement in corrosion protection of steel in saline water. The novelty of these coatings lies in the generation of corrosion inhibition by three mechanisms operating simultaneously, viz. improvement of barrier properties, formation of p–n junctions preventing easy charge transport and redox behaviour of PANI, when coating is threatened to be destroyed by scratch or scribble. Apart from the prevention of corrosion, these coatings have good gloss and shiny surface, which is not easily obtained in a conventional coating prepared with commercial micron size particle additives. Such a system can be used as a primer and on application of suitable transparent epoxy topcoat their performance in improving corrosion protection and appearance can be enhanced further [168].

From the point of view of corrosion behaviour, the high volume fraction of intergranular defects associated with nanostructured materials, such as free volumes and microvoids, could lead to a poor corrosion performance since localized corrosion commonly initiates at surface heterogeneities or weak structural sites. On the other hand, it has been pointed out for alloys with elements that are capable of forming passive films, that the atoms of these elements can diffuse easily through the grain boundaries to the surface of the alloy to form a protective passive layer [169].

Also, it can be seen from Figure 2.53 that temperature has an important influence on the grain size effect of zirconium metal. This is because, with an increase in temperature, the lattice expands and effective electron mean free path, l_{eff}, varies. So the grain size effect varies with a change in temperature [170].

The corrosion behaviour of nanocrystalline passive alloys has been reported, but the results are not consistent. The corrosion resistance of nanocrystalline AISI 304 stainless steel in NaCl solution was greater than in coarse-grained 304. Similarly, improved corrosion resistance of nanocrystalline N06022 nickel alloy in hot acid chloride solution has been reported. In contrast, the corrosion resistance of nanocrystalline Ni in H_2SO_4 was found to be inferior to that of coarse-grained Ni [167].

CrN hard coatings are widely used due to their excellent mechanical properties, which make them useful in a wide variety of industrial applications. However, in spite of their excellent mechanical and tribological properties, their corrosion resistance has always been conditioned by the presence of structural defects such as pores, pinholes and cracks that appear during use. The presence of these defects is a key factor that influences the integrity of the coating, not only in terms of corrosion resistance, but also the tribological properties [171].

Denser coatings are conducive to better corrosion protection because there are fewer pathways for the corrosive media to penetrate the coating to the substrate surface. All growth defects are potential sites for localized pitting corrosion. Therefore, the increase in corrosion resistance at higher bias voltage is predictable

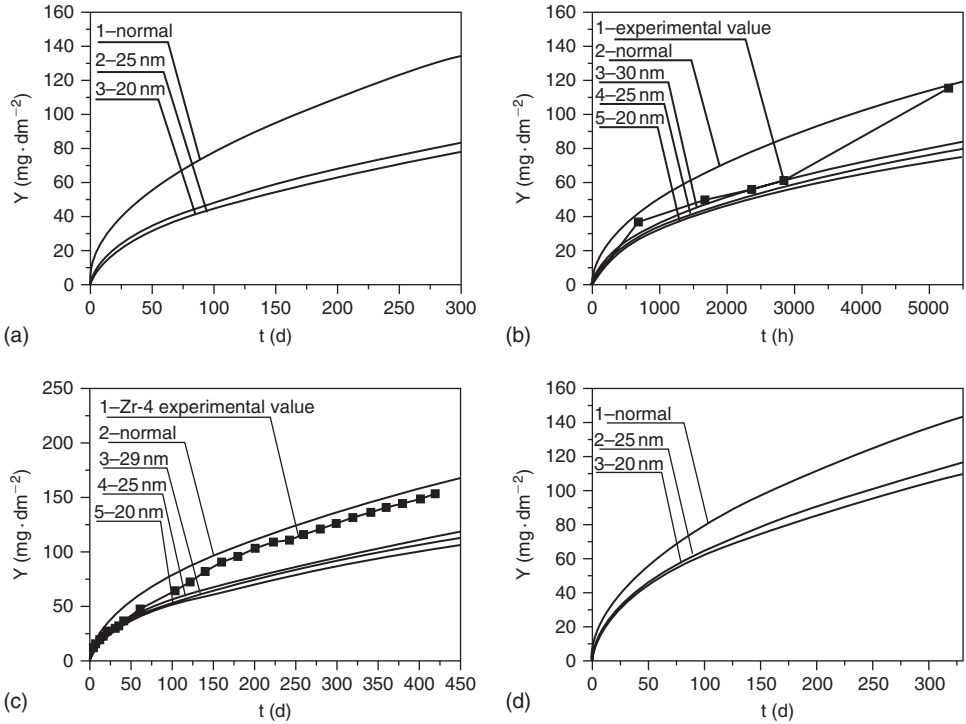

FIGURE 2.53 Corrosion kinetics of zirconium metal with different grain sizes: (a) 200°C, (b) 360°C, (c) 400°C, (d) 500°C. Normal means coarse-grain size [170].

on the basis of increased densification and reduction in the number of growth defects. The corrosion resistance of coatings deposited at lower temperatures is less than that of similar coatings deposited at higher temperatures. Coatings with higher residual-stressed areas adjacent to growth defects are prone to cracking, once corrosion has commenced. Such behaviour is typical of internally stressed coatings, where corrosion can initiate microcracks or pits, which can then grow. It would appear, however, that the beneficial effects of an increase in bias voltage in terms of denser coatings and fewer growth defects more than offset the deleterious effects of an increase in residual stresses resulting from the increase in bias voltage. A higher deposition temperature results in denser coatings with fewer voids and pores because of increased ad-atom mobility and, therefore, better corrosion resistance results. In the case of both low and high temperature ranges, a higher bias voltage, which leads to fewer pores and growth defects, exhibits better corrosion resistance, despite the higher residual stresses present in the coatings [165].

8. RELIABILITY DURING FATIGUE

Fatigue damage becomes an important limit state for the design of structures because, most of the time, materials with high static strength are used in service

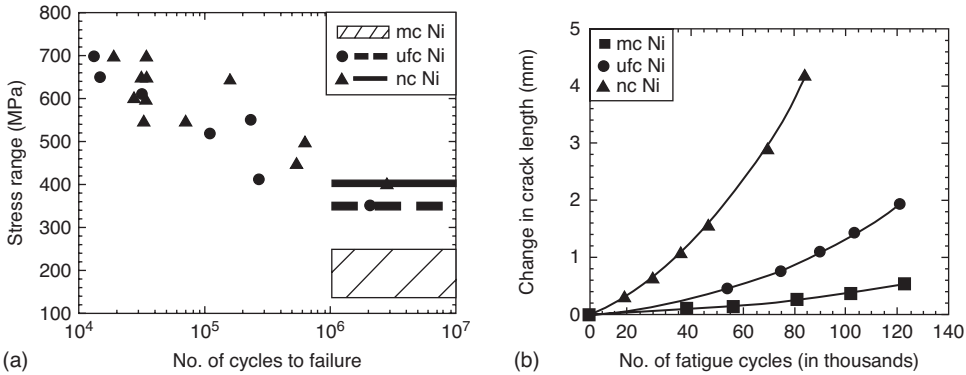

FIGURE 2.54 A comparison of (a) S–N fatigue response, (b) variation of fatigue crack length as a function of the number of fatigue cycles for mc, ufc and nc pure Ni subjected to an initial stress intensity factor range of 11.5 MPa $m^{1/2}$ at R = 0.3 at a fatigue frequency of 10 Hz at room temperature [172].

and there is no simple correlation between the static strength and the fatigue strength. Structures that experience significant dynamic loading are prone to develop fatigue damage during their service lives, especially when their use is extended beyond the design life. The aircraft industry was the first to introduce fatigue as a criterion for design and, later, other industries followed, such as the nuclear, steel bridge engineering, offshore and shipping industries. In the latter, the use of high strength steels led to the definition of an explicit fatigue limit state for design. Design criteria against fatigue failure are based on the S–N curve (stress vs. number of cycles to failure) obtained from tests on typical structural details. The introduction and development of fracture mechanics (FM) and reliability-based methods for crack growth assessment have signified substantial benefits and led to an understanding of the different parameters and the uncertainties involved in the fatigue damage process.

The resistance of metals and alloys to fatigue crack initiation and propagation is known to be influenced significantly by grain size. The coarse-grain structure can lead to an increase in the fatigue crack growth threshold stress intensity factor range and a decrease in the rate of crack growth owing to periodic deflections in the path of the fatigue crack at grain boundaries during crystallographic fracture, especially in the near-threshold regime of fatigue crack growth. The trends extrapolated from conventional microcrystalline (mc) alloys to ultrafine-crystalline (ufc) metals (grain size typically in the 100 nm to 1 μm range) and nanocrystalline (nc) metals (grain size typically less than 100 nm) have not yet been established. Such a lack of understanding is primarily a consequence of the rarity of experimental data on the fatigue response of metals with very fine grain sizes [172].

The effect of grain size on the total fatigue life of pure Ni is plotted in Figure 2.54a in terms of the stress-life (S–N) diagram. It is observed that the nc Ni with an average grain size of approximately 30 nm has slightly greater resistance to stress-controlled fatigue loading than the ufc Ni with an average grain size of

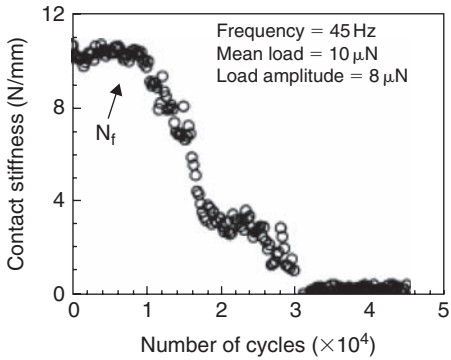

FIGURE 2.55 Contact stiffness as a function of the number of cycles for a 20-nm thick carbon overcoat [174].

approximately 300 nm. This trend is observed both in the stress range at a given number of cycles to failure and in the endurance limit. It is also seen that the range of endurance limit values observed for mc pure Ni is significantly below those of nc and ufc pure Ni. The results shown in Figure 2.54a thus clearly illustrate that grain refinement leads to an enhancement in the resistance to high cycle (S–N) fatigue. Also, fully dense nanocrystalline and ultrafine grained Ni produced by electrodeposition exhibited much higher resistance to stress-controlled fatigue compared with conventional microcrystalline Ni. On the other hand, it is understood from Figure 2.54b that the fatigue crack length increases at a much faster rate with fatigue cycling in the nc Ni than in the ufc or mc Ni under identical loading conditions [172].

Therefore, it could be said that a high-strength nanostructure is desirable at the surface where the cracks initiate. However, nanostructures would have a generally deleterious effect on the resistance to the growth of a fatigue crack once it starts. In other words, one would prefer a less-refined microstructure in the interior in order to suppress crack growth. In this context, the micro/nanostructure gradient observed offers naturally a microstructurally graded material for such applications [173].

A recently developed technique, continuous stiffness measurement (CSM), offers a significant improvement in nanoindentation testing. The CSM is accomplished by imposing a small, sinusoidally varying signal motion on the indenter. This allows the measurement of contact stiffness at any point along the loading curve and not just at the point of unloading, as in conventional measurement. A substantial decrease in the contact stiffness would indicate fatigue failure of the nanocoating. N_f is the number of cycles to failure [174]. Figure 2.55 shows the contact stiffness as a function of the number of cycles for a 20-nm thick amorphous carbon coating on a silicon substrate cyclically deformed by an oscillation load amplitude of 8 mN under a mean load of 10 mN at a frequency of 45 Hz. The abrupt decrease in contact stiffness at 0.8×10^4 cycles indicates that fatigue damage has occurred [174].

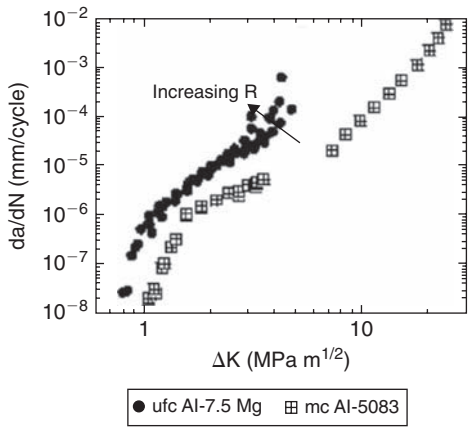

FIGURE 2.56 Variation of fatigue crack growth rate, da/dN, as a function of stress intensity range, ΔK, for the cryomilled Al-7.5 Mg at R = 0.1–0.5 at a fatigue frequency of 10 Hz at room temperature [14].

Figure 2.56 shows the da/dN versus ΔK curve for the ultrafine grained Al–Mg alloy tested at R = 0.1–0.5 over the entire range of fatigue crack growth rates. This is compared with the crack growth data for commercial 5083 aluminium alloy at R = 0.33. Although the processing conditions for these two alloys are different, it is evident from Figure 2.56 that, consistent with expectations, grain refinement from the mc to the ufc range results in a noticeable reduction in ΔK_{th} and a significant increase in the rate of fatigue crack growth from threshold to final failure [14]. If extrapolation is valid, it could be said that the situation would be worse as one reaches the nanograin size range.

The latest work of Sriraman et al. [174] discusses the effect of crystallite size on the hardness and fatigue life of steel samples coated with electrodeposited nanocrystalline Ni–W alloys containing 0.72 to 9.33 at% W. The Ni–W alloys were electrodeposited on steel samples at four different current densities to achieve varying crystallite density. Figure 2.57 shows the variation of microhardness with $(\text{crystallite size})^{-0.5}$. The best fit line is also shown by a continuous line. The hardness of the Ni–W alloy coatings was found to be in the range of 575–638 HV. The microhardness value increased with increasing content of tungsten. The alloy containing 9.33 at% tungsten and having a crystallite size of 13 nm exhibited the maximum hardness of 638 HV. The crystallite size decreased as the tungsten content increased. In the case of nanocrystalline alloys, two different factors may be responsible for strengthening, namely, solid solution strengthening and grain boundary hardening. It has been shown [175] that the solid solution strengthening effect of tungsten is about an order of magnitude smaller than the intrinsic hardness of nickel and much smaller than the grain size contribution. The alloy coatings obeyed the Hall–Petch relationship, i.e. hardness increased as the crystallite size decreased.

The reliability of structures mainly depends on crack initiation and crack growth. Sometimes the initiation of cracks dominates in nanostructured materials.

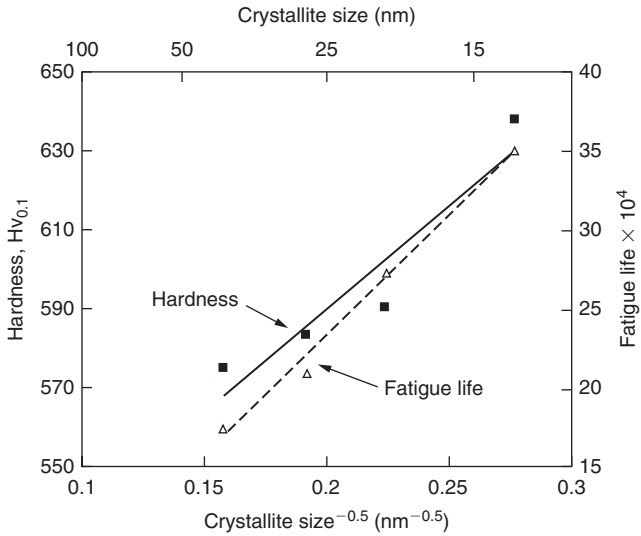

FIGURE 2.57 Dependence of hardness and fatigue life on crystallite size in Ni–W alloys containing 0.72 to 9.33 at% W [175].

Uncoated steel specimens tested at a maximum stress of 325 MPa did not fail even after 2.5×10^6 cycles. In contrast, the coated samples failed within 3.5×10^5 cycles. The inferior fatigue lives of the coated specimens could be attributed to the presence of tensile residual stresses and inherent microcracks in the coatings causing an early nucleation of fatigue cracks in the substrate [175].

Compressive residual stress is the most crucial factor in increasing the fatigue resistance [176]. Ultrasonic cold forging technology (UCFT) is a surface modification technology to produce nanostructures, which can improve the surface compressive stresses. Hence, the fatigue reliability could be improved. Figure 2.58 shows the reliability improvement during fatigue on tool steel (SKD-61) after UCFT. The 10^7 cycles fatigue limit before UCFT was 719 MPa, whereas the value after UCFT was 899 MPa, which represented a 25% increase [176].

This improvement in the reliability of the material was due to the compressive residual stresses introduced by the UCFT treatment (Figure 2.59) [176]. It has been reported that a newly developed surface modification technique, known as cavitation shotless peening (CSP), can also improve the fatigue strength and corrosion resistance of polycrystalline materials [167].

The fatigue life of surface-treated metallic materials and components depends in a complex way on a multitude of factors among which near-surface residual stresses, microstructures and roughness are just the most important ones [101]. Nanocrystalline surface layers significantly affect the mechanical behaviour by restricting or impeding dislocation slip and the formation of slip bands at the surface, which act as preferred crack initiation sites. Therefore, tailored nanocrystalline surfaces are highly desirable in order to delay or prevent surface fatigue damage [101].

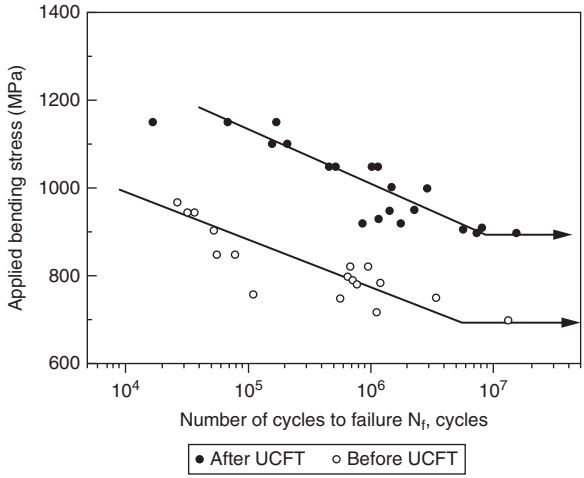

FIGURE 2.58 S–N curves of smooth specimens before and after the UCFT treatment [176].

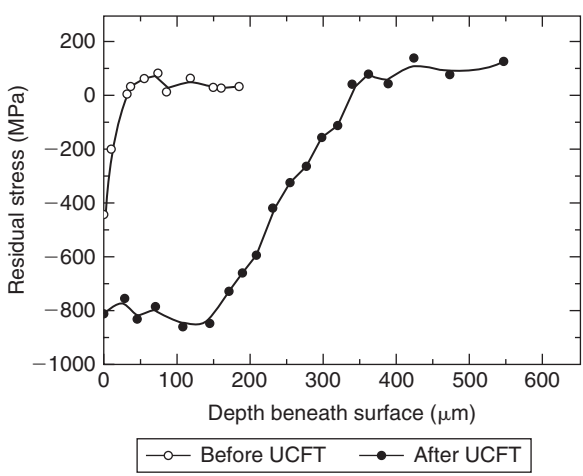

FIGURE 2.59 Variation of compressive residual stress with depth, brought about by the UCFT treatment [176].

One critical issue of mechanically induced nanocrystalline surface layers is their mechanical and thermal stability. First, thermodynamically, nanocrystalline regions are in a non-equilibrium state with a large number of lattice defects that tend to anneal out and finally recrystallize if the temperatures are elevated enough to provide substantial diffusion. Secondly, according to recent *in-situ* TEM studies, dislocation slip occurs in nanocrystalline materials if the grain size is in the range of 20–50 nm or greater. Thus, it appears probable that mechanical

(cyclic or monotonic) loading will affect the long-term or even short-term stability of nanocrystalline surface regions [176].

Therefore, the reliability of nanostructured materials (including coatings) in fatigue mainly depends on the:

1. processing methodology;
2. size of the nanostructure, e.g. average grain size;
3. coating thickness and morphology of coating;
4. stress intensity range.

However, it is safe to note that compared to what is known on the fatigue behaviour of microcrystalline materials, knowledge about the fatigue response of nc materials is rather limited.

References

1. Kendall K, Yong CW, Smith W. Powder Technol. 2007; 174:2–5.
2. Dao M, Lu L, Shen YF, Suresh S. Acta Mater. 2006; 54:5421–5432.
3. Padmanabhan KA, Nitsche R, Hahn H. Proceedings of the 4th European conference on Advanced Materials and Processes, Symposium G, Associazone Italiana Di Metallurgia, Milano, Italy, 1995; pp.289–298.
4. Hahn H, Padmanabhan KA. Phil. Mag. B 1997; 76:559–571.
5. Hahn H, Padmanabhan KA. Proceedings of the 2nd Pacific Rim International Conference on Advanced Materials and Processing, eds. K.S. Shin, J.K. Yoon and S.J. Kim, Korean Institute of Metals and Materials,1995; 2119–2125.
6. Alexandrov IV, Zhu YT, Lowe TC, Islamgaliev RK, Valiev RZ. Nanostructured Mater 1998; 10:45–54.
7. Goujon C, Goeuriot P. Mater. Sci. Engin. A 2001; 315:180–188.
8. Padmanabhan KA, Mondal P, Hahn H. J. Mater. Sci. 2005; 40:6113–6120.
9. Zhou J, Li Y, Zhu R, Zhang Z. Mater. Sci. Engin. A 2007; 445–446:717–724.
10. Chaim R. Mater. Sci. Engin. A 2007; 443:25–32.
11. Padmanabhan KA. Mater. Sci. Engin. A 2001; 304–306:200–205.
12. Wei Q, Zhang HT, Schuster BE et al. Acta Mater. 2006; 54:4079–4089.
13. Lee SW, Choi HJ, Kim Y, Bae DH. Mater. Sci. Engin. A 2007; 449–451:782–785.
14. Meyers MA, Mishra A, Benson DJ. Prog. Mater. Sci. 2006; 51:427–556.
15. Qin XY, Cheong SH, Lee JS. Mater. Sci. Engin. A 2003; 363:62–66.
16. Tjong SC, Chen H. Mater. Sci. Engin. R 2004; 4:51–88.
17. Moon KI, Lee KS. J. Alloys Compounds 2002; 333:249–259.
18. Veprek S, Reiprich S. Thin Solid Films 1995; 268:64–71.
19. Andrievski RA, Anisimova IA, Anisimov VP. Thin Solid Films 1991; 205:171–175.
20. Veprek S, Neslhdek P, Niederhofer A, Clatz F. Nanostructured Mater. 1998; 10:479–489.
21. Schiøtz J. Mater. Sci. Engin A 2004; 375–377:975–979.
22. Wang DL, Kong QP, Shui JP. Scripta Metall. Mater. 1994; 31:47–51.
23. Benson DJ, Fu HH, Meyers MA. Mater. Sci. Engin. A 2001; 319–321:854–861.
24. Liu KW, Mücklich F, Birringer R. Mat. Res. Soc. Symp. Proc. Mater. Res. Soc. 2001; 676:Y3.21.1–Y3.21.6.
25. Chokshi AH, Rosen A, Karch J, Gleiter H. Scr. Metal. 1989; 23:1679.
26. Nieh TG, Wang JG. Intermetallics 2005; 13:377–385.
27. Carlton CE, Ferreira PJ. Acta Mater. 2007; 55:3749–3756.
28. Zhou J, Li Y, Zhu R, Zhang Z. Mater. Sci. Engin. A 2007; 445–446:717–724.
29. Bellosi A, Sciti D, Guicciardi S. J. Eur. Ceramic Soc. 2004; 24:3295–3302.
30. Koch CC, Narayan J. Mat. Res. Soc. Symp. Mater. Res. Soc. 2001; 634:B5.1.1–B5.1.11.

31. Padmanabhan KA, Dinda GP, Hahn H, Gleiter H. Mater. Sci. Engin. A 2007; 452–453:462–468.
32. Zhu B, Asaro RJ, Krysl P, Zhang K, Weertman JR. Acta Mater. 2006; 54:3307–3320.
33. Gutkin MYu, Ovid'ko IA, Mikaelyan KN. Nanostruct. Mater. 1995; 6:779–782.
34. Haslam AJ, Moldovan D, Yamakov V, Wolf D, Phillpot SR, Gleiter H. Acta Mater. 2003; 51:2097–2112.
35. Zheng GP, Wang YM, Li M. Acta Mater. 2005; 53:3893–3901.
36. Wei Y, Su C, Anand L. Acta Mater. 2006; 54:3177–3190.
37. Yamakov V, Wolf D, Salazar M, Phillpot SR, Gleiter H. Acta Mater. 2001; 49:2713–2722.
38. Torre F, Spaetig P, Schaublin R, Victoria M. Acta Mater. 2005; 53:2337–2349.
39. Pande CS, Masumura RA. Mat. Res. Soc. Symp. Proc. Mater. Res. Soc. 2003; 740:I1.1.1–I1.1.12.
40. Farkas D, Van Petegem S, Derlet PM, Van Swygenhoven H. Acta Mater. 2005; 53:3115–3123.
41. Wolf D, Yamakov V, Phillpot SR, Mukherjee A, Gleiter H. Acta Mater. 2005; 5:31–40.
42. Yamakov V, Wolf D, Phillpot SR, Gleiter H. Acta Mater. 2002; 50:61–73.
43. Haslam AJ, Yamakov V, Moldovan D, Wolf D, Phillpot SR, Gleiter H. Acta Mater. 2004; 52:1971–1987.
44. Markmann J, Bunzel P, Rösner H et al. Scripta Mater. 2003; 49:637–644.
45. Cairney JM, Hoffman MJ, Munroe PR, Martin PJ, Bendavid A. Thin Solid Films 2005; 479:193–200.
46. Noskova NI. J. Alloys Compounds 2007; 434–435:307–310.
47. Zhang S, Bui XL, Fu Y. Thin Solid Films 2004; 467:261–266.
48. Ma E. Scripta Mater. 2003; 49:663–668.
49. Dollar M, Dollar A. J. Mater. Process. Technol. 2004; 157–158:491–495.
50. Sergueeva AV, Mukherjee AK. Rev. Adv. Mater. Sci. 2006; 13:1–5.
51. Ovid'ko IA, Pande CS, Masumura RA. Nanomaterials Handbook. CRC Press, Florida, 2005; pp. 531–552.
52. Padmanabhan KA, Davies GJ. Superplasticity. Springer Verlag, 1980.
53. Imayev RM, Kaibyshev OA, Salishchev GA. Acta Metall. 1992; 40:581–587.
54. Schuh CA, Nieh TG, Yamasaki T. Scripta Mater. 2002; 46:735–740.
55. Padmanabhan KA, Schlipf J. Proc. First Int. Conf. on Transport Phenomena in Processing, Technomic Publ. Co., 1993, pp.491–505.
56. Padmanabhan KA, Schlipf J. Mater. Sci. Technol. 1996; 12:391–399.
57. Hahn H, Padmanabhan KA. Nanostruct. Mater. 1995; 61:91–200.
58. Padmanabhan KA, Gleiter H. Mater. Sci. Engin. A 2004; 381:28–38.
59. Pande CS, Masumura RA, Armstrong RW. Nanostruct. Mater. 1993; 2:323–331.
60. Masumura RA, Hazzledine PM, Pande CS. Acta Mater. 1998; 46:4527–4534.
61. Yang HC, Kim KT. Acta Mater. 2006; 54:3779–3790.
62. Pearson CE. J. Inst. Metals 1934; 54:111–116.
63. Ball A, Hutchison MM. J. Mater. Sci. 1969; 3:1–8.
64. Padmanabhan KA. Mater. Sci. Engin. 1977; 29:1–18.
65. Wolf . Acta Metall. Mater. 1990; 38:781–790.
66. Wolf . Acta Metall. Mater. 1990; 38:791–798.
67. Hahn H, Mondal P, Padmanabhan KA. Nanostruct. Mater. 1997; 9:603–609.
68. Hahn H, Padmanabhan KA. Z. Metallkunde 2003; 94:1046–2051.
69. Gutkin MYu, Ovidko IA, Skiba NV. Acta Mater. 2004; 52:1711–1720.
70. Mei QS, Lu K. Prog. Mater. Sci. (in Press).
71. Zhou YH, Harmelin M, Bigot J. Mater. Sci. Engin. A 1991; 133:775–779.
72. Tadaki T, Murai Y, Koreeda A, Nakata Y, Hirotsu Y. Mater. Sci. Engin. A 1996; 217–218: 235–238.
73. Li W, Ni C, Lin H, Huang CP, Shah SL. J. Appl. Phys. 2004; 96:6663–6668.
74. Zarkevich NA, Johnson DD, Smirnov AV. Acta Mater. 2002; 50:2443–2459.
75. Van Huis MA, Chen JH, Zandbergen HW, Sluiter MHF. Acta Mater. 2006; 54:2945–2955.
76. Estrin Y, Gottstein G, Rabkin E, Shvindlerman LS. Scripta Mater. 2000; 43:141–147.
77. Rong Y. Curr. Opin. Solid State Mater. Sci. 2005; 9:287–295.
78. Asaka K, Hirotsu Y, Tadaki T. Mater. Sci. Engin. A 1999; 273–275:262–265.
79. Kitakami O, Sato H, Shimada Y. Phys. Rev. B 1997; 56:849–854.
80. Nicula R, Stir M, Schick C, Burkel E. Thermochim. Acta 2003; 403:129–136.

81. Thompson GB, Banerjee R, Dregia SA, Fraser HL. Mat. Res. Soc. Symp. Proc. Mater. Res. Soc. 2002; 72:7R5.8.1–7R5.8.6.
82. Heuer AH, Clausen N, Kriven WM, Ruhle M. J. Am. Ceramic Soc. 1982; 65:642.
83. Ehre D, Gutmanas EY, Chaim R. J. Eur. Ceramic Soc. 2005; 25:3579–3585.
84. Chaim R, Margulis M. Mater. Sci. Engin. A 2005; 407:180–187.
85. Sturm U, Betz G, Scipione , Hahn H. Nanostructured Mater. 1999; 11:651–661.
86. Chen I-W, Xue LA. J. Am. Ceramic Soc. 1990; 73:2585.
87. Millett PC, Selvam RP, Saxena A. Acta Mater. 2007; 55:2329–2336.
88. Liang S, Islam R, Smith DJ, Bennett PA. J. Crystal Growth 2006; 295:166–171.
89. Zhou L, Wei X, Zhou N. Comput. Mater. Sci. 2004; 303: 314–319.
90. Hibbard GD, Aust KT, Erb U. Materials Science and Engineering A, 433 (2006) 195–202.
91. Mannling H-D, Patil DS, Moto K, Jilek M, Veprek S. Surface Coatings Technol. 2001; 146–147:263–267.
92. Musil J, Kunc F, Zeman H, Pola´kova H. Surface Coatings Technol. 2002; 154:304–313.
93. Cairney JM, Hoffman MJ, Munroe PR, Martin PJ, Bendavid A. Thin Solid Films 2005; 479:193–200.
94. Andrievski RA. Surface Coatings Technol. 2007; 201:6112–6116.
95. Veprek S, Veprek-Heijman MGJ, Zhang R. J. Phys. Chem. Solids 2007; 68:1161–1168.
96. Varesi E, Pavia G, Zenkevich A et al. J. Phys. Chem. Solids 2007; 68:1046–1051.
97. Musil J, Daniel R, Solda´na J, Zemana P. Surface Coatings Technol. 2006; 200:3886–3895.
98. Mayrhofer PH, Mitterer C, Hultman L, Clemens H. Prog. Mater. Sci. 2006; 51:1032–1114.
99. Naka M, Shibayanagi T, Maeda M, Mori M, Mori H. Vacuum 2004; 73:619–622.
100. Lewandowska M, Kurzydyowski KJ. Mater. Characterization 2005; 55:395–401.
101. Nikitin I, Altenberger I, Maier HJ, Scholtes B. Mater. Sci. Engin. A 2005; 403:318–327.
102. Zukerman I, Raveh A, Shneor Y, Shneck R, Klemberg-Saphieha JE, Martinu L. Surface Coatings Technol. 2007; 201:161–166.
103. Mayrhofer PH, Rovere F, Moser M, Strondl C, Tietema R. Scripta Mater. 2007; 57:249–252.
104. Veprek S, Mannling H-D, Karvankova P, Prochazka J. Surface Coatings Technol. 2006; 200:3876–3885.
105. Tien SK, Duh JG. Thin Solid Films 2006; 515:1097–1101.
106. Veprek S, Nesladek P, Niederhofer A, Glatz F, Jilek M, Sima M. Surface Coatings Technol. 1998; 108:138.
107. Veprek S, Argon AS. Surface Coatings Technol. 2001; 146–147:175–182.
108. Veprek S, Mukherjee S, Karvankova P et al. Thin Solid Films 2003; 436:220–231.
109. Veprek S, Jilek M. Vacuum 2002; 67:443–449.
110. Veprek S, Veprek-Heijman MGJ. Surface Coatings Technol. 2007; 201:6064–6070.
111. Raveh A, Zukerman I, Shneck R, Avni R, Fried I. Surface Coatings Technol. 2007; 201:6136–6142.
112. Lu YH, Shen YG, Li KY, Chen H. Surface Coatings Technol. 2006; 201:1228–1235.
113. Mayrhofer PH, Stoiber M. Surface Coatings Technol. 2007; 201:6148–6153.
114. Santana AE, Karimi A, Derflinger VH, Schütze A. Mater. Res. Soc. Symp. Proc. Mater. Res. Soc. 2004; 795:U8.10.1–U8.10.6.
115. Veprek S, Männling H-D, Jilek M, Holubar P. Mater. Sci. Engin. A 2004; 366:202–205.
116. Veprek S, Veprek-Heijman MGJ, Karvankova P, Prochazka J. Thin Solid Films 2005; 476:1–29.
117. Zhang RF, Veprek S. Mater. Sci. Engin. A 2006; 424:128–137.
118. Veprek S, Nesla´dek P, Niederhofer A, Glatz F, Jılek M, Sıma M. Surface Coatings Technol. 1998; 108–109:138–147.
119. Donohue LA, Smith IJ, Muntz W-D, Petrov I, Greene JE. Surface Coatings Technol. 1997; 94–95:226.
120. Zhu Y, Tan M. Mater. Sci. Engin. A 1995; 201:Ll–L4.
121. Jin HJ, Zhou F, Wang LB, Lu K. Scripta Mater. 2001; 44:1083–1087.
122. Men H, Pang SJ, Zhang T. Mater. Sci. Engin. A 2007; 538–540:449–451.
123. Concustell A, Sort J, Woodcock TG et al. Intermetallics 2006; 14:871–875.
124. Qin FX, Wang XM, Inoue A. Intermetallics 2007; 15:1337–1342.
125. Pang SJ, Men H, Shek CH, Chaoli Ma, Inoue A, Zhang T. Intermetallics 2007; 15:683–686.
126. Yang HW, Dong P, Wang JQ, Li Y. Mater. Sci. Engin. A 2007; 449–451:273–276.

127. Gilbert CJ, Lippmann JM, Ritchie RO. Scripta Mater. 1998; 38:442–537.
128. Liu DY, Sun WS, Wang AM, Zhang HF, Hu ZQ. J. Alloys Compounds 2004; 370:249–253.
129. Liu DY, Sun WS, Zhang HF, Hu ZQ. Intermetallics 2004; 12:1149–1152.
130. Amiya K, Urata A, Nishiyama N, Inoue A. Mater. Sci. Engin. A 2007; 449–451:356–359.
131. Wollgarten M, Mechler S, Davidov E, Wanderka N, Macht M-P. Intermetallics 2004; 12:1251–1255.
132. Kato H, Inoue A, Chen H. Acta Mater. 2006; 54:891–898.
133. Fátay D, Gubicza J, Szommer P, Lendvai J, Blétry M, Guyot P. Mater. Sci. Engin. A 2004; 387–389:1001–1004.
134. Yan M, Zou J, Shen J. Intermetallics 2007; 15:961–967.
135. Inoue A. Mater. Sci. Engin. A 1994; 57:179–180.
136. Qin SH, Qin DQ, Ford WT, Resasco DE, Herrera JE. J. Am. Chem. Soc. 2004; 126:170.
137. Qiu KQ, Zhang HF, Wang AM, Ding BZ, Hu ZQ, Acta Mater. 2002; 50:3567–3578.
138. Hanlon T, Kwon Y-N, Suresh S. Scripta Mater. 2003; 49:675–680.
139. Revesz A, Donnadieu P, Simon JP, Guyot P, Ochin P. Phil. Mag. Lett. 2001; 81:767–772.
140. Xia M, Zheng H-X, Liu J, Ma C, Li J. J. Non-Crystalline Solids 2005; 351:3747–3751.
141. Senkov ON, Scott JM. Mater. Lett. 2004; 58:1375–1378.
142. Zhu SL, Wang XM, Qin FX, Inoue A. Intermetallics 2007; 15:885–890.
143. Liu L, Wu ZF, Zhang J. J. Alloys Compounds 2002; 339:90–95.
144. Gao YL, Shen J, Sun JF, Wang G, Xing DW, Xian HZ., Mater. Lett. 2003; 57:1894–1898.
145. Zhang QS, Zhang W, Xie GQ, Nakayama KS, Kimura H, Inoue A. J Alloys Compounds 1999; 293–295:821–824.
146. Bletry M, Guyot P, Blandin JJ, Soubeyroux JL. Acta Mater. 2006; 54:1257–1263.
147. Inoue A, Zhang T, Zhang W, Takeuchi A. Mater. Transact. Jap. Inst. Metals 1996; 37:99.
148. Lin XH, Johnson WL, Rhim WK. Mater. Transact. Jap. Inst. Metals 1997; 38:473.
149. Gebert A, Eckert J, Schultz L. Acta Mater. 1998; 46:5475–5482.
150. Leonhard A, Xing LQ, Heilmaier M, Gebert A, Eckert J, Schultz L. Nanostructured Mater. 1998; 10:805–817.
151. Hu Y, Liu L, Chan KC, Yang YZ. J. Alloys Compounds 2006; 419:251–255.
152. Ravi Kumar NV, Prinz S, Cai Y et al. Acta Mater. 2005; 53:4567–4578.
153. Kaiser A, Vassen R, Stiver D, Buchkremer HP. Nanostruct. Mater. 1997; 8:489–497.
154. Besson J-L, Doucey B, Lucas S, Baloul D. Eur. Ceramic Soc. 2001; 21:959–968.
155. Chan KC, Wang GF, Wang CL, Zhang KF. Scripta Mater. 2005; 53:1285–1290.
156. Descamps P, O'Sullivan D, Poorteman M, Descamps JC, Leriche A, Cambier F. J. Eur. Ceramic Soc. 1999; 19:2475–2485.
157. Sanders PG, Rittner M, Kiedaisch E, Weertman JR, Hung H, Lu YC. Nanostruct. Mater. 1999; 9:433–440.
158. Wang YM, Hamza AV, Ma E. Acta Mater. 2006; 54:2715–2726.
159. Cai B, Kong QP, Lu L, Lu K. Mater. Sci. Engin. A 2000; 286:188–192.
160. Dickenscheid W, Birringer R, Gleiter H, Kanert O, Michel B, Gunther B. Solid State Commun. 1991; 79:683.
161. Yin WM, Whang SH, Mirshams RA. Acta Mater. 2005; 53:383–392.
162. Wei Y, Liu B, Hou L, Xu B, Liu G. J. Alloys Compounds (in Press).
163. Kang DH, Park SS, Oh YS, Kim NJ. Mater. Sci. Engin. A 2007; 449–451:318–321.
164. Lewis DB, Creasey SJ, Wustefeld C, Ehiasarian AP, Hovsepian PEh. Thin Solid Films 2006; 503:143–148.
165. Hamdy AS. Mater. Lett. 2006; 60:2633–2637.
166. Kwok CT, Cheng FT, Man HC, Ding WH. Mater. Lett. 2006; 60:2419–2422.
167. Patil RC, Radhakrishnan S. Prog. Organic Coatings 2006; 57:332–336.
168. Mato S, Alcal´a G, Woodcock TG, Gebert A, Eckert J, Schultz L. Electrochim. Acta 2005; 50:2461–2467.
169. Zhang XY, Shi MH, Lic C, Liu NF, Wei YM. Mater. Sci. Engin. A 2007; 448:259–263.
170. Conde A, Navas C, Cristóbal AB, Housden J, de Damborene J. Surface Coatings Technol. 2006; 201:2690–2695.
171. Hanlon T, Kwon Y-N, Suresh S. Scripta Mater. 2003; 49:675–680.

172. Sun Chang Q. Progress in Solid State Chemistry 2007; 35:1–159.
173. Li X, Bhushan B. Mater. Characterization 2002; 48:11–36.
174. Sriraman KR, Ganesh Sundara Raman S, Seshadri SK. Mater. Lett. 2007; 61:715–718.
175. Suh C, Song G, Suh MS, Shik Y. Mater. Sci. Engin. A 2007; 443:101–106.
176. Nikitin I, Altenberger I, Maier HJ, Scholtes B. Mater. Sci. Engin. A 2005; 403:318–327.

CHAPTER 3

Mechanical Properties of Nanocomposite Materials

A.V. Sergueeva, D.M. Hulbert, N.A. Mara and A.K. Mukherjee

1. INTRODUCTION

For more than a decade, researchers have been attempting to harness the promise of nanostructured metals and ceramics. The motivation for this work was the realization that reducing the grain size of single- or multiphase materials to nanoscale dimensions offered the potential of dramatic improvements in properties. Data are now emerging that support these expectations, especially in the area of mechanical properties. However, despite the property improvements in nanocrystalline materials being significant, the ability to realize these increases faced a formidable barrier. For example, when ceramic nanopowders are processed by conventional sintering methods, rapid grain growth occurs due to the high driving force caused by the large surface area. Thus, the high surface to volume ratio that gives rise to mechanical property improvements is also responsible for coarsening the nanoscale grain size during sintering. Thus, it was quickly recognized that unless the grain growth encountered during sintering could be mitigated, the promise of nanoceramic materials would not be easily realized.

In this chapter, an attractive processing methodology, spark plasma sintering (SPS), is described (Section 2); using this as a processing tool, one can engineer microstructures of ceramic-based nanocomposites that have either much improved fracture toughness (Section 3.1), or significantly enhanced superplastic formability (Section 3.2), or much improved creep resistance (Section 3.3). Some very attractive functional properties might also be achieved (Section 3.4).

In metal-based nanocomposites, designed nanostructure might be obtained by various methods that include crystallization from amorphous (metallic glass)

Chemical Engineering & Materials Science Department, University of California, One Shields Avenue, Davis, CA 95616

Nanostructured Materials © 2009 Elsevier Ltd.
978-0-08-044965-4 All rights reserved.

state (Section 4.1, 4.3) or magnetron sputtering (Section 4.2). Not only grain size, but grain size distribution and phase morphology were found to affect significantly mechanical response of the nanocomposites.

2. SPS AS AN ADVANCED SINTERING TECHNIQUE

Spark plasma sintering (SPS), also known as field assisted sintering (FAS), pulsed electric current sintering (PECS), plasma assisted sintering (PAS), or plasma pressure consolidation (PPC), is a newly developed rapid sintering technique with a great potential for achieving fast densification results with minimal grain growth in a short sintering time [1–3]. A pulsed DC current with typical pulse durations of 10 ms flows through the punches, die and, depending on the electrical properties of the specimen, also through the specimen (Figure 3.1a).

SPS is based on the theory of high-temperature plasma momentarily generated in the gaps between powder materials by electrical discharge during DC pulsing [1–4] and has gained a reputation as new industrial processes for the processing of a broad variety of materials including metals, intermetallics, ceramics, composites and polymers. Application of rapid heating results in bypassing of low-temperature regions where surface transport controlled sintering is dominant. This preserves the powder surface area to temperature levels where bulk transport is significant. However, the nature of activation effects, especially in regard to acceleration of diffusion processes, is not clearly established. It has been suggested [4] that the On–Off DC pulse energizing method could generate:

1. spark plasma
2. spark impact pressure
3. Joule heating, and
4. an electrical field diffusion effect.

SPS can rapidly consolidate powders to near theoretical density through the combined actions of a rapid heating rate, pressure application and proposed powder surface cleaning. However, the appearance of thermal plasma during SPS is a controversial issue and plasma–particle interaction is a complex phenomenon. Nevertheless, SPS is proven by obtained experimental data of enhanced sinterability of powders subjected to SPS mainly associated with particle surface activation and increased diffusion rates on the contact zones caused by applied pulse current. In nanocrystalline materials, which are difficult to sinter by conventional methods, the advantages of SPS are more directly evident. With low sintering temperatures and short sintering times, SPS can result in better control of the microstructure and final properties of materials. All ceramic-based nanocomposites described in this chapter were synthesized by SPS.

Advanced ceramic materials are attractive because of their low density, chemical inertness, high strength, high hardness and high temperature capability. Nanocrystalline ceramics are commonly defined as having a grain size of 100 nm or less. While this definition is rather arbitrary, nanocrystalline ceramics are known to possess unique mechanical properties, including enhanced superplasticity and superior strength. Pilot-scale facilities for nanopowder synthesis and the

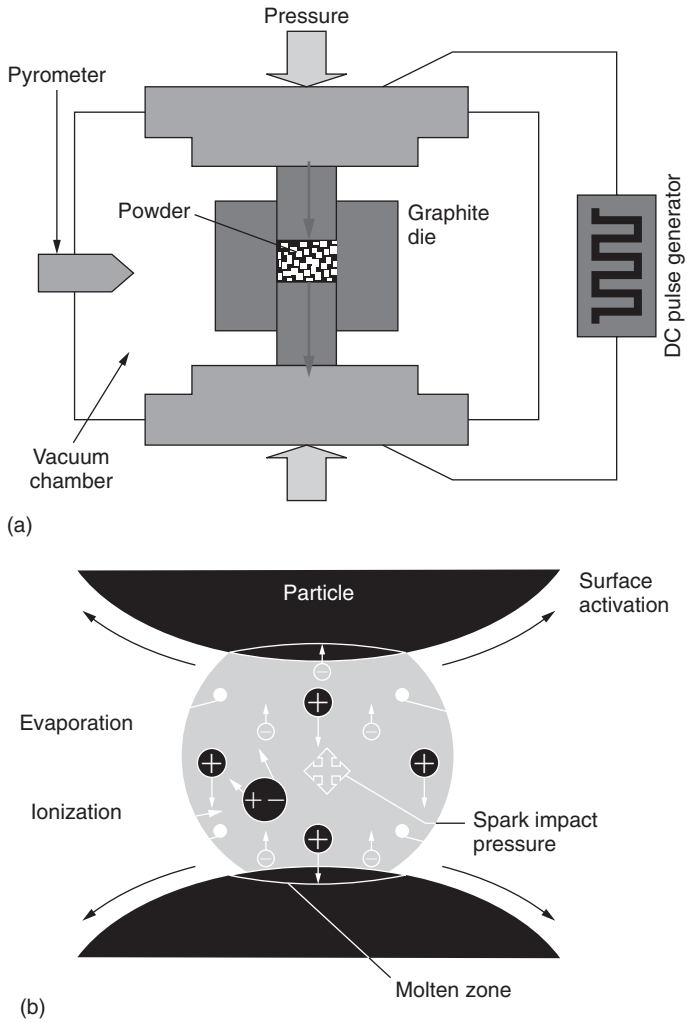

FIGURE 3.1 Schematic of spark plasma sintering: (a) set-up of SPS and (b) possible SPS mechanisms.

commercialization of sizable quantities of certain types of nanosize powders have been achieved. The fabrication of nanopowders into fully dense components that retain a nanocrystalline grain size has lagged behind powder synthesis and characterization. In part, the gap between powder synthesis and bulk fabrication is related to an incomplete theoretical understanding of the mechanisms associated with densification and sintering when grain interfacial regions comprise a large volume fraction of the material. Equally relevant is the incomplete understanding of the particular experimental conditions that yield high-density compacts without microstructural coarsening. The available experimental work in this area clearly demonstrates that the conditions for densification and sinterability of nanocrystalline ceramics is system-specific and is not readily deduced from theory alone at the present time.

The system of nano Al_2O_3-based composites with single-wall carbon nanotubes (SWCN) as a second phase is one of the most difficult to produce since Al_2O_3 possesses one of the highest homologous temperatures for full-density sintering. In the open literature [5–11], carbon nanotubes reinforced with ceramic composites have been consolidated by hot-pressing methods that require higher temperatures and longer duration. These sintering parameters damage the carbon nanotubes in the composites, leading to decreases in, or total loss in, reinforcing effects and electrical conductivity. For example, in carbon nanotubes–metal–ceramic composite systems [6–10], some of the hot-pressing temperatures were as high as 1600°C, which damaged most of carbon nanotubes and decreased the quantity and quality of carbon nanotubes in the sintered composites. Moreover, high sintering temperatures lead to aggressive grain growth as the compacts reach full density. Siegel et al. [11] used the hot-pressing method at 1300°C/h to obtain fully dense multiple-wall carbon nanotube filled alumina nanocomposites but the matrix grain size was in the sub-micron range. Utilization of SPS significantly reduced sintering temperatures and sintering times and has achieved remarkable success in producing nanocomposites [12,13]. A network of undamaged SWCN homogeneously distributed in a nanocrystalline Al_2O_3 matrix was produced that resulted in an incredible increase in fracture toughness of the nanocomposites (see Section 3.1), as well as very attractive electrical and thermal properties (see Section 3.4).

Another example of the successful application of SPS is the synthesis of highly creep resistant silicon nitride/silicon carbide composite. Covalent ceramics such as silicon nitride and silicon carbide require liquid phase sintering to reach high density [14–16]. This is usually realized by addition (either singularly or in combination) of sintering aids, such as Al_2O_3, MgO, AlN, SiO_2, Y_2O_3 and rare earth oxides, to the starting powder [17–20]. At the temperature of sintering, the sintering additives react with the silicon oxide layer, which is always present at the surface of silicon nitride particles, and form a silicate liquid phase to promote sintering. The liquid phase then forms a glassy phase with a thickness of about 0.5–2 nm at the grain boundaries upon cooling [16,19,21]. It is now well established that the superplasticity and creep deformation of silicon nitride ceramics is dictated by the behaviour of this glassy grain boundary phase [22–27]. Generally, it has been realized that compressive creep takes place through grain boundary sliding, mainly accommodated by the solution–precipitation process [27–33]. The intergranular glassy phase plays a role in high diffusivity paths for atomic diffusion. The structural change in intergranular film leads to a greater resistance to creep under compressive force [34]. Therefore, the focus of efforts in enhancing creep property has been on controlling the chemistry and amount of the glassy phase, which is determined by the amount/species of additive as well as the oxygen content at the particle surface of the starting powders. A number of approaches have been attempted for this purpose [35–38]. However, owing to the thermodynamically stable nature of the glassy phases and the fact that it is impractical to prevent surface oxidation of the powders, these efforts have led to only limited success. Even in the case where no oxide additive was used in sintering, glassy phases were still found at grain boundaries [39]. SPS of the amorphous Si–C–N powder derived from pyrolysis of a liquid polymer precursor

allowed for a nano-nano structure (nano-sized SiC and Si_3N_4 in dual-phase mixture) in the composites by decreasing, and even avoiding, sintering additive. Such a material with mean grain of 50 nm did reveal a creep rate at which most creep testing equipment is at the limit of transducer resolution (see Section 3.3).

In addition, SPS has been demonstrated not only to be an effective sintering process to fabricate fully dense nanocrystalline ceramics and composites, but also to be a new forming method to enhance ceramic ductility [40,41]. Using an advance of this method, high strain rate superplasticity of ceramics and ceramic-based composites at relatively low temperatures might be achieved (see Section 3.2).

3. CERAMIC-BASED NANOCOMPOSITES

3.1 Toughening by SWCN

Nanocrystalline ceramics do not appear to possess higher fracture toughness than conventional microcrystalline ceramics. Therefore, it is very likely that, in spite of the significant advantage in other properties, toughness is likely to be the bottleneck that controls the application of nanocrystalline ceramics in both structural and functional applications. In the last two decades, significant advances have been made in the understanding of toughening mechanisms in microcrystalline ceramics. Unfortunately, many of the microcrystalline material systems with improved fracture toughness have shown significant degradation of strength and hardness. This has led to interest in nanocrystalline ceramic composites where the possibility exists to offset this property degradation through the increases in strength and hardness typically seen in nanocrystalline materials. Production of nanoceramic composites provides a promising route to enhance toughness. Most nanocomposites currently investigated are actually composites with microcrystalline matrices and nanoscale second phases; very few composites with truly nanocrystalline matrix have been produced. Toughening mechanisms in ceramic composites, which have been reasonably investigated in microcrystalline ceramics, need to be re-investigated in their applicability to nanoceramics. Advanced consolidation techniques, such as SPS, can be used to produce nanocrystalline ceramic composites from nanopowders (see Section 2). These composites can then be analysed for a comparison of toughening data and microstructural details versus material system variables to develop analytical models for toughening mechanisms in ceramic composites with nanocrystalline matrices.

In the effort to produce ceramic nanocomposites, the introduction of a second phase is helpful in two ways: one is that the second phase will prevent grain growth of the matrix to some extent; the other is that toughening of the material can be made possible if the second phase is chosen with appropriate properties. Depending on the matrix grain size and second phase particle size, Niihara et al. have classified the nanocomposites into four groups [42]. The first three types of nanocomposite fall into the micro-nano category, i.e. with nanosized second phase dispersed in a microcrystalline matrix. With only very few exceptions, the large majority of so-called nanocomposites developed to date are micro-nano composites, rather than nano-nano composites (where both the matrix and inclusion grain size

are in the nanometre range). Advances in the synthesis of nanocrystalline ceramics call for a reclassification that has been proposed by Kuntz et al. [43]. In this new classification, the matrix phase is continuously nanocrystalline while the second phase varies leading to four nanocomposite types: the nano-nano type, the nano-micro type, the nano-fibre type and the nano-nanolayer type.

The enthusiasm in developing nanocomposites was triggered by Niihara's pioneering work. In the late 1980s, they reported a significant increase in flexure strength from 350 MPa to 1–1.5 GPa accompanied by increase in fracture toughness from 3.5 MPa $m^{1/2}$ to 4.8 MPa $m^{1/2}$, by introducing 5% SiC nano-particles into microcrystalline Al_2O_3 [44,45]. Since then, the research activity on this topic has been very intense; the new concept of adding nanometric particles has been introduced into various material systems. An extensive review has been made by Sternitzke [46] and by Awaji et al. [47]. Some of the more recent results [6,11,48–56] are listed in Table 3.1. The selected examples are on alumina-based nanocomposites.

Table 3.1 Strength and fracture toughness of alumina-based 'nanocomposites'

Material system	Microstructural description (grain size)	Strength (MPa)	Fracture toughness (MPa $m^{1/2}$)	Reference
Micro-nano composites				
Al_2O_3	3.5 μm monolith	475	3.6	Ji and Yeomans, 2002 [48]
Al_2O_3/5%Cr	Al_2O_3-0.68 μm, Cr-124 nm	736	4.0	
Al_2O_3	1.2 μm monolith	683	3.5	Sekino et al., 1997 [49]
Al_2O_3/15%Ni	Al_2O_3-1 μm, Ni-180 nm	1090	4.2	
Al_2O_3	0.89 μm monolith	536	3.57	Oh et al., 1998 [50]
Al_2O_3/5%Cu	Al_2O_3-0.63 μm, Cu-200 nm	707	4.28	
Al_2O_3 Al_2O_3/5%W	N/A W < 100 nm intragranular 1 μm intergranular	528 645–1105	3.2 3.6–3.8	Sekino and Niihara, 1995 [51]
Al_2O_3	N/A	–	3.5	Siegel et al., 2001 [11]
Al_2O_3/10%MWCN*	Al_2O_3-0.5 μm	–	4.2	

(*Continued*)

Table 3.1 (Continued)

Material system	Microstructural description (grain size)	Strength (MPa)	Fracture toughness (MPa $m^{1/2}$)	Reference
Al_2O_3	≈1 μm monolith	335	4.4	Flahaut et al., 2000 [6]
Al_2O_3/8.5%SWCN† - 4.3%Fe	Al_2O_3-0.5 μm	400	5.0	
Al_2O_3/10%SWCN † - 4.3%Fe	Al_2O_3-0.5 μm	296	3.1	
Al_2O_3	4.1 μm monolith	371	2.6	Maensiri and Roberts, 2002 [52]
Al_2O_3/1%SiC	Al_2O_3-6.85 μm, SiC-200 nm	369	2.3	
Al_2O_3/2.5%SiC	Al_2O_3-6.66 μm, SiC-200 nm	409	2.2	
Al_2O_3/5%SiC	Al_2O_3-2.82 μm, SiC-200 nm	417	2.6	
Al_2O_3	3.5 μm monolith	430	3.2	Anya, 1999 [53]
Al_2O_3/5%SiC	Al_2O_3-4.0 μm, SiC-200 nm	646	4.6	
Al_2O_3/10%SiC	Al_2O_3-2.9 μm, SiC-200 nm	560	5.2	
Al_2O_3/15%SiC	Al_2O_3-2.6 μm, SiC-200 nm	549	5.5	
Al_2O_3	2–3 μm monolith	460	3.1	Davidge et al., 1997 [54]
Al_2O_3/5-10%SiC	Al_2O_3-2–3 μm, SiC-200 nm	760–800	3.3–3.6	
Al_2O_3	≈1 μm monolith	380	3.91	Zhu et al., 1997 [55]
Al_2O_3/15%Si_3N_4	Al_2O_3-~ μm Si_3N_4-200–300 nm intergranular 80 nm intragranular	820	6.00	
Nano-nano composites				
Al_2O_3-10%ZrO_2	Al_2O_3-35–44 nm ZrO_2-20–30 nm	–	8.38	Bhaduri and Bhaduri, 1997 [56]

*MWCN: multi-walled carbon nanotubes
†SWCN: single-wall carbon nanotubes

Most of the work on ceramic/ceramic nanocomposites is concentrated on SiC nanoparticle strengthened materials. The large majority of the work has found obvious enhancement in strength or toughness or both. The increase in strength is usually more remarkable than that in toughness. A number of mechanisms were proposed to account for the toughening in Al_2O_3/SiC micro-nano composites, e.g. switch from intergranular to transgranular fracture because of the intergranular SiC particles, crack deflection by the internal stress around the intragranular particles (also resulting in a switch from intergranular to transgranular fracture), crack-bridging by SiC particles or clinched rough crack surfaces [57,58]. Reduction in critical flaw size in the nanocomposites is commonly accepted as an important reason for the increase in strength.

Adding a small amount of metallic phases to alumina can also effectively increase both the strength and toughness of the material, as shown by the examples in Table 3.1. The metallic phases in these nanocomposites are all in the form of particles, either intergranular or intragranular, with the alumina forming the continuous phase. The enhancement is attributable to metal plasticity, or to crack deflection due to residue stress, or to crack bridging.

In the sole example of nano-nano composite shown in Table 3.1, remarkable toughness was achieved. The authors [56] did not attribute the high toughness to phase-transformation; they declared that only 5% of the total zirconia undergoes t-m transformation under stress. The toughening might be due to ferroelastic domain switching or crushing of well-distributed pores under the indenter.

Certain toughening mechanisms in microcrystalline ceramic systems have been reasonably well developed and investigated. It has yet to be determined whether these same mechanisms will be germane to the corresponding nanocrystalline systems. The most common toughening mechanism that is associated with the incorporation of fibres into a ceramic matrix is fibre bridging [43]. This toughening mechanism involves the bridging of the crack wake by the second-phase fibres. The toughening effect is achieved when the fibres shed load from the crack tip while remaining intact, the interface debonds between the fibre and the matrix followed by pull out, and/or the individual fibres fracture followed by energy adsorption through pull out of the broken fibre. These effects lead to increased extrinsic toughness. Another possible toughening mechanism, as seen in fibre reinforced ceramic composites, is crack deflection. When the fibre is of a particular orientation, the crack propagation direction can be deflected away from the axis of highest stress to a less efficient orientation directed by the longitudinal orientation of the fibre. This leads to increased fracture energy through increased fracture surface area and lower driving forces due to the reduced resolved normal stresses at the crack tip. This phenomenon will enhance the intrinsic toughness. Both crack deflection and fibre bridging should be pertinent to nanoceramic composites, since neither method is inherently dependent on the matrix grain size. For example, addition of SiC whiskers to an alumina nanocrystalline matrix has been able to produce toughness values as high as 6.17 MPa $m^{1/2}$ while improving the hardness to 26 GPa [59]. A more detailed investigation on fibre toughening of nanocomposites was conducted by introducing single-wall carbon nanotubes into nanocrystalline alumina [12].

Carbon nanotubes, originally discovered as a byproduct of fullerene research, are attracting increasing interest as constituents of novel nanostructured materials for a wide range of applications [60–62]. There are two main types of carbon nanotubes, single-wall carbon nanotubes (SWCN) and multiwall carbon nanotubes (MWCN). Both of these types can have high structural perfection, however, SWCN have a particularly desirable combination of mechanical properties. Specifically, they have an elastic stiffness comparable to that of diamond ≈1.5 TPa, and they are several times as strong (yield strength 52 GPa) [60]. The size, shape and properties of SWCN make them prime candidates for use in the development of potentially revolutionary composite materials. Attempts have been made to develop advanced engineering materials with improved mechanical properties through the incorporation of carbon nanotubes in various matrices (polymers, metals and ceramics) by taking advantage of the exceptional strength of the nanotubes [9–11,13,60,63]. Most of the investigations on carbon nanotube-containing composites have so far focused on polymer-based composites with improved electrical and mechanical properties. For example, their addition to a polymer matrix leads to a very low electrical percolation threshold and improved electrical conductivity. Work on carbon nanotubes in metals and ceramics has been much less focused.

SWCN tend to self-organize into 'ropes' that consist of many (typically, 10–100) tubes running together along their length in van der Waals bonding with one another (Figure 3.2). Due to their high surface area and high aspect ratio, the ability homogeneously to disperse the nanotubes into the matrix is a processing challenge. In the open literature [9,11], all the other carbon nanotubes-reinforced ceramic composites have been consolidated by hot-pressing methods that require higher temperatures and longer duration. These sintering parameters damage the carbon nanotubes in the composites, leading to decreases in, or total loss of,

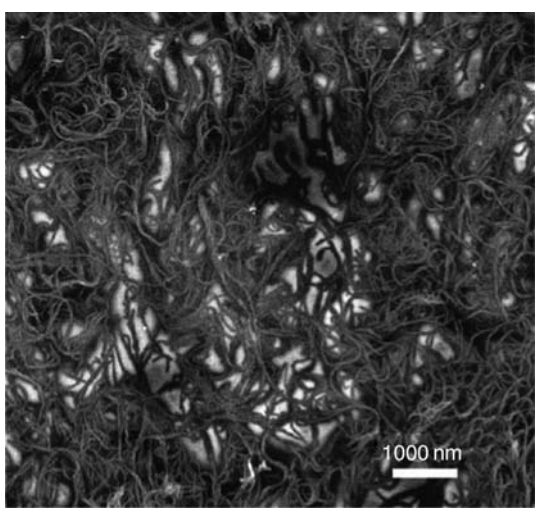

FIGURE 3.2 Ropes of single-wall carbon nanotubes.

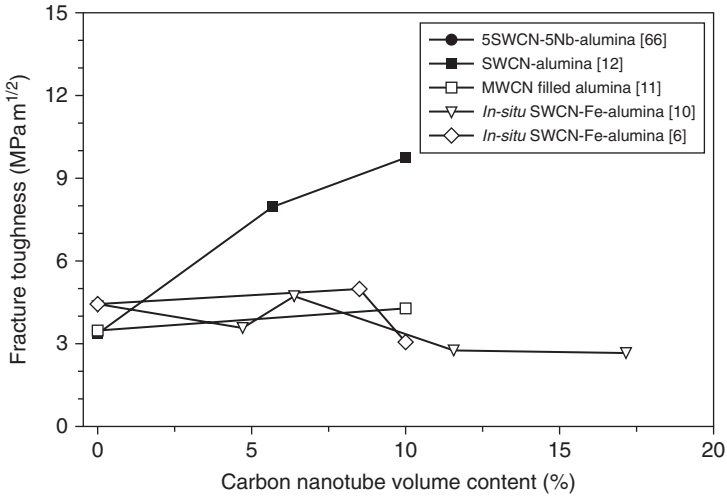

FIGURE 3.3 Fracture toughness versus carbon nanotube volume content in alumina-based composites [64].

reinforcing effects. For example, in carbon nanotubes–metal–ceramic composite systems, some of the hot-pressing temperatures were as high as 1600°C. This damaged most of the carbon nanotubes and decreased the quantity and quality of carbon nanotubes in the sintered composites. No reinforcing effect was noted in the *in-situ* carbon nanotubes-Fe-Al_2O_3 nanocomposites in the investigation of Peigney et al. [9,10]. The best reported result by Siegel et al. [11] was a 24% increase in toughness in 10 vol% MWCN/Al_2O_3 nanocomposites produced by the hot-pressing method at 1300°C/1 h. Full density of alumina-based nanocomposites with incorporated multiwall carbon nanotubes was achieved, but the matrix grain size was in the sub-micron range.

SPS technique, as was shown earlier (Section 2), allows much lower sintering temperatures and shorter times for obtaining dense nanocrystalline ceramics as compared to conventional sintering techniques. As a result, in the alumina/SWCN system, the best results to date have a toughness value of 9.7 MPa $m^{1/2}$ (nearly three times pure alumina) with only 10 vol% SWCN added [12]. This stands out as the only ceramic composite to realize the promise of significant toughening through the addition of carbon nanotubes into nanocrystalline matrix (Figure 3.3, solid squares).

Structural investigation of the nanocomposites has shown that carbon nanotubes are fairly homogeneously distributed along grain boundaries to develop an intertwining network microstructure (Figure 3.4), some of them being entangled with encapsulated alumina nanoscale grains with good bonding [12]. This microstructure simultaneously provides stiffness, toughness and strength to the ceramic.

A strong toughening effect in these nanocomposites is likely to be related to a number of factors. First, to the extraordinary mechanical properties and the closer-to-perfect structure of SWCN. MWCN are similar to SWCN, but contain

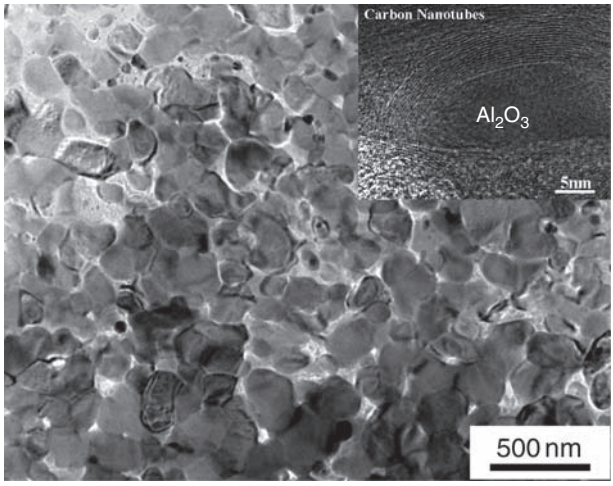

FIGURE 3.4 Bright-field TEM image (with high resolution TEM image as insert) of the nanocomposites showing the intertwining network structure of carbon nanotubes in the matrix of the 10 vol% SWCNT/Al_2O_3 composite. Light regions are filled with SWCN bundles.

more defects, which limit their properties. Furthermore, there are differences in the ability to transfer load from the matrix to the nanotubes between SWCN and MWCN. Second, the crack deflection along the continuous interface between carbon nanotubes and nanocrystalline matrix grains might significantly contribute to the toughening effect [12]. Such toughening mechanisms as fibre bridging and fibre pull-outs were also experimentally observed in alumina/SWCN nanocomposites [65]. Third, it is related to the fast sintering technique that allows lower sintering temperatures and shorter durations. Therefore, the high quality ropes of single-wall carbon nanotubes can be retained in the sintered compacts, which was confirmed by Raman spectroscopy of the sintered Al_2O_3/SWCN nanocomposites [65]. This is also consistent with the results by Flahaut et al. [6] where the increase in the quality and quantity of SWCN may result in an easier transfer of the stress and, thus, can account for the increase in the toughness in the *in-situ* SWCN/Fe/Al_2O_3 nanocomposites. In order to be effective as reinforcing elements, high quality carbon nanotubes, without damage during consolidation, must be effectively bonded to the matrix so that they can actually carry the loads. The dependence of toughness on density directly supports this statement.

The addition of certain ductile phases (metals) to ceramic matrixes has proven also to be an effective toughening mechanism. The ductile phase can lead to the toughening of the composite through two distinct mechanisms. The first is through ductile yielding in the process zone of a propagating crack to increase intrinsic toughness. The stress field around the crack tip can be relieved through adsorption of energy through the deformation of the ductile phase or blunting of the crack tip at a ductile particle. The second manner by which a ductile phase can lead to toughening of a ceramic composite is by ductile bridging ligaments in the crack wake, increasing extrinsic toughness. This occurs when the crack tip

propagates past a ductile phase grain that then bridges the crack wake and must be pulled to failure or debond from the surrounding matrix. These toughening effects should be applicable in nanocrystalline ceramic matrix composites as long as the ductile phase grain size is large enough to support plastic deformation.

The addition of a ductile phase to examine the effect of ductile phase toughening in a nanocomposite has been investigated through the addition of niobium to an alumina matrix [42,64,66]. Nb was added through high-energy ball milling (HEBM) with the nano-Al_2O_3 powder followed by sintering by SPS at only 1100°C for 3 minutes [64]. The product was a nan-nano type composite combined with a nano-nano layer type. The 10 vol% Nb nanocomposite has a fracture toughness value of $7\,\mathrm{MPa\,m^{1/2}}$ without a decrease in hardness [66]. This is twice as tough as a pressureless sintered composite of the same composition reported in work by Garcia et al. [67]. This increase in toughness may be attributed to the novel microstructure in the nanocomposite where the Nb phase distributed as particles of ≈20 nm along with a continuous 3–4 nm layer at boundaries between Al_2O_3 grains [64]. This microstructure should lead to toughening by increasing ductility at the crack tip instead of the traditional ligament bridging in the crack wake which is typical of micron-scaled metallic-phase toughened ceramics. An addition of Nb to the alumina/SWCN system resulted in an exceptional value of the fracture toughness of $13.5\,\mathrm{MPa\,m^{1/2}}$ (see Figure 3.3).

The above research indicates a promising future for application of carbon nanotubes in reinforcing both structural ceramic composites and other materials systems.

3.2 Formability

Ceramics are usually very hard, brittle and hard to machine. These characteristics of ceramics have discouraged potential users from exploiting their beneficial properties. Forming advanced ceramics into dense desired shapes in an economic manner has always been a challenge. The application of superplastic deformation is attracting considerable interest as a novel method for net-shape fabrication of ceramic components. In developing superplastic ceramics, high deformation rate and high ductility are the primary objectives. Practical considerations further require that these properties should be achieved at the lowest temperature possible. In ceramics, high formability by superplastic flow might be achieved either by increasing grain boundary diffusivity due to introducing transient liquid phase or more viscous liquid phase [68–73] or by decreasing grain size. Generally, superplasticity of ceramics requires a microstructure with a fine grain size ($<1\,\mu\mathrm{m}$) that is stable against coarsening during sintering and deformation [26]. Nanocrystalline ceramics can be pressed and sintered into various shapes at significantly lower temperatures, whereas it would be very difficult, if not impossible, to press and sinter conventional ceramics even at high temperatures. In most cases, sintering aids and grain-growth inhibitors are used to achieve such structure [26]. Second-phase particles are especially effective in inducing superplasticity in ceramics [24–27,74,75].

Superplasticity in ceramics has been studied since the first observation of the phenomenon in yttria-stabilized tetragonal zirconia (YTZP) by Wakai in 1986 [76].

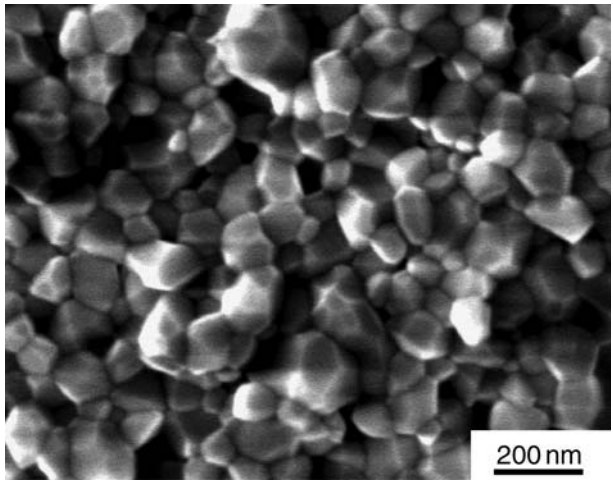

FIGURE 3.5 Nanostructure of AZM composite synthesized by SPS.

A number of fine-grained polycrystalline ceramics have demonstrated superplasticity, such as YTZP [77], magnesia-doped alumina [78] and alumina reinforced YTZP [79]. Unfortunately, the superplastic temperatures were typically above 1450°C and the strain rates were relatively low ($10^{-4}\,s^{-1}$ or lower). Kim et al. [75] realized a high strain rate of $0.1\,s^{-1}$ in zirconia–alumina–spinel (AZM) triphase composite (volume ratio 4:3:3), but at a rather high temperature of 1650°C.

More recently, superplasticity of the AZM triphase ceramic composite at temperatures as low as 1350°C was demonstrated in samples processed by SPS [Kuntz et al., unpublished results] [80]. Because of the rather low sintering temperatures (1100–1200°C) and the very short sintering time (a few minutes), the grain sizes in the synthesized AZM triphase ceramic composite were about 50–100 nm (Figure 3.5). This material was fully dense after SPS and revealed superplasticity at a relatively low temperature of 1350°C (vs. Japanese researchers at 1650°C) and at strain rate of $10^{-2}\,s^{-1}$.

Moreover, SPS has been demonstrated not only to be an effective sintering process to fabricate fully dense nanocrystalline ceramics and composites, but also to be a new forming method to enhance ceramic ductility [40,41]. The first attempt to apply the SPS approach to speed up superplastic forming was carried out by Shen et al. [41], who started with fully dense ceramics that sinter via either transient or permanent liquid phase modes. The observed enhanced ductility is thought to be associated with the enhanced grain sliding at the boundary of the glassy/liquid phase resulting from the electric-field induced motion of charged species. Despite remarkable success (rapid superplastic deformation with high strain rates in the range 10^{-2} to $10^{-3}\,s^{-1}$), the deformation temperatures were still extremely high (1500°C is typical).

Deformation of AZM nanocomposite using SPS as forming equipment allowed the deformation temperature to decrease down to 1200°C at the same stain rate. Figure 3.6 shows a ceramic-metal laminate which was formed superplastically

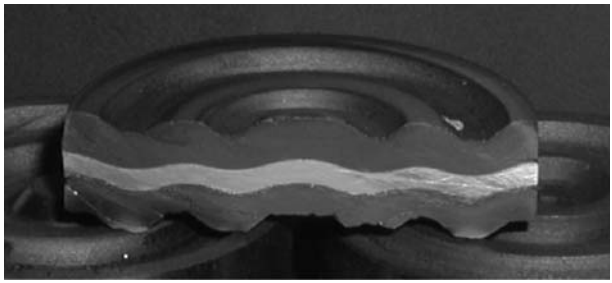

FIGURE 3.6 SPS co-formed/bonded AZM and Ti–6Al–4V alloy at 1200°C and at strain rate of $3 \times 10^{-3}\,s^{-1}$.

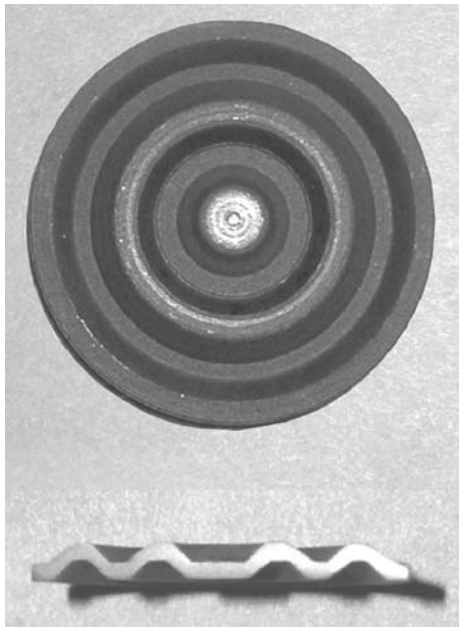

FIGURE 3.7 Top view and cross-section of the fully dense sample with diameter of 20 mm after powder forming.

by SPS. This material demonstrates superb formability of AZM nanoceramic and good quality bonding of this ceramic with Ti–6Al–4 V alloy. Such a material combines the hardness/strength of AZM with the toughness of Ti and it is an excellent candidate for lightweight threat resistant armour.

Instead of using an already consolidated disc, another strategy used to form the ceramic part was directly to put the well-mixed powder mixture into the graphite mould and then concurrently sinter and form by SPS. This further decreases the processing time to form a part without surface cracks. As shown in Figure 3.7, the final shape has been successfully achieved (in 3 minutes at 1150°C) by using

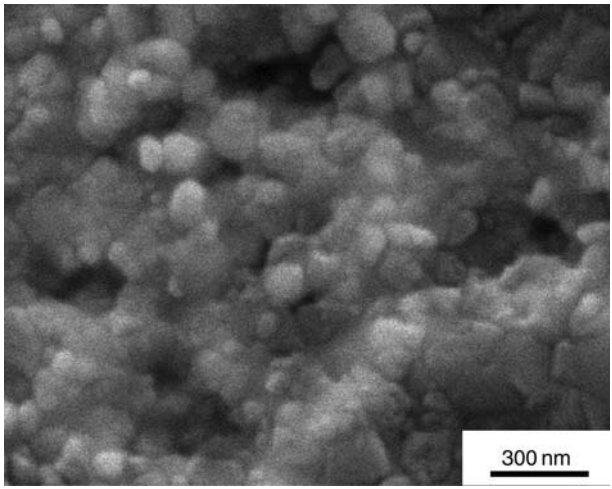

FIGURE 3.8 SEM image of the fracture surface of AZM composite after powder forming.

this one-step method. This temperature is remarkably lower than those found for conventional superplastic ceramics and it is comparable to that of Ni-based superalloys (typically, 950°C), suggesting that an existing type of metallic superplastic shape tooling might be applied to nanoceramic composites. The strain rate of the deformation process was about $10^{-2}s^{-1}$ and the final density was 100%. The same composites did not exhibit superplasticity by conventional deformation methods since both static grain growth during the slow heating and dynamic grain growth during high temperature deformation, occur. The microstructure of the formed part is shown in Figure 3.8. In the case of the powder forming, deformation takes place during the transient porous state of the composite, which takes advantage of inhibition of grain growth due to the presence of pores [81,82]. In contrast, significant grain growth was observed for the bulk formed composite [83].

An analysis of deformation parameters of the process of the powder forming has revealed a strain rate sensitivity ($m = 0.55$) and activation energy of the deformation process ($Q = 620\,kJ/mol$) that are similar to parameters observed during deformation of consolidated samples during bulk forming [64] [Kuntz et al., unpublished results] and correspond to superplastic flow. This new SPS forming approach provides a new route for low-temperature and high-strain-rate superplasticity for nanostructured materials and should impact and interest a broad range of scientists in materials research and superplastic forming technology.

3.3 Creep Resistance

Marked improvement in creep resistance of nanocomposite ceramics has been achieved by dispersing hard secondary phase nanoparticles such as SiC into the intergranular glassy phase in the matrix [84–86], in so-called micro-nano composites (nano-sized SiC included in sub-micron Si_3N_4). For the silicon nitride-based

ceramics, it is not possible to establish a deformation mechanism under general conditions because it is a very complex system which generally contains more than one phase and their intrinsic properties are greatly influenced by external factors [27]. Also, the deformation mechanisms for tensile and compressive creep are different. Thus, it has been necessary to explain the creep of silicon nitride ceramics by a series of mechanisms occurring simultaneously [27]. Generally, it has been realized that compressive creep takes place through grain boundary sliding, mainly accommodated by a solution–precipitation process [27–33]. The intergranular glassy phase plays a role in high diffusivity paths for atomic diffusion. The structural change in the intergranular film leads to a greater resistance to creep under compressive force [34]. Tensile creep is largely affected by the nucleation and growth of cavities when the tension stress field favours the formation of cavitation [27].

In most cases, the solution–precipitation process associated with the deformation mechanism for steady state compressive creep of silicon nitride involves three distinct processes. The first step is the dissolution of the crystalline grains into the glassy phase followed by diffusion of the dissolved atoms through the glassy phase and, finally, the reprecipitation of these atoms onto some other crystalline grains [87,88]. This multistep process can be controlled by the interface reaction or diffusion through glassy phases. Therefore, the focus of efforts in enhancing creep property has been on controlling the chemistry and amount of the glassy phase, which is determined by the amount/species of additive as well as the oxygen content at particle surface of the starting powders. A number of approaches have been attempted for this purpose [35–38]. However, owing to the thermodynamically stable nature of the glassy phases and the fact that it is impractical to prevent surface oxidation of the powders, these efforts have led to only limited success. Even in the case where no oxide additive was used in sintering, glassy phases were still found at grain boundaries [39].

The formation of a nano-nano structure (nano-sized SiC and Si_3N_4 in dual-phase mixture) by a novel synthesis method [89] resulted in an exceptional creep resistance of the material [90]. Starting from an amorphous Si–C–N powder derived from the pyrolysis of a liquid polymer precursor, nanocrystalline silicon nitride/silicon carbide ceramic composites with varied grain size were synthesized by SPS (see Section 2). With the amount of yttria additive decreasing from 8 wt% to 1 wt% and eventually to zero, the structure underwent a transition from micro-nano (nano-sized SiC included in sub-micron Si_3N_4) to nano-nano type (Figure 3.9). Nanocrystalline silicon nitride/silicon carbide ceramic composite with 30–50 nm grain size was also synthesized without using sintering additive [90]. The grain size distribution in such nanocomposites was fairly narrow. It is quite clear that the two phases in this material, Si_3N_4 and SiC, were randomly mixed with roughly equal grain size. High-resolution transmission electron microscopy (HRTEM) of the grain boundary regions of the synthesized material revealed that a prominent population of grain boundaries does not have an apparent amorphous layer, while some of the dual-grain junctions (grain boundaries) do contain an amorphous layer [90]. As in microcrystalline silicon nitride or silicon carbide, most of the glassy grain boundary phase exists at multigrain junctions.

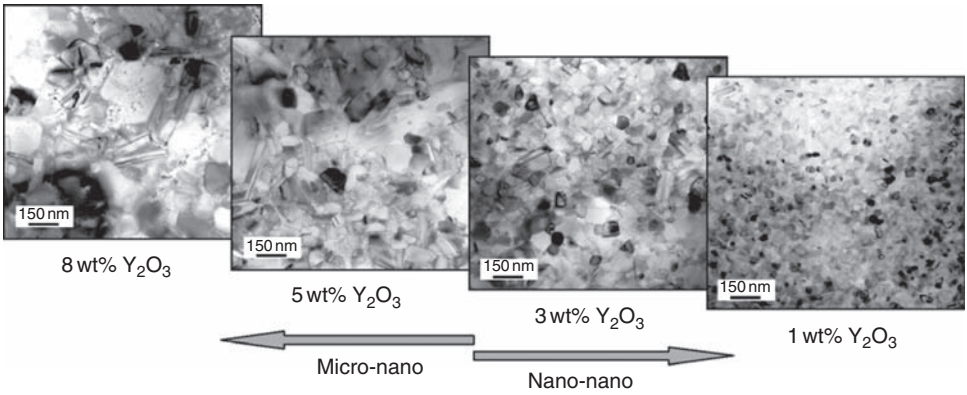

FIGURE 3.9 A transition from micro-nano (nano-sized SiC included in sub-micron Si_3N_4) to nano-nano (nano-sized SiC included in nanomatrix of Si_3N_4) structure in silicon nitride/silicon carbide composites with decreasing quantity of yttria additive.

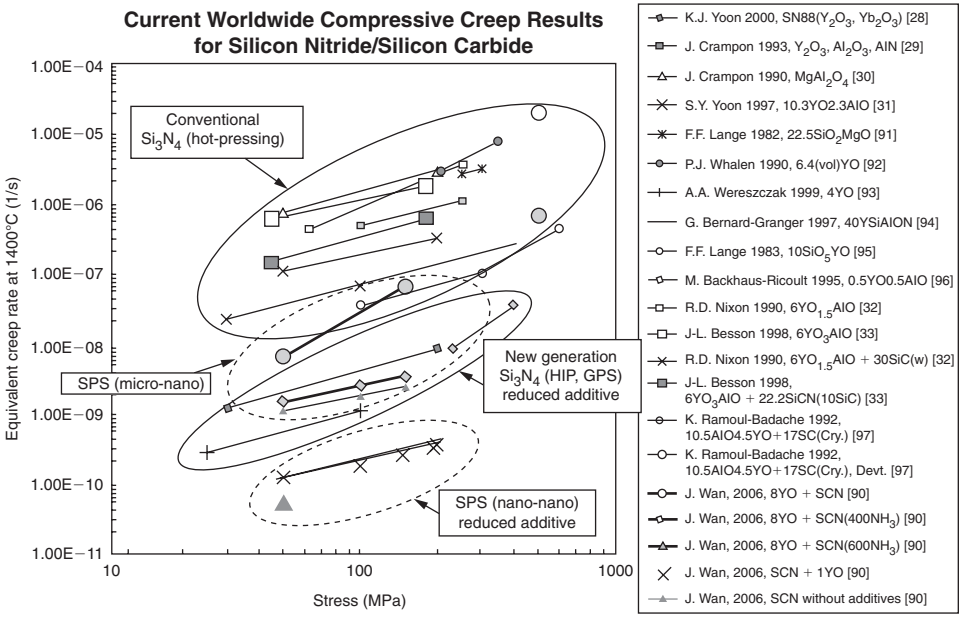

FIGURE 3.10 Comparison of the compression creep property of nanocomposites with those of existing silicon nitride ceramics (additive in weight percentage unless specified, molecular formula simplified for clarity. For instance, '6YO' in figure legend stands for '6 wt% Y_2O_3').

The comparison between the creep property of nano-nano composites and that of microcrystalline silicon nitride ceramics from literature data is given in Figure 3.10. The data can be divided into four groups. The first group is composed of conventional silicon nitride ceramics (including silicon nitride/silicon carbide

microcrystalline composites) with a high level of additive (various additives are used by different researchers, as indicated in the legend of this plot [29–33,90–97]); most were sintered by hot-pressing. This group has the lowest creep resistance of the silicon nitride ceramics. For example, the steady state creep rate at the reference test condition 1400°C/100 MPa ranges from about 3×10^{-8} to $3 \times 10^{-6} s^{-1}$. Using high purity silicon nitride powder, incorporation of less additive (e.g. less than 4 wt% Y_2O_3) and applying hot-isostatic pressing or gas pressure sintering generates silicon nitride ceramics of higher creep property, which are included in the group of new generation ceramics with reduced additive. These ceramics show secondary creep rate of about 1×10^{-9} to $3 \times 10^{-8} s^{-1}$, roughly two or three orders of magnitude lower than for ceramics in the first group. The micro-nano composites have approximately similar levels of additives as do conventional ceramics but exhibit higher creep resistance. However, their creep rate is faster than that of ceramics with reduced additive. The nano-nano composites demonstrate the highest creep resistance of all, as shown in Figure 3.10. At the reference testing condition of 1400°C/100 MPa, the steady state creep rate of the nanocomposite sintered with 1 wt% Y_2O_3 is about $1.67 \times 10^{-10} s^{-1}$, while the nanocomposite sintered without additive shows a creep rate as low as $6.3 \times 10^{-11} s^{-1}$ at 50 MPa stress. At this creep rate, most creep testing equipment is at the limit of transducer resolution.

It is generally agreed that the steady-state creep for silicon nitride (and silicon carbide) with a grain boundary glassy phase proceeds by a solution–precipitation mechanism through the amorphous (liquid) grain boundary phase, which has been modelled by Raj [87] and by Wakai [88]. Grain-size dependence p takes a value of about 1–3 [75,76,98]. This means a strong dependence of creep rate on grain size: The creep rate is supposed to increase at least for 1–3 orders of magnitude with a grain size decrease from micron size (500–1000 nm or larger), as in most of the microcrystalline silicon nitride studies, to nanometre size [90]. The extraordinarily high creep resistance found in the nanocomposites strongly suggests a fundamental change in creep mechanism. Another indication that the creep mechanism may be different in nano-nano composites is the low activation energy found in these materials. For example, the apparent activation energy for the 1 wt% Y_2O_3 nanocomposite was determined to be about 205 kJ/mol, significantly lower than that of microcrystalline silicon nitride. Comparison of the measured activation energy in the nano-nano composites suggests that the creep is controlled neither by diffusion processes in silicon carbide nor by the lattice diffusion in β-Si_3N_4 [90]. The only option left is the grain boundary diffusion in β-Si_3N_4, for which, unfortunately, there is no established diffusion data. Considering that N is the slower-diffusing species in Si_3N_4 and that the activation energy for grain boundary diffusion is lower than that for lattice diffusion, N diffusion through (oxygen enriched) grain boundaries might be the controlling mechanism in the creep of the nano-nano composites. It should be noted that the final grain size in the nano-nano composites is much smaller than the particle size of the starting powder. Normally, silicon nitride ceramics start with a fine powder (several tens or hundreds of nanometres), and the grain size of the sintered materials is larger than, or at least close to, the particle size (or crystallite size in the case of agglomerated powder) of the starting powder. The oxygen

content at grain boundaries, therefore, would very likely be greater than, or at least close to, the oxygen content at the particle surfaces. In contrast, the grain size of the nano-nano microstructure is determined by the concurrent crystallization process during sintering from an amorphous powder and there the sintered materials can have a grain size much smaller than the original particle size. If, as in silicon nitride powders, oxygen also mainly exists at particle surfaces of the amorphous Si–C–N powder (it should be pointed out that there might be a small amount of net-work oxygen in the amorphous powder) and the oxygen diffuses from the original particle surfaces into the interior regions (the grain boundaries), as the EELS mapping confirmed [90], the oxygen content at each individual grain boundary can be much lower than that at the particle surface. This 'diluting' effect possibly reduces the oxygen content to the extent that, in some of the grain boundaries, no effective glassy grain boundary layer can be formed. Thus, diffusion-based mechanisms other than solution–precipitation become the dominant mechanisms. This transition in creep mechanism has such a strong effect that it produces a lower creep rate in nanostructure, with no effective glassy phase in the intergranular region, than that observed with the microcrystalline matrix with a significant amount of glassy phase having a much larger grain size. It is apparent that, in order further to establish this concept, quantitative (and statistically valid) examination of the grain boundary chemistry and structure is called for. Nonetheless, the low creep rate observed in the nano-nano composites brings us one step closer to the extremely high creep resistance that is promised by the strong covalent bonds and low diffusivity in silicon nitride and silicon carbide.

3.4 Functional Properties

In addition to extraordinary mechanical properties, some nanocomposite materials have demonstrated very attractive functional properties. A brief description of electrical, thermal and thermoelectrical characteristics of nanocrystalline alumina reinforced with SWCN is presented below.

3.4.1 Electrical properties

It is well known that pure alumina is an insulator with extremely low electrical conductivity (10^{-10}–10^{-12} S/m). It is interesting to note that the SWCN/Al_2O_3 composites became much more electrically conductive when small amounts of carbon nanotubes were incorporated into alumina [99,100]. It was found that the electrical conductivity increases with carbon nanotube content. As shown in Table 3.2, the room-temperature electrical conductivity is up to 1050 S/m in 5.7 vol% SWCN/Al_2O_3 nanocomposite. More than three times the best reported conductivity of the carbon nanotubes/Fe/Al_2O_3 nanocomposites ($\approx$400 S/m) has been obtained in the 10 vol% SWCN/Al_2O_3 nanocomposite. An additional increase in conductivity (up to 3345 S/m) has been achieved in the 15 vol% SWCN/Al_2O_3 nanocomposite. This value is 735% higher than that of the hot-pressed CNT–Fe–Al_2O_3 nanocomposites. These values lie in the semiconductor range of conductivity but are very close to the metallic conductor threshold (10^4 S/m) [101], as shown in Figure 3.11. This dependence of the electrical

Table 3.2 Electrical and transverse thermal conductivities of carbon nanotube nanocomposites

Materials	Processing conditions	Electrical conductivity (S/m)	Thermal conductivity (W/mK)	Reference
Pure Al_2O_3	SPS 1150°C/3 min	10^{-10}–10^{-12}	27.3	[99,100]
5.7 vol% carbon black/Al_2O_3	SPS 1150°C/3 min	15	–	[99,100]
5.7 vol% SWCNT/Al_2O_3	SPS 1150°C/3 min	1050	–	[99,100]
10 vol% SWCNT/Al_2O_3	SPS 1200°C/3 min	1510	11.4	[99,100]
15 vol% SWCNT/Al_2O_3	SPS 1150°C/3 min	3345	7.3	[99,100]
8.5 vol% CNT/4.3 vol% Fe/Al_2O_3	HP 1500°C/15 min	40–80	–	[6]
10 vol% CNT/4.3 vol% Fe/Al_2O_3	HP 1500°C/15 min	280–400	–	[6]
10 vol% CNT/4.3 vol% Fe/Al_2O_3	HTE 1500°C/15 min	80–160	–	[103]
19.6 vol% CNT/3.2 vol% Fe-Co/$MgAl_2O_4$	HTE 1500°C/15 min	60–2000	–	[103]
20 vol% MWCNT/ polymer	–	≈30	–	[155]
10 wt% CNT/ aluminium	HP 520°C/30 min	1.8×10^7	–	[102]

Under the processing conditions heading SPS denotes spark-plasma-sintering, HP denotes hot-pressing, and HTE denotes high-temperature extrusion.

conductivity on carbon nanotube content in the present ceramic nanocomposites is in contrast to the carbon nanotube metal matrix composites where the electrical conductivity decreases with carbon nanotube content [102].

The conductivity of the present nanocomposites increases with increasing temperature. The largest conductivity increase, from 2060 S/m at −194°C to 3375 S/m at 77°C, is in the 15 vol% SWCN/Al_2O_3 nanocomposite. This behaviour is also opposite to the trend in metal matrix composites containing carbon nanotubes [102]. It has also been reported that carbon nanotube–metal-oxide nanocomposites can be aligned to improve the electrical conductivity by high-temperature extrusion [103]. The best reported conductivity measured along the extrusion direction is 2000 S/m, whereas much lower values are measured in the transverse direction (≈60 S/m) in carbon nanotubes/Fe/Co-$MgAl_2O_4$ systems. Note that the best conductivity in the aligned $MgAl_2O_4$-based systems could be only obtained in the centre of the extrusion while other regions were quite low due to the damage of the nanotubes by exposure to high-temperature extrusion.

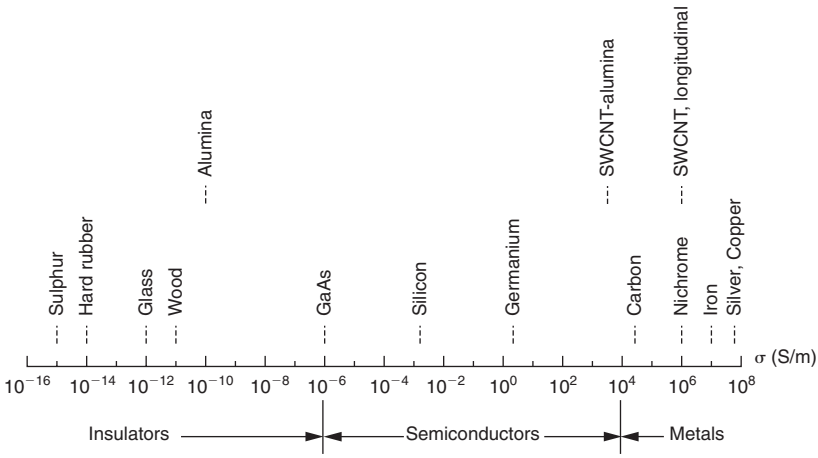

FIGURE 3.11 The electrical conductivity of various representative materials at room temperature. Note the more than 13 orders of magnitude increase in conductivity of the 15 vol% SWCN-alumina composite compared to pure alumina.

The significant increase in electrical conductivity may be related to the use of high-quality ropes of SWCN that were distributed along grain boundaries to develop an intertwining network of electrically conducting pathways (see Figure 3.2). In order directly to compare the effects of the network structure an additional composite was produced. The experimental procedure and materials were identical to the 5.7 vol% SWCN/Al_2O_3 composite except carbon black was substituted for the SWCN. The carbon black is composed of mixed fullerenes and has an average particle size of 42 nm. The 5.7 vol% carbon black/Al_2O_3 composite had a measured conductivity of 15 S/m, nearly two orders of magnitude less than the corresponding SWCN containing composite.

Thus, SWCN were shown to be successfully used to convert insulating nanoceramics to metallically conductive composites. The combined effects of the mixing of the SWCN and ceramics powders while dispersed in solution and the low temperature and time required for consolidation by SPS led to the preservation of the intertwining network structure. This network structure allows for percolation of the nanotubes at low volume fractions and thus increases the electrical conductivity significantly when compared to similar carbon–alumina composites.

3.4.2 Thermal properties

Theory predicts an extremely high value (6000 W/mK) for the room temperature thermal conductivity of an individual SWCN [104], suggesting that SWCN should be ideal for high-performance thermal management [105]. Although this speculation has not yet been proven for SWCN, a recent measurement of 3000 W/mK for the room temperature thermal conductivity of an *individual* MWCN has been reported [106]. However, the experimental measurements indicated that aligned bundles of SWCN show a measured thermal conductivity of only 250 W/mK at room temperature [107] and, surprisingly, only 2.3 W/mK for the sintered sample

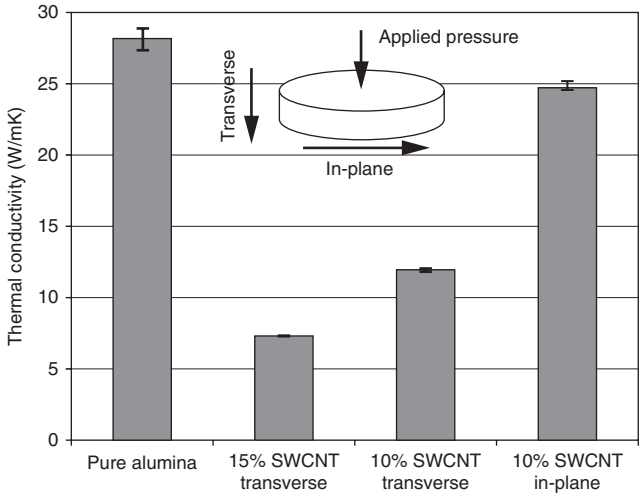

FIGURE 3.12 Bar graph comparing thermal diffusivities of various materials in different materials and orientations.

[108]. These results suggest that ropes of SWCN would have the potential to be ideal thermal barrier materials for thermal management application [13].

Figure 3.12 shows a bar graph giving the thermal diffusivities of various samples. The first three sets of bars each represent measurements taken directly on sintered discs in the transverse direction, while the last two sets represent measurements in transverse and in-plane directions taken on bars cut from sintered discs. It is very interesting to note that the incorporation of ropes of SWCN does not change the in-plane thermal diffusivity of the matrix [99,100]. By contrast, the transverse thermal diffusivities are significantly decreased when the carbon nanotubes are present and an increase in the level of carbon nanotubes produces a greater drop in thermal diffusivity in the transverse direction. These findings are directly in contrast to the results observed for SWCN/polymer composites [109].

The anisotropic thermal conductivity of the composites may be directly related to the certain degrees of alignment of ropes in the composites and the anisotropic characteristics of the thermal conductivity of ropes of SWCN [107]. The decrease in thermal conductivity by introduction of ropes of SWCN may be attributed to the difference of thermal properties of an individual tube and ropes [107,108]. Numerous highly resistive thermal junctions between the tubes, possibly due to additional extrinsic phonon scattering mechanisms such as tube–tube interactions, are the dominant barriers to thermal transport in ropes of nanotubes. Recently, it was found that the composites exhibit much improved mechanical and electrical properties [12,13], suggesting that the inter-tube coupling in the ropes is strong. The strong tube–tube coupling can decrease the thermal conductivity of SWCN bundles by an order of magnitude relative to individual tubes [104]. Moreover, the bending or twisting of the nanotubes decreases their electrical transport properties due to the fact that bending induces σ–π hybridization

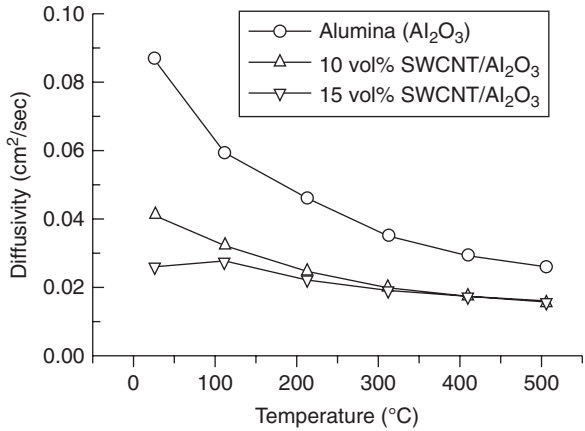

FIGURE 3.13 Thermal diffusivity temperature dependence in single-wall carbon nanotube-alumina nanocomposites.

or mixing [110,111]. Microstructural observations indicated that ropes of SWCN intertwined with alumina matrix (see Figure 3.4), suggesting that larger curvature or bending occurred in the ropes. The application of pressure in the transverse direction during SPS consolidation will further enhance such a mechanical effect on the ropes, inducing a directionality, thus leading to decrease in transverse thermal properties. Furthermore, when ropes are introduced into alumina matrix, one has to consider the effect of interface, i.e. the Kapitza effect [112], on the thermal conductivity of the composites, which will have a tendency to reduce the thermal flux because of reflection of phonons from the sidewalls of somewhat aligned carbon nanotubes bundles.

The temperature dependence of the transverse thermal diffusivity for pure alumina and composites has been measured in the temperature range of 25°C to 500°C. As shown in Figure 3.13, the thermal diffusivity of the pure alumina and carbon nanotube composites decreases with increasing temperature. This is consistent with the results observed for other carbon materials [113]. The observed reduction in thermal diffusivity with increasing temperature can be designated the dominant effect of Umklapp scattering (phonon–phonon scattering) in reducing phonon mean-free path length.

Thus, anisotropic thermal properties in the dense nanocrystalline ceramic composites have been successfully developed through the incorporation of ropes of SWCN. Such anisotropic thermal diffusivity is a quality that is sought after in materials that might be used in a wide range of applications.

3.4.3 Thermoelectric properties

Typically, thermoelectric power of metallic carbon nanotubes is in the range of $-50 - +65\,\mu V/K$ at 300 K. Greatly enhanced values ($\approx 260\,\mu V/K$) were discovered in semiconducting SWCN devices. This opens up the possibility of using SWCN for thermoelectric applications. However, finding an effective way to utilize carbon

nanotubes in a thermoelectric application has been elusive since the high electrical conductivity and also high thermal conductivity of carbon nanotubes, the calculated so-called 'figure of merit', *ZT*, of pure carbon nanotubes, can be expected to be very low ($\approx 10^{-4}$). The figure of merit depends on the Seebeck coefficient (S), the electrical conductivity (σ), the thermal conductivity (k) and the absolute temperature (T):

$$ZT = \frac{S^2\sigma}{k}T \tag{3.1}$$

Usually, any increase in S in conventional materials leads to a decrease in σ. Moreover, an increase in S also increases the electronic contribution to thermal conductivity. As a result, the overall value of ZT remains low. Recently, we discovered that incorporation of single-wall carbon nanotubes into nanoceramics leads to a dramatically improved electrical conductivity of the composites, combined with a significant decrease in thermal conductivity, suggesting that the carbon nanotube-reinforced nanoceramic composites might make promising thermoelectric materials [40,114,115].

The thermopower measurement of the 10 vol% SWCN/20 vol% 3Y-TZP/Al_2O_3 composite synthesized by SPS was carried out in air atmosphere [100]. It was found that thermoelectric power (Seebeck coefficient) increases approxiately linearly with increasing temperature (Figure 3.14a). The measured values range from 28.5 μV/K at 345 K to 50.4 μV/K at 644 K. The lowest temperature data are comparable to those of aligned ropes of SWCN (≈27 μV/K at 300 K). The positive value of thermopower is consistent with the oxygen-doping p-type semiconducting behaviour of SWCN. The electrical conductivity of the composite decreases with increasing temperature (Figure 3.14a), indicating the metallic conducting behaviour. It was found that the residual catalyst remaining in the SWCN plays a critical role in the charge and thermal transport of the composites. This is different from the equivalent case for purified SWCN/ceramic composites. Also, the electrical conductivity of the composite is extremely low, more than two orders of magnitude lower than that of purified SWCN/ceramic composites. Previous studies found that the in-plane thermal conductivity of the carbon nanotube ceramic composites depends on that of the matrix and it decreases with increasing temperatures [40]. It has been reported that incorporation of SWCN into zirconia leads to the development of the lowest thermal conductivity of the composites. The measured thermal conductivity of the composites was in the range of 0.2–0.4 W/mK in the temperature range of 27–1100°C. A 10 vol% SWCN/3Y-TZP composite has the highest electrical conductivity among all the composites [100]. It is interesting to note that the electrical conductivity decreases with increasing temperature until 545 K and then increases slowly with increasing temperature above that value. The thermopower also has a positive value and it increases with increasing temperature. Based on these data, the calculated ZT of the composite is shown in Figure 3.14b. It was found that the ZT increases with increasing temperature and has a value of 0.018 at 850 K. This is two orders of magnitude higher than that of pure SWCN.

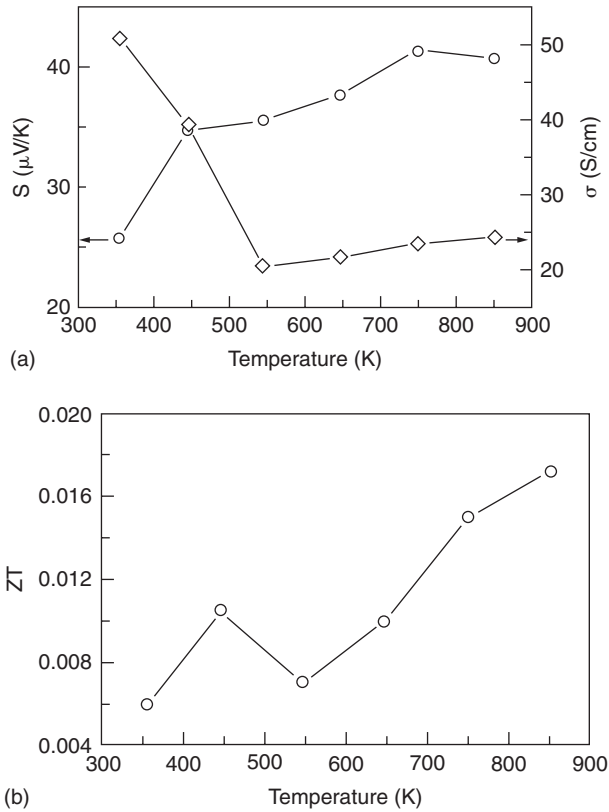

FIGURE 3.14 Variable temperature charge transport and thermal transport data for 10 vol% SWCN/3Y-TZP nanocomposite: (a) thermopower (*S*) and electrical conductivity (σ) and (b) thermoelectric figure of merit, *ZT*, as a function of temperature.

4. METAL-BASED NANOCOMPOSITES

4.1 Nanocomposites Derived from Metallic Glasses

Nanocrystalline materials crystallized from metallic glasses usually have a very complicated phase composition and are a good example of nanocomposite materials. In this section, the high potential of nanostructured iron-based composites produced by controlling solidification and subsequent devitrification is demonstrated.

Crystallization of metallic glasses has been successfully used as one of the methods for nanocrystalline material production in various alloy systems, e.g. in Fe-, Ni- and Co-based alloys [116]. This type of transformation involves decomposition of single-phase supersaturated solid solutions into multiphase nanoscale microstructures. During the solid-state transformation, the newly formed phases self-assemble directly into characteristic nanoscale structures with an intimate mixture of phases dependent on the type of transition. This class of nanostructure can be derived using a number of distinct metallurgical approaches such as

spinodal decompositions, eutectoid transformations or glass devitrification in a wide variety of metallic systems [116,117]. To obtain a nanoscale structure, the crystallization process should proceed with the largest nucleation rate possible while suppressing the crystal growth rate as much as practicable. Such conditions can be obtained for some alloy compositions by applying specific methods of heat treatment. It was shown theoretically by Crespo et al. [118] and experimentally by Köster et al. [119] that, among metallic glasses, those that undergo primary crystallization with a time-dependent, long-range diffusion controlled growth rate are the most suitable candidates for nanocrystallization.

In iron-based systems, depending on the specific composition, the crystallization temperature generally varies from 500 to 650°C and the enthalpy of the glass to crystalline transformation varies from -75 to $-200\,\mathrm{Jg^{-1}}$ [DJ Branagan, The Nanosteel Company, Idaho Falls, ID; unpublished research]. Since the melting temperature is often reduced to 1100–1200°C, this means that glass devitrification occurs at low fractions of the melting temperature ($\approx 0.5\,T_m$) where the driving force for crystallization, due to the metastable nature of the undercooled liquid, is extremely high but grain growth is still sluggish. This results in a very high nucleation frequency with limited time for grain growth before impingement between neighbouring grains occurs. Thus, the solid/solid state glass devitrification can be represented as an enabling transformation towards the development of nanoscale microstructures. Additionally, these devitrified microstructures can be stable from 0.7 to 0.8 Tm [116,120]. An additional advantage of this route is that macrodefects such as porosity or cracks, inherent in many other approaches, can be virtually eliminated. Many Fe-based metallic glasses do not require any special heat treatment to be converted into nanocrystalline materials [121–123]. Isothermal annealing at temperatures close to the crystallization temperature for a typical time of 1 h, i.e. so-called conventional annealing, is widely used by many researchers [122]. On the other hand, it was found [124] that application of relatively low temperature and longer annealing times also facilitates the creation of a nanocrystalline structure. The size and morphology of crystallites, mechanism of crystallization and crystallization products themselves depend on the temperature of thermal treatment of a metallic glass. By varying the composition of the alloys, a wide range of mechanical properties can be engineered. For example, a new Fe-based commercial alloy (SHS7170) demonstrates strength, of more than 6 GPa at room temperature (Figure 3.15, curve 1), that is much stronger than the commonly used high strength (0.24 to 0.9 GPa) or even ultra high strength steels (0.9 to 1.5 GPa) of today. Due to the conventional densities achieved in these nanostructured iron-based alloys, incredible strength to weight ratios are obtained which allows them to be superior to more expensive but lower density materials such as aluminium, magnesium and titanium based alloys. The SHS7170 alloy has a density of $7.59\,\mathrm{g/cm^3}$, which gives it a specific strength of $8.3 \times 10^4/\mathrm{m}^3$ – four times higher than that for the archetypical Ti-6-Al-4 V alloy ($2.2 \times 10^4/\mathrm{m}^3$). However, plastic strain of this alloy is only about 1% (Figure 3.15, curve 1). In another glass forming iron-based alloy with atomic stoichiometry of $(Fe_{0.8}Cr_{0.2})_{79}B_{17}W_2C_2$, around 10–20% uniform tensile elongation at an incredible level of strength of 4–5 GPa was detected (Figure 3.15, curve 2). This combination

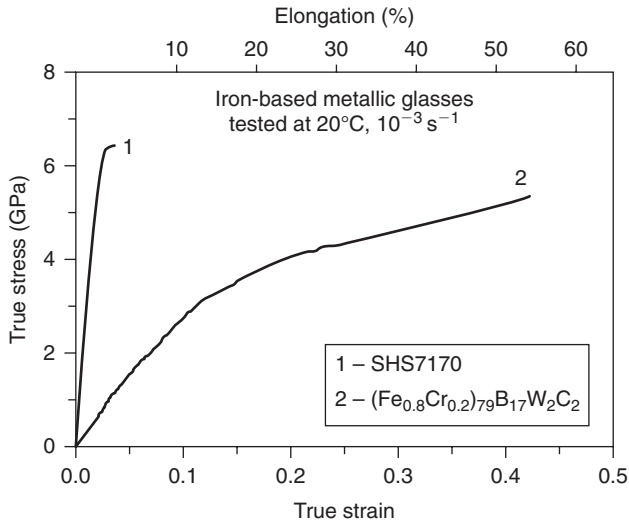

FIGURE 3.15 True stress–true strain curve for two different iron-based metallic glasses at room temperature.

of strength and plasticity may be among the highest ever measured. Moreover, this alloy has demonstrated strength levels of 1.8 GPa at 750°C [125], which is higher than for conventional steels at room temperature.

The microstructure of the alloy after devitrification consists of three phases (α-Fe, $Fe_{23}C_6$ and Fe_3B) of almost identical size (Figure 3.16). The α-Fe phase forms a distinctly mottled structure (due to magnetic interaction with the electron beam), the $Fe_{23}C_6$ type phase forms a featureless smooth structure and the Fe_3B phase forms a heavily multitwinned structure. Note that the $Fe_{23}C_6$ and Fe_3B phases are not known to form in their respective binary systems but can form as stable phases due to the presence of impurities or solute atoms [127,128]. The EDS scans taken on the individual phases revealed that each phase also contained dissolved Cr, W, B and C atoms. Lattice parameters of the phases calculated from X-ray diffraction patterns were determined to be different as compared with their respective unalloyed binary phases, confirming significant amounts of dissolved solute atoms.

A glass devitrification transformation is incredibly complex and even when the composition is fixed, even more variability is obtained by varying the transformation pathway of the glass devitrification transformation. The thermal history of the transformation is important and glass relaxation, recovery, crystallization and recrystallization phenomena are all important factors in microstructural development [128]. By manipulating these effects, the microstructure can be engineered in a variety of fashions including varying the average phase size, causing precipitation in the glass or in the nanocomposite and even forming anisotropic or isotropic microstructures. Thus, manipulation of the heat treatment parameters makes it possible to form different structures in the same alloy by varying the crystallization conditions of amorphous $(Fe_{0.8}Cr_{0.2})_{81}B_{17}W_2$ alloy [129]. Uniform

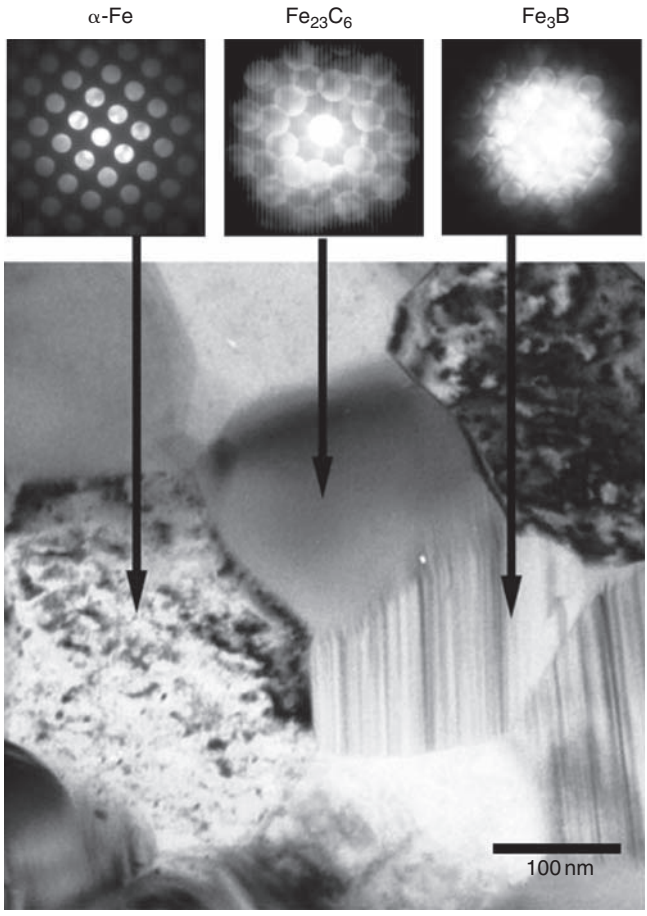

FIGURE 3.16 TEM micrograph showing the microstructure after devitrification.

nanocrystalline structure and high thermal stability of the devitrified structures result in exceptional strength of of 2.3 GPa at 600°C with plasticity of about 5% (Figure 3.17, curve 1). Increasing the deformation temperature to 750°C produced an elongation of 180% (Figure 3.17, curve 2). A clear example of the phase morphology effect, for example, is shown in Figure 3.18. After annealing at 600°C for 100 h, the alloy shows much higher yield stress and considerably lower ultimate strength and a garland of fine phase distributed along the boundaries of equiaxed grains (Figure 3.18, curve B) as compared to the equiaxed grained structure with approximately same grain sizes as in curve A (Figure 3.18). In this case, test temperature was chosen to be higher than annealing conditions for both states of the alloy microstructure. These results have clearly demonstrated the influence of annealing conditions on the nature of crystallization products and, as a result, on the mechanical behaviour of the alloy. Hence, depending upon the microstructure that is produced and the deformation conditions that are chosen, a wide variety of strength/elongation properties can be generated for various potential applications.

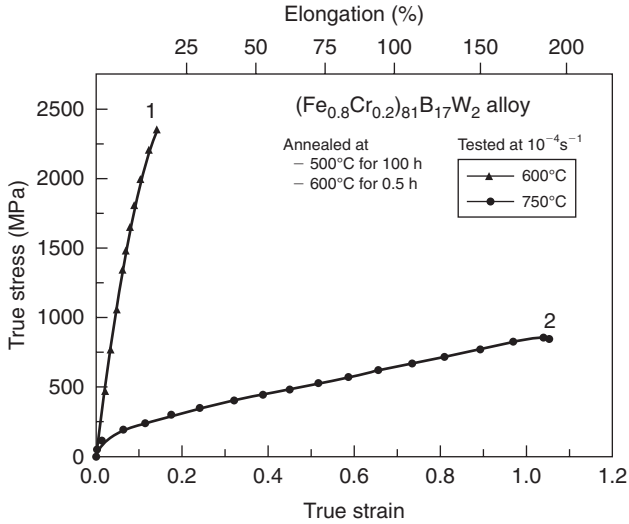

FIGURE 3.17 True stress–true strain curve for devitrified iron-based alloy at elevated temperatures.

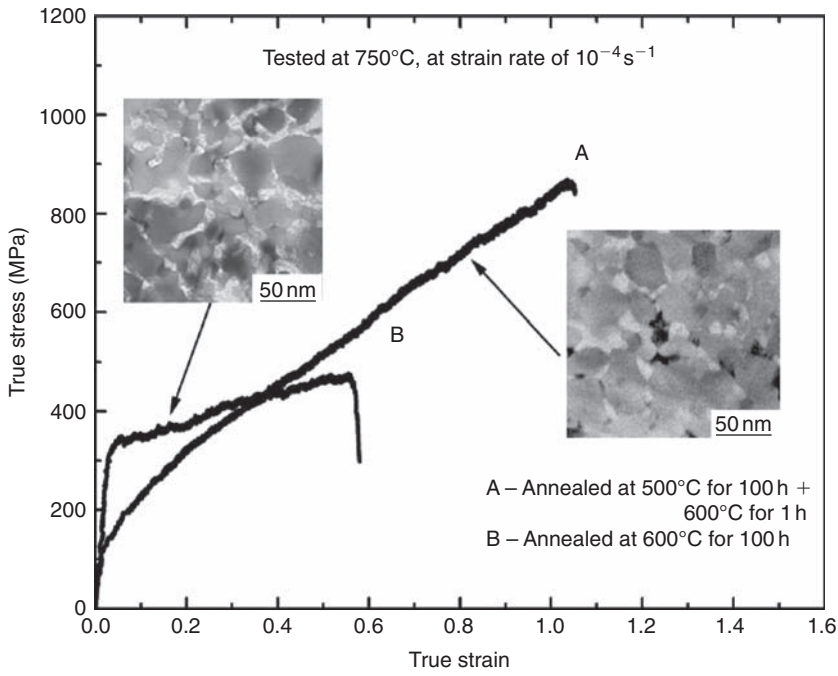

FIGURE 3.18 Stress–stain curves and microstructures of the iron-based alloy crystallized by different thermal treatments.

The real promise of this approach is to separate out the physical mechanisms governing strength and hardness from those governing toughness and ductility and then, subsequently and independently, optimize both to overcome the existing inverse relationship between strength and toughness found in conventional materials. Towards this end, we have recently shown that superplasticity can be obtained with a very high tensile elongation of 230% in a nanocomposite iron-based alloy produced from metallic glass precursors [125]. The measured strain rate sensitivity of 0.51 shows that the primary mechanism controlling deformation was not dislocation motion but grain boundary sliding and grain rotational processes. The ability to shrink the scale of the microstructure to the nanoscale will enable new mechanisms to control mechanical properties to be found, allowing new combinations of properties to emerge, such as strength and toughness, which are not possible on conventional length scales.

4.2 Multilayered Materials

Nanometre-scale polycrystalline multilayered films (nanolayered composites) with layer thickness less than 100 nm have been the subject of many recent experimental and theoretical studies due to their unique, and sometimes unexpected, combinations of properties. For instance, two nominally mechanically soft materials, such as Cu and Nb, can be combined in nanolayered form to produce composite materials with yield strengths exceeding 2 GPa [130]. Despite the fact that much has been done to evaluate the room temperature mechanical properties of multilayers [130–133], very little experimental evidence is available to shed light on the high-temperature mechanical properties of these materials which have features of nanometre length. The earlier work on creep of metallic multilayers was primarily focused on micrometre-scale multilayers [134,135]. This is, in part, due to the fact that the large number of high-energy interfaces found in nanolayers drives the initial microstructure to instability during high-temperature testing. As such, systems that would otherwise make good candidates and which have been extensively studied at room temperature are not appropriate for elevated-temperature studies. Additionally, the use of nanoindentation as a tool for measuring mechanical properties, which is prevalent in the literature, does not lend itself to straightforward evaluation of properties such as yield strength or terminal ductility, especially at elevated temperatures, and relies on a significant amount of modelling to give an idea of these values. For multilayer foils, the best way to avoid artifacts and gain a clear vision of the dominating deformation mechanism is through freestanding tensile testing, where parameters such as applied stress and strain rate are directly controlled and/or evaluated at high temperature. Recently, Cu/Nb multilayers prepared by magnetron sputtering ranging in layer thicknesses from 75 to 40 nm have been tested in tension at elevated temperature [136,137].

The as-deposited microstructure of the 75 nm Cu/75 nm Nb samples is shown in Figure 3.19. Flat interfaces and a columnar grain structure is evident and the selected area diffraction pattern (SADP) shows a {110}bcc//{111}fcc texture. The equilibrium phase diagram for the Cu/Nb system indicates negligible solubility and no intermetallic formation under temperatures of 800°C. Additional work by

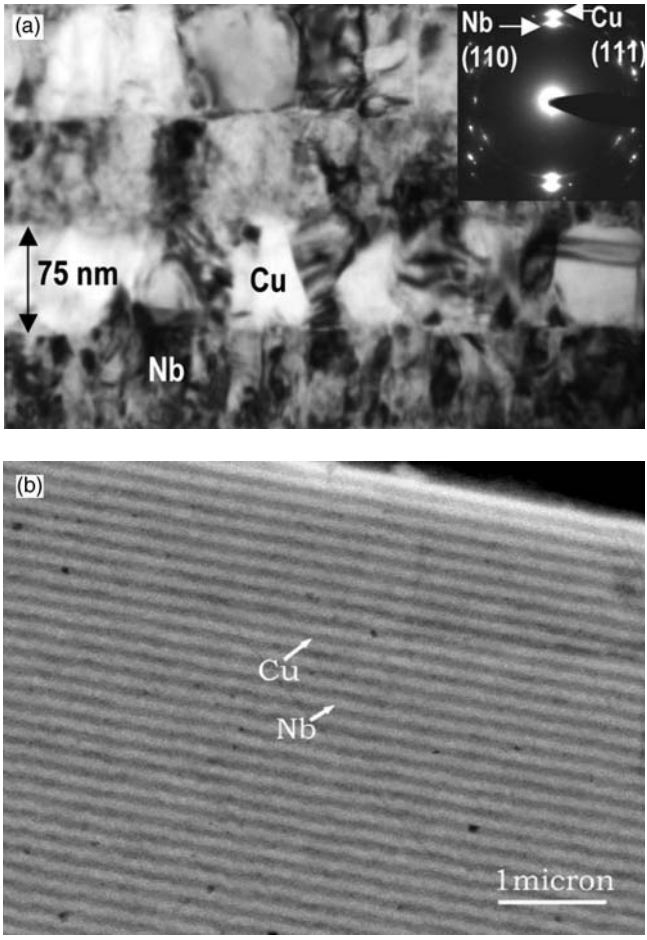

FIGURE 3.19 (a) TEM micrograph of 75 nm Cu/75 nm Nb multilayers before deformation. (b) SEM backscatter micrograph of 75 nm Cu/75 nm Nb multilayers before deformation.

Misra et al. [138] shows that this structure is stable for 75 nm layers up to 800°C for times up to 1 h. Similarly, the 60 nm Cu–Nb multilayer is stable up to 700°C, while the 40 nm layer thickness showed evidence of layer pinch-off at 700°C after annealing times of 4–8 h [139].

Figure 3.20 depicts the elevated-temperature properties of the 75 nm Cu/75 nm Nb layers under monotonic (Figure 3.20a) and varying (Figure 3.20b) strain rates. The two curves of Figure 3.20a result from identical tests at 700°C and show good repeatability between samples. One of the challenges of working with freestanding multilayer foils is the propensity for embedded or surface flaws to dominate the measured mechanical behaviour due to small sample thicknesses. That is, a very small (less than 2–3 μm) flaw can significantly alter flow curve characteristics. The repeatability of these tests indicates good sample integrity and actually shows increased elongation over prior results [136,137], while still indicating the

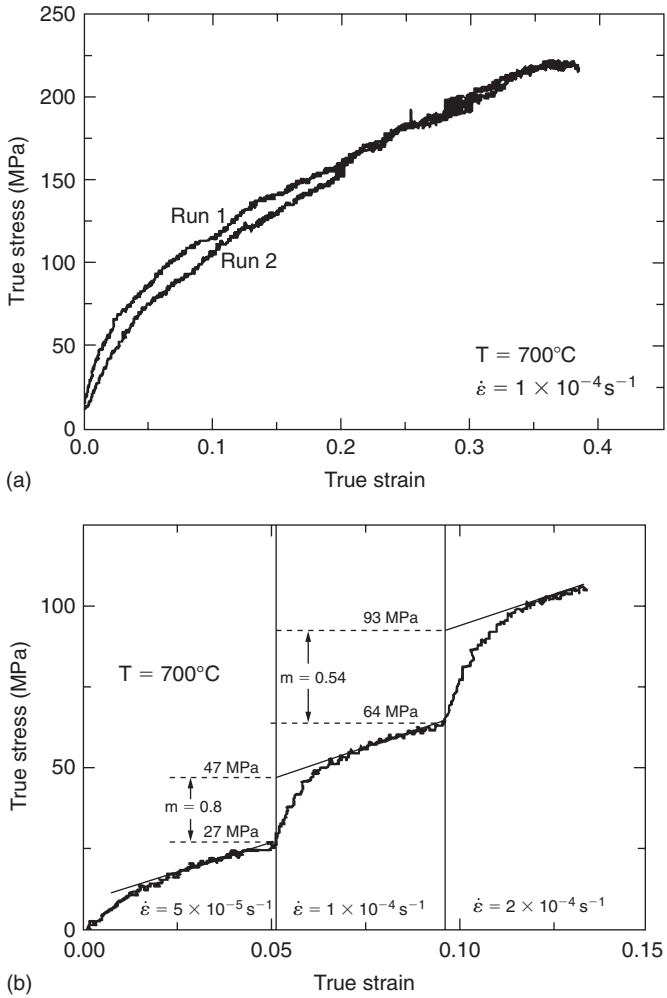

FIGURE 3.20 Tensile curves of 75 nm Cu/75 nm Nb multilayers deformed at 700°C. (a) Two separate monotonic strain rate tests carried out at a strain rate of $1 \times 10^{-4}\,s^{-1}$. (b) Strain rate jump test from strain rate $5 \times 10^{-5}\,s^{-1}$ to $1 \times 10^{-4}\,s^{-1}$ to $2 \times 10^{-4}\,s^{-1}$, respectively.

same yield point and degree of strain hardening. Figure 3.20b is a strain rate jump-test consisting of three separate strain rate jumps at a constant temperature of 700°C. Of note is the decrease in strain rate sensitivity with increasing strain rate and, in particular, the strain rate sensitivity of 0.54 at strain rates of approximately $1 \times 10^{-4}\,s^{-1}$, which usually corresponds to grain boundary sliding [98]. It is important to point out that the flow characteristics at all three strain rates show nearly identical rates of work hardening, identified by the three data-fit lines of equal slope. By extrapolating these lines to an equivalent point of strain, ≈0.09 true strain in the case of the jump from 1×10^{-4} to $2 \times 10^{-4}\,s^{-1}$, stresses at the exact point of the change in strain rate can be used for strain rate sensitivity measurements.

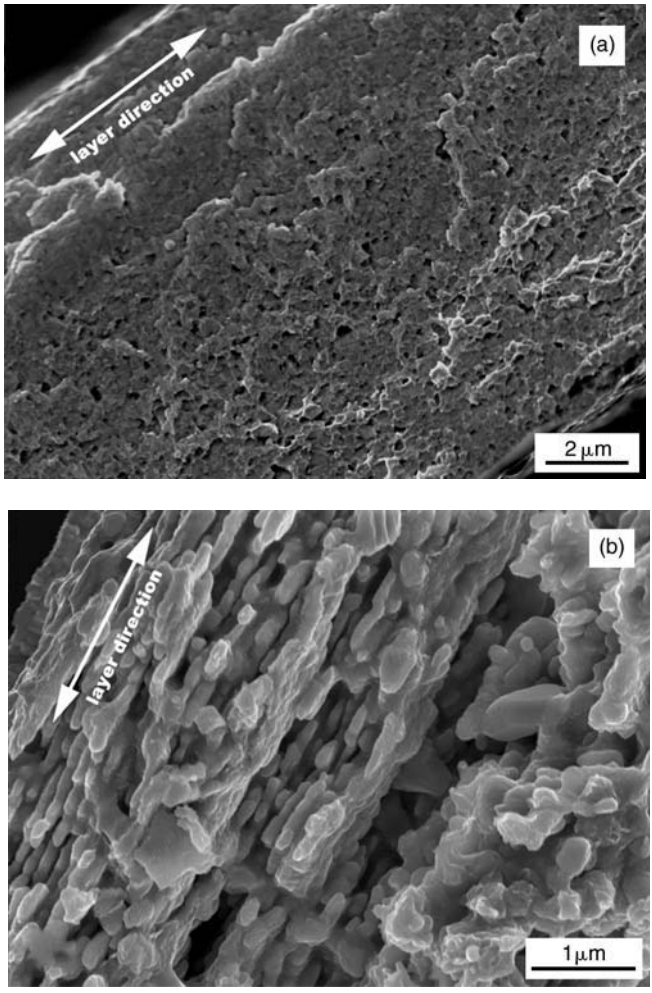

FIGURE 3.21 SEM micrographs of the fracture surfaces of samples tested at (a) 700°C and (b) room temperature.

As layer thicknesses were decreased to 60 nm and to 40 nm, the mechanical properties were not significantly altered. The same general trend of increasing ductility and decreasing strength with increasing temperature spans all three layer sizes chosen for this investigation [136,137]. The 60 nm layered structure resulted in lower overall values for the strain rate exponent m, but the same general trend, decreasing strain rate sensitivity with increasing strain rate, was observed as in the coarser 75 nm samples. A strain rate sensitivity close to that usually associated with grain boundary sliding ($m = 0.51$) was observed at strain rates of about 1×10^{-4}.

Figure 3.21 shows SEM micrographs of the fracture surfaces of 75 nm samples at 700°C (Figure 3.21a) and at room temperature (Figure 3.21b). In all samples with different layer thickness, the fracture surface at room temperature is indicative of microvoid coalescence and the high-temperature fracture surface shows

definite signs of grain pull-out and retention of a layered structure after testing. The extent of layer retention will be the focus of a future cross-sectional TEM study. The relief seen in the high-temperature fracture surfaces could be due to grains sliding apart from one another and correlates well with the mechanical results showing a strain rate exponent close to 0.5 under these testing conditions ($\approx$700°C and strain rate $\approx 1 \times 10^{-4} s^{-1}$).

The authors' previous work [136,137] on the high-temperature properties of Cu/Nb nanolayers points out through TEM observation of post-tested 75 nm samples that the grain coarsening within the layers, as well as an alignment of in-layer grain boundaries, was observed after static annealing at 600°C for 1 hour (Figure 3.22a). Straining of the material at the same time shows qualitatively similar microstructure with the energetically unfavourable quadruple points formed by the alignment of in-layer grain boundaries having started to break up into two triple points each (Figure 3.22b). No dislocation substructure is formed within the grains, although few dislocations are observed. In the absence of any cell structure formation within layers, the dislocation storage may be confined to interfaces (the interface plane is not imaged in these cross-section images). Annealing at high temperature (700°C) results in the formation of a stable triple point structure with additional coarsening of the grains within the layers (Figure 3.22c). When strain is applied at the same temperature, the degree of layer offset is less

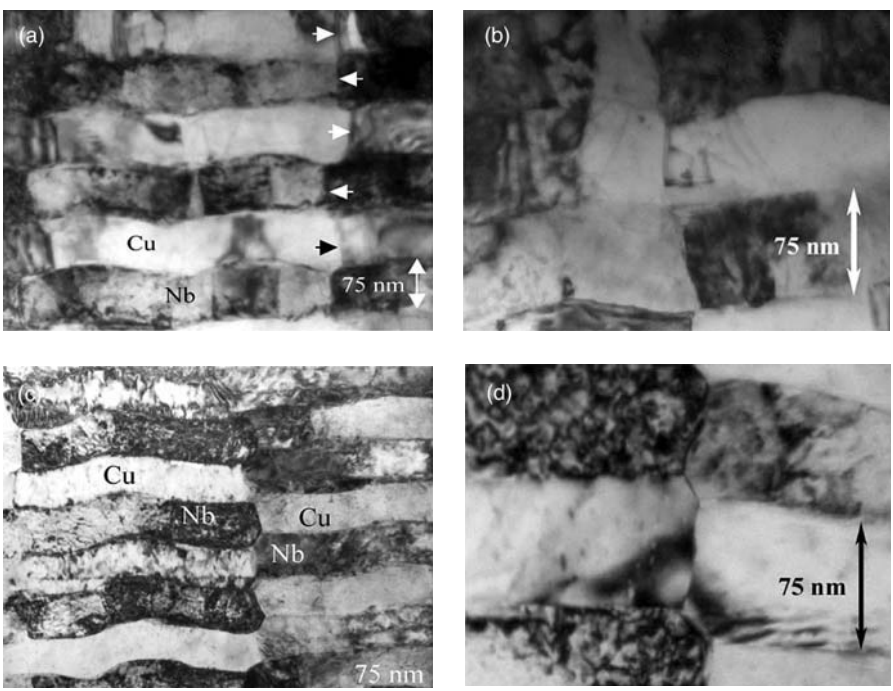

FIGURE 3.22 Bright-field TEM image of 75 nm Cu/75 nm Nb after (a) 600°C 1 h static anneal; (b) after tensile deformation at 600°C at strain rate 10^{-4}; (c) after 700°C 1 h static anneal; (d) after tensile deformation at 700°C at strain rate 10^{-4}.

than that demonstrated in the static anneal (Figure 3.22d). At test temperature in both the static and strained states, the layers are slightly offset, but still maintain a layered structure. The tendency to retain a layered structure, as well the migration of triple points during in-plane grain growth, could drive a deformation mechanism that is critically dependent on sliding at interface boundaries. This sliding, in turn, is only possible through accommodation by mass transport to areas of stress concentration such as triple points or grain boundary ledges. Without such accommodation, these stress concentrations would lead to void formation within the individual layers, followed by shearing/sliding of the fractured layers until macroscopic failure occurs. At these length scales, dislocation glide will be aided by high diffusion rates and the resulting enhanced ability for dislocation climb. Uniform elongations in excess of 30% at elevated temperatures do indicate co-deformation of Cu and Nb layers, presumably due to combined dislocation glide and boundary diffusive processes.

Cu/Nb multilayers offer an excellent opportunity for studying the high-temperature properties of extremely fine grained materials and allow for the tailoring of microstructural length scales in at least one direction. Recently, other authors such as Lewis et al., have made new headway into this area of study [140], with creep testing of Cu/Nb multilayers at lower strain rates and using coarser layering than those found in the present work. Their results, along with some from the present study, are summarized in Figure 3.23. The creep work carried

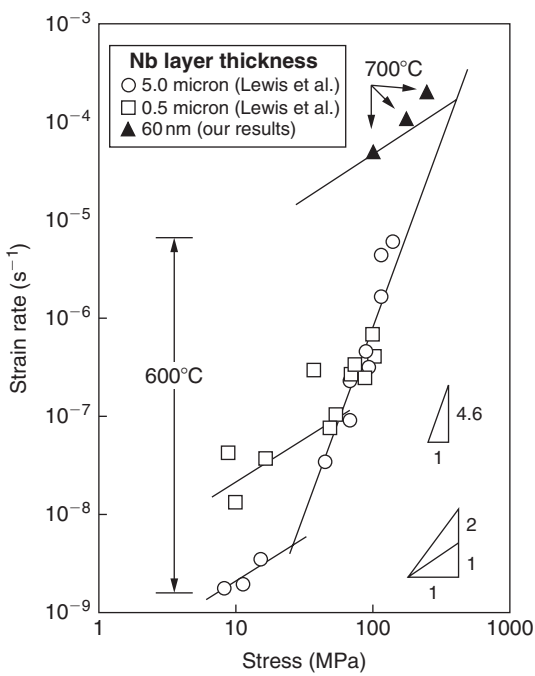

FIGURE 3.23 Logarithmic strain rate vs. logarithmic stress for a variety of Cu/Nb multilayers under various testing conditions. (Some data are from Ref. [140].)

out using 5 and 0.5 μm Cu/Nb layering shows a transition from a strain rate sensitivity of approximately one (diffusional creep) to that correlating to power law creep (stress exponent of 4.6, strain rate exponent of 0.21). This trend of a decrease in strain rate sensitivity with increasing strain rate is the same as observed in this study for both 60 and 75 nm Cu/Nb layers. While our results were obtained at 700°C as opposed to 600°C by Lewis et al., a plot of our jump-test results along with their earlier creep observations gives a good general correlation. In this case, our results include a reference line with slope of 1, which does not represent a linear fit of the new data, and is only shown as a reference to the other two lines from earlier work by Weihs et al. [134]. For the two strain rate jumps in the 60 nm, 700°C test, the strain exponents of 0.51 and 0.35 correspond to stress exponents of $n = 2$ and $n = 3$, respectively. If the test temperatures in the current study were to be lowered to 600°C, one would expect a shift in the data points to higher stresses for equivalent strain rates, giving even closer agreement between the two studies.

4.3 Bimodal Structure

Obtaining a high strength from nanocrystalline materials seems to be straightforward, but that alone may not be sufficient for many applications if the material suffers from ductility problems. The lack of a work hardening mechanism is entirely compatible with the lack of accumulation of dislocations, as suggested by both simulation and experiment [141]. It was noticed that for most of the nanocrystalline materials that showed some strain hardening and respectable ductility, the microstructure usually contained a distribution of grain sizes even though the volume fraction of the larger grains may be low [142–147]. Wang et al. [148] have reported on the preparation and tensile testing of ufg grained Cu. They rolled the Cu to 93% at liquid nitrogen temperatures and then annealed it at low temperatures up to 200°C. The original heavily cold worked Cu had a high dislocation density along with some resolvable grains less than 200 nm in size. Annealing resulted in development of well-defined grains with high angle boundaries. The annealing treatment (3 min at 200°C) that optimized strength and ductility produced a mixture of ufg grains (80–200 nm) along with about 25% volume fraction of coarser grains (1–3 μm). The coarser grains were the result of secondary recrystallization. The authors suggest that the excellent combination of strength and ductility is the result of:

1. multi-axial stress states in the confined grains;
2. twinning in the larger grains; and
3. preferential accommodation of strain in the larger grains.

Zhang et al. [144,149,150] varied the microstructure of Zn by changing the milling times at either liquid nitrogen or room temperature. The sample with the optimum combination of strength and ductility contains about 30% volume fraction of grains larger than 50 nm along with smaller nanoscale grains. This optimum microstructure, which exhibits more strain hardening than samples milled for shorter or longer times, combines the strengthening from the reduced grain size along with the strain hardening provided by dislocation activity in the larger

grains. At the longer milling times where all the grain sizes are <50 nm, the strain hardening is absent since dislocation activity is negligible. At the shorter milling times, e.g. 3 h, the existence of a distribution in grain size allows the smaller grains to provide the strength component and the larger grains the ductility component because of the latter's ability to accommodate the increase in dislocation density producing plasticity. Thus, the optimum microstructure gives a value of σ_y, about twice that of conventional grain size Zn, along with increased ductility. Tellkamp et al. [145] and Legros et al. [147] observed ductility enhancements in tensile tests of copper and Al 5083 alloy, respectively, through the incorporation of larger grains in a fine-grained matrix. In both cases, considerable strengthening was achieved relative to conventional counterparts, with a yield strength of 535 MPa for Cu and 334 MPa for Al 5083. The tensile fracture strains were 2.1% and 8.4%, respectively, both of which are higher than for typical nanocrystalline metals. The formation of larger grains was achieved by recrystallization during warm compaction [147] or bimodal grain growth during consolidation by hot isostatic pressing and extrusion [145]. This approach was demonstrated by the thermomechanical treatment of nanocrystalline Cu sheet deliberately to grow larger grains, producing dramatic improvements in strength *and* ductility [148]. Thus, a formation of bimodal grain size distribution (so-called structural composites) seems to be a very promising method for ductility improvement in nanomaterials with retention of their strength characteristics. In this section, data on mechanical response of NiTi and Fe-based (Vitroperm) alloys with bimodal grain size distribution are presented.

A bimodal grain size distribution when grains with a size of about 100–200 nm were incorporated in nc matrix with mean grain size of 40–70 nm has been achieved in NiTi alloy after high pressure torsion (HPT) with subsequent annealing [151]. High pressure torsion of NiTi leads to amorphization of the alloy [151]. Two types of annealing were applied to crystallize the material. In order to obtain a homogeneous structure, the material was subjected to two-step annealing: at 200°C for 1 h and at 500°C for 0.5 h. In this case, the first annealing step at low temperature was used to increase the number of possible nucleation sites for the following crystallization step at higher temperature [151]. The obtained structure with mean grain size of 70 nm is shown in Figure 3.24a. Annealing at 500°C for 0.5 h right after HPT results in formation of a microstructure with bimodal grain size distribution (Figure 3.24b) where large grains (d = 100–200 nm) are embedded in a nanocrystalline matrix with d = 40–70 nm.

Annealed material was tested in tension at 400° and 500°C and at strain rates of $10^{-3}\,s^{-1}$. At lower temperature (400°C), more pronounced strain hardening was observed in the sample with bimodal grain size distribution (Figure 3.25a). The ultimate tensile strength of this sample was 13% less than that of the sample with homogeneous nanostructure. The material also revealed extensive necking. Uniform plastic strain was approximately the same in the two materials (<5%). An increase in test temperature leads to a more pronounced difference in plasticity of the material with different grain size distribution while the difference in strength characteristics is insignificant (Figure 3.25b). In both cases, NiTi alloy displayed yielding at 220 MPa and ultimate strength of more than 900 MPa. At

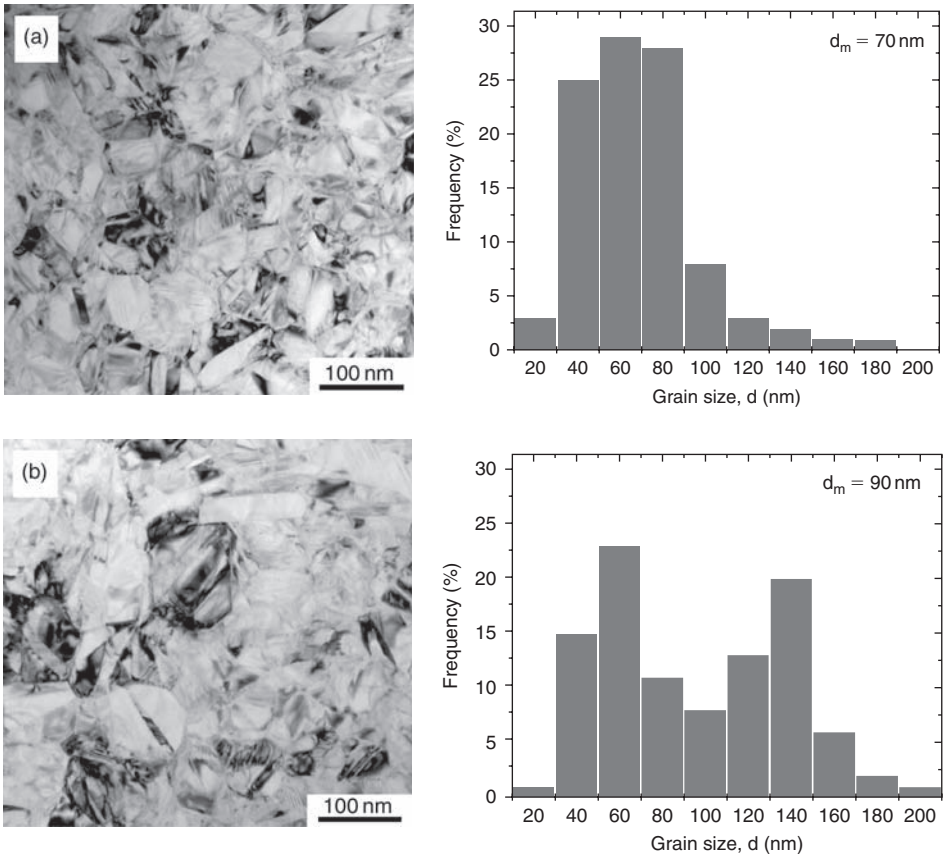

FIGURE 3.24 Microstructure of NiTi alloy and histograms of grain size distribution after HPT and annealing (a) at 200°C for 1 h and (b) at 500°C for 0.5 h.

the same time, the ductility was increased more than twice in the sample with initial bimodal grain size distribution (170% vs. 367%).

Similar trends in grain size distribution effect on mechanical behaviour were observed in Vitroperm alloy tested at 600°C ($0.4T_m$). As-received strips of this alloy were amorphous and its annealing at different temperatures resulted in different structures. Thus, homogeneous one phase (α-Fe) structure with mean grain size of 15 nm was formed in this alloy after annealing at 600°C for 1 h (Figure 3.26a). An increase in annealing temperature to 650°C leads to formation of large non-equaxed grains (100–200 nm in length) embedded in nanocrystalline matrix with mean grain size of 15 nm (Figure 3.26b). The appearance of a second phase was detected in SAED pattern. True stress–true strain curves at 600°C and at $10^{-4}s^{-1}$ are shown in Figure 3.27. Yielding of the alloy in the presence of large grains started at about 400 MPa (curve 1) with an extensive strain hardening while a nanocrystalline material with homogeneous structure (curve 2) has demonstrated elastic, perfectly plastic behaviour. No strain hardening was revealed

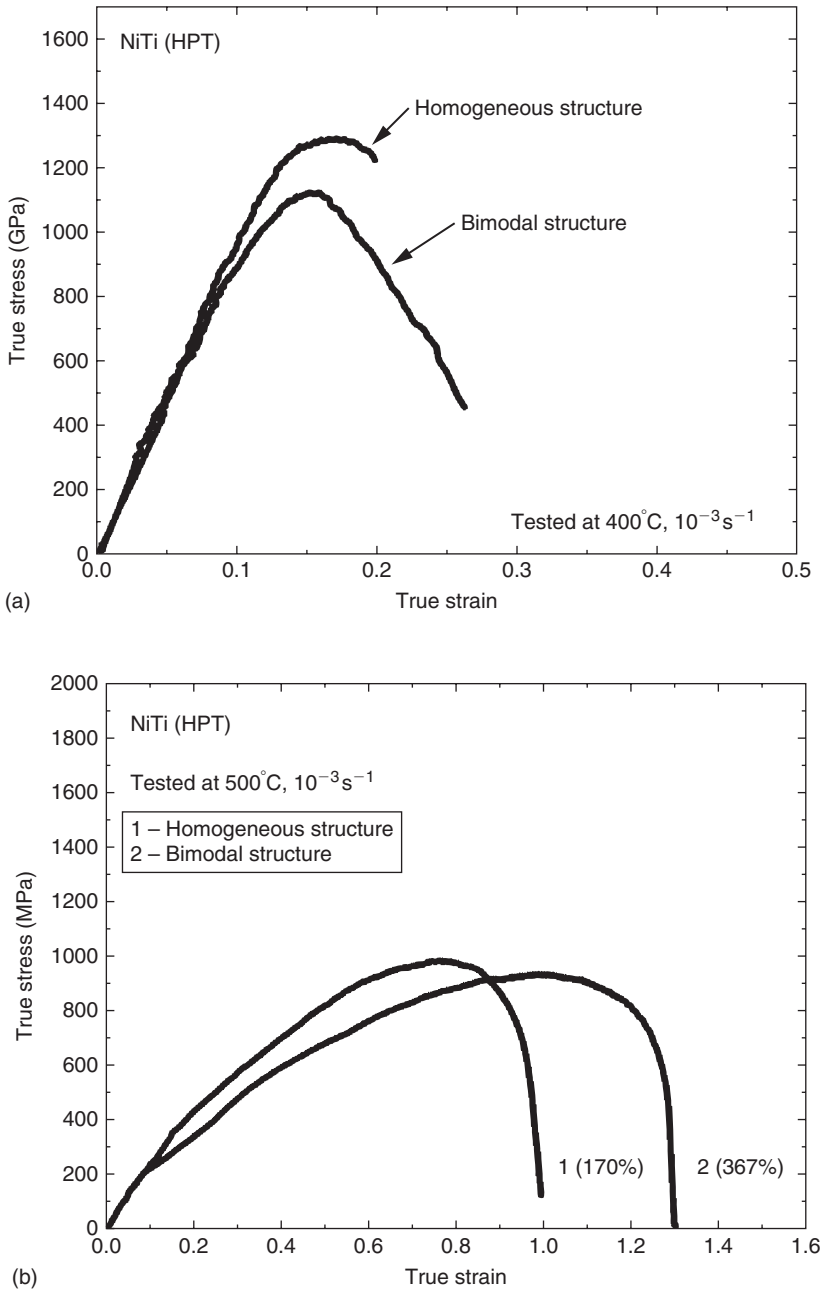

FIGURE 3.25 True stress–true strain tensile curves for NiTi alloy after HPT and annealing at (a) 400°C; (b) 500°C.

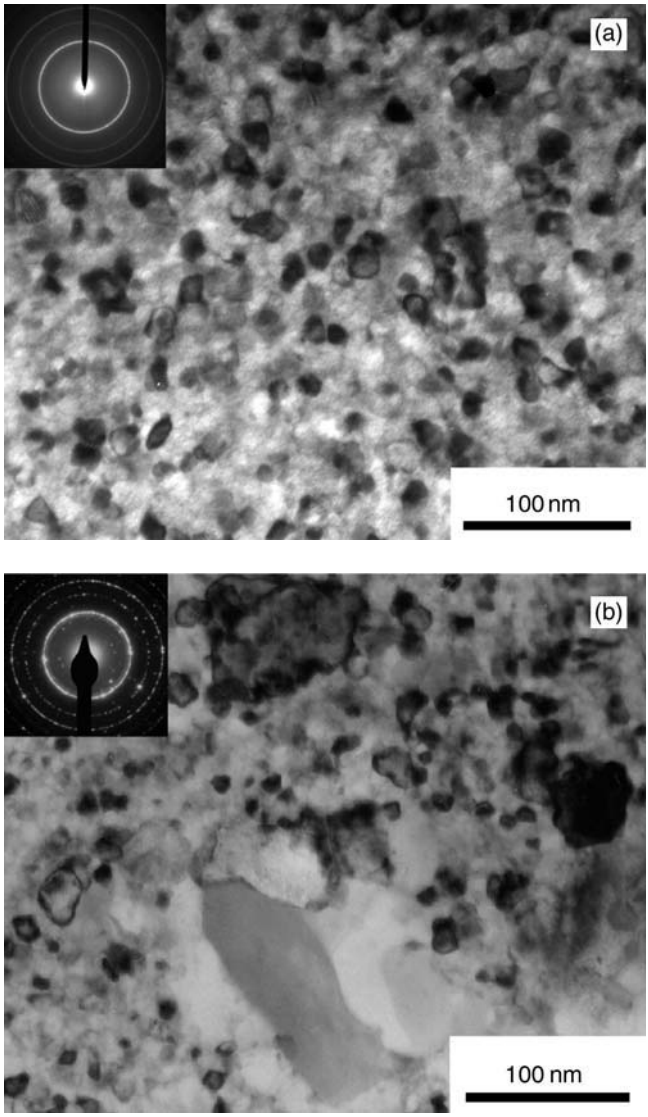

FIGURE 3.26 Microstructure with corresponding SAED patterns of Vitroperm alloy after crystallization (a) at 600°C and (b) at 650°C.

after yielding at 1270 MPa. The alloy exhibited low plasticity in both states (2% in the case of homogeneous structure and 4% at wide grain size distribution). Wide grain size distribution led to necking similar to that observed in NiTi.

The results of the current study confirmed a strong effect of the grain size distribution on mechanical behaviour of nanocrystalline materials. At the same time, our work represents a different approach to the understanding of deformation processes at extremely diminished length scale. First of all, both our materials

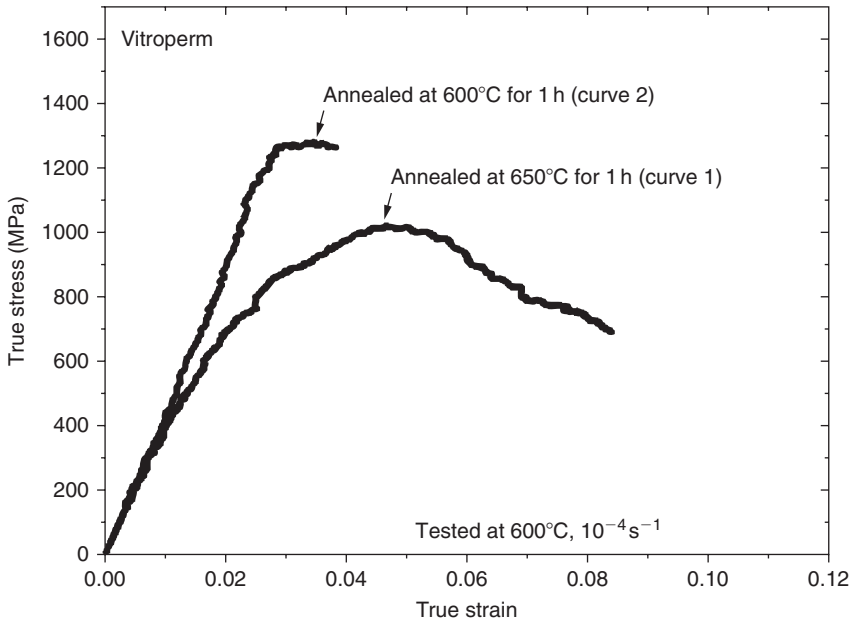

FIGURE 3.27 True stress–true strain tensile curves for Vitroperm alloy after crystallization at different temperatures.

were obtained by crystallization from the amorphous state that assumes a formation of equilibrium structures with high angle grain boundaries of random misorientations. Secondly, the size of the large grains embedded in nanocrystalline matrix is twice the mean grain size of the matrix and might be considered to be at the upper level of the definition of a nanocrystalline range (<500 nm).

It was shown that, at relatively low temperatures ($<0.4\,T_m$, where T_m is a melting point), the presence of such grains leads to the yielding of the materials at significantly lower stresses with well defined strain hardening. A homogeneous matrix of nanocrystalline grains (d = 15 nm) had displayed almost zero strain hardening in Vitroperm alloy (see Figure 3.27). Nitinol had demonstrated some hardening (see Figure 3.25), but this alloy has a wider grain size distribution with mean size of 70 nm (see Figure 3.24a). Formation of a bimodal structure in this alloy results in lower yielding stress and significant hardening during deformation as compared with the alloy with homogeneous structure (see Figure 3.25). One of the possible reasons for such behaviour might be related to an increase in dislocation activity in the grains larger than some critical grain size. Such a critical size can be different depending on the material. Vitroperm alloy with $d \approx 15$ nm seems to be below such critical value and the material exhibited elastic, perfectly plastic behaviour. Some dislocation activity is suggested to occur in nanocrystalline NiTi alloy with homogeneous structure ($d \approx 70$ nm). Actually, dislocations formed at grain boundaries have been observed in the materials with grain size down to 30–50 nm by molecular dynamic simulations [152] and experimentally

[153,154]. The presence of larger grains seems to accelerate dislocation activity. Extensive necking of the materials with wide grain size distribution also confirms this assumption.

At higher temperatures ($T > 0.4T_m$), diffusion processes, especially grain boundary diffusion, start to play an important role, leading to extensive grain growth during deformation. The initial grain size distribution seems not to be so important for the material yield stress while a significant increase in ductility was observed.

5. CONCLUDING REMARKS

It was shown that the ability to design the mechanical properties of new materials in the nanocrystalline range depends upon the design and production of novel microstructures. This requires control of grain size and grain size distribution, reinforcement-particle (or fibre) morphology, the amount and distribution of dopants and reinforcement elements, etc.

Single-wall carbon nanotube (SWCN) reinforced alumina-based nanocomposites consolidated by the SPS process yielded very significant increase in fracture toughness that has not been attained before. Incorporating a nanocrystalline layer of niobium between the alumina grains in such alumina/SWCN nanocomposites yielded a fracture toughness value equal to that for metallic materials.

By retaining nanosized grains in alumina/zirconia/magnesia spinel nanocomposites due to low temperature/short time sintering by SPS, a significant formability of this material by superplastic flow was demonstrated. Furthermore, by using the SPS chamber as a forming environment, superplasticity was obtained at an astonishingly low temperature (1150°C) with an extremely fast forming time (3 to 4 minutes).

A ceramic nanocomposite based on silicon nitride and silicon carbide produced by pyrolysis of a liquid polymer precursor with subsequent SPS processing of nanopowder has demonstrated one of the lowest creep rates (greatest creep strength) as compared to all other results on silicon nitride-based materials at a common reference temperature. This was achieved by either eliminating or minimizing the amount of oxynitride glassy phase in the intergrain and interphase boundaries of the microstructure.

Incorporating SWCN into alumina nanomatrix results not only in improved mechanical properties but was also successfully used to convert insulating nanoceramics to metallically conductive composites. Additionally, novel anisotropic thermal properties and thermoelectric properties have been observed in such carbon nanotube nanocomposites.

An exceptional strength even at elevated temperatures has been demonstrated in iron-based nanocomposites devitrified from metallic glasses. The control of this transformation is the primary factor resulting in wide variety of microstructures and resulting properties found in these materials. A formation of bimodal grain size distribution leads to an increase in ductility of the nanomaterials with retention of their exceptional strength.

Variation of layer thickness in a nanorange affects high temperature properties of layered composites produced by magnetron sputtering. These results present further understanding of and provide new insights to the strengthening mechanisms operative in nanoscale multilayered materials.

ACKNOWLEDGEMENTS

This investigation was supported in part by a grant (G-DAAD19-00-1-0185) from US Army Research Office with Dr William Mullins as the Program Manager, a grant (N00014-03-1-0148) from the Office of Naval Research with Dr Lawrence Kabacoff as Program Manager, NSF grant NSF-DMR-0240144 from Division of Materials Research, the HTML Proposal #2003-025 by Oak Ridge National Laboratory, and the EMSL Proposal No. 3385 (2003) by Pacific Northwest National Laboratory. The authors would like to acknowledge Dr DJ Branagan, Dr G-D Zhan, Dr X Zhou, Dr M Gasch, Dr J Wan, Dr R-G Duan, Dr J Kuntz and Dr D-T Jiang for their input to the current investigations.

References

1. Chen W, Anselmi-Tamburini U, Garay JE, Groza JR, Munir ZA. Mater. Sci. Eng. A 2005; 394:132.
2. Anselmi-Tamburini U, Gennari S, Garay JE, Munir ZA. Mater. Sci. Eng. A 2005; 394:139.
3. Anselmi-Tamburini U, Garay JE, Munir ZA. Mater. Sci. Eng. A 2005; 407:24.
4. Omori M. Mater. Sci. Eng. A 2000; 287:183.
5. Ma RZ, Wu J, Wei BQ, Liang J, Wu DH. J. Mater. Sci. 1998; 33:5243.
6. Flahaut E, Peigney A, Laurent Ch, Marliere C, Chastel E, Rousset A. Acta Mater. 2000; 48:3803.
7. Laurent Ch, Peigney A, Dumortier O, Rousset A. J. Eur. Ceram. Soc. 1998; 18:2005.
8. Peigney A, Laurent Ch, Dobigeon F, Rousset A. J. Mater. Res. 1997; 12:613.
9. Peigney A, Laurent Ch, Dumortier O, Rousset A. J. Eur. Ceram. Soc. 1998; 18:1995.
10. Peigney A, Laurent Ch, Flahaut E, Rousset A. Ceram. Inter. 2000; 26:677.
11. Siegel RW, Chang SK, Ash BJ et al. Scripta Mater. 2001; 44:2061.
12. Zhan G-D, Kuntz JD, Wan J, Mukherjee AK. Nature Mater. 2003; 2:38.
13. Zhan G-D, Kuntz JD, Garay J, Mukherjee AK. Appl. Phys. Lett. 2003; 83:1228.
14. Riley FL. J. Am. Ceram. Soc. 2000; 83:245.
15. Ziegler G, Heinrich J, Wötting G. J. Mater. Sci. 1987; 22:3041.
16. Duan RG, Roebben G, Vleugels J, Van der Biest O. J. Eur. Ceram. Soc. 2002; 22:1897.
17. Trice RW, Halloran JW. J. Am. Ceram. Soc. 1999; 82:2633.
18. Choi H-J, Lee J-G, Kim Y-W. J. Eur Ceram. Soc. 1999; 19:2757.
19. Roebben G, Duan RG, Sciti D, Van der Biest O. J. Eur. Ceram. Soc. 2002; 22:2501.
20. Okada K, Fukuyama K, Kameshima Y. J. Am. Ceram. Soc. 1995; 78:2021.
21. Kleebe H-J, Cinibulk MK, Cannon RM, Rüle M. J. Am. Ceram. Soc. 1993; 76:1969.
22. Pabst RF. In Creep Behavior of Crystalline Solids, Vol. 3, B Wilshire and RW Evans (eds). Pineridge Press: Swansea, 1985; 254.
23. Wakai F, Kodama Y, Sakaguchi S, Murayama N, Izaki K, Niihara K. Nature 1990; 344:421.
24. Wakai F, Kato H. Adv. Ceram. Mater. 1988; 3:71.
25. Rouxel T, Wakai F, Izaki K. J. Am. Ceram. Soc. 1992; 75:2363.
26. Chen I-W, Xue LA. J. Am. Ceram. Soc. 1990; 73:2585.
27. Meléndez-Martínez JJ, Domínguez-Rodríguez A. Prog. Mater. Sci. 2004; 49:19.
28. Yoon KJ, Wiederhorn SM, Luecke WE. J. Am. Ceram. Soc. 2000; 83:2017.
29. Crampon J, Duclos R, Rakotoharisoa N. J. Mater. Sci. 1993; 28:909.

30. Crampon J, Duclos R, Rakotoharisoa N. J. Mater. Sci. 1990; 25:1203.
31. Yoon SY, Akatsu T, Yasuda E. J. Mater. Sci. 1997; 32:3813.
32. Nixon RD, Koester DA, Chevacharoenkul S, Davis RF. Composites Sci. Tech. 1990; 37:313.
33. Besson J-L, Mayne M, Bahloul-Hourlier D, Goursat P. J. Eur. Ceram. Soc. 1998; 18:1893.
34. Gasdaska CJ. J. Am. Ceram. Soc. 1994; 77:2408.
35. Mandal H, Thompson DP. J. Mater. Sci. 2000; 35:6285.
36. Cinibulk MK, Thomas G. J. Am. Ceram. Soc. 1992; 75:2037.
37. Mitomo M. J. Mater. Sci. 1976; 11:1103.
38. Tsuge A, Nishida K, Komatsu M. J. Am. Ceram. Soc. 1975; 58:323.
39. Tanaka I, Pezzotti G, Okamoto T, Miyamoto Y, Koizumi M. J. Am. Ceram. Soc. 1989; 72:1656.
40. Hawsey RA, Murphy AW, Koncinski WS. ORNL Superconducting Technology Program for Electrical Power Systems, Annual Report, FY 2001. 2002; 45.
41. Shen Z, Peng H, Nygren M. Adv. Mater. 2003; 15:1006.
42. Niihara K, Nakahira A, Sekino T. In Nanophase and Nanocomposite Materials Symposium, S Komarneni, JC Parker and GJ Thomas (eds). Materials Research Society, 1993; 405.
43. Kuntz JD, Zhan G-D, Mukherjee AK. MRS Bulletin 2004; January 22.
44. Niihara K, Nakahira A, Sakai G, Hirabayashi M. In Composites, Corrosion/Coating of Advanced Materials, Vol. 4, S Kimura, A Kobayashi, S Umekawa, K Nii, S Saito and M Yoshiura (eds). MRS: Pittsburgh, 1989; 129.
45. Niihara K, Nakahira A. In Advanced Structural Inorganic Composites, P Vincenzini (ed.). Elsevier: New York, 1991; 637.
46. Sternitzke M. J. Eur. Ceram. Soc. 1997; 17:1061.
47. Awaji H, Choi S-M, Yagi E. Mech. Mater. 2002; 34:411.
48. Ji Y, Yeomans JA. J. Eur. Ceram. Soc. 2002; 22:1927.
49. Sekino T, Nakajima T, Ueda S, Niihara K. J. Am. Ceram. Soc. 1997; 80:1139.
50. Oh ST, Sekino T, Niihara K. J. Eur. Ceram. Soc. 1998; 18:31.
51. Sekino T, Niihara K. Nanostr. Mater. 1995; 6:663.
52. Maensiri S, Roberts SG. J. Eur. Ceram. Soc. 2002; 22:2945.
53. Anya CC. J. Mater. Sci. 1999; 34:5557.
54. Davidge RW, Brook RJ, Cambier F et al. Br. Ceram. Transact. 1997; 96:121.
55. Zhu WZ, Gag JH, Ding ZS. J. Mater. Sci. 1997; 32:537.
56. Bhaduri S, Bhaduri SB. Nanostr. Mater. 1997; 8:755.
57. Levin I, Kaplan WD, Brandon DG, Layyous AA. J. Am. Ceram. Soc. 1995; 78:254.
58. Ohji T, Young-Keun J, Yong-Ho C, Niihara K. J. Am. Ceram. Soc. 1998; 81:1453.
59. Zhan G-D, Kuntz JD, Duan RG, Mukherjee AK. J. Am. Ceram. Soc. 2004; 87:2297.
60. Yu M-F, Files BS, Arepalli S, Ruoff RS. Phys. Rev. Lett. 2000; 8:5552.
61. Thess A, Lee R, Nikolaev P et al. Science 1996; 273:483.
62. Baughman RH, Zakhidov AA, de Heer WA. Science 2002; 297:787.
63. Zhan G-D, Kuntz JD, Wang H, Wang C-M, Mukherjee AK. Phil. Mag. Lett. 2004; 84:419.
64. Kuntz JD, Wan J, Zhan G-D, Mukherjee AK. In Ultrafine Grained Materials II, YT Zhu, TG Langdon, RS Mishra, SL Semiatin, MJ Sharan and TC Lowe (eds). The Minerals, Metals and Materials Society: Warrendale, 2002; 225.
65. Sergueeva AV, Jiang DT, Thomson KE, Hulbert DM, Mukherjee AK. In Bulk Nanostructured Materials, MJ Zehetbauer (ed.). Wiley-VCH: Weinheim, 2007.
66. Kuntz JD, Zhan G-D, Mukherjee AK. Mat Res. Soc. Symp. Proc. Vols. 2004; 821:7.5.1.
67. Garcia DE, Schicker S, Bruhn J, Janssen R, Claussen N. J. Am. Ceram. Soc. 1998; 81:429.
68. Wu X, Chen IW. J. Am. Ceram. Soc. 1992; 75:2733.
69. Hwang SL, Chen IW. J. Am. Ceram. Soc. 1994; 77:2575.
70. Rosenflanz A, Chen IW. J. Am. Ceram. Soc. 1997; 80:1341.
71. Xie RJ, Mitomo M, Zhan GD, Emoto H. J. Am. Ceram. Soc. 2000; 83:2529.
72. Xie RJ, Mitomo M, Zhan GD. Acta Mater. 2000; 48:2049.
73. Zhan GD, Mitomo M, Nishimura T, Xie RJ, Sakuma T, Ikuhara Y. J. Am. Ceram. Soc. 2000; 83:841.
74. Shinoda Y, Nagano T, Gu H, Wakai F. J. Am. Ceram. Soc. 1999; 82:2916.
75. Kim B-N, Hiraga K, Morita K, Sakka Y. Nature 2001; 413:288.

76. Wakai F, Sakaguchi S, Matsuno Y. Adv. Ceram. Mater. 1986; 1:259.
77. Nieh TG, Wadsworth J. Acta Metall. Mater. 1990; 38:1121.
78. Yoshizawa Y, Sakuma T. Acta Metall. Mater. 1992; 40:2943.
79. Wakai F, Kato H. Adv. Ceram. Mater. 1988; 3:71.
80. Zhan GD, Kuntz J, Wan J, Garay J, Mukherjee AK. J. Am. Ceram. Soc. 2002; 86:200.
81. Uchic M, Hofler HJ, Flick WJ, Tao R, Kurath P, Averback RS. Scrip. Metal. Mat. 1992; 26:791.
82. Burke JE. J. Am. Ceram. Soc. 1957; 40:80.
83. Jiang D, Hulbert DM, Kuntz JD, Anselmi-Tamburini U, Mukherjee AK. Mater. Sci. Eng. 2006.
84. Ohji T, Nakahira A, Hirano T, Niihara K. J. Am. Ceram. Soc. 1994; 77:3259.
85. Hirano T, Niihara K, Ohji T, Wakai F. J. Mater. Sci. Lett. 1996; 15:505.
86. Thompson AM, Chan HM, Harmer MP. J. Am. Ceram. Soc. 1997; 80:2221.
87. Raj R. J. Geophys. Res. 1982; 87:4731.
88. Wakai F. Acta Metall. Mater. 1994; 42:1163.
89. Wan J, Gasch MJ, Mukherjee AK. J. Mater. Res. 2000; 15:1657.
90. Wan J, Duan R-G, Gasch MJ, Mukherjee AK. J. Am. Ceram. Soc. 2006; 89:274.
91. Lange FF, Davis BI. J. Mater. Sci. 1982; 17:3637.
92. Whalen PJ, Gasdaska C, Silvers RD. Ceram. Eng. Sci. Proc. 1990; 11:633.
93. Wereszczak AA, Ferber MK, Kirkland TP, Barnes AS, Frome EL, Menon MN. J. Eur. Ceram. Soc. 1999; 19:227.
94. Bernard-Granger G, Crampon J, Duclos R, Cales B. J. Eur. Ceram. Soc. 1997; 17:1647.
95. Lange FF, Davis BI, Graham HC. J. Am. Ceram. Soc. 1983; 66:C98.
96. Backhaus-Ricoult M, Eveno P, Castaing J, Kleebe HJ. In Plastic Deformation of Ceramics, RC Bradt, CA Brookes and JL Routbort (eds). Kluwer Academic Pub: 1995; 555.
97. Ramoul-Badache K, Lancin M. J. Eur. Ceram. Soc. 1992; 10:369.
98. Mukherjee AK. In Materials Science and Technology: A Comprehensive Treatment, Vol. 6, RW Cahn, P Haasen, EJ Kramer (eds). Weinheim, 407.
99. Zhan G-D, Mukherjee AK. Int. J. Appl. Ceram. Technol. 2004; 1:161.
100. Zhan G-D, Mukherjee AK. Rev. Adv. Mater. Sci. 2005; 10:185.
101. Shackelford JF. Introduction to materials science for engineers. Macmillan: New York, 1985.
102. Xu L, Wei BW, Ma RX, Liang J, Ma XK, Wu DH. Carbon 1999; 37:855.
103. Peigney A, Flahaut E, Laurent C, Chastel F, Rousset A. Chem. Phys. Lett. 2002; 352:20.
104. Berber S, Kwon YK, Tomanek D. Phy. Rev. Lett. 2000; 84:4613.
105. Hone J, Batlogg B, Benes Z, Johnson AT, Fischer JE. Science 2000; 289:1730.
106. Kim P, Shi L, Majumdar A, McEuen PL. Phys. Rev. Lett. 2001; 87, 215502.
107. Hone JM, Llaguno C, Nemes NM et al. Appl. Phys. Lett. 2000; 77:666.
108. Hone J, Whitney M, Piskoti C, Zettl A. Phys. Rev. 1999; B59:R2514.
109. Biercuk MJ, Llaguno MC, Radosavlievic M, Hyun JK, Johnson AT, Fischer JE. Appl. Phys. Lett. 2002; 80:2767.
110. Stahl H, Appenzeller J, Martel R, Avouris Ph, Lengeler B. Phys. Rev. Lett. 2000; 85:5186.
111. Rochefort A, Avouris Ph, Lesage F, Salahub DR. Phys. Rev. B 1999; 60:13824.
112. Torquato S, Rintoul MD. Phys. Rev. Lett. 1995; 75:4067.
113. Delhaàs P. Graphite and Precursors. Gordon and Breach Science Publishers, 2001.
114. Sales BC. Science 2002; 295:1248.
115. Hone J, Ellwood I, Muno M et al. Phys. Rev. Lett. 1998; 80:1042.
116. Lu K. Mater. Sci. Eng. Rep. 1996; 16:161.
117. Clavaguera-Mora MT, Clavaguera N, Crespo D, Pradell T. Prog. Mater. Sci. 2002; 47:559.
118. Crespo D, Pradell T, Clavaguera N, Clavaguera-Mora MT. Mater. Sci. Eng. A 1997; 238:160.
119. Köster U, Schünemann U, Blank-Bewersdorff M, Brauer S, Sutton M, Stephenson GB. Mater. Sci. Eng. A 1991; 133:611.
120. Branagan DJ, Kramer MJ, McCallum RW. J. Alloys Comp. 1996; 244:27.
121. Leu MS, Chin TS. Mat. Res. Soc. Symp. Proc. Vols. 1999; 577:557.
122. Kulik TJJ. Non-Cryst. Solids 2001; 287:145.
123. Wuy Q, Bitoh T, Hono K, Makimo A, Inoue A. Acta Mater. 2001; 49:4069.
124. Kulik T, Ferenc J, Matyja H. Mater. Sci. Forum Vols. 1997; 235–238:421.
125. Branagan DJ, Tang YL, Sergueeva AV, Mukherjee AK. Nanotechnology 2003; 14:1228.

126. Coehoorn R, De Mooij DB, De Waard C. J. Magn. Magn. Mater. 1989; 80:101.
127. Honeycomber WK, Bhadeshiah KDH. Steels: Microstructure and Properties, 2nd edn. Halsted Press: New York, 1995; 192.
128. Kappes BB, Meacham BE, Tang YL, Branagan DJ. Nanotechnology 2003; 14:1216.
129. Branagan DJ, Sergueeva AV, Mukherjee AK. Adv. Eng. Mater. 2006.
130. Simunovich D, Schlesinger M, Snyder D. J. Electrochem. Soc. 1994; 141:L10.
131. Misra A, Hirth JP, Kung H. Phil. Mag. A 2002; 82:2935.
132. Misra A, Verdier M, Lu YC et al. Scripta Mater. 1998; 39:555.
133. Schlesinger TE, Cammarata RC, Kim C, Qadri SB, Edelstein AS. Mat. Res. Soc. Symp. Proc. 1989; 18:L295.
134. Weihs TP, Josell D, Gao H. MRS Bull. 2002; 27:39.
135. Josell D, Spaepen F. Acta Metall. Mater. 1993; 41:3017.
136. Mara NA, Sergueeva AV, Misra A, Mukherjee AK. Scripta Mater. 2004; 50:803.
137. Mara NA, Sergueeva AV, Tamayo T, Zhang X, Misra A, Mukherjee AK. Thin Solid Films, 2006.
138. Misra A, Kung H, Hoagland RG. Phil. Mag. 2004; 84:1021.
139. Misra A, Hoagland RG. J. Mater. Res. 2005; 20:2046.
140. Lewis AC, Van Heerden D, Josell D, Weihs TP. JOM 2003; 55:34.
141. Van Swygenhoven H, Budrovich Z, Derlet PM, Hasnaoui A. In Processing and Properties of Structural Nanomaterials. TMS Publications: Warrendale, 2003; 3.
142. Wang YM, Chen MW, Zhou F, Ma E. Nature 2002; 419:912.
143. Zhang X, Wang H, Scattergood RO, Narayan J, Koch CC. Acta Mater. 2002; 50:3527.
144. Zhang X, Wang H, Scattergood RO et al. Acta Mater. 2002; 50:4823.
145. Tellkamp VL, Melmed A, Lavemia E. Metall. Mater. Trans. A 2001; 32:2335.
146. Witkin D, Lee Z, Rodriguez R, Nutt S, Lavernia E. Scripta Mater. 2003; 49:297.
147. Legros M, Elliot BR, Rittner MN, Weertman JR, Hemker KI. Phil. Mag. A 2000; 80:1017.
148. Wang YM, Chen MW, Zhou FH, Ma E. Nature 2002; 419:912.
149. Zhang X, Wang H, Scattergood RO, Narayan J, Koch CC. Acta Mater. 2002; 50:3527.
150. Zhang X, Wang H, Scattergood RO, Narayan J, Koch CC. Acta Mater. 2002; 50:3995.
151. Sergueeva AV, Song C, Valiev RZ, Mukherjee AK. Mater. Sci. Eng. A 2003; 339:159.
152. Yamakov V, Wolf D, Philpot SR, Mukherjee AK, Gleiter H. Nat. Mater. 2002; 1:45.
153. Mukherjee AK. In Creep Deformation: Fundamentals and Applications, RS Mishra (ed.). TMS-AIME: Pittsburgh, 2003; 3.
154. Youngdahl CJ, Weertman JR, Hugo RC, Kung HH. Scripta Mater. 2001; 44:1475.
155. Kymakis E, Alexandou I, Amaratunga GAJ. Synth. Met. (Switzerland) 2002; 127:59.

CHAPTER 4

Nanostructured Supported Catalysts for Low-Temperature Fuel Cells

Suk BonYoon, Baizeng Fang, Minsik Kim, Jung Ho Kim and Jong-Sung Yu

1. INTRODUCTION

A fuel cell is an electrochemical cell which can continuously convert the chemical energy of a fuel and an oxidant to electrochemical energy by a process involving electron transfer during oxidation and reduction reactions with an essentially invariant electrode–electrolytic system [1]. The invention of the fuel cell as an electrical energy conversion system can be traced back to Sir William Grove in the middle of the 19th century. The development of fuel cells, however, lacked a driver during their first century of use, as primary energy sources were abundant, unrestricted and inexpensive. At the beginning of the 20th century, the conversion of chemical energy into electrical energy became more important due to the increase in the use of electricity. The growing need for more efficient energy conversion systems is presently evident as world fossil fuel sources become scarcer and the cost of fuels rises. Moreover, the urgent necessity of reducing pollution in large urban centres imposes the use of non-polluting fuels, like hydrogen and renewable primary fuels, on a large scale. The share of renewable energy from wind, water and sun will increase further, but these sources are not suited to cover the electrical base load due to their irregular availability. Fuel cells on the other hand have proved to be an interesting and very promising alternative, which can realize the promise of clean electric power generation with high efficiency.

This chapter will focus on some recent developments and investigations of supported metal nanoparticles for applications as electrocatalysts for fuel cells, excluding electrolyte membranes and other parts of fuel cells. The structure, dispersity and morphology of the supported catalysts, which are closely related to

Department of Chemistry, Hannam Univerisity, Daejeon, 306–791, Korea

Nanostructured Materials © 2009 Elsevier Ltd.
978-0-08-044965-4 All rights reserved.

utilization and performance, are strongly influenced both by the preparation methods and the carbon supporting methods. In this chapter, the development of low-temperature fuel cell catalysts in recent years is reviewed, mainly focusing on the two most active areas, i.e. catalyst preparation and carbon supporting approaches. A comprehensive review of the literature has not been attempted. Our focus will be on low-temperature fuel cells including only proton and methanol fuelled polymer electrolyte (or proton exchange) membrane fuel cells (H-PEMFCs and DMFCs [direct methanol fuel cells]). The direct formic acid fuel cell (DFAFC) is also occasionally included in low-temperature fuel cells. The term 'PEMFC' has been used often to include the situations where DMFC is also applicable unless otherwise specifically mentioned separately.

1.1 Working Principle of a Fuel Cell

A fuel cell is an electrochemical device for the direct conversion of the free energy of a chemical reaction of fuel (e.g. hydrogen, natural gas, methanol, gasoline, formic acid) and oxidant (oxygen) into electrical energy. Since this process is not governed by Carnot's law, high operating temperatures are not necessarily required to obtain a good efficiency. Apart from being efficient, fuel cells have the advantage of being silent and non-polluting.

A fuel cell consists of the fuel electrode (anode) and the oxygen electrode (cathode), which are interconnected by an ion-conducting electrolyte. The electrodes are electrically coupled to an electricity consumer (e.g. an electric motor) by external metallic lines outside the cell. In this section of the electric circuit, the electric current is transmitted by electrons while it is transferred by means of ions in the electrolyte, which may be protons in acidic electrolytes whereas hydroxyl ions are predominantly involved in alkaline electrolytes. The Gibbs free energy change (ΔG) of a chemical reaction is related to the cell voltage via the following reaction [2]:

$$\Delta G = -nF\Delta E_0 \tag{4.1}$$

where n is the number of electrons involved in the reaction, F is the Faraday constant, and ΔE_0 is the voltage of the cell for thermodynamic equilibrium. The anode reaction in fuel cells is oxidation of fuel, while the cathode reaction is reduction of oxidant. The principle of a fuel cell is illustrated in Figure 4.1 and, for simplicity, a hydrogen/oxygen fuel cell is demonstrated as an example, in which hydrogen is oxidized at the anode according to the following equation:

$$\text{Anode reaction: } H_2 \rightarrow 2H^+ + 2e^- \quad E_0 = 0\text{V} \tag{4.2}$$

Protons enter the electrolyte and are transported to the cathode. Electrons flow into the cathode from the anode through the external circuit during these reactions. Reduction of oxygen takes place at the cathode with incoming electrons according to the following equation:

$$\text{Cathode reaction: } O_2 + 4e^- \rightarrow 2O^{2-} \tag{4.3}$$

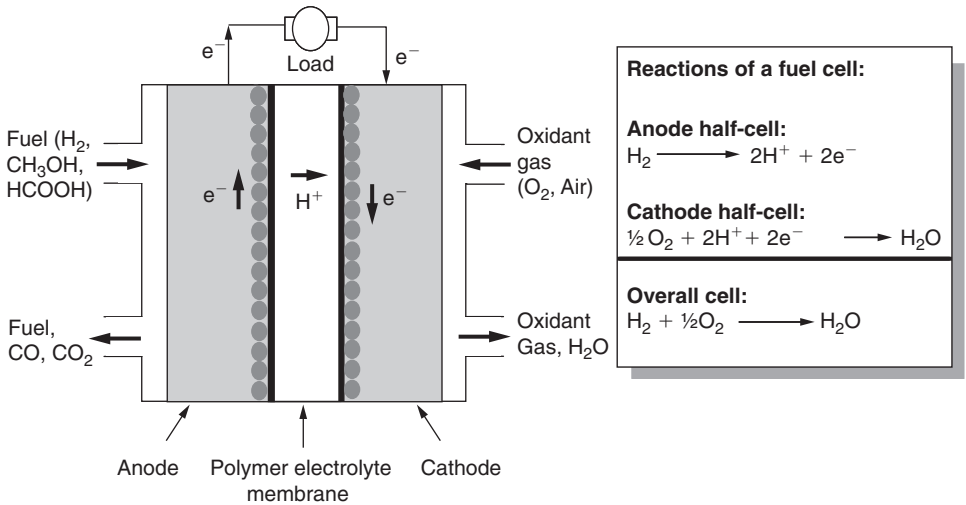

FIGURE 4.1 Schematic of operational principle of a hydrogen/oxygen fuel cell.

The oxygen ions recombine with protons to form water:

$$O^{2-} + 2H^{+} \rightarrow H_2O \tag{4.4}$$

The product of this reaction is water, which is formed at the cathode in fuel cells with proton conducting membranes. Therefore, for hydrogen/oxygen fuel cells, the overall reaction is generation of water by the electrochemical reaction of hydrogen and oxygen:

$$\text{Cell reaction: } H_2 + \tfrac{1}{2}O_2 \rightarrow H_2O \tag{4.5}$$

with $\Delta G = -237\,\text{kJ/mol}$ and $\Delta E_0 = -\Delta G/nF = 1.229\,\text{V}$ (at a pressure of 1 atmosphere and 25°C). The fuel cell reaction is thermodynamically spontaneous and thus proceeds even without any external input, producing positive cell potential. However, the fuel cell reaction is kinetically very slow and thus needs good electrocatalysts for the reaction to take place to the level of practical use.

Electrochemical reactions in a fuel cell are characterized by the thermodynamic equilibrium potential described by the Nernst equation as shown in Eq. (4.1). However, the open circuit voltage is lower than the Nernstian thermodynamic value even under no-current conditions due to the formation of mixed potential and other parasitic processes [3]. When current flows, a deviation from the equilibrium value is called the overpotential (η). One of the reasons for the overpotential is the finite rate of the reaction at the electrodes. Other limiting factors such as mass transport hindrance are present in real fuel cell systems and also contribute to the overpotential. The overpotential loss is much higher at the cathode due to slower kinetics of the oxygen reduction reaction compared with the hydrgen or methanol oxidation.

In addition to the overpotentials, fuel cells experience further losses due to the resistance R_e of the electrolyte in between both electrodes and due to contact resistances and, thus, the cell voltage ΔE_{cell} can be expressed simply as:

$$\Delta E_{cell} = E_c - E_a = \Delta E_0 - (|\eta_a| + |\eta_c| + R_e) \tag{4.6}$$

The cell voltage of a fuel cell is the polarization potential difference between cathode and anode, as illustrated in Figure 4.2a. Both cathode and anode reactions suffer from increasing polarization potential losses with increasing current density; i.e. the absolute values of polarization overpotentials, $|\eta|$, increase with

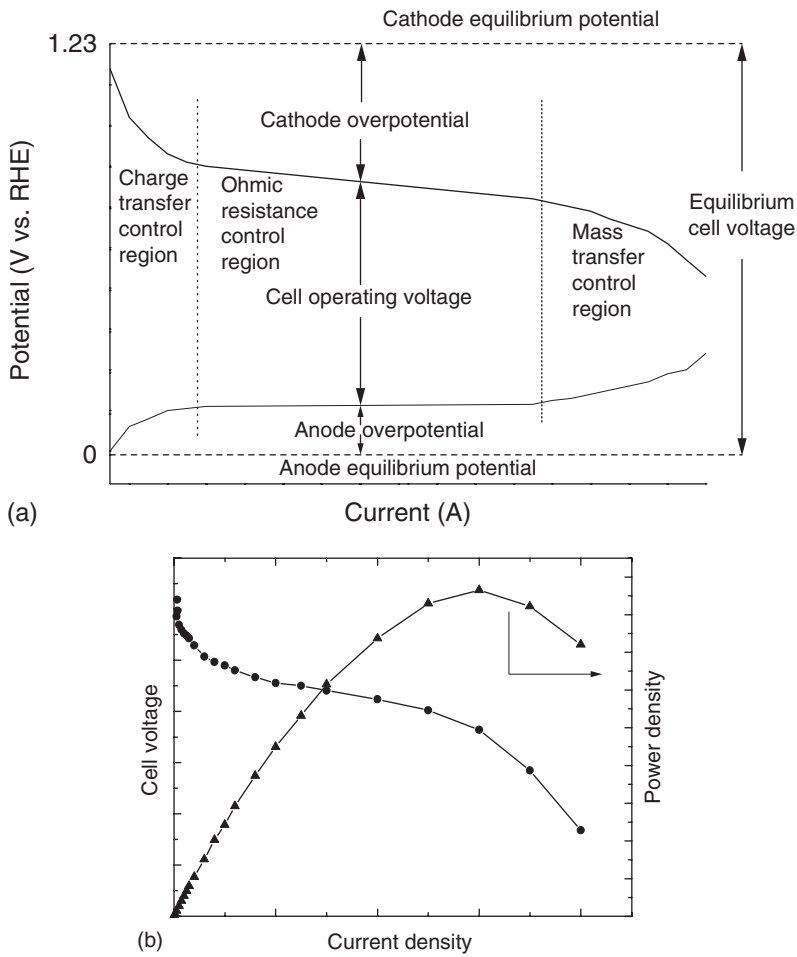

FIGURE 4.2 Schematic illustrations of polarization curves for the electrodes (a) and for the cell (b). Power density plot is derived from the i–v curve for the cell (b).

increasing current density. Thus, the cell voltage decreases with increasing current density.

In addition, in Figure 4.2a, three major polarization regions are also illustrated, where the overall electrode reaction of the cell is under control by distinct reaction mechanisms, namely, charge transfer kinetics, ohmic resistance and mass transport. The voltage decreases sharply in the low current density region of the potential–current curve. This is generally known as charge transfer kinetics polarization or activation polarization mainly because of the sluggish kinetics intrinsic to both oxygen reduction and fuel oxidation at the electrode surface. In particular, the former suffers much slower kinetics loss at the cathode. The slower voltage decrease in the mid-to-high current density region, known as the ohmic polarization region, is due to limitations to proton transport through the electrolyte membrane from the anode to cathode and/or limitations to electron flow in the electrode materials. The deviation from linearity at the higher current density of the polarization curves is due to intrusion of mass transfer effects of fuel, oxidant and their reaction products. From the cell polarization curve a plot of power density against current density can be obtained (Figure 4.2b) and this is a useful representation for comparing different fuel cells.

1.2 Electrode Reactions at Low-Temperature Fuel Cells

Hydrogen-fuelled and methanol-fuelled polymer electrolyte membrane (PEM) fuel cells (PEMFCs and DMFCs) demonstrate great promise as future energy sources for applications such as electric vehicles and electronic portable devices, due to their high power density, relatively quick startup, rapid response to varying loading and low operating temperature [1]. In particular, hydrogen-fuelled PEMFCs produce no emissions such as NO_x, SO_x or CO_2 and are therefore considered to be environmentally friendly. However, the widespread commercialization of PEMFCs has been hindered by a number of factors, including the challenges of implementing a hydrogen infrastructure, the cost of fuel cell manufacturing and limitations in terms of fuel cell performance and durability. For example, the difficulty of on-board storage and refuelling of hydrogen has limited the potential use of hydrogen fuel cells for vehicular applications. One possible source of hydrogen is the on-board generation of hydrogen by steam reforming of hydrocarbons such as methanol. The typical gas composition from steam reforming contains about 1% CO, 24% CO_2 and 75% H_2. Because CO poisons the fuel cell anode, CO removal measures, such as the water–gas shift reaction and/or CO selective oxidation, must be taken to operate a PEMFC with reformate at reasonable efficiency.

Liquid-fuelled fuel cells such as DMFCs and DFAFCs have advantages in terms of fuel storage and infrastructure and low manufacturing cost. However, the crossover of liquid fuels through the polymer membrane poses serious problems such as fuel loss and mixed potentials at the cathode electrode, lowering the overall fuel efficiency. The power density of a DMFC is about a factor of 10 lower than that of a PEMFC operated on hydrogen if the same Pt/Ru anode catalyst loading is used. The situation is similar with the DFAFC. Thus, DMFCs and DFAFCs are considered for applications in small portable devices. To date,

most research has focused on the exploration of new anode and cathode catalysts that can effectively enhance the fuel electro-oxidation and oxygen reduction kinetics.

1.2.1 Fuel oxidation

1.2.1.1 Hydrogen oxidation The oxidation of hydrogen occurs readily on Pt-based catalysts and the reaction at higher current densities is usually controlled by mass-transfer limitations. The oxidation of hydrogen involves the adsorption of the gas onto the catalyst surface followed by a dissociation of the molecule and electrochemical reaction to two hydrogen ions as follows:

$$2\ Pt_{(s)} + H_2 \rightarrow Pt\text{-}H_{ads} + Pt\text{-}H_{ads} \tag{4.7}$$

$$Pt\text{-}H_{ads} \rightarrow H^+ + e^- + Pt_{(s)} \tag{4.8}$$

where $Pt_{(s)}$ is a free Pt site and $Pt\text{-}H_{ads}$ is an adsorbed H-atom on the Pt active site. The overall reaction of hydrogen oxidation is shown in Eq. (4.2).

Operating a fuel cell with pure hydrogen gives the best performance, but pure hydrogen is expensive and difficult to store. Alternatives to pure hydrogen are natural sources such as natural gas, propane or alcohols. However, these alternatives have to be reformed into hydrogen. Hydrogen produced by reforming carbon-based fuels contains small amounts of CO apart from relatively large amounts of CO_2 ($\approx$25%). CO can block the surface of the Pt catalyst and hinder any further reaction. This poisoning effect of CO leads to a decrease of the anode performance, even in the presence of mere traces of CO at concentrations as low as a few parts per million. For example, with 25 ppm CO, the maximum power density obtained in a PEM fuel cell operating at 80°C and 0.24 MPa pressure with anode and cathode noble metal loading of 1 mg/cm^2 drops to 0.3 W/cm^2 from 0.75 W/cm^2 for pure hydrogen [4]. Thus, the search for new electrocatalyst materials with significantly lower affinity to carbon monoxide has been a paramount task for the successful development of more efficient PEMFC systems. An ideal catalyst for the anode would be fully tolerant to CO poisoning, while maintaining its activity for the oxidation of hydrogen. A number of metals are usually added to the Pt catalyst to facilitate oxidative removal of adsorbed CO to CO_2, which can be achieved by oxidizing the CO with oxygen-containing species adsorbed at the surface either from the water in solution or hydroxide ions [5]. Binary Pt-based alloys, such as PtRu, PtOs, PtSn, PtW, and PtMo, have been investigated in order to improve the electro-oxidation activities of fuels. One of the most important and extensively investigated promoters is Ru. Ru is believed to assist in the oxidation of the CO through chemisorbed -OH at potentials as low as 0.25 V [6]. The PtRu alloy with atomic ratio of 1:1 has been found to be the most active binary catalyst and is the state-of-the-art anode catalyst for the low-temperature fuel cell. The oxidation kinetics of fuel is improved significantly reaching a practicable level. PtRu alloys have similar fuel (H_2 or methanol) oxidation kinetics to Pt electrocatalysts [7] but a much higher CO tolerance [8]. The use of Pt alloy is also beneficial in terms of cost reduction by partly replacing Pt with less noble metals

as well as performance improvement. Improvements in the CO tolerance of anode catalysts would reduce the number of fuel-processing steps required and reduce the cost of a fuel cell power plant.

Various types of mechanism have been proposed to explain the enhancement of H_2/CO electro-oxidation on alloying Pt with Ru. Those most often proposed are the bifunctional catalyst effect (promoted mechanism) and the modification of the electronic properties of the Pt (intrinsic mechanism).

(a) Promoted mechanism According to Oetjen et al. [4], the electrocatalysis of H_2 in the presence of CO can be described by the competitive adsorption of hydrogen and carbon monoxide on platinum sites:

$$3Pt + H_2 + CO \rightarrow Pt\text{-}CO_{ads} + 2Pt\text{-}H_{ads} \tag{4.9}$$

The degradation of cell performance is related to CO adsorption, which blocks sites for electro-oxidation of hydrogen. The possibility to eliminate adsorbed CO depends on the following reactions [9]:

$$Pt + H_2O \rightarrow Pt\text{-}OH_{ads} + H^+ + e^- \tag{4.10a}$$

$$Ru + H_2O \rightarrow Ru\text{-}OH_{ads} + H^+ + e^- \tag{4.10b}$$

$$Pt\text{-}CO_{ads} + Pt\text{-}OH_{ads} \rightarrow 2Pt + CO_2 + H^+ + e^- \tag{4.11a}$$

$$Pt\text{-}CO_{ads} + Ru\text{-}OH_{ads} \rightarrow Ru + Pt + CO_2 + H^+ + e^- \tag{4.11b}$$

The reactions (4.10b) and (4.11b) occur at lower potentials than reactions (4.10a) and (4.11a). The oxidation of the strongly adsorbed CO present in the fuel is facilitated in the presence of Ru by supplying oxygen atoms at an adjacent site at a lower potential than that accomplished by pure Pt.

(b) Intrinsic mechanism The intrinsic mechanism is based on electron donation/back donation acting in the Pt-CO bond. This mechanism proposes that the presence of Ru modifies H_2 and CO chemisorption properties, reducing CO coverage with respect to H_2 oxidation sites [10]. The CO adsorption on Pt is stabilized by two simultaneous effects [11]: (i) electron transfer from the CO-filled 5σ molecular orbital to the empty $d\sigma$ band of Pt; (ii) back donation of electrons from the metal $d\pi$ orbital to the empty $2\pi^*$ antibonding orbital of CO. If the Pt-C bonding force is weakened, CO chemisorption on Pt will be suppressed.

Fourier transform infrared spectroscopy studies show a higher frequency for the CO stretch on PtRu, suggesting lower absorption energy for CO on the PtRu alloy than on pure Pt [12], which can be explained by electronic effects on alloying, namely, intra-alloy electron transfer from Ru to Pt [13]. Alloying with Ru causes increased d vacancies, leading to reduced contribution of back-donation of Pt 5d electrons to the CO $2\pi^*$ orbital and, accordingly, the chemisorption of CO on Pt

must depend on donation of CO 5σ electrons, resulting in weakened Pt-C bonding force and suppressed CO coverage [14].

1.2.1.2 Methanol oxidation Few electrode materials have been shown to be capable of adsorbing methanol in acidic media and, of these, only Pt-based materials display sufficient stability and activity to be attractive as catalysts. Many studies have been carried out on methanol oxidation [15–19]. The overall reaction mechanism for methanol oxidation is:

$$CH_3OH + H_2O \rightarrow CO_2 + 6H^+ + 6e^- \qquad E_0 = 0.046\,V \tag{4.12}$$

It is assumed that the oxidation of methanol on Pt-based catalysts proceeds by the adsorption of the molecule followed by several steps of deprotonation. CO is probably formed as an intermediate species during the oxidation of methanol. For the same reason due to CO, a bimetallic alloy consisting of Pt and Ru supported on porous carbon has been one of the major research interests in direct methanol fuel cells.

1.2.1.3 Formic acid oxidation Aqueous solution of formic acid is a potentially attractive fuel for fuel cells. Formic acid, especially when dissolved in water, is relatively benign and non-explosive, which makes it facile in handling and distribution, as compared with hydrogen. It can be activated even on neat platinum and then decomposes to smaller fragments – protons, electrons and CO_2 – at high efficiency as compared with methanol. In addition, oxidation of formic acid commences at less positive potential than methanol oxidation [20] and crossover of formic acid through the polymer membrane is lower than that of methanol [21].

Electrochemical oxidation of formic acid:

$$HCOOH \rightarrow CO_2 + 2H^+ + 2e^- \qquad E_0 = -0.25\,V \tag{4.13}$$

has been investigated on platinum since the early work of Breiter [22] and the results have been reviewed by Parsons and VanderNoot [23] and Jarvi and Stuve [24]. In the last several years, this reaction has been attracting more attention [25,26] because a direct formic acid–oxygen fuel cell with polymer electrolyte membrane has some advantages over a DMFC.

It has been widely accepted in the literature that HCOOH is oxidized to CO_2 via dual path mechanisms [27], where one involves a reactive intermediate (dehydrogenation), the other involving adsorbed CO as a poisoning species (dehydration):

$$HCOOH \rightarrow \text{Reactive intermediate} \rightarrow CO_2 + 2H^+ + 2e^- \qquad \text{(dehydrogenation)}$$

$$HCOOH \rightarrow CO + H_2O \rightarrow CO_2 + 2H^+ + 2e^- \qquad \text{(dehydration)}$$

The dehydrogenation pathway has been considered, since adsorbed -COH or CHO, -COOH, or formate (HCOO) [28], was detected based on electrochemical *in-situ* IR measurements. The dehydration pathway is also accepted as a possible mechanism, which is somewhat similar to that of methanol oxidation, forming adsorbed CO as a reaction intermediate. Formic acid oxidation reaction via dehydration pathway can be expressed as follows [24]:

$$HCOOH + Pt^0 \rightarrow Pt\text{-}CO + H_2O \tag{4.14}$$

$$Pt^0 + H_2O \rightarrow Pt\text{-}OH + H^+ + e^- \tag{4.15}$$

$$Pt\text{-}CO + Pt\text{-}OH \rightarrow 2Pt^0 + CO_2 + H^+ + e^- \tag{4.16}$$

Formic acid adsorbs onto the Pt surface generating an intermediate adsorbed CO species. Adsorbed OH groups are required further to oxidize the adsorbed CO intermediate into the gaseous CO_2 end product as in reformate PEMFC and DMFC.

1.2.2 Oxygen reduction

The oxygen reduction reaction (ORR) on the cathode is a key reaction in the fuel cell system, especially those operating at low temperatures such as PEMFC, DMFC and DFAFC. Pt supported on carbon black is widely used as an electrocatalyst for the oxygen reduction reaction in the PEMFCs due to its high catalytic activity and excellent chemical stability in the fuel cell environment [29]. Generally, H_2 oxidation is kinetically rapid at the Pt anode, while the kinetics of ORR are extremely sluggish even at Pt catalysts, resulting in a significant voltage loss at the Pt cathode, as illustrated in Figure 4.2a [30]. The cathode polarization of the ORR is usually about 0.3–0.4 V under typical PEM fuel cell operating conditions [31]. Alloying of Pt with other transition metals (M) such as Fe, Co, Ni or Cu has been pursued to lower the cost and increase the performance. In addition to lowering the overall catalyst cost, some of the Pt–M alloys have been found to show enhanced catalytic activity compared to pure Pt for oxygen reduction in both phosphoric acid fuel cells and PEMFC [32,33].

The ORR is a multielectron reaction that may include a number of elementary steps involving different reaction intermediates. The overall reaction mechanism still remains unsolved. The ORR has been known to proceed along two parallel pathways in aqueous electrolytes, i.e. a direct 4-electron reduction from oxygen to water and an indirect 2-electron pathway involving the formation of hydrogen peroxide as intermediate. The direct 4-electron pathway is preferable as it does not involve peroxide species in solution and the Faradaic efficiency of the reaction is greater. This pathway, however, consists of a number of steps in which molecular oxygen has to be dissociated at the surface and recombined with hydrogen ions to form water. The adsorption of an oxygen species on the surface of the metal particles is necessary for electron transfer.

The direct 4-electron pathway is as follows:

$$O_2 + 4H^+ + 4e^- \rightarrow 2\ H_2O \tag{4.17}$$

and the indirect 2-electron pathway is as follows:

$$O_2 + e^- \rightarrow O_2^- \tag{4.18}$$

$$O_2^- + H_2O \rightarrow HO_2^- + OH \tag{4.19}$$

$$OH + e^- \rightleftharpoons OH^- \tag{4.20}$$

Detailed mechanisms of these steps for the oxygen reduction reaction on different catalysts can be found elsewhere [34,35].

2. SUPPORTED CATALYSTS

Great progress has been achieved during the last decade in fuel cell science and technology, especially in some application areas such as portable, transportation and stationary power sources [36]. However, the commercialization of low-temperature fuel cells is still hindered by some technical challenges. The major challenge among them is sluggish electrochemical kinetics even on some state-of-the-art anode and cathode catalysts. Since up to now only platinum is known to have the ability to activate and break H–H and C–H bonds in the low reaction temperature range of 25 to 130°C, all presently available anode catalysts contain significant amounts of Pt [18,37]. However, the high price and the limited world supply of platinum poses serious problems for a widespread commercialization of the fuel cell technology. These difficulties have created enormous interest in the search of less expensive, more efficient electrocatalysts as well as in lowering the catalyst loading.

With regard to new catalyst exploration, performance improvement including activity, reliability and cost reduction are the two major challenges. For catalyst performance improvement, an alloying approach including noble and non-noble metals for the development of new electrocatalysts is one of the R&D directions. The other is a supporting approach. Rapid development of nanotechnology, especially in the area of the synthesis of carbon nanomaterials will create more stable and active supported catalysts by helping to improve the utilization efficiency of catalysts. Supported electrocatalysts for low-temperature fuel cells were reviewed recently [38,39]. The supported catalysts are believed to be the most promising materials for catalysis in PEMFCs such as H_2, CH_3OH or HCOOH fuelled fuel cells. Reduction of the catalyst loading through increasing Pt utilization is one of the research avenues for catalyst cost reduction. The catalytic activity of the Pt-based catalysts is strongly dependent on the composition, structure, morphology, particle size, alloying degree [40–47] and catalyst supports [48–55]. The synthesis of these metal particles as electrocatalytic materials with uniform size and good dispersion on the carbon supports has thus become of paramount importance.

Alloying and supporting approaches enable both performance increase and cost reduction for fuel cells by dramatically reducing the Pt content in the catalysts without performance compromise.

2.1 Catalyst Preparation

In recent years, various catalyst preparation methods have been developed for the generation of electrode catalysts with high activity and low cost. Methods for preparation of catalysts can be simply classified into two main categories, i.e. physical and chemical methods. Generally, nanoparticles produced by a physical method, i.e. atomization of metals in a vacuum by thermal evaporation or sputtering, do not have good penetration into the catalyst support (substrate), especially in the case of high loading of catalyst, resulting in uneven dispersions of catalyst particles and low utilization of catalysts. Chemical methods, in contrast, can generate catalyst nanoparticles with a high dispersion on the catalyst support and even with controllable particle size, and thus become very popular methods for preparation of supported catalyst nanoparticles. The synthesis of mixed metal nanoparticles is a complex problem because of the composition control in addition to size and size-distribution control. A good control over the size, composition and shape of nanoparticles should be pursued for preparation of catalyst for low-temperature fuel cells. Some innovative and cost-effective preparation methods have been developed and show promise for reaching performance optimization by controlling synthetic procedures and conditions. Three main chemical synthetic methods have been demonstrated for preparing carbon-supported catalysts:

1. impregnation method
2. colloidal method, and
3. microemulsion method.

All of these include a reduction step for forming nanoparticles and a deposit step for dispersing the catalyst onto the carbon particles, as summarized schematically in Figure 4.3.

2.1.1 Impregnation method

Impregnation means penetration and soaking up of a dissolved metallic catalyst precursor into a support prior to its reduction to metallic nanoparticles. The procedure is shown schematically in the top flow line of Figure 4.3. During the impregnation step, the catalyst precursor mixes with the catalyst support, typically porous or nanostructured carbon, and penetrates into its pores. Among the three methods mentioned above, the impregnation method is a simple, straightforward and the most frequently used chemical approach for Pt-based catalyst preparation.

The catalyst support plays a key role in terms of penetration and wetting of the precursor during this step. The reduction step can be chemical or electrochemical and can be conducted in liquid phase or gas phase. Common reducing agents such as $Na_2S_2O_3$, $Na_4S_2O_5$, N_2H_4, $NaBH_4$, HCOOH, ethylene glycol and

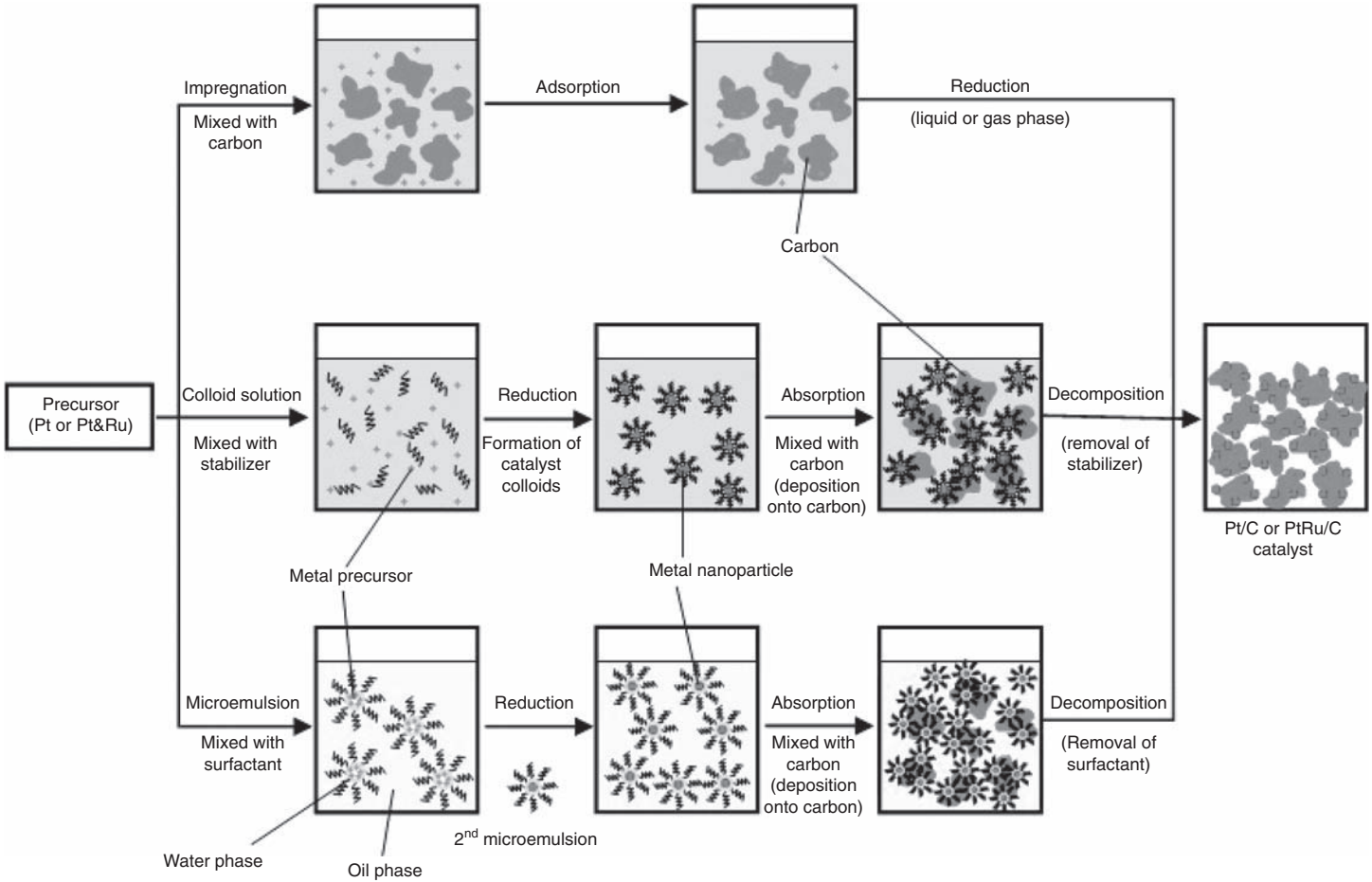

FIGURE 4.3 Illustration for synthetic approaches of supported catalysts using impregnation, colloidal and microemulsion methods.

formaldehyde are used for liquid-phase reduction, and flowing H_2 at high temperature (>300°C) for gas-phase reduction. The catalyst support confines the growth of catalyst particle size during the reduction step. Various synthetic routes and synthetic conditions, such as the metal precursor nature, the reduction method, the pH and heating temperature, have been taken and investigated in the impregnation method for preparation of catalysts [53–76]. Table 4.1 summarizes some typical, distinct synthetic routes of the impregnation method using various catalyst precursors, supports and reduction step for the preparation of Pt and its alloy catalysts.

Catalyst precursors also play key roles in terms of catalytic activity of the supported catalyst. Metal chloride salts (e.g. H_2PtCl_6 and $RuCl_3$), commonly used as precursors in the impregnation methods due to their easy availability, however, might lead to chloride poisoning, resulting in relatively lower catalytic activity and stability of the chloride-salt derived catalyst. For this reason, chloride-free synthetic routes of the impregnation method have been suggested, using metal nitrate/nitrite salts such as $Pt(NH_3)_2(NO_2)_2$ and $RuNO(NO_3)x$ [56], carbonyl complexes such as $Ru_3(CO)_{12}$ [60] and metal sulphite salts such as $Na_6Pt(SO_3)_4$ and $Na_6Ru(SO_3)_4$) [61] as metal precursors in the impregnation method, respectively. These chloride-free routes have been proven effective for higher dispersion and better catalytic activity in comparison with the conventional Cl-containing route. A current density of 8, 32 and 57 mA/mg has been observed for CH_3OH oxidation at 500 mV (vs. RHE) and at 60°C, respectively for carbon-supported $Pt_{50}Ru_{50}$ catalysts using chloride, nitrate and carbonyl as precursor salts [56]. Carbon-supported $Pt_{50}Ru_{50}$ catalyst through carbonyl complexes as precursor also showed higher catalytic activity [60].

In addition, reaction time, kinetics and mass-transfer of the reducing agent also affect the growth of the catalyst particles. Hydrogen can penetrate better into the micropores of the porous support. However, elevated temperature and inert atmosphere are required during the hydrogen reduction step, which may result not only in high costs for the preparation of catalysts, but also in the increase in particle size due to particle aggregation. It is also unfavourable for synthesis of catalysts on a large scale. The synthetic routes with liquid-phase reduction possess great possibility for scaling up preparation of supported catalysts, which might lower the cost for the production of catalysts.

Reaction time and thus the size of the catalyst particle can be somewhat controlled through the amount of current passed, if an electrochemical reduction route is taken [73]. However, three-dimensional homogeneity is difficult to realize because the nucleation and growth of catalyst particles depend greatly on the connectivity and uniformity of the electron-conductive network of the porous support and hence are restricted to the charged interface.

The catalyst support also plays a very important role in determining the size and dispersion degrees of catalyst and contributes a lot to catalytic activity. Ordered porous carbons with tunable pore sizes have been shown to be very effective in improving the catalytic activity to CH_3OH oxidation [74, 75]. The supporting approach will be discussed in further detail in the section on Catalyst Supports.

Table 4.1 Selected carbon-supported catalysts prepared through various routes of the impregnation method for low-temperature fuel cell applications

Catalyst	Precursor/ reducing agent	Support/ loading	Particle size	Activity	Ref.
Ni	$Ni(OH)_2/H_2$	VC/10%	15 nm	lower activity to ORR than Pt	64
Co	$Co(OH)_2/H_2$	VC/10%	53 nm	Lower activity to ORR than Pt	64
Pt	H_2PtCl_6/HCHO	MWCNT/ 10%	2–5 nm	14.7 mA/mg at 700 mV(vs. DHE, DMFC, 60°C)	67
Pt	$H_2PtCl_6/NaBH_4$	MCMB/ 12%	3–5 nm	lower CH_3OH oxidation overpotential than VC	66
Pt	$Pt(NO_3)_2$/HCHO	VC/20%		500 mA/cm^2 at 630 mV (PEMFC, 80°C)	65
Pt	$H_2PtCl_6/NaBH_4$	CNF/20%		500 mA/cm^2 at 645 mV (PEMFC, 80°C)	70
Pd	$PdCl_2$/HCHO	VC/20%		500 mA/cm^2 at 265 mV (PEMFC, 80°C)	65
Pd	$PdCl_2/NaBH_4$	VC/20%		372 mA/cm^2 at 390 mV (DFAFC, 30°C)	72
$Pt_{50}Pd_{50}$	$Pt(NO_3)_2$, $PdCl_2$/HCHO	VC/20%	1.4–2.0 nm	500 mA/cm^2 at 620 mV (PEMFC, 80°C)	65
$Pt_{50}Ru_{50}$	H_2PtCl_6, $RuCl_3/NaBH_4$	VC/20%	2.7–4.7 nm	4 mA/cm^2 at 468 mV (2 M CH_3OH, RT)	63
$Pt_{50}Ru_{50}$	$Pt(NH_3)_2(NO_2)_2$/ $RuNO(NO_3)_x/H_2$	VC/30%	2.6–3.6 nm	32 mA/mg at 500 mV (1 M CH_3OH, 60°C)	56
$Pt_{50}Ru_{50}$	$(\eta\text{-}C_2H_4)(Cl)Pt(\mu\text{-}Cl)_2$-Ru(Cl)	VC/30%	3.5–5.4 nm	120 mA/cm^2 at 400 mV (1 M CH_3OH, 90°C)	62

(η^3:η^3-2,7-dimethyloctadienediyl)/H_2					
$Pt_{50}Ru_{50}$	$Na_6Pt(SO_3)_4$, $Na_6Ru(SO_3)_4/H_2$	VC/50%	2 nm	60 mA/mg at 400 mV(1 M H_2SO_4 + 1.5 M CH_3OH, 65°C)	61
$Pt_{50}Ru_{50}$	H_2PtCl_6, $RuCl_3/NaBH_4$	VC/50%	3–15 nm	90 mA/mg at 500 mV(1 M H_2SO_4 + 1.5 M CH_3OH, 65°C)	61
$Pt_{50}Ru_{50}$	$[Pt(CO)_2]_x$,$Ru_3(CO)_{12}/H_2$	VC/50%	2.5 nm	85 mA/mg at 415 mV(1 M H_2SO_4 + 1.5 M CH_3OH, 65°C)	60
$Pt_{50}Ru_{50}$	H_2PtCl_6, $RuCl_3/NaBH_4$	VC/60%	2–3 nm	117 mW/cm^2 (DMFC, 2 M CH_3OH, 70°C)	75
$Pt_{50}Ru_{50}$	H_2PtCl_6, $RuCl_3/NaBH_4$	OC/80%	2–3 nm	175 mW/cm^2 (DMFC, 2 M CH_3OH, 70°C)	75
$Pt_{50}Ru_{50}$	H_2PtCl_6, $RuCl_3/NaBH_4$	POBPC/80%	2–3 nm	190 mW/cm^2 (DMFC, 2 M CH_3OH, 70°C)	53
$Pt_{50}Ru_{50}$	H_2PtCl_6, $RuCl_3/NaBH_4$	CNF/80%	3.4 nm	199 mW/cm^2 (DMFC, 2 M CH_3OH, 70°C)	54
$Pt_{50}Ru_{50}$	H_2PtCl_6, $RuCl_3/NaBH_4$	HCMS/80%	2–3 nm	214 mW/cm^2 (DMFC, 2 M CH_3OH, 70°C)	76
$Pt_{77}Ru_{17}Mo_4W_2$	H_2PtCl_6, $RuCl_3$, $MoCl_5$,	Glassy carbon	3.4 nm	higher activity to CH_3OH oxidation than $Pt_{50}Ru_{50}$	69
$(NH_4)_6W_{12}O_{39}/NaBH_4$					
$Pt_{60}Mo_{40}$	H_2PtCl_6, $(NH_4)_6W_{12}O_{39}$/HCHO	VC/20%	3–3.2 nm	higher ethanol oxidation potential than $Pt_{60}Ru_{40}$	68

Notes: 1. VC, MWCNT, MCMB, CNF, OC, POBPC, HCMS stand for Vulcan CX-72 R, multiwalled carbon nanotube, mesoporous carbon microbeads, carbon nanofibre, ordered porous carbon, periodically ordered bimodal porous carbon and hollow core mesoporous shell carbon, respectively. 2. All electrode potentials refer to reversible hydrogen electrode (RHE) potential except that stated otherwise. DHE stands for dynamic hydrogen reference electrode.

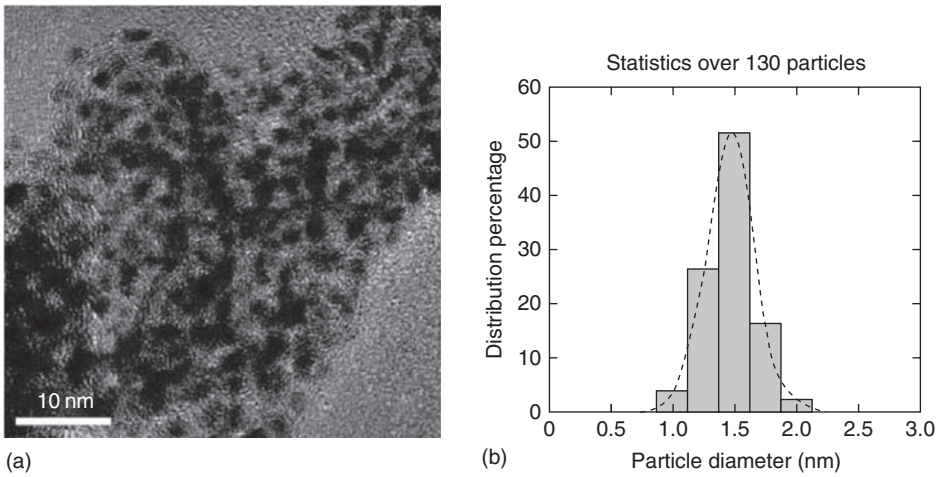

FIGURE 4.4 (a) HRTEM images and (b) statistics histogram of the particle size distribution for $Pt_{40}Ru_{20}$/C electrocatalyst prepared by the impregnation method (from [78]).

In comparison with the other two methods, the impregnation method is simple and easy to operate and scale up the preparation of catalyst. However, in general, it has some difficulties in the control of catalyst nanoparticle size and distribution especially in the case of catalyst support without a well-defined narrow pore size distribution, resulting in relatively poor dispersions of catalyst nanoparticles in the support and low utilization and catalytic activity of the catalyst host [59,77]. Despite the disadvantages in synthesis by the impregnation method, a highly dispersed Pt-Ru/C catalyst can still be obtained through careful control of appropriate preparation conditions. Yang et al. [78] recently prepared a highly dispersed Pt-Ru/C catalyst with metal loading as high as 60 wt% and a narrow size distribution (1.5±0.5 nm, as shown in Figure 4.4) even using chlorine containing precursors. More recently, Chai et al. also reported the preparation of highly dispersed $Pt_{50}Ru_{50}$ catalyst supported on periodically ordered bimodal porous carbon [53] and hollow core/mesoporous shell carbon [76] with a narrow size distribution (2.5±0.5 nm) and even with metal loading as high as 80 wt%.

2.1.2 The colloidal method

The colloidal method has been also extensively explored for the preparation of Pt-based fuel cell catalysts, which provides catalyst with tailored nanoparticle size and a narrow distribution [79–81]. This method usually includes the following three common steps:

1. preparation of metal containing colloids, e.g. organometallic colloids or metal oxide colloids;
2. chemical reduction of the colloids; and
3. deposition of the reduced colloids onto the carbon support.

Typical synthetic procedures of the colloidal method are illustrated schematically in the second flow line of Figure 4.3. However, there are some distinct synthetic routes with different preparation conditions in the steps, which are summarized in Table 4.2.

In the presence of a protective agent (i.e. NR41, PPh_3, PVP, SB12 or PVA), colloidal catalyst metal nanoparticles are formed by chemical reduction of catalyst precursor in the organic medium or aqueous medium. A narrow size distribution is achieved through the stabilization of the colloidal metal nanoparticles either by steric hindrance or by electrostatic charges. In the case of adsorbed ions or charged colloids, merging into large particles is limited by the electrostatic repulsion of like charges. On the other hand, steric stabilization can be provided by coating the metal core with organic chain molecules [82–83]. Although the colloidal method can provide a narrow size distribution of metal nanoparticles, the major drawback is the presence of the protecting agent, which may also hinder the catalytic function of the nanoparticles. The organic protecting shell can be removed by washing in an appropriate solvent or by decomposition at elevated temperature in an inert atmosphere. Before the removal of the protecting agent, adsorption into a protecting catalyst support is necessary to prevent agglomeration into larger metal particles.

As mentioned above, precursors of PtRu catalyst synthesized using the colloid method can be metal oxide colloids or organometallic colloids. Watanabe et al. prepared PtRu catalyst through a metal oxide colloid route in aqueous media, followed by reductive annealing under a stream of hydrogen gas [84,85]. The resulting PtRu catalyst had a much higher specific surface area (ca. $80\,m^2\,g^{-1}$), which is about three times larger than that obtained by the conventional method, i.e. the impregnation method [85]. However, the particle growth and agglomeration control seemed to present problems in using the metal oxide colloid route. Alternatively, Bönnemann et al. [86–90] developed an organometallic colloid route by stabilizing the Pt/Ru metal particles with organic molecules, resulting in easy control of particle size and distribution. This route mainly consists of three steps, i.e. pre-forming surfactant-stabilized Pt–Ru colloids (e.g. PtRu-$N(oct)_4Cl$ colloids), adsorbing the colloids on high-surface area carbon and, finally, removing the organic stabilizer shell by thermal treatment in an O_2 atmosphere and H_2 atmosphere, respectively. By this route, PtRu catalysts with well-defined, completely alloyed particles and a very narrow particle size distribution (<3 nm) were obtained and showed activity of around 70 mA/mg (PtRu) at 500 mV (versus RHE) in 0.5 M CH_3OH + 0.5 M H_2SO_4 at 60°C, which is comparable with that of the state-of-art commercially available catalyst at similar testing conditions (80 mA/mg (PtRu)) [90].

A simple modified route using organoaluminium molecules (i.e. $Al(CH_3)_3$) as both the reductive agent and chloride-free stabilizer was developed to produce PtRuAl/C catalyst with narrow size distribution (1.3 ± 0.4 nm) and good thermal stability and durability [91]. However, this catalyst showed slightly lower electrocatalytic activity to methanol oxidation than PtRu (NR_4)/C catalyst due to residual aluminium oxide on the catalyst surface. Therefore, although the colloidal method can prepare metal nanoparticles with a narrow size distribution, one

Table 4.2 Typical carbon-supported catalysts synthesized by different preparation routes of the colloidal method

Catalyst	Precursor/reducing agent	Support/loading	Particle size/stabilizer	Activity	Ref.
$Pt_{50}Ru_{50}$	H_2PtCl_6, $RuCl_3/H_2O_2 + H_2$/none	Vulcan XC-72/30 wt%	3–4 nm	200 mA cm^{-2} at 400 mV (vs. RHE)	[85]
$Pt_{50}Ru_{50}$	$PtCl_2$, $RuCl_3/NOct_4[BEt_3H]$/itself	Vulcan XC-72/20 wt%	1.5±0.4 nm	20 mA mg^{-1} at 400 mV (vs. RHE)	[90]
$Pt_{50}Ru_{50}$	$Pt(acac)_2$, $Ru(acac)_3/Al(CH_3)_3$/itself	Vulcan XC-72/20 wt%	1.5±0.5 nm	27 mA mg^{-1} at 400 mV (vs. RHE)	[91]
$Pt_{50}Ru_{50}$	$Pt(dba)_2$,$Ru(COD)(COT)(C_8H_{17})_4$ NDCTA/itself	Vulcan XC-72/30 wt%	<2 nm	18 mA mg^{-1} at 400 mV (vs. RHE)	[92]
PtRu	H_2PtCl_6, $RuCl_3$/methanol/SB12	Vulcan XC-72/20 wt%	2–3.5 nm	700 mA at 400 mV	[93]
$Pt_{67}Ru_{33}$	H_2PtCl_6, $RuCl_3$/1-propanol/PVP	Ketjen black/27 wt%	2–3.2 nm	220 mA mg^{-1} at 400 mV	[94]
$Pt_{50}Ru_{50}$	H_2PtCl_6, $RuCl_3$/ethylene glycol/itself	Vulcan XC-72/20 wt%	3–6 nm	1.1 mA at 400 mV (vs. SCE)	[96]
PtRu	$Pt(acac)_2$, $Ru(acac)_3$/1,2-hexadecanediol/oleylamine, oleic acid	Vulcan XC-72/30 wt%	2.4±0.1 nm	32.9 mW cm^{-2} at 0.21 V (vs. SCE)	[99]
PtRuIr (1:1:0.2)	H_2PtCl_6, $RuCl_3$, H_2IrCl_6/ethylene glycol/sodium citrate	MWNT/20 wt% (Pt)	1–1.5 nm	27.3 mW cm^{-2} at 0.7 V	[100]
$Pt_{67}Ru_{33}$	H_2PtCl_6, $RuCl_3$/ethylene glycol/itself	Vulcan XC-72/30 wt%	2.0±0.3 nm	300 mA cm^{-2} at 400 mV	[101]
Pt_xRu_y	$PtCl_2$, $RuCl_3/NOct_4[BEt_3H]$/itself	Vulcan XC-72/30 wt%	<2 nm	30 mW cm^{-2} at 50°C, 110 mW cm^{-2} at 110°C	[102]
PtRu/Pt_3Sn	$PtCl_2$, $RuCl_3$ or $SnCl_2/NOct_4[BEt_3H]$/itself	Vulcan XC-72/20 wt%	1.5±0.4 (PtRu) nm 2.2±0.4 (PtSn) nm	0.35 mA mg^{-1} at 347 mV (vs. RHE)	[103]

major drawback is the presence of residual protective agent, degrading the catalytic activity of the nanoparticles. Due to its flexibility of the preparation method, Bönnemann's route is favourable for controlling the composition, size and shape of the catalyst and hence it possesses some advantages over other synthetic routes of the colloidal method [92]. However, the organometallic colloid route is still not favourable in practical applications due to the complexity of the preparation steps and the relatively high cost.

Other colloid routes using various reducing agents, organic stabilizers or shell-removing approaches have also been developed in recent years. Wang and Hsing [93] and Kim et al. [94] prepared PtRu catalysts based on an alcohol reduction method using dodecyldimethyl(3-sulpho-propyl) ammonium hydroxide (SB12) and polyvinylpyrrolidone (PVP) as a stabilizer, respectively. Bensebaa et al. [95] reported the preparation of PtRu nanoparticles using ethylene glycol as both solvent and reducing agent and PVP as a stabilizer. The microwave method was used to remove the organic shell from these colloids as well as to obtain the alloyed bimetallic particles instead of separate monometallic particles. Due to the difference in the reduction temperature of both metals, the microwave method has an advantage over conventional heating [95,96]. The electrocatalytic performance of supported platinum nanoparticles prepared with this method has been reported recently [96].

Recently, an alternative route without using any protecting agents has been developed to prepare metal nanoparticles. Wang et al. reported the preparation of a number of metal nanoparticles, especially for platinum, by using sodium hydroxide dissolved in ethylene glycol as solvent. Importantly, ethylene glycol used to dissolve the unprotected Pt nanoclusters is then used for the synthesis of various Pt core nanoclusters [97]. Also, Bock et al. [98] prepared PtRu/C catalysts ($0.7 \approx 4$ nm, as shown in Figure 4.5) using ethylene glycol as both the solvent and reducing agent. In this work, the formation of PtRu catalysts mainly involves the reduction of respective precursor salts by the solvent itself, ethylene glycol, which is oxidized in the reaction. The metal ions are reduced absorbing the electrons produced in this oxidation process. Initial studies showed that particular PtRu catalysts prepared in this work display better CH_3OH electro-oxidation activities than those of commercial catalysts tested.

Most recently, Lee et al. [99] prepared colloidal PtRu nanoalloy from the co-reduction of $Pt(acac)_2$ and $Ru(acac)_3$ (acac = acetylacetonate) by 1,2-hexadecanediol in octyl ether as a reducing agent in the presence of oleylamine and oleic acid as surfactants. Protecting surfactants could be removed by acetic acid treatment without altering the overall catalyst morphology and composition. The average diameter of 2.4 nm was accompanied by a relatively narrow particle size distribution, as shown in Figure 4.6. The electrochemical experiments exhibited that the synthesized PtRu/VC catalyst had remarkably higher catalytic activity toward methanol oxidation reaction compared to that of commercially available PtRu catalysts. Liao and his coworkers [100] have used acetone as the solvent, ethylene glycol as the reducing agent, citrate as a complexing agent and stabilizer, multiwall carbon nanotubes as the support and Ir as the promoter, to form highly active PtRuIr/CNT catalysts. The particle size has

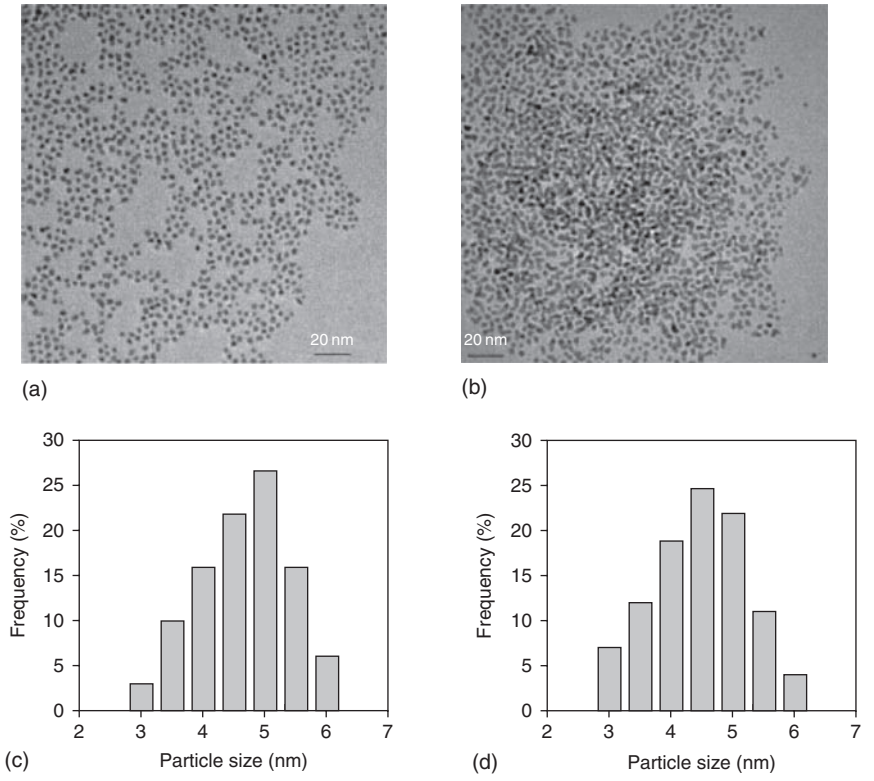

FIGURE 4.5 TEM images of the synthesized (a) Pt and (b) PtRu colloid catalysts. Histograms of particle size distributions for the synthesized (c) Pt and (d) PtRu colloids (from [98]).

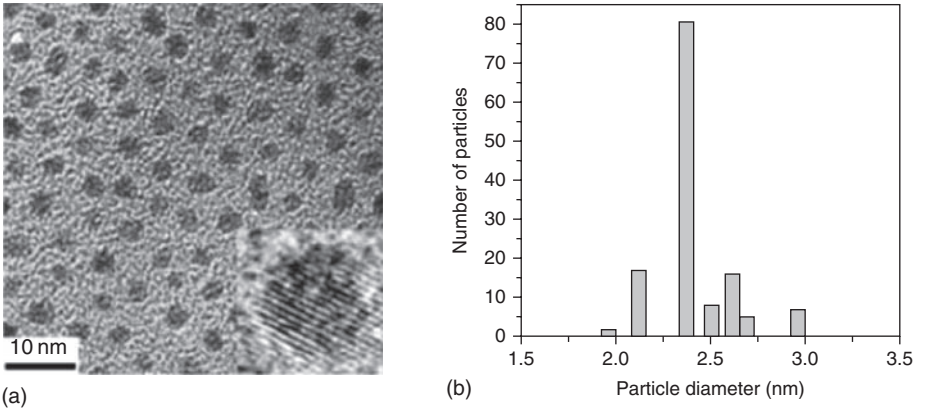

FIGURE 4.6 (a) TEM image of the colloidal PtRu nanoalloy (the inset represents the HRTEM image). (b) Histograms of the particle distributions for colloidal PtRu nanoalloy as measured from 180 particles in TEM micrographs (from [99]).

been found to be <1 nm and the catalyst has shown excellent activity toward methanol oxidation.

In comparison with the impregnation method, the colloidal method has the advantage of preparing catalyst with tailored nanoparticle size and a narrow size distribution; however, this method has also some intrinsic disadvantages, being complex, time-consuming and of high cost, which will bring difficulty for scaling up.

2.1.3 Microemulsion method

A microemulsion consists of nanosized water droplets surrounded by an organic phase and stabilized by a surfactant. If a metal precursor is contained within the water droplets, the addition of a reducing agent may render the formation of nucleus. The growing of such nucleus would be somehow hindered by the surfactant rendering metal particles of a controlled size. A major advantage of the microemulsion technology is its potential for the synthesis of bi-metallic particles at low temperature [104]. The interest in preparing nanoparticles using microemulsions has increased since Boutonnet et al. [105] successfully synthesized platinum nanoparticles by using water/oil (w/o) microemulsions. Many kinds of nanoparticles have been prepared in w/o microemulsions, including metals [106–108], metal oxides and hydroxides [109–111], metal sulphides and selenides [112,113], metal borides [114], metal carbonates [115] and organic polymers [116]. A microemulsion method is generally defined as a system composed of a mixture of water or brine, hydrocarbon(s) and amphiphilic compound(s) in the form of a thermodynamically stable and optically isotropic solution [117]. The term amphiphile refers to surfactants as well as co-surfactants, such as a short-chain alcohol. A transparent microemulsion can be formed as droplets of oil-swollen micelles dispersed in water (known as oil-in-water (o/w) microemulsions), or water-swollen micelles dispersed in oil (known as water-in-oil (w/o) microemulsions). Between the o/w and w/o microemulsion regions, there may exist bicontinuous microemulsions, where oil and water domains are randomly interconnected to form sponge-like nanostructures. In any case, the size of nanostructures in microemulsions may range from about 5 to 70 nm. Due to these unique nanosized structures, microemulsion processing is deemed to be a novel method for producing nanostructural materials, such as polymers, inorganic materials and inorganic/polymer nanocomposites [118,119]. Water-in-oil microemulsions are transparent, isotropic, thermodynamically stable liquid media with nanosized water droplets dispersed in a continuous oil phase and stabilized by surfactant molecules at the water/oil interface. The surfactant-stabilized water pools provide a microenvironment for the preparation of a nanoparticle by exchanging their contents via the fusion–redispersion process and preventing the excess aggregation of particles. As a result, the particles obtained in such a medium are generally very fine and monodispersed [120].

In this method, the first step is the formation of metal nanoparticles through a w/o microemulsion reaction, followed by a reduction step. Here, the microemulsion serves as a nanoscaled reactor in which the chemical reaction takes place. The microemulsion is a nanoscaled aqueous liquid droplet containing a noble metal precursor. The droplets are engulfed by surfactant molecules and

uniformly dispersed in an immiscible continuous organic phase. The reduction step can be carried out either by adding a reducing agent (e.g. N_2H_4, HCHO or $NaBH_4$) into the microemulsion system, or by mixing it with another reducing agent-containing microemulsion system. As a result, the reduction reaction is confined to the inside of the nanoscaled microemulsion and the formed metal particle sizes can be easily controlled by the magnitude of the microemulsion size. The surfactant molecules can function as protective agents to prevent the metal nanoparticles from agglomerating. Control of particle size has been achieved by the presence of protective agents such as soluble polymers and organic ligands or by the adsorption of anions on the particle surface. It has been shown that the size, structure and composition distribution of the resultant particles depends on the preparation conditions. The removal of surfactant molecules can be easily carried out by heat-treating high-surface-area carbon supported nanoparticles [121].

Therefore, catalyst preparation methods that can offer a high degree of alloy homogeneity with small particle size and high surface area at moderate temperatures are needed. In this context, colloidal assemblies such as reverse micelles (w/o microemulsion) offer an attractive approach to prepare multimetallic alloy compositions with a high degree of homogeneity and good control of particle size. Surfactant stabilized reverse micelles not only serve as microreactors for chemical reactions but also as steric stabilizers to inhibit particle growth. The main advantage of the microemulsion method is the ability easily to control the particle size by varying the synthesis conditions [122]. The microemulsion method has been used to synthesize a wide variety of nanoparticles. Due to the specific structure of a microemulsion, it was expected to be a suitable environment for producing small metal nanoparticles of narrow size distribution, as well as bimetallic particles of controlled composition [123]. With the promise of a better control of particle size, shape, size distribution and chemical composition, the preparation of nanoparticles with w/o microemulsion has attracted increasing attention but systematic investigation is needed [124]. Water-in-oil microemulsions have been used to synthesize a wide variety of nanoparticles with narrow size distribution and high surface area [125–128]. The low synthesis temperature associated with the microemulsion method can help to keep the grain size small and thereby to achieve better catalytic activity.

For example, PtRu/C catalysts obtained by a reverse microemulsion method have been found to exhibit higher activity than the commercial PtRu/C for methanol oxidation in a mixture of sulphuric acid and methanol [129] and activity comparable to the commercial PtRu/C for hydrogen oxidation in proton exchange membrane fuel cells (PEMFCs) [130]. In addition, the microemulsion-derived PtRu/C catalysts have been found to show higher electrocatalytic activity for methanol oxidation than the emulsion-derived PtRu/C electrocatalysts [131]. However, the evaluation of the PtRu/C catalysts prepared by the microemulsion method in practical DMFC conditions is not available in the literature to the best of our knowledge. Additionally, no information is available on the influence of synthesis conditions such as the ratio of surfactant to water and heat treatment on the electrochemical performance and the optimization of the particle size of the PtRu catalysts. The advantage of the microemulsion method is the ability to

control particle size easily by varying the synthesis conditions [132]. However, and in spite of the fact that it is a very easy and reproducible technique, very few works have been devoted to the use of this method to synthesize nanoparticles to be used as electrocatalysts [129,130,133]. From an electrochemical point of view, the key problem of the synthesis of nanoparticles in microemulsions is that the nanoparticles obtained are coated with a film of surfactant molecules that blocks the surface sites, modifying their surface properties and, particularly, their electrocatalytic properties. For that reason, in previous works, we have developed some procedures to clean, without surface damage or composition changes, Pt, Pd and Pt/Pd alloy nanoparticles prepared with this methodology [130,133–135]. Moreover, this method can be very easily scaled-up for industrial applications. The microemulsion method can be used for synthesizing PtRu nanoparticles of different compositions with electrocatalytic activity very similar to that obtained with other nanoparticles and bulk alloys synthesized using more complicated procedures. The method allows a very controlled change of composition still keeping constant the dimension of the nanoparticles (Figure 4.7). Given the characteristics of the synthesis, the scale-up of the process for obtaining bigger amounts of nanoparticles for industrial use should be easy. A controlled procedure allows cleaning the surface of the particles avoiding contamination and change of the surface structure [136].

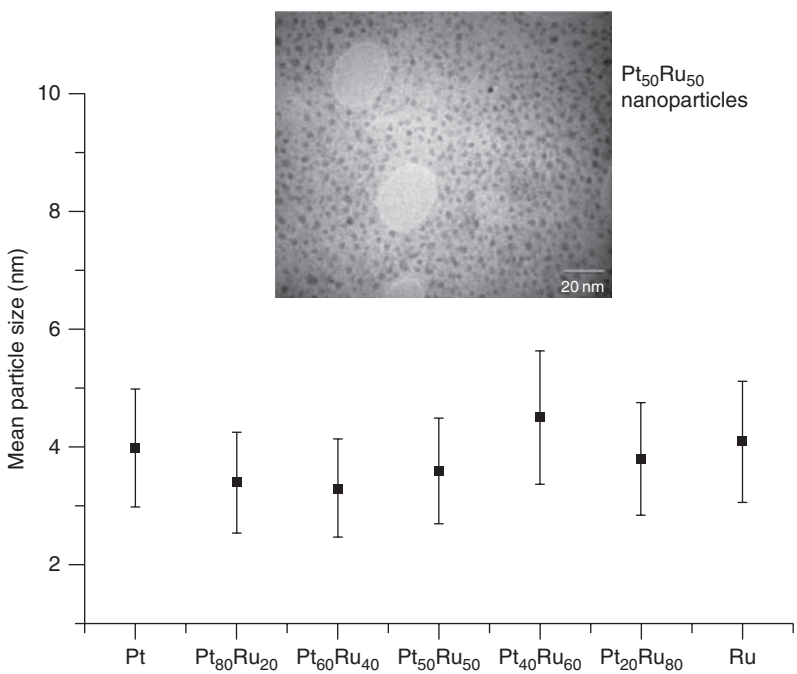

FIGURE 4.7 Mean particle size of Pt/Ru nanoparticles vs. atomic composition synthesized by microemulsion method. TEM image of $Pt_{50}Ru_{50}$ nanoparticles (from [136]).

Table 4.3 summarizes the literature results for metal nanoparticle catalysts synthesized by the microemulsion method, together with their characterization and activity evaluation.

Raghuveer and coworkers [122] applied this method to Pd–Co–Au/C catalysts, prepared by sodium bis-(2-ethylhexyl)-sulphosuccinate (AOT) microemulsion, which exhibit a higher degree of alloying at lower temperatures compared to those prepared by the conventional borohydride reduction method due to a slow and controlled reduction of the metal ions within the nanometer-sized aqueous domains or droplets. The high degree of alloying, while keeping the particle size small and surface area high, leads to a better catalytic activity for the oxygen reduction reaction in PEMFCs.

Zhang and Chan [138] synthesized some PtRu/C catalysts by a two-microemulsion route. The synthesis of PtRu nanoparticles has been achieved through microemulsions of water/Triton X-100/propan-2-ol/cyclohexane (w/o) and the reduction of aqueous PtRu precursor solution with a parallel hydrazine microemulsion system. Their catalysts exhibited a very narrow size distribution (2.5 ± 0.2 nm) and were highly alloyed. The relationship between PtRu nanoparticle size and the metal precursor concentration displays two levels of stable particle size in the plot. The low particle size level appears to be the nucleation limit, which is the minimum size required for a stable particle to exist. The upper particle size level appears to be limited by the size of the microemulsion or the mass transfer limitation on growth.

Liu et al. [119] studied the formation conditions of microemulsion in a (H_2PtCl_6 + $RuCl_3$ + NaOH)–(NP5 + NP9)–cyclohexane system. A limited region in the phase diagram was identified to be suitable for microemulsion formation. The microemulsion produced PtRu/C catalyst, which has smaller particle sizes, and shows higher anodic peak current density (0.24 mA/cm^2 (metal)) towards methanol oxidation in CV measurement, compared with the catalyst produced by a conventional emulsion method (0.05 mA/cm^2 (metal)).

Xiong and Manthiram [132] reported that the nanoparticle size depends on the ratio (W) of water to surfactant (i.e. sodium bis-(2-ethylhexyl)-sulphosuccinate (AOT)) in their case. These results demonstrated that a mono-size distribution could be easily obtained by controlling the synthetic conditions. Nanostructured PtRu/C catalysts have been synthesized by a reverse microemulsion method and their particle size could be varied from 3 to 6 nm by varying the molar ratio of water to the surfactant. Some of the PtRu/C catalysts obtained by this method are found to show higher catalytic activity than the commercial PtRu/C catalyst. The PtRu sample prepared with water to surfactant molar ratio of 10 is found to exhibit the maximum activity with the lowest charge transfer resistance with a particle size of around 5.3 nm. The better performance of the samples prepared by the microemulsion method is attributed to a better control of the particle size, crystallinity and microstructure. Also, Xiong and Manthiram [139] synthesized carbon-supported Pt–M (M = Fe and Co) alloy catalysts prepared by an ambient temperature microemulsion method and a high-temperate route. The alloy catalysts prepared by the microemulsion method show higher electrochemical active surface area than those that prepared by the high-temperature route.

Table 4.3 Summary of the reported metal alloy/C catalysts synthesized by different routes of the microemulsion method

Catalyst	Water phase/oil phase	Reducing agent/ surfactant	Particle size (nm)	Activity	Reference
20% $Pd_{70}Co_{20}Au_{10}$	$(NH_4)_2PdCl_6$, $Co(NO_3)_2$, H_2AuCl_4/heptane	$NaBH_4$/AOT	6.1<	4 A/m^2 at 700 mV, 0.2 mg/cm^2	137
20% $Pt_{50}Ru_{50}$	H_2PtCl_6, $RuCl_3$/cyclohexane	N_2H_2/ Triton X-100	2.5±0.2	7 mA/cm^2 at 200 mV (vs. Ag/AgCl), 0.4 mg/cm^2	138
40% $Pt_{50}Ru_{50}$	H_2PtCl_6, $RuCl_3$/cyclohexane	HCHO/NP5 + NP 9	4.3±1.6	0.03 mA/cm^2 at 200 mV (vs. SCE), 0.008 mg/cm^2	119
20% $Pt_{50}Ru_{50}$	H_2PtCl_6, $RuCl_3$/haptane	$NaBH_4$/AOT	3–6	50 mA/cm^2 at 400 mV, 1 mg/cm^2	132
20% $Pt_{80}M_{20}$ (M = Co, Fe)	H_2PtCl_6, $Co(NO_3)_2$ or $Fe(NO_3)_3$/haptane	$NaBH_4$/AOT	2.5–4.0	112 mA/cm^2 at 800 mV (vs. SCE), 0.3 mg/cm^2	139
20% $Pt_{60}Ni_{40}$	H_2PtCl_6, $NiCl_2$/haptane	$NaBH_4$/Brij®30	4.7±0.9	0.108 mA/cm^2 at 800 mV (vs. RHE), 0.014 mg/cm^2	140
40% $Pt_{50}Ru_{50}$	H_2PtCl_6, $Ru(NO_3)_3$/isooctane	N_2H_2/Berol050	3.2–13.7	0.02 mA/cm^2 at 400 mV (vs. RHE), 0.01 mg/cm^2	104

The Pt–Co/C catalysts prepared by the microemulsion method show superior electrocatalytic activity towards oxygen reduction in single-cell PEMFCs compared with Pt. Post-heat treatments at 200°C in a reducing atmosphere are found to increase the catalytic activity of particularly the Pt–Fe/C catalysts due to a cleaning of the surface and increase in the electrochemical surface area.

Santos and coworkers [140] prepared Pt–Ni alloys supported on carbon in three different compositions. The catalysts have been synthesized by a microemulsion method using Brij®30 as surfactant. This method produced homogeneous Pt–Ni/C particles with a narrow size distribution (4.7±0.9 nm). It was found that the Pt atoms in the alloys present higher activity than in pure Pt. A larger effect was observed for the material with a higher amount of non-noble metal. The lowest lattice parameter and the highest activity for ORR is for Pt–Ni/C with 40% Ni (atomic), probably due to the higher changes in electronic properties of the platinum caused by higher amount of non-noble metal. Similarly to the colloidal method where protecting agents are used, they should be adsorbed onto a porous support before the surfactant molecules are removed. Nevertheless, the microemulsion method requires the use of costly surfactant molecules with extra washing steps and may not be economical for a large-scale synthesis.

2.2 Catalyst Supports

Supporting materials are greatly needed to distribute and stabilize the catalyst particles in the catalytic system. The ideal support material should have the characteristics such as high inertness in harsh chemical and electrochemical conditions, high surface area and electrical conductivity, well-developed porosity to allow efficient diffusion of reactants and products, adequate water-handling capability and low cost. Carbon is the most promising candidate that can satisfy most such characteristics to be attractive as a catalyst support for fuel cells. The use of such carbon support in the catalyst layer results in finer dispersion of the metal catalyst and thus higher electrochemically active surface area, providing a means to increase the activity, stability and utilization of precious Pt or Pt alloy catalysts and thus to lower the catalyst loading and operation cost in electrode preparation for fuel oxidation and oxygen reduction in low-temperature fuel cells.

Carbon supports have strong effects on many fundamental properties of supported metal catalysts, in particular:

1. metal particle size, morphology and size distribution [141,142];
2. alloyed degree [44];
3. stability of supported metal nanoparticles;
4. mass transport in the catalytic layer [75];
5. electronic conductivity of the catalyst layer and thus its ohmic resistance, etc. [45,48].

These effects are also closely related to the catalyst utilization and electrocatalytic performance of the supported catalysts. Hence, the optimization of the carbon support is of crucial importance for the development of PEMFCs and DMFCs. The

physical and chemical origins of the effects are not fully understood yet, although considerable efforts have been made in the last few decades to optimize the supporting approaches. The three-phase reactive zone is very important in terms of utilization efficiency of the supported catalysts. At the three-phase boundary on the anodes, for example, the following elementary steps may take place: dissociative adsorption of H_2 on the electrode or the electrode catalysts; electron transfer from adsorbed H atoms to the electrode with formation of protons, and proton transportation from the electrode to the electrolyte polymer. Therefore, an electrode with a higher population of the triple-phase reactive zones is important for the development of efficient electrode catalysts. Recently, carbon support can be prepared with better control of surface area, porosity, morphology, surface functional groups, electronic conductivity and corrosion resistance in the framework. In this regard, the carbon support can play more important roles in the generation of the triple-phase reactive zones in the catalyst layer. In recent years, many researches have concentrated on unravelling the influence of carbon support properties and exploring new carbon supports [143–193] [M. Kim et al., unpublished material].

2.2.1 Carbon black

Carbon blacks (CBs) are the most commonly used catalyst supports which disperse active catalyst nanoparticles. There are many types of carbon blacks, such as Acetylene Black, Vulcan XC-72, Ketjen Black, etc., and they are usually manufactured by pyrolysing hydrocarbons such as natural gas or oil fractions taken from petroleum processing. These carbon blacks show different physical and chemical properties, such as specific surface area, porosity, electrical conductivity and surface functionality. Among these factors, specific surface area has a significant effect on the preparation and performance of supported catalysts [44,51]. High specific surface area Ketjen blacks are beneficial in terms of providing high dispersion of the active catalyst component. On the other hand, such high surface area carbons as supports for fuel cell electrocatalysts resulted in high ohmic and mass transport limitations [51]. Hence, Vulcan XC-72 carbon black with specific surface areas around $230\,m^2\,g^{-1}$ is the most widely used carbon support for the preparation of fuel cell catalysts because of its good compromise between electronic conductivity and the BET surface area [194,195].

Although it is known that the catalyst supports with high surface area allow high catalyst dispersion, which may result in better catalyst performance, the relationship between surface area for high catalyst dispersion and catalyst performance is still controversial depending on practical situations. The effects of the specific surface area of carbon black support on the particle size and homogeneity of $Pt_{50}Ru_{50}$ catalysts and on the catalytic activity toward the oxidation of hydrogen or methanol were studied in fuel cell systems. It was found that the alloyed degree and the size of $Pt_{50}Ru_{50}$ particles decreased with an increase in the specific surface area of the carbon black support. For $Pt_{50}Ru_{50}$ (30 mass%)/C catalysts, the specific activity for the oxidation of methanol increased as the specific surface area of the carbon black increased [44].

Carbon blacks are now produced in large scale at relatively low cost on a commercial basis and have good electrical conductivity and relatively high surface

area to be attractive as catalyst support. Commercial E-TEK and Johnson-Matthey supported Pt or other Pt-based alloy catalysts are prepared by using Vulcan XC-72 carbon black as support. However, Vulcan XC-72 carbon contains primary pores which are too small to be filled by the electrolyte polymer and, thus, many Pt particles trapped in the micropores (less than 1 nm) of the carbon black were not involved in the electrochemical reactions on electrodes due to absence of the triple-phase boundaries (gas–electrolyte–electrode). Other factors, such as pore size and distribution and surface functional groups of carbon blacks, also affect the preparation and performance of carbon-black-supported catalysts [196–200]. The metal catalyst utilization is determined by an electrochemical accessible active area rather than carbon specific surface area. Uchida et al. [197] found that metal nanoparticles residing in carbon pores below 40 nm in diameter had no access to Nafion® ionomer and thus did not contribute to the electrochemical activity, decreasing the extent of catalyst utilization. Rao et al. [52] also reported that a higher content of small pores (<20 nm) containing metal particles where the Nafion® ionomer could not easily enter, resulted in poor contact between the metal nanoparticles and Nafion® micelles and, accordingly, a lower level of methanol oxidation activity. Carbon materials of the Sibunit family are prepared through pyrolysis of natural gases on carbon black surfaces as supports for the anode catalysts of DMFCs [199]. It was noticed that mass activity and specific activity of PtRu anode catalysts change dramatically with S_{BET} of the support, increasing with the decrease of the latter; 20% PtRu supported on Sib-19P ($S_{BET} = 72\,m^2g^{-1}$) showed a mass specific activity of 180 mA mg^{-1} (metal) at 500 mV during DMFC half-cell testing, which is almost six times higher than that for PtRu/Sib-619P ($S_{BET} = 415\,m^2g^{-1}$). Pai et al. [200] reported a new approach for dispersing carbon black nanoparticles by introducing clay in order to prolong the dispersion stability and to increase the utilization efficiency of Pt-based catalysts.

A recent study also indicates that the oxidation problem of the carbon black in the cathode and impurities such as Cl, S in the framework could destabilize the supported catalysts and lower their catalytic performance [198]. Despite the several intrinsic drawbacks in carbon blacks as support, they are still the most widely used for fundamental and practical applications and also as a reference support due to easy availability and low cost.

In addition, the mesocarbon microbead (MCMB), a type of spherical carbon particle with many nodular lumps and pores at its surface, was also investigated as Pt or PtRu catalyst support for methanol oxidation [201–203]. MCMB is usually derived from pitch and is one of the commercially available carbon materials, having a unique spherical structure with a diameter of approximately 1–40 nm. MCMB has several benefits as an electrode material, as follows:

1. Spherical particles give a close-packed arrangement, resulting in electrodes with high density.
2. The low surface area of MCMB results in fewer side-reactions on the surface.

Although the particle size of MCMB-supported PtRu nanoparticles is comparatively larger (12–13 nm), better performance compared with Vulcan XC-72R carbon support catalyst was observed. The overpotential of a PtRu/MCMB electrode was 0.39 V (versus SCE) at 300 mAcm^{-2}, which was 70 mV lower than that of a PtRu/Vulcan XC-72 electrode [202].

2.2.2 Nanostructured carbon

In recent years, several novel nanostructured carbon materials have been reported and utilized for various applications. Among them, the family of carbon nanotubes (CNTs) is the most well-known example, which has attracted tremendous interest from both a fundamental and an applied point of view since their discovery in early 1990 [204]. Large-scale syntheses have been explored owing to their high mechanical and unique structural and electrical properties [205]. These materials have been considered to be not only ideal candidates for supports in heterogeneous catalysts [206]; recently, carbon nanotubes have been proposed to replace traditional carbon powders in fuel cells and have been used as electrode materials for both oxidation and reduction reactions in hydrogen-fuelled PEMFCs [207–209] and DMFCs [67,210,211].

Generally, the carbon nanotubes are classified as two categories: single-walled nanotubes (SWNTs) and multiwalled nanotubes (MWNTs). A SWNT is a single graphene sheet rolled into a cylinder. An MWNT consists of several coaxially arranged graphene sheets rolled into a cylinder. SWNTs can be either metallic or semi-conducting depending on the tube diameter and helicity [212]. The bandgap is proportional to the reciprocal diameter, $1/d$ [213]. For MWNTs, the conduction is mainly due to the outer shell [214]. Therefore, MWNTs have a relatively high electrical conductivity. The growth methods for MWNTs are usually simpler than those for SWNTs. SWNTs generally form bundles, which decrease their surface area available for supporting Pt particles. Due to the synthetic convenience, low production cost and property control, MWNTs have been more widely utilized as supporting medium for catalysts in fuel cells than have SWNTs.

Deposition, distribution and crystallite size of Pt-based nanoparticles supported on CNTs are significantly affected by factors including the synthesis method, oxidation treatment of the CNTs and Pt precursors. Some early investigations indicated better performance in PEMFC [208,209] and DMFC [67,210] by simply replacing carbon black particles with disordered MWNTs as the support for Pt catalyst nanoparticles. Nakamura and his group reported that the Pt/MWNT showed two to three times higher voltages per Pt atom at current densities below 600 mA/cm^2 compared with the Pt supported on carbon black in PEMFC, increasing the Pt usage by 60%. The power density per Pt atom of the Pt/CNT electrode is also twice as high as that of the Pt/CB electrode [209]. Li et al. reported that the synthetic method had great impacts on the crystallite size of Pt-based nanoparticles and on their deposition and distribution over the support, which would affect the catalytic property of the supported catalyst [67]. TEM images in Figure 4.8 show dispersion of spherical Pt metal clusters on Pt/MWNT prepared by the EG (ethylene glycol) reduction method and by the HCHO method. The former had not only better dispersion, but also a narrower size distribution ranging from 2 to 5 nm than the latter with a size distribution of 2 to 9 nm. Better structural properties such as higher dispersion and smaller particles size with narrower pore size distribution contributed to catalytic performance of the supported catalyst. At a cathodic potential of 700 mV (vs. DHE in the activation-controlled region), the current densities at 90°C were 5.7 mA/mg, 14.7 mA/mg and 2.5 mA/mg for Pt/MWNTs (HCHO method), for Pt/MWNTs

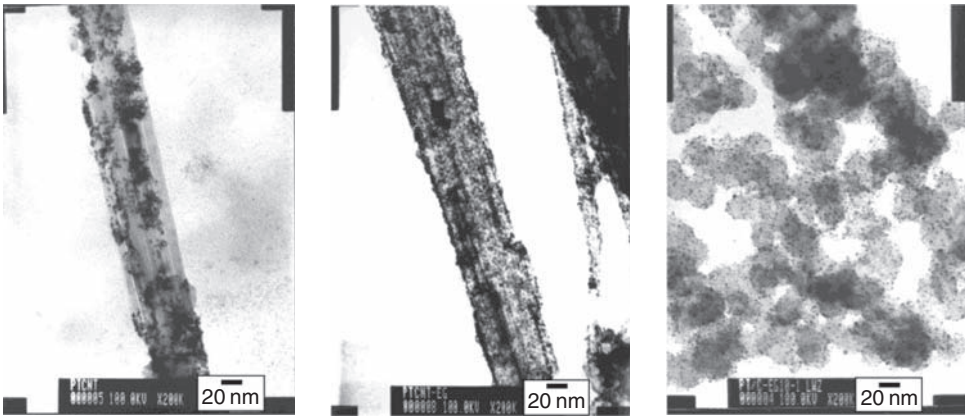

(a) (b) (c)

FIGURE 4.8 Bright-field TEM images of Pt/MWNT prepared by (a) the HCHO method and (b) by the ethylene glycol (EG) method; (c) image of Pt/XC-72 nanocomposites prepared by the EG method (from [67]).

(EG method) and for Pt/XC-72, respectively. Rajesh et al. studied a methanol oxidation catalysed by Pt, PtRu and Pt-WO_3 nanoparticles supported on CNTs and Vulcan XC-72R. The Pt-WO_3/CNTs showed better catalytic activity and stability compared with Pt or PtRu/CNTs and Pt-Ru/Vulcan XC [210]. The possible reasons were that the CNT-based catalysts could create more efficient formation of triple-phase boundaries and special metal-support interaction and also had higher conductivity and lower organic impurities than the traditional carbon black based ones. The experiments and theoretical calculations carried out by Britto et al. showed that a large number of defects of CNTs, such as pentagons at the nanotube tip and pentagon-heptagon defect pairs in the lattice and curvature were beneficial to the oxygen reduction reaction [215].

There was also an effort to employ SWNTs as a nanostructured carbon support in PEMFCs by either casting a film with a polymer binder or growing the carbon nanotubes directly onto the carbon paper or cloth [216, 217]. Although the use of binders provides a convenient method to cast SWNT films, they often pose the problem of increased resistivity. Electrophoretic deposition was also used as another effective and comparatively facile approach for assembling SWNTs on the desired electrode surface [218,219]. The Pt/SWNT electrodes cast on carbon electrodes showed 20% higher power density than Pt/carbon black electrodes for hydrogen fuel cells [219].

Since the external walls of CNTs are chemically inert and cannot be well wetted by liquid with high surface tension, it is essential to activate their surfaces before metal deposition in order to generate some anchoring sites (i.e. oxygen-containing functional groups) on the surface for achieving optimal interaction between the support and the catalyst precursor. Chemical treatments are common methods to generate functional groups on CNTs [220,221]. The common chemical

activation of the CNT surface includes oxidative reaction of the CNT with HNO_3 or a H_2SO_4–HNO_3 mixture. The oxygen-containing surface functional groups produced on CNTs can improve the reactivity and greatly affect the catalyst particle dispersion by manipulating Pt anchoring and/or nucleating sites [208].

The durability of carbon black supported Pt (Pt/C) and multiwalled carbon nanotubes supported Pt (Pt/MWNTs) catalysts for potential application in PEMFCs was investigated using an accelerated durability test. The electrochemical surface area of Pt/CB degraded by 49.8% compared with 26.1% for Pt/MWNTs during the 192-h test time due to Pt particle growth and Pt loss from the support in the forms of Pt ions and Pt particles, indicating that Pt/CNTs were more stable under electrochemical operation, which could be attributed to specific interaction between Pt and the support and the higher resistance of the support to electrochemical oxidation [222].

However, realistic applications for CNTs have been hindered by several difficulties associated with their processes involving synthesis, purification, dispersion and surface activation. The synthetic methods such as carbon-arc discharge, laser ablation of carbon or chemical vapour deposition have their limitations in terms of large-scale production and cost-effectiveness. Their harsh synthetic conditions and low production yields are major disadvantages. Currently, SWCNTs are produced only on a very small scale and the process is extremely costly [223]. It is necessary to develop further industrial large-scale production of CNTs to meet the needs of all the possible applications. It is also, in general, difficult to decorate metal nanoparticles on the surface of CNTs with uniform size and good dispersion because the metal nanoparticles are spontaneously formed at the defect sites on the surface of CNTs. Moreover, carbon nanotubes tend to agglomerate without any pretreatments, leading to uneven distribution of metal particles. To date, several methods have been developed to prepare highly dispersed metal/CNT catalysts, as summarized in Table 4.4.

The utilization efficiency of catalyst metal nanoparticles supported on the CNTs in regard to the catalyst particles' size and distribution still remains a challenge in low-temperature fuel cells. The high dispersion of nanosized Pt or Pt alloy nanoparticles is important in order to utilize fully the advantages of high surface area, conductivity and porosity of CNT-based materials. Various methods of decorating the CNT surfaces with metal nanoparticles have been developed to make active supported catalysts. Although it is difficult adequately to control particle shape and size with conventional wet impregnation and chemical reduction methods, the impregnation method was frequently used to deposit metal nanoparticles onto CNTs [71,211,226]. Alternatively, other methods such as the electrodeposition method [227–229], electroless plating [207] or a potential-step method [212] have been used to make CNT supported catalyst because of its high purity and simplicity. However, it was difficult to estimate the loading of the metallic catalyst and/or to attain small nanoparticles by using the methods, as shown in Table 4.4. Recently, Lin et al. [231] used a supercritical fluids (SCFs) method as a rapid, direct and clean approach to prepare Pt/CNT catalyst for DMFCs. It was claimed that the supercritical fluid technology could result in products (and processes) that are cleaner, less expensive and of higher quality

Table 4.4 Preparation and fuel cell performances for Pt or $Pt_{50}Ru_{50}$ catalysts supported on carbon black and nanostructured carbons

Catal loading/support	Pretreatment	Catalyst prep. method	Particle size	Activity	Ref.
20% PtRu/VC	untreated	Impregnation in H_2PtCl_6, $RuCl_3$/HCHO	≈7.8 nm	20.6 μA at 370 mV (0.5 M CH_3OH, 25°C)	[149]
20% PtRu/VC	O_3	Impregnation in H_2PtCl_6, $RuCl_3$/HCHO	≈5 nm	68.3 μA at 370 mV (0.5 M CH_3OH, 25°C)	[200]
30% PtRu/CNT	untreated	Impregnation in H_2PtCl_6, $RuCl_3$/EG, 700 W	2–5 nm	18 mA/cm^2 at 670 mV (2 M CH_3OH, 50 mV/s)	[211]
30% PtRu/VC	untreated	Impregnation in H_2PtCl_6, $RuCl_3$/EG, 700 W	2–5 nm	13 mA/cm^2 at 670 mV (2 M CH_3OH, 50 mV/s)	[211]
42% PtRu/GCNF	untreated	Impregnation in (η-C_2H_4)(Cl) Pt(μ-Cl)$_2$-Ru(Cl)	≈6 nm	210 mA/cm^2 at 400 mV (DMFC, RT)	[224]
η^3:η^3-2,7-dimethyloctadienediyl)/H_2					
60% PtRu/CNC	untreated	Impregnation in H_2PtCl_6, $RuCl_3$/$NaBH_4$	≈2.5 nm	500 mA/cm^2 at 400 mV (DMFC, 60°C)	[48]
67% Pt/C_{60}	untreated	Electrolysis of H_2PtCl_6/−350 mV(vs. SCE)	100–150 nm	3.6 mA/cm^2 at 660 mV (2 M CH_3OH, 20 mV/s)	[225]

29% Pt/CB		Commercially available		270 mA/cm^2 at 700 mV (PEMFC, 80°C)	[209]
12% Pt/CNT	HNO_3-H_2SO_4	Impregnation in K_2PtCl_4/EtOH	2–4 nm	560 mA/cm^2 at 700 mV (PEMFC, 80°C)	[209]
10% Pt/MWNT	HNO_3-H_2SO_4	Impregnation in H_2PtCl_6/HCHO	2–9 nm	5.7 mA/mg at 700 mV (DMFC, ORR, 90°C)	[67]
10% Pt/MWNT	HNO_3-H_2SO_4	Impregnation in H_2PtCl_6/EG	2–5 nm	14.7 mA/mg at 700 mV (DMFC, ORR, 90°C)	[67]
2% Pt/VC	HNO_3-H_2SO_4	Impregnation in H_2PtCl_6/EG	2–4 nm	2.5 mA/mg at 700 mV (DMFC, ORR, 90°C)	[67]
PtRu/MCMB	H_2PtCl_6, $RuCl_3$		13.1 nm	0.41 V vs. SCE at 300 mA/cm^2 (DMFC, O_2, 90°C)	[201]
PtRu/MCMB	H_2PtCl_6, $RuCl_3$/ $Na_2S_2O_4$		13.1 nm	0.39 V vs. SCE at 300 mA/cm^2 (DMFC, O_2, 90°C)	[202]
10.9–16.4% Pt/MCMB	H_2PtCl_6, $RuCl_3$/ $Na_2S_2O_4$		3–5 nm	(1 M H_2SO_4 + 1 M CH_3OH, RT)	[203]

EG: ethylene glycol; GCNF: graphitic carbon nanofibre; CNC: carbon nanocoil; MCMB: mesocarbon mesophase pitch.

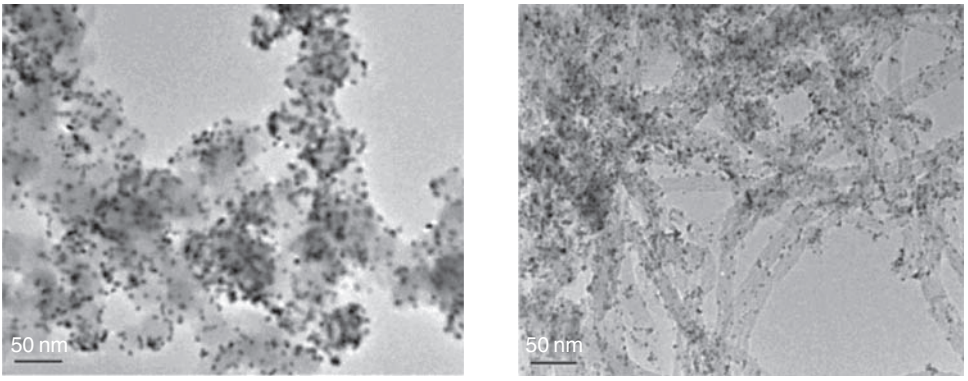

(a) (b)

FIGURE 4.9 TEM images of microwave-synthesized PtRu (20 wt% Pt-10 wt% Ru) nanoparticles supported (a) on Vulcan XC-72 and (b) on CNT (from [211]).

than those produced using conventional technologies and solvents. Recently, a microwave-assisted polyol preparation of carbon-supported PtRu nanoparticles was developed to realize a uniform dispersion of metal nanoparticles on its support, especially CNT, as shown in Figure 4.9b [211].

Another challenge of CNTs as a catalyst support for DMFCs is how to use them to fabricate high performance working electrodes. If the electrode had been prepared by a conventional ink process, it was estimated that only 20–30% of the platinum catalyst was utilized because of the difficulty for reactants to access inner electrocatalytic sites [218]. Recently, some novel techniques [227,232–234] have been developed to grow or assemble CNTs directly on the fuel cell carbon paper fibres to produce a three-dimensional nanotube-based hierarchical structure, which could make use of CNTs' advantages of structural, electronic and mechanical properties. Platinum or platinum alloys are expected to deposit directly onto these novel CNT-based catalyst supports, which seem to possess high potential in promoting the performance of the Pt/CNTs-based fuel cell by increasing noble metal utilization.

In addition to CNTs, new forms of carbon such as fullerenes, graphite nanofibre and nanohorns, which have become more available recently, have also drawn interest in recent years for performance improvement of fuel cells [224,225,235,236]. Graphite nanofibres (GNFs) have been considered to be a potential support for electrocatalysts. Bessel et al. [45], in a cyclic voltammetry study, reported that the GNF-supported Pt electrocatalysts not only exhibited higher activity of electrochemical oxidation of methanol but also showed better stability. Recently, Lukehart's group [224,236] also prepared a Pt–Ru/herringbone GNF nanocomposite using a single-source molecular precursor as the metal source. The performance of the DMFC with this nanocomposite as the anode catalyst was enhanced by 50% relative to that recorded by an unsupported Pt–Ru colloid anode catalyst. More recently, carbon nanocoils (CNCs), a new form of nanostructured carbon supports, were synthesized by a solid-phase synthetic method and used as DMFC

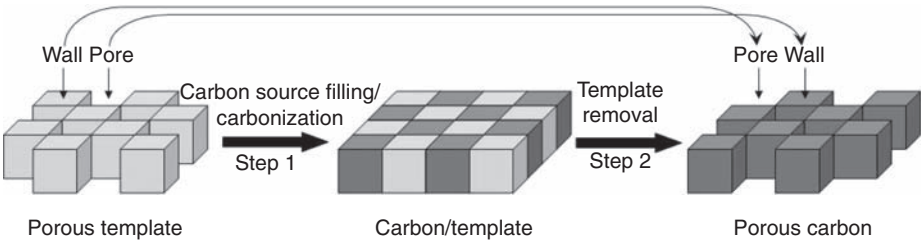

FIGURE 4.10 Schematic illustration for the fabrication of a porous carbon using template method.

catalyst supports [194]. It was found that under identical testing conditions, the maximum power density realized by CNCs-supported catalyst was much higher than those of Vulcan-supported catalyst and the commercial catalyst. A fullerene (C_{60}) film electrode was also suggested as a catalyst support for methanol oxidation after electrodeposition of Pt on the fullerene nanoclusters [225].

2.2.3 Nanoporous carbon

Nanoporous carbon materials have found wide applications in a variety of fields such as catalysis, adsorption and environmental technology because of their high surface area and well-developed pore structure coupled with many other physical and chemical properties [237,238]. Recently, remarkable progress has been made in the synthesis of carbon networks with ordered nanoporous structures consisting of uniform pores or channels in the range of micropores (<2 nm), mesopores (2–50 nm) and macropores (>50 nm) [143–193] [239–246] [Kim et al., unpublished material]. These nanoporous carbon networks are usually synthesized through a nanocasting method using solid hosts called 'templates' such as zeolites [247], mesoporous molecular sieves [248–253] and self-assembled colloidal silica gels [180]. A template is a solid nanostructured master with nanoscale pores or channels in its framework, as in zeolites and mesoporous molecular sieves, whose pores or channels can be utilized for incorporation of other materials with new compositions and thus can allow the preparation of novel materials with new structures and compositions which cannot be obtained by traditional chemical synthesis methods such as the sol–gel method. The template-fabrication approach can afford a variety of porous networks with a wide range of pore sizes, well-defined morphologies on controllable length scales and various chemical functionalities to match the needs of different applications.

Figure 4.10 shows the representative schematic illustration for the two-step fabrication of a porous carbon through the nanocasting method using a solid template. In the synthesis, the sacrificial porous template was initially infiltrated with carbon precursor, which is properly treated and carbonized under non-oxidizing conditions, and then removed from the template/carbon composite by dissolving in HF or NaOH solution to generate a template-free nanostructured porous carbon. During the replication process, the pores and walls of the host template are transformed to the walls and pores, respectively, of the resulting carbon network,

which is thus a negative replica of the parent silica template. Thus, the host scaffold materials are required to have interconnected pore systems which allow for structural integrity of the templated carbon after removal of the host. Structural periodicity in the resulting carbon originates from the structural ordering in the template framework. Most recently, new ordered mesoporous carbons, which are synthesized directly from polymer nanostructured frameworks and not by the above-mentioned hard template-replication, emerged in the mesoporous carbon world, extending their application scope and potential [254–259]. Some of these periodically ordered porous carbons have demonstrated high potential as catalyst supports for fuel cells [53,54,74–76,171–176].

2.2.3.1 Microporous carbon Zeolites are aluminosilicate materials possessing ordered and uniform sub-nanometre-sized pores or channels in their framework [247]. Because the walls of zeolites have a uniform thickness of <1 nm, the microporous carbon materials controlled at the nanometre level have been fabricated by using zeolites as a template. Rodriguez-Mirasol et al. [239] reported on microporous carbon prepared by a chemical vapur infiltration method using zeolite Y as a template and propylene as a carbon precursor, and went on to examine the oxidation behaviour of the resulting porous carbon. However, the carbon packing in the channels was not complete and there were still some spaces unoccupied by carbon. Kyotani et al. [241] reported microporous carbon with a long-range periodic ordering (d = 1.4 nm) for the first time by a template carbonization technique using zeolite Y. A two-step method was employed for the synthesis: the filling of furfuryl alcohol into the nanochannels of zeolite Y followed by the heat treatment of the zeolite/poly-(furfuryl alcohol) (PFA) composite at 700°C for 4 h and then further carbon deposition from propylene at 800°C for 4 h. The resultant carbon was liberated from the zeolite framework by acid washing. Zeolite Y consists of a tetrahedral network structure of sodalite units, which results in a supercage with a diameter of 1.3 nm [247]. Due to this framework topology, many sharp XRD peaks appeared, as shown in Figure 4.11a. However, the carbon replica gave only one sharp XRD peak at the angle corresponding to the (111) diffraction (Figure 4.11b). This implies that the carbon retains only the structural ordering of the (111) stacking plane of zeolite Y. Recently, the microporous carbons with very high surface area of 3600 m^2/g and with a three-dimensional nano-array structure were also reported by the same group by using various zeolites and carbon precursors [242,243]. Although the above-mentioned microporous carbon materials possess high specific surface area, large pore volume and uniform pore sizes, the micropore size is less than 1.0 nm and thus a portion of the metal nanoparticles may be sunk into the micropores of the carbon supports. This portion inside the micropores will have difficulty in reactant accessibility and less or no contact with electrolytes, which will significantly reduce electrochemical activity. Generally, a high-performance anode requires an efficient three-phase reaction zone at the nanoscale, in which the electrochemical reactions occur on the surface of the metal nanoparticle involving electron and proton transport. In addition, it also requires the provision of an efficient transport passage for reactants (H_2, CH_3OH, H_2O) and the product (CO_2). Too many small micropores (<2 nm) in

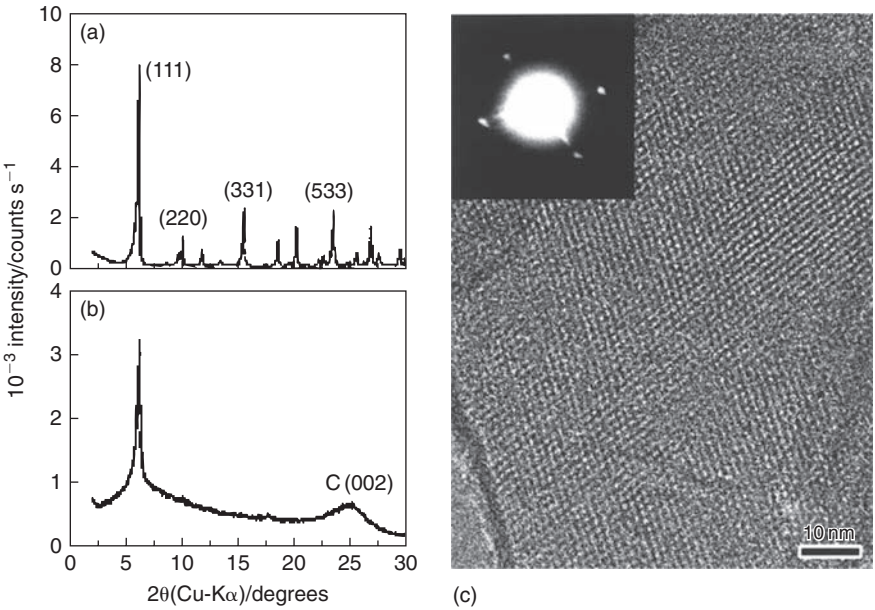

FIGURE 4.11 XRD patterns of (a) zeolite Y, (b) carbon liberated from the carbon/zeolite composite (from [248]) and (c) HRTEM image of the carbon prepared in [243]. The inset corresponds to a diffraction pattern taken from this image.

carbon supports decrease catalyst utilization because the mass transport of reactants and product is poor in these micropores, as in Vulcan XC-72 [196–206].

Although micropores are not very useful in terms of catalyst utilization, Su et al. have used zeolite Y as a template to prepare microporous carbons via a direct infiltration method or chemical vapour deposition (CVD) method of organic carbon sources for catalyst support application [244]. The use of CVD of benzene can not only enhance carbon infiltration, but also promote the formation of a graphitic carbon shell on the external surface of the carbon particles, creating a porous carbon structure with an amorphous core and a graphitic shell. These workers reported the methanol oxidation activities of Pt nanoparticles supported on the microporous carbon with and without a graphite shell [245]. Pt/microporous carbon with graphitic carbon shell was found to show better catalytic activity than a commercial E-TEK counterpart and also to have higher mass-normalized activity and CO-resistance in the room temperature electro-oxidation of methanol relative to Pt catalyst prepared similarly on a totally amorphous microporous carbon support. The amorphous microporous carbon support without a graphite shell rendered Pt nanoparticles inaccessible to reactions by engulfing the nanoparticles and increased the transport problems in the overall process. It was insisted that a good carbon support should have a minimum number of micropores and have graphitized surfaces.

2.2.3.2 Mesoporous carbon In early 1990, Mobil Corporation researchers reported the synthesis of a family of mesoporous M41S silica materials from the sol–gel polymerization of silica precursors in the presence of a surfactant self-assembly [248]. Since then, many other silicate-based mesoporous materials with various pore sizes and structures such as MCM-41 (2D hexagonal) [248], MCM-48 (cubic) [248], HMS (worm-like) [249], SBA-1 (cubic) [250], SBA-3 (2D hexagonal)[250] and SBA-15 (2D hexagonal)[251], have been reported by using different templating approaches. Various organic structure-directing agents such as cationic surfactant [248], neutral amine surfactants [249], alkyl(PEO) surfactants [250] and triblock copolymers [251], have been utilized for the synthesis of ordered mesostructured silica (OMS) materials. In comparison with microporous zeolites, the pore sizes of the mesoporous materials can be controlled in the range of 2–30 nm simply by choosing an appropriate surfactant template and/or by adding a swelling agent of the micelles. Wall thickness was less controllable and was in the range of 2–4 nm. Corma reviewed the synthesis, properties and applications of the mesoporous molecular sieves [252].

These OMS materials, in turn, provide new opportunities as scaffolds for the templated fabrication of new novel nanostructured materials such as polymers, carbons and ceramics [143–178,194]. Ryoo et al. [143] reported for the first time the synthesis of ordered mesoporous carbon (OMC) (denoted CMK-1) using MCM-48 silica of *Ia*3*d* symmetry, which exhibits cubic porous structures consisting of two disconnected interwoven three-dimensional pore systems [248,253]. The two-step template synthesis of OMC includes the following detailed multistep procedures:

1. removal of surfactant molecules in the OMS channels either by burning off (calcinations) at high temperature of 500–800°C or by washing with copious amounts of weak acidic water or alcohol solution;
2. infiltration of OMS mesopores with carbon precursors, usually monomers, and polymerization of the monomers;
3. curing the composites followed by pyrolysis under non-oxygen atmospheres; and
4. dissolution of OMS template with HF or NaOH solution to release the templated carbon.

Many research groups have successfully reported the synthesis of the CMK-1-type OMC materials by using MCM-48 mesoporous silica template and different synthetic methods [144–148].

The use of SBA-15 silica as the template led to the synthesis of another new ordered mesoporous carbon, designated as CMK-3, in which parallel carbon fibres are interconnected through thin carbon spacers, which are formed inside the pores between adjacent carbon fibres [149]. Interestingly, while the resulting CMK-1 experienced a structural transformation into a new cubic structure of $I4_132$ from cubic MCM-48 with the *Ia*3*d* structure [143–146], the CMK-3 maintained the ordered structure of SBA-15, being an exact inverse replica without structural transformation when the silica framework template was removed from the silica–carbon composite [149–161]. Many liquid carbon precursors, such as sucrose [143], phenol resin [144], divinyl benzene [145,146], furfuryl alcohol

[160], mesophase pitch [162], acenaphthene [163], polypyrrole [164], anthracene [165], polypyrrole [166] and polyacrylonitrile [167,168], have been employed to infiltrate the pores of mesoporous silica template.

Interconnected hollow tube-type mesoporous carbon, designated as CMK-5, was also reported from the partial wetting of poly(furfuryl alcohol) onto the SBA-15 silica channels and subsequent carbonization and removal of the silica template [151]. The ordered carbon tubes were rigidly interconnected into a highly ordered hexagonal array by the carbon spacers. The pore size distribution curve exhibited bimodal pores, corresponding to the inside diameter of the carbon nanotubes (5.9 nm) and the pores formed between the adjacent nanotubes (4.2 nm), respectively. Figure 4.12 shows high-resolution TEM images of the optimized CMK-5 sample. Figure 4.12a shows a hexagonally ordered array of circles and can be interpreted as a projection of the CMK-5 structure in the direction parallel to the pore channels. Figure 4.12b shows a pattern of uniformly spaced, parallel, dark lines.

In the synthesis of OMC using the OMS template, the surfactant molecules in as-synthesized silica templates were usually completely removed by the calcination process. Such processes may often cause some partial lattice collapse or shrinkage even in well-prepared mesoframeworks as observed by line broadening or signal shift in powder X-ray diffraction patterns [146]. Yu et al. reported for the first time a simple synthetic method denoted 'a direct template synthesis' of porous carbons by using as-synthesized mesostructures as templates [146,152]. This method directly used intact as-synthesized hosts containing surfactant molecules in the framework without going through a surfactant removal process. In this case, the surfactant molecules were also used as a part of the carbon source. Thus, this work could save extra labour, time and energy required for

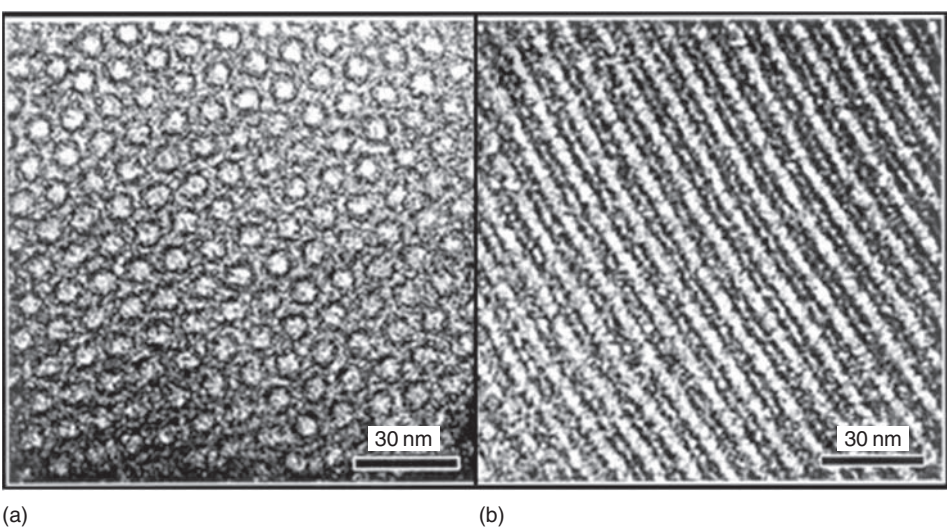

FIGURE 4.12 TEM images of CMK-5 taken (a) along the channel direction and (b) perpendicular to it, respectively (from [151]).

the calcination process and yet was found to be an efficient way of synthesizing high quality OMC with greater mechanical stability compared with OMC generated using calcined silica frameworks. Review articles concerning template synthesis of mesoporous carbon have appeared recently [169,170].

OMC materials have attracted great attention as catalyst supports for fuel cells due to their unique characteristics, including high surface areas easily reaching to more than 1000 cm^3/g and much increased pore sizes compared with those of microporous materials. Mesoporous carbons with tunable pore sizes in the range 2–50 nm are attractive for use as catalyst supports and have the potential to enhance both the dispersion and utilization of metal catalysts. The tube-type CMK-5 carbon was applied as a catalyst support for platinum nanoparticles and electrocatalytic mass activities of the Pt/CMK-5 catalysts showed a high peak activity amounting to 100 A per g Pt at the 33 wt% Pt loading for the oxygen reduction, which is important for fuel-cell applications [151].

Choi et al. reported a novel procedure to synthesize Pt nanoparticles studied in the hexagonally arranged ordered mesoporous carbon nanofibres by the pyrolysis of carbon and Pt precursors in the silica mesopore of SBA-15 [171]. The Pt/C showed higher current density for oxygen reduction and more methanol-tolerance compared with the commercial Pt/VC-72. Liu et al. report a novel route for fabrication of OMC materials with well-dispersed, highly stable Pt nanoparticles of ca. 2–3 nm on the pore walls using platinum acetylacetonate as the co-feeding carbon and Pt precursor [175]. They reported that the electrocatalytic activity of Pt-supported ordered mesoporous carbon during methanol oxidation reaction exhibited a catalytic activity surpassing that of the commercial Pt/C catalyst (Johnson-Matthey; 20 wt% Pt on Vulcan XC-72).

The CVD method has been demonstrated to be a better approach because it has a number of advantages over the liquid-phase impregnation method, such as a high degree of pore filling, and easy control over the amount of pyrolytic carbon deposited in the template pores, enabling the formation of graphitic pore walls and avoiding the formation of additional microporosity [157,176]. Recently, Su et al. reported the preparation of highly ordered graphitic mesoporous carbon through the CVD method using large-pore SBA-15 pure silica as the template and benzene as the carbon precursor [176]. The resulting carbon materials were used as Pt catalyst supports for room-temperature methanol oxidation. Pt catalyst supported on the mesoporous carbon was found to display a higher specific activity for methanol oxidation than a commercial catalyst, Pt/C (E-TEK), which is a Pt catalyst supported on Vulcan XC-72 carbon black.

Core-shell type structures are unique structures attracting great attention due to a large application potential. Yeon et al. reported the fabrication of carbon capsules with hollow core and mesoporous shell (HCMS) structures using submicrometre-size solid core/mesoporous shell (SCMS) silica spheres as templates [177]. Figure 4.13a displays a representative SEM image of HCMS carbon capsules, showing that the HCMS carbon particles were roughly uniform and spherical with a particle diameter of 300 nm with a hollow core of 220 nm diameter and a mesoporous shell with thickness of 40 nm. The HCMS carbon capsules revealed a pore size distribution centred at 3.8 nm and exhibited a very high BET

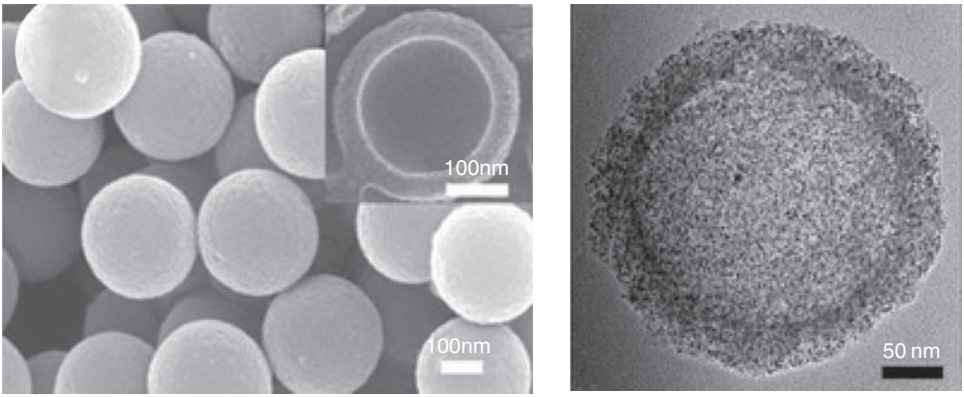

(a) (b)

FIGURE 4.13 (a) SEM image of HCMS carbon capsules (inset shows the image of a broken capsule) and (b) TEM image of an HCMS carbon capsule after catalyst loading. The small black spots represent Pt–Ru catalyst nanoparticles (from [76]).

surface area of 1876 m^2/g and a total pore volume of 1.87 cm^3/g. The HCMS carbon capsules loaded with $Pt_{50}Ru_{50}$ catalysts showed that most of the Pt–Ru alloy nanoparticles are dispersed homogeneously as small, spherical and uniform dark spots over the surface, as shown in Figure 4.13b. Figure 4.14 shows the unit cell performance of a direct methanol fuel cell at 30°C and 70°C using a PtRu/HCMS catalyst compared with those using Vulcan carbon supported PtRu (PtRu/VC) and E-TEK catalysts [76]. PtRu/HCMS catalysts exhibited much higher specific activity for methanol oxidation than the commonly used PtRu/E-TEK catalyst by about 80% at 30°C, proving that the HCMS carbon capsules are an excellent support for electrode catalysts in DMFC. In this case, the mesopores of the hollow carbon wall had uniform pore size, but were disordered unlike those of the OMCs which had ordered channel directions. Porous carbon with similar disordered mesopore channels was also reported [178,179].

Although the OMCs possessed properties to be attractive as catalyst supports, such as high surface area and pore volume, well developed ordered pore array with uniform pore size and controllable pore geometries, relatively small mesopore size of the carbon may put some limitation for the application of OMCs as catalyst supports. In addition, the limited mobility of reactants and products through confined nanochannels can be a problem in the OMC. The pore of OMC originates from the wall of the parent mesoporous silica template. In a very few cases, the wall thickness can be tuned in a large range [150]. Consequently, the OMC pore size near 2–5 nm in diameter can be good for controlling the size of catalyst nanoparticles, but may not be sufficient for contact with electrolyte polymers to form a triple-phase reaction zone at the nanoscale. Yeon et al. [154] tried to solve the problem through a novel synthetic control method for generating either highly ordered carbon nanofibre networks (denoted as OCNFs) or disordered carbon nanofibres (denoted as DCNFs) by using a pretreatment of SBA-15 silica

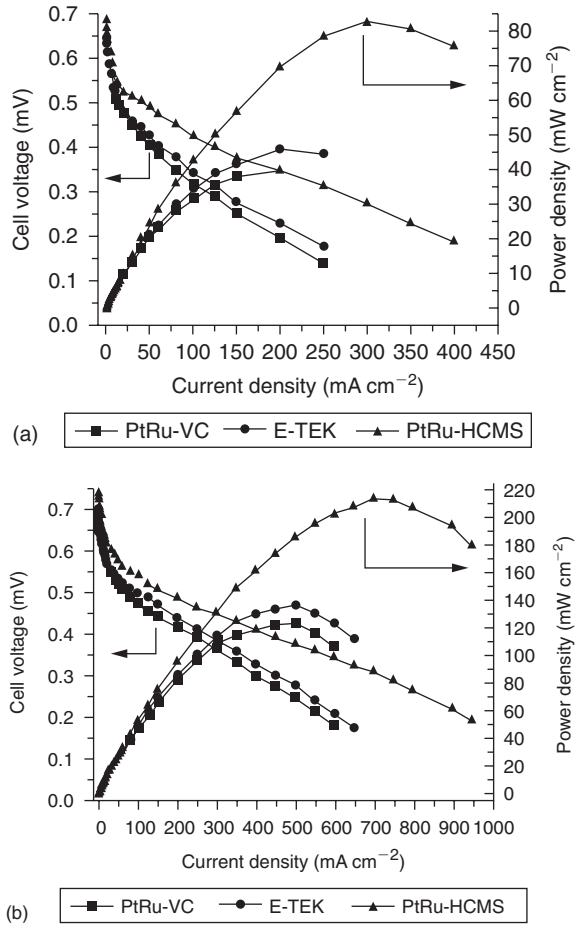

FIGURE 4.14 The polarization curves for a direct methanol fuel cell using a PtRu-HCMS catalyst (▲), a PtRu-VC catalyst (■) and a commercial E-TEK catalyst as an anode (●) determined (a) at 30°C and (b) at 70°C, respectively (from [76]).

template, as shown in Figure 4.15. Figure 4.16 shows TEM images of ordered and disordered CNFs and of their corresponding CNFs loaded with $Pt_{50}Ru_{50}$ catalyst [54]. OCNFs (Figure 4.16a) exhibited highly ordered nanofibres evenly separated by void channels. On the other hand, DCNFs (Figure 4.16b), prepared using SBA-15 calcined at 750°C, appeared to have largely disordered arrays of loose nanofibres with a few clusters and thus were easily accessible from/to the outside. PtRu alloy nanoparticles were dispersed nearly homogeneously as small, spherical and uniform dark spots on the surface of the CNFs, as shown in Figure 4.16c and d. The maximum power densities are 78 mW/cm^2 for PtRu/DCNFs, 59 mW/cm^2 for PtRu/OCNFs and 44 mW/cm^2 for the E-TEK catalyst under the same test conditions at 30°C. This indicates that the CNFs-supported catalysts exhibited 34–77% higher power density than the E-TEK catalyst. The PtRu/DCNFs exhibited a maximum power density of 199 mW/cm^2 at 70°C. In comparison, the

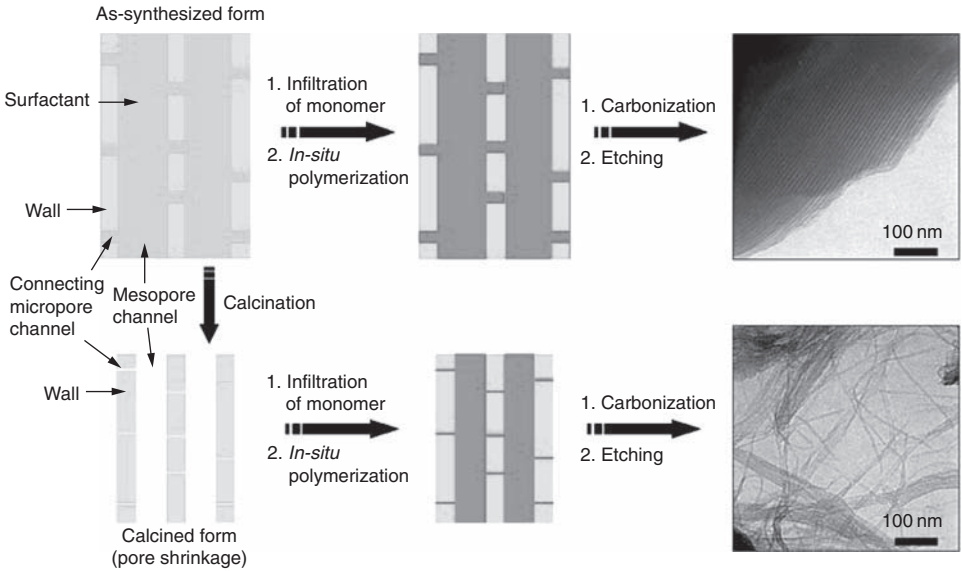

FIGURE 4.15 Schematic procedure for the synthesis of ordered and disordered arrays of carbon nanofibres (from [154]).

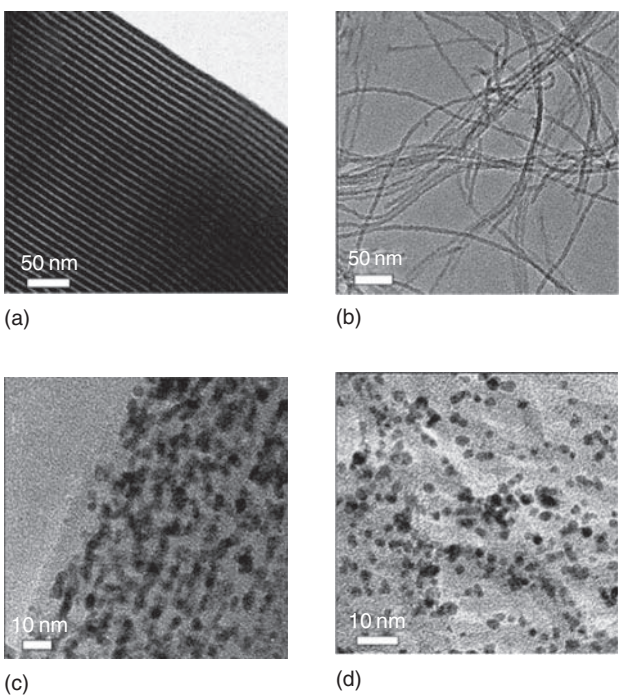

FIGURE 4.16 TEM images of (a) ordered and (b) disordered array of carbon nanofibres and high resolution TEM images of corresponding (c) ordered and (d) disordered CNFs after catalyst loading. The small black spots represent $Pt_{50}Ru_{50}$ catalyst nanoparticles (from [54]).

PtRu/OCNFs catalyst and the E-TEK catalyst showed maximum power densities of 160 mW/cm^2 and 124 mW/cm^2, respectively. PtRu/CNFs revealed higher catalytic activity in the fuel cell performance than commercial E-TEK catalyst. Such increase in catalyst activity was attributed to the supporting effect and better utilization of catalyst nanoparticles in PtRu/DCNFs. Interestingly, the PtRu nanoparticles supported on DCNFs with lower surface area of 325 m^2/g outperformed those on OCNFs with surface area of 602 m^2/g in the DMFC test. This is because the PtRu nanoparticles at DCNFs were well supported mostly on the accessible carbon surfaces with even and small particle size and could also make good contact with the Nafion® ionomers as well as methanol fuel, while the inner catalyst particles in OCNFs could hardly make contact with Nafion® ionomers during methanol oxidation reaction with little contribution to the activity.

OMCs with larger pore sizes have received much attention because of their potential applications involved with large molecules. Recently, some innovative preparation methods for new mesoporous carbon with much wider channel size have been developed by devising new synthetic strategies. An organic-organic self-assembly approach has been successfully developed to generate new ordered mesoporous polymer (OMP) materials, similar to the inorganic-organic assembly for OMS materials [254–259]. The OMP materials were synthesized by a solvent evaporation induced self-assembly method (EISA) by using amphiphilic triblock copolymers (PEO-PPO-PEO) as templates and a soluble low-molecular-weight polymer of phenol and formaldehyde (resol; MW = 500–5000) as organic precursors, followed by a thermopolymerization process. A family of the new OMC mesostructures, including two-dimensional (2D) hexagonal (space group of *p*6*m*), 3D bicontinuous (*Ia*3*d*), body-centred cubic (*Im*3*m*) and lamellar symmetries, was prepared by using phenolic resins as a carbon source and triblock copolymers PEO-PPO-PEO as templates. However, the pore sizes of the new OMC were limited by the molecular weight of copolymers, the same as mesoporous silicas. The OMP materials were then carefully carbonized to produce well-ordered and ultrastable (>1400°C) open new OMC frameworks. This method enabled a direct synthesis of new OMC from carbonization of the OMP, not from the conventional indirect nanocasting approach employing OMS as a hard template mentioned above [143–168, 246]. Figure 4.17 shows the schematic representation of the procedure used to prepare the new OMPs and corresponding OMC frameworks. Figure 4.18 displays a TEM image of an OMP denoted as FDU-15 calcined at 350°C viewed in the [001] direction (Figure 4.18a) and HRTEM image of C-FDU-15 calcined at 1400°C (Figure 4.18b), respectively. However, the large structural shrinkage during the pyrolysis and carbonization leads to pore sizes lower than 4 nm [257]. The BET surface area and the total pore volume of the FDU-15 calcined at 350°C are calculated to be 652 m^2/g and 0.63 cm^3/g, respectively. The pore diameter is about 6.8 nm with a narrow distribution. The wall thickness is estimated to be 5.3 nm, which indicates a thick organic network. C-FDU-15 obtained at 900°C has a large BET surface area of 968 m^2/g and a pore volume of 0.56 cm^3/g. A narrow pore size distribution at about 2.9 nm is obtained due to the structural shrinkage. A triconstituent co-assembly strategy has been developed to incorporate rigid components such as inorganic silicates into carbon

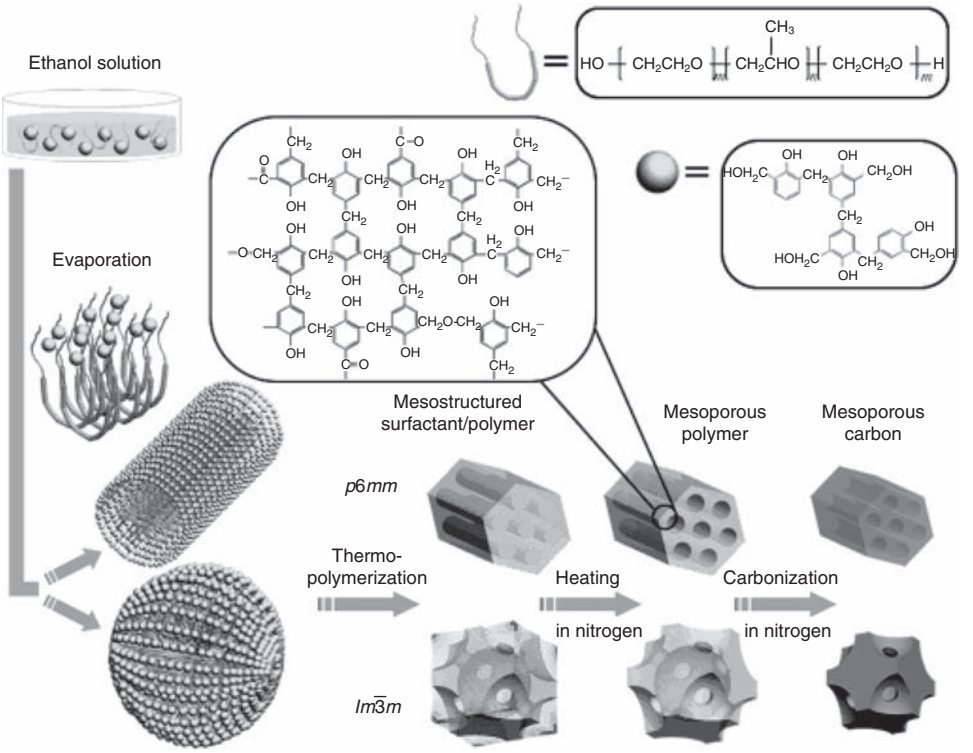

FIGURE 4.17 Schematic representation of the procedure used to prepare new ordered mesoporous polymers and, subsequently, carbon frameworks (from [257]).

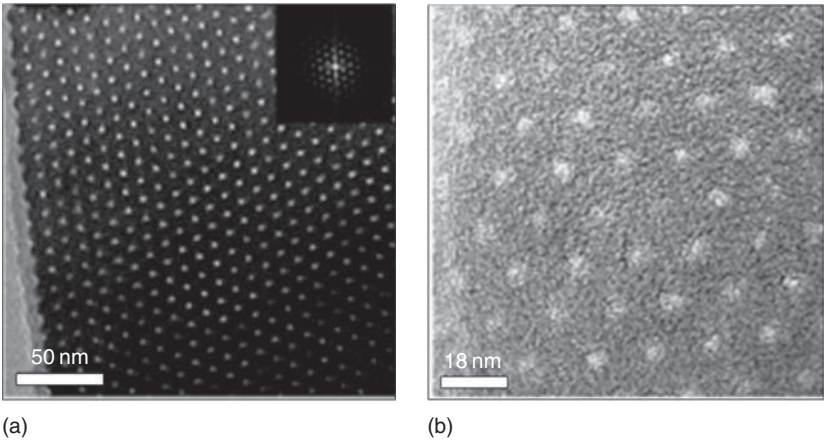

FIGURE 4.18 (a) TEM image of FDU-15 calcined at 350°C viewed in the [001] direction and (b) HRTEM image of C-FDU-15 calcined at 1400°C, respectively. Scale bar indicate 50 nm and 10 nm, respectively (from [257]).

frameworks to reduce the shrinkage [259]. The pore sizes of the obtained mesoporous carbons could be enlarged only to about 6 nm. Reminiscent of the research on mesoporous silicates, the design of high-molecular-weight copolymers would be feasible for the synthesis of new large-pore mesoporous carbons.

The combination of inorganic and organic properties at the atomic or molecular level has been also explored for the development of multifunctional hybrid materials. Recently, novel so-called periodic mesoporous organosilica (PMO) materials have been synthesized by employing organosilicate precursor instead of pure silica or polymer precursor [260–265]. Various organic moieties, including methylene, ethane, ethylene, thiophene, allyl, phenyl, biphenyl, two- or three-substituted phenyl, large heterocyclic groups and three-ring precursors have been tried uniformly to incorporate them into the pore walls of the PMO materials. Lu and co-workers reported the direct synthesis of mesoporous carbon/silica nanocomposites with unique pore walls that are composed of molecularly integrated silica and carbon from phenyl-bridged organosilica [265]. The final mesoporous carbon/silica nanocomposites were obtained by a carbonization process that decomposes the surfactant and converts the phenylene moieties into carbon [266]. The final new mesoporous carbon could be obtained from etching off the silica moiety from the carbon/silica nanocomposites. This method also provided a direct synthetic method to produce new ordered mesoporous carbon, compared with the conventional indirect two-step synthesis of mesoporous carbon (an inverse replica of silica) in which the infiltration of carbon precursors into preformed OMS is followed by carbonization and silica removal. Figure 4.19 shows the schematic illustration of the proposed mechanism for formation of mesoporous carbon/silica composite and mesoporous carbon.

In this case, the resulting new mesoporous carbon is not a negative replica whose pore size is determined from the wall thickness of the parent silica and can retain the mesopore size of the original mesoporous carbon/silica composite, providing the new means to control the pore size in large range, which possesses a high potential in preparing more efficient catalyst support for fuel cells.

2.2.3.3 Synthesis of nanoporous carbon using colloidal crystalline array templates
Self-assembled colloidal crystal arrays consisting of silica or polystyrene spheres are also frequently used as templates to synthesize a variety of highly ordered nanoporous carbon (ONC) materials with uniform pore size in the range of

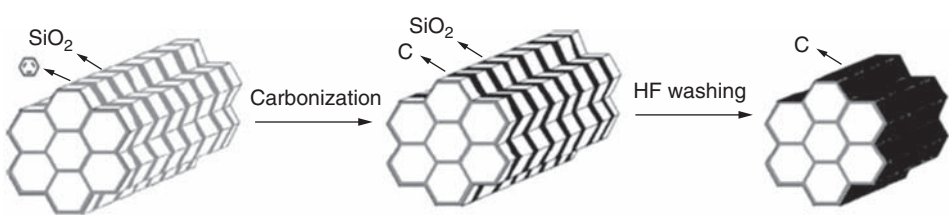

FIGURE 4.19 Schematic illustration of the proposed mechanism for formation of mesoporous carbon/silica composite and mesoporous carbon (from [266]).

mesopore to macropore[74,75,180–185]. Yu and his group reported the fabrication of a series of new uniform ONCs with controlled pore size in the range of 10–1000 nm and regulated morphology using colloidal crystalline arrays as templates and various carbon precursors such as sugars, polydivinylbenzene, phenolic resin and mesophase pitch [74,75,180–184]. Figure 4.20 shows the synthetic procedures for the fabrication of new uniform porous carbons with different morphology. The processes of the morphology control were performed by altering the acid catalyst sites, which control the initiation sites of the acid-catalysed condensation reaction from the same precursor. Figure 4.21 shows SEM images of the silica–carbon composites (insert) and the resulting silica-free carbon replicas with different morphologies. An Al-grafted silica array resulted in surface coating (surface templating) as shown in the carbon replica in Figure 4.21a. Figure 4.21b clearly shows the formation of volume-templated ordered nanoporous carbon framework with complete filling of the entire void around the silica spheres.

Some of these porous carbons with various pore sizes were used as supports for a $Pt_{50}Ru_{50}$ alloy catalyst in DMFC [74,75]. The methanol oxidation activity increased with the decreasing pore size in the porous carbon in accordance with the increasing surface area. The porous carbon with a mesopore size of 25 nm showed the highest performance, which corresponds to a 43% increase in activity as compared with that of a commercially available PtRu/C catalyst (E-TEK). This higher performance was considered to be not only due to the higher surface areas and larger pore volumes, which allowed a higher degree of catalyst dispersion,

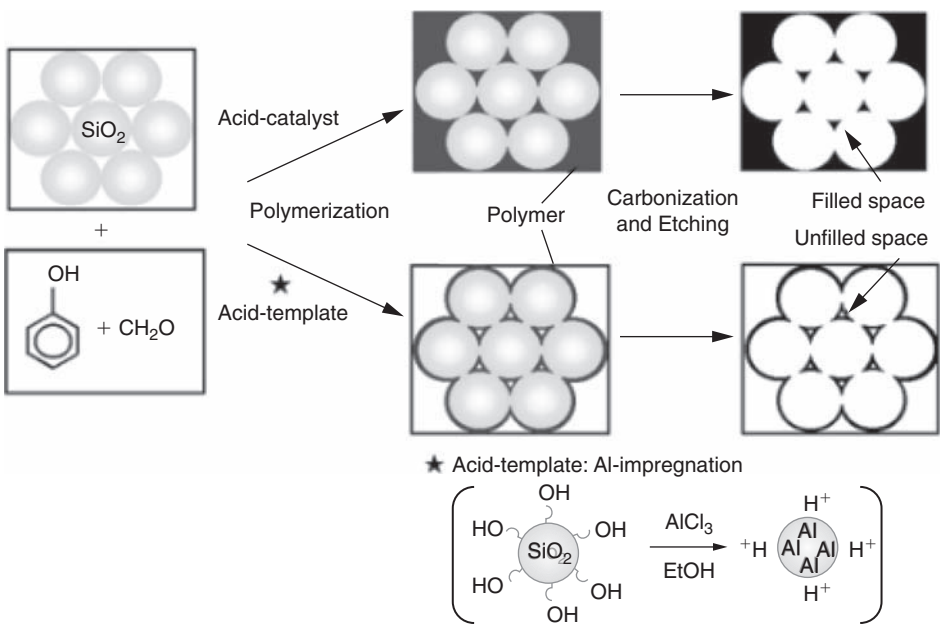

FIGURE 4.20 Synthetic procedures for the fabrication of new uniform porous carbons with a different morphology (from [74]).

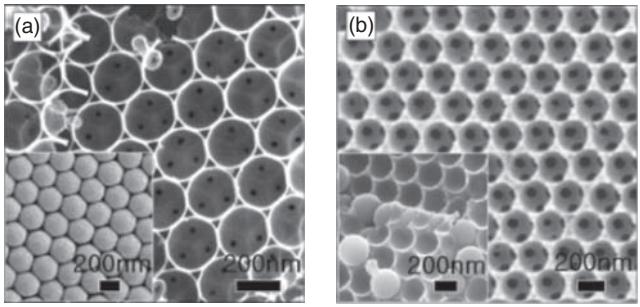

FIGURE 4.21 SEM images of carbon–colloidal silica composite (insert) and the corresponding silica-free carbon replica prepared (a) by surface templating and (b) by volume templating, using 250 nm silica spheres (from [74]).

but also due to highly integrated interconnected pore systems with periodic order, which allowed efficient transport of reactants and products.

Raghuveer et al. [186,187] used a modified colloidal template route to control the pore size of porous carbon. The obtained mesoporous carbon produced larger surface area and pore volume than the Vulcan XC-72R. They carried out the electrochemical measurements using catalyst-coated glassy carbon electrodes with a catalyst loading of $0.28\,mg\,cm^{-2}$ and found that the mesoporous carbon loaded with 5% Pt exhibited three times higher mass activity than the commercially available 20% Pt/C catalyst for methanol oxidation.

Although divinyl benzene, sucrose, phenolic resin, furfuryl alcohol and polyacrylonitrile have been usually used as carbon precursors, the resulting carbons obtained at relatively low temperatures of 700–1000°C were mainly amorphous due to poor graphitization [143–149,181–183]. There are only a few reports on ordered porous graphitized carbons, which can be synthesized usually by heating at high temperature exceeding 2000°C [158,190]. The graphitization increases electron conductivity due to delocalized π orbital electrons of carbon with sp^2 hybrid orbitals across the hexagonal aromatic units. Li et al. [190] reported the synthesis of pitch-based graphitized carbon with uniform spherical mesopores created by a colloidal imprinting method at 2400°C. Fuertes and Alvarez [158] carbonized ordered mesoporous silica-poly(vinyl chloride) nanocomposites initially by heating at 800°C and then graphitized the silica-free carbon at 2300°C after template dissolution. Pitch-based graphitized carbon with highly ordered nanopores was also synthesized by initially preparing a highly ordered porous carbon with colloidal crystals as a template and subsequently by further heating the template-free porous carbon at 2500°C [184]. Carbonization of mesophase pitch at 1000°C gave random stacking of graphene layers in the carbon matrix, while its subsequent graphitization led to the formation of relatively large graphite crystallinity in the carbonaceous pore walls having interlayer spacing of $\approx$0.33 nm. Graphitization at 2500°C of the carbonized sample reduced the BET surface area from 185 to $115\,m^2/g$. Similarly, the total pore volume is reduced from 1.63 to $1.12\,cm^3/g$. The chemical vapour deposition (CVD) method also provides an efficient way of preparing template-directed graphitic carbon. Graphitic uniform three-dimensional macroporous carbon replicas were prepared

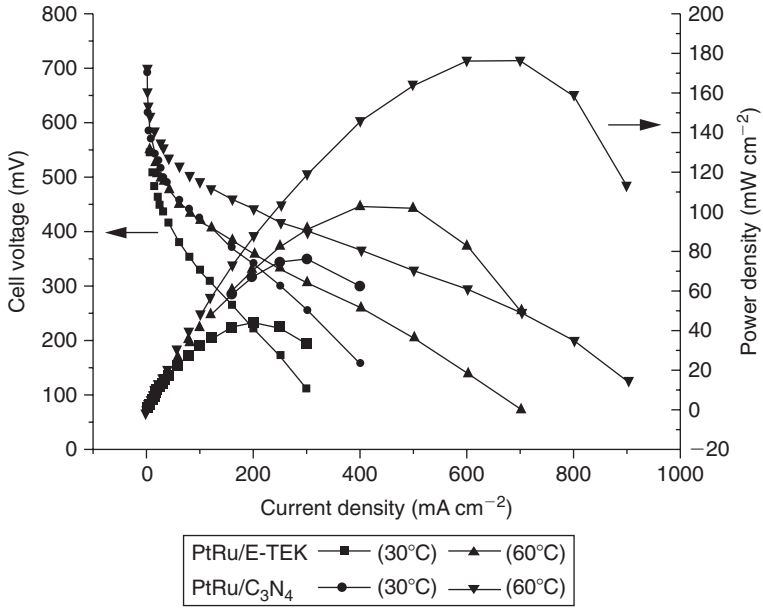

FIGURE 4.22 The polarization and power density curves for direct methanol fuel cell using Pt-Ru/C_3N_4 or commercial E-TEK catalyst as an anode determined at 30°C and 60°C. Cathode: Johnson Matthey Pt black (5.0 mg/cm^2) with O_2-feeding mode (from [Kim et al., unpublished material]).

by CVD or plasma methods of methane or propylene as a feed gas against porous synthetic silica opals [180]. Su et al. also prepared ordered macroporous carbon with a three-dimensional (3D) interconnected pore structure and a graphitic pore wall by CVD of benzene using inverse silica opal as the template [191]. The room-temperature specific activity of Pt catalyst supported on the graphitic pore carbon for electrochemical oxidation of methanol determined by cyclic voltammograms was found to be higher than that of a commercial Pt catalyst (E-TEK).

There has been also great interest in carbon materials containing heteroatoms, such as N, B and Si, due to the expectation of novel properties [192,193]. In particular, graphitic-C_3N_4 is a novel, rarely examined material which has extraordinary prospects in catalysis and hard coating and as adsorbent. Graphitic carbon nitride with a 3-dimensionally extended highly ordered pore array is prepared and the N-rich porous carbon was utilized as a support for $Pt_{50}Ru_{50}$ alloy catalyst to study the support effect on the anodic performance in a direct methanol fuel cell [Kim et al., unpublished material]. As shown in Figure 4.22, Pt-Ru/C_3N_4 catalyst showed 73–83% better performance than Pt-Ru/E-TEK catalyst under the same test conditions. The enhancement of these electrochemical characteristics is presumably related to the graphitic nature and the 3D interconnected open pore structures of the carbon materials [Kim et al., unpublished material]. The ONC materials with tunable pore size with interconnected pore structure and high surface area will suffer less diffusion and mass transport limitation compared with the ordered mesoporous carbon with small pore channels and thus can posses high potential in preparing active supported catalysts for fuel cells.

2.2.3.4 Porous carbon with hierarchically pore structure Recently, many different porous inorganic materials have been synthesized by complex multiple templating schemes employing both organic surfactants and block copolymers as template [267]. Hierarchical materials containing both interconnected macroporous and mesoporous structures can enhance properties compared with single-sized pore materials due to the combined benefits of mesoporous and macroporous networks including increased mass transport through the material and maintenance of the specific surface area on the level of fine pore systems. Particularly, the introduction of secondary larger pores in the mesoporous network can improve remarkably diffusion kinetics of reactants and products, which could be problematic in mesoporous materials, without compromise in the specific surface area.

Recently, various carbons having hierarchical structures have been synthesized based on an identical nanocasting method using hierarchically porous silica materials as templates. Thus, the resulting carbon is a replica of the silica template, having a hierarchical pore structure in the framework and preserving the macroscopic shape of the silica template [268–271]. For example, Lee et al. reported a simple and cost-effective synthesis of a hierarchical mesocellular mesoporous carbon (HMMC) composed of large, ca. 40 nm-sized cellular pores and small ordered 4.7 nm-sized mesopores derived from the dissolution of its parent hierarchical mesocellular mesoporous silicate template [268]. The BET surface area and single point total pore volume of HMMC were 853 m^2/g and 1.54 cm^3/g, respectively. Lindén and co-workers [269,270] reported the synthesis of hierarchical carbon replicas from their corresponding meso-macroporous silica and the meso-macroporous carbon had a BET surface area of over 1000 m^2/g and a specific pore volume of 1.2 cm^3/g. Interestingly, this method resulted in the generation of a significant microporosity in the carbon replicas, leading to the tri-modal porous carbons [270, 271].

Chai et al. prepared periodically ordered bimodal porous carbon (POBPC) by using a dual template strategy including both spherical polystyrene and smaller

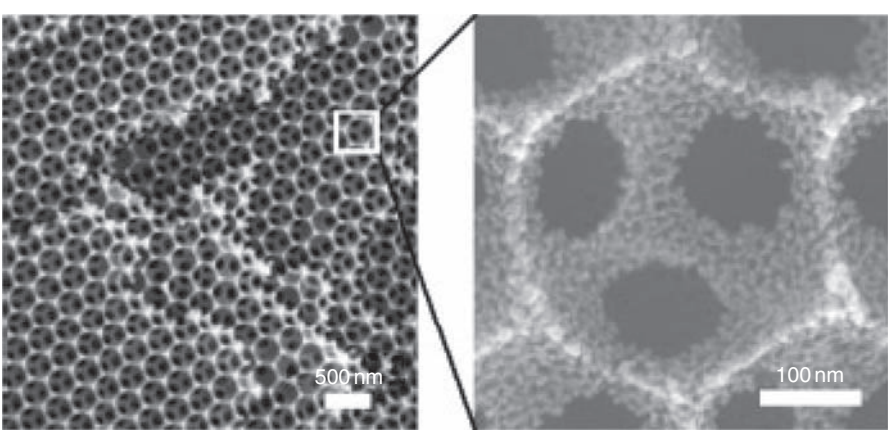

FIGURE 4.23 SEM images of periodic ordered bimodal porous carbon (POBPC) composed of macropores of about 317 nm diameter connected to small mesopores about 10 nm in size. This periodically ordered, bimodal porous carbon is termed POBPC (317-10) (from [53]).

silica particles as moulds [53]. These materials possess highly ordered adjustable and well-defined macropores, and tunable mesopores and interconnected mesopores of different size in the macropore walls (Figure 4.23). These workers also investigated Pt-Ru/POBPC catalysts for methanol oxidation at DMFC conditions. At 30°C, the POBPC catalyst showed a current density of 40 mA/cm^2, which corresponds to four times that of the E-TEK catalyst (10 mA/cm^2) at 0.5 V and exhibited a high maximum power density (70 mW/cm^2), which is 79% higher than that of E-TEK catalyst (39 mW/cm^2), as shown in Figure 4.24a. At 70°C, the maximum power densities were 190 and 121 mW/cm^2 for the POBPC catalyst and E-TEK catalyst, respectively (Figure 4.24b). This also corresponds to better

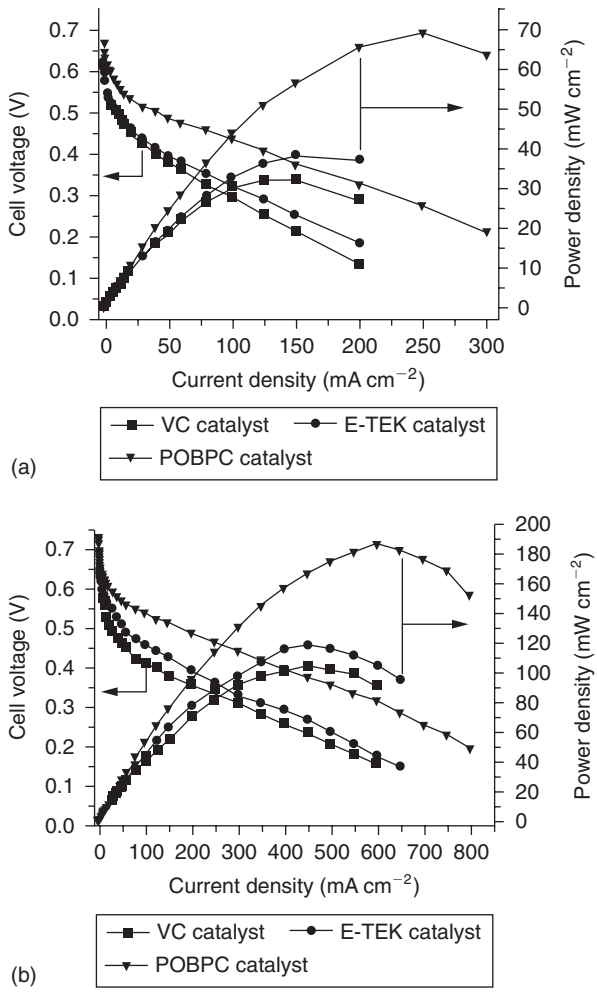

FIGURE 4.24 The polarization curves for a direct methanol fuel cell using a $Pt_{50}Ru_{50}$/VC catalyst (■), a commercial $Pt_{50}Ru_{50}$/E-TEK catalyst (●) and a $Pt_{50}Ru_{50}$/POBPC (317-10) catalyst (▼) determined at (a) 30°C and (b) 70°C, respectively (from [53]).

performance of the POBPC catalyst by about 57% in comparison with the E-TEK one. The high performance of POBPC was attributed to the structural uniqueness of the highly ordered three-dimensionally interconnected macropore array with uniform mesoporous walls, which can enhance not only both the dispersion and utilization of metal catalysts but also efficient transport of reactants and products during reaction.

Therefore, meso- and macroporous carbons appear to have great potential for catalyst supports in DMFC anode catalysis. Table 4.5 presents various Pt and/or PtRu/carbon supported catalysts prepared through various synthetic routes and their electrochemical activity for low-temperature fuel cells.

3. CONCLUSIONS

Various preparation methods for active catalyst nanoparticles have been examined with some consideration from practical view points associated with each preparation method. Types of catalyst supports and their properties along with some synthetic strategies for selected support types have been also explored based on the recent literature for fuel cell application. Recently, there has been great progress in developing efficient supported electrocatalysts for low-temperature fuel cells. The choice of the catalyst preparation method and carbon support has strong effects on size, size distribution, stability, extent of alloying degree and dispersion of active catalyst nanoparticles anchored on the carbon support. These are all closely related to the utilization and performance of the catalysts in fuel cells. Thus, the catalyst preparation along with proper selection among metals and supports are the most important means to make efficient electrode preparation for the optimization of fuel cell performance. The exploration and synthesis of mixed metal nanoparticles research extending to two and more components is a wide open and active field. Catalyst support itself also has significant influence on the catalyst preparation procedure and performance of the catalysts. The rapid development of nanotechnology, especially in the field of synthesis and nanoengineering of nanostructured carbon materials, will allow us better control of surface properties such as surface area, pore size, pore distribution, surface functionality and morphology of carbon supports. Further progress depends on the control and understanding of structures and properties at the nanoscopic level. Highly ordered nanoporous carbons offer unique opportunities for well-defined and fundamental studies, as well as possibilities of developing high performance electrocatalysts, although their application still faces some challenges in terms of synthesis, metal loading and electrode preparation. Practical applications might require nanoporous carbon materials with hierarchical pore structures at different length scales in order to achieve highly organized functions, maintaining combined beneficial advantages of fast diffusion kinetics and high surface area. Further development and improvement of the metal preparation method and the carbon supports in terms of performance and cost and integration optimization with the electrolyte membrane and other controlled macrostructures, could bring about a breakthrough in the exploration for a new generation of electrode materials in the near future.

Table 4.5 Selected carbon-supported catalysts prepared through various synthetic routes for low-temperature fuel cell applications

Catalyst	Precursor/reducing agent	Support/loading	Particle size	Activity/reaction (oxidation or reduction)	Ref.
Pt	$H_2PtCl_6/NaBH_4$	Micro-C/20%	3.8–4.7 nm		[244]
Pt	$H_2PtCl_6/NaBH_4$	Micro-C/16–17%	4.0–5.1 nm	98–244 mA/mg	[245]
Pt	$Pt(NH_3)_4(NO_3)_2$	Meso-C/8.5–24%	8–10 nm	ORR in DMFC	[171]
Pt	$H_2PtCl_6/NaBH_4$	Meso-C/9.8–22.5%			[173]
Pt	H_2PtCl_6	Meso-C/20%	3.6–4.0 nm		[174]
Pt	$Pt(CH(COCH_3)_2)_2$	Meso-C/0.6–11.5%	2–3 nm	(0.5 M H_2SO_4 + 1 M CH_3OH, RT)	[175]
$Pt_{50}Ru_{50}$	H_2PtCl_6, $RuCl_3/NaBH_4$	Meso-C/80%	2–3 nm	214 mW/cm^2 (DMFC, O_2, 70°C)	76
$Pt_{50}Ru_{50}$	H_2PtCl_6, $RuCl_3/NaBH_4$	Meso-C/80%	2.0–4.5 nm	160–199 mW/cm^2 (DMFC, O_2, 70°C)	54
$Pt_{50}Ru_{50}$	H_2PtCl_6, $RuCl_3/NaBH_4$	Col-C/60–80%	2–3 nm	122–167 mW/cm^2 (DMFC, O_2, 70°C)	75
Pt	H_2PtCl_6	Col-C/5–20%		62 mA/cm^2 at 0.75 V (1 M H_2SO_4 + 1 M CH_3OH, 25°C)	[185]
Pt	H_2PtCl_6	Col-C/20%	6 nm	0.98 mA/cm^2 at 0.66 V (0.5 M H_2SO_4 + 1 M CH_3OH, 25°C)	[191]
$Pt_{50}Ru_{50}$	H_2PtCl_6, $RuCl_3/NaBH_4$	Hierarchical-C/80%	2–3 nm	195 mW/cm^2 (DMFC, O_2, 70°C)	53

Micro-C, Meso-C, Col-C and Hierarchical-C stand for microporous carbon, mesoporous carbon, colloidal crystal array-based carbon, hierarchical carbon, respectively.

References

1. Oliveira Neto A, Franco EG, Arico E, Linardi M, Gonzalez ER. J. Eur. Ceramic Soc. 2003; 23:2987.
2. Atkins WP. Physical Chemistry, 7th edn. Oxford University Press: Oxford, 1994.
3. Carrette L, Friedrich KA, Stimming U. Fuel Cells 2001; 1:5.
4. Oetjen HF, Schmidt VM, Stimming U, Trila F. J. Electrochem. Soc. 1996; 12:3838.
5. Hogarth MP, Hards GA. Platinum Metals Rev. 1996; 40:150.
6. Liu R, Ley KL, Pu C et al. In Electrode Processes, VI, A Wieckowski, K Itaya (eds). Electrochemical Society Proceedings Series: Pennington, 1996; 341.
7. Gasteiger HA, Markovic N, Ross PN. J. Phys. Chem. 1995; 99:8290.
8. Gasteiger HA, Markovic N, Ross PN, Cairns EJ. J. Phys. Chem. 1994; 98:617.
9. Kabbabi A, Faure R, Durand R et al. J. Electroanal. Chem. 1998; 44:441.
10. Wolohan P, Mitchell PCH, Thompsett D, Cooper SJ. J. Mol. Catal. A 1997; 119:223.
11. Pozio A, Giorgi L, Antolini E, Passalacqua E. Electrochim. Acta 2000; 46:555.
12. Iwasita T, Nart FC, Vielstich W. Ber. Bunsengen. Phys. Chem. 1990; 94:1030.
13. Goodenough JB, Manoharan R, Shukla AK, Ramesh KV. Chem. Mater. 1989; 1:391.
14. McBreen J, Mukerjee S. J. Electrochem. Soc. 1995; 142:3399.
15. Burcham LJ, Wachs IE. Catalysis Today 1999; 49:467.
16. Baxter SF, Battaglia VS, White RE. J. Electrochem. Soc. 1999; 146:437.
17. Burstein GT, Barnett CJ, Kucernak AR, Williams KR. Catalysis Today 1997; 38:425.
18. Hamnett A. Catalysis Today 1997; 38:445.
19. Sobkowski J, Franaszczuk K, Dobrowolska K. J. Electrochem. Soc. 1992; 330:529.
20. Willsau J, Heitbaum J. Electrochim. Acta 1986; 31:943.
21. Wang X, Hu J-M, Hsing I-M. J. Electroanal. Chem. 2004; 562:73.
22. Breiter MW. Electrochim. Acta 1963; 8:447.
23. Parsons R, VanderNoot T. J. Electroanal. Chem. 1988; 257:9.
24. Jarvi TD, Stuve EM. In Electrocatalysis, J Lipkovski and PN Ross (eds), Wiley–VCH: Weinheim, 1998.
25. Park S, Xie Y, Weaver MJ. Langmuir 2002; 18:5792.
26. Jiang J, Kucernak A. J. Electroanal. Chem. 2002; 520:64.
27. Capon A, Parsons R. J. Electroanal. Chem. 1974; 45:205.
28. Lamy C, Leger JM. J. Chem. Phys. 1991; 88:1649.
29. Kinoshita K. Electrochemical Oxygen Technology. John Wiley & Sons: New York, 1992.
30. Salgado JRC, Antolini E, Gonzalez ER. J. Power Sources 2004; 138:56.
31. Ma Z-F, Xie X-Y, Ma X-X et al. Electrochem. Commun. 2006; 8:389.
32. Antolini E, Passos RR, Ticianelli EA. Electrochim. Acta 2002; 48:263.
33. Xiong L, Manthiram A. J. Mater Chem. 2004; 14:1454.
34. Yu EH, Scott K, Reeve RW. Fuel Cells 2003; 3:169.
35. Markovic NM, Schmidt TJ, Stamenkovic V, Ross PN. Fuel Cells 2001; 1:105.
36. Dillon R, Srinivasan S, Arico AS, Antonucci V. J. Power Sources 2004; 127:112.
37. Vielstich W, Lamm A. In Handbook of Fuel Cells, Vol. 1, HA Gasteiger (ed.), John Wiley & Sons: New York, 2002.
38. Chan K-Y, Ding J, Ren J, Cheng S, Tsang KY. J. Mater. Chem. 2004; 14:505.
39. Liu H, Song C, Zhang L, Zhang J, Wang H, Wilkinson DP. J. Power Sources 2006; 155:95.
40. Sattler ML, Ross PN. Ultramicroscopy 1986; 20:21.
41. Kinoshita K. J. Electrochem. Soc. 1990; 137:845.
42. Takasu Y, Ohashi N, Zhang X-G et al. Electrochim. Acta 1996; 41:2595.
43. Giordano N, Passalacqua E, Pino L et al. Electrochim. Acta 1991; 36:1979.
44. Takasu Y, Kawaguchi T, Sugimoto W, Murakami Y. Electrochim. Acta 2003; 48:3861.
45. Bessel CA, Laubernds K, Rodriguez NM, Baker RTK. J. Phys. Chem. B 2001; 105:1115.
46. Zhang L, Zhang J, Wilkinson DP, Wang H. J. Power Sources 2006; 156:171.
47. Simonov PA, Likholobov VA, Wieckowski A, Savinova ER, Vayenas CG (eds). Catalysis and Electrocatalysis at Nanoparticle Surfaces. Marcel Dekker: New York, 2003, 409.
48. Park KW, Sung YE, Han S, Yun Y, Hyeon T. J. Phys Chem. B 2004; 108:939.

49. Shao Y, Yin G, Gao Y, Shi P. J. Electrochem. Soc. 2006; 153:A1093.
50. Watanabe M, Sei H, Stonehart P. J. Electroanal Chem. 1989; 261:375.
51. Arico AS, Srinivasan S, Antonucci V. Fuel Cells 2001; 2:133.
52. Rao V, Simonov PA, Savinova ER et al. J. Power Sources 2005; 145:178.
53. Chai GS, Shin IS, Yu J-S. Adv. Mater. 2004; 16:2057.
54. Chai GS, Yoon SB, Yu J-S. Carbon 2005; 43:3028.
55. Lee K, Zhang J, Wang H, Wilkinson DP. J. Appl. Electrochem. 2006; 36:507.
56. Takasu Y, Fujiwara T, Murakami Y et al. J. Electrochem. Soc. 2000; 147:4421.
57. Fujiwara N, Yasuda K, Ioroi T, Siroma Z, Miyazaki Y. Electrochim. Acta 2002; 47:4079.
58. Fujiwara N, Shiozaki Y, Tanimitsu T, Yasuda K, Miyazaki Y. Electrochemistry 2002; 70:988.
59. Hills CW, Mack NH, Nuzzo RG. J. Phys. Chem. B 2003; 107:2626.
60. Dickinson AJ, Carrette LPL, Collins JA, Friedrich KA, Stimming U. Electrochim. Acta 2002; 47:3733.
61. Friedrich KA, Geyzers KP, Dickinson AJ, Stimming U. J. Electroanal. Chem. 2002; 524–525:261.
62. Boxall DL, Deluga GA, Kenik EA, King WD, Lukehart CM. Chem. Mater. 2001; 13:891.
63. Deivaraj TC, Lee JY. J. Power Sources 2005; 142:43.
64. Cote R, Lalande G, Faubert G, Guay D, Dodelet JP, Denes GJ. New Mater. Electrochem. Sys. 1998; 1:7.
65. Papageorgopoulos DC, Keijzer M, Veldhuis JBJ, de Bruijn FA. J. Electrochem. Soc. 2002; 149:A1400.
66. Liu Y-C, Qiu X-P, Huang Y-Q, Zhu W-T. Carbon 2002; 40:2375.
67. Li W, Liang C, Zhou W et al. J. Phys. Chem. B 2003; 107:6292.
68. Neto AO, Giz MJ, Perez J, Ticianelli EA, Gonzalez ER. J. Electrochem. Soc. 2002; 149:A272.
69. Choi WC, Kim JD, Woo SI. Catal. Today 2002; 74:235.
70. Yuan FL, Ryu H. Nanotechnology 2004; 15:s596.
71. Li W, Liang C, Qiu J et al. Carbon 2002; 40:791.
72. Ha S, Larsen R, Masel RI. J. Power Sources 2005; 144:28.
73. Zoval JV, Lee J, Gorer S, Penner RM. J. Phys. Chem. B 1998; 102:1166.
74. Yu J-S, Kang S, Yoon SB, Chai GS. J. Am. Chem. Soc. 2002; 124:9382.
75. Chai GS, Yoon SB, Yu J-S, Choi JH, Sung YE. J. Phys. Chem. B 2004; 108:7074.
76. Chai GS, Yoon SB, Kim JH, Yu J-S. Chem. Commun. 2004; 2766.
77. Lu Q, Yang B, Zhuang L, Lu J. J. Phys. Chem. B 2005; 109:1715.
78. Yang B, Lu Q, Wang Y, Zhang L, Lu J, Liu P. Chem. Mater. 2003; 15:3552.
79. Liu Z, Ling XY, Su X, Lee JY. J. Phys. Chem. B 2004; 108:8234.
80. Rojas S, Garcia-Garcia FJ, Jaras S, Martinez-Huerta MV, Fierro JLG, Boutonnet M. Appl. Catal., A 2005; 285:24.
81. Bensebaa F, Farah AA, Wang D et al. J. Phys. Chem. B 2005; 109:15339.
82. Bönnemann H, Richards RM. Eur. J. Inorg. Chem. 2001; 10:2455.
83. Roucoux A, Schulz J, Patin H. Chem. Rev. 2002; 102:3757.
84. Watanabe, Saegusa S, Stonehart P. J. Electroanal. Chem. 1989; 271:213.
85. Watanabe M, Uchida M, Motoo S. J. Electroanal. Chem. 1987; 229:395.
86. Bönnemann H, Nagabhushana KS. J. New Mater. Electrochem. Syst. 2004; 7:93.
87. Schmidt TJ, Noeske M, Gasteiger HA et al. Langmuir 1997; 13:2591.
88. Schmidt TJ, Noeske M, Gasteiger HA et al. J. Electrochem. Soc. 1998; 145:925.
89. Bönnemann H, Brijoux W, Brinkmann R, Dinjus E, Jouben T, Korall B. Angew. Chem. Int. Ed. Engl. 1991; 30:1312.
90. Schmidt TJ, Gasteiger HA, Behm RJ. Electrochem. Commun. 1999; 1:1.
91. Paulus UA, Endruschat U, Feldmeyer GJ, Schmidt TJ, Bönnemann H, Behm RJ. J. Catal. 2000; 195:383.
92. Bönnemann H, Brinkmann R, Kinge S, Ely TO, Armand M. Fuel Cells 2004; 4:289.
93. Wang X, Hsing I. Electrochem. Acta 2002; 47:2981.
94. Kim T, Takahashi M, Nagai M, Kobayashi K. Electrochem. Acta 2004; 50:817.
95. Bensebaa F, Patrito N, Page YL, Ecuyer PL, Wang D. J. Mater. Chem. 2004; 14:3378.
96. Liu Z, Ling X, Lee J, Su X, Gan LM. J. Mater. Chem. 2003; 13:3049.
97. Wang Y, Ren J, Deng K, Gui L, Tang Y. Chem. Mater. 2000; 12:1622.

98. Bock C, Paquet C, Couillard M, Botton GA, MacDougall BR. J. Am. Chem. Soc. 2004; 126:8028.
99. Lee YH, Lee G, Shim JH et al. Chem. Mater. 2006; 18:4209.
100. Liao S, Holmes K-A, Tsaprailis H, Birss VI. J. Am. Chem. Soc. 2006; 128:3504.
101. Xue X, Lu T, Liu C, Xing W. Chem. Commun. 2005; 12:1601.
102. Schmidt TJ, Noeske M, Gasteiger HA, Behm RJ, Britz P, Bönnemann H. J. Electrochem. Soc. 1998; 145:925.
103. Dubau L, Coutanceau C, Garnier Leger EJ-M, Lamy C. J. Appl. Electrochem. 2003; 33:419.
104. Rojas S, Garcia-Garcia FJ, Järas S, Martinez-Huerta MV, Fierro JLG, Boutonnet M. Appl. Catal. A Gen. 2005; 285:24.
105. Boutonnet M, Kizting J, Stenius P. Colloids Surf. 1982; 5:209.
106. Petit C, Lixon P, Pilei M-P. J. Phys. Chem. 1993; 97:12974.
107. Qi L, Ma J, Shen J. J. Colloid Interface Sci. 1997; 186:498.
108. Chen DH, Wu SH. Chem. Mater. 2000; 12:1354.
109. Pillai V, Kumar P, Multani MS, Shah DO. Colloid Surf. A 1993; 80:69.
110. Chhabra V, Lal M, Maitra AN, Ayyub P. Colloid Polym. Sci. 1995; 273:939.
111. Chang CL, Fogler HS. Langmuir 1997; 13:3295.
112. Hirai T, Shiojiri S, Komasawa I. J. Am. Chem. Eng. Jap. 1994; 27:590.
113. Haram SK, Mahadeshwar AR, Dixit SG. J. Phys. Chem. 1996; 100:5868.
114. Nagy J. J. Colloids Surf. 1989; 35:201.
115. Kandori K, Kon-No K, Kitahara A. J. Colloid Interface Sci. 1988; 122:78.
116. Antonietti M, Basten R, Lonmann S. Macromol. Chem. Phys. 1995; 196:441.
117. Palu BK, Moulike SP. J. Dispersion Sci. Technol. 1997; 18:301.
118. Gan LM, Chew CH. In Advanced Functional Molecules and Polymers, HS Nalwa (ed.), Gordon and Breach: New York, 1999.
119. Liu Z, Lee JY, Han M, Chen W, Gan LM. J. Mater. Chem. 2002; 12:2453.
120. Wu M-L, Chen D-H, Huang T-C. Chem. Mater. 2001; 13:599.
121. Liu H, Songa C, Zhang L, Zhang J, Wang H, Wilkinson DP. J. Power Sources 2006; 155:95.
122. Raghuveer V, Ferreira PJ, Manthiram A. Electrochem. Commun. 2006; 8:807.
123. Eriksson S, Nylé U, Rojas S, Boutonnet M. Appl. Catal. A 2004; 265:207.
124. Fendler JH. Chem. Rev. 1987; 87:877.
125. Cizeron J, Pileni MP. J. Phys. Chem. 1995; 99:17410.
126. Tanori J, Duxin N, Petit C, Veillet P, Pileni MP. Colliod. Polym. Sci. 1995; 273:886.
127. Petit C, Jain TK, Billouder F, Pileni MP. Langmuir 1994; 10:4446.
128. Pileni MP. Langmuir 1997; 13:3266.
129. Liu Y, Qiu X, Chen Z, Zhu W. Electrochem. Commun. 2002; 4:550.
130. Escudero MJ, Hontanón E, Schwartz S, Boutonnet M, Daza L. J. Power Source 2002; 106:206.
131. Liu Z, Lee JY, Han M, Chen W, Gan LM. J. Mater. Chem. 2002; 12:2453.
132. Xiong L, Manthiram A. Solid State Ionics 2005; 176:385.
133. Solla-Gullón J, Montiel V, Aldaz A, Clavilier J. Electrochem. Commun. 2002; 4:716.
134. Solla-Gullón J, Montiel V, Aldaz A, Clavilier J. J. Electrochem. Soc. 2003; 150:104.
135. Solla-Gullón J, Rodes A, Montiel V, Aldaz A, Clavilier J. J. Electroanal. Chem. 2003; 554:273.
136. Solla-Gullón J, Vidal-Iglesias FJ, Rodes A, Montiel V, Aldaz A. Electrochim. Acta 2004; 49:5079.
137. Solla-Gullón J, Montiel V, Aldaz A, Clavilier J. J. Electroanal. Chem. 2000; 491:69.
138. Zhang X, Chan K. Chem. Mater. 2003; 15:451.
139. Xiong L, Manthiram A. Electrochim. Acta 2005; 50:2323.
140. Santos LGRA, Oliveira CHF, Moraes IR, Ticianelli EA. J. Electroanal. Chem. 2006; 596:141.
141. Arico AS, Pino L, Antonucci PL, Giordano N. Carbon 1990; 28:599.
142. Simonov PA, Likholobov VA. In Catalysis and Electrocatalysis at Nanoparticle Surfaces, A Wieckowski, ER Savinova, CG Vayenas (eds). Marcel Dekker: New York, 2003; 409.
143. Ryoo R, Joo SH, Jun S. J. Phys. Chem. B 1999; 103:7743.
144. Lee J, Yoon S, Hyeon T, Oh SM, Kim KB. Chem. Commun. 1999:2177.
145. Yoon SB, Kim JY, Yu J-S. Chem. Commun. 2001; 559.
146. Yoon SB, Kim JY, Yu J-S. Chem. Commun. 2002:1536.
147. Jun S, Joo S, Kim S-S, Pinnavaia TJ. Chem. Commun. 2001:2418.
148. Vix-Cuterl C, Boulard S, Parmentier J, Werckmann J, Patarin J. Chem. Lett. 2002; 1062.

149. Joo SH, Ryoo R, Kruk M et al. J. Am. Chem. Soc. 2000; 122:10712.
150. Ryoo R, Joo SH, Kruk M, Jaroniec M. Adv. Mater. 2001; 13:677.
151. Joo SH, Choi SJ, Oh I et al. Nature 2001; 412:169.
152. Yu C, Fan J, Tian B, Zhao D, Stucky GD. Adv. Mater. 2002; 14:1742.
153. Kruk M, Jaroniec M, Kim T-W, Ryoo R. Chem. Mater. 2003; 15:2815.
154. Yoon SB, Kim JY, Kooli F, Lee CW, Yu J-S. Chem. Commun. 2003:1740.
155. Che SN, Garcia-Bennett AE, Liu XY et al. Angew. Chem. Int. Ed. 2003; 42:3930.
156. Wang T, Liu XY, Zhao DY, Jiang ZY. Chem. Phys. Lett. 2004; 389:327.
157. Xia Y, Yang Z, Mokaya R. Chem. Mater. 2006; 18:140.
158. Fuertes AB, Alvarez S. Carbon 2004; 42:3049.
159. Lee J, Han S, Hyeon T. J. Mater. Chem. 2004; 14:478.
160. Lu A, Schmidt W, Spliethoff B, Schüth F. Adv. Mater. 2003; 15:1602.
161. Yang H, Yan Y, Liu Y et al. J. Phys. Chem. B 2004; 108:17320.
162. Vix-Guterl C, Saadallah S, Vidal L, Reda M, Parmentier J, Patarin J. J. Mater. Chem. 2003; 13:2535.
163. Kim TW, Park IS, Ryoo R. Angew. Chem. Int. Ed. 2003; 42:4375.
164. Fuertes AB, Centeno TA. J. Mater. Chem. 2005; 15:1079.
165. Kim CH, Lee DK, Pinnavaia TJ. Langmuir 2004; 20:5157.
166. Yang CM, Weidenthaler C, Spliethoff B, Mayanna M, Schuth F. Chem. Mater. 2005; 17:355.
167. Lu A, Kiefer A, Schmidt W, Schüth F. Chem. Mater. 2004; 16:100.
168. Kruk M, Dufour B, Celer EB, Kowalewski T, Jaroniec M, Matyjaszewski K. J. Phys. Chem. B 2005; 109:9216.
169. Schuth F. Angew. Chem. Int. Ed. 2003; 42:3604.
170. Lee J, Han S, Hyeon T. J. Mater. Chem. 2004; 14:478.
171. Choi WC, Woo SI, Jeon MK, Sohn JM, Kim MR, Jeon HJ. Adv. Mater. 2005; 17:446.
172. Ding J, Chan KY, Ren J, Xiao FS. Electrochim. Acta 2005; 50:3131.
173. Wlkander K, Ekstrom H, Palmqvist AEC, Lundblad A, Holmberg K, Lindbergh G. Fuel Cells 2006; 6:21.
174. Joo JB, Kim P, Kim W, Kim J, Yi J. Catal. Today 2006; 111:171.
175. Liu S-H, Lu R-F, Huang S-J, Lo A-Y, Chien S-H, Liu S-B. Chem. Commun. 2006:3435.
176. Su F, Zeng J, Bao X, Yu Y, Lee JY, Zhao XS. Chem. Mater. 2005; 17:3960.
177. Yoon SB, Sohn K, Kim JY, Shin CH, Yu J-S, Hyeon T. Adv. Mater. 2002; 14:19.
178. Yu J-S, Yoon SB, Lee YJ, Yoon KB. J. Phys. Chem. B 2005; 109:7040.
179. Kawashima D, Aihara T, Kobayashi Y, Kyotani T, Tomita A. Chem. Mater. 2000; 12:3397.
180. Zakhidov AA, Boughman RH, Iqbal Z et al. Science 1998; 282:897.
181. Yu J-S, Yoon SB, Chai GS. Carbon 2001; 39:1421.
182. Kang S, Yu J-S, Kruk M, Jaroniec M. Chem. Commun. 2002:1670.
183. Gierszal KP, Yoon SB, Yu J-S, Jaroniec M. J. Mater. Chem. 2006; 16:2819.
184. Yoon SB, Chai GS, Kang S, Yu J-S, Gierszal KP, Jaroniec M. J. Am. Chem. Soc. 2005; 127:4188.
185. Gundiah G, Govindaraj A, Rao CNR. Mater. Reser. Bull. 2001; 36:1751.
186. Raghuveer V, Manthiram A. Electrochem. Solid-State Lett. 2004; 7:336.
187. Raghuveer V, Manthiram A. J. Electrochem. Soc. 2005; 152:1504.
188. Li ZJ, Jaroniec M. J. Phys. Chem. B 2004; 108:824.
189. Li ZJ, Jaroniec M. Chem. Mater. 2003; 15:1327.
190. Li ZJ, Jaroniec M, Lee YJ, Radovic LR. Chem. Commun. 2002:1346.
191. Su F, Zhao XS, Wang Y, Zeng J, Zhou Z, Lee JY. J. Phys. Chem. B 2005; 109:20200.
192. Reculusa S, Agricole B, Derré A et al. Electroanalysis 2007; 19:379.
193. Sung IK, Yoon SB, Yu J-S, Kim DP. Chem. Commun 2002:1480.
194. Arico AS, Srinivasan S, Antonucci V. Fuel Cells 2001; 2:1.
195. Ravikumar MK, Shukla AK. J. Electrochem. Soc. 1996; 143:2601.
196. Wu G, Li L, Li JH, Xu BQ. Carbon 2005; 43:2579.
197. Uchida M, Fukuoka Y, Sugawara Y, Ohara H, Ohta A. J. Electrochem. Soc. 1998; 145:3708.
198. Anderson ML, Stroud RM, Rolison DR. Nano Lett. 2002; 2:235.
199. Mastragostino M, Mossiroli A, Soavi F. J. Electrochem. Soc. 2004; 151:1919.
200. Pai Y-H, Ke J-H, Chou C-C, Lin J-J, Zen J-M, Shieu F-S. J. Power Source.

201. Liu Y-C, Qiu X-P, Huang Y-Q, Zhu W-T, Wu G-S. J. Appl. Electrochem. 2002; 32:1279.
202. Liu Y-C, Qiu X-P, Huang Y-Q, Zhu W-T. J. Power Sources 2002; 111:160.
203. Liu Y-C, Qiu X-P, Huang Y-Q, Zhu W-T. Carbon 2002; 40:2375.
204. Iijima S. Nature 1991; 354:56.
205. Li W-Z, Xie S-S, Qian L-X et al. Science 1996; 274:701.
206. Luo J-Z, Gao L-Z, Leong Y-L, Au C-T. Catal. Lett. 2000; 66:91.
207. Liu Z, Lin X, Lee J-Y, Zhang W-S, Han M, Gan LM. Langmuir 2002; 18:4054.
208. Li X, Hsing I-M. Electrochim. Acta 2006; 51:5250.
209. Matsumoto T, Komatsu T, Arai K et al. Chem. Commun. 2004; 7:840.
210. Rajesh B, Thampi KR, Bonard JM, Xanthopoulos N, Mathieu HJ, Viswanathan B. J. Phys. Chem. B 2003; 107:2701.
211. Liu Z, Lee J, Chen W, Han M, Gan L. Langmuir 2004; 20:181.
212. Saito R, Fujita M, Dresselhaus G, Dresselhaus MS. Appl. Phys. Lett. 1992; 60:2204.
213. Dresselhaus MS, Hishi RA, Dresselhaus G, Inomta D, Nakao K, Saito R. Mol. Cryst. Liq. Cryst. Sci. Technol. Sect. C: Mol. Mater. 1994; 4:27.
214. Kasumov AY, Bouchiat H, Reulet B et al. Europhys. Lett. 1998; 43:89.
215. Britto PJ, Santhanam SV, Rubio A, Alonso JA, Ajayan PM. Adv. Mater. 1999; 11:154.
216. Sun X, Li R, Villers D, Dodelet JP, Desilets S. Chem. Phys. Lett. 2003; 379:99.
217. Choi W-B, Chu J-U, Pak C-H, Chang H. In US Pat. Appl. Publ, Vol. 01. Samsung SDI Co. Ltd.: South Korea, 2004; A1.
218. Girishkumar G, Vinodgopal K, Kamat PV. J. Phys. Chem. B 2004; 108:19960.
219. Girishkumar G, Retter M, Underhile R et al. Langmuir 2005; 21:8487.
220. Jiang L, Gao L. Carbon 2003; 41:2923.
221. Ellis AV, Vijayamohanan K, Goswami R et al. Nano Lett. 2003; 3:279.
222. Shao Y, Yin G, Gao Y, Shi P. J. Electrochem. Soc. 2006; 153:A1093.
223. Baughman RH, Zakhidov AA, De Heer WA. Science 2002; 297:787.
224. Steigerwalt ES, Deluga GA, Cliffel DE, Lukehart CM. J. Phys Chem B 2001; 105:8097.
225. Vinodgopal K, Haria M, Meisel D, Kamat P. Nano Lett. 2004; 4:415.
226. Che G, Lakshmi BB, Martin CR, Fisher ER. Langmuir 1999; 15:750.
227. Wang C, Waje M, Wang X, Tang J-M, Haddon RC, Yan Y. Nano Lett. 2004; 4:345.
228. He Z, Chen J, Liu D, Tang H, Deng W, Kuang Y. Mater. Chem. Phys. 2004; 85:396.
229. Quinn BM, Dekker C, Lemay SG. J. Am. Chem. Soc. 2005; 127:6146.
230. Tang H, Chen J-H, Huang Z-P et al. Carbon 2004; 42:191.
231. Lin Y, Cui X, Yen C, Wai C-M. J. Phys. Chem. B 2004; 109:14410.
232. Sun X, Li R, Stansfield B, Dodelet JP, Desilets S. Chem. Phys. Lett. 2004; 394:266.
233. Sun X, Li R, Stansfield B, Dodelet JP, Desilets S. Int. J. Nano Sci. 2002; 1:223.
234. Li W, Wang X, Chen Z, Waje M, Yan Y. Langmuir 2005; 21:9386.
235. Serp P, Corrias M, Kalck P. Appl. Catal. A 2003; 253:337.
236. Steigerwalt ES, Deluga GA, Lukehart CM. J. Phys. Chem. B 2002; 106:760.
237. Marsh H, Heintz EA, Rodriguez-Reinoso F. Science of Carbon Materials. Universidad de Alicante. Secretariado de Publications: Alicante, 2000.
238. Patrick JW. Porosity in Carbons: Characterization and Applications. Arnold: London, 1995.
239. Rodriguez-Mirasol J, Cordero T, Radovic LR, Rodriguez JJ. Chem. Mater. 1988; 10:550.
240. Johnson SA, Brigham ES, Olliver PJ, Mallouk TE. Chem. Mater. 1997; 9:2448.
241. Ma Z, Kyotani T, Tomita A. Chem. Commun. 2000:2365.
242. Ma Z, Kyotani T, Liu Z, Terasaki O, Tomita A. Chem. Mater. 2001; 13:4413.
243. Hou P-X, Yamazaki T, Orikasa H, Kyotani T. Carbon 2005; 43:2618.
244. Su F, Zeng JH, Yu YS, Lv L, Lee JY, Zhao XS. Carbon 2005; 43:2366.
245. Zeng J, Su F, Lee JY, Zhou W, Zhao XS. Carbon 2006; 44:1713.
246. Kim JY, Yoon SB, Kooli F, Yu J-S. J. Mater. Chem. 2001; 11:2912.
247. Breck DW. Zeolite Molecular Sieves: structure, chemistry, and use. John Wiley & Sons: New York, 1974; Chapter 1.
248. Beck JS, Vartuli JC, Roth WJ et al. J. Am. Chem. Soc. 1992; 114:10834.
249. Tanev PT, Pinnavaia TJ. Science 1995; 267:865.
250. Huo Q, Margolese DI, Ciesla U et al. Nature 1994; 368:317.

251. Zhao D, Feng J, Huo Q et al. Science 1998; 279:548.
252. Corma A. Chem. Rev. 1997; 97:2373.
253. Carlsson A, Kaneda M, Sakamoto Y, Terasaki O, Ryoo R, Joo SH. J. Electron Microsc. 1999; 48:795.
254. Kim TW, Solovyov LA. J. Mater. Chem. 2006; 16:1445.
255. Liang C, Hong K, Guiochon GA, Mays JM, Dai S. Angew. Chem. Int. Ed. 2004; 43:5785.
256. Tanaka S, Nishiyama N, Egashira Y, Ueyama K. Chem. Commun. 2005:2125.
257. Meng Y, Gu D, Zhang F et al. Angew. Chem. Int. Ed. 2005; 44:7053.
258. Liu R, Shi Y, Wan Y et al. J. Am. Chem. Soc. 2006; 128:11652.
259. Wan Y, Yang H, Zhao D. Acc. Chem. Res. 2006; 39:423.
260. Kapoor MP, Inagaki S, Ikeda S, Kakiuchi K, Suda M, Shimada T. J. Am. Chem. Soc. 2005; 127:8174.
261. Xia YD, Mokaya R. J. Mater. Chem. 2006; 16:395.
262. Sayari A, Wang W. J. Am. Chem. Soc. 2005; 127:12194.
263. Olkhovyk O, Jaroniec M. J. Am. Chem. Soc. 2005; 127:60.
264. Morell J, Wolter G, Froba M. Chem. Mater. 2005; 17:804.
265. Lu Y, Fan H, Doke N et al. J. Am. Chem. Soc. 2000; 122:5258.
266. Pang J, John VT, Loy DA, Yang Z, Lu Y. Adv. Mater. 2005; 17:704.
267. Ying JY, Mehnert CP, Wong MS. Angew. Chem. Int. Ed. 1999; 38:57.
268. Lee J, Kim J et al. Small 2005; 1:744.
269. Taguchi A, Smatt JH, Lindén M. Adv. Mater. 2003; 15:1209.
270. Lu AH, Smatt JH, Backlund S, Lindén M. Microporous Mesoporous Mater. 2004; 72:59.
271. Shi ZG, Feng YQ, Xu L, Da SL, Zhang M. Carbon 2003; 41:2677.

CHAPTER 5

Nanocrystalline Solar Cells

Gary Hodes* and Arieh Zaban**

1. INTRODUCTION

At one time in the not very distant past, an important key to making efficient photovoltaic cells was to use large crystal size semiconductors, preferably large single crystals. This was logical based on the higher carrier diffusion lengths expected from large crystals (fewer grain boundaries). For thin films cells, however, it became clear that polycrystalline material could be even better than single crystals. This was most evident in the $CuInS_2$ cell, where initial experiments using single crystals were soon abandoned in favour of polycrystalline material. Of course, initially this was due to ease of manufacturing considerations. However, it was eventually realized that polycrystalline films exhibited certain inherent advantages over single crystals for this material and this was explained by beneficial effects of band bending at the grain boundaries, which promoted electron-hole separation [1,2]. The next stage of this reduction in particle size, and the one that is the subject of this chapter, is the use of nanoporous semiconductors. The main breakthrough for nanoporous semiconductors used in photovoltaic cells came with the publication in 1991 of a 9% dye-sensitized solar cell (DSSC) based on a very high surface area nanoporous TiO_2 film [3].

The logic for the DSSC was that the quantum efficiency for injection of electrons from single dye molecules to many oxides is very high but, if more than a monolayer of dye is adsorbed on the oxide, then quenching occurs and the quantum efficiency drops drastically. To prevent this, the surface area of the oxide was increased to allow strong light absorption by the dye on the one hand, yet maintain only monolayer coverage of the oxide on the other. While modest increases in surface area had been attained previously, the breakthrough of O'Regan and

*Department of Materials and Interfaces, Weizmann Institute of Science, Rehovot 76100, Israel
**Department of Chemistry, Bar Ilan University, Ramat Gan, 52900, Israel

Nanostructured Materials © 2009 Elsevier Ltd.
978-0-08-044965-4 All rights reserved.

Grätzel [3] was the use of a very high surface area, nanoporous TiO_2 which increased the geometric surface area by ca. 1000 times. The lesser-investigated semiconductor-sensitized solar cell (SSSC) works on the same principle but, since a semiconductor particle does not suffer from quenching to the same extent as dye molecules, thicker 'layers' of the semiconductor can be used. However, even in this case, each semiconductor crystal should ideally be connected directly to the oxide to allow electron injection directly into the oxide rather than having to pass through additional semiconductor crystals first. Also, it is a decided advantage to make the semiconductor dimension small so that all photogenerated electrons have only a short distance to travel before they are injected into the oxide and thus separated from the holes.

One of the major differences between the DSSC and conventional photovoltaic cells is the essential lack of a built-in electric field throughout most of the DSSC. Most conventional solar cells are based on a p-n semiconductor junction, which results in a built-in electric field (the space charge layer). The purpose of this field is rapidly to separate photogenerated electrons and holes before they recombine. Less commonly, this field may also be established by a semiconductor–electrolyte junction (the photoelectrochemical cell – PEC) or by a semiconductor–metal junction (such as the Schottky diode). The width of the field is inversely proportional to the square root of the semiconductor doping density; for semiconductors used in solar cells, it is typically hundreds of nanometres.

Since a space charge layer extends over a certain distance, what happens if the semiconductor unit is much smaller than this distance? In this case, very little electric field will exist in the semiconductor. Consider a simple case of a (medium- or low-doped) semiconductor–electrolyte junction, where the semiconductor is in the form of a nanoparticle several nanometres in size. In such a system, there will be (almost) no field in the semiconductor nanoparticle [4,5]. If a large number of nanoparticles are connected together as in an aggregate, it could be argued that the total size of the semiconductor is large enough to support a space charge layer. However, even in this case, and assuming the aggregate is porous (as an aggregate normally would be), electrolyte can percolate into the aggregate and contact individual nanoparticles, thus screening any field which might be set up. Similarly for the high bandgap oxide, for the typical size of nanocrystal used in the DSSC (tens of nanometres), the electrolyte will result in essentially total depletion of the oxide nanocrystals and charge flow in the nanocrystalline porous network will be by diffusion rather than by migration in a field.

For much larger nanocrystals (whether oxide or absortbing semiconductor), particularly if the doping level is high, this assumption will gradually break down with increasing size. Also, for solid state nanocrystalline cells, the situation may be different, since screening by an interpenetrating solid is likely to be less effective than by a liquid.

In this chapter, we discuss the various types of nanocrystalline solar cell, explain their mode and mechanism of operation and give some examples of such cells. The report is divided according to the different types of cell. First, we treat the dye-sensitized solar cell (DSSC): this is the best known and by far the most widely studied of this class of cell. Both liquid junction and solid state DSSCs

are considered. Following this, we discuss the semiconductor-sensitized solar cell (SSSC), which is a DSSC where the absorber is a semiconductor instead of a dye. We start this section with liquid junction SSSCs, which have many similarities to the DSSC, but also some important differences. Solid state SSSCs, more commonly known as ETA cells (extremely thin absorber cell) conclude this chapter. ETA cells are separated into the two main types – three-component and two-component cells. The three-component cell is discussed first, since it is conceptually more similar to the liquid junction SSSC, with the difference being use of a solid hole conductor instead of a liquid electrolyte. The two-component ETA cell differs from the three-component one in that the semiconductor absorber functions also as a hole conductor. While a two-component cell does not necessarily have an extremely thin absorber, it is often considered to belong to the ETA family.

All the cells in this chapter share the common phenomenon of electrons injected from an excited absorber to a porous, large bandgap oxide. There are other types of nanoparticle cell which are not included in this report. These include porous nanocrystalline cells where light is absorbed in the non-porous semiconductor itself, organic and hybrid organic–inorganic cells (other than the DSSC itself) and various concepts of multiple exciton and hot electron cells.

2. DYE-SENSITIZED SOLAR CELLS (DSSCs)

2.1 Cell Operation

Figure 5.1 presents a basic energy diagram of DSSC operation. The basic system contains a wide bandgap semiconductor electrode, a dye that is attached to the semiconductor, a redox electrolyte and a counter electrode (the specific materials are discussed later). Upon illumination of the DSSC, an electron is injected from the dye into the semiconductor film (Figure 5.1a). Following the injection, a hole is transferred to the redox electrolyte, thus regenerating the dye (Figure 5.1b).

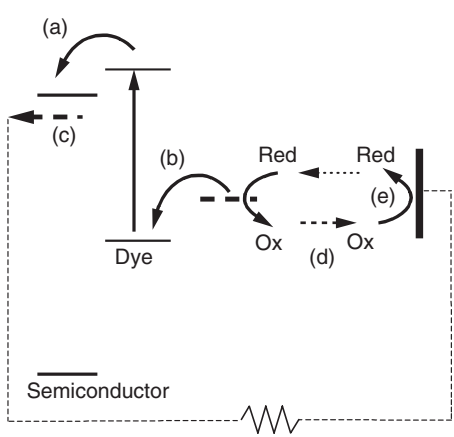

FIGURE 5.1 A basic energy diagram of dye-sensitized solar cell operation (a–e: see text).

The injected electrons must cross the semiconductor layer and reach the conducting substrate (Figure 5.1c), while the oxidized ions diffuse towards the counter electrode (Figure 5.1d) where they are reduced to their original state by the electron travelling through the external wire (Figure 5.1e). Consequently, while there is no net change in the system, electrons flow through the external wire.

The processes involved in the operation of the DSSC are quite efficient. In particular, the initial charge separation, i.e. the electron injection, is an ultrafast, efficient process [6–9]. However, to obtain a sufficiently high optical density that is required for efficient solar energy conversion necessitates the use of high surface area semiconductor electrodes [3,10]. These electrodes consist of nanosized semiconductor colloids that are sintered onto a transparent conducting substrate. The sintering process forms electrical contact between the various colloids and between the colloids and the substrate [11,12]. The electrodes have a porous geometry and a very large surface area. For example, when 10–20 nm colloids are used, the surface area of a 10 μm thick electrode is approximately one thousand times greater than the substrate area [13]. Consequently, the operation of the DSSC is better described in the schematic presentation of Figure 5.2. In this figure, the transport issues regarding both the photoinjected electron (see Figure 5.1c) and the electrolyte ions (see Figure 5.1d) are highlighted. The charge transport issues will be detailed later; however, at this point, we note that the transport of both electrons and ions in the nanoporous region must be taken into account.

The electron injection from the excited dye to the semiconductor (see Figure 5.1a) is an ultrafast process occurring in the ps time scale [6–9]. The variation in the reported injection rate values may be attributed to differences between the measured systems, since the injection rate depends on the specific dye–semiconductor system [14] and possibly also the nature of the TiO_2 [15]. The measurements of these ultrafast reactions can be altered by phenomena such as the surrounding

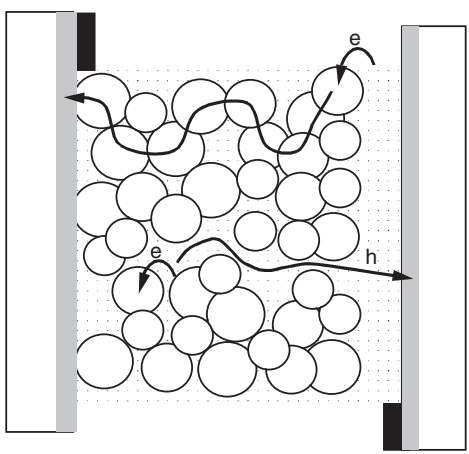

FIGURE 5.2 The transport of the photoinjected electrons and electrolyte ions in the nanoporous film (see text and Figure 5.1).

atmosphere, thus providing different values for what can be considered similar systems.

The ultrafast injection rate is explained by good coupling between the dye and the semiconductor [6–9]. In efficient dye–semiconductor systems, the injection rate is much faster than the characteristic decay time of the dye, which results in a quantum yield that is close to one. From the point of view of dye design, the ultrafast injection enables the use of dyes whose decay time is relatively short [16]. Furthermore, research has shown that even hot electrons can be transferred in some dye–semiconductor couples [17]. In some systems, it was even suggested that the electrons are excited directly into the semiconductor instead of internal excitation followed by injection [18]. It is important to note, however, that at this point a comprehensive understanding of the dye–semiconductor system that will enable dye design has not yet been developed.

The dye regeneration process (see Figure 5.1b) refers to the electron transfer from the redox electrolyte to the ground state of the oxidized dye. The oxidized ion carries the photogenerated hole to the counter electrode. Dye regeneration is a slow process compared with the injection [19]. The regeneration rate is influenced by both the potential difference between the solution and the ground state of the dye and by the quality of the interaction between the dye and the ions [20,21]. The regeneration rate is a significant factor in dye-sensitized solar cells because it determines the average lifetime for the oxidized dye. An oxidized dye acts as a recombination centre that can recapture injected electrons. In addition, most dyes are not stable in their oxidized form. Thus, slow dye regeneration decreases both the efficiency and the stability of a DSSC. Measurements of cells containing the N3 dye and the I^-/I_3^- redox couple (see details in the materials section) found that the regeneration rate in this composition allows approximately 10^8 redox turnovers, which corresponds to 15 years of outdoor operation [10].

The charge transport of both the photogenerated electrons in the semiconductor and the redox ions in the electrolyte (see Figure 5.1c,d) is controlled by diffusion. On a macroscopic scale, electroneutrality is maintained in the electrode volume by the mutual charge screening of the electrons and holes that are closely packed in the different phases of the nanoporous structure [10,22]. These issues will be discussed in detail in the section relating to various aspects of DSSC operation. At this point, we highlight the fact that the counter movement of the electrons and holes (oxidized ions) across the electrode (see Figure 5.2) increases the probability that they will react with each other. The description of this recombination process in an energy diagram is provided in Figure 5.3a. Furthermore, the electron travelling across the porous electrode can react with the oxidized dye that has not yet been regenerated by the electrolyte. This recombination process, presented in Figure 5.3, is negligible in most liquid electrolyte-based DSSCs, depending on the specific dye used.

The electric circuit of the DSSC is closed at the counter electrode (see Figure 5.1e). At this side, the oxidized ions are reduced to their original state by the electrons travelling through the external wire. This is the final process that occurs in the cell since it requires the arrival of the oxidized ions at the counter electrode. The counter electrode utilizes standard electrochemical concepts in order

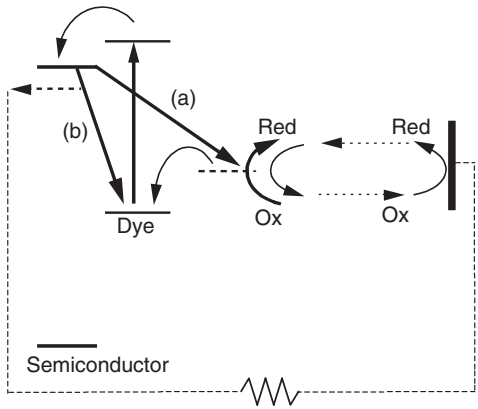

FIGURE 5.3 The two major recombination processes of dye-sensitized solar cells, shown by thick, straight arrows (a,b: see text).

to efficiently reduce the ions [23]. Inefficient reduction leads to polarization of the counter electrode and loss of photovoltage. Furthermore, inefficient operation of the counter electrode increases the hole concentration in the cell. This, in turn, increases the rate of the recombination loss process (see Figure 5.3) [24].

2.2 Materials

The DSSC consists of a nanoporous electrode, sensitizing dye, hole conducting mediator and a counter electrode. The highest solar energy conversion efficiency was achieved with the type of cell shown schematically in Figure 5.4 [10,19]. The cell was a 10–15 μm thick nanoporous TiO_2 electrode made from particles having a 15–20 nm diameter and a light scattering layer made of larger TiO_2 particles; an adsorbed monolayer of the N3 (cis-di(isothiocyanato)-N-bis(4,4′-dicarboxy-2,2′-bipyridine) ruthenium(II)) or the black (tri(cyanato)-2,2′2″-terpyridyl-4,4′,4″-tricarboxylate)Ru(II) [25] dye; a liquid electrolyte consisting of ca. 0.5 M LiI, 0.05 M I_2 and 0.2 M TBP (4-tert-butylpyridine) in acetonitrile or 3-methoxypropionitrile; a platinized conducting substrate as counter electrode; and a polymer-based sealing. Efforts to increase the conversion efficiency of DSSCs include the application of new materials aiming at a high efficiency, stable, solid state cell that will be much less expensive than the alternatives. The literature contains several reviews of the current status of dye-sensitized solar cells which discuss available and prospected materials [10,19]. Here, we will briefly mention some of these important aspects.

Figure 5.5 presents a diagram of the DSSC, emphasizing the relative energetics in the cell. The cell operation requires the presence of driving forces for two processes:

1. $\Delta E_{injection}$ for the electron injection from the excited level of the dye (E_{D^*}) to the conduction band of the semiconductor (E_{CB}); and

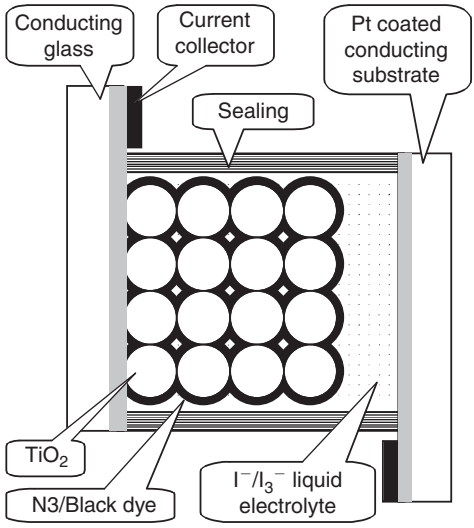

FIGURE 5.4 Schematic cross-section of a state-of-the-art dye-sensitized solar cell consisting of a nanoporous electrode, sensitizing dye, hole conducting mediator and a counter electrode.

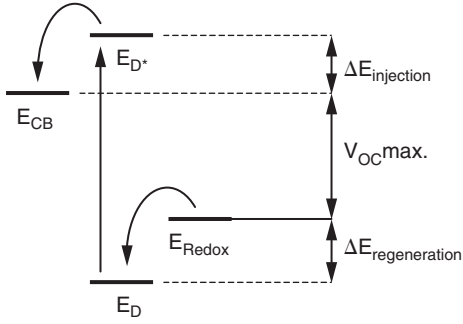

FIGURE 5.5 The relative energetics in a dye-sensitized solar cell that determine the maximum photovoltage and influence the kinetics of the injection and regeneration processes.

2. $\Delta E_{regeneration}$ for the dye regeneration by an electron transfer from the redox electrolyte (E_{Redox}) to the ground state of the oxidized dye (E_D).

The remaining potential ($E_{CB} - E_{Redox}$) defines the maximum photovoltage that the cell can generate. From the point of view of kinetics, efficient cell performance is achieved when these electron transfer processes occur rapidly. Thus, when selecting materials for DSSCs, a balance must be achieved between the thermodynamics and kinetics.

Figure 5.5 represents a simplified picture of the DSSC which is convenient for the basic understanding of the system. As will be discussed later, during the cell operation, the potential of the various cell components can vary with respect to an external reference. Thus, Figure 5.5 shows, at best, the relative energetics in the system independent of an external scale [26,27].

By definition, DSSCs utilize wide bandgap semiconductors, while the sensitization to the solar spectrum is performed by the dye. Many materials have been tested in DSSCs including SnO_2 [28–30], rutile TiO_2 [31], ZnO [32,33], anatase TiO_2 [3], Nb_2O_5 [17,34] and $SrTiO_3$ [17,34]. (This list was ordered by the conduction band potential, starting with the most positive one.) Until now the best performance has been achieved with anatase TiO_2.

The limited choice of oxides motivated new approaches in which treatments are used to alter the basic properties of the oxides. These treatments include molecular or inorganic modification of the semiconductor surface that shifts the bands to a different potential [35,36]. Composite materials in various configurations were also shown to improve the electrode performance [37–39]. Finally, different porous geometries based on nanorods or mesoporous colloids were tested, although with limited success so far [40,41].

The main benefit in using nanoporous electrodes is their high surface area. The electrode design involves the optimization of two factors: the surface area per electrode volume and the pore size. Both factors are controlled primarily by the particle size, i.e. decreasing the particle diameter results in both an increase of the surface area per electrode volume and a decrease of the pore average diameter. The surface area per electrode volume is important because it defines the electrode thickness for a desirable surface area. We provide below some characteristics of nanoporous electrodes that are thickness dependent. For example, an applied bias is unequally distributed across the electrode and electrons diffuse across the electrode only for a limited distance. Thus, it is always preferable to use a relatively thin electrode. On the other hand, one has to keep the pores large enough to allow sufficient electrolyte diffusion. Both parameters are highly dependent on the specific application in which the electrodes are used. In the typical DSSC, the electrode thickness does not exceed 15 μm with particles of 15–25 nm. However, when poor conductors are used as hole mediators (e.g. solid electrolytes), much thinner electrodes and larger pores are needed. Consequently, the primary particle sizes range from 50 to 60 nm in diameter and the electrode thickness is limited to ca. 5 μm.

Many different types of dye have been tested in DSSCs; however, only a few dyes have been found to be highly efficient. The leading dyes are the ruthenium complexes, of which the N3, N917 and the black dye are the most efficient [10,19]. The black dye has a wide absorption spectrum, which extends up to ca. 900 nm, thus providing an excellent match to the solar spectrum. However, since the black dye is less stable than the N3 and N917, the latter are usually preferred.

Other types of dyes were tested, but these usually resulted in limited performance. The ultrafast injection rate enables the use of dyes that have a short excited lifetime such as iron or osmium complexes [16,42]. Molecular dyes such as perylenes, porphyrins and phthalocyanines were tested because of their

unique advantages: stability, spectrum, environmental compatibility and price [29,43–48].

Another important aspect of dye design relates to its interaction with the hole mediator. The original dyes are optimized for liquid cells containing organic, typically non-polar, solvents. Attempts to move to less volatile mediators like polymers, molten salts, ionic liquids and inorganic semiconductors (see below), result in different interaction between the dye and the mediator. Consequently, several series of dyes having different substituents were synthesized and tested in DSSCs showing the importance of the dye mediator interface [49–51].

Different cell designs related to the dyes have been developed, although to date these attempts have not resulted in efficient cells. One such cell design features the use of two dyes that match the solar spectrum more efficiently than does a single one. Usually, dyes having a band at long wavelengths were added to the N3 dye which covers the spectrum up to ca. 650 nm. The failure in this approach is attributed to the low efficiency of the co-adsorbed dye that contributes much less than the N3 per occupied electrode surface [19]. Another approach relates to organic semiconductors. These materials can be applied in a multilayer configuration in which the photoexcited state is transferred by excitons [39,52,53]. The use of inorganic semiconductors instead of dyes will be discussed later.

The electrolyte is currently the weakest point in the application of DSSCs to outdoor conditions [19]. It is difficult to seal a cell containing volatile solvents for extended operation under extreme environmental conditions. The sealing should prevent both evaporation of the solvent and the penetration of humidity into the cell. Currently, a major effort in DSSC research is directed towards replacement of the liquid electrolyte by a solid mediator that will transfer the holes from the dye to the counter electrode efficiently. Different materials such as p-type semiconductors [54–64], polymers [19,65–71], ionic liquids and molten salts [72–78] were tested, but the efficiency achieved with these materials is lower than that of a compatible liquid electrolyte-based cell. This low performance is usually attributed to the conducting performance of the solid mediator and to a poor contact with the dye. However, it is also possible that the lower performance is related to the nanoporous geometry of the cell [22].

At this point, most efficient DSSCs utilize the I^-/I_3^- couple in dry solvents such as acetonitrile or 3-methoxypropionitrile [79,80]. Other electrolytes reduce the cell performance significantly [81,82]. The unique performance of the I^-/I_3^- couple is explained by the negative charge of both ions in the couple that reduces the recombination rate from the negative electrode to the solution and by a good charge transfer coupling between the dye and this couple [20]. However, attempts to replace this couple are motivated by the anticipated higher photovoltage that could be achieved if a more positive redox electrolyte were used (see Figure 5.5) [81,82].

The counter electrode completes the electrical photogenerated circuit by the re-reduction of the oxidized ions. Efficient reduction requires electrocatalytic properties. The simplest electrode is based on platinum which is deposited by various methods as a thin layer on a conductive substrate. When plated on a transparent conductive substrate, the platinized electrode can be semitransparent.

However, if transparency is not needed, it is preferable to use other substrates due to the high cost of the transparent electrodes. Typical replacements are carbon electrodes of various morphologies [83–86]. Carbon is one of the few materials that are stable in the corrosive environment associated with the electrolyte. Recently, stainless steel and other alloy materials have been tested, although long-term stability in operating DSSC is not yet proven [87–89].

2.3 Important Issues Regarding Cell Operation

The geometry of the nanoporous electrodes imparts special characteristics that differentiate these electrodes from their compact analogues. These porous electrodes are strongly influenced by the following factors: the open structure of the electrodes that permits electrolyte penetration through the entire electrode; the small size of the individual colloidal particles that cannot support a high space charge; and the low inherent conductivity of the semiconductor with respect to the penetrating electrolyte. These inherent properties of the nanoporous semiconductor electrodes have several implications for the functioning of dye-sensitized solar cells [22]:

1. Transient electric fields generated upon illumination are neutralized under steady state conditions, although they may be an important factor in transient measurements.
2. Charge carrier motion through the TiO_2 occurs primarily via diffusion rather than drift.
3. The activity of the electrolyte ions may change upon charge accumulation in the solid nanoporous electrode, thus being different in the dark and under illumination.
4. Systems without excess supporting electrolyte, such as some solid state versions of the DSSCs, may not be able to efficiently neutralize the field generated by photoinduced charge separation, leading to enhanced charge recombination.

Like in any other photovoltaic system, the performance of DSSCs is limited by the recombination processes (discussed above). In brief, during the operation of a DSSC, the injected electrons diffuse through the TiO_2 film towards the conducting substrate, while the oxidized ions move in the opposite direction to be regenerated at the counter electrode. The porous geometry that permits electrolyte contact through the entire electrode also provides a high surface area for the recombination of the photoinjected electrons with the holes in the dye layer or reducible species in the electrolyte [81,90–92]. The small size of the individual particles in the nanoporous electrode, screened by the interpenetrating electrolyte, cannot support an appreciable space charge [90,93,94]. Thus, in contrast to a conventional photovoltaic cell where the space charge layer prevents majority charge from reaching the surface, there is usually no energy barrier in the semiconductor to prevent electrons from being back-injected in to the dye or electrolyte. Other factors must dominate the recombination in the DSSC.

Most of the effort to improve the efficiency of DSSCs by suppression of the recombination process involves two basic approaches [95,96]. The first approach

physically blocks the electrode area that is not covered with dye. The second approach involves the formation of an energy gradient that directs the electrons towards the substrate. The physical blocking involves adsorption of insulating molecules or polymerization of an insulating layer on the semiconductor surface after the dye adsorption [30,53]. This approach is complicated by mutual effects between the insulating layer and the dye. Furthermore, the approach requires a complex process to ensure that the coating will not prevent contact between the dye and solution. The energy gradient approach involves composite nanoporous electrodes where the conduction band levels (electron affinities) of the two materials in the composite differ [39,95,96]. Arranging these materials in the correct geometry is expected to drive the electrons in the desired direction, i.e. the electrons will flow to the material having the more positive (lower lying) conduction band. A common geometry for this composite is a core-shell structure [39]. This core-shell electrode is made by coating a nanoporous TiO_2 matrix with a thin layer of another wide bandgap semiconductor whose conduction band potential is more negative than that of the TiO_2 (e.g. Nb_2O_5, Al_2O_3, MgO) [97–103]. The potential difference between the core and shell materials forms an energy barrier at the electrode–electrolyte interface. Thus, electrons injected into the electrode are driven away from the electrode surface into the TiO_2 core, which slows the recombination rate and increases the cell efficiency. In other words, the coating forms an inherent energy barrier at the electrode surface [37–39]. Passivation of surface states at the TiO_2 through which back electron transfer to both the electrolyte and the oxidized dye could occur was also proposed as a reason for the beneficial effect of thin Al_2O_3 on TiO_2 [104]. While this core-shell approach was found to improve liquid-based cells quite significantly, it was found to be crucial for solid state systems, especially where thin semiconductor absorber films were used (discussed later).

Another important recombination centre of the DSSC is the conductive substrate. The conductive substrate is exposed to the electrolyte solution at regions that are not covered with the TiO_2 particles. If the substrate is a poor electrocatalyst, as is the case for the common tri-iodide electrolyte, then recombination by electron injection from the substrate to the electrolyte is usually not serious. Most liquid-based cells show only a small decrease in efficiency at the maximum power point. However, in cases where the substrate is significantly more active, typically in solid state systems, where the hole conductor usually acts as a short to the substrate, [105], the substrate contribution to cell efficiency may be very significant [22,93,106–108].

Various methods for passivation of the exposed substrate have been reported [105,109,110]. The passivation material need not necessarily be similar to that of the porous film. Usually passivation is achieved by the formation of a compact semiconductor layer prior to the oxide particle deposition or by coating the entire electrode after its formation [19,111]. Typically, the compact semiconductor layer consists of TiO_2, although recently other semiconductors like Nb_2O_5 were used successfully [110,112]. Blocking can also be achieved by electrochemical deposition of insulating polymers at potentials at which the semiconductor is inactive, thus ensuring specific coating of only the substrate [53].

The mechanism by which electrons move through the nanoporous semiconductor film is an important factor in DSSCs. Models describing the electron motion by diffusion have been developed based on various measuring techniques [43,113,114]. The diffusion model may be rationalized by the short range screening of the semiconductor by the electrolyte mentioned previously. Because of the porous nature of the electrode, ions can migrate through the film to neutralize any electric fields (including those caused by the moving electrons) over very short distances. Therefore, under normal operating conditions, there should be essentially no macroscopic electric fields in the TiO_2 film [22,23,93]. Accordingly, during steady state illumination of a DSSC, the injected electrons experience little or no electric field, so their motion is governed primarily by concentration gradients, i.e. diffusion.

The diffusional motion of the electrons in the semiconductor film was found to be trap-limited [115–120]. Electronic states that are located in the bandgap trap release electrons, thus significantly slowing the diffusion rate. Filling the traps by photo- or electro-injected electrons decreases the trapping depth and thus the trapping time shortens. In other words, the electron mobility in the semiconductor film changes as a function of the electron concentration in the film [115–120]. Another important factor is the coordination number of the semiconductor nanoparticles forming the electrode. Recent reports showed that densification of the particles (porosity decrease) increases the diffusion rate by a power law defined in the percolation theory [121–123]. Several attempts to increase charge mobility in the nanoporous electrodes involve the use of better conducting nanowires [124–126]. So far, these attempts have not yielded better photovoltaic efficiencies in comparison with the standard electrodes.

Finally, it is important to address one of the most fundamental aspects of DSSCs: the relative energies at the semiconductor/dye/electrolyte interface. In a DSSC, the dye's excited state potential must be more negative than the semiconductor conduction band potential to enable the electron injection, and the oxidation potential of the dye must be more positive than the redox couple in the electrolyte solution to provide the driving force for the hole transfer [111,127]. Within these limits, the cell performance is affected by the exact position of the relative potentials. A change in either of the two driving forces impacts both the short circuit photocurrent and the open circuit photovoltage of the cell [111,128]. Therefore, optimization of the cells must involve consideration of the semiconductor, dye and electrolyte energetics [127].

The following four potentials that affect the semiconductor/dye/electrolyte interface can be measured separately:

1. the conduction band potential of the high surface area semiconductor;
2. the oxidation potential of the dye in solution;
3. the potential of the redox couple; and
4. the excited state potential of the dye.

However, measurements of these potentials under working cell conditions, i.e. when the dye is adsorbed onto the semiconductor and the electrolyte solution is present, are more complicated. It is, therefore, usually assumed that the potentials measured individually are still valid when the complete solar cell is assembled.

Various measurements of potentials in operating cells show that the closely packed materials affect each other energetically. The adsorbed dye potential shifts with the semiconductor potential [26,27]; the electrolyte changes composition (and thus potential) in the nanopores and the semiconductor is affected by the dipole moments of the dye [36]. In other words, the various components in the cell alter the original energetic values. Most of the effect is attributed to the ionic double layer (Helmholtz and diffuse layers). There is no similar information for solid state systems in which ion motion is much less.

3. SEMICONDUCTOR-SENSITIZED SOLAR CELLS (SSSC)

The DSSC discussed up to now is by far the most studied of the possible nanocrystalline solar cell types. An obvious alternative is to replace the dye by a relatively low bandgap semiconductor as light absorber (the semiconductor-sensitized solar cell or SSSC). In a number of studies of this cell type, the advantages of using a semiconductor rather than a dye are given as:

- higher absorption of the semiconductor, which is not subject to quenching and therefore is not limited to molecular monolayers;
- greater expected stability of the inorganic semiconductor compared to the (usually organometallic) dye;
- tailoring of bandgap (as well as electron affinity) through size quantization, which should allow greater flexibility.

In spite of these perceived (not always so simple) advantages, the DSSC possesses one major advantage at this time over the SSSC: the maximum obtained efficiency of the DSSC is ca. 11% compared with <3% for the SSSC (5% for the two-component solid state ETA cell). This major difference cannot be simply attributed to the greater body of research carried out on the DSSC, since right from the early days of the DSSC, efficiencies over 9% were obtained. While we cannot provide a simple answer to this question in this section, we will consider possible reasons in the course of describing studies carried out on the SSSC. We consider first the liquid junction SSSC (which constitutes most of the SSSC research up to now) followed by all solid state SSSCs (ETA cells) containing (1) three components (electron transporter, usually nanoporous TiO_2; absorbing semiconductor; and hole transporter) and (2) two components (where the absorbing semiconductor doubles also as the hole transporter).

3.1 Liquid Junction SSSCs

3.1.1 History and general principles

The idea of electron transfer from one semiconductor to another (coupled semiconductors) was recognized before the advent of the efficient DSSC. In 1984, a mixed CdS/TiO_2 particle system demonstrated how, prior to semiconductor–electrolyte charge transfer, photogenerated electrons (from the lower bandgap CdS) were transferred to the TiO_2 while the holes remained in the CdS [129].

Shortly afterwards, this same sensitization was demonstrated for CdS on a (flat) n-TiO_2 single crystal [130]. This concept was gradually extended to other coupled semiconductor systems with increasing emphasis on SSSC cells. Early studies concentrated first on CdS and PbS sensitization of TiO_2 (and, less frequently, ZnO), where the CdS and PbS were deposited on the porous oxide by alternate dipping in solutions of metal ions and sulphide [131–133], and extended to a wider range of absorbing semiconductors and, to a lesser extent, of wide bandgap porous oxides. CdSe, in particular, was a popular absorber due to its relatively suitable bandgap for solar absorption and ease of deposition by various solution methods, in particular by electrodeposition [134,135] and chemical bath deposition (CBD) [136–140]. Other absorbing semiconductors include Bi_2S_3 [141,142], FeS_2 [143–145], InP [146] and InAs [147], Sb_2S_3 and Ag_2S [141].

It is important to point out that solution methods for deposition of the absorbing semiconductor are favoured since they allow infiltration of the semiconductor into the porous oxide network, rather than just preferential deposition on the geometric surface of the oxide as is more likely to occur using other methods of semiconductor deposition. Electrodeposition, in particular, may be expected initially to occur preferentially near the substrate, growing outward from the substrate and near substrate region. This is because the porous oxides are normally poorly conducting, although it is possible that the cathodic bias used in the electrodeposition may drive the oxide into accumulation and therefore make it conducting during the deposition.

Since the absorbing semiconductor is required to inject electrons into the porous oxide, its conduction band must lie higher (i.e. its electron affinity must be lower) than that of the oxide. An example of this is illustrated in Figure 5.6 for PbS on TiO_2. The conduction band of bulk PbS lies well below that of TiO_2 and, indeed, no photocurrent is generated for bulk PbS on TiO_2. However, for highly quantized PbS (≤ca. 4 nm crystal size), photocurrent has been observed and explained by the upward shift in the conduction band (or more correctly for quantum dots, conduction level) with increasing size quantization [132]. This is

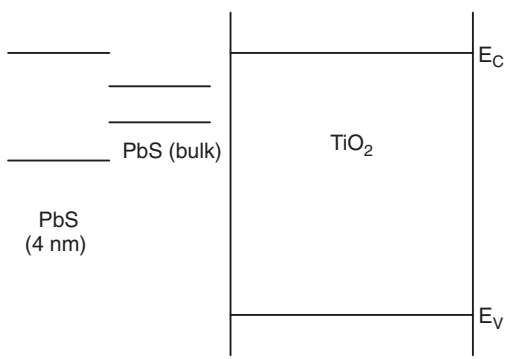

FIGURE 5.6 Relative energy levels of TiO_2 and PbS, the latter in bulk form (Eg = 0.4 eV) and 4 nm crystal size (Eg ≈ 1.2 eV).

seen in seen in Figure 5.7, where the photocurrent drops after two sets of dips (due to increasing crystal size). The same effect has been observed for FeS_2 [144], Bi_2S_3 [142] and InAs [147]. The ability to tune the conduction band level of quantized semiconductors through size quantization is clearly demonstrated in these cells by the cut-off in photocurrent with increasing crystal size, when the conduction band level falls below that of the porous oxide. This effect can be seen particularly clearly in FeS_2, where absorption spectra often show an absorption onset considerably red-shifted compared to the photocurrent spectra of the same samples [143–145]. Only the smaller crystals in these samples have a conduction band lying high enough to inject electrons into the oxide. The same has been observed for Bi_2S_3 in a sulphide-free electrolyte ([142]; see below).

Another way of adjusting the relative conduction band levels of the absorbing and porous oxide semiconductors is through electrolyte-controlled band shifts. Oxide band edges shift in a Nernstian manner (60 mV/pH unit) with change in pH. Chalcogenide semiconductors, on the other hand, do not change in a regular manner with pH (although shifts do occur), but do shift strongly if chalcogenide ions are present. Thus, by adding sulphide to an electrolyte, the conduction band of a chalcogenide semiconductor will shift upward relative to the underlying oxide. This has been demonstrated for Bi_2S_3 on TiO_2 where larger Bi_2S_3 nanoparticles, which cannot inject electrons into the TiO_2 in the absence of sulphide, do so when sulphide ions are added to the electrolyte [142]. This capability is particularly important in liquid junction cells; however, it may also apply in solid cells where interactions between the three main constituents (absorbing semiconductor,

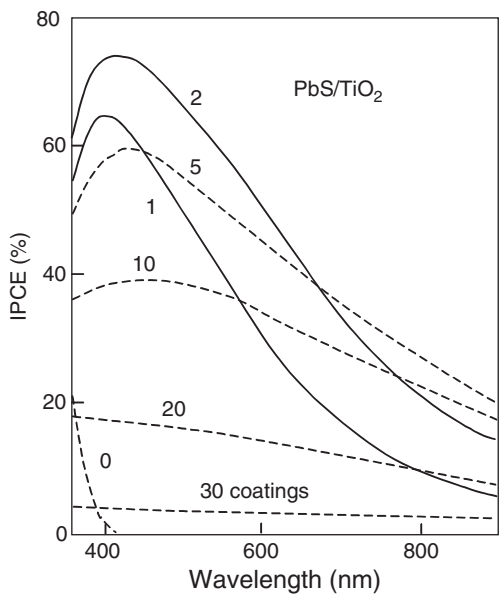

FIGURE 5.7 Photocurrent spectra of porous TiO_2 electrodes dip-coated with different numbers of PbS coatings (adapted with permission from [132]).

porous oxide and solid electrolyte) may result in dipole-induced shifts of one semiconductor relative to another. This means that common vacuum measurements of band lineups between two semiconductors, while being a useful first step in predicting combinations of semiconductors for SSSCs, may not be valid in a particular cell configuration, in parallel to the same problem mentioned above in determining energy lineups for the DSSC.

3.1.2 Electron injection from absorbing semiconductor into the porous oxide

One of the factors responsible for the efficient operation of the DSSC is the high rate of electron injection from the dye to the TiO_2 – as high as tens of fs for the standard Ru bipyridyl dye. In order to compare the DSSC and SSSC, we have to consider the equivalent rate from the absorbing semiconductor to the oxide. There are a limited number of such studies, which usually measure the increased rate of luminescence decay of the absorbing semiconductor when it is attached to the oxide; this decay is equated with the rate of injection of electrons from the absorbing semiconductor into the oxide. More recently, transient optical absorption measurements have been used for the same purpose. These rates are summarized in Table 5.1. Two points should be stressed: many of these measurements were carried out on colloidal systems, rather than on films, and many values are given as upper limits for electron lifetimes (or conversely, lower limits for electron transfer rates), being limited by the exciting pulse width.

Taking into account that most of these values are lower limits for electron transfer rates, it seems reasonable to take the value of 2 ps measured by Evans et al. [151] as typical, assuming that there is a typical rate. The relatively long value of 10–100 ps measured by Robel et al. [152] for CdSe on TiO_2 is for CdSe linked through an organic molecule (mercaptopropionic acid) to the TiO_2. It is expected that the electron transfer rate for such a linkage is slower than would be

Table 5.1 Electron injection times measured from an absorbing semiconductor to TiO_2 or ZnO colloids or nanoporous films

System	Electron transfer time	Reference
CdS/TiO_2	3 ns	[148]
CdS/TiO_2	<20 ps	[149]
Cd_3P_2/TiO_2	<1 ps	[150]
CdS/ZnO	<18 ps	[133]
CdS/TiO_2	2 ps	[151]
CdS/TiO_2	10–50 ps	[151a]
CdSe-linked toTiO_2	5–100 ps	[152]
$CdSe/TiO_2$	16 ps	[153]

the case were the CdSe to be directly deposited on the TiO_2, although it should be noted that photocurrent quantum efficiencies for mercaptopropionic acid and for mercaptohexadecanoic acid, a much longer chain, were essentially identical.

The experiments described are for colloidal semiconductors with typical sizes (of the absorbing semiconductor) of several nanometres. In contrast to molecular dyes, we should consider the time needed for the photogenerated electrons to reach the interface between the absorbing semiconductor and the oxide (assuming every absorbing semiconductor particle contacts an oxide particle directly). Grätzel and Frank [154] used a simple diffusion calculation to estimate a diffusion time for an electron in the centre of a 20 nm diameter TiO_2 particle to reach the surface of 10 ps. Since this time is proportional to the square of the radius and TiO_2 has a much lower electron diffusion coefficient than typical chalcogenide semiconductors, we estimate sub-ps diffusion times for several nm-sized chalcogenide semiconductors. In addition, these semiconductors are often more or less highly quantized and the photogenerated electron delocalized over the whole particle. Again, assuming single particles in contact with the oxide semiconductor, we can consider the electron to be generated at the absorbing semiconductor–oxide interface, which would obviate the need for any electron diffusion to occur. It is possible that the photogenerated electrons are preferentially trapped at sites far from the oxide interface. If so, we would expect much slower injection times than are observed, unless the traps were very shallow indeed.

For 'thick' absorbing semiconductor layers on oxides and, in particular, where many of the semiconductor particles are not in direct contact with the oxide particles, the diffusion time for photogenerated electrons to reach the interface becomes increasingly important, since recombination may increasingly occur before the electrons reach the interface and are separated from the holes. This recombination is considered in the following section.

The ps injection rate should be compared with the tens of fs measured for some dye/TiO_2 systems. Assuming a degree of generality for these results, this means that the injection rates for semiconductor–semiconductor systems are around one to two orders of magnitude slower than for dye–TiO_2 systems. Whether this difference is important or not depends both on the recombination rate in the absorbing semiconductor and on the back-transport rate from the oxide to the absorbing semiconductor.

Finally, there was expectation of relatively long hot electron lifetimes in excited quantum dots due to the 'phonon bottleneck mechanism', where hot electron relaxation via relatively widely-spaced levels, mediated by phonons, was expected to be slow compared with the sub-ps relaxation times in bulk semiconductors. It was shown by Klimov et al. [155] that, contrary to these expectations, electron relaxation in CdSe quantum dots with varying surface properties (passivations) was even faster than in bulk CdSe and independent of the surface passivation used. This understanding is relevant to expectations of hot electron transfer from an excited semiconductor to an oxide support, even if the relaxed excited state (conduction 'band' edge or LUMO) of the excited semiconductor lies below that of the oxide. It suggests that we should not expect such hot electron injection to occur at high efficiency.

3.1.3 Recombination rates in semiconductors

Accepting that recombination rates in semiconductors can vary over many orders of magnitude, we can make some generalizations, limiting ourselves to the most commonly used absorbing semiconductors in SSSCs – CdS, CdSe and PbS. We consider also charge trapping times, since recombination most often occurs between trapped charges.

Zhang [156] has provided an overview of measured recombination (and trapping) rates in many semiconductor nanoparticles. We consider first CdS and CdSe nanoparticles, which were most commonly used in SSSCs. Typical 'band-to-band' (involving shallow traps only) recombination rates are often in the ns range. Trapping times for electrons vary between 100 fs to hundreds of ps or more. Holes are trapped within 1–2 ps. More specifically, Klimov et al. [155] found that, for CdSe quantum dots, the hole trapping occurs within 1 ps and is independent of surface passivation, while electron trapping occurs over a range of time scales (up to ns) and is dependent on the surface treatment. The recombination rate of trapped charge can vary over many orders of magnitude, probably depending to a large extent on trap depth, with deeper trapped charge having longer lifetimes. Values between some ps and $>\mu$s can be found (for very deeply trapped charge, particularly in insulating semiconductors, carrier lifetimes of hours can be found). To give some specific examples of luminescence decay times in CdS colloids, Duonghong et al. [157] measured 0.3 ns, while Spanhel et al. [148] measured 50 ns (the main difference was a higher pH and excess Cd in the latter, probably forming a hydroxide-rich surface). Zhang et al. [158] found a value of ca. 50 ps which, however, was dependent on the solution composition as expected (hole scavengers and higher pH increased the electron lifetime).

CdSe is most commonly deposited in SSSCs by CBD. Maly et al. [159] reported luminescence decay times for CBD CdSe films of typically 100 ps, but varying considerably with emission wavelength, being much faster for shorter wavelengths. While close to band-to-band emission, the emission was reported to occur between trapped carriers. For similar films, Ai et al. [160] used fs techniques and were unable to measure long times scales (beyond 50 ps). However, it was clear that a major part of the (trapped) recombination occurred at time scales much longer than this, consistent with the results of Maly et al. They also found that electron trapping occurred in sub-ps times.

For PbS quantum dots, Patel et al. [161], using transient absorption measurements (they observed no emission at room temperature), obtained results suggesting recombination times of ca. 45 ps, independent of crystal size, shape or surface capping. This fast recombination was believed to be mediated by a high density of surface states. In contrast, Warner et al. [162] and Wehrenberg et al. [163] measured luminescence with very long electron-hole lifetimes of ca. 1 μs for PbS and PbSe quantum dots. (Warner et al. also confirmed, in agreement with many other studies, many tens of ns lifetimes for CdSe nanocrystals). These reports on PbS indicate the caution required when extrapolating lifetimes from one set of samples (even the broad range of samples used by Patel et al.) to different samples of the same material.

Electron trapping in semiconductors is important in the context of the SSSC for two main reasons. One is that typical electron trapping rates are comparable to typical electron injection (to the oxide) rates. This means that photogenerated electrons may be trapped before being injected into the oxide. Since the energy of the trapped electrons has been lowered, possibly below the oxide conduction band edge, this raises the question: can trapped electrons in the semiconductor be transferred to the oxide? We cannot answer this, since, even if trapping occurs (or ends up) well below the oxide conduction band edge, the electron might still be transferred to the oxide via surface states on the oxide. However, we should be aware of this possibility. Trapping may also reduce the possible open circuit voltage, due to lowering of the electron energy (the opposite of hot electrons). However, there are also possible reasons why it may not do so, e.g. if the trapped electrons are still above the oxide conduction band edge or if the open circuit voltage is limited by trapping in the oxide. Such effects are likely to be light intensity dependent, in the same way that transport in the porous oxide is light dependent (e.g. trap saturation).

A second effect of electron trapping is that the lifetime of the electron in the semiconductor will be increased, increasing the chances of recombination with the photogenerated hole. In such a case, a short injection time for the hole into the electrolyte becomes even more important than usual. Hole trapping is usually very rapid (ca. 1 ps as noted above), but this is not serious in itself unless the trapping depth is such that the hole cannot be injected to the electrolyte rapidly. In fact, hole transfer, as well as electron transfer from a semiconductor to an electrolyte, is believed to be often mediated by surface states [164].

From a fundamental point of view, the electron injection time:electron-hole recombination time ratio is more favourable for the DSSC than for the typical SSSC. For the DSSC, it is typically 10^{-13}:10^{-7} (typically six orders of magnitude difference) while, for the SSSC, it is typically 10^{-12}:10^{-9} (three orders of magnitude difference, although this will be very dependent on trapping and the difference could be much less). However, this three orders of magnitude difference may still be ample, to allow high quantum efficiencies for injection which, as we will describe later, are actually measured in many cases.

3.1.4 Back transport of electrons from oxide to absorbing semiconductor

This is an area which suffers from lack of experimental data. We therefore consider it from a more fundamental viewpoint, discussing (briefly) the factors that are expected to influence this back transport.

The first consideration for back transport is the relative level line-up of the conduction level (or band edge) of the two semiconductors. To inject electrons into the oxide, the absorbing semiconductor normally should have a higher conduction band edge. This means that back transport is relatively unlikely (the difference between the rates of the two directions increasing rapidly with the difference in band lineup). This would suggest that, as long as the absorbing semiconductor injection level is not too close to the oxide conduction band edge, little back transport should occur. However, most semiconductors have surface trapping sites (we have already alluded to the fast trapping typical of

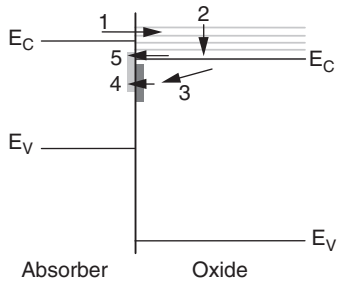

FIGURE 5.8 Possible electron transfer processes between an absorbing semiconductor and wide bandgap oxide with overlapping surface states (light grey – absorber; dark grey – oxide). 1. Electron injection from absorber to oxide. 2. Intraband relaxation of injected electron down oxide conduction band states. 3. Trapping of electron. 4. Back transfer of electron from oxide surface states to absorber surface states. 5. Back transfer of electron from oxide E_C to absorber surface states.

photogenerated electrons). Figure 5.8 demonstrates how back injection could occur from the oxide to absorbing semiconductor through overlapping surface states on the two semiconductors or from the oxide conduction band to the semiconductor surface states.

Even if no charge trapping sites existed, in contrast to molecular dyes which have essentially a single excited level (although broadened by solvent interactions), semiconductors have a range of levels. This means that there are, in principle, more levels for a back-injecting electron to transfer to and therefore higher probability. Another way of looking at this is that, for the dye–oxide system, electron transfer from dye to oxide involves an increase in entropy (from a single level to multiple levels), making it more favourable, and therefore less favourable in the opposite direction (back transfer). This may be a reason why dye-to-oxide electron injection appears to be, in the most favourable cases, faster than semiconductor-to-oxide injection and, conversely, will favour oxide-to-semiconductor injection relative to oxide-to-dye injection. Based on this consideration, the DSSC wins in both directions: faster injection to oxide and slower back transfer. Quantization of the absorbing semiconductor, however, brings the semiconductor closer to the concept of a molecule in that the closely spaced levels of the bulk semiconductor become farther apart as the degree of quantization increases. This, therefore, may be another advantage of using size-quantized semiconductors as absorbers and one which is not normally recognized. The oxide crystals are normally relatively large and non-quantized and therefore the conduction band level density will be much higher than in an adsorbed size-quantized semiconductor.

3.1.5 Electron injection from the oxide/substrate into the electrolyte

We have already discussed this earlier in the section on the DSSC. Since the DSSC and the SSSC are almost the same in this respect (for the same electrolyte), we discuss only cases where the SSSC might be different in this aspect from the DSSC.

The most obvious one is that iodide is not used in most SSSCs for the simple reason that the simple chalcogenide semiconductors most commonly used are not stable in this electrolyte. In view of the fact that it appears to be the best, by far, electrolyte for the DSSC (in non-aqueous form), with low rates of back reaction between electrons in the oxide and the electrolyte, the difference between the DSSC and SSSC could conceivably be due to this factor.

Another potential difference which could affect this recombination is the coverage of the oxide either by dye or by semiconductor. In general, the semiconductor coverage is expected to be greater (the dye is limited to a single monolayer). In view of the earlier discussion of back electron transport from the oxide to the semiconductor, this coverage might be expected to decrease the recombination. However, as for electron injection from oxides to an electrolyte, such electron transfer is likely to be very dependent on electron traps on the semiconductor surface. This is an area where more experimental work is needed. However, in view of the beneficial effect of relatively large bandgap semiconductors (buffer layers) deposited between the sensitizing semiconductor and oxide, particularly for solid state cells (discussed below), it is likely that conduction band lineup is a major factor here as discussed above for core-shell structures in the DSSC.

3.1.6 Losses in semiconductor 'aggregates' on oxides

An important clue to the difference in performance between the two types of cells may lie in the fact that high monochromatic incident photon to current efficiencies (IPCE) – often 70–80% – have been seen for *small* amounts of deposited semiconductor [131,132,141,165], but that the IPCE usually decreases when the amount of the semiconductor deposited increases further. Figure 5.9 shows this behaviour for CdS on TiO_2. The maximum quantum efficiency reaches a maximum after 5 dip coatings and then drops gradually as the CdS becomes thicker (although the long wavelength response improves due to the expected better

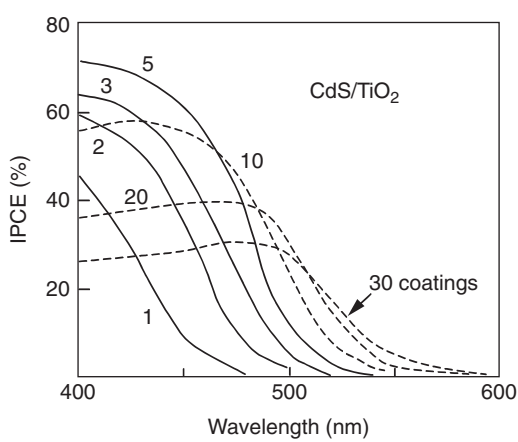

FIGURE 5.9 Photocurrent spectra of porous TiO_2 electrodes dip-coated with different numbers of CdS coatings. Adapted with permission from [131].

'red' response for thicker films). It should be noted that, in contrast to the case of PbS in Figure 5.7, the conduction band of CdS is always above that of TiO_2 and, therefore, size quantization does not play a direct role here. For PbS, the maximum quantum efficiency drops much more rapidly with number of dips (crystal size) due to the lowering of the PbS conduction band below that of TiO_2 and the problem of PbS grain boundaries is probably less important.

This suggests that the loss in these cells, when enough semiconductor is deposited to give a strong absorption of the incident light, is in a transfer process not considered above – electron transfer from semiconductor to semiconductor before being injected into the oxide. In other words, the efficiency can be high for semiconductor particles directly contacting the oxide, but drops considerably when semiconductor-to-semiconductor charge transfer is necessary. This concept has been suggested by Vogel et al. [131] and their SEM micrographs of CdS-coated TiO_2 indeed shows CdS particle aggregation at high coverages.

3.1.7 Multilayer semiconductors

This section deals with multiple 'absorbing' semiconductors deposited on the porous oxide. Vogel et al. [141] and Yang et al. [166] showed that coating a PbS/TiO_2 electrode with CdS both increased the IPCE and the photocurrent stability in sulphide-based electrolytes. The latter study also added a further ZnS coating after the CdS and found an additional small increase in photocurrent and more noticeable increase in open circuit voltage. Yang et al. [166] explained the increase in IPCE by invoking a fast cascade of photogenerated electrons from CdS and PbS to TiO_2. Such a scenario does not explain why the IPCE improves also at wavelengths where CdS does not absorb. It is also not clear how holes in the PbS reach the electrolyte through the much lower valence band of the CdS. The two most likely explanations are tunnelling through a very thin CdS layer or lack of complete coverage of the PbS by CdS.

It is also not clear why the recombination is less (greater IPCE) for the CdS-coated PbS. Possible explanations are:

- passivation of the PbS surface by CdS decreasing surface recombination of photogenerated electrons and holes;
- coverage of uncovered TiO_2 by CdS, thus decreasing recombination by electron transfer from the TiO_2 to the electrolyte;
- blocking of electron flow from PbS to electrolyte by the higher-lying conduction band of the CdS (but note that this same logic should prevent hole transfer from PbS to the electrolyte).

Finally, the increase in stability of the coated PbS, while also not obvious, is most likely attributable to the known much greater photostability of CdS in sulphide electrolyte compared with PbS. This would then imply that holes from the PbS do reach the CdS (maybe through traps). The greater stability of CdS-coated PbS may appear to provide evidence against uncovered PbS being the route for hole transfer from the PbS to the electrolyte, as postulated above to explain why holes reach the electrolyte at all. However, if the degradation of the PbS is due to crystal growth (therefore lowering of the conduction band below that of

the TiO_2), rather than PbS dissolution, then the CdS could act to limit the size of the PbS. It should be noted that metal chalcogenide photoanodes operating in polysulphide electrolytes are known to undergo a dynamic exchange of the surface chalcogen with S from the electrolyte, rather than dissolution [167].

CdS has also been successfully used as an underlayer for CdSe in porous TiO_2 cells [140], where both the CdS and the CdSe were deposited by CBD. The conduction band of CdSe lies below that of CdS, so a simple series energy level picture would suggest that the CdS should block electron transfer to the oxide. Possible reasons why electron transport occurs from CdSe to CdS (if it indeed does) are:

- electron storage in the CdSe due to fast hole removal by the polysulphide electrolyte, thus raising the energy bands of the CdSe relative to the CdS;
- as discussed for the CdS-coated PbS, trap-mediated charge transfer or breakdown of the simple series-connected semiconductors model.

As to why the CdS improves the cell so much, an explanation, which may be valid for all the composite-coated oxides, is simply reduction of back electron transfer from the TiO_2 to the electrolyte, probably by the higher conduction band of the CdS. Note that for the CdS-coated PbS, the coverage of the TiO_2 by the PbS is much lower than the CdS and CdSe coverages of the CBD samples. Therefore, a subsequent CdS layer can block the free TiO_2 in the former, while it is not expected to make much difference in the latter.

In_2S_3 has also been used as a buffer layer between PbS and TiO_2 [168]. This study was in the framework of a solid state cell using $CuInS_2$ (see below) and the PbS/In_2S_3/TiO_2-electrolyte system was used more as a reference system and was therefore not studied in depth. However, it was seen that addition of PbS to the In_2S_3/TiO_2 system resulted in an increase of photocurrent (as expected due to the lower bandgap of the PbS), but a decrease in photovoltage, with values of the two parameters between those of the In-free and the Pb-free systems.

3.1.8 Other porous oxides

There are only a limited number of studies on the use of oxides other than TiO_2 in SSSCs. Both CdS/ZnO [133] and CdSe/SnO_2 [135] have been reported. Monochromatic quantum efficiencies in both cases reach ca. 15%. These are much lower than the better quantum efficiencies seen for CdS(e)/TiO_2 systems. Hara et al. [169] studied an In_2S_3-sensitized porous In_2O_3 system (prepared by sulphiding the porous In_2O_3). The maximum quantum efficiency (33% at 400 nm) was reasonable, but the photovoltage was low (0.23 V), which was explained by a low-lying conduction band of the In_2O_3.

A systematic study using different oxides was carried out by Vogel et al. [141]. Using dip-coated CdS and PbS as sensitizing semiconductors and TiO_2, ZnO, SnO_2, Nb_2O_5 and Ta_2O_5 as the porous oxides, they found that, in general, the photocurrent quantum efficiencies decreased in the order (using the metal to denote the oxide): Ti > Zn > Nb > Sn»Ta, while the photovoltages decreased in the order: Ta > Nb > Ti > Zn > Sn. There is a general correlation with the oxide electron affinity (conduction band position): currents increase for lower conduction band

level (easier electron injection) while maximum photovoltage requires highest conduction band position, as long as electron injection can reasonably occur. The higher electron affinity SnO_2 was an exception, giving both low currents as well as the expected low voltage. It is noteworthy quantum efficiencies up to 80% were obtained for the CdS/ZnO system, indicating the potential of ZnO as the porous oxide. PbS gave low or zero injection efficiencies to Nb and Ta oxides and only a little better to ZnO (which has a similar electron affinity to TiO_2). Also, surprisingly, PbS gave no photoactivity whatsoever with SnO_2, with which it might be expected to work best.

Regarding the electron transfer time from CdS into ZnO of <18 ps listed in Table 5.1 [133], we can only note that this is comparable to times found for the CdS/TiO_2 system.

Since ZnO is the next best studied oxide after TiO_2, a few words on the differences between the two oxides are in order. The bandgaps and electron affinities of the two oxides are very similar. The higher mobility of electrons in ZnO (particularly in nanowires, which is the most commonly used form of ZnO in these cells) is well documented. ZnO also has a smaller density of states in the conduction band; this would tend to favour the electron injection rate into TiO_2 compared to ZnO. The chemistry of the two surfaces is very different: this may be expected to be more important for the DSSC, where binding of the dye to the oxide is more important, but it should not be ignored in the SSSC. Finally, if the ZnO nanowires are thick enough and not too intrinsic (the length is not important here assuming electrolyte penetration throughout the film and resulting depletion of the ZnO), appreciable space charge layers may occur in the wires in a direction perpendicular to the wire axis. Since ZnO is normally n-type, this space charge layer will tend to confine the electrons to the interior of the wires, thus reducing recombination at the surface. In this context, we note that the CuSCN/CdSe/ZnO solid state cell [170,171] (see section on three-component ETA cell below) is the only one we are aware of using such a low bandgap absorber which does not require a buffer layer between oxide and semiconductor.

While virtually all studies on semiconductor-sensitized porous high-bandgap semiconductors use oxides as the porous high bandgap semiconductor, in principle, a non-oxide high bandgap semiconductor could be used. Oxides have the great advantages of higher bandgaps compared with other chalcogenides, relative stability, environmental preferability and greater cheapness. However, non-oxides should not be dismissed out of hand. One study has considered ZnS (prepared by sulphidation of a ZnO sintered disc, therefore probably not very porous), sensitized by In_2S_3 [172]. The photocurrents obtained were several orders of magnitude lower than from comparable (non-porous) TiO_2 and ZnO. ZnS possesses a very high-lying conduction band and it would be difficult to find a light-absorbing injecting semiconductor which could inject into it. Also, the use of sulphide electrolyte, which can lift the bands of sulphide (and selenide) semiconductors up relative to oxides (due to specific adsorption of the sulphide) is of no benefit here since the ZnS levels will also rise, probably to the same extent. However, the use of non-oxide large bandgap semiconductors would be of interest for fundamental studies. For example, would the coupling between two sulphide semiconductors

be stronger than between a sulphide and an oxide semiconductor, allowing an increased rate of electron transfer?

3.2 Solid State SSSCs – the ETA Cell

There are two different types of ETA cell. One is the three-component cell, comprising a porous electron acceptor, most often TiO_2, an absorbing semiconductor and a p-type hole acceptor. The other is the two-component cell (which if not strictly an ETA cell, is often considered as such as noted earlier) where the absorber also functions as hole conductor. We begin with the three-component cell which is structurally closer to the liquid junction cell discussed above. A recent review of ETA cells [173] treats these cells in more detail and, in particular, gives much more detail on different fabrication methods, which we treat only very superficially.

3.2.1 Three-component ETA cell

CuSCN, a high bandgap (3.6 eV and therefore transparent), hole-conducting p-type semiconductor, is the most commonly used hole acceptor in these cells. CuI was used in some earlier cells, but appears to suffer more from instability problems.

The first reported use of CuSCN in an SSSC was in a Se/porous TiO_2 cell, where Se was electrodeposited from a SeO_2 solution onto the porous TiO_2 and CuSCN, dissolved in acetonitrile, was sprayed onto the film [174]. A photocurrent of $3\,mA\,cm^{-2}$ and a photvoltage of 600 mV were obtained under simulated sunlight. Photocurrent was confined mainly to the spectral range between 600 and 700 nm (the red as-deposited Se was gently annealed to give grey Se). While the Se was electrodeposited into the pores of the TiO_2, it is not clear whether the Se filled the pores and the CuSCN was deposited as a separate layer on top or whether some of the (10 μm thick) CuSCN also penetrated the pores. Since CuSCN forms an ohmic contact with SnO_2-glass [175], a blocking layer is normally used in solid state cells (both DSSC and SSSC) employing CuSCN (and other hole conductors) to prevent short circuiting between the SnO_2 and infiltrated CuSCN. Since such a blocking layer was not used in this case, the reasonable results obtained suggest that the CuSCN did not reach the substrate.

This system emphasized a fundamental difference between these sensitized cells and normal photoelectrochemical cells. Se is a p-type semiconductor and normally gives a (usually weak) p-type response as a photoelectrode, even when deposited on a planar TiO_2 film. However, on a porous TiO_2 film, current flow is that of an n-type semiconductor (electron injection to the substrate and hole injection to the electrolyte). Semiconductor nanocrystals are often relatively intrinsic and the direction of photocurrent flow can be dominated by factors other than conductivity type normally exhibited in the bulk semiconductor [176]. In the above case, the directionality imposed by the lineups of the Se and TiO_2 energy levels will direct the photocurrent flow.

$CuInS_2$ has been successfully used as an absorber in ETA cells in the absence of a separate hole conductor (see next section). Earlier attempts with $CuInS_2$ on TiO_2 using CuSCN as a hole conductor resulted in low photocurrents (up to ca.

$1\,mA\,cm^{-2}$ under bias; $1\,\mu A\,cm^{-2}$ at zero bias), but demonstrated the potential of this absorber [177].

CuSCN was also used as a hole conductor in electrodeposited ZnO nanorod-based cells. Using MOCVD CdTe, some photoactivity was obtained ($30\,\mu A\,cm^{-2}$; 0.2 V; fill factor = 0.28 under simulated solar irradiation) [178]. Much better results were obtained using CdSe-sensitized ZnO [170,171]. Both the nanocolumnar ZnO and the CdSe were deposited by electrodeposition, following spray pyrolysis of a compact ZnO layer on the SnO_2-coated glass substrate. The CdSe-coated ZnO was air-annealed at 350°C (one of the few cases in SSSCs where annealing was found to be useful; the short circuit current increased by more than a factor of two after annealing (see below); open circuit voltage and fill factor increases were less dramatic but still appreciable). CuSCN was then deposited on the CdSe/ZnO by solution (propyl sulphide) infiltration, followed by an evaporated Au contact. This cell gave a top efficiency of 2.3% (under $360\,W\,m^{-2}$ simulated 1/3 sunlight) with an IPCE of ca. 25% over a fairly wide spectral range. Figure 5.10 shows SEM images of various stages of formation of this cell (the image in Figure 5.10b was deliberately chosen to include a section of ZnO where the CdSe had peeled off, since this shows the CdSe layer more clearly). The nanostructured ZnO resulted in a 10–20 times increase in the real surface

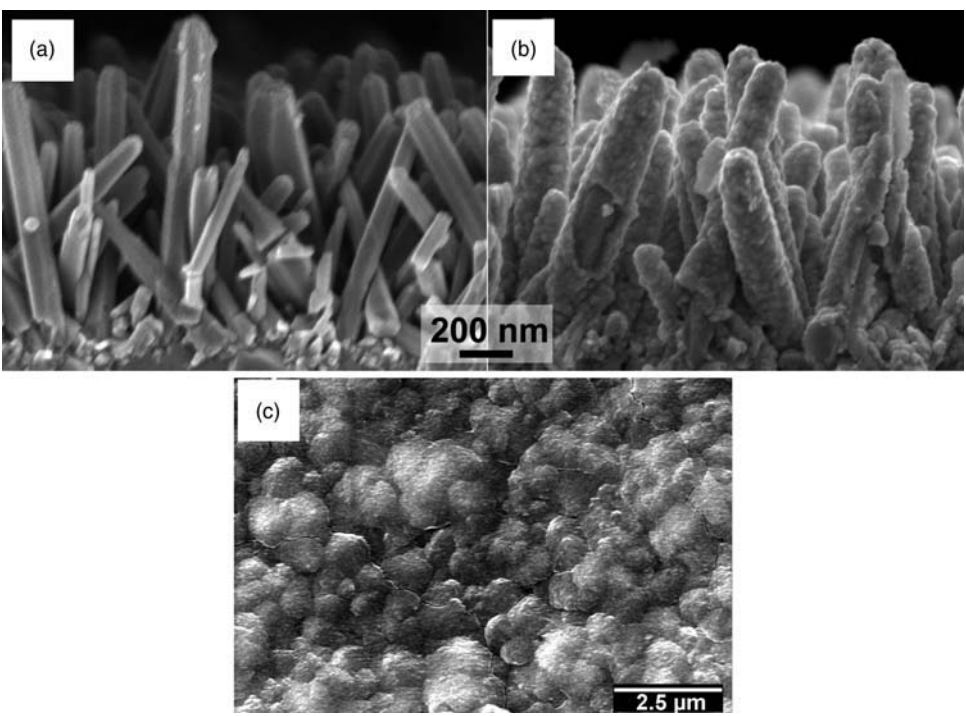

FIGURE 5.10 SEM micrographs of (a) electrodeposited ZnO; (b) CdSe electrodeposited on electrodeposited ZnO and annealed; (c) top view of the CuSCN layer on CdSe-coated ZnO. (With permission from C. Lévy-Clément.)

area, much less than the many hundreds of times typical of nanoporous TiO_2. The CdSe thickness on the individual ZnO nanorods was 30–40 nm, enough to give a good optical absorption, even at this relatively low coverage, but clearly thin enough to keep the electron/hole recombination in the CdSe low.

The effect of annealing in this cell is instructive. The local CdSe thickness (30–40 nm) means that in the as-deposited cell (CdSe crystal size ca. 4 nm), electrons photogenerated in the outer layers of the CdSe (i.e. those furthest from the ZnO rods) have to cross up to 10 grain boundaries before reaching the ZnO. In a liquid junction configuration (ZnO/CdSe/electrolyte), this cell exhibited at least a doubling of photocurrent after annealing at 350°C (as with the solid state version). Normally, this could be explained by a number of different reasons: change in optical absorption; surface oxidation; electronic changes in the CdSe or the CdSe/ZnO interface; and reduction in number of grain boundaries. While low-temperature annealing does cause some improvement, the main clue comes from the fact that the main improvement in quantum efficiency occurs between 250°C and 350°C [179]. This is the temperature range where CdSe (and many other nanocrystalline II–VI semiconductors) undergo major crystal growth (a crystal size of 9 nm was measured by Tena-Zaera et al. [179] after such annealing). Relatively small changes in optical absorption occurred at lower annealing temperatures and little change in this parameter was observed above 350°C. The presence of oxygen in the annealing atmosphere (known to be favourable for polycrystalline CdSe photoelectrodes) caused only a small improvement. Thus, it is reasonable to correlate the doubling of quantum efficiency between 250°C and 350°C with the grain growth of the nanocrystalline CdSe and possibly also better electronic contact between CdSe crystals.

Comparing the ZnO with the usual nanoporous TiO_2, there are a number of fundamental differences. The one-dimensional nature of the ZnO nanotubes provides faster transport for injected electrons to the substrate. Typical decay times for the photovoltage (and surprisingly also the photocurrent) were 14 μs; for porous TiO_2-based cells, it is usually orders of magnitude longer. The relatively open nature of the ZnO deposit made it easier to infiltrate the CuSCN, resulting in essentially complete infiltration of the CuSCN to the CdSe/ZnO films.

A third property of the ZnO – a measured doping density of $10^{20}cm^{-3}$ – begs the question as to the mechanism of charge separation in this cell (and similar cells). Is it just a solid equivalent of the liquid junction cell, where band offsets and concentration differences are the main driving forces for charge movement, or is the CdSe a 'dielectric' in the field generated by the p- and n-type semiconductors (CuSCN and ZnO respectively), i.e. a p-i-n cell. These two types of cell are different in principle since, in one case, the photovoltage is generated by the change in Fermi level in the (depleted) oxide due to electron injection and, in the other, photovoltage arises from the electric field in the system formed by equilibration of the Fermi levels of the n- and p-type semiconductors. Since a highly doped porous oxide would not generate much photovoltage from electron injection (the Fermi level is already close to the conduction band and will not change very much with a further increase in electron concentration), this suggests that this cell is indeed a p-i-n device, but with a distributed geometry.

A CdS-sensitized TiO_2 cell using CuSCN as hole transporting phase was fabricated yielding 1.3% solar conversion efficiency [180]. This is an encouraging efficiency, considering the high bandgap (2.4 eV) of the CdS absorber. Also, the open circuit voltage (0.86 V) was higher than usually found for such cells. This cell included the all various methods known to improve cell efficiencies: blocking layer on the substrate to prevent short circuiting by the CuSCN; deposition of a very thin Al_2O_3 layer on the porous TiO_2 to minimize recombination of electrons from the TiO_2 to the CuSCN; LiSCN (or KSCN) solution treatment of the TiO_2 prior to CuSCN deposition (which lowers cell resistivity). It is noteworthy that the Al_2O_3 layer did not make a clear difference; essentially similar, or at most only slightly inferior performance was obtained with no blocking layer on the TiO_2. This strongly suggests that CdS itself is a good (if not necessarily optimal) blocking layer and provides further support for the idea, put forward earlier, that CdS, whether deposited before or after the main absorber deposition, might improve porous cells by acting as a blocking layer.

Another factor discussed in this paper was the strong effect of TiO_2 particle size on cell efficiency: the best cells were made using 40–50 nm sized particles; 100 nm particles caused a fairly large loss in quantum efficiency and small particles (10–15 nm) a much greater loss. This is an important issue and needs careful investigation, not only as a function of TiO_2 size, but also other properties of the TiO_2, such as shape (the particles in the best cells were irregularly shaped) and doping.

SpiroOMeTAD (an organic hole conductor discussed in the DSSC section) was used in one study of PbS-sensitized TiO_2 cells [181]. Quantum efficiencies up to 45% were obtained together with a moderate solar conversion efficiency of nearly 0.5%. This demonstrates the potential for reasonable efficiencies in SSSCs using this hole conductor. This was the only SSSC study in which some charge transfer times were measured. Electron trapping in the PbS was found to be of the order of 1 ps (from liquid junction measurements on PbS, discussed above, electron/hole recombination times in the PbS are orders of magnitude longer); hole transfer time from PbS to the spiro was 4 ps and the recombination time of electrons with holes in the spiro was 2 μs. Probably much of the recombination occurred by electron injection from TiO_2 to the spiro. Based on the liquid junction results, we might expect a blocking layer on the porous TiO_2 to further increase the quantum yield.

PEDOT:PSS (poly (3,4-ethylenedioxythiophene):polystyrene sulphonic acid) is an organic hole conductor used for In(OH)S/Pb(OH)S cells [182–184]. CBD and dip coating were both used to deposit the In(OH)S and PbS, while the TiO_2 was deposited either by spray pyrolysis or by sol–gel dipping. The PbS bandgaps (ca. 0.7–0.8 eV) were about double the normal bulk PbS gap and this was ascribed to oxygen in the deposits. Solution-deposited PbS is normally oxidized at the surface and it is not clear if the increased bandgap was due to oxygen incorporation, size quantization or some other reason. The cell parameters depended strongly on annealing conditions of the In(OH)S, which changed both stoichiometry and bandgap upon annealing: the photocurrent increased and the photovoltage decreased with increase in annealing temperature up to 200°C. Efficiencies up to ca. 1% were obtained. The wide variation in cell performance upon modest

changes in preparation parameters, together with the respectable performance that can be obtained, suggests that this cell is worthy of further study.

The mode of operation of these three-component cells is normally considered to be similar to that of a p-i-n photovoltaic cell. The electron and hole transporters are considered to be at least moderately doped and, therefore, essentially all of the electric field in the device falls across the thin absorbing semiconductor, which is considered to be essentially insulating. In fact, due to the small characteristic sizes of all components, it could be argued that they are all largely depleted. However, since the absorber crystal size tends to be smaller than that of the other components, it is not unreasonable, at least as a first assumption, to expect most of the field arising from the p-n junction to fall across the 'insulating' absorber. This is the model which appears to be commonly accepted in three-component ETA cells.

If this model is correct, then, as pointed out by Taretto and Rau [185], if the absorber, which ideally should be very thin in an ETA cell, is too thin, then losses can occur due to field enhanced recombination through defects in the absorber. The thinner the absorber, the greater the field strength across it and therefore the greater this recombination. This would lead to an optimum thickness for the absorber, depending among, other parameters, on the built-in field strength and the defect energies.

3.2.2 Two-component ETA cells

Two-component cells are a cross between standard photovoltaic cells and high surface area porous cells. The absorber is deposited on a porous oxide, but contact to the non-oxide side of the cell is made directly to the absorber, rather than via an electrolyte or a hole conductor. This geometry requires that the absorbing semiconductor also acts, at least reasonably well, as a hole conductor.

An early cell of this type was amorphous Si deposited by RF discharge of SiH_4 on/into nanoporous TiO_2 (ca. 6 nm crystal size) [186]. A semitransparent Schottky contact was made to the amorphous Si by Pt. Although the Si did not infiltrate very far into the porous TiO_2, almost 1% conversion efficiency was found (at 17 mW cm^{-2} illumination). Since the contact to the absorber was reported to be Schottky, rather than ohmic (as per others described below), it could be argued that this is a three-component cell (i.e. the Pt contact is considered as an active component rather than just a charge extracting electrode).

The next generation of cells of this type were based on the idea of CdTe as absorber [187], although the conceived cell structure in this paper was that of a three-component cell, using ZnTe as hole carrier. While CdTe was successfully electrodeposited onto moderately porous (spray pyrolysis; ca. ten times surface enhancement) TiO_2 in this work, cell parameters were only given for the two-component ZnTe (electrodeposited)/TiO_2 cell. Quantum efficiencies up to 4% were measured with this configuration. Two-component cells using electrodeposited CdTe ($CdCl_2$-treated and annealed at 400°C) on this moderately porous TiO_2 were later evaluated [188]. Conversion efficiencies up to 1.2% were obtained with reasonable currents (quantum efficiency up to 45%) and voltages, but very low fill factors (ca. 0.2). Attempts to increase the fill factor by using a buffer layer of

CdS increased the fill factor (still low), but at the expense of the other parameters. The low fill factor, seen as an S-shaped I-V characteristic, was explained, through a high offset between the conduction bands of CdTe and TiO_2 (0.7 V), by the formation of a barrier to electron transport from CdTe to TiO_2 once the forward bias exceeded 0.2 V (the built-in voltage) [189].

By alloying the CdTe with HgTe, a lower bandgap absorber was obtained with a large increase in photocurrent (a reduction in photovoltage was more or less offset by an increase in fill factor), resulting in an efficiency of ca. 2% [190]. If the bandgap was lowered below 1.28 eV (by increasing the Hg concentration), the photocurrent dropped again. This was explained by the decreasing offset between the (Cd,Hg)Te and TiO_2 conduction bands, resulting in a decreased driving force for electron injection from absorber to the oxide.

$Cu_{1.8}S$ was tried as an absorber in these cells [191]. Flat (sprayed) TiO_2 films with very thin (35 nm) $Cu_{1.8}S$ layers, deposited by atomic layer CVD, were used as a model system to test the concept of this absorber. A photocurrent of 30 $\mu A\,cm^{-2}$ and photovoltage of 0.2 V were obtained at ca. three times solar intensity and an internal conversion efficiency of 6% at 500 nm. While the $Cu_{1.8}S$ was also deposited into porous TiO_2, no solar cell characterization of this structure was given.

While the Cu-S absorber does not appear to have been pursued further in these cells, $CuInS_2$ (abbreviated here as CISu) has been successfully used and gives the best performing cells up to now. We previously mentioned a three-component cell using CISu and CuSCN, which gave a very small output [177]. In 2003, a two-component flat cell using atomic layer deposition (ALD) was described, which was optimized by annealing in S, then in O_2 (the latter to convert the CISu to p-type) and resulted in cell parameters of 3 $mA\,cm^{-2}$ and 0.19 V (photocurrent and photovoltage) and a quantum efficiency of ca. 20% averaged over the photocurrent spectrum [192].

A buffer layer of $In_x(OH)_yS_z$ (deposited by CBD, which results in In_2S_3 films with varying OH content) improved similar cells by reducing back injection of the electrons in the TiO_2 back to the CISu [168]. For a flat cell with 100 nm of CISu, a cell efficiency of 2.1% was obtained (10.7 $mA\,cm^{-2}$; 0.45 V; 43.1% fill factor). A similar cell, but using nanoporous TiO_2 (on a compact TiO_2 layer) cell gave lower photocurrent (2.5 $mA\,cm^{-2}$) and 0.35% efficiency. It was believed that this was due to incomplete pore filling by the sprayed CISu.

A 4% cell was reported the following year [193,194]. This cell employed the usual compact TiO_2 on SnO_2-glass, with a porous TiO_2 layer made up of 50 nm particles. Two successive buffer layers (2 nm Al_2O_3 followed by ca. 30 nm of In_2S_3, both deposited by AL-CVD, were followed by CISu deposited by the same technique and annealed in the same way as described in Nanu et al. [192]). The CISu fills the pores and is in intimate contact with the TiO_2, thus maximizing charge transfer between the CISu/buffers and the TiO_2. The buffer layers fulfilled two purposes: to prevent the diffusion of Cu into TiO_2 and reduce back transfer of electrons from the TiO_2 into the absorber. (The cell output was two orders of magnitude poorer in the absence of the buffer layers.) The maximum quantum efficiency was 80% at 700 nm. One year later, the same group reached 5% efficiency by using sprayed $In_2S_3(OH)$ and CISu, resulting in an increase mainly of

the V_{OC} and fill factor from 0.49 V and 44% (the 4% cell) to 0.53 V and 55% (5% cell) [195]. This (unsealed) cell was reported to be stable in storage for months and also under illumination for an unspecified time. Most solar cells require sealing to be stable and, therefore, this stability is very encouraging.

A study of the effect of TiO_2 crystal size on these two-component cells using three different TiO_2 crystal sizes (9, 50 and 300 nm), found that the performance improved as crystal size increased (0.21, 0.81, 2.80% efficiencies respectively for 1 μm thick nanoporous TiO_2 films) [196]. This was explained mainly by better charge transport due to better infiltration of buffer/absorber in the larger pores of the larger-grained films and therefore better contact with TiO_2. Also, improved absorption due to light trapping in the larger-grained scattering films contributed to the improvement with increasing crystal size. In this respect, it is interesting to return to the study of the three-component TiO_2/CdS/CuSCN cell by Larramona et al. [180], discussed previously. Here also, the particle size of the TiO_2 was found to be important, although not exactly in a parallel manner. The best cells were made with 40–50 nm particle size and, in agreement with O'Hayre et al. [196], very small particle size (10–15 nm) resulted in a large drop in performance. However, larger particle sizes (100 nm) resulted in a fairly large loss in performance compared to the 40–50 nm particles in this case. Also, and possibly an important issue, the size distribution of the particles was large. This should result in many large pores, therefore good infiltration of absorber, but also higher effective surface area. Additionally, the shape distribution of the TiO_2 particles in the Larramona study was large (many of the particles were highly elongated). As noted previously, a comprehensive study of the effect of the nature of the porous TiO_2 on all these nanocrystalline cells requires investigation of all these factors (as well as doping and surface properties) and not just variation in crystal size.

3.2.3 The issue of built-in fields in SSSCs

The most widely-held view of the mechanism of the liquid junction nanoporous cells is that both the photocurrent and photovoltage are not dependent on built-in fields in the system. There may be electric fields in the cells (notably the Helmholzt layers at the various solid–liquid interfaces and at the substrate-TiO_2 contact). However, these fields extend over very narrow regions and are not believed to control the short current photocurrent or open circuit photovoltage. In solid nanoporous cells, on the other hand, extended electric fields (space charge layers) are routinely drawn in the energy diagrams. This leads to the question: are solid state nanoporous cells defined by space charge layers or are there cases where the kinetic model is dominant? More specifically, is the maximum photovoltage determined by built-in fields or not?

If we model a two-component cell by moderately-doped TiO_2 and absorber semiconductor and a characteristic size of 50 nm, then we have 25 nm in which to build up a space charge layer. Figure 5.11a illustrates this situation where we consider alternating slabs, 50 nm wide, of TiO_2 and the absorbing semiconductor, with the TiO_2 connected to the substrate and the absorbing semiconductor connected (with a thin additional layer of the semiconductor to prevent possible shorting between the TiO_2 and contact) with a second contact. The main features

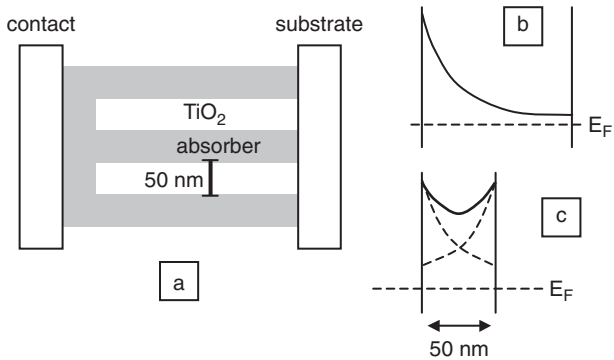

FIGURE 5.11 (a) Simplified schematic of alternating TiO_2 and absorbing semiconductor structures (both 50 nm wide) connected to a substrate (normally conducting glass together with a dense blocking layer) and a contact (usually Au or graphite) on the other side. (b) The space charge layer in a semiconductor structure just wide enough to support the entire field (taken as 100 nm in the present case). (c) A 50 nm sized semiconductor structure showing both the incomplete development of the space charge layer due to contact with TiO_2 from both sides individually (light broken curves) and taken together (solid dark curve).

of this model are valid also for three dimensions, since the pore structure is also three-dimensional.

Figure 5.11b shows the space charge layer (only one band is considered) assuming that the width of the semiconductor is the same as the space charge layer width (of the order of 100 nm for moderately doped semiconductors: the space charge layer width may be much greater for very small nanocrystals which are sometimes close to intrinsic). If we then consider a 50 nm wide semiconductor, then not all the space charge layer can be built up in the semiconductor and it is partially depleted. However, in this example, a large fraction of the full space charge layer could still be present. If, however, we consider that the semiconductor is in contact with the TiO_2 on *both* sides (in three dimensions, on all sides), then consideration of overlapping space charge layers means that only a relatively small fraction of the space charge layer will occur and the semiconductor will be depleted to a large extent (Figure 5.11c). From Figure 5.11c, whatever field does exist in the semiconductor will direct the electrons (holes) toward the centre of the n-(p-)type structures and the holes (electrons) to the surface and toward the second phase. Thus, while charge transport in the desired direction perpendicular to the electrodes should be by diffusion (there should be little or no field in this direction (except possibly very close to the electrodes)), what space charge layer does exist in a lateral direction may still promote electron-hole separation. This argument is equally valid for the oxide; the distribution of space charge layers between the semiconductor and oxide will depend largely on their doping densities: most of the field will be in the lower-doped material. If both are totally depleted, then the photovoltage is generated by changes in the charge concentration in the two materials, comparable to the case of the liquid junction DSSC but with change in Fermi levels in both materials and not just the oxide. There is also

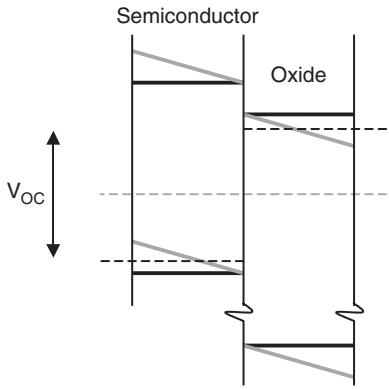

FIGURE 5.12 Energy diagram of an absorbing p-type semiconductor (left side) – high bandgap n-type oxide (right side) junction, where the built-in field is shared equally between the two materials, both of which are partially depleted. Broken lines represent (pseudo)Fermi levels. Grey thick lines: in the dark. Black thick lines: illumination to flat band.

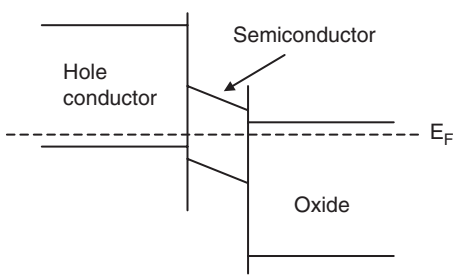

FIGURE 5.13 Energy diagram of a three-component solid state cell with the built-in field dropping across the absorbing semiconductor (p-i-n configuration).

the possibility of an intermediate case where the photovoltage arises both from band flattening and from changes in charge concentration (Figure 5.12).

The three-component cell can be treated similarly, except that there are now three materials over which the field can be distributed, assuming there is a built-in field. As discussed earlier, the favoured energy structure for the three-component cell is a p-i-n type, where the field falls across the absorbing semiconductor (Figure 5.13). If this model is correct, then the field across the semiconductor will separate the electron-hole pair immediately and is probably the optimum situation. If the field is in either/both the oxide or hole conductor, then initial charge separation arises due to band offsets (surface states may also play a role) and the lateral field in the oxide (hole conductor) will act to confine the electron (hole) to the centre of the relevant conductor. The three-component system may be further complicated by (a) direct contact between oxide and hole conductor and, in common with the two-component system, (b) contacts between the buffer layer normally present in solid state cells and the other components.

4. CONCLUDING REMARKS

The DSSC has led not only to a solar cell which is in the early stages of commercialization, but to much interesting physics and debate on the nature of its operation. Additionally, it has spawned several other types of cell that, to a greater or lesser extent, share some of this interesting (and sometimes controversial) physics. Much has been learned in the past 15 years and much is still being learned. The complexity of the various systems and the differences between them ensure that there will also be much to be learned and debated for the future. In particular, the mechanisms involved in charge transport in the various solid state cells, along with the electronic structures of these cells, are far from understood.

References

1. Visoly-Fisher I, Cohen SR, Ruzin A, Cahen D. Adv. Mater. 2004; 16:879–883.
2. Azulay D, Millo O, Balberg I, Schock H-W, Visoly-Fisher I, Cahen D. Sol. Ener. Mater. Sol. Cells 2007; 91:85–90.
3. O'Regan B, Grätzel M. Nature 1991; 353:737–740.
4. Bard AJ. J. Phys. Chem. 1982; 86:172–177.
5. Hodes G, Grätzel M. Nouveau J. Chim. 1984; 8:509–520.
6. Burfeint B, Hannappel T, Storck W, Willig F. J. Phys. Chem. 1996; 100:16463–16465.
7. Ellingson RJ, Asbury JB, Ferrere S et al. J. Phys. Chem. B 1998; 102:6455.
8. Ghosh HN, Asbury JB, Lian TQ. J. Phys. Chem. B 1998; 102:6482.
9. Rehm J, McLendon GL, Nagasawa Y, Yoshihara K, Moser J, Grätzel M. J. Phys. Chem. 1996; 100:9577.
10. Hagfeldt A, Grätzel M. Acc. Chem. Res. 2000; 33:269.
11. Gerfin T, Grätzel M, Walder L. In Molecular Level Artificial Photosynthetic Materials, 44, KD Karlin (ed.). John Wiley & Sons, Inc: New York, 1997; 345–393.
12. Kamat PV. In Molecular Level Artificial Photosynthetic Materials, 44, KD Karlin (ed.). John Wiley & Sons, Inc: New York, 1997; 273–343.
13. Kavan L, Grätzel M, Gilbert SE, Klemenz C, Scheel HJ. J. Am. Chem. Soc. 1996; 118:6716.
14. Asbury JB, Hao E, Wang YQ, Ghosh HN, Lian TQ. J. Phys. Chem. B 2001; 105:4545.
15. Tachibana Y, Haque SA, Mercer IP, Durrant JR, Klug DR. J. Phys. Chem, B 2000; 104:1198–1205.
16. Ferrere S, Gregg BA. J. Am. Chem. Soc. 1998; 120:843.
17. Lenzmann F, Krueger J, Burnside S et al. J. Phys. Chem. B 2001; 105:6347.
18. Ramakrishna G, Ghosh HN. J. Phys. Chem. B 2001; 105:7000–7008.
19. Grätzel M. Prog. Photovoltaics 2000; 8:171.
20. Huang SY, Schlichthorl G, Nozik AJ, Grätzel M, Frank AJ. J. Phys. Chem. B 1997; 101:2576–2582.
21. Park NG, Schlichthorl G, van de Lagemaat J, Cheong HM, Mascarenhas A, Frank AJ. J. Phys. Chem. 1999; 103:3308–3314.
22. Zaban A, Meier A, Gregg BA. J. Phys. Chem. B 1997; 101:7985.
23. Bard AJ, Faulkner LR. Electrochemical Methods Fundamental and Applications. John Wiley & Sons: New York, 1980.
24. Zaban A, Zhang J, Diamant Y, Melemed O, Bisquert J. J. Phys. Chem. B 2003; 107:6022–6025.
25. Nazeeruddin MK, Pechy P, Grätzel M. Chem. Commun. 1997:1705.
26. Zaban A, Ferrere S, Sprague J, Gregg BA. J. Phys. Chem 1997; 101:55–57.
27. Zaban A, Ferrere S, Gregg BA. J. Phys. Chem. B 1998; 102:452–460.
28. Chappel S, Zaban A. Sol. Ener. Mater. Sol. Cells 2002; 71:141–152.
29. Ferrere S, Zaban A, Gregg BA. J. Phys. Chem. B 1997; 101:4490–4493.
30. Kamat PV, Bedja I, Hotchandani S, Patterson LK. J. Phys. Chem. 1996; 100:4900–4908.
31. Park NG, van de Lagemaat J, Frank AJ. J. Phys. Chem. B 2000; 104:8989.
32. Hoyer P, Weller H. J. Phys. Chem. 1995; 99:14096–14100.

33. Rensmo H, Keis K, Lindstrom H et al. J. Phys. Chem. B 1997; 101:2598.
34. Sayama K, Sugihara H, Arakawa H. Chem. Mater. 1998; 10:3825–3832.
35. Kruger J, Bach U, Grätzel M. Adv. Mater. 2000; 12:447.
36. Rühle S, Greenshtein M, Chen SG et al. J. Phys. Chem. B. 2005; 109:18907–18913.
37. Chappel S, Chen SG, Zaban A. Langmuir 2002; 18:3336–3342.
38. Chen SG, Chappel S, Diamant Y, Zaban A. Chem. Mater. 2001; 13:4629–4634.
39. Zaban A, Chen SG, Chappel S, Gregg BA. Chem. Comm. 2000; 22:2231–2232.
40. Chen SG, Vijaya Kumar R, Gedanken A, Zaban A. Israel J. Chem. 2001; 41:51–54.
41. Wang YQ, Chen SG, Tang XH et al. J. Mater. Chem. 2001; 11:521–526.
42. Kuciauskas D, Sauve G, Freund MS, Gray HB, Winkler DR, Lewis NS. Abstr. Papers Am Chem. Soc. 2001.
43. Boschloo GK, Goossens A, Schoonman J. J. Electroanal. Chem. 1997; 428:25–32.
44. Deng HH, Lu ZH, Mao HF, Xu HJ. Chem. Phys. 1997; 221:323–331.
45. Deng HH, Mao HF, Lu ZH, Li JM, Xu HJ. J. Photochem. Photobiol. A 1997; 110:47–52.
46. Fang JH, Wu JW, Lu XM, Gu JH, Lu ZH. J. Vac. Sci. Tech. B 1997; 15:1468–1470.
47. Kay A, Grätzel M. J. Phys. Chem. 1993; 97:6272–6277.
48. Sayama K, Hara K, Mori N et al. Chem. Comm. 2000; 1173.
49. Kawano R, Nazeeruddin MK, Sato A, Grätzel M, Watanabe M. Electrochem. Commun. 2007; 9:1134–1138.
50. Klein C, Nazeeruddin MK, Liska P et al. Inorg. Chem. 2005; 44:178–180.
51. Nazeeruddin MK, Bessho T, Cevey L et al. J. Photochem. Photobiol. A 2007; 185:331–337.
52. Diamant Y, Zaban A. J. Electrochem. Soc. 2001; 148:C709–C714.
53. Gregg BA, Pichot F, Ferrere S, Fields CL. J. Phys. Chem. B 2001; 105:1422.
54. Bandara J, Yasomanee JP. Semicond. Sci. Technol. 2007; 22:20–24.
55. Chen ZG, Yang H, Li XH, Li FY, Yi T, Huang CH. J. Mater. Chem. 2007; 17:1602–1607.
56. Han HW, Bach U, Cheng YB, Caruso RA. Appl. Phys. Lett. 2007; 90:213510.
57. Howie WH, Harris JE, Jennings JR, Peter LM. Sol. Ener. Mater. Sol. Cells 2007; 91:424–426.
58. Kroeze JE, Hirata N, Schmidt-Mende L et al. Adv. Funct. Mater. 2006; 16:1832–1838.
59. Lan Z, Wu JH, Wang DB, Hao SC, Lin JM, Huang YF. Sol. Ener. 2007; 81:117–122.
60. O'Regan B, Schwartz DT. Chem. Mater. 1995; 7:1349–1354.
61. O'Regan B, Schwartz DT. J. Appl. Phys. 1996; 80:4749.
62. Ramirez RE, Sanchez EM. Sol. Ener. Mater. Sol. Cells 2006; 90:2384–2390.
63. Tennakone K, Kumara GRRA, Kumarasinghe AR, Wijayantha KGU, Sirimanne PM. Semicond. Sci. Technol. 1995; 10:1689.
64. Tennakone K, Kumara GRRA, Wijayantha KGU, Kottegoda IRM, Perera VPS, Aponsu GMLP. J. Photochem. Photobiol. A 1997; 108:175–177.
65. Huang ML, Yang HX, Wu JH et al. J. Sol-Gel Sci. Technol. 2007; 42:65–70.
66. Ikeda N, Miyasaka T. Chem. Commun. 2005; 1886–1888.
67. Kang MS, Kim JH, Kim YJ, Won J, Park NG, Kang YS. Chem. Commun. 2005; 889–891.
68. Kang MS, Kim JH, Won J, Kang YS. J. Photochem. Photobiol. A 2006; 183:15–21.
69. Kim MR, Jin SH, Park SH, Lee HJ, Kang EH, Lee JK. Mol. Cryst. Liq. Cryst. 2006; 444:233–239.
70. Li MY, Feng SJ, Fang SB et al. Electrochim. Acta 2007; 52:4858–4863.
71. Nogueira AF, Durrant JR, De Paoli MA. Adv. Mater. 2001; 13:826.
72. Kuang DB, Ito S, Zakeeruddin SM, Grätzel M. Abstr. Papers Am. Chem. Soc. 2006:231.
73. Kuang DB, Wang P, Ito S, Zakeeruddin SM, Grätzel M. J. Am. Chem. Soc. 2006; 128:7732–7733.
74. Lee HJ, Lee JK, Kim MR et al. Mol. Cryst. Liq. Cryst. 2007; 462:75–81.
75. Papageorgiou N, Athanassov Y, Armond M et al. J. Electrochem. Soc. 1996; 143:3099.
76. Santa-Nokki H, Busi S, Kallioinen J, Lahtinen M, Korppi-Tommola J. J. Photochem. Photobiol. A 2007; 186:29–33.
77. Wang M, Xiao XR, Zhou XW, Li XP, Lin Y. Sol. Ener. Mater. Sol. Cells 2007; 91:785–790.
78. Yamanaka N, Kawano R, Kubo W et al. J. Phys. Chem. B 2007; 111:4763–4769.
79. Nakade S, Kanzaki T, Kubo W, Kitamura T, Wada Y, Yanagida S. J. Phys. Chem. B 2005; 109:3480–3487.
80. Nakade S, Makimoto Y, Kubo W, Kitamura T, Wada Y, Yanagida S. J. Phys. Chem. B 2005; 109:3488–3493.

81. Oskam G, Bergeron BV, Meyer GJ, Searson PC. J. Phys. Chem. B 2001; 105:6867.
82. Pichot F, Gregg BA. J. Phys. Chem. B 2000; 104:6.
83. Cai FS, Chen J, Xu RS. Chem. Lett. 2006; 35:1266–1267.
84. Huang Z, Liu XH, Li KX et al. Electrochem. Commun. 2007; 9:596–598.
85. Murakami TN, Ito S, Wang Q et al. J. Electrochem. Soc. 2006; 153:A2255–A2261.
86. Ramasamy E, Lee WJ, Lee DY, Song JS. Appl. Phys. Lett. 2007; 90:173103.
87. Fang XM, Ma TL, Akiyama M, Guan GQ, Tsunematsu S, Abe E. Thin Solid Films 2005; 472:242–245.
88. Kang MG, Park NG, Ryu KS, Chang SH, Kim KJ. Sol. Energ. Mater. Sol. Cells 2006; 90:574–581.
89. Tan B, Toman E, Li YG, Wu YY. J. Am. Chem. Soc. 2007; 129:4162.
90. Hagfeldt A, Didriksson B, Palmqvist T et al. Sol. Ener. Mater. Sol. Cells 1994; 31:481.
91. Nelson J, Haque SA, Klug DR, Durrant JR. Phys. Rev. B 2001; 6320:5321.
92. Tachibana Y, Moser JE, Grätzel M, Klug D, Durrant JR. J. Phys. Chem. 1996; 100:20056.
93. Bisquert J, Garcia-Belmonte G, Fabregat-Santiago F. J. Solid State Electrochem. 1999; 3:337.
94. Cahen D, Hodes G, Grätzel M, Guillemoles JF, Riess I. J. Phys. Chem. B 2000; 104:2053.
95. Bedja I, Kamat PV. J. Phys. Chem. 1995; 99:9182.
96. Tada H, Hattori A. J. Phys. Chem. B 2000; 104:4585.
97. Diamant Y, Chapple S, Chen SG, Melamed O, Zaban A. Coord. Chem. Rev. 2004; 248:1271–1276.
98. Jung HS, Lee JK, Nastasi M et al. Langmuir 2005; 21:10332–10335.
99. Kim KE, Jang SR, Park J, Vittal R, Kim KJ. Sol. Ener. Mater. Sol. Cells 2007; 91:366–370.
100. Law M, Greene LE, Radenovic A, Kuykendall T, Liphardt J, Yang PD. J. Phys Chem. B 2006; 110:22652–22663.
101. O'Regan BC, Scully S, Mayer AC, Palomares E, Durrant J. J. Phys. Chem. B 2005; 109:4616–4623.
102. Wang ZS, Yanagida M, Sayama K, Sugihara H. Chem. Mater. 2006; 18:2912–2916.
103. Yum JH, Nakade S, Kim DY, Yanagida S. J. Phys Chem. B 2006; 110:3215–3219.
104. Fabregat-Santiago F, García-Cañadas J, Palomares E et al. J. Appl. Phys. 2004; 96:6903–6907.
105. Snaith HJ, Grätzel M. Adv. Mater. 2006; 18:1910.
106. Fabregat-Santiago F, Garcia-Belmonte G, Bisquert J, Zaban A, Salvador P. J. Phys. Chem. B 2002; 106:334–339.
107. Fabregat-Santiago F, Garcia-Belmonte G, Bisquert J, Bogdanoff P, Zaban A. J. Electrochem. Soc. 2003; 150:E293–E298.
108. Xia JB, Masaki N, Jiang KJ, Wada Y, Yamagida S. Chem. Lett. 2006; 35:252–253.
109. Goto H, Hattori R. Electrochemistry 2006; 74:484–486.
110. Xia JB, Masaki N, Jiang KJ, Yanagida S. J. Photochem. Photobiol. A 2007; 188:120–127.
111. Hagfeldt A, Grätzel M. Chem. Rev. 1995; 95:49–68.
112. Xia JB, Masaki N, Jiang KJ, Yanagida S. J. Phys. Chem. C 2007; 111:8092–8097.
113. Cao F, Oskam G, Meyer GJ, Searson PC. J. Phys. Chem. 1996; 100:17021.
114. Schwarzburg K, Willig F. J. Phys. Chem. B 1999; 103:5743–5746.
115. de Jongh PE, Vanmaekelbergh D. J. Phys. Chem. B 1997; 101:2716–2722.
116. Dloczik L, Ileperuma O, Lauerman I et al. J. Phys. Chem. B 1997; 101:10281.
117. Franco G, Gehring J, Peter LM, Ponomarev EA, Uhlendorf I. J. Phys. Chem. B 1999; 103:692.
118. Konenkamp R. Phys. Rev. B 2000; 61:11057.
119. Meulenkamp EA. J. Phys. Chem. B 1999; 103:7831.
120. Solbrand A, Henningsson A, Södergren S, Lindstrom H, Hagfeldt A, Lindquist SE. J. Phys. Chem. B 1999; 103:1078.
121. Dittrich T, Ofir A, Tirosh S, Grinis L, Zaban A. Appl. Phys. Lett. 2006; 88:182110.
122. Ofir A, Dittrich T, Tirosh S, Grinis L, Zaban A. J. Appl. Phys. 2006; 100:74317.
123. Tirosh S, Dittrich T, Ofir A, Grinis L, Zaban A. J. Phys. Chem. B. 2006; 110:16165–16168.
124. Asagoe K, Ngamsinlapasathian S, Suzuki Y, Yoshikawa S. Cent. Eur. J. Chem. 2007; 5:605–619.
125. Law M, Greene LE, Johnson JC, Saykally R, Yang PD. Nat. Mater. 2005; 4:455–459.
126. Tan B, Wu YY. J. Phys Chem. B 2006; 110:15932–15938.
127. Parkinson BA, Spitler MT. Electrochim. Acta 1992; 37:943.
128. Södergren S, Hagfeldt A, Olsson J, Lindquist SE. J. Phys. Chem. 1994; 98:5552.
129. Serpone N, Borgarello E, Grätzel M. J. Chem. Soc. Chem. Commun. 1984; 342–344.
130. Gerischer H, Lübke M. J. Electroanal. Chem. 1986; 20:225–227.

131. Vogel R, Pohl K, Weller H. Chem. Phys. Lett. 1990; 174:241–246.
132. Weller H. Ber. Bunsenges. Phys. Chem. 1991; 95:1361–1365.
133. Hotchandi S, Kamat PV. J. Phys. Chem. 1992; 96:6835–6839.
134. Liu D, Kamat PV. J. Phys. Chem. 1993; 97:10769–10773.
135. Nasr C, Kamat PV, Hotchandani S. J. Electroanal. Chem. 1997; 420:201–207.
136. Fang JH, Lu XM, Zhang DG, Fu DG, Lu ZH. Supramol. Sci. 1998; 5:709–711.
137. Rincon ME, Jiminez A, Oriuhela A, Martinez G. Sol. Ener. Mater. Sol. Cells 2001; 70:163–173.
138. Shen Q, Arae D, Toyoda T. J. Photochem. Photobiol. A 2004; 164:75–80.
139. Toyoda T, Tsuboya I, Shen Q. Mater. Sci. Eng. C 2005; 25:853–857.
140. Niitsoo O, Sarkar SK, Pejoux C, Rühle S, Cahen D, Hodes G. J. Photochem. Photobiol. A 2006; 181:306–313.
141. Vogel R, Hoyer P, Weller H. J. Phys. Chem. 1994; 98:3183–3188.
142. Peter LM, Wijayantha KGU, Riley DJ, Waggett JP. J. Phys. Chem. B 2003; 107:8378–8381.
143. Ennaoui A, Fiechter S, Tributsch H, Giersig M, Vogel R, Weller H. J. Electrochem. Soc. 1992; 139:2514–2518.
144. Fang JH, Wu JW, Su LY, Zhang XY, Lu ZH. Chem. Lett. 1997; 149–150.
145. Shen Y-C, Deng H, Fang J, Lu Z. Colloids Surf. A 2000; 175:135–140.
146. Zaban A, Micic OI, Gregg BA, Nozik AJ. Langmuir 1998; 14:3153–3156.
147. Yu P, Zhu K, Norman AG, Ferrere S, Frank AJ, Nozik AJ. J. Phys. Chem. B 2006; 110:25451–25454.
148. Spanhel L, Weller H, Henglein A. J. Am. Chem. Soc. 1987; 109:6632–6635.
149. Gopidas KR, Bohorquez M, Kamat PV. J. Phys. Chem. 1990; 94:6435–6440.
150. Kietzmann R, Willig F, Weller H et al. Mol. Cryst. Liq. Cryst. 1991; 194:169–180.
151. Evans JE, Springer KW, Zhang JZ. J. Chem. Phys. 1994; 101:6222–6225.
151a. Blackburn JL, Selmarten DC, Nozik AJ. J. Phys. Chem. B, 2003; 107:14154.
152. Robel I, Subramanian V, Kuno M, Kamat PV. J. Am. Chem. Soc. 2006; 128:2385–2393.
153. Shen Q, Katayama K, Yamaguchi M, Sawada T, Toyada T. Thin Solid Films 2005; 486:15–19.
154. Grätzel M, Frank AJ. J. Phys. Chem. 1982; 86:2964–2967.
155. Klimov VI, McBranch DW, Leatherdale CA, Bawendi MG. Phys. Rev. B. 1999; 60:13740–13749.
156. Zhang JZ. J. Phys. Chem. B 2000; 104:7239–7253.
157. Duonghong D, Ramsden J, Grätzel M. J. Am. Chem. Soc. 1982; 104:2977–2985.
158. Zhang JZ, O'Neill RH, Roberti TW. J. Phys. Chem. 1994; 98:3859–3864.
159. Maly P, Kudrna J, Trojanek F et al. Appl. Phys. Lett. 2000; 77:2352–2354.
160. Ai X, Jin R, Ge C et al. J. Chem. Phys. 1997; 106:3387–3392.
161. Patel AA, Wu F, Zhang JZ et al. J. Phys. Chem. B 2000; 104:11598–11605.
162. Warner JH, Thomsen E, Watt AR, Heckenberg NR, Rubinsztein-Dunlop H. Nanotechnology 2005; 16:175–179.
163. Wehrenberg BL, Wang C, Guyot-Sionnest P. J. Phys. Chem. B 2002; 106:10634–10640.
164. Meissner D, Lauermann I, Memming R, Kastening B. J. Phys. Chem. 1988; 92:3484.
165. Yang S, Wang Z, Huang C. Synth. Metals 2001; 123:267–272.
166. Yang S, Huang C, Zhai J, Wang Z, Jiang L. J. Mater. Chem. 2002; 12:1459–1464.
167. Cahen D, Hodes G, Manassen J. J. Electrochem. Soc. 1978; 125:1623–1628.
168. Wienke J, Krunks M, Lenzmann F. Semicond. Sci. Technol. 2003; 18:876–880.
169. Hara K, Sayama K, Arakawa H. Sol. Ener. Mater. Sol. Cells 2000; 62:441–447.
170. Lévy-Clément C, Tena-Zaera R, Ryan MA, Katty A, Hodes G. Adv. Mater. 2005; 17:1512–1515.
171. Tena-Zaera R, Ryan MA, Katt A, Hodes G, Bastide S, Lévy-Clément C. CR Chim. 2006; 9:717–729.
172. Yasaki Y, Sonoyama N, Sakata T. J. Electroanal. Chem. 1999; 469:116–122.
173. Lévy-Clément C. In Nanostructured Materials for Solar Energy Conversion, T Soga (ed.). Elsevier: Amsterdam, 2007; 447–484.
174. Tennakone K, Kumara GRRA, Kottegoda IRM, Perera VPS, Aponsu GMLP. J. Phys. D Appl. Phys. 1998; 31:2326–2330.
175. Rost C, Sieber I, Siebentritt S, Lux-Steiner MC, Könenkamp R. Appl. Phys. Lett. 1999; 75:692–694.
176. Kronik L, Bachrach-Ashkenasy N, Leibovitch M et al. J. Electrochem. Soc. 1998; 145:1748–1755.
177. Kaiser I, Ernst K, Fischer Ch-H et al. Sol. Ener. Mater. Sol. Cells 2001; 67:89–96.

178. Tena-Zaera R, Katty A, Bastide S, Lévy-Clément C, O'Regan B, Muños-Sanjose V. Thin Solid Films 2005; 483:372–377.
179. Tena-Zaera R, Katty A, Bastide S, Lévy-Clément C. Chem. Mater. 2007; 19:1626–1632.
180. Larramona G, Chone C, Jacob A et al. Chem. Mater. 2006; 18:1688–1696.
181. Plass R, Pelet S, Krueger J, Grätzel M, Bach U. J. Phys. Chem. B 2002; 106:7578–7580.
182. Bayon R, Musembi R, Belaidi A et al. Sol. Ener. Mater. Sol. Cells 2006; 89:13–25.
183. Gavrilov S, Oja I, Lim B et al. Phys. Stat. Sol. 2006; 203:1024–1029.
184. Oja I, Belaidi A, Dloczik L, Lux-Steiner M-Ch, Dittrich Th. Semicond. Sci. Technol. 2006; 21:520–526.
185. Taretto K, Rau U. Thin Solid Films 2005; 480–481:447–451.
186. Könenkamp R, Hoyer P, Wahi A. J. Appl. Phys. 1996; 79:7029–7035.
187. Ernst K, Sieber I, Neumann-Spallart M, Lux-Steiner M-Ch, Könenkamp R. Thin Solid Films 2000; 361–362:213–217.
188. Ernst K, Engelhardt R, Ellmer K et al. Thin Solid Films 2001; 387:26–28.
189. Grasso C, Ernst K, Könenkamp R, Burgelman M, Lux-Steiner MC. Proc. 17th Eur. PV Conf., Munich, Germany, Oct. 2001, 2001; 211.
190. Ernst K, Belaidi A, Könenkamp R. Semicond. Sci. Technol. 2003; 18:475–479.
191. Reijnen L, Meester B, Goossens A, Schoonman J. Mater. Sci. Eng. C 2002; 19:311–314.
192. Nanu M, Reijnen L, Meester B, Goossens A, Schoonman J. Thin Solid Films 2003; 431–432:492–496.
193. Nanu M, Schoonman J, Goossens A. Adv. Mater. 2004; 16:453–456.
194. Nanu M, Schoonman J, Goossens A. Adv. Funct. Mater. 2005; 15:95–100.
195. Nanu M, Schoonman J, Goossens A. Nanoletters 2005; 5:1716–1719.
196. O'Hayre R, Nanu M, Schoonman J, Goossens A, Wang Q, Grätzel M. Adv. Funct. Mater. 2006; 16:1566–1576.

CHAPTER 6

Nanoscale Materials For Hydrogen and Energy Storage

Maximilian Fichtner

1. INTRODUCTION

Energy experts have predicted that the world's energy demand will double to 28 terawatts in the next 50 years [1]. At the same time, global oil resources will dwindle and a considerable increase of the oil price is expected, which may lead to severe economic, social and political problems [2]. In order to meet this challenge, scientific breakthroughs have been demanded by energy agencies and political leaders. The increasing need for more energy will require enormous growth in energy generation capacity, more secure and diversified energy sources and a successful strategy to tame greenhouse gas emissions. In this regard, nanoscience and nanotechnology offer promising approaches, as all the elementary steps of energy conversion (charge transfer, molecular rearrangement, chemical reactions, etc.) take place on the nanoscale. Thus, the development of new nanomaterials, as well as the methods to characterize, manipulate and assemble them, have created a new paradigm for developments in the field of energy technologies. First examples are new light-harvesting systems and solar cells, new materials for energy storage and highly efficient fuel cells. This chapter will give a short introduction on methods and materials for energy storage and focus on the storage of hydrogen in nanoscale materials.

2. METHODS FOR ENERGY STORAGE

An increasing fraction of renewable energies is expected to contribute to covering the global energy demand in the future and energy storage systems are needed

Forschungszentrum Karlsruhe, Institute for Nanotechnology, PO Box 3640,
D-76021 Karlsruhe, Germany

Nanostructured Materials © 2009 Elsevier Ltd.
978-0-08-044965-4 All rights reserved.

for an efficient use of discontinuous sources, such as wind and solar power. In this context, nanostructured architectures employing a 3D structure for power storage and conversion (batteries, supercapacitors, fuel cells, photovoltaics) offer many advantages over existing technologies to minimize power losses, improve charge/discharge rates and enhance energy densities, because functional units in these architectures consist of interconnected ≈0 nm domains and mesopores (10–50 nm), for example.

For practical reasons, it is one of the favourable options to store energy in electrical and chemical storage devices, such as batteries, supercapacitors and hydrogen storage systems. Other options may have disadvantages in mobile applications. For example, advanced flywheels can store up to 250 Wh/kg, but powerful mobile systems would be problematic because of their big mass, high rotation speed (30 000 rpm) and, hence, the high moment of inertia.

2.1 Energy Storage in Supercapacitors and Batteries

The supercapacitor resembles a regular capacitor, with the exception that it offers much higher capacitance in a small package. Energy is stored by means of static charge rather than an electrochemical process that is inherent to the battery. Applying a voltage differential to the positive and negative plates charges the supercapacitor. Whereas a regular capacitor consists of conductive foils and a dry separator, the supercapacitor crosses over with battery technology by using special electrodes and an electrolyte. Three types of electrode material have been used for the supercapacitor: high-surface-area activated carbons, metal oxide and conducting polymers. The high-surface electrode material, also called a double layer capacitor (DLC), is least costly to manufacture and the most common. It stores the energy in the double layer formed near the carbon electrode surface [3]. The gravimetric energy density of the supercapacitor is 1–10 Wh/kg and low compared with other storage technologies. However, the charge time of a supercapacitor is about 10 seconds only and mainly limited by the size of the charger. Due to the high power, but low storage capacity, their high reliability and extraordinarily long cycle life, supercapacitors are commonly used as memory backup to bridge short power interruptions or to improve the current handling of a battery. The supercapacitor is also suitable for enhancing peak-load performance. Due to their ability to charge rapidly, large supercapacitors are meanwhile used for regenerative braking on vehicles and to improve the agility of hybrid cars.

During the last few decades, rechargeable batteries have experienced only moderate improvements in terms of higher capacity and smaller size. However, research has brought about a variety of battery chemistries and, with today's increased selection, better choices are available to suit a specific user application [3]. The highest energy densities of more than 200 Wh/kg are currently obtained with Li-ion batteries, which also have the advantage of showing no memory effect. However, due to a maximum charge and discharge current, conventional types have only been used in low-load applications, such as notebook computers and cellular phones. These limitations in power density have been considerably improved by new lithium batteries with nanostructure electrodes. Such systems

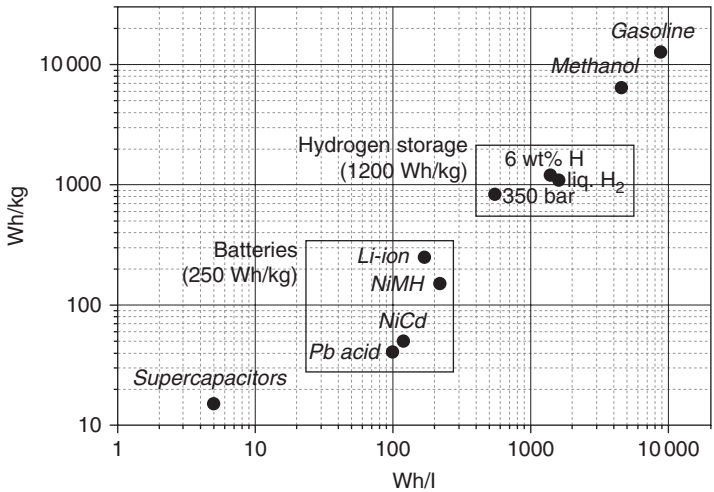

FIGURE 6.1 Volumetric and gravimetric energy densities of different energy storage systems.

reach over 2500 watts per kilogram power density, which is 10 times larger than that of conventional lithium batteries.

In summary, energy storage directly in electrical form would be a simple and convenient option. However, the energy densities that can be obtained by second generation batteries and by supercapacitors are still low and far below the demands of vehicular applications (Figure 6.1).

As an alternative, hydrogen storage systems offer a storage capacity which exceeds that of current batteries by a factor of 5–10. Moreover, energy-related problems of energy security, air pollution and climate change, technological advances and growing competition in the energy industry are reasons why hydrogen as a future energy carrier is regarded to be increasingly attractive. As a consequence, major efforts are being devoted to building an energy infrastructure that uses hydrogen as the primary energy carrier, connecting a host of energy sources to diverse end uses. A major challenge in implementing a hydrogen economy is the development of efficient and safe storage materials for hydrogen. The storage of hydrogen is one of the key issues which have to be solved for the implementation of a hydrogen economy [4,5].

3. METHODS FOR HYDROGEN STORAGE IN MOBILE APPLICATIONS

Three ways of storing hydrogen for fuel cell-driven applications have been proposed. Of the various options, the conventional storage systems based on pressurized and liquefied hydrogen have a high development status. However, they also exhibit principal drawbacks and have reached their theoretical limit of storage density (Figure 6.2).

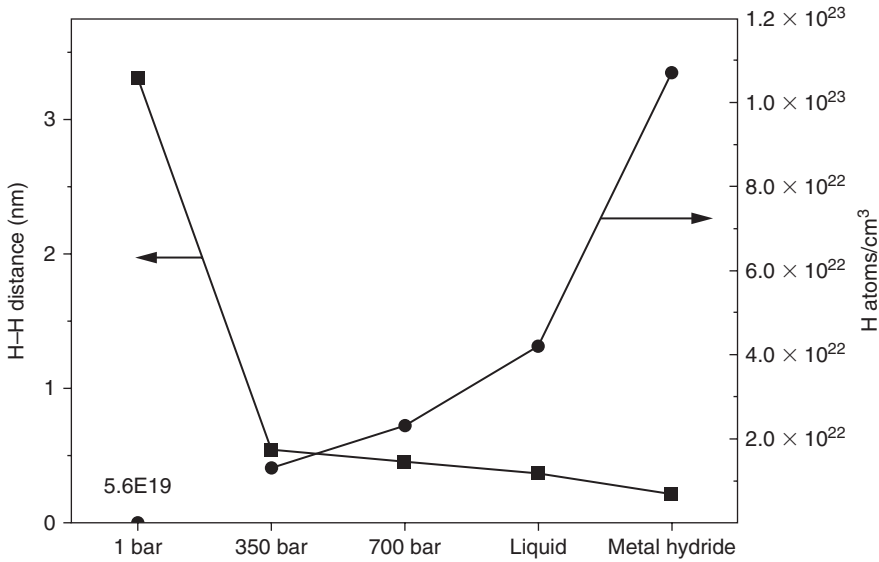

FIGURE 6.2 Mean H–H distances and theoretical volumetric storage densities of hydrogen stored as a compressed gas, as a liquid, or in a solid storage material.

Pressurized hydrogen can be stored in containers made of composite materials that have to withstand high pressures in order to carry enough fuel for an envisaged driving cycle of some 400 km or more. One of the drawbacks of such a system is that the already limited volumetric density does not increase proportionally to the operating pressure at high values because of the real gas behaviour of the hydrogen. Moreover, there are safety concerns related to a tank rupture in an accident. Technical problems arise from, for example, adiabatic effects when expanding and compressing the hydrogen during refuelling of a composite tank. Furthermore, it may be risky to fill and empty current containers at temperatures below the freezing point due to the risk of failure of the composite structure.

As an alternative, liquefied hydrogen with a density of 70.8 kg/m^3 is particularly attractive to reach higher storage densities per volume. For this purpose, the hydrogen is cooled down to 21 K which, however, needs about one third of the energy content of the stored hydrogen. Overall, efficiency is further reduced by the so-called boil-off phenomenon which means that the stored cryogenic liquid starts to evaporate after a certain period of time due to unavoidable heat input into the storage vessel, leading to a loss of 2–3% of vaporized hydrogen per day. This cannot be prevented even with a very sophisticated vacuum insulation and heat radiation shield in place. The low critical temperature of hydrogen of 32 K would lead to a high pressure build-up in the tank. Hence, the overpressure must be released, e.g. via a catalytic converter.

To circumvent these drawbacks, several fuel storage alternatives have been proposed over the past few years which are all based on storage in a material that

can readily take up and release large amounts of hydrogen. According to the technical targets specified by the US Department of Energy (US-DoE) for 2010 and 2015, more than 6 wt% of hydrogen should be contained in such a system, including tank and valves, and the filling time should not exceed 5 min. Furthermore, the thermal properties of the material should match the operation conditions of the fuel cell, which means that the temperature necessary to release the hydrogen from storage should not exceed the temperature of the exhaust gas of the fuel cell.

Recent investigations have shown that nanoscale materials may offer advantages for hydrogen storage, if certain physical and chemical effects related to the nanoscale can be used efficiently. Associated phenomena, such as surface interactions, material transport, defects, phase transitions, grain boundary phenomena and the formation of new and metastable phases, may also play an important role in the development of reversibly working hydrogen storage materials with a high cycling stability.

In practice, two basic mechanisms are considered for hydrogen storage in nanoscale materials:

1. *chemisorption*, including dissociation of hydrogen molecules and chemical bonding of the hydrogen atoms by integration in the lattice of a metal or an alloy or by formation of a new chemical compound;
2. *physisorption* of molecular hydrogen in a nanomaterial.

A principal advantage of storing hydrogen in chemical form, e.g. as an atom in a metal hydride, is the high volumetric storage density which can be achieved by this method (see Figure 6.2). Hydrogen in the gaseous (70 MPa, 300 K) or liquid state (0.1 MPa, 20 K) consists of H_2 molecules at a mean distance of approximately 0.45 nm or 0.36 nm, respectively. These distances result from repulsive molecular interactions. The minimum H–H separation in ordered binary metal hydrides is 0.21 nm. This limit is due to the repulsive interaction generated by the partially charged hydrogen atoms [6]. A principal drawback of the method is the necessity to split or recombine the hydrogen molecule and form chemical bonds with the material. This makes thermal management of the storage necessary in order to supply or remove the heat of reaction.

Storing hydrogen by physisorption is not subject to this constraint because the hydrogen stays in its molecular form. The problem rather is to provide light carrier materials with a sufficient number of bonding sites for the hydrogen per volume. Moreover, physisorption interaction between the H_2 molecule and the surface is in the lower kJ/mol range, as a result of which it may be necessary to work at very low working temperatures.

4. CHALLENGES IN MATERIALS DEVELOPMENT

Figure 6.3 shows the main target properties of hydrogen storage materials which have to be optimized and may depend on each other. Over the last few years, a new multidisciplinary approach combining physics, chemistry, materials science and engineering science has tried to deal with this complex field. Such activities

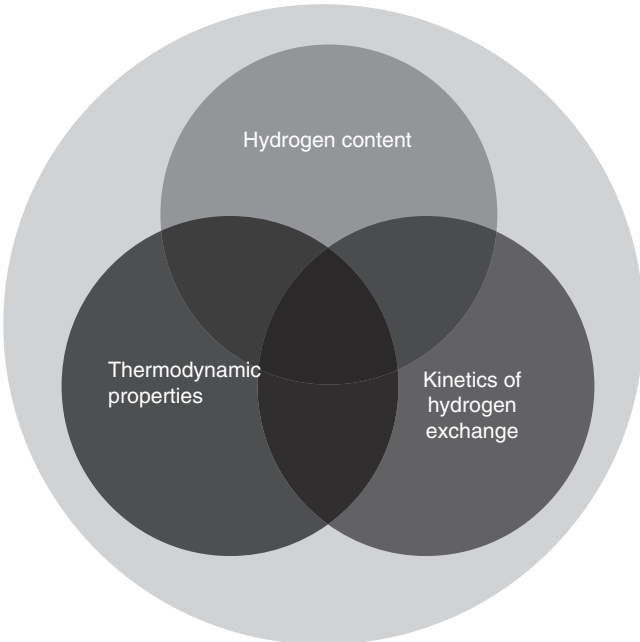

FIGURE 6.3 Target properties of hydrogen storage materials.

aim at combining experiment and theory, model building and simulation not only better to understand experimental data, but also to identify core parameters for the further development of the materials.

Recent investigations showed that nanomaterials may offer a particular advantage for hydrogen storage if scale-dependent physical and chemical properties can be used efficiently. Typical nanoscale-related phenomena may play an important role. Hence, understanding of the sometimes interrelated properties on the nanoscale has been regarded as a key issue for the further development of hydrogen storage materials.

Below, an overview will be given of the current state of the art of nanomaterials developed for hydrogen storage. Material-relevant nanotechnological aspects of preparation and properties will be outlined and strategies will be presented for the further development of the materials. The contribution will close with a technical section about handling, synthesis and investigation of nanoscale materials for hydrogen storage.

5. PHYSISORPTION MATERIALS

The intermolecular forces involved in typical physisorption systems are weak (van der Waals forces) and do not cause any significant change in the electronic orbital patterns of the relevant species. This is a challenge for the physisorption

of hydrogen, because H_2 is the smallest molecule and has two electrons only. Hence, it is hard to polarize and dispersion forces created by temporarily induced dipoles are weak. Nanomaterials may offer advantages for molecular hydrogen storage when they exhibit high specific surface areas and when the chemical and spatial environment of the hydrogen can be designed on a molecular level.

An alternative for storing hydrogen by physisorption on large surfaces is hydrogen storage by encapsulation or trapping in microporous media. The working principle is that the guest molecules are forced into the cavities of the nanostructured host. Upon cooling, hydrogen is trapped inside the cavities. It can be released again by raising the temperature. Thus, trapping may be an instrument to overcome the low binding energies between the molecular hydrogen and the support by implementing kinetic restrictions for the sorption process. Of the physisorption materials currently investigated, nanostructured zeolites and chabazites, carbons, metal–organic frameworks and clathrates will be discussed. Nanoporous materials are generally defined as those porous materials with pore diameters smaller than 100 nm.

5.1 Nanoporous Inorganic Materials

5.1.1 Zeolite structures

Zeolites are the first systems that were studied systematically as media for hydrogen storage. Weitkamp et al. [7] found a relationship between the amount of encapsulated hydrogen and the size of the exchanged cation in zeolite A. The number of zeolite cages per gram of the material is between 3.58×10^{20} for NaA and NaX and 1.41×10^{21} for sodalite; the number of H_2 molecules per cage was found to be between 0.1 and 0.25 for the different materials. Storage capacity is generally higher for zeolites having a high number of small cavities in their structure and sodalite shows the highest hydrogen uptake of 9.2 cm^3/g (0.082 wt%) when loaded at 573 K and 10 MPa hydrogen pressure. This implies that only one out of four to five sodalite cages can be occupied by a hydrogen molecule. The reason why not every cage takes up at least one hydrogen molecule is unknown. However, the storage capacity is increased considerably at liquid nitrogen temperatures. Kazansky et al. [8] studied hydrogen adsorption on sodium forms of faujasite and found a hydrogen storage capacity of 1.2 wt% H at 77 K. Moreover, a maximum hydrogen storage capacity of 1.81 wt% (15 bar) was obtained for NaY zeolite in a recent study [9]. The authors noticed a close correlation between the BET surface area of the zeolite measured with nitrogen and the storage capacity for hydrogen at low temperatures. For all zeolites investigated, a type I isotherm was observed at 77 K, with desorption closely following the same path as adsorption. This indicates a process of microporous hydrogen physisorption in the zeolite structure at low temperatures.

H-SSZ-13, a highly siliceous zeolite (Si/Al = 11.6) with a chabazitic framework, stores 1.3 wt% H at 77 K and 0.9 bar hydrogen pressure [10]. The behaviour in terms of hydrogen uptake was explained by the presence of an isolated, strongly polarizing site in the small cages. The cooperative role played by the high surface area, internal wall topology and presence of high binding energy sites (protons) probably allows the hydrogen to densify inside the nanopores

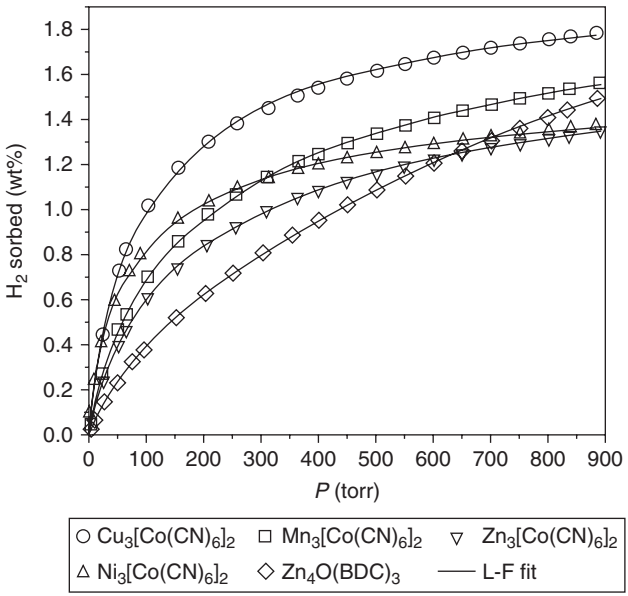

FIGURE 6.4 Hydrogen sorption isotherms for the Prussian blue analogues $M_3[Co(CN)_6]_2$ (M = Mn, Ni, Cu, Zn) and $Zn_4O(BDC)_3$. Isotherms of $Fe_3[Co(CN)_6]_2$ and $Co_3[Co(CN)_6]_2$ are not shown for clarity, but are similar to those of $Zn_3[Co(CN)_6]_2$ and $Mn_3[Co(CN)_6]_2$, respectively. Solid lines represent the best fit of the Langmuir–Freundlich (L-F) equation to the data (reproduced with permission from [13], Copyright 2005, American Chemical Society).

under favourable temperature and pressure conditions. It was pointed out in the study that a proper balance between available space (volume accessible to hydrogen), high contact surface and specific interaction with strong and isolated polarizing centres can be helpful to design better materials for molecular H_2 storage.

5.1.2 Transition metal-based structures

First reports of the hydrogen storage properties of dehydrated Prussian blue analogues of the type $M^{II}{}_3[Co^{II}(CN)_6]_2$ (M^{II} = Mn, Fe, Co, Ni, Cu, Zn, Cd) revealed that interactions with bridging cyanide ligands and/or coordinatively unsaturated metal centres may lead to higher adsorption enthalpies compared with nanostructured carbon or metal–organic framework materials, such as $Zn_4O(BDC)_3$ (Figure 6.4) [11,12].

In Prussian blue itself, $Fe_4[Fe(CN)_6]_3{\cdot}14H_2O$, charge balance with the Fe^{3+} ions leads to vacancies at one quarter of the $[Fe(CN)_6]^{4-}$ sites in the framework. The cavities are normally filled by water molecules, which can be removed, leaving the residual Fe-CN framework intact. Prussian blue analogues of the formula $M_3[M'(CN)_6]_2{\cdot}\,xH_2O$ feature even more vacancies, at one third of the hexacyanometalate sites. The polarizable π-electron clouds of the cyanide bridges in these materials are expected to have some affinity to H_2. In addition, H_2 may also be able to interact with the vacant coordination sites on the M^{2+} ions.

The compounds investigated exhibited type I sorption isotherms characteristic of microporous materials. The BET surface areas range from 560 m^2/g for $Ni_3[Co(CN)_6]_2$ to 870 m^2/g for $Mn_3[Co(CN)_6]_2$. Interestingly, this is far below the values of nanostructured carbon and metal–organic framework materials having BET surface areas of several thousand m^2/g, although the storage gravimetric capacities are comparable. The highest capacity of 1.8 wt% H at 77 K and 119 kPa H_2 was found for $Cu_3[Co(CN)_6]_2$, which has a BET surface area of 730 m^2/g.

It is likely that the total hydrogen uptake is a combined function of surface area and the comparably high enthalpy of adsorption [11], the latter of which is influenced both by surface chemistry and the pore geometry which best complements the hydrogen dimensions (0.41 nm diameter).

5.2 Nanoporous Organic and Carbon Materials

Nanoporous organic materials have gained considerable interest as physisorption materials, since natural activated carbon is able to store fair amounts of hydrogen and chemistry offers ways to synthesize materials with tailor-made pore geometries for hydrogen, which gives room for further development.

5.2.1 Activated carbon

Activated carbon materials are known for their very high specific surface areas of up to 2500 m^2/g and their unique physisorption capacities. It was found that these materials are capable of storing 4–5 wt% H_2 at 77 K. The adsorption isotherm of carbon can be explained by the Langmuir model at low temperatures, while the storage capacity at room temperature is a linear function of the pressure [14,15]. There is a relationship between the hydrogen storage capacity of the different carbon samples at 77 K and their specific surface area. The slope of the fit is 1.91×10^{-3} wt% $m^{-2}g$ [15]. Accordingly, the maximum hydrogen storage capacity per specific surface area of carbon can be calculated theoretically to amount to 2.28×10^{-3} wt% $m^{-2}g$ by assuming the density of the liquid adsorbate.

The intrinsic interaction of hydrogen with carbon materials seems to be slightly stronger than that with oxidic materials, such as zeolites and porous SiO_2 [14]. Due to the various sizes and shapes of the micropores in activated carbon, however, it is as yet impossible to comment on the optimum pore size and shape.

5.2.2 Carbon nanotubes and nanofibres

The chemistry of non-planar carbon structures differs from that of planar carbon or graphite, because the curvature of the backbone leads to a reduced orbital overlap of the π electrons. This causes a localization of the double bonds, which affects the overall chemistry. Hence, nanostructured carbon materials, such as single-walled carbon nanotubes (SWNT), multiwalled carbon nanotubes (MWNT), graphitic nanofibres (GNF) and carbon nanohorns, exhibit novel properties and yield unusual scientific phenomena, as was reported in a number of studies.

Hydrogen was expected to undergo a particular interaction with carbon nanomaterials, too. After a storage capacity of 67 wt% H had been reported for graphitic nanofibres [16] in 1998, a number of experimental studies were conducted,

but such high values could not be reproduced by other groups. The first publications reporting high storage capacities in carbon nanotubes (CNT) also resulted in extensive research activities, yielding many experimental data and a similar controversy [17]. Figure 6.5 gives an overview of data published in this field.

Recent studies of hydrogen uptake at 77 K in various carbon nanostructures, including CNT and GNF, indicated that the storage capacity depends on the surface area only and not on the long-range order or curvature of the graphene sheets [18]. Nijkamp et al. [14] and Zuettel et al. [19] found that the amount of adsorbed hydrogen was proportional to the specific surface area (BET) of various carbon materials and limited to 2 wt% hydrogen at 1 bar H_2 and 77 K. When cathodically charging GNF, SWNT and MWNT with hydrogen under ambient conditions, the reversible hydrogen uptake was 1.5 wt% H per 1000 m^2/g [19].

Orimo et al. [20] tried to improve the binding interaction between hydrogen and the support by introducing defects and stacking faults in the material. Thus, nanostructured graphite can bind up to 7.4 wt% hydrogen when the graphite is prepared by 80 h reactive ball milling under a 1.0 MPa hydrogen atmosphere. However, hydrogen desorption does not start before 600 K with maxima around 800 K and 1050 K [21,22]. Therefore, it was concluded [22,23] that the uptake of hydrogen was mainly due to the formation of strong covalent C–H bonds during ball milling rather than to bonding by physisorption.

Supported catalyst particles may be a source of atomic hydrogen and enhance the overall hydrogen uptake of a carbon material [13,24]. Lueking and Yang [24] found that 1–3 cm^3 H_2/g (STP) were adsorbed on various undoped carbon materials (SWNT, MWNT, GNF and activated carbon) at 300 K and 0.1 MPa H_2. The hydrogen uptake of the carbons could be increased by a factor of three when mixing CNT with small palladium nanoparticles. The effect was explained by

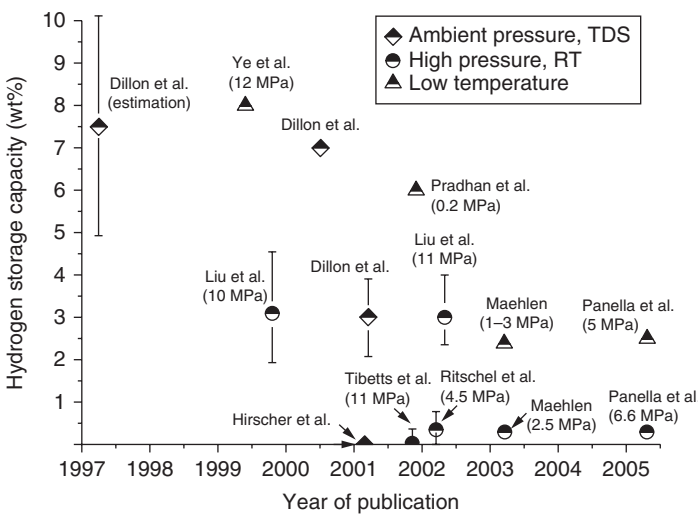

FIGURE 6.5 Experimental data regarding hydrogen storage capacities in SWNTs versus publication year for different methods, pressures and temperature regimes [M. Hirscher, private communication].

hydrogen spill-over from the catalyst particles to carbon receptors at the surface of the nanotubes. However, the adsorbed amount of hydrogen did not exceed 0.3 wt%. An increase of a factor of 2.9 for the activated carbon AX-21 and 1.6 for single-walled nanotubes at 298 K and 1 bar was obtained when using a Pd/carbon catalyst [25]. It was also shown that a spill-over mechanism may enhance adsorption density in the MOF-5 and IRMOF-8 metal–organic frameworks by a factor of 3.3 and 3.1, respectively [26]. This was achieved using a catalyst containing 5% Pt supported by activated carbon (primary receptor). The spill-over effect was obtained by grinding the catalyst and the MOF at a 1:9 ratio (wt). The maximum density observed was 1.8% at 298 K and 10 MPa for IRMOF-8.

5.2.3 Carbide-derived carbons

A new type of nanoporous carbon with a controlled microporous or mesoporous structure was presented recently [27]. The material is produced by a chlorination process from carbides which yields a regular porous structure with a narrow pore size distribution depending on the type of carbide and the conditions of chlorination. The specific surface area is up to 2000 m^2/g; the pore volume is up to 1 cm^3/g of the material. Figure 6.6 shows that up to 3 wt% hydrogen can be adsorbed at 77 K and 1 bar H_2 pressure. It was concluded in the study that a uniform and open porosity with pore diameters smaller than 1 nm is the key to storing large amounts of hydrogen by physisorption.

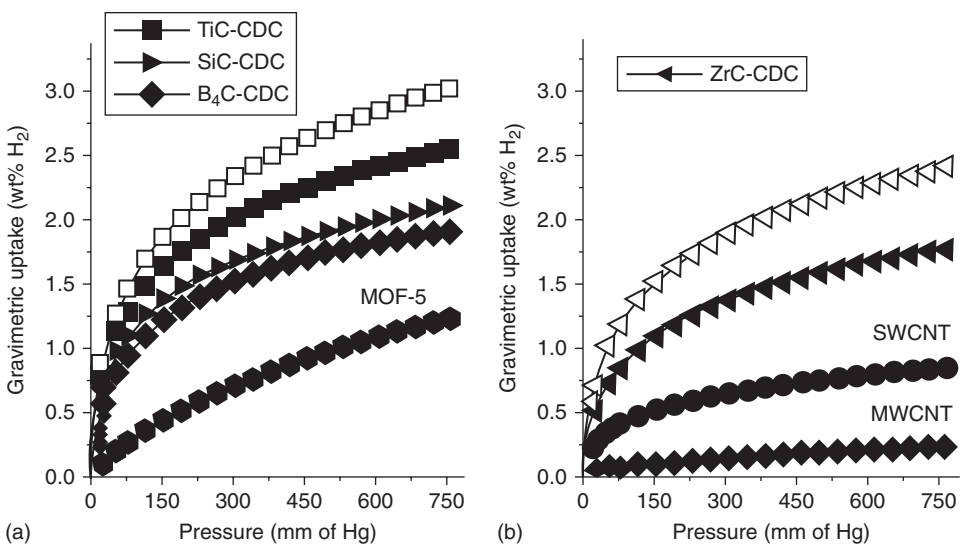

FIGURE 6.6 Hydrogen sorption isotherms of different CDC materials produced from different carbides compared to (a) MOF-5 and (b) nanotubes. Solid symbols stand for as-produced and empty for hydrogen-annealed CDC. All isotherms are completely reversible, without hysteresis (reproduced with permission from [27], copyright 2005, American Chemical Society).

5.3 Metal–Organic Frameworks

In principle, the gravimetric storage capacity of physisorption materials is limited by the relatively large mass of the inorganic or organic framework itself. Moreover, materials can have unnecessarily large diameters of their voids. Hence, the following bottom-up strategy can be pursued in order to improve the storage capacity in microporous systems:

- design of a light-weight framework with high interaction energy between hydrogen and the constituents of the framework;
- avoidance of inessential free space in the structure with space for optimal interaction between H_2 and the pore walls.

Metal–organic frameworks (MOFs) have been proposed as suitable systems for a bottom-up approach to the design and synthesis of a wide range of nanomaterials with different structures and properties. Li et al. [28] presented a synthesis strategy based on reticulating metal ions and organic carboxylate links into extended networks. The method uses a self-organizational process and allows for the design of porous structures in which pore size and functionality can be varied systematically. MOFs have therefore gained considerable interest because of their capability of storing in their framework hydrogen, light hydrocarbons and other organic substances [29].

A cubic MOF structure of $Zn_4O(L)_3$ consists of Zn_4O clusters forming the corners and linked by linear carboxylates L. Other metal ions, such as copper or differently structured carboxylates, lead to different structures. An example is shown in Figure 6.7, where the structure is formed by a trigonal carboxylate linking Zn_4O clusters. Sorption isotherms for heavier gases in MOFs are of type I as is typical of microporous materials [30]. Their specific surface areas were calculated from nitrogen sorption isotherms with values ranging between 1466 m^2/g for IRMOF-8 and 4500 m^2/g for IRMOF-177. At 77 K and 0.1 MPa H_2 pressure, the maximum uptake of hydrogen was 7.6 wt% for IRMOF-177. The latter value is more than what was expected from the simple rule-of-thumb for carbon materials presented above (approx. 1.5 wt% H_2 uptake per 1000 m^2/g at 77 K). At room temperature and 2 MPa hydrogen pressure, the experimentally determined hydrogen uptake was 1 wt% [32].

The nature of the organic linkers seems to have a certain influence on the number of hydrogen molecules attached to a linking unit [30]. This assumption is supported by the results of a theoretical study, where the interaction energies of molecular hydrogen with different aromatic molecules were studied by *ab-initio* calculations [32]. According to the study, the binding energies between H_2 and differently substituted benzene rings vary systematically depending on the nature of the functional group. Electron-drawing groups lower the interaction energy and electron-pushing groups increase the values. However, the role of the metal oxide clusters has not yet been elucidated and there are indications that they may be responsible for a fraction of more tightly bound hydrogen in the material. The dynamics of hydrogen is another important factor and, hence, a critical aspect of pore quality is the relative size of the pores with regard to the

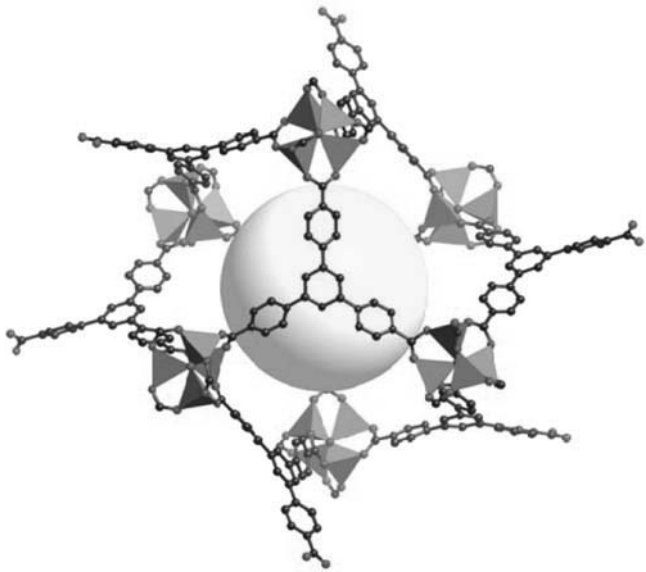

FIGURE 6.7 Structure of MOF-177, $Zn_4O(btb)_2$ (btb = benzene-1,3,5-tribenzoate). The ball in the centre represents the free volume in the structure (reproduced with permission from [29], copyright 2005, Wiley-VCH Verlag GmbH & Co, KGaA, Weinheim, Germany).

hydrogen and its interaction energy with the pore's surface. A design strategy should therefore focus on the minimization of the pore diameters to increase both the number of pores and the number of binding sites per volume, which would also enhance the volumetric storage density of the material.

A retardation of the hydrogen uptake and release can be achieved by spatial obstruction of the pores, as was reported by Zhao et al. [33]. Nickel-based metal–organic frameworks with small pore openings were synthesized and it was found that some of them exhibited a remarkable hysteresis in the adsorption and desorption of hydrogen at 77 K. Of the different materials investigated, the compound with the most distinctive isotherm hysteresis had the smallest window dimensions (smaller than the kinetic diameter of 0.29 nm of H_2) and cavities that were much larger than H_2.

Hysteresis decreases at higher temperatures and was therefore explained by kinetic trapping of the gas. This is supposed to result from the flexibility of the organic ligands (4,4′-bipyridine) in the nickel-based MOF. It was proposed that desorption is kinetically limited at lower temperatures, such that hydrogen can be loaded at high pressures, but then stored at lower pressures.

6. CHEMISORPTION MATERIALS

Current bulk materials with high gravimetric and volumetric storage capacities for hydrogen are almost exclusively based on nanocompositic chemisorption

systems, where a hydrogen carrier material is treated in, for example, a high-energy ball mill together with a dopant, leading to a material with a high hydrogen content and fast kinetics for hydrogen exchange.

Mechanical synthesis has the advantage of simplicity, as it represents a technique of preparation that offers a free choice of various kinds of alloys [34,35]. The technique also allows for the mass production of non-equilibrium phases of alloys over a wide range of composition. Moreover, a number of difficulties in synthesis and processing of metal hydrides can be solved by applying this method.

First improvements were made with respect to the so-called 'activation' of hydride materials. This is a process by means of which possibly present oxidic barriers at interfaces are broken by a mechanical treatment and high isotropic and anisotropic lattice strains are induced in the material, such that a high density of dislocations in the order of 10^{12} cm^{-2} is produced [36]. Thus, the transformation of the alloy is promoted as a forming hydride phase may not coherently precipitate in a perfect lattice due to the large elastic energy associated with precipitation and the comparably small enthalpy of formation for hydrides [37].

A number of hydride materials that could be synthesized under severe conditions or in a complicated process only, have been made accessible by the mechanical alloying of the constituting elements. One of the first examples was $LaNi_5$, which is hard to obtain with a high purity in a melting process because La and Ni possess different melting vapour pressures. The cooling process has to be controlled carefully to avoid a peritectic reaction and to obtain the product with the right composition. At the same time, the product can be produced easily by ball milling [38]. In most cases, nanocomposites produced by ball milling exhibit better hydrogenation kinetics and reversible capacities for hydrogen than the same material produced by sintering. An example is the activation temperature reduced by 100–150 K of Mg_2FeH_6 which was produced by ball milling the immiscible metals Fe and Mg and subsequent hydrogenation [39].

Milling under a hydrogen atmosphere at elevated pressures is another method for the synthesis of ternary hydrides. The hydride phase forming during the process is more brittle than the raw materials and facilitates the milling process. A number of complex and interstitial hydrides have been produced in this way, for example Mg_2FeH_6 [40], Mg_2NiH_4 [41], $TiFeH_x$ [42] and $Zr_{1-\delta}NiH_x$ [43]. To circumvent pressurizing the milling vial with hydrogen, mixtures of a brittle metal hydride and a metal can be milled to produce ternary compounds, as was shown by Huot et al. [44]. Synthesis of alkali metal and strontium alanates (i.e. complex aluminium hydrides, see below) is feasible using the principle according to Dymova et al. [45,46]. Adding a Ti-based dopant, such as $Ti(OBu)_4$ [47], enhances the hydrogen exchange kinetics of the material produced.

Hence, mechanical alloying also provides the opportunity to form nanocomposites consisting of hydrogen carrier materials and suitable dopants, leading to reduced kinetic barriers associated with hydrogen chemisorption and/or phase transformation. This is advantageous for practical use, as in some important cases, e.g. in automotive applications, short refuelling times are needed which can only be achieved when using such a nanocomposite.

Meanwhile, carrier materials consisting of light main group metals have moved into the focus of research because they offer high gravimetric storage densities for hydrogen. An overview of nanocomposites based on magnesium hydride, complex hydrides and combined systems will be given in the following sections.

6.1 Magnesium Hydride

Magnesium is of interest to hydrogen storage applications because of its low costs and high content of 7.6 wt% hydrogen. However, hydrogenation of untreated Mg is very slow and numerous attempts have been made to both increase the hydrogenation rate and decrease the desorption temperature of 573 K. This high temperature is largely due to the high enthalpy of formation of −76 kJ/mol. On the other hand, these properties make magnesium hydride a favourable material for, for example, thermal and solar-thermal applications.

The absorption and desorption kinetics may be enhanced considerably by simple ball milling of pure MgH_2, and dehydrogenation curves of both unmilled and milled samples exhibit a sigmoidal shape which suggests that a nucleation and growth process governs the transformation rate. The effect of milling was explained qualitatively by an increasing influence of grain boundaries and enhanced diffusion of hydrogen.

Further to improve the H exchange kinetics, composite materials were prepared by ball milling of Mg with a series of transition metals either absorbing hydrogen (e.g. V, Nb, Pd, Pt [48,49]) or not (e.g. Ni, Fe, Cu, Co [50,51]). V, Nb and Pd do not alloy with Mg and small hydrogenated particles in the composite are supposed to act as gateways for the hydrogen to the magnesium matrix. For V- and Nb-doped nanocomposites, the dehydrogenation rate at temperatures below 573 K again was found to be limited by nucleation and two-dimensional growth. At higher temperatures, the reaction is interface-controlled, with a two-dimensional growth of the forming Mg phase [52]. The role of the transition metals has not been settled yet, but the formation of hydrides was observed in the case of TiH_x and VH_x which may act as hydrogen donors [53].

Metal oxides may have a strong catalytic effect, even in small amounts, as was found for the oxides of Ti, V, Cr, Mn, Fe and Mo [53,54]. Oelerich et al. [54] reported that Cr_2O_3 yields the fastest hydrogen absorption, whereas V_2O_5 and Fe_3O_4 cause the most rapid desorption of hydrogen. The best metal oxides allow for hydrogen absorption at room temperature (p = 8.4 bar) and desorption at 200°C (under a vacuum) within a few minutes.

6.2 Complex Hydrides

In the 1940s, it was found that aluminium hydride (alane, AlH_3) is able to bind a hydride ion (H^-) and forms a stable tetrahydroaluminate complex or 'alanate' ion, $[AlH_4]^-$, with a tetrahedral structure [55]. Alanates are therefore ternary, salt-like compounds and belong to the so-called 'complex hydrides' like the boranates $[BH_4]^-$ and amides $[NH_2]^-$. Another stable form of an Al–H complex also exists, $[AlH_6]^{3-}$, the structure of which is similar to that of the cryolite anion which has

an octahedral configuration. The Al–H bond can be described as covalent with a strong ionic character [56]; the bond to the cation is ionic. Negatively charged hydrogen atoms are the reason for the reduction power and the high chemical reactivity of alanates with protons, e.g. in water.

The directed covalent bonding of the hydrogen in the complex ion leads to differences in the transformation behaviour of alanates (and other complex hydrides) and interstitial metal hydrides. In the case of the 'classical' interstitial metal hydrides, the H atoms are incorporated in tetrahedral and octahedral interstices of a metallic host lattice. When a metal lattice is loaded with hydrogen, the lattice expands, the electron from the H atom is transferred to the conducting band and a hydride phase precipitates from a saturated solid solution. Most hydriding metals and alloys therefore remain metallic upon hydrogenation. On the other hand, the reversible hydrogenation reaction with the alanates is a solid-state reaction between metallic aluminium, a binary metal hydride and H_2, thus forming the alanate salt. Another principal difference is the hydrogen mobility which remains high for the interstitial hydrides. Due to the covalent bond, hydrogen exchange is slower in the case of alanates. However, recent nuclear magnetic resonance (NMR) and inelastic spectroscopy studies revealed a considerable increase of H mobility when the material is doped with a catalyst [57,58].

Cycling experiments with hydrogenation and dehydrogenation steps were not attempted with the pure material, because the direct synthesis of $NaAlH_4$ from the elements [59] or from NaH and Al in a solvent [60] is possible at high pressures and temperatures only and takes a long time. From the thermodynamic point of view, however, such harsh conditions are not necessary, as the equilibrium pressure of the first decomposition step of $NaAlH_4$ is 1 bar hydrogen at around room temperature [59,61]. Obviously, hydrogen exchange with the pure substance is kinetically inhibited and operating conditions closer to the thermodynamic values are supposed to be possible if the kinetic barriers can be lowered. This was first realized by Bogdanovic and Schwickardi [62], who were able to lower considerably the operating temperatures and pressures of the reverse reactions of the sodium alanate system by using transition metal catalysts, Ti in particular, which were added to the alanate first by wet impregnation.

The pure, macrocrystalline $NaAlH_4$ melts at 186°C. Then, the melt starts to decompose and release H_2 at around 240°C, forming the hexahydride Na_3AlH_6 and elemental Al as solid decomposition products. Pure Na_3AlH_6 decomposes at temperatures above 300°C and releases H_2, such that a mixture of two solid phases, NaH and Al, is obtained [59] (see Eqs (6.1) and (6.2)). The third step is the decomposition of NaH, which occurs at temperatures above 450°C; this is considered too high for practical applications. The maximum reversible storage capacity for hydrogen therefore is 5.5 wt% H:

$$3NaAlH_4 \rightleftharpoons Na_3AlH_6 + 2Al + 3H_2 \quad (+\Delta H = 37\ \text{kJ/mol}\ H_2;\ 3.7\ \text{wt\% H}) \tag{6.1}$$

$$Na_3AlH_6 \rightleftharpoons 3NaH + Al + 3/2H_2 \quad (+\Delta H = 47\ \text{kJ/mol}\ H_2;\ 1.8\ \text{wt\% H}) \tag{6.2}$$

Equilibrium pressures of 1 bar H_2 of catalysed and non-catalysed material are reached at 33°C for step (6.1) and at 110°C for step (6.2) [59,61].

When the pure material is ball milled, desorption already starts below the melting point of $NaAlH_4$, which is probably due to the lowering of kinetic barriers [63]. Although milling leads to such a pronounced effect, it is not yet clear whether this effect is the result of an increasing influence of interfaces and grain boundaries, or introduced defects or a combination of reasons.

As was shown in a number of studies, about 4.5 wt% H are reversible under practical conditions when an appropriate dopant is added that lowers the kinetic barriers for the transformation of the material. Bogdanovic and Schwickardi [62] studied a number of transition and rare-earth metal catalyst precursors (Ti, Zr, V, Fe, Ni, Nb, Y, La, Ce, Pr, Nd, Sm) for this purpose and found that Ti precursors had the best catalytic properties. The doping method used in these studies was a standard wet impregnation procedure based on a solution or a slurry. Later, it was shown that dry or liquid precursors can be added directly to the alanate and, upon ball milling, a nanocomposite forms with superior kinetic properties [64]. Of the dopants available, addition of 2 mol% $TiCl_3$ to the $NaAlH_4$ has been considered a good compromise between the catalytic activity and the loss of storage capacity due to the storage-inactive Ti and other by-products from the reduction of the precursor in the ball mill [65] according to the following equation:

$$TiCl_3 + 3NaAlH_4 \rightarrow Ti + 3Al + 3NaCl + 6H_2 \tag{6.3}$$

To avoid or reduce the amount of inactive material, several attempts have been made, e.g. by using $TiAl_3$ as dopant [66], which might be an active component in the system, or Ti powder [67], which was added to $NaAlH_4$ and ball milled for 5 hours under hydrogen atmosphere. In both cases, however, the kinetics may be considered insufficient for fast recharging and considerably more Ti would be needed for reaction rates comparable to those of a $TiCl_3$-doped material.

Several efforts have been taken in the meantime further to accelerate the hydrogen exchange reaction. An interesting synergetic effect of co-dopants was described recently by Wang et al. [68]. It was reported that Fe (which has only poor catalytic properties, if used alone) is able to enhance the catalytic activity of Ti when one-third of the amount of Ti is added.

The system currently with the best performance is based on a solvent-stabilized Ti cluster, Ti_{13}·6THF [69,70] or Sc and Ce halides [71]. $ScCl_3$ was found to be highly efficient with respect to both storage capacity and kinetics: $NaAlH_4$ ball milled with 2 mol% of $ScCl_3$ exhibited a nearly theoretical hydrogen storage capacity (4.5–4.9 wt%; expected 5.0 wt%) which persisted throughout a test of seven cycles. Moreover, the improvement of storage properties was found to be much more pronounced under low-pressure rehydrogenation conditions, which is of particular importance to practical applications.

6.2.1 State of the dopant

Ti was identified to be the most active element for doping in many studies. However, little is known about its state and function in the material. The by-product

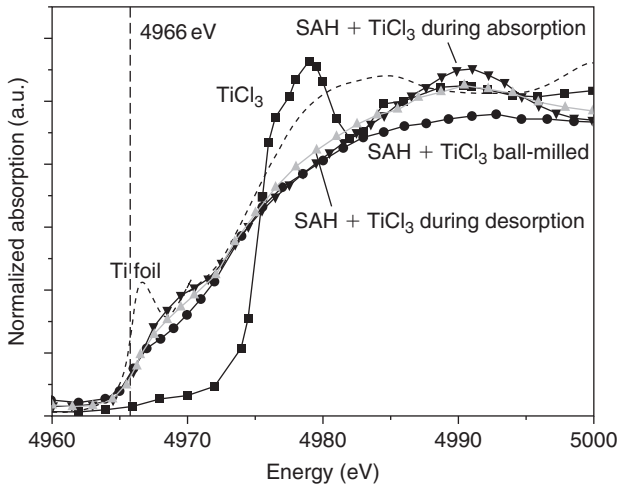

FIGURE 6.8 Normalized Ti K-edge XANES spectra of $NaAlH_4$ doped with 2 mol% of $TiCl_3$ in different stages. Spectra of pure Ti metal and $TiCl_3$ are shown for comparison.

NaCl of Eq. (6.3) was detected in XRD measurements and it was concluded that Ti is reduced upon ball milling with the alanate [71,72]. Recently, X-ray absorption near-edge structure (XANES) and extended X-ray absorption fine structure (EXAFS) studies [73,74] confirmed this assumption and provided more insight into the chemical state of Ti and its next neighbours during the doping and cycling procedure. Figure 6.8 shows the K absorption edge of Ti for five different samples: Ti foil, $TiCl_3$, and doped alanate samples in the early stage of the cycling process, one freshly prepared by ball milling, one partly desorbed and one partly reabsorbed. The dashed line is at the position of the absorption edge of metallic Ti and it can be concluded from these data that Ti^{3+} is indeed reduced to Ti^0 when $TiCl_3$ is ball milled with the alanate. Behind the edge, at around 4970 eV, there are low-energy features caused by changes in the electronic band structure, which can be attributed to an ordering inside particles or to particle size effects. The changes in this region suggest that there is a growth or ordering of Ti particles from the ball milled to the partly desorbed to the partly reabsorbed state. This is supported by an increasing EXAFS amplitude and an increasing number of Ti next neighbours. After the first absorption, the next neighbour distances of Ti were found to be 0.283 nm and 0.299 nm, which may be explained by a strongly distorted *hcp* structure of Ti metal particles.

Samples that have been treated extensively by ball milling [73] or samples that have been cycled several times exhibit features in the XANES spectra that may be explained by the formation of small entities of $TiAl_3$ phase (13–35 atoms), which have a distorted structure [75]. The formation of $TiAl_3$ is thermodynamically favoured by an enthalpy of formation of -136 kJ/mol. A $TiAl_3$ phase was also detected by XRD in dehydrogenated material [66]. As no intermetallic phase was found in the initial phase, where the sample exhibits the fastest kinetics,

however, it does not seem likely that $TiAl_3$ plays a direct and decisive role in the rate-limiting step of the transformation of the alanate [76].

6.2.2 Transformation mechanism of alanates

Several attempts have been made to clarify the role in catalysis and the potential mechanistic influence of Ti. DFT calculations of Ti-enhanced $NaAlH_4$ indicated [77] that there is a certain preference for Ti to replace Al and stay at Al sites in the outer layers of an alanate host lattice where it is able to increase the mobility of hydrogen species. Another theoretical study found that a particular local arrangement around Ti atoms may be important to the rehydrogenation reaction and that the diffusion of hydride species on the Al–metallic phase and the formation of mobile alane species might play a role in the synthesis of the next products in the rehydrogenation reaction [78]. Recently, experimental evidence was found in inelastic neutron scattering experiments for the formation of AlH_3 as an intermediate species [79]. Furthermore, it was shown in kinetic isotope experiments that both absorption and desorption are slower when deuterium is ab- or desorbed instead of hydrogen. The results indicate that a species heavier than H is responsible for the mass transport [80]. This means that the transformation of the material during hydrogen uptake and release probably is a transport reaction with an aluminium hydride species as the transport agent. In such a case, the Ti plays multiple roles in the process and the overall transformation reaction may be regarded a consecutive reaction of fast and slow, rate-determining steps. The latter are governed by nucleation and growth processes.

Nucleation and growth: Kinetic studies of the different absorption and desorption steps have revealed that the transformation kinetics follow a sigmoidal behaviour [69,81]. The absorption steps can be fitted well by a nucleation and growth model according to the Johnson–Mehl–Avrami theory. The Avrami coefficient of the first step was 0.8, which indicates that transport in the solid is the rate-determining process. This means that diffusion of the solid constituents NaH and Al or an interface process limits the reaction rate when the hexahydride phase is formed during absorption. Kinetic measurements mainly reflect the influence of the dopant on the rate-determining, i.e. slowest, step. It can therefore be concluded that Ti must have an accelerating influence on the materials transport, too.

6.3 Other Complex Hydrides

Other complex hydrides based on boron and nitrogen as complex centres (boranates and amides, respectively) have even higher gravimetric hydrogen contents of up to 18.4 wt% ($LiBH_4$). Some of them show reversible hydrogen storage properties.

Most of the boranates exhibit a high thermodynamic stability due to the strong B−H bond, and the working temperatures and pressures achieved in dehydrogenation/hydrogenation experiments are too high for current PEM fuel cell applications [81,82]. Some compounds, such as $Mg(BH_4)_2$ or $Ce(BH_4)_3$, show promising thermodynamic stabilities, but reversibility has not been demonstrated up to now [83,84]. It is known from early works on boranates that volatile

boranes may develop upon the decomposition of certain compounds. The gases are toxic and may poison the catalytic membranes of the fuel cell. Future work in this field will therefore be aimed at finding ways of destabilizing the complex hydride and avoiding the production of boranes.

In the search for other systems for hydrogen storage, Chen et al. [85] presented their work on the reversible hydrogenation behaviour of lithium nitride which transforms in a stepwise manner similar to the alanates:

$$Li_3N + 2H_2 \rightleftharpoons Li_2NH + LiH + H_2 \rightleftharpoons LiNH_2 + 2LiH \tag{6.4}$$

The amount of H_2 absorbed by Li_3N is 10.4 wt% in this reaction, which is a very high value. However, the overall heat of reaction is −161 kJ/mol and operation temperatures above 520 K were reported, which is a daunting value for low-temperature fuel cell applications. Nonetheless, successive activities have led to an interesting and promising new approach, as will be shown in the next chapter.

6.4 Reaction Systems

Shortly after the work of Chen et al. [85], other groups presented their work on amide systems [86,87]. Ichikawa et al. [88] pointed out that the enthalpy change of the second reaction of Eq. (6.4) is −44.5 kJ/mol only, which is almost ideal from the thermodynamic point of view because the free enthalpy of reaction is close to zero at room temperature. To perform the reaction, they produced composite materials containing $LiNH_2$ and LiH by ball milling and investigated the hydrogenation/dehydrogenation behaviour according to Eq. (6.5), with a theoretical amount of 6.5 wt% H being involved.

$$Li_2NH + LiH + H_2 \rightleftharpoons LiNH_2 + 2LiH \tag{6.5}$$

Compared to the binary and interstitial hydrides and the alanates, reactions of the type of Eq. (6.5) open up a new field in the development of hydrogen storage materials. The systems may be considered solid-state reactions of binary (or interstitial) metal hydrides with complex metal hydrides under the exchange of hydrogen.

Another interesting boranate-based combination is the $LiBH_4/MgH_2$ system. The reaction between the two hydrides proceeds as follows:

$$2LiBH_4 + MgH_2 \rightleftharpoons 2LiH + MgB_2 + 4H_2 \tag{6.6}$$

The gravimetric density is 11.5 wt% hydrogen of the reaction, the calculated enthalpy is 45.8 kJ/mol-H_2 and T(1 bar) = 168°C. Combining $LiBH_4$ with MgH_2 may decrease T(1 bar) by 240°C. As T(1 bar) for pure MgH_2 is ≈280°C, the T(1 bar) indicates that both $LiBH_4$ and MgH_2 are destabilized by incorporation in this combined system [89].

In spite of their additional degree of complexity, the reaction systems offer additional opportunities to design a storage system. In principle, many

combinations of binary and complex hydrides are conceivable, so that an optimization can be made with respect to the exchangeable amount of hydrogen and the thermodynamics, i.e. reaction enthalpy and reaction entropy. Even compounds with originally unfavourable thermodynamic properties for low-temperature fuel cell applications, such as MgH_2, may be considered for use again when combined with an appropriate reaction partner. An example was presented by Luo [90], where a nanocomposite was prepared by high-energy ball milling of a MgH_2:$LiNH_2$ mixture at a molar ratio of 1.1:2. The reversible behaviour of the material was tested at temperatures between 473 K and 573 K and 6–6.5 wt% H were gained upon absorption and desorption. At 473 K, hydrogen absorption took place at 3.2 MPa hydrogen pressure. Leng et al. [91] investigated a composite material produced by ball milling of a 3:8 molar mixture of $Mg(NH_2)_2$ and LiH under a 1 MPa H_2 atmosphere. The results showed that a large amount of hydrogen (approx. 7 wt%) started to be desorbed at 413 K and desorption peaked at 463 K. Hydrogenation was achieved, for example at 473 K and 3 MPa H_2 pressure. As in the case of boranate systems, unwanted by-products may also be formed when using amides. It was shown by several studies that desorption of hydrogen is accompanied by the emission of ammonia, which may be toxic for the catalyst of the fuel cell.

The challenges associated with this new type of system are the number of solid phases that are involved in the transformations. At lower working temperatures, severe kinetic barriers may interfere with the phase transformations and, hence, with H exchange. In any case, a transport in the solid and an interface reaction are necessary and means such as

- shortening the diffusion path,
- enhancing the mobility, e.g. by introducing defects, and
- an intimate contact along the reactive phase boundaries

may be considered prerequisites for a properly and fast working system. All these requirements are influenced by the particle size and structure of the grain boundaries.

Accordingly, a nanotechnological approach is deemed advantageous for the development of this promising new type of system.

In the last section, an overview will be given of experimental methods for materials synthesis and investigation of the most important properties of hydrogen storage materials.

7. EXPERIMENTAL ASPECTS

7.1 Materials Handling

A principal recommendation for working with hydrogen storage materials is to handle them under inert gas atmosphere and to prevent any contact with air and moisture. This is of particular importance to the nanoscale powders produced in the doping procedure of the hydrides. Nanoscale metal hydrides are oxidized

easily when in contact with oxygen and water and catalytically active nanoscale metal dopants may be destroyed or degraded in efficiency. Physisorption materials may incorporate heavier gases which can block adsorption sites in the material or lead to erroneous results when hydrogen storage properties are being investigated using gravimetric methods. Hence, for sample preparation and handling under inert conditions, argon-filled glove boxes with recirculation systems and the use of clean hydrogen, noble gases or nitrogen for cycling experiments are indispensable.

7.2 Synthesis Methods

Wet chemical synthesis and reconditioning of the product can be carried out by the so-called Schlenk technique, where a vacuum line (10^{-3} mbar) and a feed line with purified nitrogen are used for evacuating and inertizing the Schlenk glassware, which is equipped with plugs and stop cocks. Almost every chemical operation, from heating under reflux to filtering and evaporation, extraction and drying, can be carried out under inert conditions by using this technique.

Mechanical synthesis is performed by ball milling in a high-energy ball mill. To obtain inert conditions, the milling vials must be sealed properly under argon atmosphere in a glove box; otherwise, they are evacuated and subsequently pressurized by hydrogen, nitrogen, argon or a reactive gas. As the transformation properties of metal hydrides may be sensitive to transition metal dopants, it is recommended to use milling vials and balls made of catalytically inert and hard silicon nitride or tungsten carbide instead of using stainless or hardened steel. The ball mill may be put up in an argon-filled glove box to ensure inert operation conditions.

Milling under argon atmosphere is used for a wide range of applications and nanocomposites for hydrogen storage have been prepared from:

- different metals (to form a hydrogen-absorbing alloy);
- a metal hydride and a dopant (to alter the kinetic properties of the hydride);
- a metal and a metal hydride (to synthesize complex hydride after subsequent hydrogen absorption).

Ball milling of a hydrogen-absorbing metal under elevated hydrogen pressure leads to the formation of brittle hydride which can facilitate the milling process. Ball milling with other reactive gases, such as NH_3, has been used to synthesize hydrogen storage compounds and composite materials.

7.3 Characterization of Hydrogen Storage Materials

Table 6.1 summarizes the most important parameters which characterize a hydrogen storage material and methods for their determination. Above all, the hydrogen content, the absorption/desorption kinetics of the hydrogen at a given temperature and the corresponding equilibrium pressure are important to an application.

For a description of the common analytical methods based on spectrometry and diffraction, the reader is referred to the appropriate textbooks. As the core parameters of the storage materials are often investigated by the volumetric

Table 6.1 Parameters of hydrogen storage materials and their determination

Parameter	Investigation method
Hydrogen content	Volumetry (Sieverts apparatus) TGA Electrochemical methods
Decomposition temperature	Volumetry TDS TGA DSC
Equilibrium pressure/temperature	Volumetry HP-DSC
Thermodynamic parameters	Volumetry (Van't Hoff method for determining enthalpies and entropies) HP-DSC
Hydrogen exchange kinetics	Volumetry with kinetic reactor for isothermal and non-isothermal measurements DSC or TGA using different heating ramps
Specific surface area	BET method
Crystal structure/long-range order	Single crystal and powder X-ray and neutron diffraction
Molecular environment	Infrared and Raman spectroscopy
Local order	X-ray absorption spectrometry (XANES, EXAFS) Inelastic neutron scattering

TDS = Thermal desorption spectrometry; TGA = Thermogravimetric analysis; (HP-) DSC = (High-pressure) differential scanning calorimetry; XANES = X-ray absorption near-edge structure; EXAFS = Extended X-ray absorption fine structure.

method in a Sieverts apparatus (see Table 6.1), this method, which is among the most important ones in this field and not so commonly used elsewhere, will be introduced below.

7.3.1 Volumetry

A Sieverts-type apparatus can be described as a flow apparatus with calibrated working volumes, which is used to determine the number of hydrogen molecules absorbed by or desorbed from a sample material that is kept at a certain temperature in a reactor. For this purpose, the pressure drop or rise is measured in the

apparatus and the number of molecules is calculated using the Van der Waals equation:

$$p(V) = \frac{n \cdot R \cdot T}{V - n \cdot b} - a \cdot \frac{n^2}{V^2} \tag{6.7}$$

where p is the gas pressure, V the volume, R the gas constant, T the temperature in K, n the number of moles, a the repulsion factor and b the volume occupied by the hydrogen molecules.

Thermodynamic properties The equilibrium pressure, p_{eq}, of a hydride system is related to the changes ΔH and ΔS in enthalpy and entropy as a function of temperature. The relationship can be described by the Van't Hoff equation:

$$\ln\left(\frac{p_{eq}}{p_{eq}^0}\right) = \frac{\Delta H}{R \cdot T} - \frac{\Delta S}{R} \tag{6.8}$$

For the construction of a Van't Hoff plot (right diagram in Figure 6.9), pressure–composition isotherms (left diagram in Figure 6.9) are determined first in a Sieverts-type apparatus. The pressure is increased stepwise (absorption) or decreased (desorption) and the pressure value is taken when pressure equilibrium is reached.

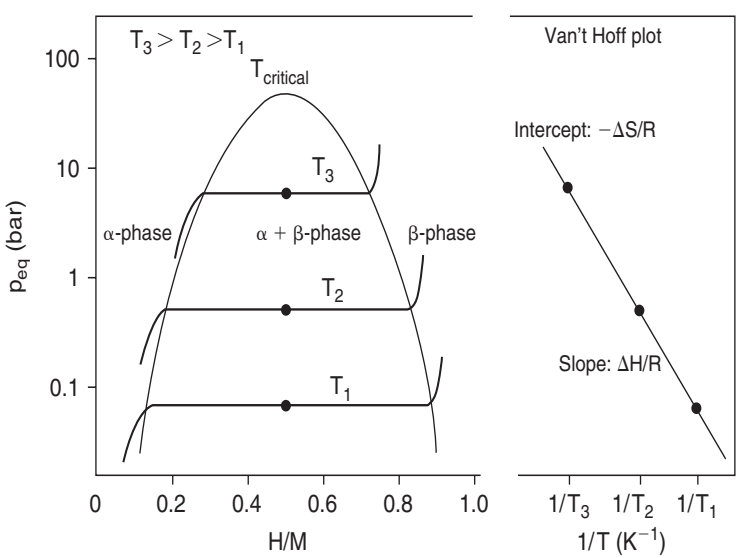

FIGURE 6.9 Pressure–composition isotherms for hydrogen absorption in a typical hydrogen-absorbing metal or alloy (left). The coexistence region of the α- and β-phases is characterized by flat plateaux and ends at the critical temperature. The pressures at H/M = 0.5 are used for the construction of the Van't Hoff plot. The enthalpy and entropy of the hydrogenation reaction can be obtained from the slope and the intercept of the plot.

At low concentrations of hydrogen, the composition/pressure relationship in the α-phase is ideal and obeys Sieverts' law

$$H/M = K_s \cdot p_{eq}^{1/2} \tag{6.9}$$

where H/M is the hydrogen to metal ratio, K_s is Sieverts' constant and p_{eq} is the equilibrium hydrogen pressure. As the hydrogen content in the metal increases, the hydrogen atoms interact via the elastic strains introduced in the metal lattice and the pressure/composition behaviour departs from ideality. This is reflected by a decrease in the slope of the isotherm. Once the material is saturated by hydrogen, the hydride phase starts to precipitate. When a solid solution of hydrogen in the metal or alloy (α-phase) and hydride phases coexist, there is a plateau in the isotherms. The reversible capacity is conservatively defined as the plateau width which may be far below the maximum capacity.

In the pure β-phase, the hydrogen pressure again rises steeply with the concentration. The two-phase region ends at a critical point, above which the transition from the α- to β-phase is continuous. In general, the plateau pressure for hydrogen loading is different from that for unloading. This pressure difference is called hysteresis and, although models have been proposed to explain the effect, further research is needed fully to understand it.

Kinetic properties The kinetics is normally changing heavily when the grain size of a hydrogen-absorbing material is reduced down to the nanoscale. Hence, kinetic data can be used to learn about the influence of reduced diffusion lengths, increasing fraction of grain boundaries or other factors and, thus, obtain a mechanistic insight into the materials transformation.

The volumetric method may also be applied for determining kinetic parameters, such as hydrogenation/dehydrogenation rates, and activation energies of a phase transformation. In principle, the same experimental procedure is used as described above. The main difference is that the focus now is on the temporal behaviour of the pressure in the apparatus. Moreover, care must be taken in an isothermal experiment to avoid kinetic contributions from poor thermal conduction or enthalpy effects in the sample. The powder material either must be spread as a thin layer with good thermal contact to the heat-transferring reactor wall [81] and/or the sample has to be mixed with an inert material with good heat conduction, copper for example.

In principle, several methods exist for determining the kinetics of a hydride transformation (e.g. [92,93] and references therein). It is possible either to conduct an isothermal experiment by suddenly changing the thermal status of the sample and detecting the pressure change with time or by using different temperature ramps for heating up and decomposing the sample. Generally, the transformation of metal hydrides can be described by a reaction rate df/dt, which depends on the temperature T and the reacted fraction f as follows:

$$\frac{df}{dt} = y(f) \cdot k(T) \tag{6.10}$$

The temperature dependence is generally assumed to follow an Arrhenius law:

$$k = k_0 \cdot \exp\left(-\frac{E_A}{RT}\right) \tag{6.11}$$

where E_A is an activation barrier, R the gas constant and k_0 a constant pre-exponential factor. In an ideal isothermal experiment, $k(T)$ is a constant and the function $y(f)$ can be determined easily. E_A can be determined in a straightforward manner by measuring k at different temperatures.

In the case of a sigmoidal behaviour of $f(t)$, a fitting procedure can be applied according to the Johnson–Mehl–Avrami (JMA) equation:

$$f = 1 - \exp\{-(kt)^{\eta}\} \tag{6.12}$$

The equation describes the reacted fraction f when the rate-limiting process for the formation of the new phase is nucleation and growth. According to Rudman [94], small exponents η between 0.5 and 1.5 denote a diffusion-limited growth process of the new phase. When a constant number of nuclei is assumed, the exponent η is equal to 0.5, 1 and 1.5 for one-, two- and three-dimensional diffusion-limited growth, respectively. Growth is then driven by the concentration gradients of the atomic species involved at the grain boundaries. The growth rate itself is limited by the specimen with the slowest diffusion.

For $E_A >> RT$, which is fulfilled for most solid-state reactions, a simple relation between the heating rate $\beta = \mathrm{d}T/\mathrm{d}t$ and T_0 (for a constant reacted fraction) can be applied:

$$\ln\left(\frac{\beta}{T_0^2}\right) = -\frac{E_A}{RT_0} + C \tag{6.13}$$

from which the activation energy E_A can be determined. This method is known as the Kissinger–Akahira–Sunose (KAS) method [95]. It belongs to the so-called isoconversion (i.e. analysis at constant reacted fraction f_0) methods. As an alternative, a certain stage of reaction may be defined at the maximum rate $\mathrm{d}f/\mathrm{d}t$ of the reacted fraction per unit time. Eq. (6.13) then changes to:

$$\ln\left(\frac{\beta}{T_{max}^2}\right) = -\frac{E_A}{RT_{max}} + C \tag{6.14}$$

where T_{max} denotes the temperature at the maximum reaction rate. This method, known as the Kissinger method [96,97], in most cases yields a good approximation of Eq. (6.14). Other instrumental techniques, such as HP-DSC and TGA-MS, can be used for temperature ramp experiments, too.

References

1. Nanoscale Science, Engineering and Technology in the Department of Energy: Research Directions and Nanoscale Research Centers, US-Department of Energy, Office of Science (2004), http://www.sc.doe.gov.

2. Dunn S. Int. J. Hydrogen Energy 2002; 27:235–264.
3. Buchmann I (ed.). Batteries in a Portable World, 2nd edn. Cadex Electronics Inc, Richmond, CND. 2001.
4. Schlapbach L, Zuettel A. Nature 2001; 414:353.
5. Ritter JA, Ebner AD, Wang J, Zidan R. Mater. Today 2003; 6:9,18.
6. Switendick AC. Z. Phys. Chem. 1979; 117:89.
7. Weitkamp J, Fritz M, Ernst S. Int. J. Hydrogen Energy 1995; 20:967.
8. Kazansky VB, Borovkov VY, Serich A, Karge HG. Microporous Mesoporous Mater. 1998; 22:251.
9. Langmi HW, Walton A, Al-Mamouri MM. et al. J. Alloys Comp. 2003; 356–357:710.
10. Zecchina A, Bordiga S, Vitillo JG. et al. J. Am. Chem. Soc. 2005; 127:6361.
11. Chapman KW, Southon PD, Weeks CL, Kepert CJ. Chem. Comm. 2005;3322–3324.
12. Kaye SS, Long JR. J. Am. Chem. Soc. 2005; 127:6506–6507.
13. Zacharia R, Kim KY, Fazle Kibria AKM, Nahm KS. Chem. Phys. Lett. 2005; 412:369–375.
14. Nijkamp MG, Raaymakers JE, van Dillen AJ, de Jong KP. Appl. Phys. A 2001; 72:619.
15. Panella B, Hirscher M, Roth S. Carbon 2005; 43:2209–2214.
16. Chambers A, Park C, Baker RTK, Rodriguez NM. J. Phys. Chem. B 1998; 102:4253.
17. Hirscher M, Becher M. J. Nanosci. Nanotech. 2003; 1/2:1.
18. Schimmel HG, Kearley GJ, Nijkamp MG, Visser C, de Jong K, Mulder FM. Chem. Eur. J. 2003; 9:4764.
19. Zuettel A, Sudan P, Mauron Ph, Kiyobayashi T, Emmenegger Ch, Schlapbach L. Int. J. Hydrogen Energy 2002; 27:203.
20. Orimo S, Majer G, Fukunaga T, Züttel A, Schlapbach L, Fujii H. Appl. Phys. Lett. 1999; 75:3093.
21. Orimo S, Matsushima T, Fujii H, Fukunaga T, Majer G. J. Appl. Phys. 2001; 90:1545.
22. Hirscher M, Becher M. Haluska M et al. J. Alloys Comp. 2003; 356–357:433.
23. Hirscher M, Becher M. Haluska M et al. J. Alloys Comp. 2002; 330–332:654.
24. Lueking AD, Yang RT. Appl. Cat. A 2004; 256:259.
25. Lachawiec AJ Jr, Qi G, Yang RT. Langmuir 2005; 24:11418–11424.
26. Li Y, Yang RT. J. Am. Chem. Soc. Commun. 2006; 128:726–727.
27. Gogotsi Y, Dash RK, Yushin G, Yildirim T, Laudisio G, Fischer JE. J. Am. Chem. Soc. 2005; 127: 16006–16007.
28. Li H, Eddaoudi M, O'Keefe M, Yaghi OM. Nature 1999; 402:276–279.
29. Rowsell JLC, Yaghi OM. Angew. Chem. Int. Ed. 2005; 44:4670–4679.
30. Rowsell J, Millward AR, Park KS, Yaghi OM. J. Am. Chem. Soc. 2004; 126:5666.
31. Rosi NL, Eckert J, Eddaoudi M. et al. Science 2003; 300:1127.
32. Huebner O, Gloess A, Fichtner M, Klopper W. J. Phys. Chem. A 2004; 108:3019.
33. Zhao X, Xiao B, Fletcher AJ, Thomas KM, Bradshaw D, Rosseinsky MJ. Science 2004; 306:5698.
34. Weebar AW, Bakker H. Physica B 1988; 153:93.
35. Zaluski L, Hosatte S, Tessier P. et al. Z. Phys. Chem. 1994; 183:45.
36. Yamamoto T, Inui H, Yamaguchi M. Intermetallics 2001; 9:987.
37. Tanaka K, Okazaki S, Ichitsubo T. et al. Intermetallics 2000; 8:613.
38. Sakaguchi H, Sugioka T, Adachi G. Chem. Lett. 1995; 7:561.
39. Konstantchuk I, Yvanov E, Pezat M, Darriet B, Boldyrev V, Hagenmuller P. J. Less-Common Met. 1987; 131:181.
40. Huot J, Hayakawa H, Akiba E. J. Alloys Comp. 1997; 248:164.
41. Orimo S, Fuji H. J. Alloys Comp. 1996; 232:L16.
42. Chiang C, Chin Z, Perng T. J. Alloys Comp. 2000; 397:259.
43. Orimo S, Fuji H, Yoshino T. J. Alloys Comp. 2000; 217:287.
44. Huot J, Boily S, Akiba E, Schulz R. J. Alloys Comp. 1998; 280:306.
45. Dymova TN, Aleksandrov DP, Konoplev VN. Koord. Khim. 1994; 20(4):279.
46. Dymova TN, Konoplev VN, Sizareva AS. Dokl. Ross. Akad. Nauk. 1998; 359(2):200.
47. Bogdanovic B, Schwickardi M. Appl. Phys. A 2001; 72:221.
48. Liang G, Huot J, Boily S, Van Neste A, Schulz R. J. Alloys Comp. 1999; 291:295.
49. Gutfleisch O, Schlorke-de Boer N, Ismail N. et al. J. Alloys Comp. 2003; 356–357:598.
50. Bobet J-L, Pechev S, Chevalier B, Darriet B. J. Mater. Chem. 1999; 9:315.
51. Zeng K, Klassen T, Oelerich W, Bormann R. J. Alloys Comp. 1999; 283:213.
52. Liang G, Huot J, Boily S, Schulz R. J. Alloys Comp. 2000; 305:239.

53. Khrussanova M, Terzieva M, Pesdhev P, Konstanchuk I, Ivanov EY. Z. Phys. Chem. Neue Folge 1989; 164:1261.
54. Oelerich W, Klassen T, Bormann R. J. Alloys Comp. 2001; 315:237.
55. Finholt AE, Bond AC, Schlesinger HI. J. Amer. Chem. Soc. 1947; 69:1199.
56. Peles A, Alford JA, Ma Z, Yang L, Chou MY. Phys. Rev. B 2004; 70:165105.
57. Majer G, Stanik E, Valiente L, Grinberg F, Kircher O, Fichtner M. J. Alloys Comp. 2005; 404–406: 738–742.
58. Palumbo O, Cantelli R, Paolone A, Jensen CM, Srinivasan SS. J. Phys. Chem. B 2005; 109: 1168–1173.
59. Dymova TN, Dergachev YM, Sokolov VA, Grechnaya NA. Dokl. Akad. Nauk SSSR 1975; 224:556.
60. Clasen H. Angew. Chem. 1961; 73:322.
61. Bogdanovic B, Brand RA, Marjanovic A, Schwickardi M, Tölle J. J. Alloys Comp. 2000; 302:36.
62. Bogdanovic B, Schwickardi M. J. Alloys Comp. 1997; 253–254:1–9.
63. Zaluska A, Zaluski L, Ström-Olsen JO. J. Alloys Comp. 2000; 298:125.
64. Jensen CM, Zidan RA, Mariels N, Hee AG, Hagen C. Int. J. Hydrogen Energy 1999; 24:461.
65. Sandrock G, Gross K, Thomas G. J. Alloys Comp. 2002; 339:299.
66. Majzoub EH, Gross KJ. J. Alloys Comp. 2003; 356–357:363.
67. Wang P, Jensen CM. J. Alloys Comp. 2004; 379:99.
68. Wang J, Ebner AD, Zidan R, Ritter JA. J. Alloys Comp. 2005; 391:245.
69. Fichtner M, Fuhr O, Kircher O, Rothe HJ. Nanotechnology 2003; 14:778.
70. Bogdanovic B, Felderhoff M, Kaskel S, Pommerin A, Schlichte K, Schüth F. Adv. Mater. 2003; 15:1012.
71. Bogdanovic B, Felderhoff M, Pommerin A, Schüth F, Spielkamp N. Adv. Mater. 2006; 18: 1198–1201.
72. Sandrock G, Gross K, Thomas G, Jensen C, Meeker D, Takara S. J. Alloys Comp. 2002; 330–332:696.
73. Felderhoff M, Klementiev K, Grünert W. et al. J. Phys. Chem. Chem. Phys. 2004; 6:4369.
74. Léon A, Kircher O, Rothe J, Fichtner M. J. Phys. Chem. B 2004; 108:16372.
75. Léon A, Kircher O, Fichtner M, Rothe J, Schild D. J. Phys. Chem B 2006; 110:1192–1200.
76. Fichtner M, Canton P, Kircher O, Léon A. J. Alloys Comp. 2005; 404–406:732–737.
77. Lovvik OM, Opalka SM. Phys. Rev. B 2005; 71:54103.
78. Chaudhuri S, Muckerman JT. J. Phys. Chem. B 2005; 109:6952–6957.
79. Fu Q, Ramirez-Cuesta A, Tsang S. J. Phys. Chem. B 2006; 110:711–715.
80. Lohstroh W, Fichtner M. Phys. Rev. B. 2007; accepted.
81. Kircher O, Fichtner M. J. Appl. Phys. 2004; 95:7748.
82. Züttel A, Rentsch S, Fischer P. et al. J. Alloys Comp. 2005; 356–357:515.
83. Nakamori Y, Miwa K, Ninomiya A. et al. Phys. Rev. B 2006; 74:045126.
84. Chłopek K, Frommen Ch, Léon A, Zabara O, Fichtner M. J. Am. Chem. Soc. (submitted).
85. Chen P, Xiong Z, Luo J, Lin J, Tan KL. Nature 2002; 420:302.
86. Hu YH, Ruckenstein E. Ind. Eng. Chem. Res. 2003; 42:5135.
87. Nakamori Y, Orimo S. J. Alloys Comp. 2004; 370:271.
88. Ichikawa T, Hanada N, Isobe S, Leng H, Fujii H. J. Phys. Chem. B 2004; 108:7887.
89. Vajo JJ, Skeith SL, Mertens F. J. Phys. Chem. B 2005; 109:3719–3722.
90. Luo W. J. Alloys Comp. 2004; 381:284.
91. Leng H, Ichikawa T, Hino S, Hanada N, Isobe S, Fujii H. J. Phys. Chem. B 2004; 108:8763.
92. Sastri MVC. Metal Hydrides. Springer Verlag: Berlin, 1998.
93. Starnik MJ. Thermochim. Acta 2003; 404:163.
94. Rudman PS. J. Less Common Met. 1983; 89:93.
95. Akahira T, Sunose T . Transactions of Joint Convention of Four Electrical Institutes 1969.
96. Kissinger HEJ. Res. Nat. Bur. Stand. 1956; 57:217.
97. Kissinger HE. Anal. Chem. 1957; 29:1702.

CHAPTER 7

Materials with Structural Hierarchy and their Optical Applications

Chantal Paquet, Andrew Paton and Eugenia Kumacheva

1. INTRODUCTION

This chapter describes recent accomplishments in the conceptualization, design, synthesis and characterization of polymer–inorganic materials with structural hierarchy, with the focus on the optical applications of these materials. In particular, we concentrate on the materials produced by combining metal or semiconductor *nano*particles and polymer *micro*spheres, such as latexes or microgels, and the organization of these hybrid materials into further hierarchical levels. In the introduction (Section 1), we provide a brief review of materials with structural hierarchy. In Section 2, we discuss the properties of the constituent materials: inorganic nanoparticles and polymer microspheres. Section 3 describes the methods for the production of polymer–inorganic hybrid microspheres. The optical properties of these hybrid structures and their corresponding applications are discussed in Section 4.

1.1 Types of Structures with Hierarchy

Materials with structural hierarchy contain structural elements of several characteristic length scales, each with its own recognizable structure and properties [1]. Such materials attract great interest since they possess unique properties arising from the *coupling* of the properties of each structural element. Similarly to a bridge, which derives its strength and utility from the arrangement of small metal beams, the properties of a successful hierarchical structure exceed those of the component parts. Nature provides many examples of exceptional properties of

Department of Chemistry, University of Toronto, Toronto, Ontario M5S 3H6 Canada

Nanostructured Materials © 2009 Elsevier Ltd.
978-0-08-044965-4 All rights reserved.

hierarchically organized materials, such as the resilience of bone and the strength of nacre [2]. Man-made materials with structural hierarchy also show improvements in their mechanical properties. Of the most recognizable examples of man-made hierarchical structures are the Eiffel Tower and Eiffel's Gabarit viaduct [1].

Recently, new building blocks have been discovered for the fabrication of materials with hierarchical structures comprising characteristic length scales below one micrometre. Because of the size-dependent properties of these new building blocks, it is important to specify a length scale that describes these properties. Typically, four size regimes are used to describe a material's structure and explain its properties: *nano* (from one to tens of nanometres); *meso* (from tens to hundreds of nanometres); *micro* (from hundreds of nanometres to 100 microns); and *macro* (100 microns and above). This classification is somewhat arbitrary as no sharp boundary exists between the *nano* and *meso* or *meso* and *micro* length scales. Herein, nanoscopic building units are used as the smallest constituent blocks in the hierarchical structures, while the upper limit in the size of the building blocks is of a microscopic length scale.

1.2 Combining Micro-, Meso- and Nano- in One Material

Nanoscopic building blocks can be represented by metal, magnetic or semiconductor nanoparticles (NPs). These particles have size- and shape-dependent properties such as the luminescence of semiconductor nanocrystals (quantum dots) [3], superparamagnetic–ferromagnetic transitions in magnetic NPs [4] or the surface plasmon absorption properties of metal NPs [5]. Representing the mesoscale are metal nanoshells [6], semiconductor nanowires [7] or NPs engulfed by silica shells [8,9]. Mesostructured materials possess properties that are distinct from those of nano- and microscopic materials [10]. Microscopic particles can be represented by inorganic or polymeric micrometre-size beads. The distribution of sizes of these particles can be controlled with a high precision; therefore, they are often used in hierarchical systems as sacrificial templates for mesoparticle growth [6], as non-sacrificial templates for the growth of NPs [11,12] or as building blocks for the fabrication of macroscopic systems (e.g. colloidal crystalline arrays) [13,14].

Materials with structural hierarchy are obtained by bringing nano-, meso- and microparticles together and, when needed, assembling them in a particular, well-defined manner. Figure 7.1 shows several representative examples of materials described in the present chapter, which are obtained from nano- and microscopic building blocks. Figure 7.1a illustrates NPs with different compositions and shapes. Figure 7.1b shows polymeric particles – microgels (top) and latex microbeads (bottom) – with dimensions from approximately one hundred nanometres to one micron.

Hybrid systems obtained from NPs and polymer microspheres are displayed in Figure 7.1c. In addition to these examples, many others have been recorded in the literature. For example, metal nanorods can be loaded into polymer microgels [15,16] or semiconductor nanocrystals can be attached to or loaded into polymer microspheres [11,12,17–19]. Such materials have interesting and useful applications.

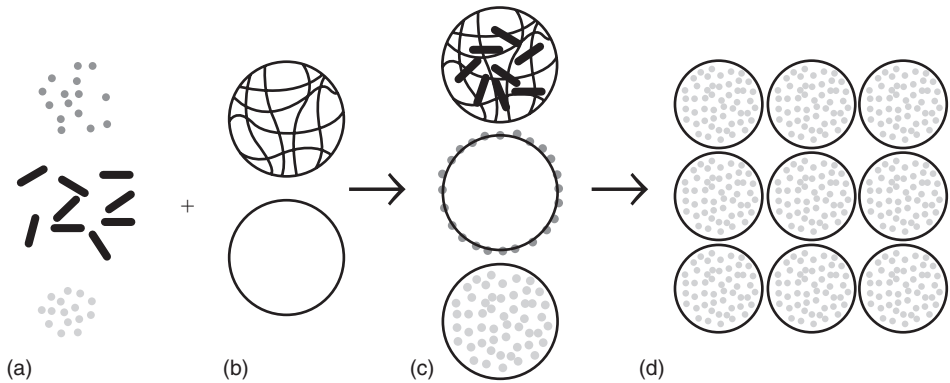

FIGURE 7.1 Strategies for the fabrication of materials with structural hierarchy described in this chapter. (a) Nanoparticles with varying compositions and shapes; (b) micrometre-size polymer particles (latexes and microgels); (c) representative combinations of nanoparticles and micrometre-size particles (polymer microspheres) in systems with structural hierarchy; (d) organization of hybrid particles in a macroscopic material with a more complex hierarchical structure.

Microgels loaded with gold nanorods show photothermally triggered volume transitions [15]. The bioconjugated microspheres loaded with quantum dots are used for simultaneous sensing of multiple target molecules or substances [17,18]. Gold NPs and nanoshells on the surface of dielectric microspheres possess tunable absorption spectra [20–22]. Polystyrene microspheres loaded with magnetic NPs form magnetically responsive colloidal crystal arrays [19].

More complicated hierarchical architectures are realized when hybrid particles, shown in Figure 7.1c, are used as the building blocks for the fabrication of macroscopic materials (Figure 7.1d). For example, photoswitchable microlens arrays were fabricated from microgel particles doped with gold NPs [23,24]. Polymer microspheres coated with metal or semiconductor NPs were organized into colloidal crystals in which the optical properties of the nanoparticles were coupled with the structure-dependent properties of colloid crystals [25,26].

2. PROPERTIES OF CONSTITUENT MATERIALS

In order to 'programme' the properties of materials with hierarchical structures, it is necessary to understand the properties of their building blocks. Below we review the optical properties of the constituent structural units for hierarchical materials. The synthesis of these building blocks is not discussed in detail, instead, the reader is later directed to reviews on the subject.

2.1 Inorganic Nanoparticles

2.1.1 Semiconductor nanocrystals

In semiconductors, the energy gap between the highest occupied band of energy levels (the valence band) and the lowest unoccupied band of energy levels (the conduction band) is of the order of that of the energy of light in or near the visible

spectral range. When an electron in a semiconductor is excited across the bandgap into the conduction band, it leaves behind an unoccupied state in the valence band known as a hole. The states occupied by the electron and its associated hole, collectively known as an exciton, by definition do not separate farther than the Bohr radius of the material. After some time, this electron returns to its initial state in the valence band through a process known as radiative recombination, thereby emitting the bandgap energy as light [27,28].

When the size of the semiconductor NP is smaller than the Bohr radius of the material, the energies of electronic states in the semiconductor are changed. Due to the wave nature of electrons, the energies become discretized and the density of states turns into a series of delta functions, i.e. the electrons can only possess distinct, well-defined energies. Thus, the excitation energy of the electrons is determined by the size of the NP: the energy stored and released as light by an exciton increases with the decreasing size of the particle [29]. There are many interband states caused by crystal defects on the surface of NPs which can reduce and quench luminescence through non-radiative recombination [30]. In addition, the ligands stabilizing the semiconductor NPs (quantum dots) and the solvents can cause quenching of the luminescence [31]. By covering the semiconductor nanocrystal with a contaminant-free layer (e.g. a thin semiconductor shell), these surface traps can be greatly reduced. By choosing a semiconductor that has a close lattice match to the core and a larger bandgap energy, surface defects and contaminants can be almost eliminated [31,32].

Typical materials that are used for the synthesis and fabrication of quantum dots (QDs) are II–VI and III–V semiconductors such as CdSe [33] and InP [34], as well as oxides (e.g. ZnO [35]) and sulphides (e.g. CdS [36] or ZnS [31]). Synthesis of semiconductor NPs includes pyrolytic [37], Stranski-Krastanow growth [38] and colloidal methods. Synthesis employing organometallic precursors [39] has become one of the main methods of the production of quantum dots, due to enhanced crystallinity, narrow size distribution and a reduced number of surface defects in the nanocrystals. Furthermore, there has been considerable effort on making this method less toxic, by the use of safer precursors and lower temperatures [40–42]. The selected stabilizing agents depend on the solvent used in the synthesis. Typical ligands include phosphine oxide-terminated alkanes for organic solvents, e.g. trioctylphosphine oxide [40], or mercapto-terminated alkyl acids for NPs stabilized in water, e.g. mercapto-undecanoic acid [43].

The interest in the optical properties of semiconductor QDs stems from their well-defined luminescence characteristics, which lead to potential applications of the NPs in materials with enhanced security [44], in LEDs and displays [45] and as fluorescence probe tags [46]. The main features of the fluorescence spectrum of semiconductor NPs are:

1. a narrow and a well-defined emission peak created by the excitonic transition;
2. a large effective Stokes shift [47] of the emission peak with respect to the absorption peak;
3. the dependence of the spectral range of luminescence on the size and type of nanocrystals.

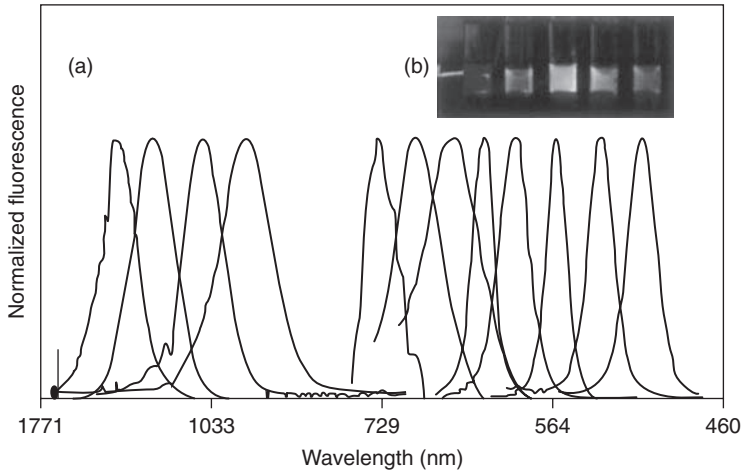

FIGURE 7.2 Dependence of the fluorescence of quantum dots on size and material. The series on the left is InAs, the middle is InP and the right is CdSe. The size of the quantum dots increases with increasing wavelength of peak fluorescence: the InAs (left) ranges from 2.8 to 6.0 nm, the InP (middle) from 3.0 to 4.6 nm and the CdSe (right) from 2.1 to 4.6 nm (all sizes increase from right to left). (Adapted, with permission, from [48]. Copyright 1998 American Association for the Advancement of Science.)

Since each semiconductor has a characteristic Bohr radius, a useful strategy for controlling fluorescence emission is to use different semiconductor materials. For example, CdSe NPs emit mainly in the visible spectrum [48], ZnO nanocrystals emit in the UV spectral range [35] and PbS quantum dots are being examined for use in the near-IR wavelength range [49]. The dependence of photoluminescence properties of QDs on the material and on the size of nanoparticles is illustrated in Figure 7.2.

2.1.2 Metal Nanoparticles

In metals, there is no bandgap over which the electrons can be excited; hence, there are many electrons in the conduction band, creating a sea of freely mobile electrons on the surface of the material. The optical properties of metal NPs stem not from the excitation of electrons into higher energy states as in semiconductor QDs, but from the collective oscillation of free electrons, known as surface plasmon. When the metal is irradiated, the electrons begin to oscillate at the frequency of the incident radiation (Figure 7.3) and, if the frequency of the incident radiation is close to the natural frequency, the energy is absorbed by the oscillator. The absorption spectra of metal NPs show a distinct peak centred on the natural frequency of the plasmon mode.

The surface plasmon resonance (SPR) frequency is governed by the density of the electrons and the effective mass of the electrons. Both properties are material-dependent (e.g. small gold NPs absorb in the green, while small silver NPs absorb in the ultraviolet spectral range) [51]. The spectral position of this peak is also

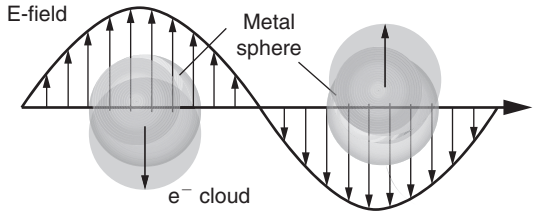

FIGURE 7.3 Schematic of the freely moveable electron cloud on the surface of metal NPs as it interacts with incident radiation. The surface plasmon (electron cloud) is forced into oscillation, creating electron-rich and electron-poor regions. (Reprinted with permission from [50]. Copyright 2003 American Chemical Society.)

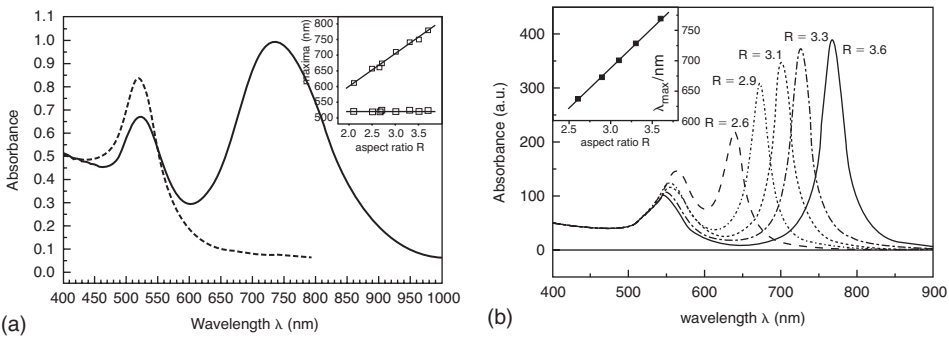

FIGURE 7.4 (a) The absorbance spectra of 22 nm-size gold NPs (dotted line) and gold nanorods with aspect ratio of 3.3 (solid line). The inset in (a) shows the dependence of the absorption peak of the longitudinal axis (circles) and the transverse axis (squares) on the aspect ratio of the NRs. (b) The effect of aspect ratio (R) of elongated gold ellipsoids on the absorption spectra. The peak on the right corresponds to the longitudinal plasmon oscillations, while the peak on the left corresponds to the transverse oscillations. The inset graph in (b) shows the linear dependence on the shift of the longitudinal absorption peak with aspect ratio. ((a) is reprinted, with permission, from the Annual Review of Physical Chemistry, Volume 54 ©2003 by Annual Reviews www.annualreviews.org. (b) is reprinted with permission from [54]. Copyright 1999 American Chemical Society.)

affected by the polarizability of the surrounding medium: the resonant wavelength of the surface plasmon red-shifts with increasing refractive index of the surrounding medium [50]. The dependence of the plasmon mode on the size of metal NPs is caused by the physical restriction of the oscillation of the electrons in small metal NPs; however, below diameters of 25 nm, the size of the NPs does not significantly affect the spectral position of the absorption peak [52]. Furthermore, surface plasmon resonance absorption is not observed for metallic NPs with dimensions smaller than 2 nm, due to predominating quantum effects [53]. Finally, the shape of NPs is a very important factor in determining their spectroscopic properties. The absorption spectra of small, spherical NPs feature a well-defined peak, due to their symmetry. For non-spherical NPs, as one of the axes increases in length, a second absorption peak appears, caused by oscillations along the longer axis (Figure 7.4) [51,54].

When the aspect ratio increases, the longitudinal absorption peak is red-shifted (Figure 7.4b). Other non-spherical shapes also alter the plasmon characteristics; metallic triangles [55], stars [56] and even 'nanorice' [22] have been studied. Generally, a sharp tip in the metallic nanostructure provides enhancement of the plasmon resonance absorption [57].

Nanoshells are another interesting group of metal nanostructures, which consist of a dielectric core coated with a thin metal layer. The plasmonic properties of nanoshells are determined by the relationship between the diameter of the dielectric core and the thickness of the metal shell [20,58]. When the ratio of the diameter of the core to the shell thickness increases, the SPR of the metal shifts towards the red end of the spectrum. This feature is explained by the existence of two interfaces of the metal nanoshell with the dielectric phases, which provide two surfaces that support plasmon modes. Due to the differing radii of these surfaces, the resonant modes of the surface plasmons possess different absorption peaks. A small separation of the surfaces allows hybridization of the plasmon modes, which results in the red-shift of the surface plasmon absorption peak for decreasing shell thicknesses [59].

The synthesis of metal NPs is described in several excellent reviews [4,60,61]. Both organic and aqueous solvents are used to produce metal NPs with tunable sizes [62–66].

2.2 Polymer Particles

Polymer particles with dimensions in the submicrometre size range have experienced revived interest in the materials science community. One of the reasons for such interest is the versatility of properties that can be readily tailored to the polymer microbeads. Polymer microbeads can be easily synthesized from a variety of materials and the surface charge of the particles can be readily tuned by functionalizing them during synthesis or by using post-synthesis modification. A number of techniques exist to date that yield particles with a predetermined size and a very narrow size distribution. Generally, polymer particles have spherical shapes; however, other 'non-conventional' shapes can be generated by thermodynamic and kinetic methods [67–69]. Using these methods, core-shell and multilayer particles can be readily produced. In macroscopic polymer-based materials, polymer microbeads introduce an additional length scale, determined by the particle diameter. Thus, polymer particles can be used as the building blocks of materials with periodic composition, structure and function.

Polymer particles in the size range from ca. 100 nm to 1 μm can be tentatively divided into latexes and microgels. Latex particles have a 'condensed' structure while microgels have an 'open' polymer network structure. This division is somewhat arbitrary: at appropriate values of pH and/or in appropriate solvents latex beads swell, transforming into microgel particles. An open structure of microgels leads to important application-related properties: the polymer network can sequester and release small molecules or nanoparticles or can change its volume in response to external stimuli, such as pH, temperature or ionic strength [70].

Polymer latexes and microgels are synthesized using emulsion, dispersion, precipitation, miniemulsion or suspension polymerizations [71]. These methods

produce particles with varying size distribution; however, the polydispersity of microbeads can be as low as 1–2%. Most polymerization schemes employ conventional free-radical polymerization; however, with the rapid development of miniemulsion polymerization, other synthetic routes have become readily available, e.g. living radical polymerization polycondensation or atom transfer radical polymerization (ATRP) [71].

Typically, most polymers used in the synthesis of latexes and microgels absorb light in the UV spectral range [72]. This property makes materials derived from polymer particles attractive for applications that require 'transparency' upon irradiation in the visible and near-IR spectral range. It should be noted, however, that synthesis of particles from polymers absorbing in the visible spectral range has been demonstrated. For example, polypyrrole, polyaniline and polyferrocene microbeads show several absorption peaks in the wavelength range from ca. 300 to 800 nm [73,74], a feature that can be employed in, for example, fabrication of photonic crystals.

Some of the materials used in the synthesis of polymer particles are fluorescent. For example, polystyrene shows weak autofluorescence. This feature can have potential applications but to be treated with caution, especially when polymer particles are loaded with fluorescent inorganic nanoparticles. In most cases, however, the optical response of latexes and microgels is induced by loading particles with photosensitizers (dye, semiconductor or metal nanoparticles).

3. FABRICATION OF HYBRID-POLYMER MICROSPHERES

3.1 Synthesis of Polymer Microspheres in the Presence of Nanoparticles

Heterogeneous polymerization of hybrid particles, as in Figure 7.1c, is realized by using dispersion, emulsion, precipitation, miniemulsion or suspension polymerizations in the presence of NPs dispersed in the liquid phase. The synthesis of NPs with pre-designed properties is conducted under well-defined conditions prior to polymerization. This approach is limited by two problems. First, heterogeneous polymerizations typically employ free radical chain polymerization of vinyl monomers [75]. During polymerization, radicals react with NPs, degrading their properties. This problem has in part been circumvented by growing inert shells around NPs. For instance, encapsulation of CdSe NPs with a shell of ZnS, helped to retain the luminescence properties of the core-shell QDs in the presence of radicals [76,77]. The second problem arises from the disruption of polymerization reactions in the presence of NPs: the processes of nucleation and growth of the polymer particles are sensitive to the presence of nanocrystals [78]. For instance, in emulsion, dispersion or precipitation polymerizations, the loci of polymerization are formed separately from the monomer droplets and the monomer and NPs must travel from the monomer droplet to the growing polymer particle through the continuous phase (usually water). Typically, solubility of monomers in water is sufficient for the monomer to diffuse from the droplet to the locus of polymerization, whereas many inorganic NPs, especially trioctylphosphine (TOPO)-covered QDs, do not have

sufficient solubility to allow efficient transfer from droplets to polymer particles. As a result, the NPs do not diffuse to the growing polymer particle.

Sheng et al. [78] circumvented the problem of poor solubility of NPs in the continuous phase by copolymerizing styrene and methyl methacrylate-functionalized CdSe-ZnCdS core-shell QDs in ethanol. The functionalized QDs were soluble in the continuous medium and thus could participate in the dispersion polymerization. However, two nucleation events occurred in the presence of QDs: the loci of polymerization were created by both precipitated QDs and polystyrene oligomers. These multiple nucleation events ultimately led to poor polydispersity of microspheres, even at low concentration of QDs.

Success in growing NP-loaded microbeads by heterogeneous polymerization has been reported by using miniemulsion and suspension polymerization routes [36,80]. In miniemulsion and suspension polymerization, the monomer droplets mixed with NPs become the loci of the polymerization [71]. Li et al. [36] used suspension polymerization for polymerizing a mixture of styrene and oleic acid-stabilized CdS NPs. Control over the diameter of the hybrid beads (from 100 nm to 500 μm) was achieved by varying the stirring speed and the concentration of the stabilizer. Joumaa et al. [77] used TOPO-stabilized CdS-ZnS QDs and styrene to produce hybrid latexes by miniemulsion techniques. Characterization of the microbeads revealed that the QDs were primarily located at the outer shell of the particles. Similar results were obtained in a study by Bradley et al. [76], who found that QDs were distributed near the interfaces of the polymer particles. Both groups explained this feature by phase separation between the QDs and the polymer during particle growth. Using similar conditions, Fleischhaker and Zentel [81] successfully prepared QD-loaded polystyrene (PS) latexes. The composite latexes were subsequently used as seeds to grow a poly(methyl methacrylate) (PMMA) shell in order to achieve the desired latex size. A somewhat different method was used when water-soluble CdTe QDs were used [80]. The CdTe QDs, stabilized by 3-mercaptopropionic acid, were mixed with the phase-transfer agent, dodecyl-p-vinylbenzylmethylammonium chloride, in order to transfer the QDs into styrene droplets. By initiating polymerization, the droplets carrying the QDs transformed into 2 μm-size particles. The degradation in photoluminescence of the QDs was attributed to the attack on the QDs by radicals in the polymerizing mixture.

3.2 Loading of Preformed NPs into Preformed Microspheres

The approach using loading preformed NPs into preformed polymer microspheres is the simplest when compared with other methods of preparing hybrid-microspheres discussed in this chapter. Three variations on this approach will be considered herein. In the first case, NPs are incorporated in the interior of polymer particles with a condensed structure. Nanoparticles are loaded into the swollen polymer particles and are subsequently confined in the particle interior by transferring the hybrid particles in a poor solvent for the polymer (Figure 7.5a). In the second strategy, preformed NPs are incorporated into the interior of polymer microgel. In the third case, the NPs are attached to the surface of microspheres by using attraction forces, e.g. electrostatic attraction between oppositely charged

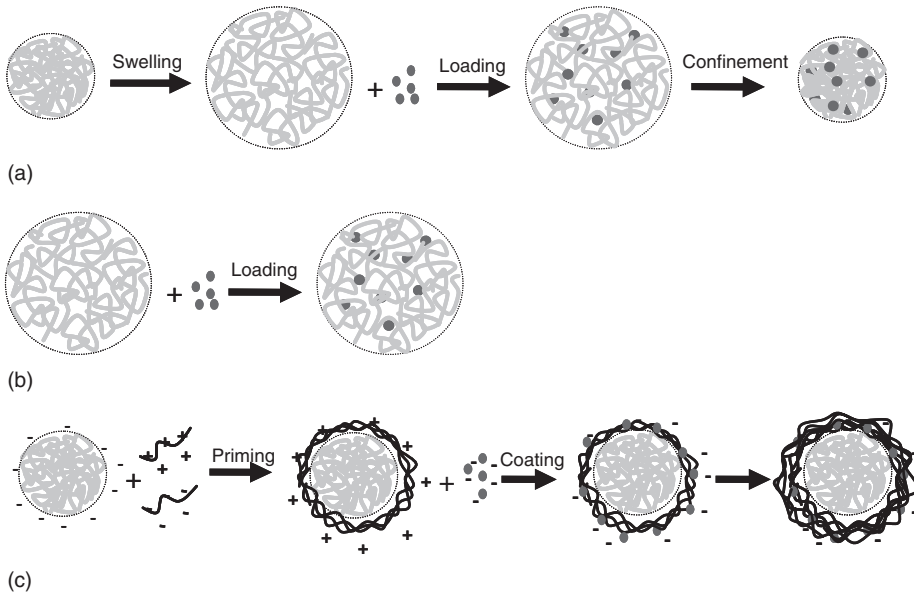

FIGURE 7.5 Schematics of three approaches to hybrid polymer–inorganic microbeads. (a) Hybrid microspheres are prepared by swelling a condensed microbead, allowing NPs to diffuse into the bead and confining the NPs by deswelling the polymer bead. (b) Loading of NPs in the interior of microgels by diffusion. (c) Consecutive deposition of layers of polyelectrolytes and nanoparticles on a polymer microsphere.

microspheres and NPs. Furthermore, the surface of microspheres can be decorated using layer-by-layer (LBL) deposition of polyelectrolytes and electrostatically charged NPs. These three schemes have a common advantage: the NPs and polymer particles are prepared separately. As a consequence, NPs whose synthesis requires complicated synthetic methodologies can be prepared apart prior to loading inside the microbeads. There is no restriction on the polymerization route used to make the polymer beads. Furthermore, because NPs are introduced into pre-made polymer microspheres, the NPs are not exposed to radicals.

3.2.1 Loading NPs into condensed polymer microspheres

Loading of NPs into condensed cross-linked polymer microbeads is carried out from a liquid medium that is a good solvent for the polymer and the NPs. The NPs diffuse in the interior of the swollen polymer beads, where they are subsequently trapped by deswelling the polymer network. For example, CdSe-ZnS core-shell NPs were loaded in PS beads by swelling the microspheres in a chloroform/alcohol mixture [17,18]. Similar work performed by Bradley et al. [76] highlighted the importance of good swelling conditions: the depth of penetration of the NPs into the PS microspheres varied from the periphery only to the homogeneous infiltration of the polymer particles, depending on the composition of liquid medium used for the swelling of PS beads. In a similar method, water-soluble

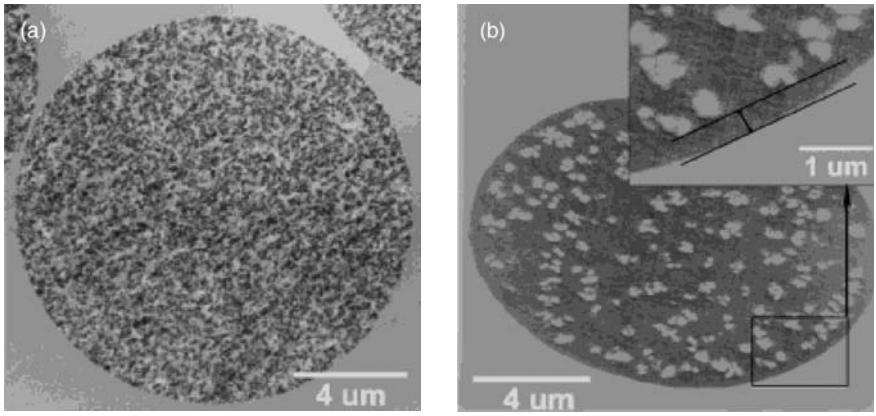

FIGURE 7.6 Transmission electron microscopy images of microtomed sections of (a) porous and (b) non-porous beads. The network of pores is more extensive in the interior of porous beads, whereas a small number of voids (bright spots) and a dense surface layer (delineated by two parallel lines) were observed in the non-porous beads. (Reprinted with permission from [17]. Copyright 2004 American Chemical Society.)

QDs were incorporated into hydrophobic PS beads [82]. To achieve loading, the anionically stabilized CdTe NPs were transferred into chloroform using a phase transfer agent, such as octadecylbenzyldimethylammonium chloride. Using isopropanol/chloroform mixtures, CdTe NPs were loaded into the cross-linked PS beads, yielding hybrid beads with ca. 2×10^2 NPs/bead.

Higher loading of NPs in polymer beads could be achieved if the microbeads possessed an extensive network of nanometre-size pores [17,18]. These mesoscale pores, with sizes ranging from 2 to 50 nm, were generated by extracting linear soluble oligomers and polymers from PS beads using organic solvents. In Figure 7.6, the TEM images show that the beads treated in this manner possess a more extensive network of pores in comparison to the non-porous beads. When the NPs were loaded into the bead, the small and large pores worked in synergy: the larger pores allowed rapid diffusion of the NPs inside the beads while the smaller pores provided a large surface area for immobilization of the NPs via strong hydrophobic interactions between the polymer and the TOPO ligands. The process of loading was found to be exceptionally efficient: in 10 minutes 3×10^6 NPs/bead were loaded into PS beads.

3.2.2 Loading NPs into microgel beads

The open network structure of hydrogels offers additional ways of loading and entrapping NPs inside hydrogel microspheres [70]. Microgel particles exist in a swollen state and therefore they sequester NPs without additional treatment, as shown in Figure 7.5b. Interactions between hydrogel particles and NPs can be driven by different processes including electrostatic forces, hydrogen bonding or specific forces. Furthermore, interesting applications of the NP loaded-microgels can be realized if they retain their stimuli-responsive nature.

In the work of Gorelikov et al. [15] poly(N-isopropylacrylamide-*co*-acrylic acid) microgels were loaded with Au nanorods (NRs). The cationic Au NRs were drawn into the microgels by strong electrostatic attraction with the negatively charged acrylic acid moieties of the hydrogel. The net positive charge of the Au NRs also ensured that they remained well isolated and evenly distributed inside the microgels. The hybrid-microgels retained the properties of their component parts, i.e. the volume-temperature transition of the microgels and the characteristic plasmon absorption band of the NRs.

Kuang et al. [83] reported loading and entrapping of NPs in microgels by the physical entanglement of the collapsed gel network. Highly cross-linked neutralpoly(N-isopropylacrylamide) and negatively charged poly(N-isopropylacrylamide-*co*-methacrylic acid) microgels were loaded with citrate-stabilized Au NPs. Since the negatively charged citrate-stabilized Au NPs were loaded into the negatively charged hydrogels, it was suggested that the incorporation of the NPs into the hydrogel is driven by an entropic process. Furthermore, the authors found that NPs with a diameter larger than 20 nm were excluded from loading due to the small pore sizes of the microgels.

In a separate study, Kuang et al. [84] demonstrated that water-soluble CdTe NCs could be entrapped in poly(4-vinylpyridine) microgels by using the response of this polymer to the variation in pH. At $pH \approx 3$, the microgels were swollen due to the charge repulsion between the protonated pyridine groups, whereas with an increasing value of pH the microgel shrank due to the deprotonation of the pyridine groups. Negatively charged CdTe NPs stabilized with thioglycolic acid were taken up by the microgel at $pH \approx 3$ (when the pore size was comparable to or larger than the diameter of the CdTe NPs). The NPs were subsequently confined within the hydrogel by collapsing the network at higher pH values. Furthermore, NPs were not released from the microgel particles for $3 < pH < 10$ while for $pH \geq 10$, the loaded NPs were released. It was speculated that, under these conditions, the sizes of pores in the polymer network decreased to sizes commensurate with the diameter of the NPs, squeezing the NPs out of the microgel.

In another study, NPs were loaded into poly(N-isopropylacrylamide) (polyNIPAm) microgels using the temperature sensitivity of the particles [83,85].

This method proved to be impractical: once the ambient temperature was brought below the lower critical solution temperature (LCST) of the polymer, the microgel swelled and the NPs were released. To circumvent this problem, Gong et al. used H-bonding firmly to attach NPs to the microgels [85]. Nanoparticles of CdTe stabilized with a mixture of thioglycerol and thioglycolic acid were loaded into poly(NIPAm) microspheres. The thioglycerol on the CdTe NPs formed hydrogen bonds with the amide groups on the polyNIPAm chains.

3.2.3 Coating polymer microbeads with NPs using layer-by-layer deposition

Layer-by-layer (LBL) deposition of polyelectrolytes has been used to modify and functionalize surfaces of polymer microspheres, as shown in Figure 7.5c. The method of LBL deposition entails consecutively adsorbing oppositely charged polyelectrolyte layers onto the surface of microspheres. The LBL method was used to decorate the surface of polymer microspheres with CdTe

NPs [86–88]. First, PS beads were primed with three layers of poly(allylamine hydrochloride)/poly(sodium-4-styrensulphonate)/poly(allylamine hydrochloride) to render the surface smooth and uniform. The outer positively charged surface attracted negatively charged QDs capped with thioglycolic acid. Multiple layers of QDs were produced that were separated by three bilayers of the polyelectrolyte to regenerate the positively charged surface. In this fashion, a controlled amount of QDs could be deposited on the surface of polymer beads.

In a similar manner, Au NP loaded capsules were prepared by depositing alternating layers of poly(allylamine hydrochloride) and poly(sodium 4-styrensulphonate) on melamine formaldehyde microbeads to produce a seven-layer coating [89,90]. Cationically stabilized Au NPs were then introduced to a dispersion of the polyelectrolyte-coated microspheres by allowing the NPs to infiltrate the polyelectrolyte layers. The melamine formaldehyde cores were then dissolved in 0.1 M HCl, yielding hybrid capsules.

3.3 *In-situ* Synthesis of NPs in Microbeads

Hybrid NP-polymer microspheres prepared by the *in-situ* synthesis of NPs generally involve introducing precursor ions within the interior of a microgel or on the surface of latex beads and subsequently reacting the ions to give NPs. Typically, the precursor ions are immobilized in the particles via covalent bonding [91], and electrostatic [92] and complexation [93–95] interactions, allowing nucleation and growth of NPs to remain localized in the polymer microbead. The resulting NPs are stabilized against aggregation by functional groups on the polymer chain. In comparison with other polymer templates such as dendrimers [96], polymer micelles [97–100] or star block copolymers [101], polymer microspheres have the advantage of easy synthesis and functionalization. In addition, polymer microbeads have a larger range of sizes: from tens of nanometres to several micrometres. Three general routes can be used for *in-situ* growth of NPs in polymer particles. When polymer microspheres have a condensed structure, the NPs can be grown on the surface of the bead (Figure 7.7a). When the polymer beads possess an open network, the NPs are grown in the interior of the particle (Figure 7.7b). The third approach combines the first two methods: NPs are grown in the hydrogel shell of the core-shell particles, as shown in Figure 7.7c.

Zhang et al. used cross-linked poly(NIPAm-*co*-AA-*co*-2-hydroxyethyl acrylate) microgels as the microreactors for semiconductor, metal and magnetic NPs [92] (Figure 7.8). Each component of the random copolymer hydrogel had a specific function: the polyNIPAm component rendered the microgel temperature sensitive, the polyacrylic acid moiety was used to complex precursor cations and the addition of poly-2-hydroxyethyl acrylate controlled the size of the microgel voids. Nanoparticles of CdS, Ag and Fe_3O_4 with narrow polydispersity were synthesized in these microgels. The concentration and structure of the NPs were controlled by varying the value of the pH of the dispersion, the composition of the hydrogel and the stoichiometry of the co-monomers.

Poly(NIPAm-*co*-AA-*co*-2-hydroxyethyl acrylate) microgels were also used to synthesize fluorescent Ag nanoclusters [102]. In this work, the microgel

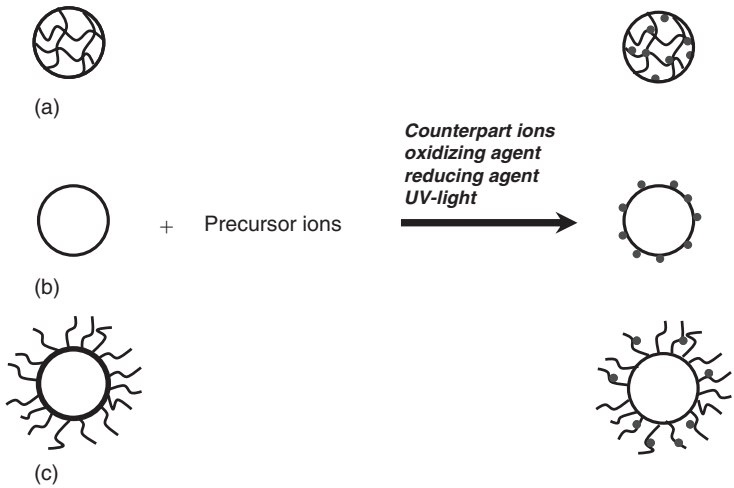

FIGURE 7.7 Approaches to *in-situ* growth of NPs in polymer microspheres. In (a) NPs are grown in the interior of microgels. In (b) NPs are grown on the surface of condensed polymer particles. (c) The NPs can also be grown in the swollen shell of a core-shell polymer microsphere.

dispersion was mixed with $AgNO_3$ and subsequently irradiated with UV light. Short (below 10 min) irradiation times generated silver nanoclusters containing from 2 to 8 atoms and/or ions, while after 100 min of illumination, the nanoclusters grew into 2–3 nm size NPs. Photoluminescence was detected in clusters produced after 6 min illumination and it gradually decayed for the NPs produced under long-time irradiation conditions.

Hybrid microgels are soft and hydrophilic particles and their size and shape depend on temperature, pH and the ionic strength of the intervening medium. These properties make the self-assembly of hydrogels into colloid crystals difficult. This problem was solved by encapsulating hybrid microgels with a hydrophobic shell [103]. Interfacial polymerization of poly(methyl methacrylate-butyl acrylate-acrylic acid) shell on the surface of hybrid poly(NIPAm-*co*-AA-*co*-2-hydroxyethyl acrylate) microgels carried out at 75°C and at a pH of 4.2 (when the microgels were in a deswollen state) yielded core-shell structures with no evidence of temperature-induced volume transitions, indicating that the hydrophilic cores were screened from the aqueous medium. These hybrid-core-shell structures crystallized into a closed-packed ordered array.

Hard polymer microbeads with functionalized surfaces have also been used to grow NPs *in situ* [11,94,95]. The advantage of using hard hybrid microbeads is that they can be readily self-assembled in colloidal crystals. In the first example, poly(vinylbenzyl chloride) microspheres were functionalized with viologen pendant groups (diquaternary derivatives of 4,4'bipyridyl that form radical monocations capable of reducing Au ions when UV-irradiated) [104]. Nanoparticles were grown onto the surface of the microspheres by mixing the dispersion of beads with gold chloride and irradiating the mixture for up to 60 min. After 60 minutes, the UV-Vis absorption spectrum of the dispersion showed the loss of

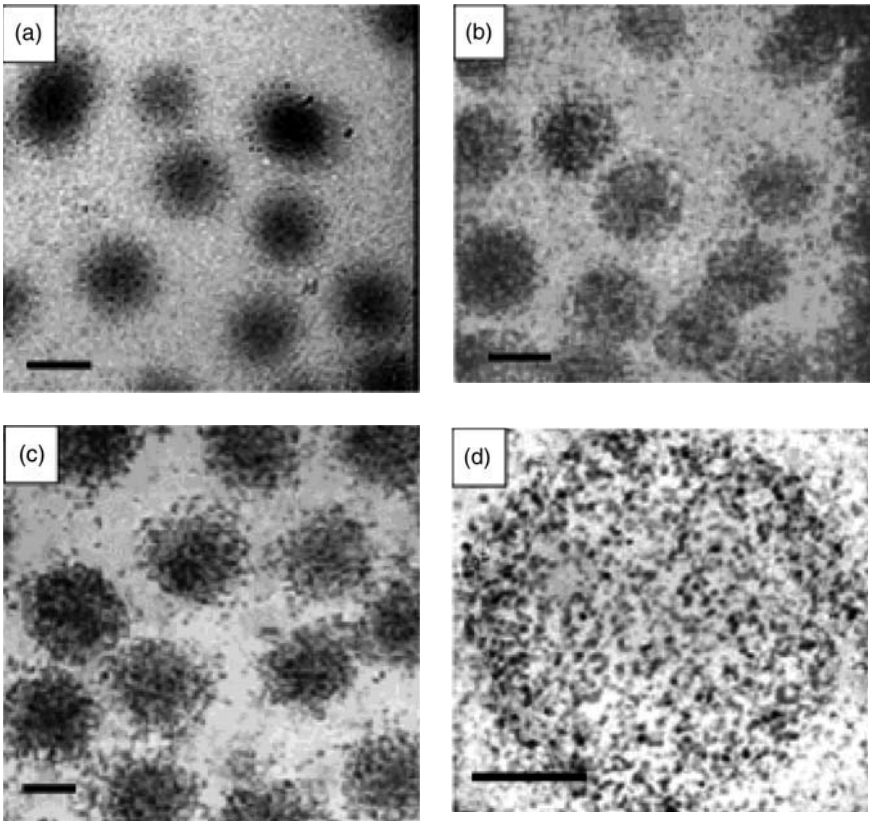

FIGURE 7.8 TEM images of hybrid poly(N-isopropyl acrylamide-*co*-acrylic acid-*co*-2-hydroxyethyl acrylate) microgels carrying (a) CdS NPs with a concentration of 0.027 $g_{NP}/g_{polymer}$; (b) Ag NPs with a concentration of 0.23 $g_{NP}/g_{polymer}$; (c) Fe_3O_4 NP with a concentration of 0.618 $g_{NP}/g_{polymer}$ (scale bar: 150 nm); (d) single microgel particle doped with CdS NPs. The scale bar is 50 nm. (Reprinted, with permission, from [92]. Copyright 2004 American Chemical Society.)

the signature absorption peak of the viologen radical cations and the appearance of a surface plasmon resonance (SPR) band associated with Au NPs. In Figure 7.9, TEM images show that NPs with a diameter of 5 nm were obtained after 10 min photoirradiation while NPs with a bimodal size distribution (5 and 15 nm in diameter) resulted after 60 min irradiation. The latter size distribution was attributed to either the result of two nucleation events or to accelerated coalescence of the NPs.

Zhang and Huang showed that complicated functionalization of the polymer bead surface was not required for *in-situ* synthesis of NPs: the COO^- groups on the surface of poly(methyl methacrylate-*co*-methacrylic acid) were used to localize Cd^{2+} or Ag^+ ions on the surface of the microbead [105]. The dispersions were then treated with Na_2S or $NaBH_4$ yielding CdS or Ag NPs, respectively. The images in Figure 7.10 reveal that the microbeads are uniformly coated with

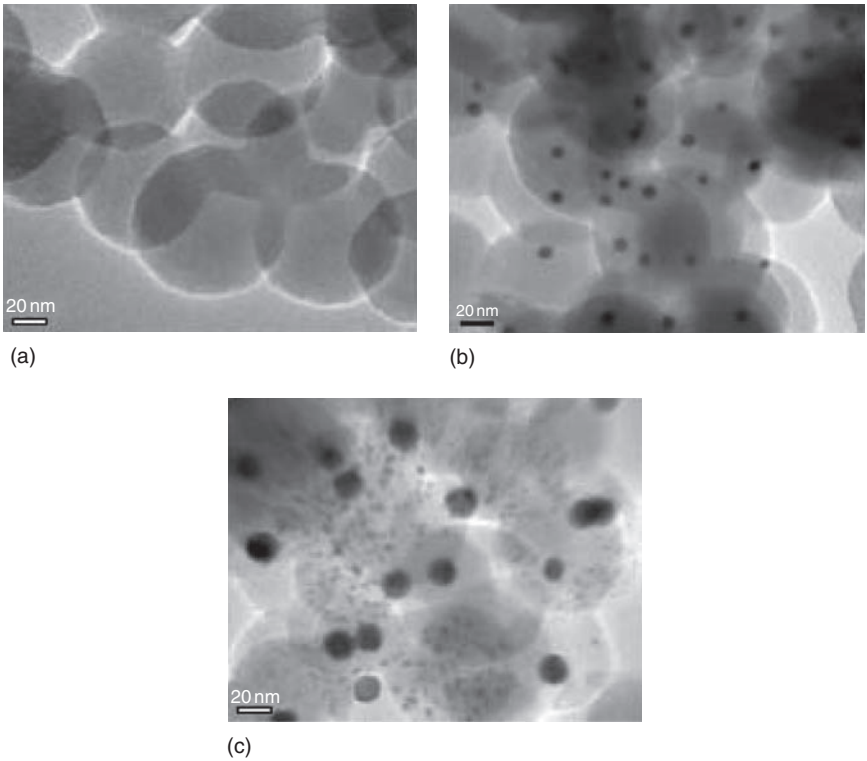

FIGURE 7.9 TEM images of viologen functionalized polymer beads (a) prior to, (b) after 10 min of and (c) after 60 min of irradiation. Nanoparticles with a diameter of 5 nm are formed after 10 minutes while NPs with a bimodal size distribution were formed after 60 min of irradiation. (Reprinted, with permission, from [104]. Copyright 1999 American Chemical Society.)

CdS and Ag NPs with a coverage of up to 40% of the surface of the beads. Two parameters determined the size of the NPs and the surface coverage of the polymer beads: the concentration of the methacrylic acid in the microbeads and the ratio of Cd^{2+}/COO^{-} or Ag^{+}/COO^{-} groups.

A number of works have focused on *in-situ* growth of NPs on the surface of polymer microgels. Since many of these hybrid NP-polymer beads were intended for use in catalysis, their structures were designed to have NPs in a porous polymer shell, leaving the NPs accessible for catalysis after *in-situ* growth [106–108]. Several of these works demonstrate the growth of NPs in soft hydrogel shells surrounding a hard core. In an early method, hybrid core-shell microbeads using a one-step dispersion polymerization of a mixture of styrene, macromonomers of polyNIPAm and $AgNO_3$ yielded core-shell microbeads decorated with Ag NPs [106]. Styrene was copolymerized with the polyNIPAm macromonomers, generating PS microbeads with the hydrophilic polyNIPAm shell. The Ag^{+}-ions coordinated to the nitrogen of the amide group of polyNIPAm and the radicals then reacted with the Ag^{+}-ions to form Ag NPs. The surface-grafted polyNIPAm served as a steric stabilizer to prevent the flocculation of the PS particles and to

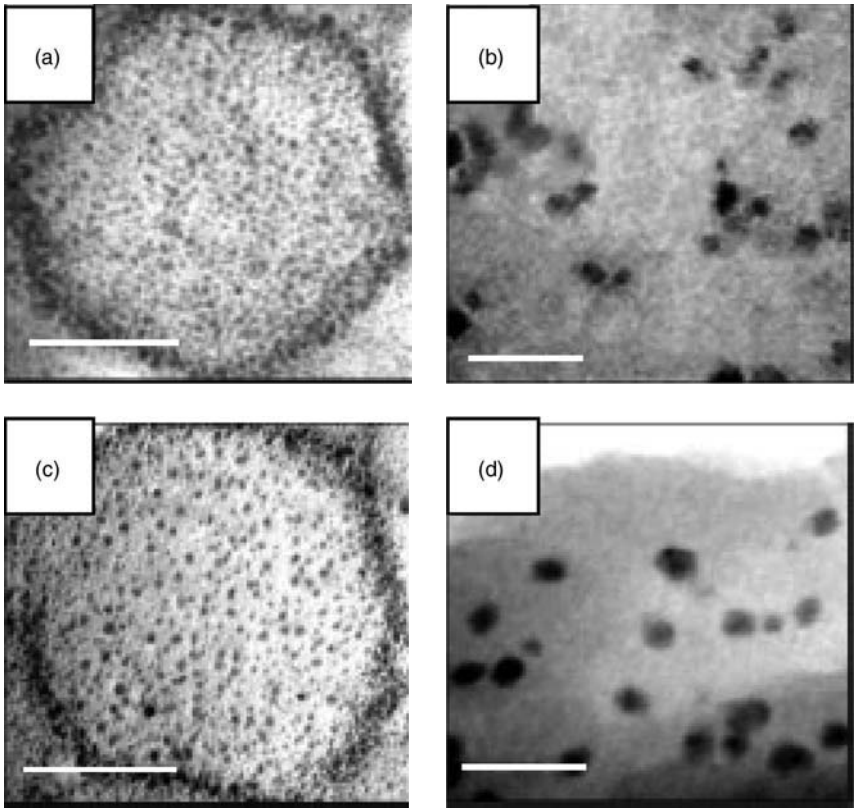

FIGURE 7.10 TEM micrographs of poly(methyl methacrylate-*co*-methacrylic acid) beads covered with NPs of CdS (a,b) and Ag (c,d). The images which show individual latex microspheres (a and c) reveal that the NPs are localized on the surface of the polymer bead (scale bar: 100 nm). Sections of the latex surface covered with CdS (b) and Ag (d) NPs show that the NPs are well isolated and well dispersed (scale bar: 20 nm). Reprinted with permission from [11]. Copyright 2002 Wiley-VCH.

immobilize the NPs on the surface of the beads. Similar core-shell beads were used for *in-situ* growth of Pt NPs [107]. This work stressed the role of the concentration of surface polyNIPAm on the structure of the NPs: with increasing concentration of polyNIPAm, the induction period for NP formation increased and the diameter of the NPs decreased.

In an alternative approach, Au NPs were immobilized in the shell of core-shell beads by functionalizing the shell with thiol and amino groups [109,110]. By controlling the amount of glycidyl methacrylate and NIPAm fed into the reaction mixture, particles with hard, glycidyl methacrylate-rich cores and soft, polyNIPAm-rich shells were synthesized. The small fraction of glycidyl methacrylate in the shell allows the shell to be modified with thiol or amino groups. *In-situ* synthesis of Au NPs in these three systems was achieved by introducing an aqueous solution containing $AuCl_4$ to the dispersion of particles and reducing the gold ions using $NaBH_4$. Figure 7.11 shows TEM images of thiol-modified hybrid

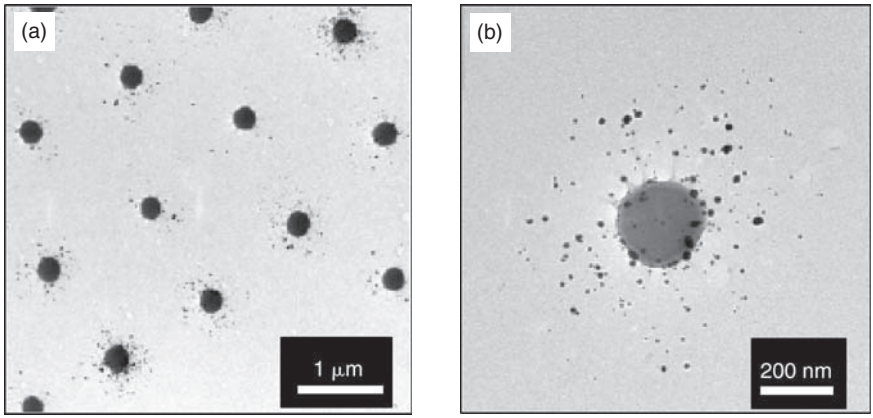

FIGURE 7.11 TEM images of Au nanoparticles in the shell of thiol-modified core-shell particles. The Au nanoparticles are immobilized via the thiol functionality of the shell. (Reprinted, with permission, from [109,110]. Copyright 2005 American Chemical Society.)

microspheres. The NPs are localized in the thiol-modified shell of the core-shell structure and the NPs are found to be well isolated.

4. OPTICAL PROPERTIES AND APPLICATIONS OF POLYMER MICROSPHERES LOADED WITH INORGANIC NANOPARTICLES

4.1 Thermally responsive Polymer Microgels Loaded with Gold Nanoparticles: Materials for Drug Delivery

Photothermally modulated volume transitions in submicrometre-sized microgel particles have promising applications in drug delivery. Generally, photosensitive moieties are embedded in a thermally reversible polymer matrix and irradiated at their absorption wavelengths. Conversion of the light energy to heat through non-radiative relaxation causes microgel heating and, for polymers with lower critical solution temperature (LCST), leads to deswelling. For applications of thermoresponsive gels as drug delivery carriers, it is important that the photosensitive species absorb in the 'water window' spectral range, i.e. at $800\,\text{nm} < \lambda < 1200\,\text{nm}$, in order to minimize the absorption of laser light by cells and tissue [111].

One of the examples of hybrid hydrogel systems is capsules produced by the LBL assembly of polyelectrolytes and loaded with gold NPs [89]. The capsules ruptured when they were irradiated with short-pulsed laser pulses (<10 ns) at $\lambda = 532\,\text{nm}$ or at $\lambda = 1064\,\text{nm}$. The degree of damage induced by the irradiation was controlled by varying the radiant exposures, as shown in Figure 7.12. In a controlled experiment using capsules without Au NPs, the capsules were unaffected by such radiation exposures.

The authors proposed that heating of the capsule shell created significant thermal stresses within the capsule, which ultimately caused the shell to rupture.

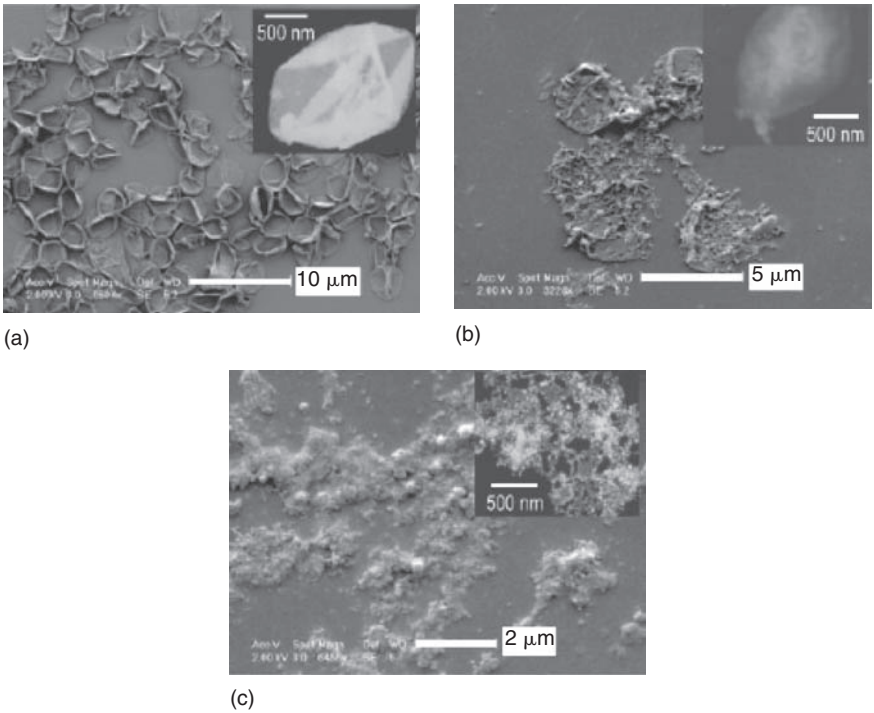

FIGURE 7.12 SEM images of polymer capsules loaded with gold NPs irradiated with multiple laser pulses: (a) before irradiation; (b) after moderate radiation exposure (30 mJ/cm^2); (c) after radiation exposures of 50 mJ/cm^2 and higher. Insets are the corresponding TEM images. (Adapted, with permission, from [89]. Copyright 2004 Wiley-VCH.)

Extremely short-lived nanometre-size bubbles forming around the gold NPs as a result of an explosive phase-transition separation could also contribute to the rupture of the capsule of the shell. These optically addressable capsules were used as carriers for the protein lysozyme loaded in the capsule interior. When irradiated with short-pulsed laser light, the capsules ruptured, releasing the protein. The protein maintained its enzymatic properties after the laser-induced release.

Using a similar strategy, laser-induced release of fluorophores from living cancer cells has been achieved [112]. The shells of the capsules obtained by the LBL assembly of polyelectrolytes were loaded with 20 nm Ag NPs, which absorb light in the near-infrared spectral range. When these capsules were incorporated in living cells and illuminated with a laser beam operating at 830 nm, they ruptured inside the cells. Figure 7.13 shows the remote light-triggered activation of the capsule inside a cell.

Gold nanorods are particularly useful in drug delivery applications since they can be pre-designed and synthesized to have SPRs in the 'water window' spectral range. Thermoresponsive poly(NIPAm-AA) microgels were loaded with Au NRs to demonstrate their utility as potential photoresponsive drug carriers [15]. When these

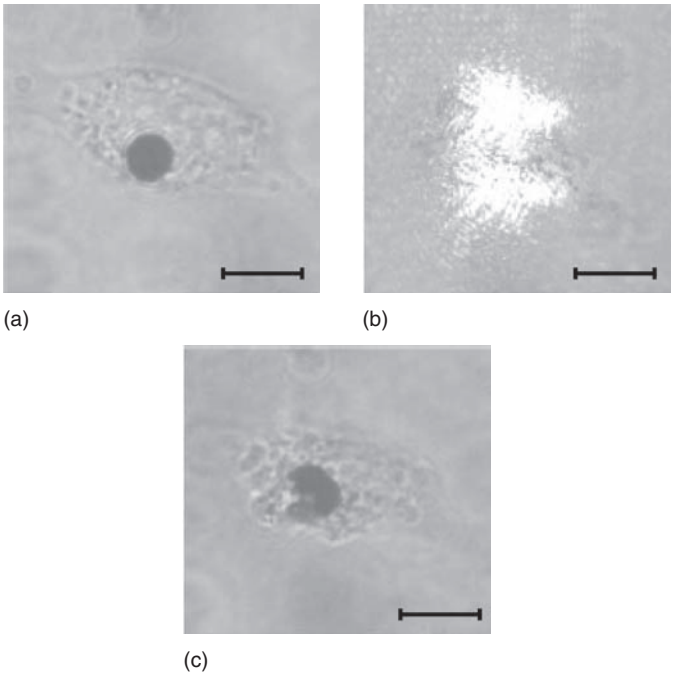

FIGURE 7.13 Remote activation of a capsule containing silver NPs in its walls. The capsule was engulfed by a living MDA-MB-435S cancer cell. The images show the cell (a) before, (b) during and (c) after illumination with a laser. Scale bar is 10 μm. (Adapted, with permission, from [112] Copyright 2006 Wiley-VCH.)

microgels were illuminated with a wavelength of $\lambda = 810$ nm (close to the plasmon band of the NRs), the NRs absorbed light energy and released it as heat, causing local heating of the microgels. The volume of the hybrid microgels decreased by 53%. These photothermally induced swelling–deswelling transitions in hybrid microgels were reproducible, suggesting that the NRs remained in the microgels during the polymer volume phase transitions (Figure 7.14). While the photothermally triggered swelling–deswelling transitions occurred at 30–35°C at pH = 4, further modification of the composition of microgels made them photoresponsive at biological temperatures and pH values [16].

4.2 Polymer Microspheres Loaded with Quantum Dots for Biological Imaging

The ability to monitor the interactions between cells and bioactive molecules (e.g. proteins) or to image cells is becoming an active area of research in the biotechnology community. Polymer microbeads loaded with QDs are ideal for this application due to the unique photoluminescence properties of quantum dots and the biocompatibility and the ease of surface functionalization of polymer microspheres.

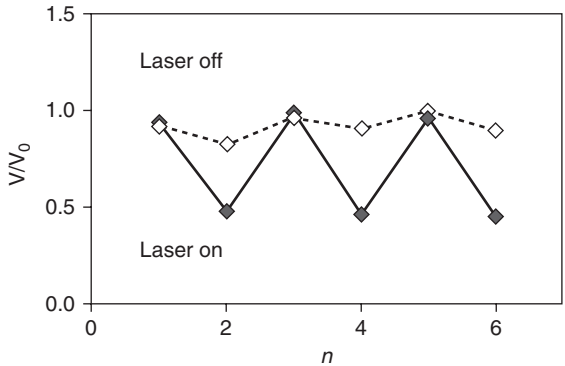

FIGURE 7.14 Variation in volume of pure (◇) and hybrid (◆) poly(NIPAm-AA) microgels plotted as a function of the number of *laser on* and *laser off* events *n*. Both microgel systems were irradiated at $\lambda = 810$ nm. The original dimensions of pure and hybrid microgels are ca. 500 nm and 450 nm, respectively, at pH = 4. (Adapted, with permission, from [16]. Copyright 2004 American Chemical Society.)

The use of organic fluorophores as biological probes has been well documented [113]. There are many dyes available that have sharp emission peaks across the visible spectrum and the near-infrared spectral range but, in order to target a specific optical range, a potentially complicated organic synthesis is necessary to change the fluorescence characteristics of the dyes. Semiconductor quantum dots, due to their size-dependent PL emission properties, require only a change in the size of the NPs to produce a new colour of fluorescence. In addition, quantum dots (QDs), especially core-shell QDs, possess high photostability and therefore their fluorescence efficiency will not decay with time [31]. The absorption characteristics of quantum dots also make them more desirable for imaging purposes over conventional organic dyes: the fluorescence of QDs with varying emission characteristics can be excited under the irradiation at a single UV-wavelength [114].

A significant drawback of the biological application of semiconductor QDs is their toxicity. It is well known that cadmium and other heavy metals, which are commonly used in the fabrication of QDs, are cytotoxic [115]; however, the degree of cytotoxicity of semiconductor nanocrystals remains under investigation [116,117]. It is the release of Cd^{2+} ions from the surface of the QDs that causes nanocrystal cytotoxicity; therefore, coating QDs with a polymer reduces the cell death rate [116]. In addition, surface functionalization on the QD affects the location in the cell or tissue where the quantum dots eventually accumulate which, in turn, could lead to increased or decreased long-term toxic effects [118].

The use of polymer microspheres carrying QDs can overcome many of the shortcomings of QDs alone and provide additional beneficial properties. The work of Han et al. [119] demonstrated the capability of these hybrid structures. The schematics of the use of polymer–QD particles is shown in Figure 7.15. Core-shell CdSe–ZnS QDs with different dimensions were loaded into PS microbeads in precisely controlled amounts. The constituent materials were synthesized separately

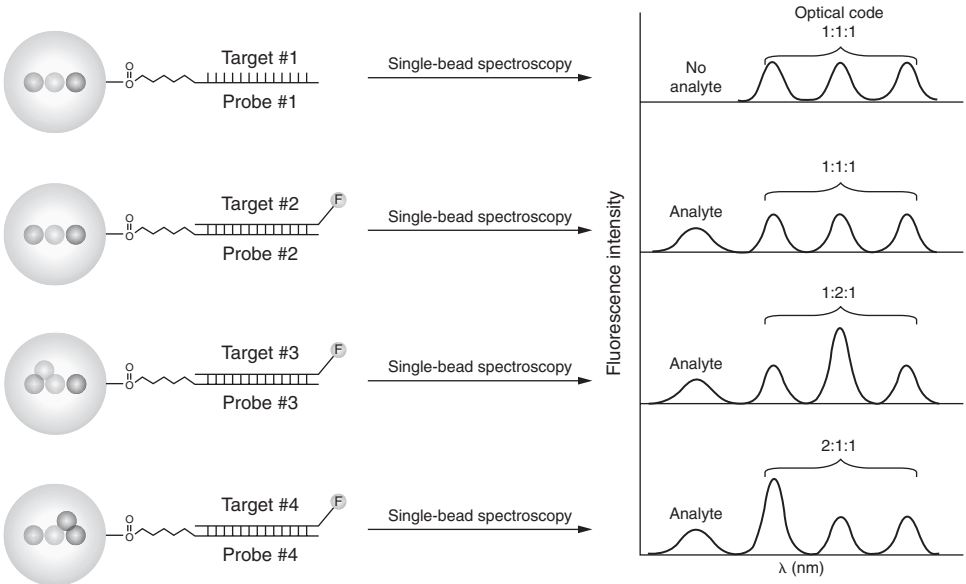

FIGURE 7.15 Schematics of biofunctionalized polymer microspheres loaded with quantum dots, used as fluorescent probes. Single beads have been functionalized to attach three target biomolecules. The different ratios of the QDs loaded inside the polymer microspheres allow simultaneous identification of the location of the target molecules inside the cells from irradiation with a single incident wavelength, through their different fluorescence spectra. (Adapted, with permission, from [119]. Copyright 2001 Nature Publishing Group.)

and the loading was performed through swelling of the PS microbeads. The QD–polymer hybrid microspheres were excited using a single UV light source and, by controlling the ratios of QDs with different emission characteristics in the polymer particles, the hybrid microspheres were identified through the variations in peaks and relative intensity of the photoluminescence. This approach provided a large number of easily discernible identification tags. For example, it was estimated that if QDs with six different peak emission wavelengths were loaded into the microspheres at ten photoluminescence intensity levels, at least 10 000 recognizable tagging codes could be produced. The polymer microspheres carrying QDs could be further biofunctionalized to target specific molecules inside the cells [114,119,120].

With this strategy, the size of the microbeads may restrict their application in biological imaging: microspheres larger than 100 nm can be useful in multiplexed biosensing; however, they are too large for subcellular detection [105]. Synthesis of QD-encoded microbeads of 30 nm in diameter enabled the uptake of these microspheres into cells, which can allow the imaging of intracellular components. Furthermore, QDs coated with silica and solubilized with PEG can create hybrid particles with sizes of the order of 10 nm [121]. The small size of QDs generated by the last method allows imaging of the smallest components of cells; however,

the advantage of the potential for multiplexing is lost, as only one population of quantum dots is contained within each particle.

4.3 Photonic Crystals Fabricated from Polymer Microspheres Loaded with Semiconductor Quantum Dots

Three-dimensional (3D) photonic crystals – materials that are periodic on an optical length scale – have attracted much attention from both fundamental and practical points of view [122,123]. The unique property of such materials is the possibility of obtaining a full photonic bandgap, a range of energy for which the photons cannot propagate in any direction inside the material. If a complete photonic bandgap is realized, 3D photonic crystals would allow one to harness light in a particular predetermined manner, thus making them useful as photonic limiters and switches.

The self-assembly method (or the bottom-to-top method) is a simple and straightforward approach to photonic crystals. In this strategy, colloid crystals (CCs) are formed by the self-assembly of submicrometre size silica or polymer microspheres. In the next step, the interstitial spaces of the CC are infiltrated with a high refractive index material and the microspheres are removed. The final (FCC) structure consists of spherical air cavities surrounded by the infiltrated material [124–127]. It should be noted that a complete bandgap can be realized when the infiltrated material has a refractive index >2.8; however, a pseudo-photonic bandgap material with interesting properties can be produced even if there is a moderate refractive index modulation in a material with periodic composition and structure. This applies to colloid crystals fabricated from microspheres that are either loaded, or coated with inorganic NPs [11,12,19,25]. Incorporation of NPs in the interior or on the surface of microspheres is achieved by the methods described in Section 2. The use of semiconductor nanocrystals is particularly interesting, because they offer the potential for strong, resonantly enhanced, optical non-linearities. The resulting structure combines the unique electronic properties of NPs with the light confinement properties of the colloidal crystal, and a CC doped with QDs can potentially act as an all-optical limiter: in response to high intensity irradiation the NPs change their refractive index which, in turn, causes the microstructures to shift their stopband.

Figure 7.16 demonstrates the predicted change in the transmission spectra for a CC loaded with quantum dots that is expected from assuming that the NPs have linear and non-linear refractive indices of 1.70 and 1.75, respectively, and the microspheres have a refractive index of 1.59. In the case of low light intensity, the CC features a stopband centred at 1480 nm (solid curve). Under high light intensity, the refractive index of the NPs increases to 1.75 and the stopband shifts to a wavelength of 1500 nm (dashed curve). The wavelengths at the low energy edge of the stopband (indicated by a vertical line) would be excluded: at low light intensity, this wavelength lies in the passband while at high light intensity, this wavelength lies inside the stopband.

Here, we describe the results of the experimental study of the properties of photonic crystals fabricated from polymer microspheres carrying semiconductor

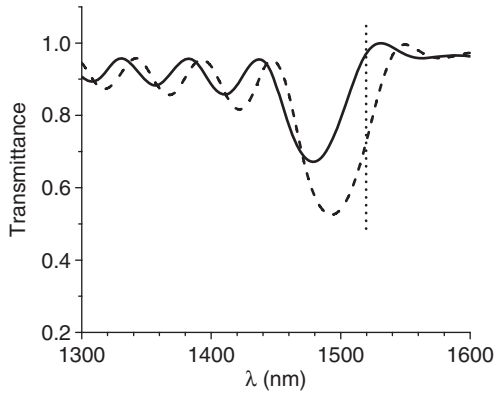

FIGURE 7.16 Multem simulations show how variations of the refractive index of the interstitial space change the transmission of the photonic crystal made from PS microspheres. The solid curve represents a CC filled with a material possessing a refractive index of 1.70. Upon irradiation, the effective refractive index of this material is assumed to increase to 1.75. The dashed curve shows the corresponding shift in the stopband. Wavelengths at the edge of the first stopband are excluded from entering the crystal under high intensity illumination. (Multem is a FORTRAN computer code which calculates the complex band structure associated with a given surface (crystallographic plane) of an infinite photonic crystal, and the transmission, reflection and absorption coefficients of a slab of the crystal (from [128]).) Simulations were provided by Dr Fumiyo Yoshino from the University of Toronto.

NPs on their surface (the schematics are depicted in Figure 7.1d). The CC was fabricated from PMMA-PMAA microspheres covered with CdS nanocrystals [25]. Coupling between the properties of semiconductor QDs and colloid crystals is illustrated in Figure 7.17. Figure 7.17a shows the absorption and PL spectra of hybrid polymer microspheres coated with ca. 6 nm-size CdS NPs. The luminescence spectrum displays band-edge emission at a wavelength close to the onset of absorption (≈480 nm) and an additional strong, broad band associated with radiative decay from a surface trap state, as shown in the three-level diagram in the inset of Figure 7.17a. Figure 7.17b shows the transmittance spectrum of the photonic crystal fabricated from the hybrid polymer spheres and illuminated at several incidence angles with respect to the normal of the (111) surface. For 0° incidence the spectrum shows a dip in the range of 640–660 nm associated with the stopband arising from Bragg diffraction at (111) planes. The stopband disappears for the sample infiltrated with index-matching dimethyl sulphoxide (DMSO), indicating the Bragg diffraction observed results from the periodic structure. Figure 7.17c shows PL spectra of the CC, acquired at several incident angles. Relative to the index-matched PL spectrum (top curve) the CC without infiltrated DMSO exhibits spectral dips in its PL spectrum, for example, at 650 nm for PL collected at 0°. Vertical arrows indicate the wavelength of the centre of the stopband for the angle at which PL is acquired. In each case, the dips in the PL spectra occur at the centre of the angular stop band due to the interaction of the photonic stop band and QD light emission.

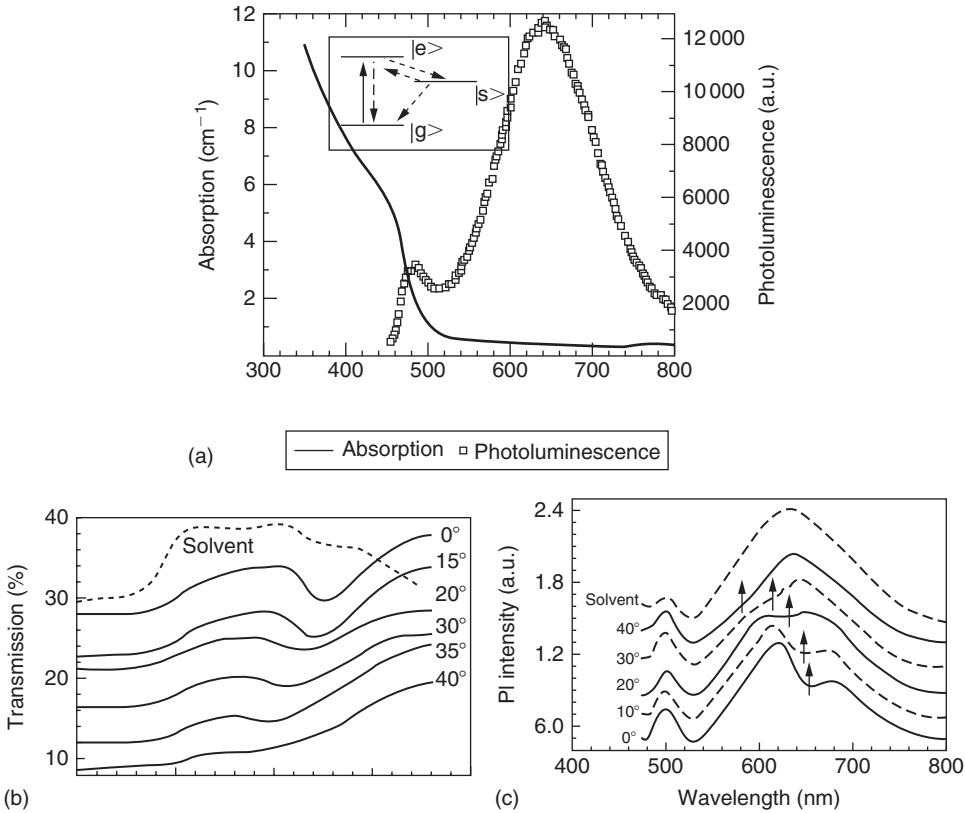

FIGURE 7.17 (a) Optical absorption from aqueous dispersions of CdS/PMMA/PMAA hybrid microspheres diluted in dimethyl sulphoxide (DMSO) with DMSO as a reference, together with a photoluminescence spectrum from colloidal CdS/PMMA-PMAA microspheres. The narrow peak corresponds to band-edge emission from the radiative decay from excited state to ground state, while the broad peak corresponds to radiative decay of the carrier captured by a nanocrystal surface trap state from the excited state, as shown in the inset. (b) Optical transmission for different incidence angles, with respect to the surface normal of the photonic crystals doped with CdS nanocrystals together with the transmission of the photonic crystals infiltrated with the index-matching solvent DMSO (dash line, shifted down). (c) PL spectra from the CdS nanocrystals in the photonic crystals as a function of observation angle with respect to the (111) surface of the photonic crystal. The spectrum from the solvent DMSO infiltrated sample is also shown. The vertical arrows indicate the wavelength of the centre of the stopband for the angle at which PL is acquired. (Adapted, with permission, from [25]. Copyright 2002 American Institute of Physics.)

Thus, the combination of self-organization of microspheres to form a photonic crystal, providing electromagnetic structural resonances, with semiconductor QDs-coated microsphere surface, provided optical functionalization with spectral control achieved through the quantum size effect. Luminescence from surface states ensured that light was emitted at energies significantly below the absorption edge of the emitting species.

SUMMARY

This chapter describes the methods of production and the optical applications of materials with structural hierarchy. The materials were created by loading or coating polymer submicrometre-size particles with inorganic (metal and semiconductor) nanoparticles. The examples of optical applications include photothermally triggered drug delivery, biolabelling and the fabrication of photonic crystals.

References

1. Lakes R. Nature 1993; 361:511–515.
2. Mayer G, Sarikaya M. Exp. Mech. 2002; 42:395–403.
3. Alivisatos PA. Science 1996; 271:933–937.
4. Lue JT. J. Phys. Chem. Solids 2001; 62:1599–1612.
5. Klar T, Perner M, Grosse S, von Plessen G, Spirkl W, Feldmann J. Phys. Rev. Lett. 1998; 80:4249–4952.
6. Zhong Z, Yin Y, Gates B, Xia Y. Adv. Mater. 2000; 12:206–209.
7. Agarwal R, Lieber CM. Appl. Phys. A 2006; 85:209–215.
8. Nann T, Mulvaney P. Angew. Chem. Int. Ed. 2004; 43:5393–5396.
9. Darbandi M, Thomann R, Nann T. Chem. Mater. 2005; 17:5720–5725.
10. Antonietti M, Ozin GA. Chem. Eur. J. 2004; 10:28–41.
11. Zhang JG, Coombs N, Kumacheva E, Lin YK, Sargent EH. Adv. Mater. 2002; 14:1756–1759.
12. Zhang JG, Coombs N, Kumacheva E. J. Am. Chem. Soc. 2002; 124(49):14512–14513.
13. Foulger SH, Kotha S, Sweyda-Krawiec B et al. Opt. Lett. 2000; 25:1300–1302.
14. Bock RD, Cathcart MJ. Proc. SPIE: Inter. Soc. Optical Eng. 2005; 5778:732–740.
15. Gorelikov I, Field LM, Kumacheva E. J. Am. Chem. Soc. 2004; 126:15938–15939.
16. Das M, Sanson N, Fava D, Kumacheva E. Langmuir 2006.
17. Gao XH, Nie SM. Anal. Chem. 2004; 76:2406–2410.
18. Gao X, Cui Y, Levenson RM, Chung LWK, Nie S. Nat. Biotechnol. 2004; 22:969–976.
19. Xu X, Majetich SA, Asher SA. J. Am. Chem. Soc. 2002; 124:13864–13868.
20. Oldenburg SJ, Averitt RD, Westcott SL, Halas NJ. Chem. Phys. Lett. 1998; 288:243–247.
21. Grady NK, Halas NJ, Nordlander P. Chem. Phys. Lett. 2004; 399:167–171.
22. Wang H, Brandt DW, Le F, Nordlander P, Halas NJ. Nano Lett. 2006; 6:827–832.
23. Jones CD, Serpe MJ, Schroeder L, Lyon LA. J. Am. Chem. Soc. 2003; 125:5292–5293.
24. Kim J, Serpe MJ, Lyon LA. Angew. Chem. Int. Ed. 2005; 44:1333–1336.
25. Lin Y, Zhang J, Sargent EH, Kumacheva E. Appl. Phys. Lett. 2002; 81:3134–3136.
26. Liang Z, Susha A, Caruso F. Chem. Mater. 2003; 15:3176–3183.
27. Bawendi MG, Carroll PJ, Wilson WL, Brus LE. J. Chem. Phys. 1992; 96:946–954.
28. Bockelmann U. Phys. Rev. B 1993; 48:17637–17640.
29. Brus LE. J. Chem. Phys. 1984; 80:4403–4409.
30. Woggon U. Optical Properties of Semiconductor Quantum Dots. Springer: Berlin, 1997.
31. Hines MA, Guyot-Sionnest P. J. Phys. Chem. 1996; 100:468–471.
32. Guénaud C, Deleporte E, Filoramo A et al. J. Appl. Phys. 2000; 87:1863–1868.
33. Brus L. Appl. Phys. A 1991; 53:465–474.
34. Guzelian AA, Katari JEB, Kadavanich AV et al. J. Phys. Chem. 1996; 100:7212–7219.
35. Lu JG, Ye ZZ, Zhang YZ, Liang QL, Fujita S, Wang ZL. Appl. Phys. Lett. 2006; 89:023122.
36. Li Y, Liu ECY, Pickett N et al. J. Mater. Chem. 2005; 15:1238–1243.
37. Coffer JL, Zerda TW, Appel R, Wells RL, Janik JF. Chem. Mater. 1999; 11:20–22.
38. Arakawa Y. Solid-State Electron 1994; 37:523–528.
39. Murray CB, Norris DJ, Bawendi MG. J. Am. Chem. Soc. 1993; 115:8706–8715.
40. Peng ZA, Peng X. J. Am. Chem. Soc. 2001; 123:183–184.

41. Talapin DV, Rogach AL, Kornowski A, Haase M, Weller H. Nano Lett. 2001; 1:207–211.
42. Mekis I, Talapin DV, Kornowski A, Haase M, Weller H. J. Phys. Chem. B 2003; 107:7454–7462.
43. Reiss P, Bleuse J, Pron A. Nano Lett. 2002; 2:781–784.
44. Chang S, Zhou M, Grover C. Opt. Express 2004; 12:143–148.
45. Ronda C, Srivastava A. Electrochem. Soc. Interface 2006; 15:55–57.
46. Klostranec JM, Chan WCW. Adv. Mater. 2006; 18:1953–1964.
47. Stavis SM, Edel JB, Samiee KT, Craighead HG. Lab Chip 2005; 5:337–343.
48. Bruchez M, Jr, Maronne M, Gin P, Weiss S, Alivisatos AP. Science 1998; 281:2013–2016.
49. Hines MA, Scholes GD. Adv. Mater. 2003; 15:1844–1849.
50. Kelly KL, Coronado E, Zhao LL, Schatz GC. J. Phys. Chem. B 2003; 107:668–677.
51. Creighton JA, Eadon DG. J. Chem. Soc. Faraday Trans. 1999; 87:3881–3891.
52. Link S, El-Sayed MA. J. Phys. Chem. B 1999; 103:4212–4217.
53. Moores A, Goettmann F. New J. Chem. 2006; 30:1121–1132.
54. Link S, Mohamed MB, El-Sayed MA. J. Phys. Chem. B 1999; 103:3073–3077.
55. Fromm DP, Sundaramurthy A, Schuck PJ, Kino G, Moerner WE. Nano Lett. 2004; 4:957–961.
56. Nehl CL, Liao H, Hafner JH. Nano Lett. 2006; 6:683–688.
57. Novotny 1997.
58. Tam F, Moran C, Halas NJ. J. Phys. Chem. B 2004; 108:17290–17294.
59. Halas N. MRS Bull. 2005; 30:362–367.
60. Schmid G, Chi LF. Adv. Mater. 1998; 10:515–526.
61. Hutter E, Fendler JH. Adv. Mater. 2004; 16:1685–1706.
62. Turkevich J, Stevenson PC, Hillier J. Faraday Soc. 1951; 11:55–75.
63. Duff DG, Baiker M. Langmuir 1993; 9:2301–2309.
64. Duff DG, Baiker M. Langmuir 1993; 9:2310–2317.
65. Gittens DI, Caruso F. Angew. Chem. Int. Ed. 2001; 40:3001–3004.
66. Shi W, Sahoo Y, Swihart MT, Prasad PN. Langmuir 2005; 21:1610–1617.
67. Okubo M, Kanaida K, Matsumoto T. Coll. Polym. Sci. 1987; 265:876–881.
68. Okubo M, Murakami Y, Fujiwara T. Coll. Polym. Sci. 1995; 274:520–524.
69. Sundberg DC, Casassa AP, Pantazopoulos J, Muscato MR, Kronberg B, Berg J. J. Appl. Polym. Sci. 2003; 41:425–1442.
70. Pelton R. Adv. Coll. Interface Sci. 2000; 85:1–33.
71. Antonietti M, Landfester K. Prog. Polym. Sci. 2002; 27:689–757.
72. Brandrup J, Immergut EH, Grulke EA. Polymer Handbook, 4th edn. Wiley & Sons: New York, 1999; VI/571.
73. Patil Ao, Heeger AJ, Wudl F. Chem. Rev. 1988; 88:183–200.
74. Stejskal J, Kratochvil P, Radhakrishnna N. Synth. Metals 1993; 61:225–231.
75. Arshady R. Coll. Polym. Sci. 1992; 270:717–732.
76. Bradley M, Bruno N, Vincent B. Langmuir 2005; 21:2750–2753.
77. Joumaa N, Lansalot M, Theretz A, Elaissari A. Langmuir 2006; 22:1810–1816.
78. Sheng WC, Kim S, Lee J, Kim SW, Jensen K, Bawendi MG. Langmuir 2006; 22:3782–3790.
79. Odian G. Principles of Polymerization, 3rd edn. Wiley-Interscience: New York, 1991.
80. Yang YH, Wen ZK, Dong YP, Gao MY. Small 2006; 2:898–901.
81. Fleischhaker F, Zentel R. Chem. Mater. 2005; 17:1346–1351.
82. Li MJ, Zhang H, Zhang JH, Wang CL, Han K, Yang B. J. Colloid Interface Sci. 2006; 300:564–568.
83. Kuang M, Wang DY, Bao HB, Gao MY, Mohwald H, Jiang M. Adv. Mater. 2005; 17:267–270.
84. Kuang M, Wang DY, Mohwald H. Adv. Funct. Mater. 2005; 15:1611–1616.
85. Gong YJ, Gao MY, Wang DY, Mohwald H. Chem. Mater. 2005; 17:2648–2653.
86. Wang DY, Rogach AL, Caruso F. Nano Lett. 2002; 2:857–861.
87. Wang DY, Rogach AL, Caruso F. Chem. Mater. 2003; 15:2724–2729.
88. Wang YJ, Yu AM, Caruso F. Angew. Chem. Int. Ed. 2005; 44:2888–2892.
89. Radt B, Smith TA, Caruso F. Adv. Mater. 2004; 16:2184–2189.
90. Angelatos AS, Radt B, Caruso F. J. Phys. Chem. B 2005; 109:3071–3076.
91. Scott RWJ, Wilson OM, Crooks RM. J. Phys. Chem. B 2005; 109:692–704.
92. Zhang JG, Xu SQ, Kumacheva E. J. Am. Chem. Soc. 2004; 126:7908–7914.
93. Lemon BI, Crooks RM. J. Am. Chem. Soc. 2000; 122:12886–12887.

94. Cen L, Neoh KG, Kang ET. Adv. Mater. 2005; 17:1656–1661.
95. Cen L, Neoh KG, Cai Q, Kang ET. J. Colloid Interface Sci. 2006; 300:190–199.
96. Scott RWJ, Datye AK, Crooks RM. J. Am. Chem. Soc. 2003; 125:3708–3709.
97. Moffitt M, McMahon L, Pessel V, Eisenberg A. Chem. Mater. 1995; 7:1185–1192.
98. Moffitt M, Eisenberg A. Macromolecules 1997; 30:4363–4373.
99. Moffitt M, Vali H, Eisenberg A. Chem. Mater. 1998; 10:1021–1028.
100. Zhao HY, Douglas EP. Chem. Mater. 2002; 14:1418–1423.
101. Youk JH, Park MK, Locklin J, Advincula R, Yang J, Mays J. Langmuir 2002; 18:2455–2458.
102. Zhang JG, Xu SQ, Kumacheva E. Adv. Mater. 2005; 17:2336–2340.
103. Xu SQ, Zhang JG, Paquet C, Lin YK, Kumacheva E. Adv. Funct. Mater. 2003; 13:468–472.
104. Dokoutchaev A, Thomas JJT, Koene SC et al. Chem. Mater. 1999; 11:2389–2399.
105. Zhang Y, Huang N. J. Biomed. Mater. Res. B: Appl. Biomater. 2005; 76B:161–168.
106. Chen CW, Chen MQ, Serizawa T, Akashi M. Adv. Mater. 1998; 10:1122–1126.
107. Chen CW, Serizawa T, Akashi M. Chem. Mater. 1999; 11:1381–1389.
108. Chen CW, Serizawa T, Akashi M. Chem. Mater. 2002; 14:2232–2239.
109. Suzuki D, Kawaguchi H. Langmuir 2005; 21:8175–8179.
110. Suzuki D, Kawaguchi H. Langmuir 2005; 21:12016–12024.
111. Simpson CR, Kohl M, Essenpreis M, Cope M. Phys. Med. Biol. 1998; 43:2465–2478.
112. Skirtach AG, Javier AM, Kreft O et al. Angew. Chem. Int. Ed. 2006; 45:4612–4617.
113. Liang S, Pierce DT, Amiot C, Zhao X. Synth. React. Inorg. Met.-Org Nano-Met Chem. 2005; 35:661–668.
114. Gao X, Yang L, Petros JA, Marshall FF, Simons JW, Nie S. Curr. Opin. Biotechnol. 2005; 16:63–72.
115. Lopez E, Figueroa S, Oset-Gasque MJ, Gonzalez MP. Br. J. Pharmacol. 2003; 138:901–911.
116. Derfus AM, Chan WCW, Bhatia SN. Nano Lett. 2004; 4:11–18.
117. Fischer HC, Liu L, Pang KS, Chan WCW. Adv. Funct. Mater. 2006; 16:1299–1305.
118. Kirchner C, Liedl T, Kudera S et al. Nano Lett. 2005; 5:331–338.
119. Han MY, Gao XH, Su JZ, Nie S. Nat. Biotechnol. 2001; 19:631–635.
120. Portney NG, Ozkan M. Anal. Bioanal. Chem. 2006; 384:620–630.
121. Zhang T, Stilwell JL, Gerion D et al. Nano Lett. 2006; 6:800–808.
122. John S. Phys. Rev. Lett. 1987; 58:2486–2489.
123. Yablonovitch E. Phys. Rev. Lett. 1987; 58:2059–2062.
124. Kulinowski KM, Jiang P, Vaswani H, Colvin VL. Adv. Mater. 2000; 12:833–838.
125. Velev OD, Kaler EW. Adv. Mater. 2000; 12:531–534.
126. Xia Y, Gates B, Yin Y, Lu Y. Adv. Mater. 2000; 12:693–713.
127. Norris DJ, Vlasov YA. Adv. Mater. 2001; 13:372–376.
128. Stefanou M, Yannopapas V, Modinos A. Comput. Phys. Commun. 1998; 113:49–77.

CHAPTER 8

Interfacial Assembly of Nanoparticles into Higher-order Patterned Structures

Xiaodong Chen and Lifeng Chi

1. INTRODUCTION

Nanoparticles (NPs) exhibit unique and tunable properties, such as blue-shifts in optical spectra of semiconductor nanocrystals [1], superparamagnetic behaviour of magnetic NP [2], resonance tunnelling and Coulomb blockade effects in metallic and semiconducting NPs [3–5], which are not existent in their bulk counterparts. Considerable progress has already been made in the synthesis of NPs extending over a wide range of materials with good control over particle size and shape over the past two decades [3,6–12]. A formidable challenge still to be faced, however, is controllable assembling and positioning NPs in desired locations to construct complex, higher-order structures and, ultimately, functional systems. Moreover, assemblies of NPs are well known to yield collective physical properties dependent on particle size, spacing and higher-order structure [13–19]. This topic has gained increasing interest over the past ten years and plays an important role for emerging applications in photonics, electronics, information storage, catalysis and biological sensing [20]. For instance, colloidal semiconducting nanocrystals can self-assemble into close-packed solids on thin films, which are interesting for their cooperative physical properties and their application in quantum-dot lasers and conducting thin films [21,22].

The controllable assembly of NPs (zero-dimensional material) into multidimensional arrangements can be approached from different directions. To date, the methods for 3-dimensional (3D) superlattices composed of one or more types

Physikalisches Institut and Center for Nanotechnology (CeNTech), Westfälische Wilhelms-Universität, 48149 Münster, Germany

Nanostructured Materials © 2009 Elsevier Ltd.
978-0-08-044965-4 All rights reserved.

of metallic and/or semiconductor NPs have relied on the differences in the sizes of component particles and on entropic, van der Waals, electrostatic, steric and dipolar interactions between them [23–25], while 2-dimensional (2D) superlattices (close-packed NP monolayers) were achieved by self-assembly from NP solutions onto a flat substrate [26,27], evaporation induced self-assembly [28] and Langmuir–Blodgett (LB) technique [29–31]. Close-packed NP monolayers can also be achieved by chemisorption of NPs onto a substrate surface by interaction between NPs and substrates. 2D NP patterns and 1-dimensional (1D) NP arrays may be obtained by traditional lithographic techniques (top-down strategies) and interfacial assembly techniques (bottom-up strategies). Among these arrangements of NPs, 2D NP patterns and 1D NP arrays serve as platforms for developing nanoscale devices whose functionalities are enabled by the physical (i.e. optical, electrical and magnetic) properties of the individual particles and their arrangement [20]. For example, 1D NP arrays provide model systems to study transport phenomena between NPs [17,20,32,33]. Moreover, the assembly of NPs into 2D patterns and 1D arrays is of interest to researchers working in fields ranging from biosystems study to magnetic information storage and from photonics to electronics. For instance, Au-NP arrays with varying lateral spacing are functionalized with self-assembled monolayers of a cyclic derivative of the Arg-Gly-Asp (cRGD) peptide (linked to mercaptopropionic acid) to study cell adhesion [34].

The purpose of this chapter is to summarize the recent development in interfacial assembly of synthesized NPs into higher-order patterned structures, especially focusing on 1D and 2D arrays of NPs. By definition, interfacial assembly is a process that occurs at the geometrical limit between two immiscible phases, the so-called interface, due to interfacial phenomena such as the dewetting instability and interfacial interactions such as capillary forces, electrostatic interaction and van der Waals forces. Figure 8.1 illustrates how an interface can play an important, often decisive, role in dictating the higher-order structure of NPs. In terms of structure, a high degree of NPs organization can be best achieved by

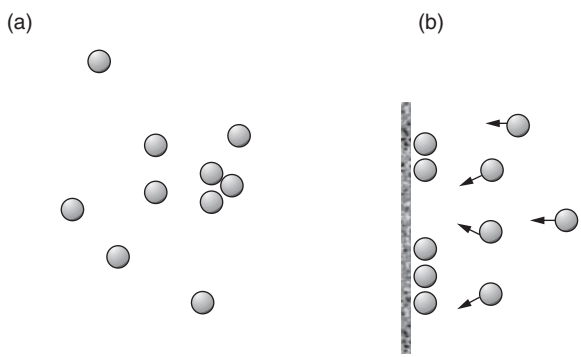

FIGURE 8.1 Schematic representations of (a) random distribution of NPs and (b) ordered organization of NPs at the interface with a matrix.

developing architectures on a matrix (solid interface, molecular template). The interface impacts the higher-order structure in three important ways. First, the interface provides a platform for extended 1D or 2D organization of the NPs. Secondly, the packing density of the active molecular species on the surface allows the extent and the strength of lateral interactions to be controlled so that interparticle communication, which may be individually weak, can collectively drive the assembly of defect-free structures. Finally, the interface of the matrix may serve as a communication interface, through which the 1D or 2D organization of the NPs can be electrically addressed, which is a necessary step for the nanoscale device integration.

In general, there are three methods for interfacial controllable assembling of NPs into 1D or 2D higher-order patterned structure: the so-called 'non-templated interfacial self-assembly', 'template-directed self-assembly' and 'nanocontact printing and writing'. The self-assembly process, defined as the autonomous organization of components into structurally well-defined aggregates without human intervention, is characterized by numerous beneficial attributes: it is cost-effective and versatile as well as facile and the process occurs towards the system's thermodynamic minima, resulting in stable structures. Non-templated interfacial self-assembly mostly based on bottom-up methods is highlighted in Section 2. It covers the main approaches that are utilized to assemble the NPs into higher-order structures without template. Section 3 addresses the template-directed self-assembly of NPs, focusing on molecular templates or preformed chemical or topographic structures. Section 4 focuses on the organization of NPs by printing and writing directly based on the pure top-down nanolithography approaches, such as soft lithography and dip-pen nanolithography (DPN).

2. NON-TEMPLATED INTERFACIAL SELF-ASSEMBLY

2.1 Instability during Dewetting and Solvent Evaporation

The events of surface pinning and convective flow during the dewetting process of a droplet of a colloidal suspension on a flat surface have received interest because potentially they can be harnessed as an extremely simple way for surface patterning [35]. Several groups have used this dewetting process to form ring-like aggregated structures of NPs. For instance, Tripp et al. [36] have shown that cobalt NPs can self-assemble into similar rings which can be formed by two different mechanisms: dipole-directed self-assembly (typically 5–12 particles, ring diameters between 50 and 100 nm) and evaporation-driven hole formation in viscous wetting layers (ring diameters ranging from 0.5 to 10 μm). Similarly, Ohara et al. described a class of annular ring-like structures which self-assemble from a solution of metal NPs on solid substrates [37,38]. Moreover, barium ferrite NPs [39] and CoPt3 NPs [40] can self-assemble into ring structures based on a similar mechanism.

Maillard et al. [41,42] found that the evaporation rate of the solvent strongly influenced the 2D arrangements of the NPs. A fast evaporation process (use of a

highly volatile solvent, hexane) induces a large temperature gradient between the interface and the substrate, which results in an increase of the surface tension perturbation and convective flow. After complete evaporation of the solvent, the nanocrystal organization is the replica of this flow. By decreasing the evaporation rate (use of a low-volatility solvent, such as decane), the system equilibrates faster than the heat loss by the evaporation process and instabilities disappear. Moreover, by increasing the particle concentration, more complex organizations such as honeycombs or chaotic structures are observed after evaporation of the solvent [41,42].

The stick-slip phenomenon during the liquid evaporation process is an efficient way to form linear pattern structures. For instance, Ray et al. [43] found that an ordered linear pattern of poly(styrene-co-vinylimidazole) latex particles is formed by drying a droplet of a positively charged colloidal suspension on a flat negatively charged hydrophilic surface, as shown in Figure 8.2. This extremely

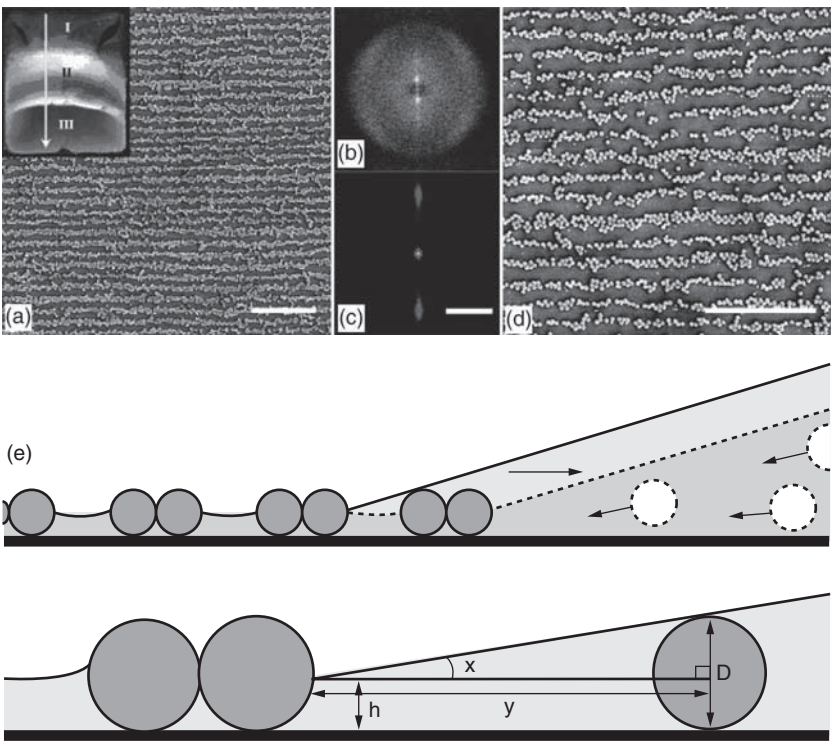

FIGURE 8.2 (a) SEM image of the linear pattern found in region II using 258 nm particles on glass. Scale bar: 10 μm. The inset (12 mm wide) shows the three regions observed with a typical sample. The arrow indicates the liquid receding direction during the drying process. (b) FFT of the linear pattern in micrograph (a). Notice the intense spots which were used to measure the centre-to-centre line spacing. The halo is caused by the particle diameter. (c) Laser diffraction pattern of a similar patterned region. λ, 632.8 nm; projection length, 25 cm; scale bar, 10 cm. (d) SEM image showing an area of region II using 391 nm particles on glass. Scale bar: 10 μm. (e) Top: schematic illustration of the ordering process. Bottom: Geometry used to describe the ordering process. (Adapted with permission from [43].)

simple method affords lines of colloidal particles with regular 1.5–4.5 μm line spacing and smaller than 2 μm line width over a broad surface area. The simultaneous deposition of the particles at a fixed distance (i.e. the line spacing) behind the previous line of particles where the contact line is pinned, is in turn responsible for the periodic stick-slip motion. The key distinguishing feature of the present system is the attractive interaction between the particles and the surface, which instigates the periodicity of the particle deposition. Similarly, Giraldo et al. presented a study of oscillatory phenomena, in which mixed-valent manganese oxide inorganic NPs are organized with a high degree of periodicity [44]. As well as dewetting, convection also could be used to form regular pattern. Porous zeolite films with surface patterns such as knotted-rope web and wrinkled honeycomb were obtained by convection-assisted dynamic self-assembly of zeolite NPs [45], but an appropriate dispersant and the presence of zeolite NPs with a specific range of particle sizes in the colloidal suspension are critical for pattern formation.

2.2 Langmuir–Blodgett Technique

The Langmuir–Blodgett (LB) technique is one of the most conventional methods for nanofilm fabrication in which organized systems of moieties are efficiently built one monolayer at a time. The method involves a monolayer transfer of the desired substance, originally adsorbed at the air–water interface, to the substrate of choice. The appealing feature of the LB technique is the intrinsic control of the internal layer structure down to a molecular level and the precise control of the resulting film thickness. The method was originally used to organize amphiphilic molecules but was extended to NP systems in the last decade. There has been progress reported on the close-packed monolayer fabrication of ligand-stabilized NPs on solid substrates [29–31,46–49].

Unlike these traditional close-packed NP monolayers on solid substrates, the LB technique itself also is a way to obtain regular NP patterned arrays on solid substrates. For instance, Chung et al. [50] confirmed the formation of aligned, high-aspect ratio nanowires at a low density Langmuir monolayer film of alkylthiol-passivated silver NPs during the film compression. Prior to monolayer compression (surface coverage $\approx$20%, $\pi \approx 0$ mN/m), the particles were found to aggregate into circular domains [51]. After compression, the particle monolayers are found spontaneously to assemble into lamellae or wire-like superstructures several micrometres in length and 20–300 nm in width; both are functions of the solvent and particle sizes. The inter-wire separation, as well as the alignment of the wires, could be controlled via compression of the wires. In addition, experiments and computer simulations performed by the standard Metropolis Monte Carlo algorithm [51], show good agreement, as shown in Figure 8.3. The patterns have been described as a result of competition between an attraction, which makes the particles aggregate, and a longer-ranged repulsion, which limits the aggregation to finite domains. Also, careful investigations showed that an increase in concentration leads to a spontaneous reorganization of the self-assembled domains from circular clusters to stripes, as the repulsions between

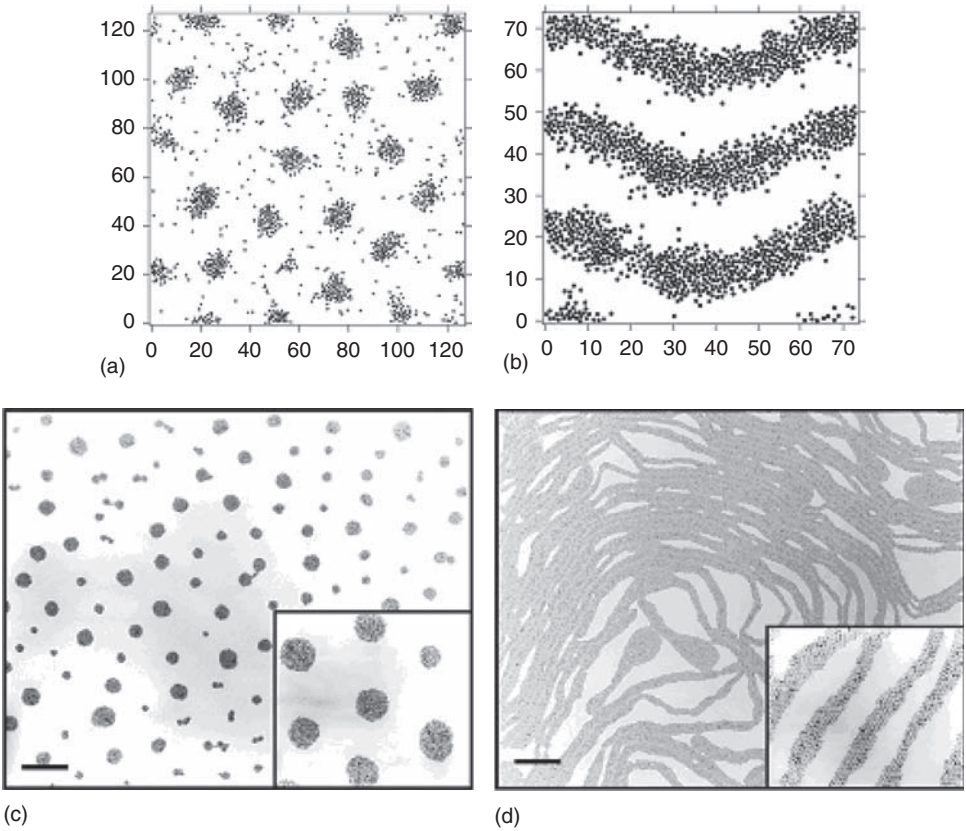

FIGURE 8.3 Results of computer simulation (a,b) and the corresponding TEM micrographs (c,d) revealing the spontaneous formation of clusters and stripe-like arrays of alkylthiol passivated Ag nanocrystals. The solution used to prepare (d) was approximately three times more concentrated (~1 mg/ml) than that of (c). The size of the scale bar shown is 0.5 μm. (Adapted with permission from [51].)

the aggregates becomes more important than those between the individual particles within them. This phenomenon is closely related to the transition between the hexagonal and lamellar phases observed commonly in concentrated surfactant solutions, where the locally preferred curvature of micelles is successively 'squeezed out' of the systems as interaggregate repulsions become dominant and the lower-curvature cylinder and bilayer geometries are found to minimize the overall interaction free energy.

Contrary to the results of Chung et al. [50], where the higher-order structures of NPs formed at the air–water interface before transferring onto the solid substrate, Schmid's group in Essen and Yang's group in Berkeley [52–54] found that the process of LB transfer also is an efficient way to obtain regular NP arrays on solid substrates with the help of dewetting. Vidoni et al. [54] were first successfully to obtain parallel rows of $Au_{55}(PPh_3)_{12}Cl_6$ clusters by the LB technique which

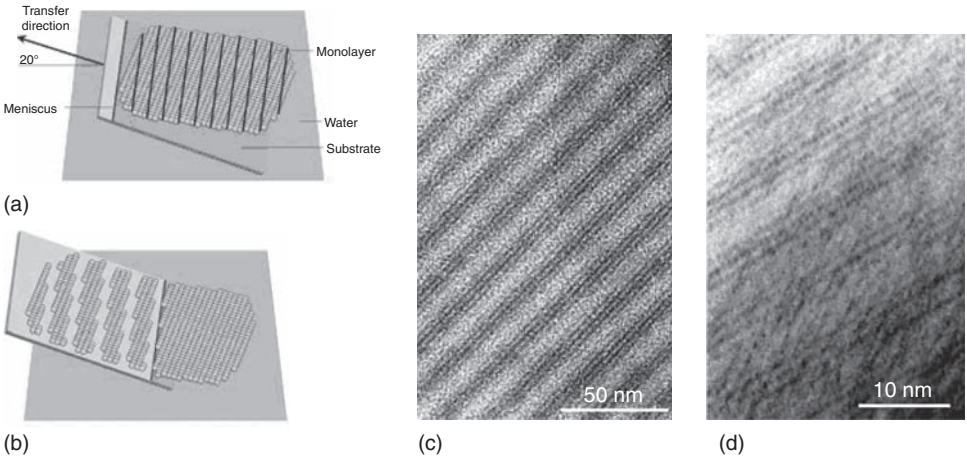

FIGURE 8.4 (a) Sketch of the formation of cluster stripes from an ordered monolayer. The monolayer is oriented toward the substrate edge and the meniscus, respectively, by a non-predetermined angle. (b) Owing to the movement of the substrate from the water and the herewith linked transfer of the monolayer onto the substrate surface, the monolayer is fractured along the black lines due to the oscillation of the meniscus. Stripes of three to four rows of clusters lying side by side are formed. The stripes run parallel to the water meniscus. (c) TEM image of cluster stripes consisting of three to four cluster rows. (d) Magnified cutout. The cluster rows consist of equidistantly ordered clusters. (Adapted with permission from reference [54].)

represents a quasi 1D structure of quantum dots of about 10 nm width. A modified LB technique (Figure 8.4a), deposited underneath the monolayer with an angle of 20°, was used to generate this kind of cluster stripes. The pattern formation is mainly dependent on the speed at which the substrate is moved. At speeds of ~10 cm/min^{-1}, the parallel stripes consisting of three to four cluster rows, show a separation of 8 nm from each other, as shown in Figure 8.4. They attributed the formation of such patterns to the existence of oscillation of the water meniscus at the substrate, inducing the generation of stripe patterns running parallel to the meniscus.

Later, Huang et al. [53] used the LB technique to generate well-spaced, parallel single particle lines on a substrate from a dilute Langmuir particle monolayer via a stick-slip motion of the water–substrate contact line. They could *in situ* observe a stick-slip motion of the three phase contact line during the transfer process by optical microscopy, which is due to the large interline distance and low density of the Langmuir monolayer at the air–water interface, compared with the work from Vidoni et al. [54]. The particle density within the lines is controllable by the particle concentration in the monolayer as well as the pulling speed of the substrate. Lines of a great variety of materials and sizes, ranging from a few nanometres to a few micrometres, have been demonstrated. The ability to assemble NPs into 1D arrays enables the construction of higher hierarchical device structures. For example, using Au-NP seeds, vertical single nanowire arrays of silicon can be grown replicating the pattern of single particle lines. Huang and coworkers [52] also found the spontaneous formation of ordered gold and silver NP stripe patterns on dewetting a dilute film

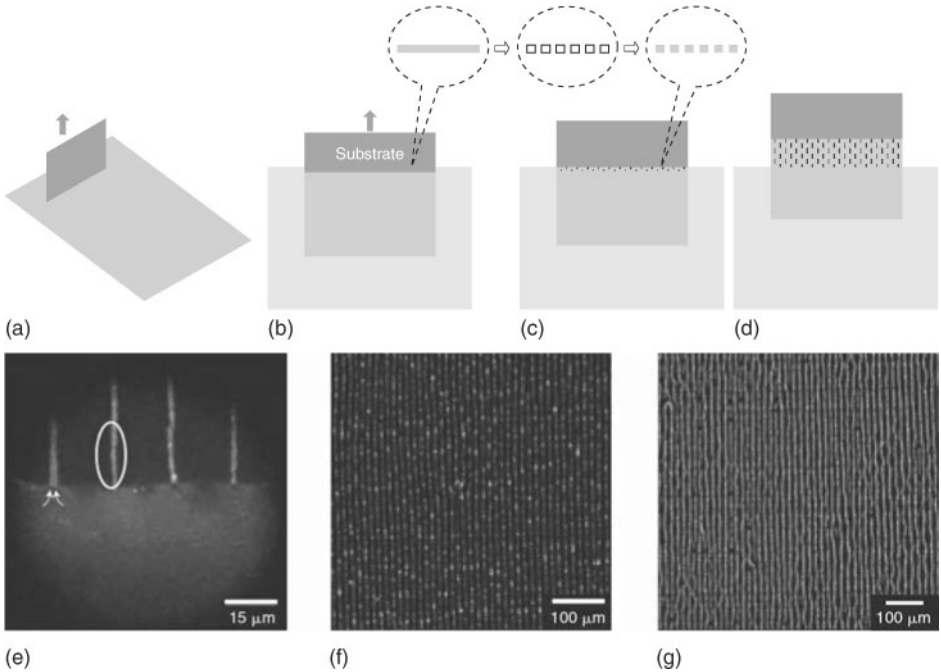

FIGURE 8.5 Extended stripe pattern formation through dip-coating. (a–d) A schematic drawing illustrating the formation of an aligned gold NP stripe pattern by vertical deposition (a,b). Only the NPs at the water–substrate contact line (gold dots in b–d) are shown for clarity. The substrate is raised slowly (a,b) so that water is evaporated when a new surface is exposed. The wet contact line containing uniformly dispersed NPs breaks up into aggregates of NPs (b,c) owing to the fingering instability during the initial dewetting stage. These fingertips then guide further deposition of NPs, finally forming the extended stripe pattern (d). (e) Direct optical microscopy observation of the water front reveals a rapid motion of NPs towards the wet tips (circled area) of the stripes, as indicated by the arrows. This leads to the unidirectional growth of the stripes across the entire substrate as shown in the optical microscopy image in (f). (g) Silver NP stripes have been obtained in the same fashion. (Adapted with permission from [52].)

of polymer-coated NPs floating on a water surface. In this case, the NP stripe patterns are perpendicular to the air–water interface (Figure 8.5), which is contrary to the above two examples. For this system, the fingering instability is responsible for the formation of vertical NP stripe patterns. These samples have shown that the LB technique opens up a new avenue for lithography-free patterning of NP arrays for various applications including, for example, multiplexed surface-enhanced Raman substrates and templated fabrication of higher-order nanostructures.

3. TEMPLATE-DIRECTED SELF-ASSEMBLY

Although non-templated interfacial self-assembly shows some possibilities for form in ordered structures, the formation of low dimensional NP arrays is most

challenging. The 1D arrangement of NPs needs the help of appropriate templates or of sophisticated techniques, since nature usually does not tend to organize in 1D for energetic reasons. Normally, there are two types of template for assembling free-standing NPs: hard and soft templates. Examples of soft templates include surfactant aggregates, polymer molecules, biomolecules, self-assembled monolayers, polymeric moulds and so on, and hard templates include silica colloidal crystal arrays, anodized alumina membranes and silicon substrates with topographic patterns. In this section, we will focus on molecular templates (surfactant, polymer and biomolecules etc.), chemical patterns on solid substrates, for which some soft templates are fabricated on the solid substrates, and topographically patterned structures.

3.1 Surfactants and Polymers

It is well-known that the surfactant molecules (such as dipalmitoylphosphatidylcholine, DPPC) can be organized into regular strucures at the air–water interface. For this reason, Hassenkam et al. [55] demonstrated the formation of continuous gold nanowires by mixing and spreading the dodecanethiol-capped Au-NP and DPPC at the air–water interface. To some extent, the morphology of these nanostructures can be controlled by adjusting the parameters that affect the self-assembly process. The unidirectional sintering of particles, which is accompanied by packing into a maze-like structure, is due to a template effect of the surfactant at the molecular level. The amphiphilic DPPC molecules energetically prefer to occupy the entire water surface if left alone, while the hydrophobic gold particles, if left alone on the water surface, form close-packed 2D hexagonal rafts floating on the water surface. When a mixture of DPPC and dodecanethiol capped gold particles is placed on the same water surface, the energetic strain between the bare water surface and the hydrophobic particles will be reduced. The DPPC molecules can only support single-particle broad lines, resulting in the formation of 1D aggregates, which is the mechanism for nanowire formation. In another work, Zhang et al. [56] used molecular aggregates as templates to assemble water-soluble nanocrystals into branched wire structures at the air–water interface. They designed and synthesized a chiral amphiphilic molecule, C12-(L)Cys-(L)Cys-C18, which consists of two short cystein peptides as hydrophilic heads and two hydrophobic alkyl chains as tails (Figure 8.6a), which formed chiral domains (Figure 8.6b) at the air–water interface. This lateral structure with chemically active end-groups (thiol groups) was further used for the specific binding of CdTe nanocrystals. After transferring a monolayer of C12-(L)Cys-(L)Cys-C18 with complexation of CdTe nanocrystals, they realized the CdTe nanowires with 10–15 nm in width and up to several micrometres in length, and branched in a certain way as shown in Figure 8.6c and d. Using self-patterned molecular aggregates as templates for interfacial assembly may provide a general method to organize metal or semiconductor NCs in a defined way.

Polymers may serve as templates to form NP arrays, if with the help of suitable interfacial assembly techniques there is a sufficient attraction between the ligand molecules and the polymer. Wyrwa and coworkers [57] demonstrated 1D

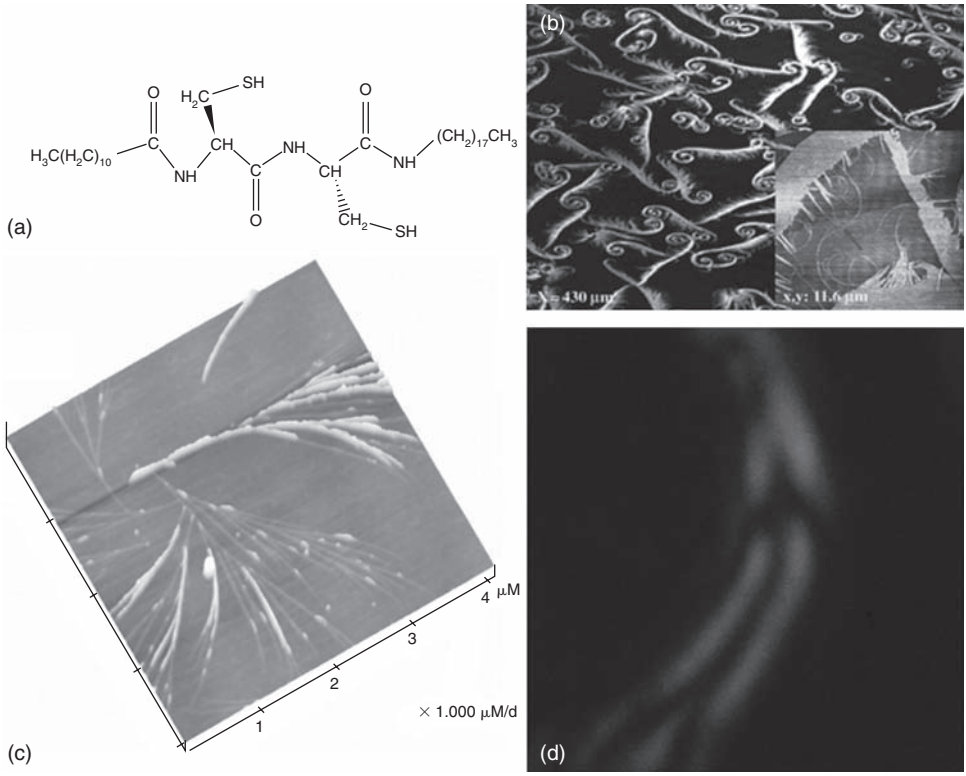

FIGURE 8.6 (a) Chemical structure of a C12-(L)Cys-(L)Cys-C18 molecule. (b) Brewster angle microscope (BAM) image of chiral domains formed by C12-(L)Cys-(L)Cys-C18 at the air–water interface (20.0 ± 0.5°C). Inset: AFM image of an LB monolayer of C12-(L)Cys-(L)Cys-C18 on mica. (c) AFM image and (d) confocal laser scanning microscopy image taken from LB monolayers of C12-(L)Cys-(L)Cys-C18 after using CdTe NCs (2×10^{-6} mM) as the subphase (transferred at a surface pressure of 20 mNm^{-1}; 20.0 ± 0.5°C). (Adapted with permission from reference [56].)

arrangements of $Au_{55}(PPh_3)_{12}C_{l6}$ NPs which are formed by self-assembly processes at the phase boundary between water and dichloromethane. On the basis of the successful generation of ordered 2D cluster architectures by self-assembly processes at the phase boundary between water and dichloromethane, the formation of single cluster rows could be initiated by dilution effects. Concentrations of 0.5 μg/l of isooctyl-substituted poly(p-phenylene ethinylenes) (PPE-i-octyl) in CH_2Cl_2 lead to thin bundles of the polymer molecules that are partially decorated with a few rows, but sometimes also with a single row of the Au_{55} quantum dots and that can be collected from the water surface after evaporation of the dichloromethane. Poly(vinyl-pyrrolidone) (PVP) is another polymer that can adsorb $Au_{55}(PPh_3)_{12}C_{l6}$ clusters via the phenyl groups in an impressive way: 2D networks consisting of $Au_{55}(PPh_3)_{12}C_{l6}$ and PVP were formed when the subphase was added with PVP acting as the linear template [58]. Without PVP, smaller

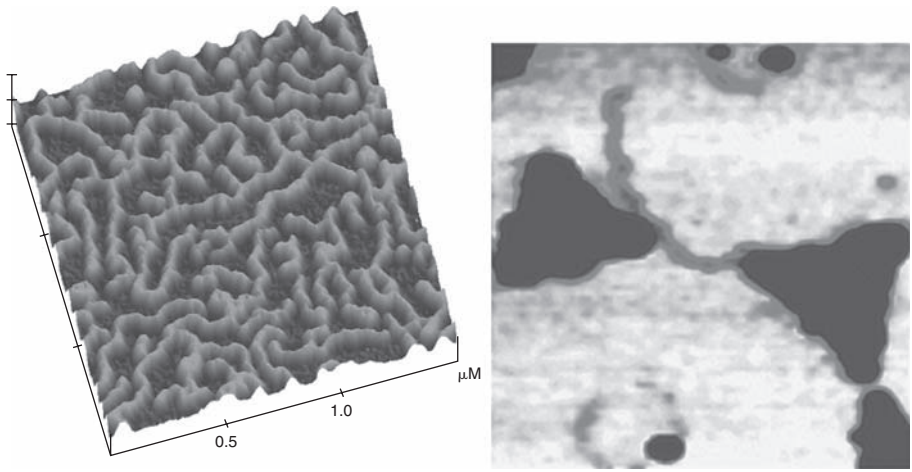

(a) (b)

FIGURE 8.7 Topographical image of network structures of Au_{55} on mica surface ($1.6 \times 1.6\,\mu m^2$) and nanowires of Au_{55} connected with model electrodes ($350 \times 350\,nm^2$). (Adapted with permission from [60].)

islands of well-ordered Au_{55} are formed instead at the air–water phase boundary [59]. The wires (30 nm in width and up to 1 μm in length) were connected by junctions of cluster islands to a complete 2D network on mica or silicon. The pattern of cluster-coated polymer molecules indicates that the NPs partially act as linking knots between polymer chains and so generate a stable network. Furthermore, Lu et al. [60] used model electrodes fabricated by nanosphere lithography [61] to connect the nanowires of Au_{55}. The model electrodes were prepared by using metal evaporation through a mask of monodispersed latex beads. At the second step, the silicon surfaces bearing such model electrodes were used as substrates for transferring nanowires consisting of Au_{55} prepared with the LB technique on a PVP subphase. By controlling the structure density on the surface, single connections (as shown in Figure 8.7) and multiconnections were obtained.

In addition to linear metal NP arrays or 2D networks, ring-like CdSe NP patterns [62] and tree-like fractal aggregates of CdS NPs in amphiphilic oligomer [63] were observed. Ring-like CdSe NP patterns with diameters ranging between 150 nm and 1200 nm are obtained by transferring a mixed monolayer of amphiphilic copolymer poly[(maleic acid hexadecylmonoamide)-co-propylene] and CdSe NPs stabilized with polystyrene-poly(4-vinylpyridine) onto solid substrates using the LB technique [62]. Due to the preferential interactions between polystyrene-functionalized NPs and the polystyrene block of an amphiphilic polystyrene-poly(ethylene oxide) block copolymer, highly stable 1D NP/polymer surface features, including branched nanowires, nanocables up to 100 μm in length were formed at the air–water interface by self-assembly [64].

3.2 Biologically Programmed Assembly

In 1996, Mirkin et al. and Alivisatos et al. [65,66] first established a process for the formation of NP aggregates using DNA as a recognition element, which opens a new way to achieve higher-order structures based on NPs [67–69]. Also, monolayer-protected NPs present a versatile scaffold for creating various bio-macromolecular receptors, because the surface properties of NPs can be engineered through introduction of different functional ligands. Currently, numerous research groups have successfully developed protocols to employ DNA, proteins and other biomolecules as molecular templates to construct higher-order structures from NPs.

The well-defined double-stranded structure of the DNA molecule provides an ideal template for the assembly of NPs into programmed structured nanomaterials. The ability to synthesize nucleic acids of pre-designed shapes and composition, and the versatile biocatalytic transformations that can be performed on DNA, for example, ligation, scission or polymerization, enable 'cut and paste' procedures to be carried out on the template DNA, thus enabling us to design and manipulate the DNA 'mould'. Furthermore, the association of metal ions to the DNA phosphate units and the intercalation of transition-metal complexes into the DNA provide a means to functionalize the DNA-template and to initiate further chemical transformations on the mould. Assembly motifs involving the sequence-specific hybridization of complementary DNA strands conjugated to NPs and the non-specific electrostatic interaction between cationic NPs and DNA have been extensively employed to produce NP chains or networks.

Alivisatos and co-workers showed for the first time that a discrete number of water-soluble Au-NP can be organized into spatially defined structures based on Watson–Crick base-pairing interactions [66]. Individual NPs attached to single-stranded DNA oligomers with defined length and sequence were assembled into dimers and trimers with addition of a complementary single-stranded DNA template. Furthermore, they realized heterodimers and heterotrimers of Au-NPs in which Watson–Crick base-pairing interactions are used to control the relative spatial arrangement of Au-NPs that are 5 and 10 nm in diameter [70], as shown in Figure 8.8. They used a well-established strategy in medicine, in which cis-$[Pt(NH_3)_2Cl_2]$ (cis-Pt) has a high affinity to nitrogen donor sites in nucleotides and therefore binds with high selectivity in neighbouring guanine–guanine nucleobases. After cis-Pt is intercalated into DNA double strands, the coupling of the NPs stabilized by cysteamine can selectively bind to Pt^{2+} by exchange of the NH_3 ligands for the NH_2-termini of the ligand shell resulting in the organization of NPs. Another example for the hetero-aggregates is CdSe/ZnS core/shell quantum dots (QDs) surrounded by a discrete number of Au-NPs which were generated via DNA hybridization and purified by gel electrophoresis [71]. The distance between Au particles and QDs, the number of Au around the central QD and the size of the Au particles and the QDs can be adjusted. The concept of self-assembled dendrimers is explored for the creation of discrete Au-NP groupings using branched DNA scaffolds [72]. Hybridization of branched DNA trimers and NP-DNA conjugates results in the synthesis of NP trimer and tetramer complexes. Asymmetric structures are also produced in which both 5 and 10 nm Au-NPs are assembled

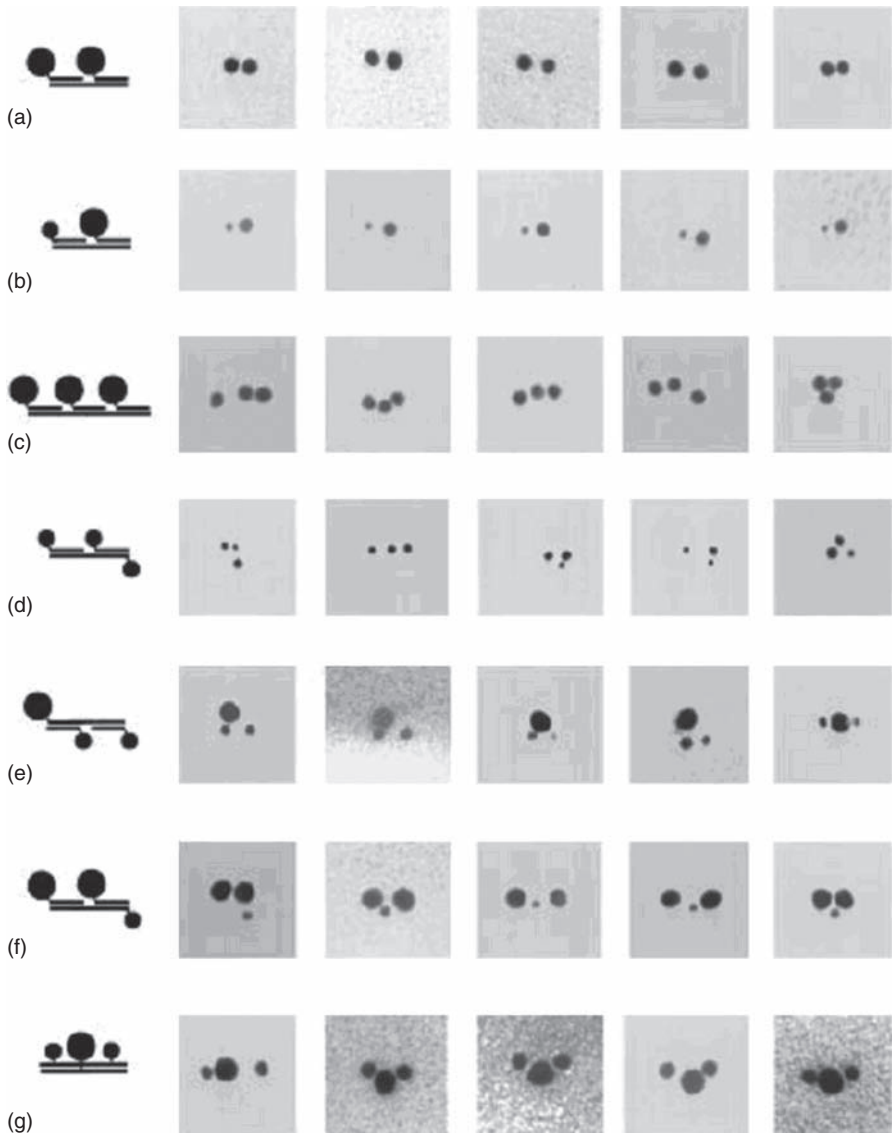

FIGURE 8.8 Schematic illustrations and representative TEM images for specific nanocrystal aggregates. (a) 10 nm homodimer; (b) 10-/5 nm heterodimer; (c) 10 nm homotrimer; (d) 5 nm homotrimer; (e) 10-/5-/5 nm heterotrimer; (f) 5-/10-/10 nm heterotrimer; (g) 5-/10-/5 nm heterotrimer. (Adapted with permission from [70].)

on branched scaffolds. Alivisatos and co-workers demonstrated that the plasmon coupling between single pairs of gold and silver NPs depends on the distances, which is studied by the directed assembly of gold and silver NP dimers in real time [73].

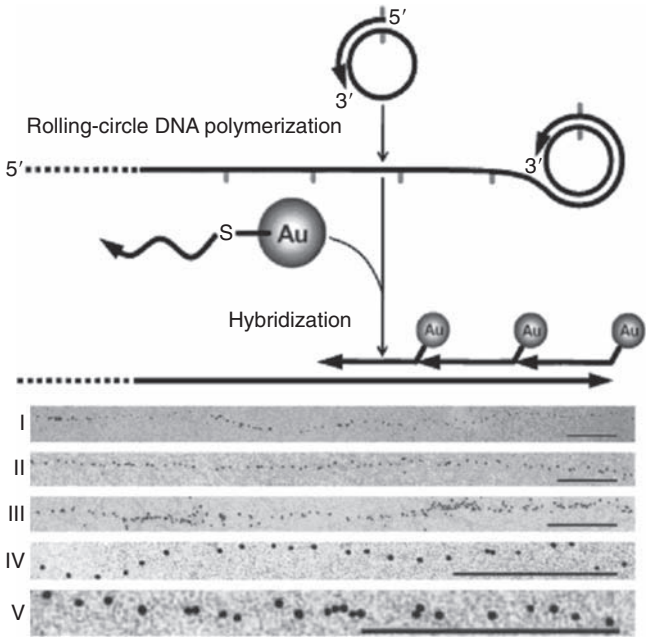

FIGURE 8.9 (Top) Synthesis of an extended gold NP array by combining DNA-encoded self-assembly and rolling-circle polymerization of DNA. (Bottom) TEM images of the extended 1D structures; (IV) and (V) are close-up views of part of the wires in (I) and (II); all scale bars are equivalent to 200 nm. (Adapted with permission from [74].)

The scheme for the assembly of NP oligomers based on hybridization of mono-DNA-functionalized Au-NPs with template-DNA strands could be used to fabricate more elongated NP aggregates due to the existence of extended and complicated DNA nanostructures. For instance, Deng et al. used this idea to get well-extended Au-NPs 1D arrays [74]. Figure 8.9 illustrates the strategy to assemble micrometres-long Au-NP arrays:

1. functionalization of 5 nm Au nanoparticles with DNA 1 (with a 5′ thiol group) to form a 1:1 Au-NP/DNA 1 conjugate (Au-DNA 1);
2. rolling-circle polymerization to synthesize DNA template with a large number of repeats complementary to DNA 1; and
3. hybridization of Au-DNA 1 with DNA template to form micrometres-long Au-NP arrays, as shown in Figure 8.9.

The resulting linear structures could potentially link the nanometric properties of materials with the convenience of micrometric manoeuvrability.

Based on the strong electrostatic interaction between cationic NPs and DNA, assemblies of monolayer-protected NPs aligned along the DNA scaffold to form 1D NP arrays can be generated. For instance, Torimoto et al. [75] fabricated CdS NP chains along DNA double strands by using the electrostatic interaction between positively charged CdS NPs and the phosphate groups of DNA molecules.

The observation with transmission electron microscopy (TEM) revealed that the CdS NPs were arranged in a quasi-1D fashion with dense packing and the line width of an NP array was equal to the diameter of CdS NPs. Diverse cationic NPs have been subjected to the assembly with DNA on solid surfaces, affording NP wires and threads [76–87]. In these systems, the scale of the individual assembly depends on the length of the DNA templates allowing variation of assembly lengths from several nanometres to a few micrometres and the interparticle spacing between NPs is determined by the monolayer thickness as well as by the ligand shell electrostatics [79,85–87]. Upon combining electrostatic deposition on DNA molecules with DNA-stretching technology, highly ordered linear assemblies of NPs along DNA molecules on substrates can be generated [80,82,88].

In a strategy of supramolecular interaction, Patolsky et al. generated Au-NP wires by intercalation of psoralen-functionalized Au-NPs (psoralen is a chemical compound) into a double-stranded DNA, followed by the photochemical covalent attachment of the intercalator with the DNA template [89]. First, amino psoralen was covalently linked to 1.4 nm Au-NPs functionalized with a single N-hydroxysuccinimide group. After that, the psoralen moiety intercalated with a double-stranded poly A/poly T duplex of ca. 900 nm to achieve a wire-like assembly, as shown in Figure 8.10. Under UV irradiation, psoralen participated in a photoinduced $2\pi + 2\pi$ cycloaddition with the thymine residues, leading to a dense covalent attachment of the NPs to the DNA. The covalent conjugates of single-stranded DNA oligomers and the streptavidin (STV) protein is another supramolecular way to organize NPs because of the biospecificity of STV's four native biotin-binding sites and the hybridization of specific oligonucleotides. Niemeyer et al. used the DNA–STV conjugates to organize Au-NPs [90]. First of all, 1.4 nm gold particles containing a single amino substitute are derived with a biotin group and the resulting biotin moiety subsequently used to organize the NPs into a tetrahedral superstructure defined by the biotin-binding sites of the STV. Subsequently, the NP-loaded proteins self-assemble in the presence of a complementary single-stranded

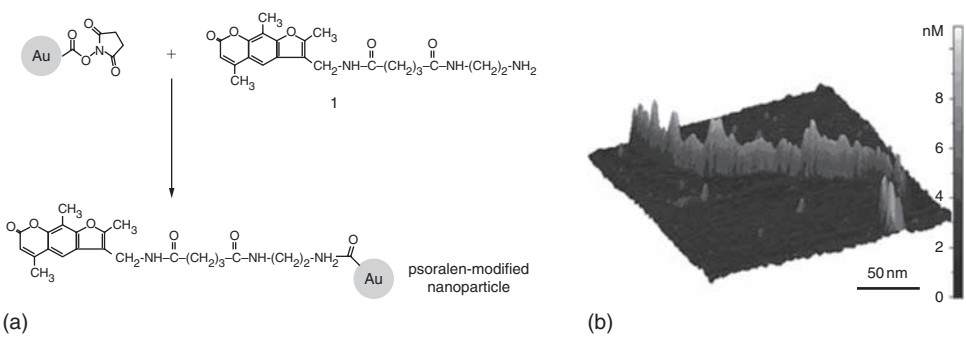

FIGURE 8.10 (a) Scheme of amino psoralen covalently linked to 1.4 nm Au NPs functionalized with a single N-hydroxysuccinimide group. (b) Atomic force microscope (AFM) image of an Au-NP wire in the poly A/poly T template. (Adapted with permission from [89].)

nucleic acid carrier molecule to form NP assemblies. The strong biotin–STV interaction together with the specific nucleic acid hybridization capabilities of DNA have recently been utilized for the controlled assembly of 5 nm Au-NPs along linear arrays of DNA triple cross-over molecules (TX) [91].

Kiehl and coworkers have used self-assembled DNA nanoarrays comprised of cross-over motifs [92] to produce regular 2D assemblies of Au-NPs [93,94]. In general, the self-assembly of Au-NP arrays was performed in three steps. First, the DNA scaffolding was grown by slowly cooling a buffered solution containing a stoichiometric mixture of the 21 strands from 90°C to room temperature to form four double-cross-over (DX) tiles (Figure 8.11a). These DX tiles further assemble by sticky-ended cohesion

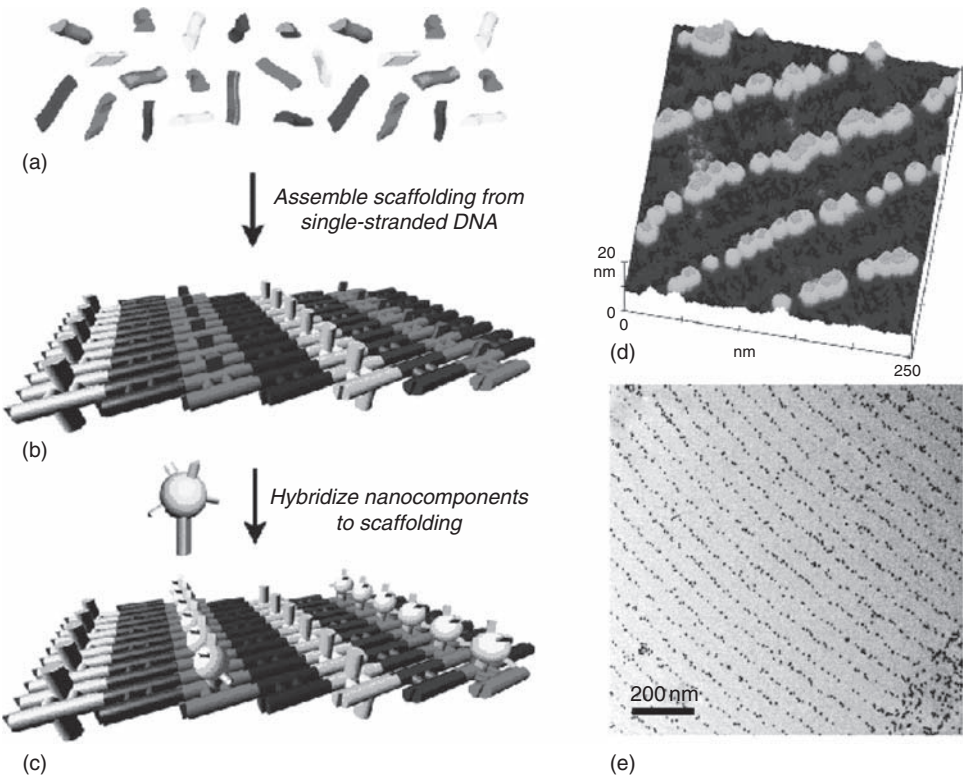

FIGURE 8.11 Assembly steps for the 2D nanocomponent arrays. (a) The DNA scaffolding is first assembled in solution from the set of 21 strands. (b) A suspension of the DNA scaffolding is deposited on mica, allowing the scaffolding to attach to the surface. The scaffolding is composed entirely of double-stranded DNA, except for the open, single-stranded hybridization sites on the B tiles. DNA hairpin topological markers extend from the D tiles. (c) The scaffolding is combined with DNA-encoded nanocomponents, which attach to the open hybridization sites. While this diagram shows one nanocomponent occupying each site, single NPs can also attach to multiple sites via hybridization of multiple, NP-bound strands. (d) Topographical AFM image of an assembled array providing a 3D visualization of the assembled DNA-Au nanocomponents, DNA marker rows and DNA scaffolding. (e) TEM image of the nanocomponent array. (Adapted with permission from [93].)

to tile the plane, thereby forming a suspension of 2D crystals. Second, a drop of the DNA scaffolding suspension was deposited on freshly cleaved mica and allowed to adsorb to the surface (Figure 8.11b). Finally, the 6 nm Au-NPs functionalized with multiple strands of 3′-thiolated $(dT)_{15}$ conjugate are deposited on the mica substrate and allowed to hybridize with DNA nanoarrays (Figure 8.11c). AFM and TEM results confirmed the formation of high density 2D NP arrays with a precisely defined inter-row spacing of ~63 nm, but the intra-row particle spacing was less well controlled, ranging from 15 to 25 nm (Figure 8.11d,e). Later, Kiehl and coworkers demonstrated that the *in-situ* Au-NP assembly strategy can be extended to organize different-sized Au-NPs each encoded with a unique DNA sequence [95]. Yan et al. [96] used a similar method to generate 5 nm Au-NP arrays of periodic square-like configurations on self-assembled DNA nanogrids. In contrast to the work reported by Kiehl and coworkers [93], the larger spacing between neighbouring tiles in the DNA lattice is used to assemble the NP arrays so that cross-hybridization between multiple sites is not possible. As a result, the centre-to-centre interparticle spacing between neighbouring particles is controlled to be ~38 nm and each particle sits on only a single DNA tile. Recently, Sharma et al. [97] used a different strategy to fabricate 2D periodical Au-NP arrays. In their strategy, 5 nm Au-NPs functionalized with a single DNA strand first participates in the formation of a single DNA-tile structure. This Au-NP-bearing DNA tile was then subsequently used to assemble with another DNA tile to form 2D NP arrays with well-defined periodical patterns and precisely controlled interparticle spacing. Zheng et al. [98] described robust three-space-spanning DNA motifs that are used to organize NPs in 2D. One strand of the motif ends in an Au-NP and only one DNA strand is attached to the particle. By using two directions of the motif to produce a two-dimensional crystalline array, one direction is free to bind Au-NPs. Identical motifs, tailed in different sticky ends, enable the two-dimensional periodic ordering of 5 and 10 nm diameter Au-NPs, as shown in Figure 8.12.

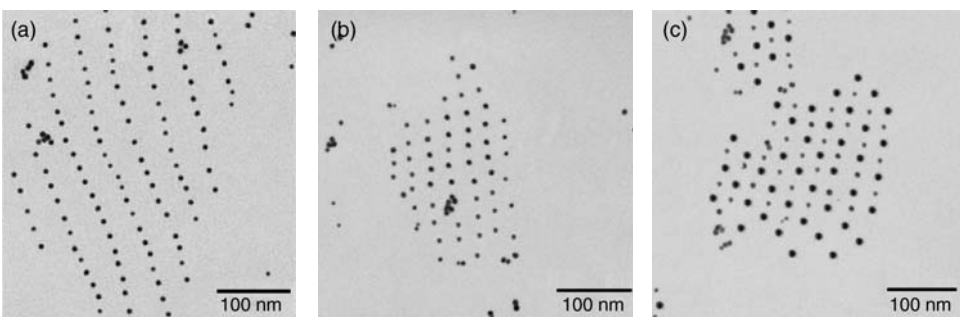

FIGURE 8.12 Transmission electron micrographs of 2D arrays of organized gold NPs. (a) An array where one tile contains 5 nm particles. It is clear that this arrangement results in one short distance and one long distance. Sometimes a particle is missing. (b) An array where both tiles contain 5 nm particles. The distances between particles are seen to be equal here. (c) An array where one tile contains a 5 nm particle and the other tile contains a 10 nm particle. The alternation of 5 nm particles and 10 nm particles is evident from this image. Note that the spacings are precise in both directions and that the pattern mimics the rhombic pattern of the tile array. (Adapted with permission from [98].)

Besides DNA, other bimolecules have also been used for the 1D or 2D assembly. Koyfman et al. [99] developed a method to organize NPs in space using a nanocrown RNA scaffold, as shown in Figure 8.13. Two small tectosquares (TS) were first generated by self-assembly of four different RNA subunits through loop–loop interactions [100], which can further self-assemble hierarchically through complementary tail–tail connectors to form ladders. The ladders possess negatively charged openings with a well-defined distribution leading to a linear arrangement of cationic NPs through encapsulation into the cavity. The NPs' spacing is dependent on the precise architecture of the RNA crown scaffolding. Because RNA can be manipulated into shapes more diverse than DNA, this study offers new opportunity in precise control over the positioning of NPs. Bae et al. [101] have demonstrated that Au-NPs can be aligned in 1D architecture by wrapping them in the helical structure of schizophyllan (SPG), a natural polysaccharide produced by the fungus *Schyzophyllum commune*.

Peptides and proteins provide useful templates and building blocks for construction of NP complex assemblies in solution or at an appropriate surface via complementary interactions. In a recent study, Li and Stupp [102] reported a strategy for the creation of 1D assemblies of lipophilic Au-NPs in non-polar solvents by using peptide-based nanofibres with surface-binding motifs. In their work, the authors co-assembled two amphiphilic tripeptide derivatives into a fibriform supramolecular structure in aprotic solvents. Upon introduction of NP, the thymine moiety provides binding sites to the diaminopyridine group present on the NP surface, leading to a large number of linear arrays of Au-NPs. In a related work,

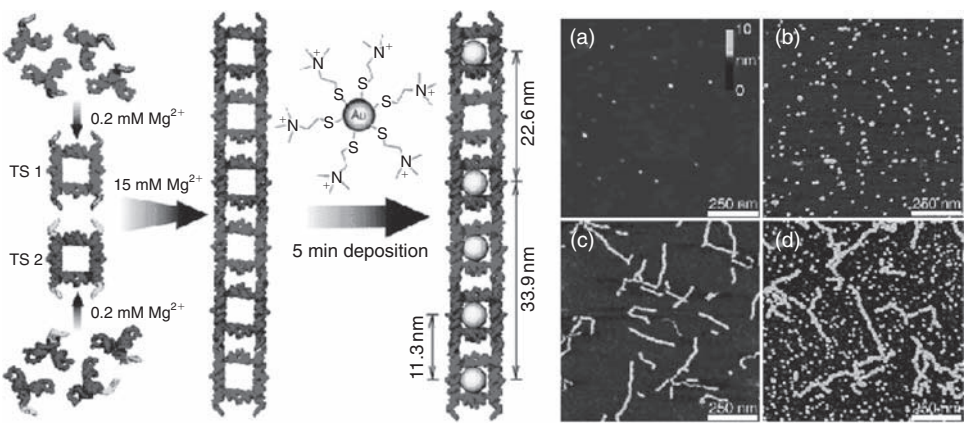

FIGURE 8.13 (Left) Hierarchical supramolecular assembly of TS ladders decorated with cationic gold NPs. TS 1 and TS 2, each made of four different RNA subunits (left), self-assemble through complementary 3' tail–tail connectors into a ladder (centre). Once the ladder is formed on the mica surface, cationic, thiocholine-modified gold NPs are electrostatically assembled in solution to the RNA (right). Thiocholines on the gold NP are not to scale. (Right) AFM images of TS RNA ladders decorated with gold NPs. (a) TS 1 alone; (b) cationic gold NPs alone; (c) TS 1–TS 2 ladder; (d) TS 1–TS 2 RNA ladder decorated with cationic gold NPs. (Adapted with permission from [99].)

Fuet et al. [103] used peptide nanofibril templates, obtained through peptide self-assembly, to prepare double-helical and single-chain arrays of NPs through complementary electrostatic binding. The structure of the resulting assemblies was further controlled by the pH of the reaction media and the size of the NPs. These studies display the use of peptide superstructures in dictating assemblies of metal NPs. A different approach to generate the Au-NP wires involves the chemical modification of polylysine with the Au-NPs functionalized with a single N-hydroxysuccinimide unit [89] or carboxylic acid group [104]. The deposition of the polylysine functionalized with the Au-NPs on mica surface yields circular NP arrays.

3.3 Chemical Pattern

Current lithography methods can either directly produce NPs in the form of arrays or predefine a surface (geometrically, chemically) to assist the assembly of NPs. In this section, we focus on the chemically patterned structures. There are several ways to prepare preformed patterned surfaces, such as optical lithography, E-beam lithography and scanning probe nanolithography. There are two approaches to chemically directed assembly: one is driven by ionic or weaker van der Waals attractions; the other is driven by covalent bonds. The former strategy has faster kinetics due to long-range electrostatic attractions and allows the assembly of ordered arrays due to the reversibility of the bonds formed. The latter has the advantage of being based on strong bonds that are more durable.

3.3.1 Self-assembled block copolymer domains

Self-assembled block copolymer systems provide an intriguing means to arrive at the nanostructured patterned surface via microphase separation, which is a well-studied phenomenon producing morphologies by phase separation that are determined by the relative lengths of the polymer blocks, ranging from spheres to lamellae, or interconnected network morphologies [105]. The size of each block of the polymer domain, from a few to several tens of nanometres, is determined by its overall chain length [106,107]. The domains of block copolymer can be used as templates to direct assembly of NPs with control over the spatial location and the particle density of NP arrays [108]. The important factor in determining the stable incorporation of the NPs within a block copolymer matrix mainly lies in the compatibility of the NPs with the block copolymer microstructures which, in turn, can be controlled considering the symmetry of both the inclusion and the block copolymer host matrix [108]. Thus, surface modification of the NPs is necessary to stabilize them against aggregation within the block copolymer matrix, which normally tends to attract the NPs by one of the blocks of a block copolymer and repel it by the other block of the copolymer. The resulting materials thus can accumulate the NPs into one microphase of a block copolymer, reflecting the pattern formed by the respective microphase.

For instance, Zehner et al. [109] have successfully decorated only the polystyrene (PS) cylindrical phase with thiol-passivated Au-NPs in microphase separated ultrathin films of PS-b-PMMA (poly(methylmethacrylate)) block copolymers, as

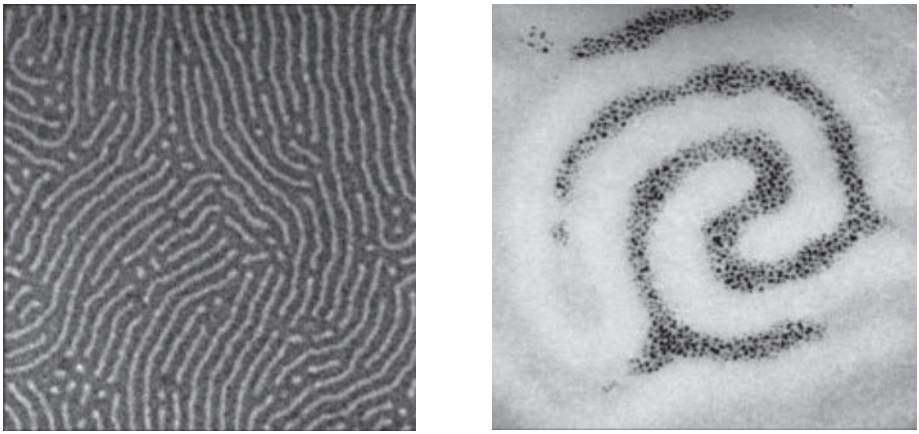

(a) (b)

FIGURE 8.14 (a) TEM micrograph of a phase-separated, 600 Å thick, PS-b-PMMA copolymer film. The light areas correspond to the PMMA phase. Image dimensions were 1.7 μm × 1.75 μm. (b) TEM micrograph of alkanethiol-coated gold nanocrystals on a microphase-separated PS-b-PMMA substrate, deposited from a dilute solution in toluene/ethanol. Image dimensions were 360 nm × 350 nm. (Adapted with permission from [109].)

shown in Figure 8.14. Figure 8.14a shows a representative area of a phase-separated polymer film before decoration. The PMMA phase appears lighter than the PS in the micrograph due to electron beam thinning of the PMMA. After addition of a dilute solution of 1–2 nm diameter alkanethiol-coated gold nanocrystals (0.1 mg/ml), portions of the PS phase are densely covered with particles (Figure 8.14b). The basis for the separation is due to the difference in interaction energies between the thiol passivants and the two polymers. There exist promising potentials for the formation of complex nanostructures with other NPs with the shape and feature size of dispersed nanophases, simply by selecting the suitable block copolymer system.

In an alternative approach, Binder et al. [110] reported the binding of Au-NPs onto microphase-separated block copolymer films deposited on surfaces by using a strong multiple hydrogen bonding interaction, as shown in Figure 8.15. Au-NPs (5 nm diameter) were coated with ligands consisting of barbituric acid moieties. Block copolymers were prepared bearing the matching receptor in one of the blocks and a fluorinated side chain in the other block in order to enhance the microphase separation. The binding of Au-NPs onto the block copolymer surface was forced by strong interactions between the barbituric acid moieties and the receptor.

Shenhar et al. [111] have created robust arrays (nanowires or nanosheets) of ordered NPs using cross-linking through coordination chemistry. They described the application of microphase-separated PS-b-PMMA diblock copolymer thin films as templates for the patterning of terpyridine-functionalized NPs [112], as shown in Figure 8.16. The Au-NPs were selectively adhered on top of a PS phase

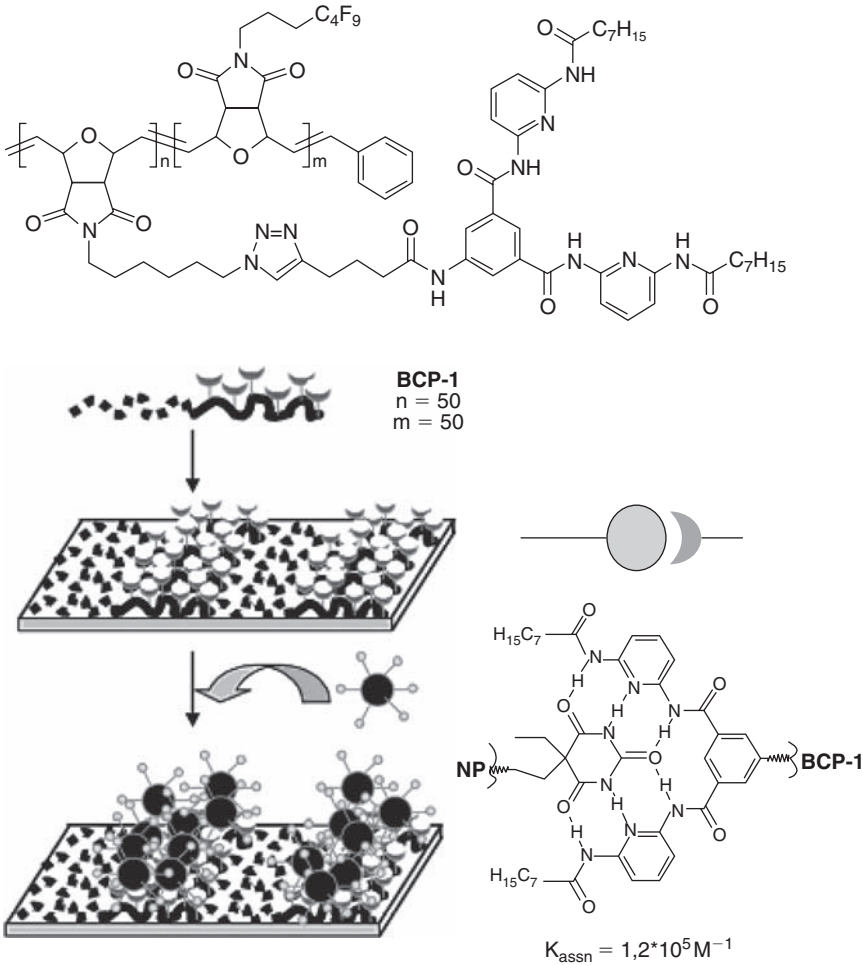

FIGURE 8.15 Strategy to bind NPs onto block copolymer surfaces via multiple hydrogen bonding interactions. Starting from block copolymer, a microphase-separated thin film is prepared, onto which NPs are bound subsequently. (Adapted with permission from [110].)

driven by differences in interaction energies between the PS and the PMMA polymer block. Cross-linking of the patterned NPs was performed by dipping the samples into a solution of $[Fe(H_2O)_6](BF_4)_2$. TEM images showed that iron–terpyridine complex formation was not affected by the patterned NP structure. NPs still retain their cross-linked nanowire structures upon swelling in chloroform vapour.

3.3.2 Langmuir–Blodgett patterning

The LB technique is an efficient way to fabricate large-area patterns with mesostructured features termed LB patterning. Chi and coworkers [113–117] have used this technique to prepare mesostructures with controlled alignment, size

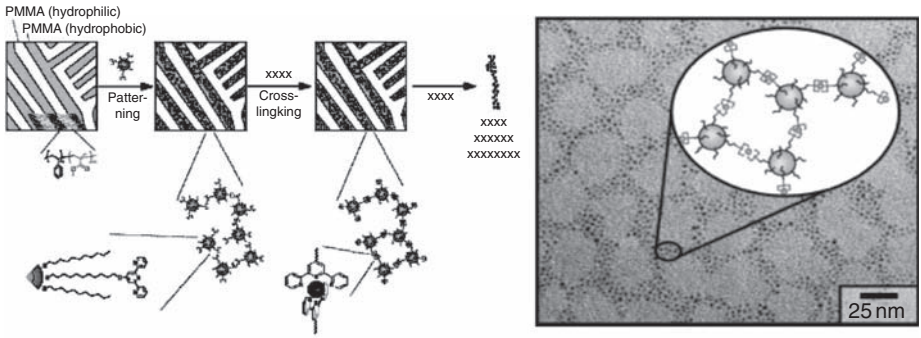

FIGURE 8.16 (Left) Formation of morphologically controlled, robust NP superstructures via orthogonal self-assembly methodologies: patterning on microphase separated diblock copolymer templates followed by cross-linking through coordination chemistry. (Right) TEM image for the gold NP arrays by selective adherence on top of a PS phase and cross-linking by coordination interaction. (Adapted with permission from [111].)

and shape, from a homogeneous DPPC Langmuir monolayer. The DPPC pattern is composed of expanded DPPC molecules in the channels and condensed DPPC molecules in the stripes and the obtained DPPC mesostructured pattern is chemical homogeneous, but topographically heterogeneous. This stripe pattern shows an anisotropic wetting property of 1-phenyloctane [118], due to the different interfacial energy for the channels ($\sim$31 mJ/m^2) and stripes ($\sim$23 mJ/m^2) [119]. As a result, this kind of mesostructured surface can be used as a template to guide the self-assembly of NPs.

The DPPC stripe pattern can serve as a template for selective deposition of NPs simply by dropping the 1-phenyloctane solutions of NPs on the DPPC chemical pattern, as shown in Figure 8.17. The work of adhesion of 1-phenyloctane on the channels is 62.0 mJ/m^2, which is larger than that of 1-phenyloctane on the stripes (53.7 mJ/m^2). As a result, the NPs accumulate in the expanded DPPC channels when the solution is removed from the sample surface after some time. The density of NP coverage is determined by the concentration of the NP solution and the duration of exposure of the patterned surface to the NP solution. As an example, quasi 1D cluster arrays (Figure 8.17b) of Au_{55} clusters stabilized by an organic ligand shell were generated [115]. Semiconductor nanocrystals have similar selective adsorption in the channels as well, which was demonstrated by topographical and near-field optical fluorescence measurements (Figure 8.17c) [120,121]. These examples show principally that NPs can be arranged one-dimensionally in a parallel manner over large areas.

Moreover, the CdSe nanocrystals are selectively deposited into green-emitting stripes [113] formed by transferring mixed monolayers of DPPC and 2-(4,4-difluoro-5-methyl-4-bora-3a,4a-diaza-s-indacene-3-dodecanoyl)-1-hexadecanoyl-sn-glycero-3-phosphocholine (BODIPY) (0.5 mol%) onto mica surfaces, for which BODIPY molecules are uniformly distributed within the expanded DPPC channels [122]. Then, a hierarchical luminescence pattern is generated, as shown in Figure 8.18, based on the photoinduced enhancement of fluorescence of CdSe

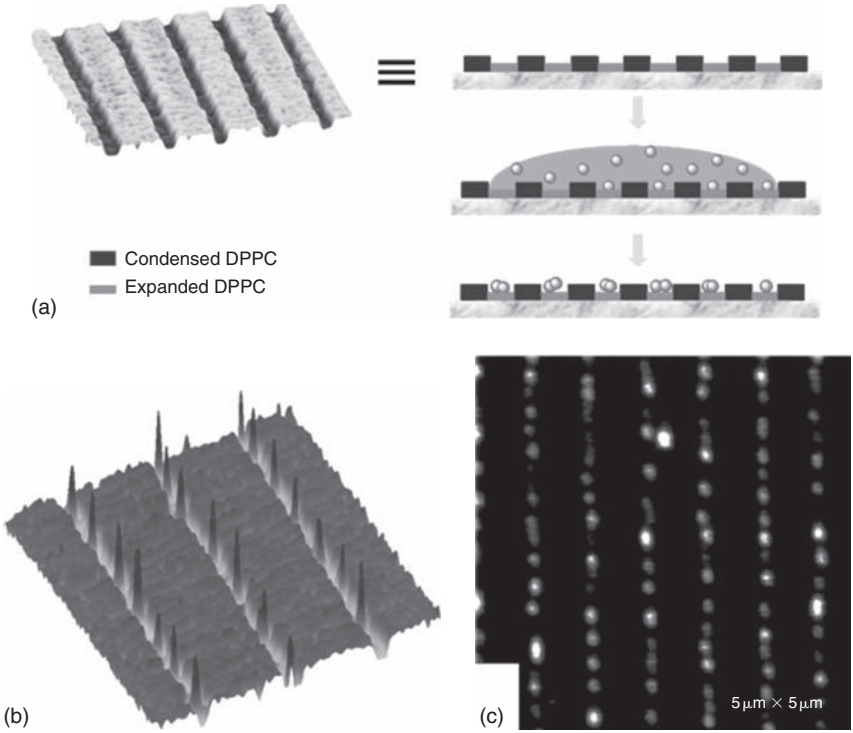

FIGURE 8.17 (a) Generalized schematic outline of the three steps used to pattern NPs on DPPC stripe pattern. Selective deposition of (b) Au_{55} clusters and (c) CdSe nanocrystals aligned along the channels on mica surface. (Adapted with permission from [120].)

nanocrystals [123] and photobleaching of dyes. Figure 8.18b shows the hierarchical luminescence pattern which was obtained by exposing the samples to light through a shadow mask (500 mesh copper grid, square holes with side 28 μm). The areas exposed to the light (the squares) appear red and the green lines correspond to the regions shielded by the mask. Furthermore, another kind of hierarchical luminescence pattern can be produced, as shown in Figure 8.18c, in which the different squares are exposed to light for different amounts of time according to the time dependence of the photobleaching of BODIPY and fluorescence enhancement of CdSe nanocrystals. The exposure time for the inside square is longer than the exposure time for the outside square, so only red dot arrays are observed in the inside square, while orange dots were obtained on the green stripes in the outside square.

3.3.3 Scanning probe based lithography

Scanning probe microscopy has proven to be an effective technique capable of identifying the structure and nature of surfaces and adsorbates on substrates down to molecular and atomic resolution. It is also an efficient technique to modify substrates, termed scanning probe based lithography (SPL), ranging from the

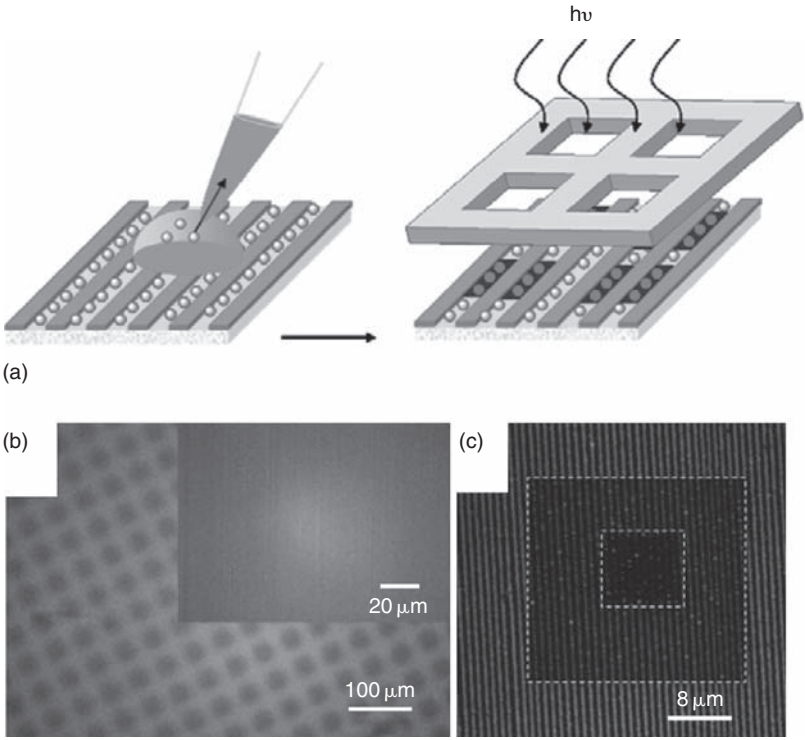

FIGURE 8.18 (a) Schematic illustration of the procedure for the formation of hierarchical luminescence patterns by exposure to light through a shadow mask. (b) Fluorescence images showing that the photoactivation of CdSe NPs and the photobleaching of BODIPY through a shadow mask reproduced the multiplexed luminescence pattern on the CdSe/BODIPY layer. (c) Confocal laser scanning microscope image of the multiplexed luminescence pattern due to different illumination time. (Adapted with permission from [122].)

subtle movement of atoms, the formation of local deformation in soft substrates using high contact force to the local application of 'inks' (dip-pen nanolithography, DPN) [124] and the local oxidation of suitable substrates (probe oxidation) [125,126]. In this section, we focus on the chemical pattern formed by SPL techniques, such as local force-induced patterning, local-probe oxidation-based techniques and DPN, to arrange the NPs into ordered arrays.

3.3.3.1 Local force-induced patterning Self-assembled layers of chemically bound NPs were mechanically patterned by Yang et al. via STM [127]. Hexanedithiolate-/decanethiolate-capped gold clusters were deposited onto gold on mica. Lithography was performed at greater than 2.55 V bias and 15.6 μm/s scan speed locally to remove the gold particles in squares corresponding to the scan dimensions. A complete removal of all particles within the pattern usually required four consecutive scans. No effect of humidity was reported, but the tunnelling current

played an important role. Tunnelling currents of 0.5 nA and a 10 mV bias removed surface bound particles.

3.3.3.2 Local-probe oxidation-based techniques Liu and co-workers chemically positioned Au-NPs on a silicon surface using a nano-oxidation technique for the preparation of quasi-1D lines [128]. The silicon substrate, modified with an octadecyltrichlorosilane (OTS) monolayer, was first subjected to a localized chemical oxidation by using conductive AFM to form silicon oxide lines. Then, the oxidized region is modified with an aminopropyltriethoxysilane (APTES) monolayer via selective chemical adsorption. Finally, 12 nm diameter Au-NPs were electrostatically bound to these amine-terminated self-assembly monolayer (SAM) regions, which is confirmed by SEM images. Using a similar methodology, Li et al. presented the fabrication of lithographic patterns that could trap single gold colloids [129].

NPs patterned on silica surfaces have also been used by Liu et al. as masks in the anodization of a silica substrate, which facilitated the fabrication of silicon nanopillars under ambient conditions [130]. Gold colloids (18 nm) were initially anchored to the surface with a mercaptopropyltriethoxysilane (MPTS) SAM. An area was scanned with an applied bias of +9 V to oxidize the silicon in this region. By comparing the height of the NPs before and after the anodization, the measured height of the NPs decreased slightly from 18 to 15 nm, which supported the assumption that the silicon around the NPs oxidized and slightly expanded. After wet etching of the sample, columns remained under the NPs. The measured diameter of these columns (in the lithographically patterned area) was 71 nm with a height (including the Au-NP) of 30 nm. The real lateral dimension of the features could be smaller due to the convolution of the tip shape and the columns.
The chemical modification of the terminal functional headgroup of the SAM can also be stimulated by electrochemical means. Sagiv and co-workers developed a different type of substitution lithography, which they termed 'constructive lithography' [131]. In this method, a conducting AFM tip was utilized selectively to induce nanoscale electrochemical oxidation to the terminal functional groups (methyl, ($—CH_3$) or vinyl, ($—CH{=}CH_2$)) of SAMs on silicon. The headgroup of a silane-based SAM is subjected to a localized redox event initiated by a conducting AFM tip. Locally modified surfaces could then be used to induce site-selective self-assembly of a number of different materials (organic, metal, semiconducting). This technique had the advantage that the surrounding non-patterned SAMs were not reactive to many *in-situ* wet chemical treatments. Constructive nanolithography was also employed to fabricate an organic bilayer terminated with top thiol functionality to immobilize selectively triphenyl phosphine ligand-stabilized Au_{55} NPs (1.4 nm core diameter) through a ligand exchange process [132]. A more complex nano-architecture based on this constructive lithography is illustrated in Figure 8.19 [133]. The tip written carboxyls are then utilized to guide, through site-selective hydrogen-bonding interactions, the self-assembly of vinyl-terminated nonadecyltrichlorosilane molecules to form a patterned bilayer architecture. These vinyl groups are then photo-reacted with formamide to create terminal amide groups in their place, which are subsequently reduced with borane-tetrahydrofuran to obtain the desired patterned terminal amine

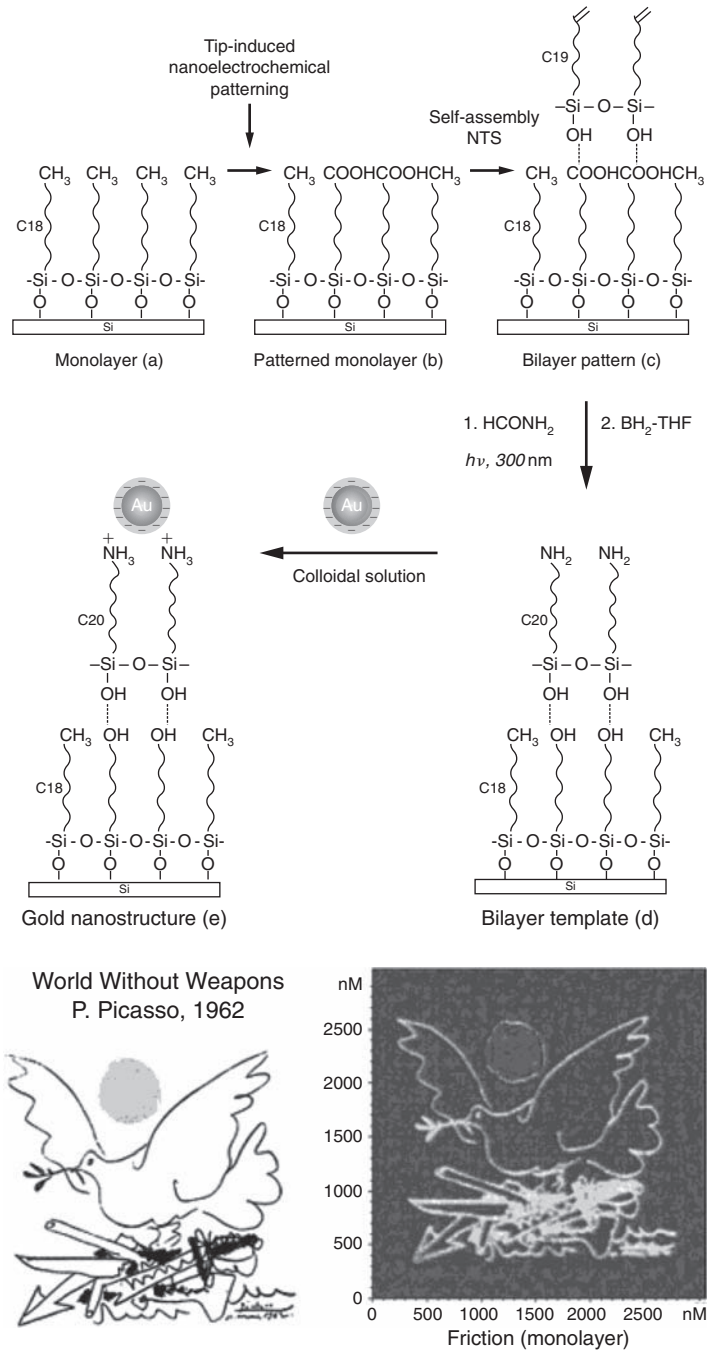

FIGURE 8.19 Scheme delineating the elctrochemical modification of a SAM and its decoration with gold NPs. Below is shown a sketch and AFM image of Pablo Picasso's World Without Weapons. (Adapted with permission from [133].)

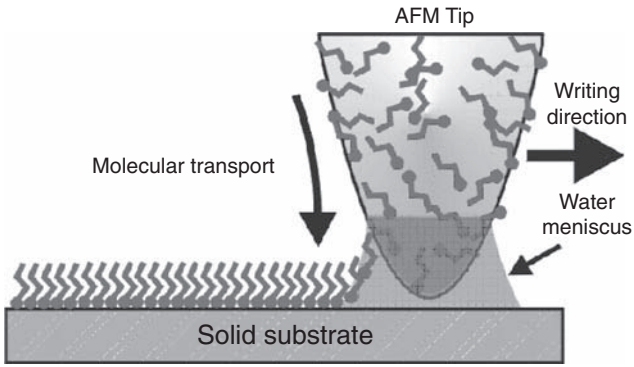

FIGURE 8.20 Scheme of dip-pen nanolithography: transport of molecules to the surface via water meniscus. (Adapted with permission from [124].)

functionality needed selectively to capture and pattern gold nanoclusters. The pattern forming the gold–amine co-assembly step is achieved in an aqueous environment through site-selective electrostatic interactions between protonated terminal amine groups and citrate capped gold nanoclusters.

Frechet et al. used the similar idea to pattern Au-NPs with nanometer resolution [134]. The pattern is defined using an AFM to apply a voltage bias between the tip and selected locations of a surface covered by a reactive monolayer containing a 3,5-dimethoxy-R,R-dimethylbenzyloxycarbonyl (DDZ)-protected thiol. During this step, thiocarbonate moieties from the bound monolayer are selectively transformed into thiols. The thiol-patterned surface is then used to direct the subsequent self-assembly of 10 nm citrate-stabilized Au-NPs. This patterning technique can be used to fabricate lines a single particle in width as well as to control the placement of individual Au-NPs.

3.3.3.3 Dip-pen nanolithography DPN, developed by Mirkin's group, is a scanning probe nanopatterning technique in which an AFM tip is used to deliver molecules to a surface via a solvent meniscus, which naturally forms in the ambient atmosphere, as shown in Figure 8.20 [124,135,136]. This direct-writing technique offers high-resolution patterning capabilities for a number of molecular and biomolecular 'inks' on a variety of substrates, such as metals, semiconductors and monolayer functionalized surfaces. DPN allows one precisely to pattern multiple patterns with near-perfect registration and is a valuable tool to make a chemical pattern with defined size and shape.

A number of DPN-based methods have been developed for controlling the immobilization of particles with diameters ranging from 5 nm to nearly 1 μm onto surfaces. Electrostatic interactions between 16-mercaptohexadecanoic acid (MHA) and amine- or amidine-coated polystyrene spheres can control the immobilization of 190 nm to 930 nm diameter particles with single-particle precision [137]. By preparing a large number of test templates on a single substrate, DPN could be used quickly to identify the optimal conditions for immobilizing single

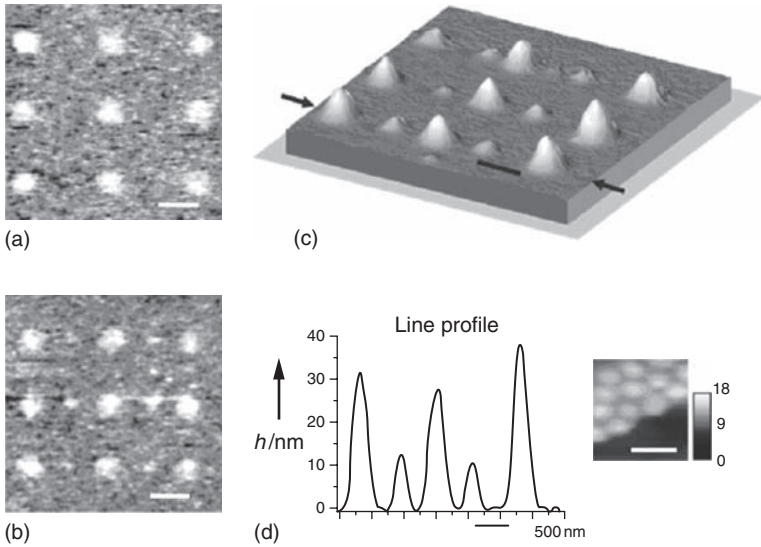

FIGURE 8.21 AFM images of patterned gold substrates. (a) Topographical image (contact mode) of the substrate after DNA has been coupled to the DPN-generated MHA pattern. (b) Topographical image of the two-component DNA pattern. (c) Non-contact AFM topography image of particles after the orthogonal assembly process. Scale bars in (a), (b) and (c) are 1 μm. (d) Line scan of the first row of particles in the image of (c). The inset shows a high resolution, tapping-mode image of one of the nanostructures comprisied of 13 nm particles (scale bar is 30 nm). Adapted with permission from [139].

particles in a single experiment [137]. Furthermore, electrostatic particle assembly can be used to form arrays of magnetic nanostructures [138]. The size of the NP dots could be controlled by changing the contact time of the modified tip with the substrate or by changing the writing speed for the creation of lines.

The potential to imprint a surface with a virtually limitless quantity of information and the possibility of doing so with the exceptional resolution of DPN has motivated the development of DPN-based DNA patterning techniques. The first approach used to control the orthogonal assembly of NPs relied on the indirect patterning of DNA: MHA was patterned using DPN and then carbodiimide chemistry was used to link amine-functionalized oligonucleotides to the surface [139]. While multiple sequences can be deposited using indirect methods, each additional sequence requires its own additional patterning and coupling steps, which can ultimately lead to cross-contamination of the patterns, which highlights the disadvantage of indirect lithographic processes. For these reasons, direct-write DPN strategies were developed for depositing DNA onto surfaces using chemically modified AFM tips and precisely controlled environmental conditions [140]. Using such a strategy, sequence-specific interactions can be used to direct the assembly of DNA-functionalized particles into a number of predefined nanopatterns.

Orthogonal approaches have also been studied in which multicomponent NP assemblies were guided to their intended positions with the help of

DPN-patterned features, as shown in Figure 8.21 [139]. The procedure began with the writing of an MHA array on a gold surface. The pattern was back-filled with 1-octadecanethiol (ODT) in order to prevent non-specific binding. The carboxylic headgroup was activated with the coupling agent 1-ethyl-3-(3-dimethylaminopropyl) carbodiimide hydrochloride (EDAC). At first, alkylamine-modified DNA was reacted with the surface ink (a). Taking advantage of the fact that ODT regions could be replaced by MHA, a second set of dots was patterned, activated and reacted with a different DNA-based ink (b). This process created two arrays comprised of two distinct oligonucleotide sequences. The surface was then incubated with a linker (a′-b′) that was partly complementary to strands a and b. The next step was to expose the surface to a solution containing two different sizes of particles (13 and 30 nm), each modified with ssDNA (a and b), structured to bind only to one of the two complementary oligonucleotide patterns. In this way, arrays of two different particles were produced, as shown in Figure 8.21. Another strategy for the orthogonal assembly of oligonucleotide-modified Au-NPs on a template surface was performed on gold substrates patterned with ω-functionalized ferrocene (Fc) tagged alkyl and acylthiol inks [141]. These electrochemically active materials had a redox potential difference of 255 mV, allowing for non-overlapping redox processes between the two molecular inks. Appropriate changes in the applied substrate potential resulted in oxidation of one or both of the patterned regions. This oxidation (to ferrocinium) made the region positively charged. Subsequent assembly of oppositely charged, polyanionic oligonucleotide coated gold colloids of two different sizes occurred in the region of interest, depending on the applied potential. Oligonucleotide-modified Au-NPs did not display non-specific binding on the neutral Fc species, suggesting they did not readily adsorb to non-ionic patterned regions.

3.3.3.4 Other lithographies Microcontact printing of SAMs represents a non-photolithographic strategy based on self-assembly and replica moulding for carrying out micro- and nanofabrication [142]. Using this technique, patterned self-assembled monolayers (SAMs) of functionalized alkanethiols can be routinely generated over large areas on metal substrates. Patterned SAMs were shown to control various area-selective processes. Based on this method, Aizenberg et al. [143] described a way to deposit polystyrene colloidal particles in a controlled way, which exploited patterned SAMs with ionic regions as templates, as shown in Figure 8.22. The direct observation of the colloidal assembly is due to a two-stage mechanism of colloidal assembly: long-range electrostatic forces between the particles and charged templated regions and lateral capillary interactions during drying, which is the driving force for the rearrangement of particles. By combining the electrostatic and capillary forces, they even realized ordered 2D patterns of single colloidal spheres. He et al. [144] patterned Au-NPs using a similar way, that is they used patterned SAMs with –NH2 terminal groups on gold substrates by a microcontact printing technique, acting as guiding templates for electrostatic adsorption. Other interactions for mediating self-assembly are hydration forces (hydrophilic and hydrophobic interactions), van der Waals forces, temperature control and capillary forces. For example, exploiting hydrophobic and/or hydrophilic interactions, Chen et al. [145] have demonstrated the ability for constructing CdSe nanocrystal

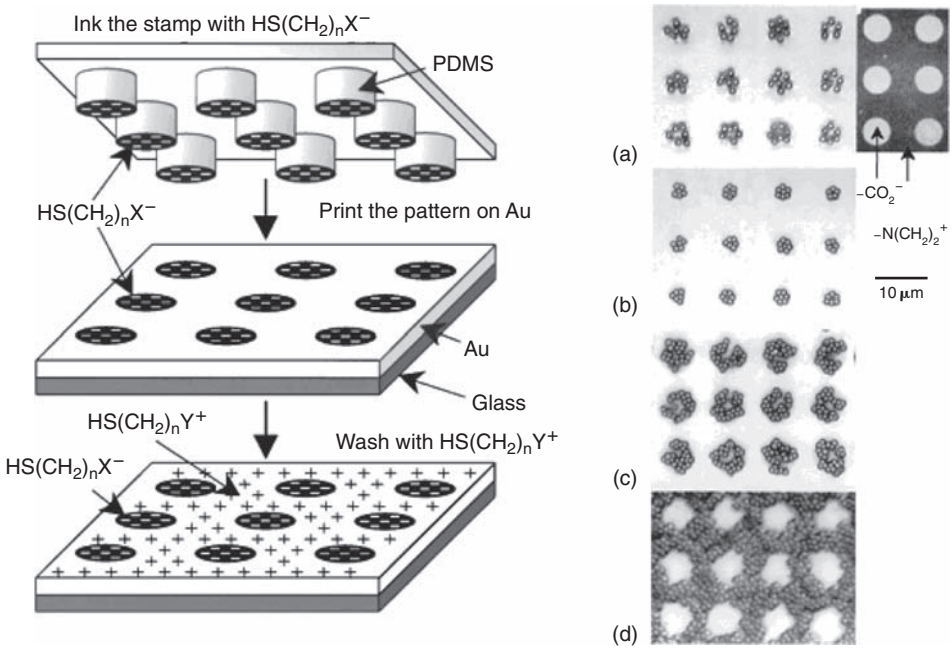

FIGURE 8.22 (Left) Schematic presentation of the fabrication procedure of a substrate chemically patterned with anionic and cationic regions using microcontact printing. (Right) Light micrographs showing localized deposition of charged colloidal particles controlled by a patterned ionic SAM. The inset presents a scanning electron micrograph of the geometry of the substrate. (a) Specific attachment of positively charged spheres to the negatively charged regions of a template (wet sample). (b) The same region as in (a) showing further focusing of the structure after drying. (c) Deposition of positively charged colloids from a 0.005 M LiCl solution. (d) Specific attachment of negatively charged spheres onto positively charged regions of the patterned surface. (Adapted with permission from [143].)

arrays on patterned SAMs on a gold substrate by microcontact printing of 1-dodecanethiol and MHA. Alternatively, covalent linkage between NPs on patterned SAMs by microcontact printing is demonstrated [146,147], which provides an efficient way for fabricating robust NP arrays on solid substrates. For instance, diamine molecules were used chemically to direct the assembly of carboxylic acid terminated monolayer-protected Au-NPs onto Au surfaces patterned with MHA by microcontact printing [147]. Song et al. [148] demonstrated that this kind of ordered 2D arrays of NPs on patterned SAMs of alkanethiolates on gold can be used as substrates for surface enhanced Raman scattering (SERS). Different SERS activities were observed on the surface of the hierarchical micro/nanostructure.

As an alternative technique, photolithography provides a way to build a chemical patterned surface, which can be used as template to direct the assembly of NPs. Xu et al. [149] reported the patterning of silicon substrates with thymine and positively charged N-methylpyridinium containing polymers using photolithography and the subsequent orthogonal modification of these surfaces

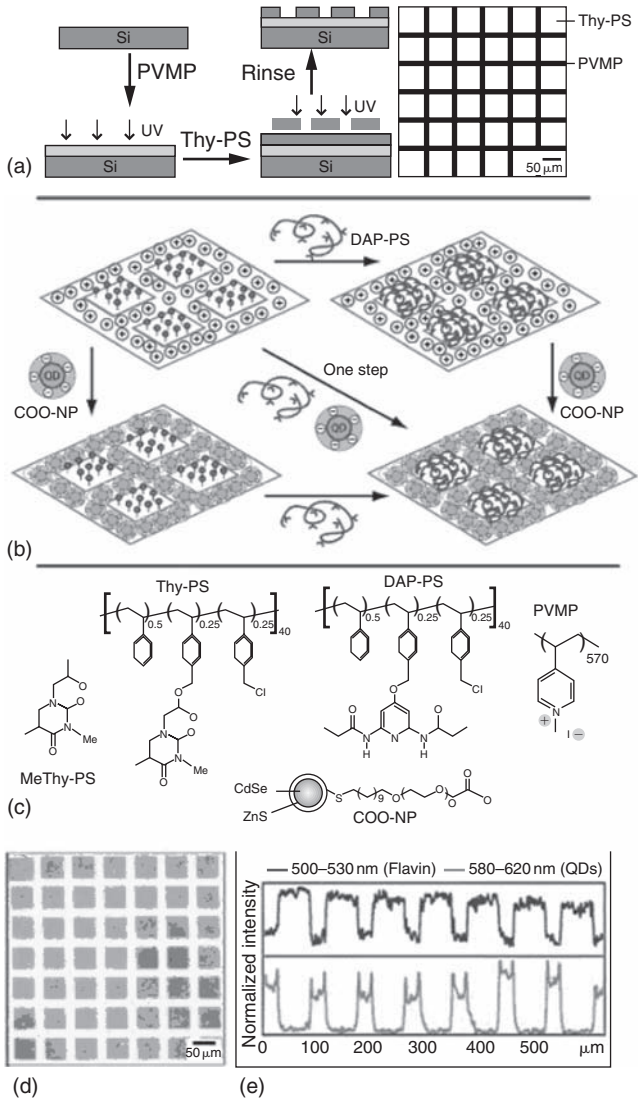

FIGURE 8.23 Schematic illustration of the fabrication process. (a) Formation of the patterned PVMP/Thy-PS surface and optical micrograph of the resulting pattern. (b) One-step and sequential orthogonal functionalization by DAP-PS and COO-NP through PS-Thy:PS-DAP recognition and PVMP: COO-NP electrostatic interactions. (c) Chemical structures of the materials, including control polymer MeThy-PS. (d) Fluorescence microscopy of modified surfaces by two components. (e) Confocal fluorescence intensity profiles of a modified surface with two different emission wavelength channels of 500–530 and 580–620 nm, respectively. (Adapted with permission from [149].)

using diaminopyridine-functionalized polystyrene and carboxylate derivatized CdSe/ZnS core-shell NPs through diamidopyridine–thymine three-point hydrogen bonding and pyridinium–carboxylate electrostatic interactions, respectively, as shown in Figure 8.23. This recognition-induced orthogonal self-assembly

provides high specificity and selectivity in both sequential and one-step functionalization of surfaces. Odom and coworkers demonstrated that templates in photoresist, generated by phase-shifting photolithography using composite poly(dimethylsiloxane) masks, can assemble CdSe/ZnS nanocrystals into any shape of 2D mesoscale structures [150]. Upon removal of the template, the CdSe/ZnS structures are found to exhibit hierarchical order over square nanometres (self-assembly of nanocrystals), square micrometres (template shape) and square centimetres (arrays of template pattern). This technique is most useful for manipulating NPs dispersed in aqueous solutions because polar and organic solvents will dissolve the resist template. In another work, a silicon wafer was modified by chemisorption of a monolayer of a cation precursor and exposed to blue light through a mask [151]. In the regions exposed to blue light, the cation precursor was converted to cations. These cations were recognized and bound selectively by NPs modified by the adsorption of crown. As a consequence, these crown-modified NPs were adsorbed at only the desired regions.

3.4 Topographically Patterned Substrates

As well as chemically patterned structures, topographically patterned structures can also be used as templates to direct the assembly of NPs into ordered arrays due to the capillary force and space confinement. A fluidic cell fabricated by sandwiching a square gasket between two glass substrates is a device to generate well-defined aggregates of spherical colloids under the physical confinement of templates [152]. The templates (e.g. a 2D array of cylindrical holes or trenches) were lithographically patterned, either on a thin film of photoresist spin-coated on the surface of the bottom substrate or on the surface of an Si(100) wafer via anisotropic wet etching. There are three major forces exerted on each colloidal particle as the liquid is dewetting across the cell: the capillary force associated with the meniscus of the liquid slug; the gravitational force due to the difference in density between the particle and the dispersion medium; and the electrostatic force caused by charges resting on surfaces of the particle and the bottom substrate. The capability and feasibility of using relief structures have been demonstrated with the organization of monodispersed spherical colloids, such as polymer latex or silica beads, into homo-aggregates, including circular rings; polygonal and polyhedral clusters; and linear, zigzag and spiral chains, as shown in Figure 8.24 [152]. It was also possible to generate hetero-aggregates in the configuration of HF and H_2O molecules that contained spherical colloids of different sizes, compositions, densities, functions or a combination of these features. These uniform, well-defined aggregates of spherical colloids can serve as a new class of building blocks to generate hierarchically self-assembled structures that are expected to exhibit interesting features valuable to areas ranging from condensed matter physics to photonics.

The packing of colloidal spheres on relief-patterned substrates depends on the deposition method as well as the commensurability between the sphere diameter and the length scale of the template. Kumacheva et al. [153] found the colloidal spheres form an ordered assembly when the template size is commensurate with the particle size and become disordered when it is incommensurate. Tanaka et al.

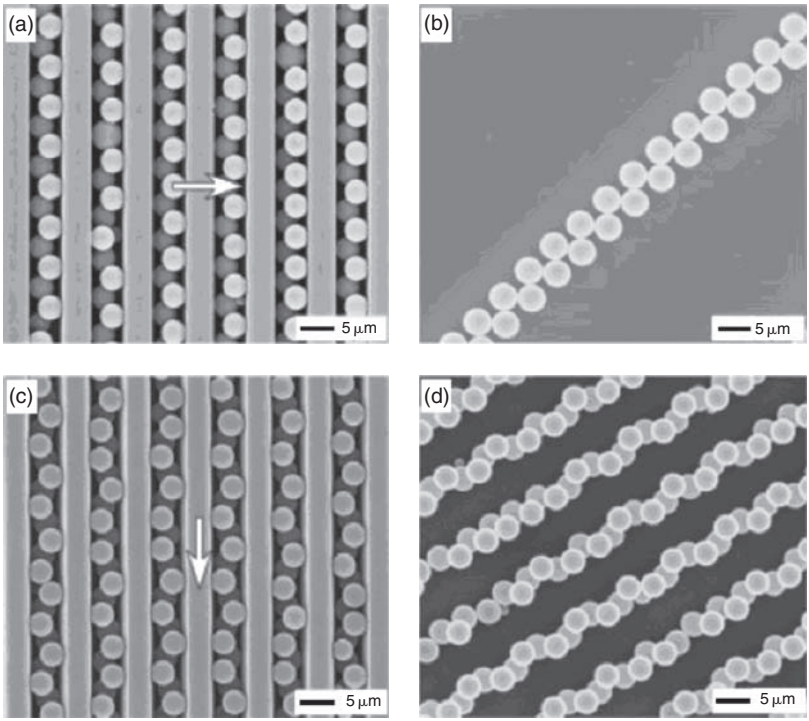

FIGURE 8.24 (a,c) SEM images of double layered zigzag chains that were fabricated by assembling PS beads in an array of channels whose cross-sections were 5.0 μm in width and 5.5 μm in height. The direction of liquid flow is indicated by an arrow. (b,d) SEM images of these aggregates after they had been annealed at a temperature slightly higher than the glass transition temperature of PS for a few minutes and then released from the templates by sonication in an ethanol bath. (Adapted with permission from [152].)

used a simple method by a dipping and pulling-up operation of a microfabricated substrate from an aqueous suspension of particles using simple handmade equipment [154,155]. This process is expected selectively to deposit polymer particles on the desired position resulting from the capillary force, i.e. the gas–liquid interfacial tension in the meniscus region. In most cases, the selectively depositing particles within the recessed patterns formed the closest packing structures. However, a special phenomenon, cubic packing structures of the particles, was observed when using square patterns with the side-length a few times larger than the particle diameter.

Although templated self-assembly of colloidal particles has been shown to produce ordered arrays of colloidal particles, there is a need to extend this technique to particles measuring much less than 50 nm in size and to develop robust fabrication techniques that would lead to defect-free, large-area arrays. Alivisatos and coworkers [156,157] used lithographically patterned structures as templates for fabricating large-scale device arrays, suitable for nanoelectronics or nanophotonics, that incorporate a controlled number of sub-50 nm diameter nanocrystals. The interfacial capillary force present during the evaporation of a nanocrystal

suspension forms the basis of the assembly mechanism. They also showed that macromolecule-sized particles down to 2 nm in diameter and complex nanostructures such as nanotetrapods can effectively be organized by the capillary interaction. A similar approach has recently been employed to template NPs using the capillary force from a moving solution front combined with topographical substrates using the dip-coating technique [158]. Although the use of capillary force to drive spherical particles into lithographically defined trench templates has been demonstrated to produce well-ordered particle structures [152,158], the quality of such structures is highly dependent upon the flow direction, speed, particle density, etc. For example, when trenches are perpendicular to the flow/dipping direction, particle chains are no longer continuous [158].

Exposure of PS-PMMA film with microdomains to UV radiation decomposes PMMA and induces cross-linking of PS, thus producing a PS film with an array of close-packed, cylindrical nanopores that span the entire thickness of the film. Such films are ideal templates wherein NPs can be sequestered with very large area densities of the particles. Misner et al. [159] demonstrated the effective use of the capillary force to drive tri-n-octylphosphine oxide (TOPO)-covered CdSe NPs into the nanopores of cylindrical diblock copolymer templates. Furthermore, they used electrophoretic deposition to drive NPs into nanopores and nanotrenches in templates prepared from PS-b-PMMA diblock copolymers [160]. The electrophoretic deposition technique has been used widely for coating ceramic surfaces with charged colloidal particles. Electrophoretic deposition involves the motion of charged particles in solution under the influence of an electric field and the subsequent deposition of the particles onto an electrode surface. The electrophoretic force is controlled by an applied voltage which, along with the deposition time and NP concentration, controls the degree of deposition.

4. NANOCONTACT PRINTING AND WRITING

4.1 Microcontact Printing

Microcontact printing, which involves transfer of a molecular ink from a patterned elastomeric stamp to the substrates, can be used directly to fabricate patterned arrays of NPs on solid surfaces. If uniform, close-packed arrays of NPs could be used to ink the stamp. One way of achieving this goal is to transfer an LB monolayer of compressed NPs on to a prepatterned stamp, which was developed by Yang and coworkers [161–163]. As shown schematically in Figure 8.25, a compressed monolayer of iron oxide NPs is transferred onto a patterned PDMS stamp; after that, the NP monolayer can be transferred onto the surface of silicon wafer by contacting the wafer with NPs-inked stamp. In this way, a patterned monolayer of NPs can be transferred on silicon and has been further elaborated to printing multilayers [164]. By putting pressure on the top of a stamp, new patterns may be obtained. This method is dubbed as overpressure contact printing and is used to print NPs arrays with different shapes, such as discs and rings of ferromagnetic Pt-Fe_2O_3 core-shell NPs [163].

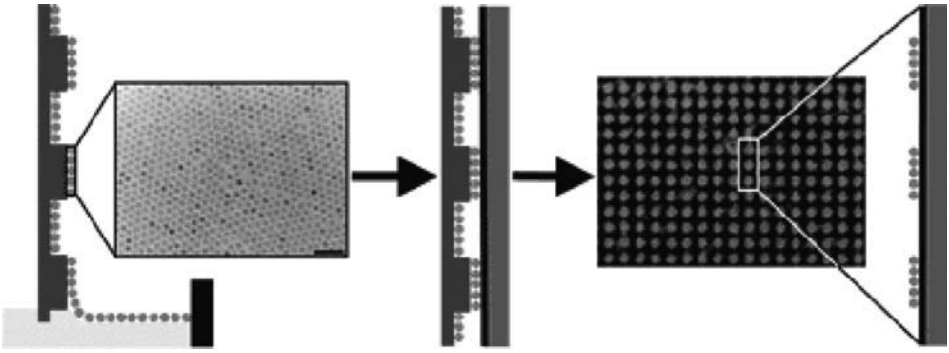

FIGURE 8.25 The processes of the formation of μ-dot arrays of γ-Fe_2O_3 NPs on a silicon wafer by microcontact printing. (Adapted with permission from [161].)

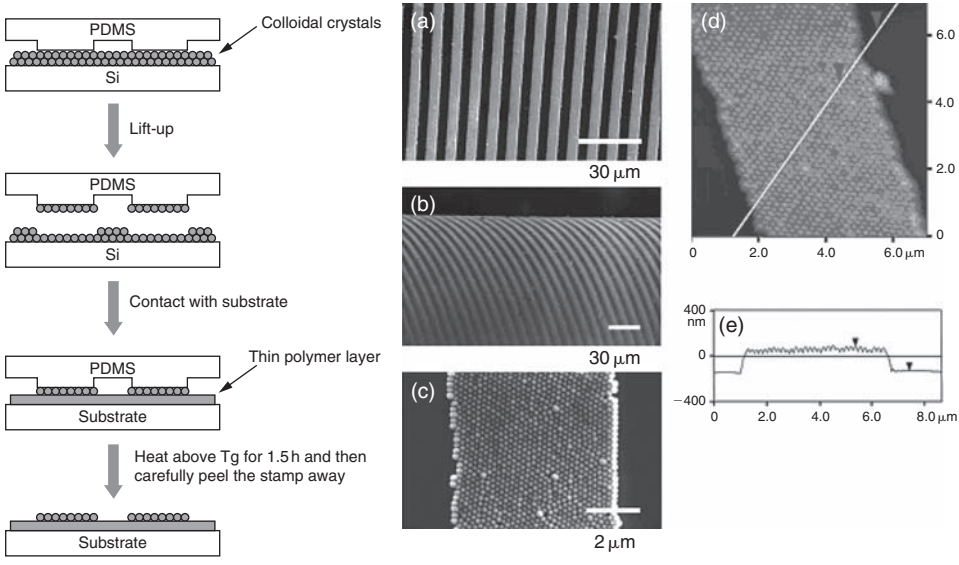

FIGURE 8.26 (Left) Illustration of the procedure for the transfer of the obtained colloidal crystals by using the modified contact printing method. (Right) Two SEM images of parallel lines of the 2D colloidal crystalline arrays made of 230 nm silica microspheres (a) on a planar substrate, (b) on the surface of a glass tube with 3.7 mm radius of curvature; (c) a highly magnified view; (d) 2D AFM image; and (e) the corresponding cross-section analysis of a line of colloidal crystal. (Adapted with permission from [165].)

Yang and coworkers [165] patterned 2D colloidal crystals by a modified microcontact printing technique that was based on the use of polymer film as 'glue' to provide an efficient interaction between the microsphere 'ink' and substrate, as shown in Figure 8.26. Before that, a lift-up soft lithography method is used for the selective transfer of a single layer of close-packed microspheres from the crystal

film to the protruding surface of a PDMS stamp [166]. The versatility of this method has been demonstrated by the patterning of a colloidal crystal on a non-planar substrate and on a heterogeneously structured colloidal crystal film. Furthermore, the same group utilized the solvent-swelling and mechanical deformation behaviours of PDMS to adjust the lattice structures of 2D arrays of spheres [167]. More importantly, the as-prepared 2D non-close-packed sphere array could be kept and transferred onto the surface of a solid substrate by using the microcontact printing technique.

Bittner and coworkers [168,169] also tried to pattern semiconductor NPs on solid substrate surfaces, but the difference from the above examples is that the semiconductor NPs are formed on the surface of the PDMS stamps. Near-spherical dendrimers are used as templates for the syntheses of semiconductor NPs. Starting from methanolic solutions of Cd^{2+}, sulphide and poly(amidoamine) dendrimers, CdS clusters precipitate at the dendrimers. The NPs have diameters above about 2 nm and show blue photoluminescence. The patterning and orientation of CdS/dendrimer clusters can be produced by microcontact printing on a hydroxyl-terminated silicon wafer surface. Depending on the ripening of the CdS/dendrimer suspension, a sub-micrometre stripe pattern develops inside the micrometre-scaled patterns and extends over the complete surface.

4.2 Dip-pen Nanolithography

Although the original idea of DPN was used to pattern alkanethiol molecules on gold surfaces, it is also possible to use DPN directly to place NPs, or generate solid nanostructures, in specific locations on surfaces. For instance, Brust, Ondarcuhu et al inked an AFM tip with a concentrated liquid solution of alkanethiol-capped gold colloids [170]. By controlling the contact force, they were then able to deposit 5 nm diameter particles in clusters of 50–200 nm in diameter depending on the contact force used [170]. Patterns of gold colloidal particles have been deposited successfully from the AFM tip onto specific regions of silicon surfaces modified by bifunctional mercaptosilane, i.e. (3-mercaptopropyl)-triethoxysilane [171]. This was used as an adhesion agent and can immobilize NPs delivered from the AFM tip onto the substrate surface. One interesting ink used in conjunction with DPN has been NPs. By scanning a predefined area, it was observed that the particles could be immobilized only in the scanned area. A high-resolution AFM image showed that the patterns were composed of loosely packed particles.

DPN has been successfully demonstrated on mica substrates employing hydrosols of polyvinylpyrrolidone-capped Pd nanocrystals as well as Au nanocrystals stabilized by tetrakishydroxymethyl phosphonium chloride [172]. Lines with widths as small as 30 nm and various aspect ratios have been successfully drawn by this method. DPN has also been employed to obtain magnetic nanopatterns of gamma-Fe_2O_3 nanocrystals on mica and silicon substrates [173].

5. SUMMARY AND OUTLOOK

A fundamental challenge in the development of nanotechnology is the assembly of nanoscale building blocks into functional nanostructured materials and/or

devices. The interfacial assembly, as one branch of self-assembly, discussed in this chapter, provides an effective and distinguished solution to fabricate highly ordered structures of NPs, such as 1D or 2D arrays. In addition to expanding the types of building blocks (nanorods, nanotubes or nanowires) that can be used in interfacial assembly of highly ordered structures, there are still some questions that remain open. The first involves orthogonal assembly of multicomponent NPs with different functions into a defined structure. The second involves the orientation control for anisotropic NPs, such as nanoprisms and tetrapods, to enhance the collective behaviours of this kind of NPs. Finally, the integration of ordered NP structures into functional device architectures also is an important issue for future application.

References

1. Murray CB, Norris DJ, Bawendi MG. J. Am. Chem. Soc. 1993; 115:8706–8715.
2. Sun SH, Murray CB. J. Appl. Phys. 1999; 85:4325–4330.
3. Schmid G, Chi LF. Adv. Mater. 1998; 10:515–526.
4. Likharev KK. Proc. Ieee 1999; 87:606–632.
5. Duncan DS, Goldhaber-Gordon D, Westervelt RM, Maranowski KD, Gossard AC. Appl. Phys. Lett. 2000; 77:2183–2185.
6. Ahmadi TS, Wang ZL, Green TC, Henglein A, El-Sayed MA. Science 1996; 272:1924–1926.
7. Peng XG, Manna L, Yang WD et al. Nature 2000; 404:59–61.
8. Burda C, Chen XB, Narayanan R, El-Sayed MA. Chem. Rev. 2005; 105:1025–1102.
9. Jin RC, Cao YW, Mirkin CA, Kelly KL, Schatz GC, Zheng JG. Science 2001; 294:1901–1903.
10. Jin RC, Cao YC, Hao EC, Metraux GS, Schatz GC, Mirkin CA. Nature 2003; 425:487–490.
11. Kim F, Connor S, Song H, Kuykendall T, Yang PD. Angew. Chem. Int. Ed. 2004; 43:3673–3677.
12. Sun YG, Xia YN. Science 2002; 298:2176–2179.
13. Collier CP, Vossmeyer T, Heath JR. Anna. Rev. Phys. Chem. 1998; 49:371–404.
14. Kim B, Tripp SL, Wei A. J. Am. Chem. Soc. 2001; 123:7955–7956.
15. Pileni MP. J. Phys. Chem. B 2001; 105:3358–3371.
16. Russier V, Petit C, Legrand J, Pileni MP. Phys. Rev. B 2000; 62:3910–3916.
17. Schmid G, Simon U. Chem. Commun. 2005:697–710.
18. Taleb A, Russier V, Courty A, Pileni MP. Phys. Rev. B 1999; 59:13350–13358.
19. Wei A, Kim B, Sadtler B, Tripp SL. ChemPhysChem 2001; 2:743–745.
20. Shipway AN, Katz E, Willner I. ChemPhysChem 2000; 1:18–52.
21. Kagan CR, Murray CB, Bawendi MG. Phys. Rev. B 1996; 54:8633–8643.
22. Kagan CR, Murray CB, Nirmal M, Bawendi MG. Phys. Rev. Lett. 1996; 76:1517–1520.
23. Kalsin AM, Fialkowski M, Paszewski M, Smoukov SK, Bishop KJM, Grzybowski BA. Science 2006; 312:420–424.
24. Shevchenko EV, Talapin DV, Kotov NA, O'Brien S, Murray CB. Nature 2006; 439:55–59.
25. Shevchenko EV, Talapin DV, Murray CB, O'Brien S. J. Am. Chem. Soc. 2006; 128:3620–3637.
26. Andres RP, Bielefeld JD, Henderson JI et al. Science 1996; 273:1690–1693.
27. Whetten RL, Khoury JT, Alvarez MM et al. Adv. Mater. 1996; 8:428.
28. Kitaev V, Ozin GA. Adv. Mater. 2003; 15:75–78.
29. Chen SW. Langmuir 2001; 17:2878–2884.
30. Huang SJ, Tsutsui G, Sakaue H, Shingubara S, Takahagi T. J. Vac. Sci. Technol. B 2001; 19:115–120.
31. Markovich G, Collier CP, Henrichs SE, Remacle F, Levine RD, Heath JR. Acc. Chem. Res. 1999; 32:415–423.
32. Maier SA, Kik PG, Atwater HA et al. Nat. Mater. 2003; 2:229–232.
33. Simon U. Adv. Mater. 1998; 10:1487–1492.
34. Arnold M, Cavalcanti-Adam EA, Glass R et al. ChemPhysChem 2004; 5:383–388.
35. Deegan RD, Bakajin O, Dupont TF, Huber G, Nagel SR, Witten TA. Nature 1997; 389:827–829.

36. Tripp SL, Pusztay SV, Ribbe AE, Wei A. J. Am. Chem. Soc. 2002; 124:7914–7915.
37. Ohara PC, Heath JR, Gelbart WM. Angew. Chem. Int. Ed. 1997; 36:1078.
38. Ohara PC, Gelbart WM. Langmuir 1998; 14:3418–3424.
39. Shafi KVPM, Felner I, Mastai Y, Gedanken A. J. Phys. Chem. B 1999; 103:3358–3360.
40. Govor LV, Bauer GH, Reiter G, Shevchenko E, Weller H, Parisi A. Langmuir 2003; 19:9573–9576.
41. Maillard M, Motte L, Ngo AT, Pileni MP. J. Phys. Chem. B 2000; 104:11871–11877.
42. Maillard M, Motte L, Pileni MP. Adv. Mater. 2001; 13:200–204.
43. Ray MA, Kim H, Jia L. Langmuir 2005; 21:4786–4789.
44. Giraldo O, Durand JP, Ramanan H et al. Angew. Chem. Int. Ed. 2003; 42:2905–2909.
45. Wang HT, Wang ZB, Huang LM, Mitra A, Yan YS. Langmuir 2001; 17:2572–2574.
46. Brust M, Stuhr-Hansen N, Norgaard K, Christensen JB, Nielsen LK, Bjornholm T. Nano Lett. 2001; 1:189–191.
47. Paul S, Pearson C, Molloy A et al. Nano Lett. 2003; 3:533–536.
48. Song H, Kim F, Connor S, Somorjai GA, Yang PD. J. Phys. Chem. B 2005; 109:188–193.
49. Tian YC, Fendler JH. Chem. Mater. 1996; 8:969–974.
50. Chung SW, Markovich G, Heath JR. J. Phys. Chem. B 1998; 102:6685–6687.
51. Sear RP, Chung SW, Markovich G, Gelbart WM, Heath JR. Phys. Rev. 1999; 59:R6255–R6258.
52. Huang JX, Kim F, Tao AR, Connor S, Yang PD. Nat. Mater. 2005; 4:896–900.
53. Huang JX, Tao AR, Connor S, He RR, Yang PD. Nano Lett. 2006; 6:524–529.
54. Vidoni O, Reuter T, Torma V, Meyer-Zaika W, Schmid G. J. Mater. Chem. 2001; 11:3188–3190.
55. Hassenkam T, Norgaard K, Iversen L, Kiely CJ, Brust M, Bjornholm T. Adv. Mater. 2002; 14:1126–1130.
56. Zhang L, Gaponik N, Muller J et al. Small 2005; 1:524–527.
57. Wyrwa D, Beyer N, Schmid G. Nano Lett. 2002; 2:419–421.
58. Reuter T, Vidoni O, Torma V et al. Nano Lett. 2002; 2:709–711.
59. Chi LF, Rakers S, Hartig M, Gleiche M, Fuchs H, Schmid G. Colloids Surfaces A Physicochem. Eng. Asp. 2000; 171:241–248.
60. Lu N, Zheng JW, Gleiche M et al. Nano Lett. 2002; 2:1097–1099.
61. Haynes CL, Van Duyne RP. J. Phys. Chem. B 2001; 105:5599–5611.
62. Fahmi AW, Oertel U, Steinert V, Froeck C, Stamm M. Macromol. Rapid Commun. 2003; 24:625–629.
63. Li LS, Jin J, Yu S, Zhao YY, Zhang CX, Li TJ. J. Phys. Chem. B 1998; 102:5648–5652.
64. Cheyne RB, Moffitt MG. Langmuir 2005; 21:10297–10300.
65. Mirkin CA, Letsinger RL, Mucic RC, Storhoff JJ. Nature 1996; 382:607–609.
66. Alivisatos AP, Johnsson KP, Peng XG et al. Nature 1996; 382:609–611.
67. Mann S, Shenton W, Li M, Connolly S, Fitzmaurice D. Adv. Mater. 2000; 12:147–150.
68. Niemeyer CM, Simon U. Eur. J. Inorganic Chem. 2005:3641–3655.
69. You CC, Verma A, Rotello VM. Soft Matter 2006; 2:190–204.
70. Loweth CJ, Caldwell WB, Peng XG, Alivisatos AP, Schultz PG. Angew. Chem. Int. Ed. 1999; 38:1808–1812.
71. Fu AH, Micheel CM, Cha J, Chang H, Yang H, Alivisatos AP. J. Am. Chem. Soc. 2004; 126:10832–10833.
72. Claridge SA, Goh SL, Frechet JMJ, Williams SC, Micheel CM, Alivisatos AP. Chem. Mater. 2005; 17:1628–1635.
73. Sonnichsen C, Reinhard BM, Liphardt J, Alivisatos AP. Nat. Biotechnol. 2005; 23:741–745.
74. Deng ZX, Tian Y, Lee SH, Ribbe AE, Mao CD. Angew. Chem. Int. Ed. 2005; 44:3582–3585.
75. Torimoto T, Yamashita M, Kuwabata S, Sakata T, Mori H, Yoneyama H. J. Phys. Chem. B 1999; 103:8799–8803.
76. Braun G, Inagaki K, Estabrook RA et al. Langmuir 2005; 21:10699–10701.
77. Ganguli M, Babu JV, Maiti S. Langmuir 2004; 20:5165–5170.
78. Gourishankar A, Shukla S, Pasricha R, Sastry M, Ganesh KN. Curr. Appl. Phys. 2005; 5:102–107.
79. Kim HJ, Roh Y, Hong B. J. Vac. Sci. Technol. A 2006; 24:1327–1331.
80. Kinsella JM, Ivanisevic A. J. Am. Chem. Soc. 2005; 127:3276–3277.
81. Kumar A, Pattarkine M, Bhadbhade M et al. Adv. Mater. 2001; 13:341–344.
82. Nakao H, Shiigi H, Yamamoto Y et al. Nano Lett. 2003; 3:1391–1394.

83. Sastry M, Kumar A, Datar S, Dharmadhikari CV, Ganesh KN. Appl. Phys. Lett. 2001; 78:2943–2945.
84. Stsiapura V, Sukhanova A, Baranov A et al. Nanotechnology 2006; 17:581–587.
85. Wang GL, Murray RW. Nano Lett. 2004; 4:95–101.
86. Warner MG, Hutchison JE. Nat. Mater. 2003; 2:272–277.
87. Woehrle GH, Warner MG, Hutchison JE. Langmuir 2004; 20:5982–5988.
88. Stsiapura V, Sukhanova A, Artemyev M et al. Opt. Spectros. 2006; 100:854–861.
89. Patolsky F, Weizmann Y, Lioubashevski O, Willner I. Angew. Chem. Int. Ed. 2002; 41:2323–2327.
90. Niemeyer CM, Burger W, Peplies J. Angew. Chem. Int. Ed. 1998; 37:2265–2268.
91. Li HY, Park SH, Reif JH, Labean TH, Yan H. J. Am. Chem. Soc. 2004; 126:418–419.
92. Winfree E, Liu FR, Wenzler LA, Seeman NC. Nature 1998; 394:539–544.
93. Le JD, Pinto Y, Seeman NC, Musier-Forsyth K, Taton TA, Kiehl RA. Nano Lett. 2004; 4:2343–2347.
94. Xiao SJ, Liu FR, Rosen AE et al. J. Nanoparticle Res. 2002; 4:313–317.
95. Pinto YY, Le JD, Seeman NC, Musier-Forsyth K, Taton TA, Kiehl RA. Nano Lett. 2005; 5:2399–2402.
96. Zhang JP, Liu Y, Ke YG, Yan H. Nano Lett. 2006; 6:248–251.
97. Sharma J, Chhabra R, Liu Y, Ke YG, Yan H. Angew. Chem. Int. Ed. 2006; 45:730–735.
98. Zheng JW, Constantinou PE, Micheel C, Alivisatos AP, Kiehl RA, Seeman NC. Nano Lett. 2006; 6:1502–1504.
99. Koyfman AY, Braun G, Magonov S, Chworos A, Reich NO, Jaeger L. J. Am. Chem. Soc. 2005; 127:11886–11887.
100. Chworos A, Severcan I, Koyfman AY et al. Science 2004; 306:2068–2072.
101. Bae AH, Numata M, Hasegawa T et al. Angew. Chem. Int. Ed. 2005; 44:2030–2033.
102. Li LS, Stupp SI. Angew. Chem. Int. Ed. 2005; 44:1833–1836.
103. Fu XY, Wang Y, Huang LX et al. Adv. Mater. 2003; 15:902–906.
104. Dai Q, Worden JG, Trullinger J, Huo Q. J. Am. Chem. Soc. 2005; 127:8008–8009.
105. Forster S, Konrad M. J. Mater. Chem. 2003; 13:2671–2688.
106. Fasolka MJ, Mayes AM. Anna. Rev. Mater. Res. 2001; 31:323–355.
107. Kickelbick G. Prog. Polym. Sci. 2003; 28:83–114.
108. Haryono A, Binder WH. Small 2006; 2:600–611.
109. Zehner RW, Lopes WA, Morkved TL, Jaeger H, Sita LR. Langmuir 1998; 14:241–244.
110. Binder WH, Kluger C, Straif CJ, Friedbacher G. Macromolecules 2005; 38:9405–9410.
111. Shenhar R, Jeoung E, Srivastava S, Norsten TB, Rotello VM. Adv. Mater. 2005; 17:2206–2210.
112. Norsten TB, Frankamp BL, Rotello VM. Nano Lett. 2002; 2:1345–1348.
113. Chen XD, Hirtz M, Fuchs H, Chi LF. Adv. Mater. 2005; 17:2881–2885.
114. Chen XD, Lu N, Zhang H et al. J. Phys. Chem. B 2006; 110:8039–8046.
115. Gleiche M, Chi LF, Fuchs H. Nature 2000; 403:173–175.
116. Lenhert S, Zhang L, Mueller J et al. Adv. Mater. 2004; 16:619–624.
117. Lenhert S, Gleiche M, Fuchs H, Chi LF. ChemPhysChem 2005; 6:2495–2498.
118. Gleiche M, Chi LF, Gedig E, Fuchs H. ChemPhysChem 2001; 2:187–191.
119. Berger CEH, Vanderwerf KO, Kooyman RPH, Degrooth BG, Greve J. Langmuir 1995; 11:4188–4192.
120. Lu N, Chen XD, Molenda D et al. Nano Lett. 2004; 4:885–888.
121. Naber A, Molenda D, Fischer UC et al. Phys. Rev. Lett. 2002; 89.
122. Chen XD, Rogach AL, Talapin DV, Fuchs H, Chi LF. J. Am. Chem. Soc. 2006; 128:9592–9593.
123. Wang Y, Tang ZY, Correa-Duarte MA et al. J. Phys. Chem. B 2004; 108:15461–15469.
124. Ginger DS, Zhang H, Mirkin CA. Angew. Chem. Int. Ed. 2004; 43:30–45.
125. Kramer S, Fuierer RR, Gorman CB. Chem. Rev. 2003; 103:4367–4418.
126. Wouters D, Schubert US. Angew. Chem. Int. Ed. 2004; 43:2480–2495.
127. Yang W, Chen M, Knoll W, Deng HL. Langmuir 2002; 18:4124–4130.
128. Zheng JW, Zhu ZH, Chen HF, Liu ZF. Langmuir 2000; 16:4409–4412.
129. Li QG, Zheng JW, Liu ZF. Langmuir 2003; 19:166–171.
130. Zheng JW, Chen ZC, Liu ZF. Langmuir 2000; 16:9673–9676.
131. Maoz R, Frydman E, Cohen SR, Sagiv J. Adv. Mater. 2000; 12:725–731.
132. Liu ST, Maoz R, Schmid G, Sagiv J. Nano Lett. 2002; 2:1055–1060.

133. Liu ST, Maoz R, Sagiv J. Nano Lett. 2004; 4:845–851.
134. Fresco ZM, Frechet JMJ. J. Am. Chem. Soc. 2005; 127:8302–8303.
135. Mirkin CA. MRS Bull. 2001; 26:535–538.
136. Mirkin CA, Hong SH, Demers L. ChemPhysChem 2001; 2:37–39.
137. Demers LM, Mirkin CA. Angew. Chem. Int. Ed. 2001; 40:3069–3071.
138. Liu XG, Fu L, Hong SH, Dravid VP, Mirkin CA. Adv. Mater. 2002; 14:231.
139. Demers LM, Park SJ, Taton TA, Li Z, Mirkin CA. Angew. Chem. Int. Ed. 2001; 40:3071–3073.
140. Demers LM, Ginger DS, Park SJ, Li Z, Chung SW, Mirkin CA. Science 2002; 296:1836–1838.
141. Ivanisevic A, Im JH, Lee KB et al. J. Am. Chem. Soc. 2001; 123:12424–12425.
142. Xia YN, Whitesides GM. Angew. Chem. Int. Ed. 1998; 37:551–575.
143. Aizenberg J, Braun PV, Wiltzius P. Phys. Rev. Lett. 2000; 84:2997–3000.
144. He HX, Zhang H, Li QG, Zhu T, Li SFY, Liu ZF. Langmuir 2000; 16:3846–3851.
145. Chen CC, Yet CP, Wang HN, Chao CY. Langmuir 1999; 15:6845–6850.
146. Bae SS, Lim DK, Park JI, Lee WR, Cheon J, Kim S. J. Phys. Chem. B 2004; 108:2575–2579.
147. Barsotti R, Stellacci F. J. Mater. Chem. 2006; 16:962–965.
148. Song W, Li W, Cheng YC et al. J. Raman Spectrosc. 2006; 37:755–761.
149. Xu H, Hong R, Lu TX, Uzun O, Rotello VM. J. Am. Chem. Soc. 2006; 128:3162–3163.
150. Babayan Y, Barton JE, Greyson EC, Odom TW. Adv. Mater. 2004; 16:1341–1345.
151. Ryan D, Nagle L, Fitzmaurice D. Nano Lett. 2004; 4:573–575.
152. Xia YN, Yin YD, Lu Y, McLellan J. Adv. Funct. Mater. 2003; 13:907–918.
153. Kumacheva E, Golding RK, Allard M, Sargent EH. Adv. Mater. 2002; 14:221–224.
154. Tanaka M, Hosaka T, Tanii T, Ohdomari I, Nishide H. Chem. Commun. 2004:978–979.
155. Tanaka M, Shimamoto N, Tanii T, Ohdomari I, Nishide H. Sci. Technol. Adv. Mater. 2006; 7:451–455.
156. Cui Y, Bjork MT, Liddle JA, Sonnichsen C, Boussert B, Alivisatos AP. Nano Lett. 2004; 4:1093–1098.
157. Liddle JA, Cui Y, Alivisatos P. J. Vac. Sci. Technol. B 2004; 22:3409–3414.
158. Juillerat F, Solak HH, Bowen P, Hofmann H. Nanotechnology 2005; 16:1311–1316.
159. Misner MJ, Skaff H, Emrick T, Russell TP. Adv. Mater. 2003; 15:221–224.
160. Zhang QL, Xu T, Butterfield D et al. Nano Lett. 2005; 5:357–361.
161. Guo QJ, Teng XW, Rahman S, Yang H. J. Am. Chem. Soc. 2003; 125:630–631.
162. Guo QJ, Teng XW, Yang H. Adv. Mater. 2004; 16:1337–1341.
163. Guo QJ, Teng XW, Yang H. Nano Lett. 2004; 4:1657–1662.
164. Santhanam V, Andres RP. Nano Lett. 2004; 4:41–44.
165. Yan X, Yao JM, Lu G, Chen X, Zhang K, Yang B. J. Am. Chem. Soc. 2004; 126:10510–10511.
166. Yao JM, Yan X, Lu G et al. Adv. Mater. 2004; 16:81–84.
167. Yan X, Yao JM, Lu G et al. J. Am. Chem. Soc. 2005; 127:7688–7689.
168. Wu XC, Bittner AM, Kern K. Adv. Mater. 2004; 16:413–417.
169. Bittner AM, Wu XC, Balci S, Knez M, Kadri A, Kern K. Eur. J. Inorg. Chem. 2005:3717–3728.
170. Ben Ali M, Ondarcuhu T, Brust M, Joachim C. Langmuir 2002; 18:872–876.
171. Liao JH, Huang L, Gu N. Chin. Phys. Lett. 2002; 19:134–136.
172. Thomas PJ, Kulkarni GU, Rao CNR. J. Mater. Chem. 2004; 14:625–628.
173. Gundiah G, John NS, Thomas PJ, Kulkarni GU, Rao CNR, Heun S. Appl. Phys. Lett. 2004; 84:5341–5343.

This page intentionally left blank

INDEX

1-dimensional (1D) NP arrays, 327, 328, 332, 334–5, 339, 343
1-octadecanethiol (ODT), 354
2-dimensional (2D) assemblies of Au-NPs, 328, 341–2
16-mercaptohexadecanoic acid (MHA), 352
Acetylene Black, 199
Activated carbon, 278, 280
Activation polarization, 177
Advanced ceramic materials, 128–9
$Al_{88}Y_7Fe_5$ *in-situ* composites, 7
Alanates, transformation mechanism of, 288
Alumina:
  electrical properties, 145–7
  thermal properties, 147–9
  thermoelectric properties, 149–50, 151
Alumina-based nanocomposites, 132–8
Aluminium hydride, 284
Amino psoralen, 340
Amphiphile, 193
Amphiphilic triblock copolymers, 216
Arrhenius law, 295
Atom transfer radical polymerization (ATRP), 305
Au_{55}, 335, 336
Au nanorods (NRs), 309, 316
Au NP loaded capsules, 310
Au-NPs, 337, 339, 340–2, 345–6
Austenitic stainless steel AISI 304, 82–3

Ball milling, 31, 53, 291
Bimodal grain size distribution, 163
Bimodal structure, 163–8
Biologically programmed assembly, 337–44
Black dye, 239
BODIPY molecules, 347, 348
Boil-off phenomenon, 273
Boundary sliding controlled flow model, 62
Bright-field (BF) image, 8
Bulk eutectic alloy, phase diagram of, 22
Bulk metallic glasses (BMGs), 94, 95
  crystallization behaviour of, 94–5
Bulk nanocrystalline alloys, interface diffusion in, 25
  experiments on diffusion along interfaces, 27–8
  hierarchic microstructures, 31–42
  production route on diffusion behaviour, effect of, 28–31
  severe plastic deformation (SPD), diffusion after, 42–7
Bulk nanocrystalline materials, 4–7
Bönnemann's route, 191

Carbide-derived carbons, 280
Carbon blacks (CBs), 199–200
Carbon nanocoils (CNCs), 206
Carbon nanotubes (CNTs), 135–8, 201, 202, 203, 206
  and nanofibres, 278–80
Carbon-supported catalysts:
  by colloidal method, 190
  for low-temperature fuel cell, 186–7
Carbon supports, 182, 198, 206, 208, 209, 224
Catalyst precursors, 185, 286
Cavitation shotless peening (CSP), 120
CdS, 249, 253, 254
CdS-coated PbS, 253
CdS/TiO_2 particle system, 244
CdS/ZnO, 254
CdSe, 249, 254
CdSe-coated ZnO, 257
CdSe nanocrystals, 347–8, 354–5
CdSe/SnO, 254
CdTe, 260, 261
CdTe NPs, 308, 309
Ceramic-based nanocomposites:
  creep resistance, 141–5
  formability, 138–41
  functional properties, 145–50
  toughening by SWCN, 131–8

Charge transfer kinetics polarization, 177
Chemical pattern:
  Langmuir–Blodgett patterning, 346–8
  scanning probe based lithography, 348–57
  self-assembled block copolymer systems, 344–6
Chemical vapour deposition (CVD) method, 53, 203, 209, 212, 220, 221
Chemisorption materials, 282
  complex hydrides, 284–9
  magnesium hydride, 284
  reaction systems, 289–90
Coatings, thermal stability of, 83
  nanocrystalline films, 85–91
  superhard coatings, 91–3
  W–Si–N films, 91
Coble creep, 62, 113
Colloid crystals (CCs), 320, 321
Colloidal method, 188–93
Complex hydrides, 284
  alanates, transformation mechanism of, 288
  state of dopant, 286–8
Constituent materials, properties of, 300
  inorganic nanoparticles:
    metal nanoparticles, 302–4
    semiconductor nanocrystals, 300–2
  polymer particles, 304–5
Constructive nanolithography, 350
Continuous stiffness measurement (CSM), 118
Conventional TEM, 8–9
Corrosive environments, stability in, 114–16
Crack deflection, 134
Creep deformation, 107
Creep resistance, of nanocomposite ceramics, 141–5
$CuInS_2$, 256–7
CuSCN, 256, 257, 259

Dark-field (DF) imaging, 8, 9
Dehydration pathway, 181
Dimethyl sulphoxide (DMSO), 321, 322
Dip-coating technique, 359
Dip-pen nanolithography (DPN), 352–4, 361
Dipalmitoylphosphatidyl-choline (DPPC), 334, 347
Direct 4-electron pathway, 181–2
Direct formic acid fuel cell (DFAFC), 174, 177, 181
Direct infiltration method, 209
Direct methanol fuel cells (DMFCs), 174, 177, 181
Disordered carbon nanofibres (DCNFs), 213–14, 215
DNA–STV conjugates, 340
Dodecyldimethyl(3-sulpho-propyl) ammonium hydroxide (SB12), 191
Double layer capacitor (DLC), *see* High-surface electrode material
Dye-sensitized solar cells (DSSCs), 232, 233
  cell operation, 234–7, 241–4
  materials, 237–41

E-TEK catalyst, 213, 214, 216, 223
EG (ethylene glycol) reduction method, 201, 202
Electrolyte-controlled band shifts, 246
Electron trapping, in semiconductors, 250
Electrophoretic deposition technique, 202, 359
Elemental nanoparticles, size-dependent melting of, 16–18
Energy storage, 270
  in supercapacitors and batteries, 271–2
Equal channel angular pressing, 4
Exciton, 301
Extended X-ray absorption fine structure (EXAFS) study, 287
Extremely thin absorber cell (ETA cells), *see* Solid state SSSCs

Fabrication process, 355, 356
Fatigue damage, 116–22
FCC structure, 320
$FeSi_2$ nanowire phases:
  structure and properties of, 79
Fibre bridging, 134
Field assisted sintering (FAS), *see* Spark plasma sintering (SPS)
'Figure of merit' (ZT), 150, 151
Fourier theory, 13–14
Fourier transform infrared spectroscopy, 179–80
Functional nanostructured materials, 1
  bulk nanocrystalline alloys, interface diffusion in, 25
    experiments on diffusion along interfaces, 27–8
    hierarchic microstructures, 31–42

production route on diffusion behaviour, effect of, 28–31
severe plastic deformation (SPD), diffusion after, 42–7
bulk nanocrystalline materials, 4–7
microstructure, of nanocrystalline materials, 8
conventional TEM, 8–9
high-resolution TEM, 9–10
nanostructured and nanocrystalline materials, 3–4
plasticity, in nanocrystalline materials, 10
geometric phase analysis, 13–15
in-situ TEM, 11–13
thermodynamic stability of, 16
elemental nanoparticles, size-dependent melting of, 16–18
multicomponent nanoparticles, thermodynamics of, 18–25

GB diffusion, 45–6
classification, 27
kinetic regimes, 32–7
GB migration on diffusion, effect of, 37–8
Geometric phase analysis (GPA), 13–15
Gibbs free energy, 20, 21, 74, 174
Glass-forming ability (GFA), 94, 99, 102
Glass transition temperature (T_{rg}), 98
Gold colloids, 350, 361
Grain boundaries (GBs), 25, 26, 56
Grain boundary sliding, 62
and high-strain-rate superplasticity, 58–9
Grain size distribution, 163–8
Graphite nanofibres (GNFs), 206, 278, 279
Graphitic carbon shell, 209

H-SSZ-13, 276–7
Hall–Petch effect, 60–2
Hard polymer microbeads, 311–12
Hard templates, 334
Hardness versus grain size, 54, 55
Harrison classification, 28
HCHO method, 201, 202
HgTe, 261
Hierarchic microstructures, interface diffusion in, 31
GB migration on diffusion, effect of, 37–8
kinetic regimes, of GB diffusion, 32–7
systematics of, 38–42
Hierarchical mesocellular mesoporous carbon (HMMC), 222
High pressure torsion straining, 4
High-resolution TEM, 9–10
High-resolution transmission electron microscopy (HRTEM), 11, 87
High-surface electrode material, 271
Hollow-cone DF imaging, 9
Hollow core and mesoporous shell (HCMS) carbon capsules, 212–13
Hot isostatic pressing (HIP), 52
Hybrid microgels, 311, 317
Hybrid-polymer microspheres, fabrication of:
in-situ synthesis, of NPs, 310–15
preformed NPs into preformed microspheres, loading of, 306
coating polymer microbeads, with NPs, 309–10
condensed polymer microspheres, loading NPs into, 307–8
microgel beads, loading NPs into, 308–9
synthesis of, 305–6
Hydride materials, activation of, 283
Hydrogen-fuelled PEMFCs, 177
Hydrogen/oxygen fuel cell, operational principle of, 175
Hydrogen storage, 272
chemisorption materials, 282
complex hydrides, 284–9
magnesium hydride, 284
reaction systems, 289–90
experimental aspects, 290
hydrogen storage materials, characterization of, 291
materials handling, 290–1
mechanical synthesis, 291
wet chemical synthesis, 291
materials development, challenges in, 274–5
in mobile applications, 272–4
physisorption materials, 275
metal–organic frameworks, 281–2
nanoporous inorganic materials, 276–8
nanoporous organic and carbon materials, 278

$In_x(OH)_yS_z$, 261
In_2S_3, 254
In_2S_3-sensitized porous In_2O_3 system, 254

Impregnation method, 183–8
In-situ Au-NP assembly strategy, 342
In-situ TEM, 11–13
Incident photon to current efficiencies (IPCE), 252
Indirect 2-electron pathway, 181, 182
Inert gas condensation (IGC) technique, 53
Inorganic nanoparticles:
  metal nanoparticles, 302–4
  semiconductor nanocrystals, 300–2
Interfacial assembly, of nanoparticles, 326
  definition, 327
  nanocontact printing and writing:
    dip-pen nanolithography, 361
    microcontact printing, 359–61
  non-templated interfacial self-assembly:
    instability during dewetting and solvent evaporation, 328–30
    Langmuir–Blodgett technique, 330–3
  template-directed self-assembly, 333
    biologically programmed assembly, 337–44
    chemical pattern, 344–57
    surfactants and polymers, 334–6
    topographically patterned substrates, 357–9
Internal-variable theory, 114
Inverse Hall–Petch effect, 62–8
Iron-based composites, 151–6

Johnson–Mehl–Avrami (JMA) equation, 295
Johnson–Mehl–Avrami–Kolmogorov (JMAK) formalism, 46

Ketjen Black, 199
Kirkendall effect, 26
Kissinger–Akahira–Sunose (KAS) method, 295
Kissinger method, 295
Langmuir–Blodgett (LB) technique, 330–3
Langmuir–Blodgett patterning, 346–8
Late transition metal (LTM), 94
Latex particles, 304, 329
Liquefied hydrogen, 273
Liquid junction SSSCs:
  absorbing semiconductor into the porous oxide, electron injection from, 247–8
  electrons from oxide to absorbing semiconductor, back transport of, 250–1
  history and general principles, 244–7
  multilayer semiconductors, 253–4
  oxide/substrate into the electrolyte, electron injection from, 251–2
  porous oxides, 254–6
  semiconductor 'aggregates' on oxides, losses in, 252–3
  semiconductors, recombination rates in, 249–50

Liquid nitrogen, 53
Lithium-ion batteries, 271–2
Living radical polymerization polycondensation, 305
Local force-induced patterning, 349–50
Local-probe oxidation-based techniques, 350–2
Low-temperature creep, 110–14
Low-temperature fuel cells, nanostructured supported catalysts for, 173, 182
  catalyst preparation, 183
    colloidal method, 188–93
    impregnation method, 183–8
    microemulsion method, 193–8
  catalyst supports, 198
    carbon blacks (CBs), 199–200
    nanoporous carbon, 207–24
    nanostructured carbon, 201–7
  electrode reactions, 177
    formic acid oxidation, 180–1
    hydrogen oxidation, 178–80
    methanol oxidation, 180
    oxgen reduction, 181–2
  working principle, of fuel cell, 174–7
Lower critical solution temperature (LCST), 309, 315

Magnesium hydride, 284
Mass-transfer limitations, 178
Materials with, structural hierarchy and their optical applications:
  constituent materials, properties of, 300
    inorganic nanoparticles, 300–4
    polymer particles, 304–5
  hybrid-polymer microspheres, fabrication of:
    in-situ synthesis, of NPs, 310–15
    preformed NPs into preformed microspheres, loading of, 306–10
    synthesis of, 305–6

micro-, meso- and nano-particles, combining, 299–300
polymer microspheres:
gold, loaded with, 315–17
quantum dots, loaded with, 317–20
semiconductor quantum dots, loaded with, 320–2
types, 298
Mechanical alloying (MA), 53
Mesocarbon microbead (MCMB), 200
Mesoporous carbon, 210–18
'Mesoscopic glide planes', 11
Metal-based nanocomposites:
bimodal structure, 162–8
metallic glasses, crystallization of, 151–6
multilayered materials, 156–62
Metal–matrix composites (MMCs), 108
Metal nanoparticles, 302–4
Metal–organic frameworks (MOFs), 281–2
Metallic glasses
nanocomposites derived from, 151–6
stability of, 94–106
Microcontact printing technique, 354, 359–61
Microemulsion method, 193–8
Microporous carbon, 208–9
Microstructure, of nanocrystalline materials, 8
conventional TEM, 8–9
high-resolution TEM, 9–10
Microwave method, 191
Mobile applications, hydrogen storage in, 272–4
Molar Gibbs free energy, variation of, 74
Molecular dyes, 239–40
Molecular dynamic (MD) simulations, 10–11, 56–7
Multicomponent nanoparticles, thermodynamics of, 18–25
Multilayer semiconductors, 253–4
Multilayered materials, 156–62
Multiwall carbon nanotubes (MWCN), 135, 136–7
Multiwalled nanotubes (MWNTs), 201

N3 dye, 239, 240
N917 dye, 239
Nafion® ionomers, 200, 216
Nanocasting method, 207, 22
Nanocomposite materials, mechanical properties of, 127
ceramic-based nanocomposites:
creep resistance, 141–5
formability, 138–41
functional properties, 145–50
toughening by SWCN, 131–8
metal-based nanocomposites:
bimodal structure, 162–8
metallic glasses, crystallization of, 151–6
multilayered materials, 156–62
SPS as advanced sintering technique, 128–31
Nanocomposites, 108–10
Nanocontact printing and writing:
dip-pen nanolithography, 361
microcontact printing, 359–61
Nanocrystalline ceramics, 128
phase instability of, 75–9
Nanocrystalline films, 85–91
Nanocrystalline materials:
bulk materials, 4–7
deformation:
Hall–Petch effect, 60–2
inverse Hall–Petch effect, 62–8
microstructure, 8
conventional TEM, 8–9
high-resolution TEM, 9–10
and nanostructured materials, 3–4
plasticity in, 10
geometric phase analysis, 13–15
in-situ TEM, 11–13
Nanocrystalline solar cells, 232
dye-sensitized solar cells (DSSCs)
cell operation, 234–7, 241–4
materials, 237–41
semiconductor-sensitized solar cells (SSSC), 244
liquid junction SSSCs, 244–56
solid state SSSCs, 256–64
Nanometre-scale polycrystalline multilayered films, 156
Nanoparticles (NPs), interfacial assembly of, *see* Interfacial assembly, of nanoparticles
Nanoporous carbon, 207
with hierarchically pore structure, 222–4
mesoporous carbon, 210–18
microporous carbon, 208–9
synthesis of, 218–21
Nanoshells, 304

Nanostructured and nanocrystalline materials, 3–4
Nanostructured aluminium alloys, 80–2
Nanostructured carbon, 201–7
Nanostructured Cr–Ni alloys, 82
Nanostructured materials:
  thermal stability of, 79
    austenitic stainless steel AISI 304, 82–3
    nanostructured aluminium alloys, 80–2
    nanostructured Cr–Ni alloys, 82
Nanostructured metallic materials, phase instability of, 68–75
Nanostructured ZnO, 257–8
Nickel-based metal–organic frameworks, 272
Non-templated interfacial self-assembly:
  instability during dewetting and solvent evaporation, 328–30
  Langmuir–Blodgett (LB) technique, 330–3

On–Off DC pulse energizing method, 128
Ohmic polarization region, 177
Oil-in-water (o/w) microemulsions, 193
Ordered carbon nanofibre networks (OCNFs), 213–14, 215
Ordered mesoporous carbon (OMC), 208, 210, 211, 212, 213, 216, 218
Ordered mesoporous polymer (OMP), 216
Ordered mesostructured silica (OMS) materials, 210, 211, 216, 218
Ordered nanoporous carbon (ONC), 218, 219, 221
Organometallic colloid route, 189, 191
Ostwald ripening, 86
Overpotential (η), 175, 176

Patterned self-assembly monolayers, 354
PbS quantum dots, 249, 253, 254
PEDOT:PSS (poly(3,4-ethylenedioxythiophene):polystyrene sulphonic acid), 259
Periodic mesoporous organosilica (PMO), 218
Periodically ordered bimodal porous carbon (POBPC), 222–4
Phase instability:
  of nanocrystalline ceramics, 75–9
  of nanostructured metallic materials, 68–75
  thermal stability, of nanostructured materials, 79–83
Phase-shifting photolithography, 357
'Phonon bottleneck mechanism', 248
Photolithography, 355–7
Photovoltaic cell, 232
Physisorption, hydrogen storage by, 274, 275
  metal–organic frameworks, 281–2
  nanoporous inorganic materials, 276–8
    transition metal-based structures, 277–8
    zeolite structures, 276–7
  nanoporous organic and carbon materials, 278
    activated carbon, 278
    carbide-derived carbons, 280
    carbon nanotubes and nanofibres, 278–80
Pile-up model, 60, 61
Plasma assisted sintering (PAS), *see* Spark plasma sintering (SPS)
Plasma pressure consolidation (PPC), *see* Spark plasma sintering (SPS)
Plasticity in nanocrystalline materials, 10
  geometric phase analysis, 13–15
  in-situ TEM, 11–13
Poly(methyl methacrylate) (PMMA), 306, 345, 346, 359
Poly(methyl methacrylate-*co*-methacrylic acid), 312
Poly(N-isopropylacrylamide) (polyNIPAm) microgels, 309
Poly(NIPAm-AA) microgels, 316, 318
Poly(NIPAm-*co*-AA-*co*-2-hydroxyethyl acrylate) microgels, 310–11
Poly(vinyl-pyrrolidone) (PVP), 335
Poly(vinylbenzyl chloride) microspheres, 311
Polymer electrolyte membrane fuel cells (PEMFCs), 174, 177, 181, 201
Polymer microspheres:
  gold, loaded with, 315–17
  quantum dots, loaded with, 317–20
  semiconductor quantum dots, loaded with, 320–2
PolyNIPAm, 310, 313, 314
Polyvinylpyrrolidone (PVP), 191, 335
Pressurized hydrogen, storage of, 273

Production route on diffusion behaviour, effect of, 28
ball milling, 31
controlled crystallization, of amorphous precursors, 30
electrodeposition, 30–1
inert gas condensation, 28–9
sintering, 31
Prussian blue analogues, hydrogen storage properties of, 277
PS beads, 310
PS-b-PMMA, 344–5
Psoralen, 340
Pt/CMK-5 catalysts, 212
Pt/CNT catalyst, 203
Pt–Co/C catalysts, 198
Pt–Fe/C catalysts, 198
Pt_{50} Ru_{50} catalysts, 213, 214
PtRu (NR 4)/C catalyst, 189
PtRu catalyst, 178, 189, 191, 194, 200
PtRu/CNFs catalyst, 216
PtRu/HCMS catalysts, 213
PtRu/OCNFs catalyst, 216
PtRu/VC catalysts, 213
PtRuAl/C catalyst, 189, 191, 196
Pulsed electric current sintering (PECS), *see* Spark plasma sintering (SPS)

QD-loaded polystyrene (PS) latexes, 306
Quantum dots (QDs), 301, 302, 306, 308, 310, 318

Radiative recombination, 301
Reliability, of nanostructured materials, 51
corrosive environments, stability in, 114–16
during fatigue, 116–22
instability due to size effects:
behaviour at ambient and low temperatures, 52–8
deformation of nanocrystalline materials, models for, 60–8
grain boundary sliding and high-strain-rate superplasticity, 58–9
metallic glasses, stability of, 94–106
phase instabilities:
of nanocrystalline ceramics, 75–9
of nanostructured metallic materials, 68–75
thermal stability, of nanostructured materials, 79–83
thermal stability, of coatings, 83
nanocrystalline films, 85–91
superhard coatings, 91–3
W–Si–N films, 91
under creep conditions, 107
low-temperature creep, 110–14
nanocomposites, 108–10
Repeated cold-rolling, 4

Saccharin, 30
Scanning electron microscopy (SEM), 59
Scanning probe based lithography (SPL), 348, 354–7
dip-pen nanolithography, 352–4
local force-induced patterning, 349–50
local-probe oxidation-based techniques, 350–2
SCMS silica spheres, 212
Se, 256
Secondary ion mass spectroscopy (SIMS), 43
Selected area electron diffraction (SAED), 9
Self-assembled block copolymer systems, 344–6
Self-assembled DNA nanoarrays, 341
Self-assembly monolayer (SAM), 350, 351
Self-assembly process, 328
Semiconductor nanocrystals, 300–2
Semiconductor nanoparticles (NPs), 301, 309, 314
Semiconductor-sensitized solar cells (SSSC)
liquid junction SSSCs:
absorbing semiconductor into the porous oxide, electron injection from, 247–8
electrons from oxide to absorbing semiconductor, back transport of, 250–1
history and general principles, 244–7
multilayer semiconductors, 253–4
oxide/substrate into the electrolyte, electron injection from, 251–2
porous oxides, 254–6
semiconductor 'aggregates' on oxides, losses in, 252–3
semiconductors, recombination rates in, 249–50
Semiconductors, recombination rates in, 249–50

Severe plastic deformation (SPD)
diffusion after, 42–7
Sieverts' law, 294
Silicon carbide, 107
Silicon nitride, 107
Silicon nitride-based ceramics, 141–2, 143
Single-wall carbon nano-tubes (SWCN), 130, 135–8, 147
Singlewalled nanotubes (SWNTs), 201, 202
SnO_2, 255
Sodium bis-(2-ethylhexyl)-sulphosuccinate (AOT), 196
Soft templates, 334
Sol–gel method, 207
Solid state SSSCs, 256
built-in fields in, 262–4
three-component ETA cell, 256–60
two-component ETA cells, 260–2
Spark plasma sintering (SPS), 128–31
SpiroOMeTAD, 259
Steady state creep rate (SSCR), 111, 112
Streptavidin (STV) protein, 340
Structural composites, *see* Bimodal grain size distribution
Supercapacitors and batteries, energy storage in, 271–2
Supercooled liquid (SCL), 94
Supercritical fluids (SCFs) method, 203
Superhard coatings, 84, 91–3
Superplasticity, 138–9
Supersaturated solid solution (SSSS), 69
Supported catalysts, *see* Low-temperature fuel cells, nanostructured supported catalysts for
Surface Mechanical Attrition Treated (SMAT), 75
Surface plasmon, 302, 304
Surface plasmon resonance (SPR) frequency, 302–4
Surfactant molecules, 334

TEM image, 14
Template-directed self-assembly, 333
biologically programmed assembly, 337–44
chemical pattern, 344–57
surfactants and polymers, 334–6
topographically patterned substrates, 357–9
Templates, 207
Tensile deformation, 58
Thermodynamic stability, of nanostructured materials, 16
elemental nanoparticles, size-dependent melting of, 16–18
multicomponent nanoparticles, thermodynamics of, 18–25
Thin films, thermal stability of, 90
Three-component ETA cell, 256–60, 264
TiO_2, 254, 255
Titanium, 286, 288
Topographically patterned substrates, 357–9
Toughening mechanisms, 131–8
Transition metal-based structures, 277–8
Transmission electron microscopy (TEM), 8
conventional TEM, 8–9
geometric phase analysis, 13–15
high-resolution TEM, 9–10
in-situ TEM, 11–13
Triple junctions (TJs), 25
Two-component ETA cells, 260–2, 263–4
'Two-phase' models, 3

Ultrafine grained (UFG) materials, 4, 26
Ultrasonic cold forging technology (UCFT), 120
US Department of Energy (US-DoE), 274

Van der Waals equation, 293
Van't Hoff equation, 293
Vulcan XC-72, 199, 200

W–Si–N films, 91
Water-in-oil (w/o) microemulsions, 193

X-ray absorption near-edge structure (XANES) study, 287

Yttria-stabilized tetragonal zirconia (YTZP), 138, 139

Zeolite structures, 276–7
Zirconia–alumina–spinel (AZM) triphase ceramic composite, 139
ZnS, 255